ISSN 2414-6331

International Association
for Hydro-Environment Engineering and Research
Ice Research and Engineering

Proceedings of the 24th IAHR International Symposium on Ice

Vladivostok, Russia

June 4-9, 2018

Scientific electronic edition

Vladivostok
Far Eastern Federal University
2018

ISSN 2414-6331

Far Eastern Federal University

School of Engineering

Proceedings of the 24th IAHR International Symposium on Ice

Vladivostok, Russia

June 4–9, 2018

Scientific electronic edition

Vladivostok
Far Eastern Federal University
2018

ISSN 2414-6331

Дальневосточный федеральный университет
Инженерная школа

Материалы 24-го Международного ледового симпозиума МАГИ Владивосток, Россия

4–9 июня 2018

Научное электронное издание

Владивосток
Дальневосточный федеральный университет
2018

УДК 551.46(98)(063) ISSN 2414-6331
ББК 26.221(00)я431
М34

Scientific Editor Tatiana Uvarova, Doctor of Engineering Sciences, Associate Professor, Department of Hydraulic Engineering, the Theory of Buildings and Structures Offshore and Structure Mechanics Department, School of Engineering

Far Eastern Federal University

Proceedings of the 24th IAHR International Symposium on Ice. Vladivostok, Russia, June 4–9, 2018. Scientific Editor T. Uvarova; School of Engineering FEFU. [Electronic resource]. Vladivostok, Far Eastern Federal University, 2018, 556 p. 1 CD.

ISBN 978-5-7444-4240-8; ISSN 2414-6331

24th IAHR International Symposium on Ice Vladivostok, Russia, June 4–9, 2018 – symposium with a great history. It was held in countries Iceland, Finland, USA, Sweden, Canada, Germany, Japan, Norway, China, Poland, New Zealand, and Singapore. In 2018, the host of the symposium is Far Eastern Federal University, School of Engineering, Russia

The symposium focuses on the following problems.

In cold regions, the effects of ice on human activities can be either harmful or beneficial. Some of the ice are floods induced by ice jams, clogging of water intakes and trash racks by frazil ice, severe impediment to winter navigation, and damage to coastal and offshore structures by moving ice. On the positive side, stable ice covers have extensively been used for transportation, recreational activities, landing of aircraft and working platforms, and also ice is a source of clear drinking water. At times, however, mishaps during these activities have resulted in loss of life. So, a major goal of ice engineering is to protect life and property against the harmful effects of ice by understanding ice phenomena and processes.

The research should aid in the solution of ice related problems affecting strong economic and environmental interests, such as hydropower production, navigation in ice-infested waters, water transfer in cold regions, mitigation of ice-jam floods, effects of ice on hydraulic structures, and exploitation of petroleum and other natural resources in polar regions. Active co-operation exists between the research community and industry in ice hydraulic engineering. This kind of co-operation should be maintained and promoted, and the importance of basic research should be recognized.

Keywords: ice mechanics, navigation in ice, permafrost, offshore & arctic technology, arctic engineering, hydrodynamics, coastal and arctic structures, energy resources and transport.

Technical Editor G. Arbatskaia
Design T. Uvarova
Design CD G. Pisareva, A. Shmykov
Published 31.05.2018
PDF format
Volume 33 MB [64,6 printed sheets]
Copies 100

The publication is prepared by Publishing Department of the School of Engineering FEFU

Far Eastern Federal University
8 Sukhanova St., Vladivostok, Russia, 690091

Producer of CD: Far Eastern Federal University
(Printing House of the Publishing House FEFU,
10 Pushkinskaya St., Vladivostok, Russia, 690091)

ISBN 978-5-7444-4240-8

CONTENTS

In cold regions, the effects of ice on human activities can be either harmful or beneficial. Some of the problems caused by ice are floods induced by ice jams, clogging of water intakes and trash racks by frazil ice, severe impediment to winter navigation, and damage to coastal and offshore structures by moving ice. On the positive side, stable ice covers have extensively been used for transportation, recreational activities, landing of aircraft and working platforms, and also ice is a source of clear drinking water. At times, however, mishaps during these activities have resulted in loss of life. So, a major goal of ice engineering is to protect life and property against the harmful effects of ice by understanding ice phenomena and processes. Ice engineering deals with ice formation, ice movement, the thermal regimes of rivers, lakes and seas, and the development of methods to

Research and engineering efforts are mainly directed toward a better understanding of ice and how best to manage it. Research topics include:
- the formation and evolution of various types of ice;
- the movement and accumulation of ice in surface waters and around structures;
- the interaction between flow and ice cover;
- the effects of ice on the environment and ecology;
- methods of ice control and use;
- the mechanical physical properties of ice;
- mathematical and physical modelling of ice engineering problems.

The research should aid in the solution of ice related problems affecting strong economic and environmental interests, such as hydropower production, navigation in ice-infested waters, water transfer in cold regions, mitigation of ice-jam floods, effects of ice on hydraulic structures, and exploitation of petroleum and other natural resources in polar regions. Active co-operation exists between the research community and industry in ice hydraulic engineering. This kind of co-operation should be maintained and promoted, and the importance of basic research should be recognised.

Research Agenda

River, lake and reservoir ice hydraulics: Important topics to be investigated include the freeze-up process, especially the development of different types of ice runs and covers starting from frazil ice formation; the hydraulic and ecological effects of frazil and anchor ice; river ice break-up, with emphases on the dynamics of ice cover interaction with river flow and the effects of basin runoff; the dynamics of surface and undercover ice runs and jam formation; the blockage of water intakes and fish hatcheries, which impedes the continuous flow of water; the impacts of ice on sediment transport, water quality, and river and lake morphology; and methods of ice control and mitigation.

Thermal regime: The great variety of complex phenomena that depend on thermodynamic processes need to be understood, because the thermal regimes of rivers, lakes and seas control the growth of ice and its properties.

Ice forces on structures: These forces depend on the mechanical strength of ice and the processes leading to its failure. There is a need to investigate the ice failure process in bending, crushing, fracture and buckling. Non-simultaneous crushing of ice at high indentation rates is caused by a combination of ductile and brittle failure, and the understanding of this process is far from complete. Study of structure's interaction with a pressure ridge should also receive emphasis.

Ice modelling: Ice modelling is used for testing the performance of icebreakers, determining the forces on an offshore structure, studying the effectiveness of hydraulic structures, etc. Although modelling techniques have improved considerably, there are still limitations on model tests because of facility size and the requirements for model ice to have low strength and brittle properties. The modelling techniques need to be improved by comparing the results from model tests with data obtained from full-scale structures. To clarify scale effects should be a main focus.

Environmental and ecological effects of ice: Important topics to be investigated include: climate changes; the effects of global climate change need to be assessed with respect to the ice regimes of rivers, lakes and seas; diffusion and dispersion of pollutants. These differ in partly and completely ice-covered waters versus ice-free waters. Oil spills, the effects of spills in ice-infested waters also need to be understood. The effects of ice on stream ecology and the presence of an ice cover influences the level of dissolved oxygen (DO) in streams, and ice control techniques may also affect the stream habitat. These are all emerging areas of research.

Instrumentation: There is a need to develop instruments suitable for cold environments, for use in both the laboratory and the field.

Numerical modelling: Numerical modelling is an essential part of ice engineering research. With the lack of understanding of many of the complex ice phenomena, theoretical formulations are usually not available. Mathematical modelling should be used in conjunction with field observations and laboratory experiments as a tool for developing solutions to ice engineering problems with known analytical formulations. Because of the intricate flow, thermal and mechanical processes in many ice phenomena, traditional numerical methods are usually not adequate. Innovative mathematical and numerical techniques should be developed. The transfer of new models from researchers to practising engineers should be promoted and supported.

Navigation in ice covered waters: To provide safe and economical vessels is an essential goal for investigators. Exploitation of petroleum and other natural resources in polar regions requires ice navigating vessels to transport massive amounts of product. Ship operators strongly request vessels that can safely and effectively navigate in ice-covered waters. The presence of an ice cover is not only a severe impediment to winter navigation in inland waters, but also affects ships and barges passing through locks and dams. Coastal regions and harbours have to be protected from ice movements and the combined actions of ice and waves. Methods to mitigate these problems need to be investigated.

Past Events

- **23rd** IAHR International Symposium on Ice, Ann Arbor, Michigan, US. 31 May – 3 June, 2016
- **22nd** IAHR International Symposium on Ice, Singapore. August 11-14, 2014.
- **21nd** IAHR International Symposium on Ice, Dalian, China. June 11-15, 2012.
- **20th** IAHR International Symposium on Ice, Lathi, Finland. June 14-17, 2010.
- **19th** IAHR International Symposium on Ice, Vancouver, Canada, July 6-11, 2008.
- **18th** IAHR International Symposium on Ice, 28 August - 1 September, 2006, Sapporo, Japan,
- **17th** IAHR International Symposium on Ice, Saint Petersburg, Russia, June 21-25, 2004.
- **16th** IAHR International Symposium on Ice, Dunedin, New Zealand, December 2-6, 2002.
- **15th** IAHR International Symposium on Ice, Gdansk, Poland, August 28 - September 1, 2000.
- **14th** IAHR International Symposium on Ice, Potsdam, NY, USA, July 27-31, 1998.
- **13th** IAHR International Symposium on Ice, Beijing, China, August 27-31, 1996.
- **12th** IAHR International Symposium on Ice, Trondheim, Norway, August 23-26, 1994.
- **11th** IAHR International Symposium on Ice, Banff, Alberta, Canada, June 15-19, 1992.
- **10th** IAHR International Symposium on Ice, Espoo, Finland, August 20-23, 1990.
- **9th** IAHR International Symposium on Ice, Sapporo, Japan, August 23-27, 1988.
- **8th** IAHR International Symposium on Ice, Iowa, USA, 1986.
- **7th** IAHR International Symposium on Ice, Hamburg, Germany, 1984.
- **6th** IAHR International Symposium on Ice, Quebec, Canada, 1981.
- **5th** IAHR International Symposium on Ice, Lulea, Sweden, 1978.
- **4th** IAHR International Symposium on Ice
- **3rd** IAHR International Symposium on Ice, Hannover, New Hampshire, USA, 1975.
- **2nd** IAHR International Symposium on Ice, Leningrad, Finland, 1972.
- **1st** IAHR International Symposium on Ice, Reykjavic, Iceland, 1970.

LOCAL ORGANIZING COMMITTEE

Chairman:

TATIANA UVAROVA – Doctor of Engineering Science, Professor, Off-shore and Structure Mechanics Department, School of Engineering, FEFU. cell: +7(902)555- 86-53

Co-Chairs:

ALEXANDER BEKKER – Doctor of Engineering Science, Professor,
Director, School of Engineering, FEFU

EGOR POMNIKOV – Candidate of Engineering Sciences associate profes-sor, Offshore and Structure Mechanics Department, School of Engineering, FEFU. cell: +7(914)650-45-29

Secretariat:

ELENA PIPKO – Research Assistant, Offshore and Structure Mechanics Department, School of Engineering, FEFU. cell: +7(914)792-64-03

EKATERINA NEPOMILUEVA – Manager, International Scientific and Educational Center «Arctic», FEFU. cell: +7(914)739-77-27

Members:

ALEXEY SHMIKOV – Research Assistant Offshore and Structure Mechan-ics Department, School of Engineering FEFU. cell: +7(984)151-75-32

ALEXEY SKLYAROV – Research Assistant Offshore and Structure Me-chanics Department, School of Engineering FEFU

VLADIMIR ZORIN – Head of the Laboratory, Offshore and Structure Me-chanics Department, School of Engineering, FEFU

IAHR ICE RESEARCH AND ENGINEERING COMMITTEE

Chair:

Dr. Matti Leppäranta, Department of Physics, University of Helsinki, Finland

Vice Chair:

Margaret (Maggie) A. Knuth, National Science Foundation, Division of Polar Programs, USA

Past Chair:

Dr. Pat Langhorne, Department of Physics, University of Otago

Members

•Knut Alfredsen, Norwegian University of Science and Technology, Norway
•Hyun Soo Kim, Inha Technical College, Korea
•Adrian Law Wing-Keung, Nanyang Technical University, Singapore
•Greg Leonard, University of Otago, New Zealand
•Peng Lu, Dalian University of Technology, China
•Arttu Polojärvi, Aalto University, Finland
•Yuntong She, University of Alberta, Canada
•Tatiana Uvarova, Far Eastern Federal University, Russia
•Jia Wang, NOAA Great Lakes Environmental Research Lab, USA
•Yasuhiro Yoshikawa, Kitami Institute of Technology, Japan
•Gesa Ziemer, Hamburg Ship Model Basin (HSVA), Germany
•Paul Barrette,Ocean, Coastal and river engineering, National Research Council, Canada
•Tomasz Kolerski, Gdansk University of Technology, Poland

International Association for Hydro-Environment Engineering and Research
Supported by Spain Water and IWHR, China

24th IAHR International Symposium on Ice
Vladivostok, Russia, June 4 to 9, 2018

Concept of the Specific Energy of the Mechanical Destruction of Ice versus the Ice Pressure-Area Relationship: Review and Discussion

Ekaterina Kim[1] and Vladimir G. Tsuprik[2]
[1] Center for Autonomous Marine Operations and Systems,
Center for Sustainable Arctic Marine and Coastal Technology,
Norwegian University of Science and Technology, Trondheim, Norway
ekaterina.kim@ntnu.no
[2] School of Engineering Far Eastern Federal University,
Russky Island, Vladivostok 690922 Russia
tsuprik.vg@dvfu.ru

For a structure-ice interaction process, a continuous record of force versus time can be converted to an ice pressure–area curve, or it can be used to find the specific energy of the mechanical destruction of ice (crushing specific energy), that is the energy required to crush a unit volume (or mass of ice). The highly empirical concept of the ice pressure–area relationship has been incorporated into design codes and practices, but use of the crushing specific energy is limited, although a theoretical and experimental basis exists for this value. In an attempt to identify the barriers to achieving the full potential of the specific energy concept, this paper reviews the development of the pressure-area concept and the development of the specific energy concept. We also discuss whether it is more convenient to use the specific energy for the description of certain ice-structure interaction scenarios, e.g., ice impact crushing with limited energy.

1. Introduction

For several decades in the 20th century, the major focus in creating computational models of ice-induced loads was on the experimental characterization of the ultimate ice strength and other parameters of the ice-structure interaction process. Uniaxial compressive strength of ice has traditionally been (and is still occasionally) used in ice load calculations. In ice load models, this parameter denotes the transition of ice from the elastic state to the fully plastic state or the broken state.

To obtain this strength characteristic, uniaxial compression tests on small-scale ice samples are used. To account for the full-scale multiaxial stress-state in ice, the correction coefficients are included in the ice load formulations, for instance, the coefficient of structural shape and the ice crushing coefficient (see, e.g., the method for predicting the ice forces on a vertical structure in Korzhavin, 1962). By the end of the 20th century, the majority of engineers and scientists have accepted that the ice load models, which are recommended in codes and standards, do not adequately cover the variety of design conditions. Ralston (1978) notes that for ice, one cannot use formulations that were derived for plastic isotropic, pressure insensitive materials. Schapiro (1983) and Palmer et al. (1983) have questioned universality of the ice load formulation for the description of ice deformation process. Usability of the strength data from small-scale ice testing for engineering problems has been subjected to criticism by Maser (1971), Weeks and Assur (1969), Croasdale et al. (1977), Truskov et al. (2001) and other authors.

The above critique was the justification for deploying a number of national and international programs for full-scale load measurements on full-scale structures exposed to ice. In recent decades, research has developed in two directions.

One of the most common ways to describe an ice structure interaction under the conditions of limit stress/limit energy is via a relation between ice pressure and contact area, where the pressure is, by definition, the amount of force applied perpendicular to the surface of the structure per unit area. We will refer to it as the *pressure-area (PA) concept.*

In contrast to the research in the direction of PA concept, the second direction of research was aimed at studying specific energy of mechanical destruction of ice (crushing specific energy) – the energy required to crush a unit volume (or mass of ice). We will refer to it as the *specific energy (SE) concept*.

The highly empirical concept of ice pressure–area relationship has found its way to design codes and practices, but the concept of crushing specific energy is not widely used, although a theoretical and experimental basis exists for this value. The purpose of this paper is first to review the development of these two concepts and later to discuss their potential for solving engineering problems.

We start by conducting a bibliometric analysis of research publications dealing with ice pressure-area relationships and specific energy absorption capacity of ice during crushing, primarily covering the period 1900-2017. This approach allowed us to explore the publication trends over time and across nations (see Table 1). We specifically analyzed publications containing ice pressure-area and specific-energy content indexed in the Scopus database, including a specific focus on ice crushing failure mode. Next, we reviewed the research publications available in national and international standards. The following section present details of the literature review.

Table 1. Publications by country*(all research publications as retrievable from the Scopus database).

Country	PA Documents	Country	SE Documents
Canada	58	Russian Federation	8
United States	20	Canada	6
Norway	18	United States	3
China	15	Finland	2
Finland	9	Norway	2

*The numbers are indicative, as the researchers in ice engineering and ice mechanics community frequently publish in journals and formats (e.g., conference proceedings, technical reports, books or books chapters) not presently covered by the Scopus database. The Scopus database very likely does not fully cover outcomes on other languages than English.

2. Development of the PA concept and SE concept

The literature review in the following chapters originates from the research publications covered in the Scopus database plus the writers' knowledge; thus, this review is limited to the publications in English and in Russian languages. We have tried to arrange the research progress chronologically while focusing on the ice crushing against a stationary structure. Details of the pressure area relationships can be found in Timco and Sudom (2013).

2.1 Origins of the PA concept

One of the first hypothesis in determining ice-induced loads on stationary structures dates back to approximately 1900: the ice-induced loads [pressures] cannot exceed the ice strength under corresponding type of loading (via Korzhavin, 1962). In earlier engineering practices (e.g., GOST 3440-46), the force on the stationary structure was calculated as a product of the ultimate compressive strength of ice and the projected contact area (width of the structure multiplied by the ice thickness). In late 1950s, in Russian practices (SN 76-59) it was accepted that the ice resistance to penetration depends on the structure's shape, i.e., the resistance is bigger for blunt structures. It was also accepted that the ice crushing strength differs from the ultimate compressive strength.

Based on the observations of ice interaction with bridge piers, Korzhavin (1962) proposed to account for limited energy interactions, i.e., the interactions in which the kinetic energy of the ice floe limits the ice force. The results of the experimental testing in Afanasyev et al. (1971) and Hirayama et al. (1973) indicate that the contact ice pressure decreases with increasing the aspect ratio (the ratio of the width of the structure to the ice thickness). In early 1980s, Russian practice (SNiP 2.06.04-82) adopted some of the experimental findings from Korzhavin (1962) and Afanasyev et al. (1971). In particular, the ice load formulation depends on the interaction scenario (limit stress/limit energy approach). For the limit stress interactions, the load depends on the aspect ratio. The ratio between the ice crushing strength and the uniaxial compressive strength was introduced (for crushing failure mode, the ratio of 2.5 was generally considered appropriate).

Around the same time, in American practice (API Bulletin 2N, 1982) the interaction of an ice sheet with a fixed offshore structure have conceptually been treated analogously to the indentation problem in metals; see, e.g., the theoretical work by Croasdale et al. (1977) and Ralston (1978). In API Bulletin 2N, ice load is calculated as a product of the unconfined compressive strength, contact area, indentation and contact factors. Both the indentation and contact factors are considered to vary with ice interaction speed and local contact geometry.

Despite the recommendations in API Bulletin 2N (1982) for marine/offshore structures and those in SNiP 2.06.04-82 for hydrotechnical structures, in both documents, the load acting on the engineering structure can conceptually be written in the following form:

Ice_load = Interaction_factor*Unconfined_compressive_strength*Contact_area **[1]**

In Eq. 1, the contact area is calculated as the product of the structural width and the ice thickness, and the interaction factor takes into account effects of multiaxial stress state in ice in front of the structure, as well as contact conditions.

Importantly, before Schwarz et al. (1981), the agreement on standardized testing methods for ice properties did not officially exist among the nations. For example, in North America, crushing ice tests were performed on samples with lengths of approximately three times the diameter, rather than cubic samples widely used in Russia. This difference made the use of semi-empirical formulas troublesome as each empirical constant had to be modified accounting for the difference in the testing methods.

During late 1970s and 1990s, the engineering community in North America and Canada experienced trouble relating the ice strength from small-scale specimens to the ice crushing strength for fixed structures (see for example Croasdale et al., 1977). During this period, a number of researchers draw attention to the discrepancy between the conditions for the destruction of ice in the samples and ice in the field that is in front of the structure. Truskov et al. (2001), based on their full-scale research on Sakhalin Island, concluded that the full-scale measurements of ice pressure are preferred over the scaling from small scale-tests. As more experimental data became available, re-analysis and compilation of global and local pressure data becomes important. Ice loads (including ice impact loads) have been defined in terms of contact areas, pressure distributions and statistical aspects. In 1988, Sanderson presented a pressure-area plot in which he included data from multiple ice failure modes and testing methods at scales ranging from small laboratory samples to mesoscale models. Effective pressures were observed to consistently decrease with increases in the loaded area. At that time, this trend was believed to be an integral part of observations from the ice crushing failure mode, due to the non-simultaneous nature of brittle ice failures (Ashby et al., 1986). Interpretations of such area-dependent pressure decrease have been suggested using flaw statistics of the specimen (Sanderson, 1988) or using the fractal theory (Palmer and Sanderson, 1991).

As offshore structures were getting wider, local strength assessments became more important. Not only was the maximum ice load required, the designers also needed to work in terms of the average (or effective) design pressures over an area appropriate for a structural member under consideration. The relationship between the pressure and area was discussed in the context of global ice loads (e.g., loads used in stability calculations) and local ice loads (e.g., loads determining the design of steel plate thicknesses). For example, Bruen et al. (1982) defined local loading as the ice pressures that occurred over the areas of 0.1 sq. m to 46.5 sq. m and suggested that the local design pressures decrease as the load area increases in size. Bruen et al. have admitted that the experimental base is too limited for a purely empirical method. Since then, the research efforts have been directed towards quantifying complexity and randomness of ice failure over the small contact areas. In Canada, modeling the local pressure spatial and temporal variation gained momentum. For example, Jordaan and Timco (1988) and Joensuu and Riska (1989) observed zones of confined ice near the center of ice sheets.

It has been generally accepted that pressure is not uniform during brittle ice crushing and that the effective (average) pressures decrease with increasing contact areas and/or the ice thickness. This pressure-area trend was included in Canadian and North American practice (CAN/CSA-S471-89 and API RP 2N 1995), whereas the derivation has been presented by Masterson and Frederking (1993) and builds on the data from large scale-field tests and measurements on full-scale structures such as ships, production platforms, etc. The ice load in Eq. 2 is given in terms of the reference ice pressure rather than the uniaxial compressive strength.

$$\text{Ice\_load} = \text{Ice\_strength\_coefficient} * \text{Contact\_area}^{\,(1+\text{ Number})} \qquad \textbf{[2]}$$

where the Ice_strength_coefficient and Number are empirically derived coefficients.

In Russia, from the beginning of the 1990s, the revision of codes and standards has almost stopped. Since that era, despite scientific progress, there was not much development in this area; see, e.g., SP 38.13330.2012 which is a revised edition of SNiP 2.06.04–82. In this context, it is difficult (if not impossible) to trace what was accepted in Russian engineering practice at that time.

Soon after the release of API RP 2N (1995), re-analysis of the measured data from Cook Inlet, Baltic Sea, Bohai Sea and the Beaufort Sea indicated that global and local ice pressure is not only a function of contact area but shape and size of the contact area. Loading rate and ice properties are also playing an important role. Deterministic and probabilistic methods have been used to account for these effects (e.g., Masterson and Spencer, 2001; Blanchet and Defranco, 2001, Jordaan et al., 1993).

From mid-1990s to present, increasingly numerous researchers have tried to explain the empirical pressure-area trends. Some researchers sought the explanation in fracture mechanics (e.g., Bažant, 1997; Palmer et al., 2009). and from the concept of the ductile-to-brittle transition (Schulson and Duval, 2009). Probabilistic failure theories (Palmer and Sanderson, 1991; Taylor and Jordaan, 2015) have been used to explain the size effect on ice pressure using a simplified model of ice crushing Kim and Schulson (2015) connected the observed size effect with the strain softening behavior of ice when indented within the regime of brittle behavior. Researchers have been trying (i) to quantify the role that confinement and aspect ratio play in the design pressure magnitude, (ii) to establish a link between local and global loads, (iii) to gain more instinct into ice ice-structure interaction mechanism at the ice-structure interface, not to mention the numerical modeling.

At present, the PA curves fall into three categories: *process curves*, (termed by Frederking 1998), *spatial-distribution* (termed by Frederking 1999) *curves* and *characteristic curves*. The latter category of curves is often viewed in the context of local or global ice loads and in the context of probabilistic or deterministic approaches to design. A process p-A curve describes the process of a structure penetrating into an ice feature or of an ice feature hitting a structure. This curve is a continuous plot of average pressure versus total contact area variation during an ice-structure interaction process. A spatial-distribution p-A curve characterizes the spatial distribution of pressure. It describes the average pressure on sub-areas of various sizes within a larger area at an instant in time. To establish such a curve, knowledge of the true contact area and pressure distribution at a particular instant in time is required.

Although recently debated (Daley 2007, Gagnon 2014, Paquette and Brown, 2017), it is generally accepted that the average pressure decreases as the total load area increases. In current offshore practice (i.e., ISO 19906, 2010), following the SCA471 approach, ice loads on offshore structures are calculated using the characteristic ice pressure-area curve. The empirical basis for these curves are measurements from the Cook Inlet, Baltic Sea, Bohai Sea and the Beaufort Sea. The pressure–area curves are used in calculations of global ice loads due to continuous ice crushing against a vertical fixed structure as well as in calculations of global ice loads resulting from impact and in estimation of local ice loads.

To summarize, upon reviewing the scientific literature, design practices and recommendations, we note that the highly empirical PA concept has found its way to engineering practice replacing the uniaxial compressive strength. The most common way of expressing a p-A relationship is by the power-law expression $p = CA^{ex}$, where C and ex are empirical constants and the exponent ex typically is a negative number between 0 and –1.

2.2 Origins of the SE concept

The concept of crushing specific energy of ice (SE) has, until recently, been viewed in the context of technical tools/methods for destruction of ice, airplane landing, ship ramming or a wave driven bergy-bit striking an offshore structure. The total amount of literature on SE is significantly less than that on PA (see Table 1).

The concept of SE was introduced first by Kheisin and Likhomanov (1973). Authors treated the amount of energy spent on crushing the unit mas of ice as a constant that can be used in the identification of ice impact loads. The energy per mass of crushed ice, or the so-called *specific energy of mechanical destruction of ice*, is defined in dynamic experiments by impacting a rigid indenter at a known velocity and measuring the indentation volume formed on the surface of the ice as

$$\psi_m = \frac{\text{energy of indenter}}{\rho \cdot V} \quad \textbf{[3]}$$

where ρ is the ice density, and V is nominal crushed volume – the volume of the remaining indentation. When multiplied by material density, SE is equivalent to rebound or *dynamic hardness* (in some ice literature also called the impact strength of ice; e.g., in Timco and Martin, 1979). The dynamic hardness of polycrystalline ice has been measured by Pounder et al. (1959), Dementyev (1961), Barness et al. (1971), Tsurikov et al. (1973) and other authors.

In contrast to small balls (with diameters of a few mm) in the hardness tests, Kheisin and his colleagues (1973) have worked with larger hemispherical indenters (with diameters of 0.565 m and mass of 156 kg and 300 kg) on freshwater lake ice. Khrapaty and Tsuprik (1976) repeated the same experiment, but on the sea ice of the Japan sea, using the additional third indenter with a diameter of 0.395 m and a mass of 103 kg. Drop-weight test studies of these two research groups indicated that SE has stable characteristics; it increases with decreasing temperature and independent of mass, velocity and indenter diameter.

In conjunction with the drop-weight testing, a hydrodynamic model of ice rigid body interaction has been developed (Kurdjumov and Kheisin, 1976) by studying the failure patterns in tested ice obtained from longitudinal and transverse slices. Their model treats a crushed-ice layer between the indenter and unbroken ice surface with simplified Navier-Stokes equations. In this model, the SE parameter is not explicitly used. A different model of ice destruction was considered by Tsuprik (1978, 2012). He provided theoretical justification of SE as a physical quantity, a constant which characterizes the transition from the undisturbed state of elastically compressed ice to the destroyed state. In this model, SE is treated as an integral characteristics of the energy-expenditure of all deformation and failure mechanisms. Possibly, this is currently the only available energy–based ice-structure interaction model that have physical justification of SE.

Already in the 1970s and 1980s, several researchers (Afanasyev et al., 1978; Iyer, 1978; Sodhi and Morris, 1984ab) paid attention to the possibility of describing the process of ice-structure interaction using SE and have tried to relate dynamic hardness/SE to the compressive strength of sea ice (e.g., Glen and Comfort, 1983; Khrapaty et al., 1986; Blanchet et al., 1990). In Sodhi and Morris (1984a), the terms "mean effective pressure" and "specific energy" are used interchangeably for the ice-structure interaction at a constant velocity. From the experiments in which the model ice was cut by the vertical rigid structure, Sodhi and Morris (1984b) found that the area under the sawtooth force-deformation curve per cycle (energy to failure) has a constant value.

Other researchers have used SE in ice impact load calculations. For example, Nevel (1986) treated iceberg impact loads using the constant strength theory in analogy to indentation into metals. He acknowledges that specific energy is a different strength criterion but treats it as equivalent to the contact ice pressure, which he considers uniform over the contact area and constant during impact.

Earlier experimental data on SE include results from laboratory and in situ drop weigh tests using cones, balls, spherically-ended indenters as well as laboratory and in situ pendulum impact tests. Overview and analysis of the available experimental data in the period from 1971 to 1986 are given in Tunik (1991). His study shows that the experimental data spread does not exceed typical data spread of standard laboratory tests of compressive ice strength; however, contradicting observations of the SE dependencies have been noted (i.e., indenter mass effect, impact velocity effect). Tunik (1991) concluded that the collected data are insufficient for clear understanding of the relationship between the ice load parameters and the impact conditions (speed, scale, contact conditions, ice temperature, salinity, microstructure).

Since the early 1990s, after general acceptance of empirical PA curves, few studies focus on the SE concept. Timco and Frederking (1990, 1993) carried out drop-weight crushing tests on laboratory freshwater ice, and Gagnon and Gammon (1997) examined natural iceberg ice. Likhomanov et al. (1998) compared the results of Timco and Frederking on laboratory ice (test series of the National Research Council of Canada) with the earlier results on natural freshwater ice (test series of Arctic and Antarctic Research Institute). Their preliminary qualitative comparison showed that SE is independent on impact velocities for warm spring ice and decreasing with increasing impact velocity for cold winter ice. As a part of the ARCDEV project, in 1998, drop-weight tests were carried out on natural sea ice (Appolonov, 2003). Obtained experimental data have been used to improve the Kurdumov and Kheisin hydrodynamic model; however, the SE parameter is not explicitly used in the modified model.

Recently, there has been an increase in SE use cases. Kim and Høyland (2014) and Kim and Gagnon (2016) re-analyzed old and new data on freshwater ice in an attempt to clarify some of the contradicting observations (e.g., velocity effect, temperature effect, indenter radius effect, and indentation size effect). These researchers' analysis shows that under certain conditions (scale and size effects are limited) for any particular test, the crushing specific energy of freshwater ice shows little if any dependency on the displaced ice volume and tends towards a constant value. Furthermore, there is no apparent correlation of the ice crushing specific energy with indenter size.

Tsuprik (2012) conducted a detailed study of the algorithm for obtaining numerical values of SE by drop ball testing. He notes that the estimation of SE by drop-ball testing is challenging and requires careful planning and experimentation. This finding is observed because the failure of ice occurs in cycles (layer by layer) with a number that depends on the indenter's initial velocity. The actual value of SE can only be obtained if the entire kinetic energy of the indenter is spent on the integer number of cycles. As an alternative to drop-ball testing, Baenkhaev et al. (2016) presented a method for experimental identification of the SE by compressing big ice samples under the laboratory conditions that are similar to the limit-stress state of ice blocks interacting with a fixed vertical structure.

A direct use of SE in calculations of layer-by-layer destruction of ice in contact with the support structure is demonstrated in Tsuprik (2016). Kinnunen et al. (2016) enhanced the ice impact load model with SE parameters. The authors concluded that the SE can be used for tuning the impact model towards the actual ice properties, even though it is not directly a parameter in the model. Kim et al. (2016) have used SE concepts to validate ice model assumptions in nonlinear finite element simulations. In discrete element models, van den Berg et al. (2017) have assumed constant energy dissipation per crushed volume to determine ice-ice and ice-structure contact parameters.

Thus, to date, the SE studies have evolved both in terms of theoretical justification of this concept and in terms of finding the optimal method for measuring this characteristic. The SE characteristic is an appendix to practical engineering problems. It is an integral energy parameter, which takes into account the energy expenditure by different failure mechanisms in the contact zone of ice with the structure. The parameter value can be determined either by drop-ball testing or by compressive testing of large samples in a laboratory while recording spatial and temporal evolution of pressures with contact area.

3. Discussion

In this study, we have traced the development of two concepts: PA and SE. Numbers in Table 1 indicate that more research effort has been put into the PA concept compared to the SE. This difference is perhaps linked with the release of the international standard for Arctic offshore structures ISO 19906, in which the PA concept is used in both limit stress and limit energy interaction problems. In contrast, the SE concept has seldom been used in research and mostly in limit energy applications. There has been an increase in the number of articles with reference to the specific energy of the destruction of ice, but not everyone agrees that SE is the parameter of ice/indenter system and that it remains constant over a certain range of system sizes and interaction speeds. This situation is improving as more researchers use the SE concept in engineering models of ice impact loads and in numerical simulations of ice crushing.

One of the practical applications of the SE concept is in the ice-induced vibration models for calculations of self-induced vibrations of structures interacting with ice fields. In the view of mechanisms causing ice-induced vibrations, Määttänen (1988) emphasized the importance of the ice-structure energy interchanges. He accepted the possibility that the stored kinetic and elastic energy in the ice cover can activate and control ice-crushing process. Tsuprik, (2017) conceptually showed that SE can be used as the parameter that determines the ice failure frequency based on calculations of the necessary and sufficient portion of energy that dissipates in the contact zone of the ice field with the structure. Perhaps, the SE concept can help resolving the controversy among the researchers on whether the structural vibration during ice crushing is auto-oscillation (Blenkarn, 1970, Määttänen, 1978 and etc.) or it is forced oscillation, as discussed in Sodhi (1988).

Another possible application is limit energy ice-impact problems, in which an ice floe (or a bergy bit) strikes a stationary (or floating) structure. According to current practice, one needs to know the process PA curve as well as the local structure and ice geometry for calculating the energy spent on crushing the ice. If the process PA curve builds on the data corresponding to the local force peaks (as shown in Fig. 1), the calculated ice crushing energy will be overestimated. This overestimation can be avoided by using the SE concept.

Despite the wide use of the PA curves, increasing numbers of authors are beginning to debate the PA trends. Validity of the empirical pressure area curves has been questioned in areas with limited data (e.g., Kara Sea). In addition, the use of the PA concept is limited (if impossible) when considering the cyclic processes of ice failure causing structure vibration. In this view, it is natural to search for an alternative ice strength criterion that is more stable and easily determined in experimental studies. Could the specific energy be a candidate parameter for introducing in physical laws?

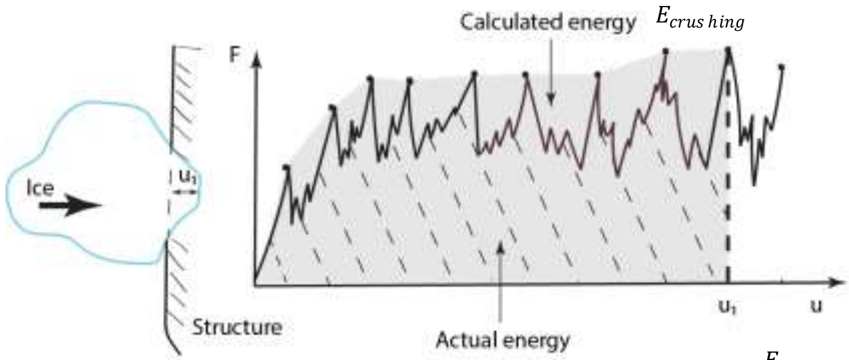

$$E_{crushing} = \int_0^{u_1} F(u)du = \int_0^{u_1} CA(u)^{ex+1}\, du$$

Figure 1. Limit energy ice-impact problem.

4. Summary remarks

For a structure-ice interaction process, a continuous record of force versus time can be converted to an ice pressure–area curve, or it can be used to find the crushing specific energy. In this study, we have traced and discussed the development of two concepts: PA and SE. After a century of research, the highly empirical concept of ice the pressure–area relationship has been integrated into the international design codes and practices. In contrast, the Russian norms and regulations seldom use this concept. Recently, the research focus has been more on the SE concept, and theoretical and experimental basis exists for this value. With further international input, it is hoped that both concepts will eventually be clarified for worldwide use.

References

Afanasyev, V.P., Dolgopolov, Yu. V., Shmeleva, L.A., Khrapaty, N.G. and Tsuprik, V.G., 1978. Effect of ice impact forces on the supports of the structures in estuaries and shelf zones. Proc. of the IAHR Symposium on Ice Problems, Luleå, Sweden, 453-461.

Afanasyev, V.P., Dolgopolov, Yu. V. and Shvainshtein, Z.I., 1971. Ice pressure on individual marine structures. G.N. Yakovlev (Ed.), Ice Physics and Ice Engineering, Leningrad, USSR, 50-68. [Translation by Israel Program for Scientific Translation, Jerusalem, Israel].

Appolonov, E.M., 2003. Решение проблем обеспечения прочности судов ледового плавания и ледоколов в условиях круглогодичной эксплуатации в Арктике. Doctoral thesis, ФГУП ГНЦ РФ Центральный научно-исследовательский институт имени академика А.Н.Крылова, [in Russian].

API Bulletin 2N Bulletin on Planning, Designing, and Constructing Fixed Offshore Structures in Ice Environments, API Bulletin 2N, 1982. American Petroleum Institute, Washington, D.C., 49p.

API Recommended Practice 2N, 1995. Planning, designing and constructing structures and pipelines for Arctic conditions. American Petroleum Institute: 2nd edition.

Ashby, M.F., Palmer, A.C., Thouless, M., Goodman, D.J., Howard, M., Hallam, S.D., Murrell, S.A.F., Sanderson, T.J.O. and Ponter, A.R.S., 1986. Nonsimultaneous failure and ice loads on Arctic structures. Offshore Technology Conference, Houston, Texas.

Baenkhaev, A.K., Bekker, A.T., Ivolgin, E.S., Pomnikov, E.E. and Tsuprik, V.G., 2016. Experimental studies of specific energy of destruction of ice by the method of testing

samples in uniaxial compression. Proceedings of Polar Mechanics Conference, 332-346, [in Russian].
Barnes, P., Tabor, D. and Walker J.C.F., 1971. The friction and creep of polycrystalline ice. Proc. Roy. Soc., Series A, 324, 127-155.
Bažant, Z.P., 1997. Scaling of quasibrittle fracture: asymptotic analysis. International Journal of Fracture, 83, 19-40.
Blenkarn, K., 1970. Measurements and analysis of ice forces on Cook Inlet structures. Offshore Tech. Conference, Houston, TX, 2, 365–378.
Blanchet, D. and Defranco, S., 2001. On the understanding of the local ice pressure area curve. In: Dempsey, J.P. and Shen, H.H. (Eds.) IUTAM Symposium on Scaling Laws in Ice Mechanics and Ice Dynamics. Solid Mechanics and Its Applications, 94, Springer, Dordrecht.
Blanchet, D., Kivisild, H.R. and Grinstead, J., 1990. Equations for local ice energy dissipations during ship ramming. Cold Regions Science and Technology, 18 (2), 101-115.
Bruen, F.J., Byrd, R.C., Vivatrat, V. and Watt, B.J., 1982. Selection of local design ice pressures for Arctic systems. Offshore Technology Conference, Houston, Texas.
CAN/CSA-S471-89, 1989. General requirements, design criteria, the environment, and loads. National Standard of Canada, Canadian Standards Association. Preliminary Edition.
Croasdale, K.R., Morgenstern, N.R. and Nuttall, J.B., 1977. Indentation tests to investigate ice pressures on vertical piers. Journal of Glaciology, 19 (81), 301-312.
Daley, C.G., 2007. Reanalysis of ice pressure-area relationships. Marine Technology 44(4), 234-244.
Dementyev, Kh.N., 1961. Determining the impact hardness of ice. Problems of Arctic and Antarctic, 7, 52–63, [in Russian].
Frederking, R. and Nakawo, M., 1984. Ice action on Nanisivik wharf, winter 1979-1980. Canadian Journal of Civil Engineering, 11, 996-1003.
Frederking, R., 1998. The pressure area relation in the definition of ice forces. Proc. of the 8th International Offshore and Polar Engineering Conference, Montreal, 2, 431-437.
Frederking, R., 1999. The local pressure-area relation in ship impact with ice. Proc. of the 15th International Conference on Port and Ocean Engineering under Arctic Conditions, Helsinki, 2, 687-696.
Gagnon, R.E., 2014. Re-analysis of load and pressure data acquired from ice impacts during the CCGS Louis St-Laurent 1994 Arctic voyage. Proc. Of the 22nd IAHR International Symposium on Ice, Singapore.
Gagnon, R. and Gammon, P., 1997. In situ thermal profiles and laboratory impact experiments on iceberg ice. Journal of Glaciology, 43 (145), 569-582.
Glen, I.F. and Comfort G., 1983. Ice impact pressure and load: investigation by experiments and sea trials. Proc. of the International Conference on Port and Ocean Engineering under Arctic Conditions, Helsinki, Finland, 1, 516-533.
GOST 3440-46, 1946. Нагрузки на гидротехнические сооружения. Нагрузки ледовые. Moscow, [in Russian].
Hirayama, K., Schwarz, J. and Wu, H.C., 1973. Model technique for the investigation of ice forces on structures. Proc. of the 2nd Conference on Port and Ocean Engineering under Arctic Conditions, 332-344.
ISO 19906, 2010. Petroleum and natural gas industries – Arctic offshore structures. International standard: 1st edition.

Iyer, S.H., 1978. Existing ice codes and suggested criteria. Proc. IAHR Ice Symposium, Lulea, Sweden, 363-378.

Joensuu, A. and Riska, K., 1989. Contact between ice and structure, Helsinki University of Technology, Laboratory of Naval Architecture and Marine Engineering Report M-88, Otaniemi, Finland, [in Finish].

Jordaan, I.J. and Timco, G.W., 1988. Dynamics of the ice-crushing process. Journal of Glaciology, 34 (118), 318-326.

Jordaan, I.J., Maes, M.A., Brown, P.W. and Hermans, I.P., 1993. Probabilistic analysis of local ice pressures, Journal of Offshore Mechanics and Arctic Engineering 115 (1), 83-89.

Kheisin, D.E. and Likhomanov, V.A., 1973. An experimental determination of the specific energy of mechanical crushing of ice by impact. Problemi Arktiki i Antarktiki, 41, 69-77, [in Russian].

Khrapaty, N.G, Takhteyev, V.A., Gomolsky, S.G., 1986. Ball penetration into a floating ice plate Proc. of the IAHR International Symposium on Ice, Iowa City, Iowa, 1, 319-327.

Khrapaty, N.G. and Tsuprik, V.G., 1976. Экспериментальное определение удара твердого тела о лед. Тр. коорд. совещ. по гидротехн.: Регулир. ледовых явлений на каскадах гидроузлов. Вып.111. Л.: Энергия, 166-169, [in Russian].

Kim, E. and Schulson, E.M., 2015. A phenomenological explanation of the pressure–area relationship for the indentation of ice: Two size effects in spherical indentation experiments. Cold Regions Science and Technology, 115, 48-55.

Kim, E. and Høyland, K.V., 2014. Experimental investigations of the energy absorption capacity of ice during crushing: Is the specific energy scale independent? Proc. of the 22nd IAHR International Symposium on Ice.

Kim, E. and Gagnon, R., 2016. A preliminary analysis of the crushing specific energy of iceberg ice under rapid compressive loading. Proc. of the IAHR International Symposium on ice.

Kim, E., Song, M. and Amdahl, J., 2016. On ice model validation and calibration strategies for damage assessment of structures subjected to impact actions. Proc. of the 7th International Conference on Collision and Grounding of Ships and Offshore Structures.

Kinnunen, A., Tikanmäki, M. and Heinonen J., 2016. An energy model for ice crushing in ice-structure impact. Proc. of the 23rd IAHR International Symposium on Ice, Ann Arbor, Michigan, USA, 1-8.

Korzhavin, K.N., 1962. Action of ice on engineering structures, Draft Translation Report No. 260, U.S. Army Corps Eng. Cold Reg. Res. Eng. Lab, Hanover, NH.

Kurdjumov, V. and Kheisin, D., 1976. Hydrodynamic model of the impact of a solid on ice. Prikladnaja Mekhanika, 12 (10), 103-109, [in Russian].

Likhomanov, V., Stepallov, I., Frederking, R. and Timco, G.W., 1998. Comparison of results of impact tests on laboratory and natural freshwater ice with hydrodynamic model predictions. Proc. of the Eighth International Offshore and Polar Engineering Conference, Montreal, Canada, 452-459.

Määttänen M., 1978. On conditions for the rise of self-excited ice-induced autonomous oscillations in slender marine pile structures. Finnish-Swedish Winter Navigation Board. Research report No 25, Helsinki, Finland. [PhD thesis on ice induced vibrations and numerical model]

Määttänen, M., 1988. Ice-induced vibrations of structures − self-excitation. Proc. of the Ninth IAHR International Symposium on Ice, 2, 658–663, Sapporo, Japan.

Maser, K.R., 1971. The Interpretation of small scale data for ice. Proc. of the first International Conference on Port and Ocean Engineering under Arctic Conditions, Trondheim, Norway, 1, 632-657.

Masterson, D.M. and Frederking, R.M.W., 1993. Local contact pressures in ship/ice and structure/ice interactions, Cold Regions Science and Technology, 21, 169-185.

Masterson, D.M. and Spencer, P.A., 2001. Ice force calculation for large and small aspect ratios. In: Dempsey J.P. and Shen H.H. (Eds.) IUTAM Symposium on Scaling Laws in Ice Mechanics and Ice Dynamics. Solid Mechanics and Its Applications, Springer, Dordrecht, 31–42.

Nevel, D.E., 1986. Iceberg impact forces. Proc. IAHR Symposium on Ice, Iowa City, Iowa, 3, 345-369.

Palmer, A., Goodman, D., Ashby, M., Evans, A., Hutchinson, J. and Ponter, A., 1983. Fracture and its role in determining ice forces on offshore structures. Annals of Glaciology, 4, 216-221.

Palmer, A.C. and Sanderson, T.J.O., 1991. Fractal Crushing of Ice and Brittle Solids. Proceedings of the Royal Society A: Mathematical, Physical and Engineering Sciences, 433 (1889) 469-477.

Palmer, A.C., Dempsey, J.P. and Masterson, D.M., 2009. A revised ice pressure-area curve and a fracture mechanics explanation. Cold Regions Science and Technology, 56, 73-76.

Paquette, E. and Brown, T.G., 2017. Ice crushing forces on offshore structures: Global effective pressures and the ISO 19906 design equation. Cold Regions Science and Technology, 142, 55-68.

Pounder, E.R. and Little, E.M., 1959. Some physical properties of sea ice. Canadian Journal of Physics, 37, 345–369.

Ralston, T.D., 1978. An analysis of ice sheet indentation. Proc. of the IAHR Ice Symposium, Luleå, Sweden, 1, 13-31.

Sanderson, T.J.O., 1988. Ice mechanics. Risks to offshore structures. Graham and Trotman, London, UK.

Schapiro, G.S., 1983. Об уравнениях деформирования льда. Механика и физика льда (под ред. Ишлинского, А.Ю.), 164−167, [in Russian].

Schulson, E.M. and Duval, P., 2009. Creep and Fracture of Ice. Cambridge University Press.

Schwarz, J., Frederking, R., Gavrillo, V., Petrov, I.G., Hirayama, K.-I., Mellor, M., Tryde, P. and Vaudrey, K.D., 1981. Standardized testing methods for measuring mechanical properties of ice. Cold Regions Science and Technology, 4 (3), 245-253.

SN 76-59, 1959. Технические условия определения ледовых нагрузок на речные сооружения. Госстрой СССР, Moscow, [in Russian].

SNiP 2.06.04-82, 1982. Нагрузки и воздействия на гидротехнические сооружения (волновые, ледовые и от судов), Госстрой СССР, [in Russian].

Sodhi, D.S., 1988. Ice induced vibrations of structures. Proc of the IAHR Ice Symposium, Sapporo, Japan, 625–657.

Sodhi, D.S. and Morris, C.E., 1984a. Dependence of crushing specific energy on the aspect ratio and the structure velocity. Proc. of the 16th Annual Offshore Technology Conference, Houston, Texas, USA, 363-374.

Sodhi, D.S. and Morris, C.E., 1984b. Ice forces on rigid, vertical, cylindrical structures. Research report 84-33, US Army Corps of Engineers, Cold Regions Research and Engineering Laboratory, Hanover, New Hampshire.

SP 38.13330.2012, 2014. Нагрузки и воздействия на гидротехнические сооружения (волновые, ледовые и от судов), Минрегион России, [in Russian].
Taylor, R.S. and Jordaan, I.J., 2015. Probabilistic fracture mechanics analysis of spalling during edge indentation in ice. Engineering Fracture Mechanics, 134, 242-266.
Timco, G.W. and Frederking R.M.W., 1990. Drop impact tests on freshwater ice: spherical head. Proceeding of the 10th IAHR Ice Symposium, Espoo, Finland, 776-787.
Timco, G.W. and Frederking, R.M.W., 1993. Laboratory impact tests on freshwater ice. Cold Regions Science and Technology, 22 (1), 77-97.
Timco, G.W. and Martin, R.A., 1979. Impact strength tests on Ottawa River ice. National Research of Canada, Report No. LTR-LT-97.
Timco, G.W. and Sudom, D., 2013. Revisiting the Sanderson pressure–area curve: Defining parameters that influence ice pressure, Cold Regions Science and Technology, 95, 53-66.
Truskov P. A., Vershinin S.A., Kouzmitchev, K.V. and Tazov, D.N., 2001. Substantiation of the Design Parameters of Ice Features for Load Calculations Acting on Sakhalin Offshore Structures (South Sakhalin). Proc. of the 16th International Conference on Port and Ocean Engineering under Arctic Conditions, 223-232.
Tsuprik V.G., 1978. Модель динамического взаимодействия льдины с отдельной опорой. В сб. статей: Гидротехнические сооружения. - Владивосток.: изд-во ДВГУ, 1978, 82-89, [in Russian].
Tsuprik, V.G., 2012. Theoretical and experimental studies of specific energy of mechanical failure of sea ice. Proc. 22nd International Offshore and Polar Engineering Conference, Rhodes, Greece, 1242-1246.
Tsuprik, V.G., 2016. Методология определения ледовой нагрузки на ледостойкие основания с использованием удельной энергии разрушения льда. Материалы международной научной конференции «Полярная механика-2016» (IPMC), Владивосток, 306-319, [in Russian].
Tsuprik, V.G., 2017. The forming cyclic loads on the offshore structures during ice field edge fracture. Journal of Civil Engineering, 6, 118-139.
Tsurikov, V.L. and Veselova, L.E., 1973. Dynamic hardness of the Caspian Sea ice. Trans. Studies of Ice of the USSR Southern Seas, Moscow, Nauka Publishing House, 60–68, [in Russian].
Tunik, A.L., 1991. Impact ice pressure: more questions than answers. Ice-Structure Interaction (Eds. Jones, S.J., McKenna, R.F., Tillotson, J. and Jordaan, I.J.) Springer-Verlag, 693-714.
van den Berg, M., Lubbad, R. and Løset, S., 2017. Accuracy of a non-smooth time stepping scheme with non-rigid contacts for ice-structure interaction. Proceedings - International Conference on Port and Ocean Engineering under Arctic Conditions.
Weeks, W.F. and Assur, A., 1969. Fracture of lake and sea ice. Research report 269, Corps of Engineers, U.S. Army Cold Regions Research and Engineering Laboratory, Hanover, New Hampshire.

Ice blasting with explosives to prevent ice disasters in the Heilongjiang River

Tao Wang [1], Xinlei Guo[1], Hui Fu [1], Yongxin Guo [1], Li Jiazheng[1]
1. State Key Laboratory of Simulation and Regulation of Water Cycle in River Basin, China Institute of Water Resources and Hydropower Research, Beijing, China

Ice cover or ice jam blasting with explosives is an important measure for ice flood mitigation. In order to conduct a successful blasting, it is the key to properly determine the relations between varies parameters including radius of the blasting crater, amount of the explosive, the water depth and the thickness of the ice cover. Field experiments have been conducted to study ice breaking process with explosive in the upper reach of the Heilongjiang River (Amur River) for several years. A theoretical model are developed to correlate the blasting crater radius and the thickness of the ice cover, the water depth below the ice cover, and the explosive weight. The blasting crater radius determined by the proposed equation result in average errors of less than 8.5% when compared with the measured values. This equation is used on ice blasting with explosives in the Mohe reach of the Heilongjiang River in 2015-2017, which successfully prevented ice jam from occurring during river breakup. This research provides scientific basis for ice breaking with explosives to prevent ice disaster in the river in Alpine region.
Key words: Blasting, Blasting crater radius, Explosive weight, Ice cover, Ice jam

1. Background

The Heilongjiang River, serving as the border of China and Russia, is located in the most northern region of China. The annual average temperature in the region is about below -2°C and the freeze up period lasts up to 6 months. Significant ice jam events occur every 3 years on average in the upper reach of Heilongjiang River. Due to its remote location, transportation and communication systems are undeveloped in this region and observation equipment and technologies are behind. As a result, research on ice jam flood prevention and mitigation in this region has experienced very slow progress. Since the Heilongjiang River serves as the border river, it is impossible to construct hydraulic structures to control and mitigate ice flooding on the river. The only available non-structural measures are to prevent ice jam formation and to remove ice jams (Beltaos, 1995, 2008). Field measurements have shown that ice covers on the Heilongjiang River can reach 2.0m thick, which makes the ice covers extremely strong. In addition, there is usually about 20cm thick snow covering on ice. It is difficult to breach and remove a large area of such thick ice covers or ice jams by mechanical destruction, surface treatment, and thermal modification. Therefore, ice blasting by explosives become the most effective tool for ice jam prevention and mitigation on the Heilongjiang River.

Although explosives have been used to break ice cover for about 200 years, systematic research for ice blasting has been still progressing slowly because the implementation of such research is highly limited by the river condition, the surrounding environment, and the difficulty and risks from the field operations (Shen, 2003; Shen & Knach, 2015). Based on ice blasting experience, Mellor (1982) from the United States Army Corps of Engineers (USACE, 1982, 2002) developed empirical prediction curves to express the relations between the blasting radius and the ice cover thickness, explosive weight. In China, Ding et al. (2010) proposed the ice blasting technologies of dropping bombs into the Yellow River by airplane and shooting bombs from the river bank. Liang et al. (2012) analyzed the characteristics of blasting vibration and shock pressure in water based on two ice blasting technologies of laying explosives on the ice and below the ice on the Yellow River in Inner Mongolia. Tong et al. (2012) summarized ice cracks and loading distributions on the ice after ice blasting based on field data from ice blasting on the Yellow River and mathematical models. Regarding blasting technologies, Duan et al. (2003) and Yin et al. (2010) summarized the proper layout for blasting holes and the blasting range of a river channel based on engineering practice. The average ice cover thickness for the studies mentioned above was around 0.5m or less, which is different from the thick ice cover on the Heilong River. Heilongjiang River has these characteristics of thick and strong ice covers and shallow water depth. In this study ice blasting experiments were performed in the Mohe reach of the upper Heilongjiang River. Based on these experiments, effective ice blasting technologies are developed and theoretical models are established between the blasting crater radius and the explosive weight, ice cover thickness, and water depth below the ice covers. These results provide scientific and theoretical basis for high efficiency ice blasting technologies.

2. Experiment Scheme Setup for Ice Blasting

Ice blasting for ice jam mitigation can be divided into two categories of ice cover blasting and ice jam blasting according to the blasting stage. Ice cover blasting before breakup is undertaken to prevent severe ice jam formation. Preventative ice blasting breaks ice covers into smaller blocks, which can smoothly flow downstream during the breakup before the ice jam formation. It can also allow the radiant heat of the sun to penetrate into the water under the ice cover and weaken the ice cover in the vicinity of the blasting area through heat transfer. In addition, ice jam blasting during or after ice jam formation is used to break or destroy ice jams, and, as a result, prevent or mitigate ice flooding. Prevention is considered to be a priority measure for the flood damage reduction. Thereby, ice cover blasting before ice jam formation bases on the ice forecast (Wang et al., 2008, 2013) and field measurements has been undertaken as an important technique for ice jam prevention in the Heilongjiang River.

2.1 Selection of explosive type, amount, and timing

Research by the USACE (Mellor, 1987) showed that, there were negligible differences in the blasting effects when using different types of explosives. In China, the Institute of Engineer Crops in China (Xia, 2014; Shi et al., 2008) used TNT Explosive for ice blasting under water. TNT Explosive (Liang, 2014) and Rock Emulsion Explosive (Tong et al., 2012) have been used for ice blasting on the Yellow River. Rock Emulsion Explosives (Dai et al., 2012) has been used for ice blasting on the Heilongjiang River from 2011 through 2017. The above studies have shown that the types of the explosives has no apparent effects on the blasting results.

A key factor of ice blasting is the determination of the explosive mass. The USACE published an equation to calculate the optimal explosive mass:

$$W_{opt} = 21t^3 \qquad \textbf{[1]}$$

Where W_{opt}= the optimal amount for explosives, kg; and t = the ice cover thickness, m. This equation was fitted based on a large amount of measured data. As shown in this equation, the optimal amount for explosives is positively correlated to t^3. In practice, once the ice cover thickness exceeds 1.0 m, the amount for explosives increases quickly. For natural rivers with small water depth below the ice cover, the full effect of a large explosive dosage cannot be carried out through the explosive blasting shock wave. Therefore, for the Heilongjiang River, which has thick ice, snow cover and small water depth, this equation is not a good fit. The objective of the current study was to develop a blasting technology which is appropriate for natural rivers in high latitude regions like the Heilongjiang River based on blasting experiments.

Ice blasting before breakup is usually performed before the formation of ice jams and after the temperature becomes positive. Ice blasting on the Heilongjiang River was performed 15 days before breakup, which made sure that the ice cover was sufficiently thick and strong for the blasting operations and the broken ice cover after blasting would not freeze again. Therefore, accurate forecasting of breakup date and ice jam occurrence is a prerequisite of the date selection of the ice blasting.

2.2 Selection of blasting location

The tributaries, geographical location and river flow direction of the Heilongjiang River are shown in Fig.1. The Argun River and the Shilka River are two large tributaries as the sources flowing into the Heilongjiang River. Both rivers flow from southwest to northwest, as shown in Fig. 1, and from low latitude to high latitude with a 700km distance difference. This condition causes breakup to occur in the upstream reach and tributaries before the downstream reach, resulting in reversed breakup condition. Fig.2 shows that the characteristics of the upper Heilongjiang River, which include: narrow and meandering main channel, connecting islands, a large number of branches and trenches, and steep change in river gradient, resulting in uneven distribution of the flow and water depth along the river. The above factors lead to frequent occurrence of ice jams during breakup. Furthermore, based on historical records, as shown in Table 1, 19 out of the 21 years, the center of the ice jam events occurred in the Mohe country reach on the upper Heilongjiang River, where the average temperature is about -5°C, with the lowest winter temperature being as low as -59.5°C. Through the above analysis, it is concluded that the Mohe reach is an appropriate location for ice breaking experiments with explosives.

Fig 1. River locations and flow direction of the Heilongjiang River.

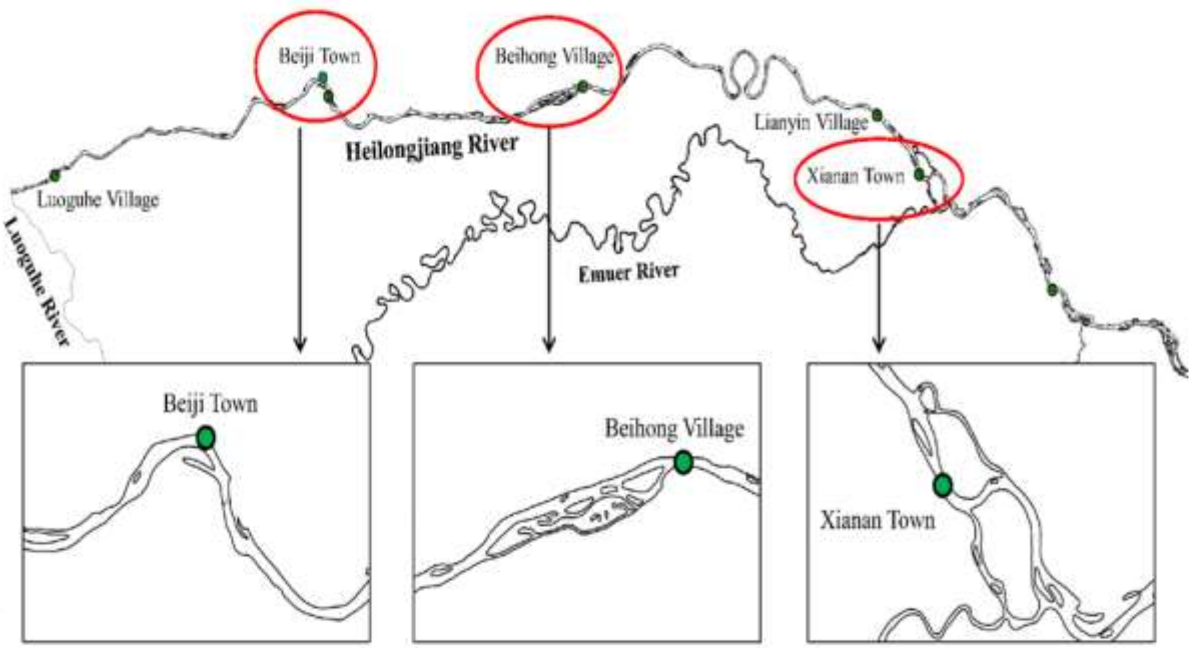

Fig 2. Location map of the Mohe reach, Heilongjiang River.

Table 1. Ice jam Events on the Heilongjiang River.

Year	Breakup Date (Month-Date)	Location of Ice jam	Maximum Head Increase(m)	Period of Ice Jam (Month-Date)
1950	/	Jialinda-Oupu in Tahe reach	9.40	05-09 ~ 05-11
1953	/	Luoguhe—Mohe city in Mohe reach	7.46	05-05 ~ 05-08
1956	/	Luoguhe—Mohe city in Mohe reach	7.39	05-08 ~ 05-10
1958	05-01	Lianyin-Hutong Tahe reach	10.14	05-05 ~ 05-10
1960	04-26	Luoguhe-Huoermojin in Mohe reach	13.56	04-27 ~ 05-10
1961	04-27	Lianyin in Mohe reach	8.03	/
1964	04-30	Jialinda-Malun in Mohe reach	8.00	05-02 ~ 05-14
1970	04-27	Huma city in Huma reach	5.22	/
1971	04-23	Luoguhe-Sandaoka in Mohe reach	9.90	04-23 ~ 05-04
1973	05-05	Jialinda-Hutong in Mohe reach	8.20	05-06 ~ 06-01
1977	05-03	Mohe-Kaikukang in Mohe reach	6.65	/
1981	04-23	Luoguhe-Mohe city in Mohe reach	7.46	04-28 ~ 04-30
1985	04-18	Luoguhe-Huoermojin in Mohe reach	12.60	04-17 ~ 05-29
1986	05-04	Luoguhe—Malun/ Mohe city-Kaikukang in Mohe reach	9.25	05-04 ~ 05-08
1987	05-08	Kaikukang-Oupu in Tahe reach	6.17	/
1988	04-22	Kaikukang in Tahe reach	5.11	/
1991	05-01	Luoguhe—Malun in Mohe reach	8.80	04-28 ~ 05-04
1994	04-29	Luoguhe—Kaikukang in Mohe reach	10.93	04-29 ~ 05-10
1995	05-03	Luoguhe—Mohe city in Mohe reach	10.10	05-05 ~ 05-09
2000	04-28	Jinshan-Huma in Mohe reach	9.23	04-29 ~ 05-01
2009	04-14	Beihong—Hongqiling /Beihong—Oupu in Mohe reach	/	04-16 ~ 04-21
2010	04-25	Beihong-Xingan in Mohe reach	8.34	05-03 ~ 05-09
2013	05-01	Mohe-Huma in Mohe reach	/	05-02 ~ 05-07

Note, / represents that no historical records were found.

3. Analysis of Experiments

A basic requirement in ice blasting is to predict the size of the crater as the dependent variable. An important task for ice blasting is to establish the relation between the blasting crater radius (R_c) and other relevant variables based on a large amount of measurement data and field observations. The relevant variables, representing the input data for the prediction, include the explosives weight (W), water depth below the ice (h_c), explosives depth under the ice cover (d_c), and ice cover thickness (t). The relation between the blasting crater radius and other relevant variables is built by regression analysis. However, the number of data sets available for regression analysis is rather small, it is necessary to somehow reduce the number of variables. One of the ways to reduce the number of variables is to express one variable in terms of another. Based on Mellor (1972)'s conclusions for underwater blasting, an expedient parameter is cube root scaling, which has been adopted in his study. All linear dimensions of this variables are divided by the cube root of explosive weight. In this case of constant explosive density, the lengths are effectively dimensionless since the dimension of the cube root of explosive weight represents that of the crater radius. For scaling the crater radius, these scaled parameters of the ice cover thickness and water depth are defined by Equations (2) – (4).

The scaled crater radius Y is

$$Y = R_c/W^{1/3} \quad \textbf{[2]}$$

Where R_c = the scaled blasting crater radius, m; and W = the explosive weight, kg.
The r scaled ice cover thickness X_1 is

$$X_1 = t/W^{1/3} \quad \textbf{[3]}$$

Where t = the ice cover thickness.
The scaled water depth below the ice cover X_2 is

$$X_2 = h_c/W^{1/3} \quad \textbf{[4]}$$

Where h_c = the water depth below the ice cover, m.
The chosen regression equation is a polynomial equation with cross-products and terms up to the third power as shown in equation (5)

$$Y = b_0 + b_1X_1 + b_2X_2 + b_3{X_1}^2 + b_4X_1X_2 + b_5{X_2}^2 + b_6{X_1}^3 + b_7{X_1}^2X_2 + b_8X_1{X_2}^2 + b_9{X_2}^3 \quad \textbf{[5]}$$

3.1 Relation between blasting crater radius and ice cover thickness
Several challenges exist for ice blasting and observation on the Heilongjiang River: (1) Due to the effects of factors such as thick ice cover and snow on the river, a lack of topographic information of the entire river channel as a boundary river, harsh weather, inconvenient transportation system and insufficient skill level of blasting technicians, the accuracy of measured ice blasting data is limited. (2) Some blasting craters have a clear demarcation between the fragmented ice of the central crater and the surrounding intact ice. Other craters have a central zone with heavy fragmented ice, surrounded by ice which has been flexed and cracked, and there is no clear demarcation in place. Moreover, the edge of the blasting crater and surrounding cracks are usually covered by snow and broken ice, which makes it difficult to accurately determine the blasting boundary and the length of the cracks. (3) It is dangerous for the researchers to get too close to the blasting crater after the blasting. Therefore, the measurement of the blasting crater radius is usually performed outside the crater, which can also lead to errors from different surveyors. (4) Due to constraints on site conditions, the range of some experiment data, such as ice cover thickness and water depth, is limited. A total of 214 sets of effective data based on hundreds of field conditions were collected during 2015～2017. In order to make sure that the diameters of all the blasting craters can be independently measured, a sufficient distance was kept between each blasting craters. The explosives were placed under the ice cover based on the principal proposed by the USACE, i.e. the optimal location of the explosives was 0～0.6 t below the ice cover. Therefore, the impact of the location of the explosive below the ice cover was neglected during this study. Fig. 3 shows the relation between the blasting crater diameter and ice cover thickness based on measured data. The measured ice

cover thickness is between the range of 0.51~1.55m, and the measured blasting crater diameter is between the range of 4.6~21.6m. As shown in Fig. 3, as the amount of the explosives increases, the blasting crater diameter also increases obviously. When the amount of the explosives is kept the same, the blasting diameter increases with the increase of the ice cover thickness. Other researches have shown that, under the same explosive weight, when the ice cover thickness exceeds a certain value, the blasting crater diameter starts to decrease as the ice cover thickness increases (USACE, 1982).

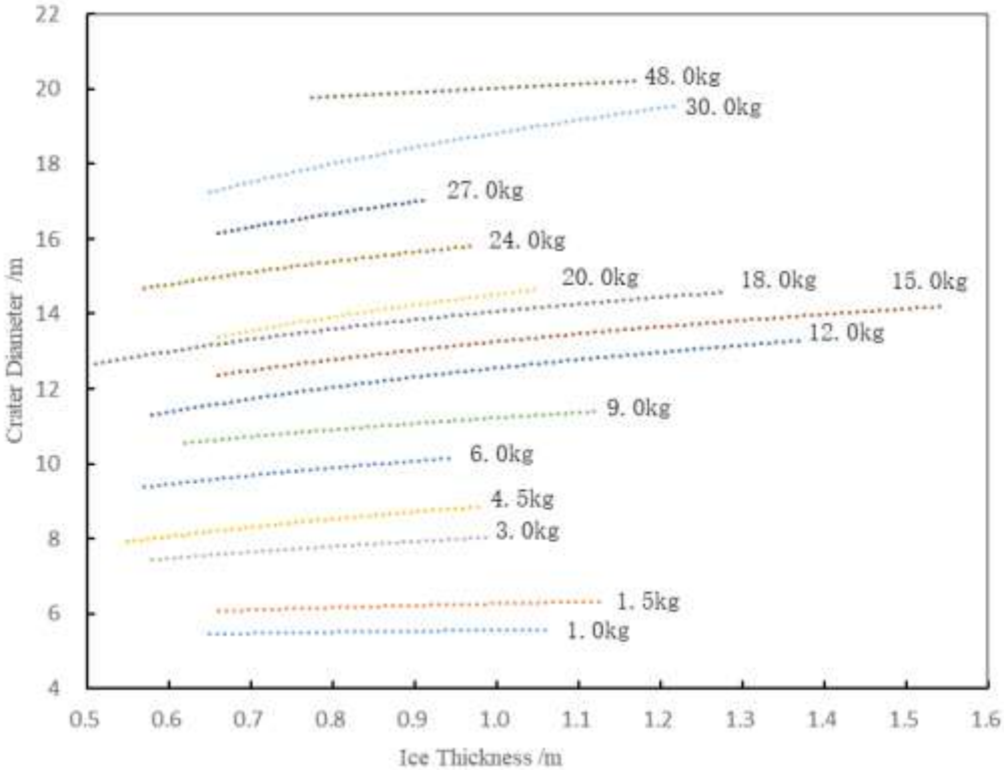

Fig 3. Relation between measured blasting crater diameter and ice cover thickness.

Based on the regression equation in Equation (5), the trinomial and binominal forms are shown in Equations (6) and (7), which express the relation between the scaled blasting crater radius and the scaled ice cover thickness.

$$Y = 3.0815 - 2.6944X_1 + 5.5689X_1^2 - 3.2568X_1^3 \quad \textbf{[6]}$$

$$Y = 2.6722 + 0.0640X_1 + 0.0546X_1^2 \quad \textbf{[7]}$$

3.2 Relations between blasting crater radius and ice cover thickness, water depth

When explosives are detonated well below the surface of water, instant gas with high temperature and pressure are produced, which leads to propagation of spherical shock waves and create gas bubbles. The bubble expands against the hydrostatic pressure. After the internal pressure drops below the water pressure, the bubbles continue to expand due to inertia. When the internal pressure drops to 1/5 to 1/10 of the external water pressure, the bubbles start to shrink due to external pressure (Yu et al., 2003). Also due to inertia, the bubbles continue to shrink even after the internal pressure exceeds the external water pressure. This back-and-forth process continues to take place. Meanwhile, the bubbles keep rising in the water under the effect of buoyance and has a tendency to move toward the water surface, solid boundaries and away from free boundaries. Eventually the bubbles collapse until the internal pressure becomes greater than the external pressure. This processes gives rise to successive bubble pulsations which transmit to the water surface or solid boundaries. Therefore, it is necessary to have adequate water depth for the explosives to take full effect during under water blasting.

Natural rivers such as the Heilongjiang River have many branches and shallow sand bars. Furthermore, blasting locations are limited to the right side of the river center line within the Chinese territory since the Heilongjiang River is the border of China and Russia. The above factors lead to relatively shallow water in the blasting area, where the maximum measured water depth is less than 5.0m. When a large amount of explosives are used, the explosives could not take full effect in areas with shallow water. The relation between the measured blasting crater diameter and water depth is shown in Fig.4. Fig.4 shows that: (1) When the explosive weight was 1.0~6.0kg, as the water depth increased between 2.0 and 5.0m, under the same amount of explosive, the blasting crater diameter more or less remained the same, demonstrating that the explosives can take full effect when the water depth is larger than 2m. (2) When the explosive weight was 9kg, as the water depth increased, the blasting crater diameter increased, however, as the water depth exceeded 3.0m, the blasting crater diameter has little change with the increase of the water depth. (3) When the explosive weight was 12~15kg, as the explosives amount increased, the blasting crater diameter increased, and as the water depth exceeded 4.5m, the diameter increased slightly as the water depth increased. (4) When the explosive weight was 20~30kg, due to limitations of the field conditions, the measure water depth was limited to 0.5~2.5m in explosive area, and the blasting crater diameter increased rapidly as the water depth increased.

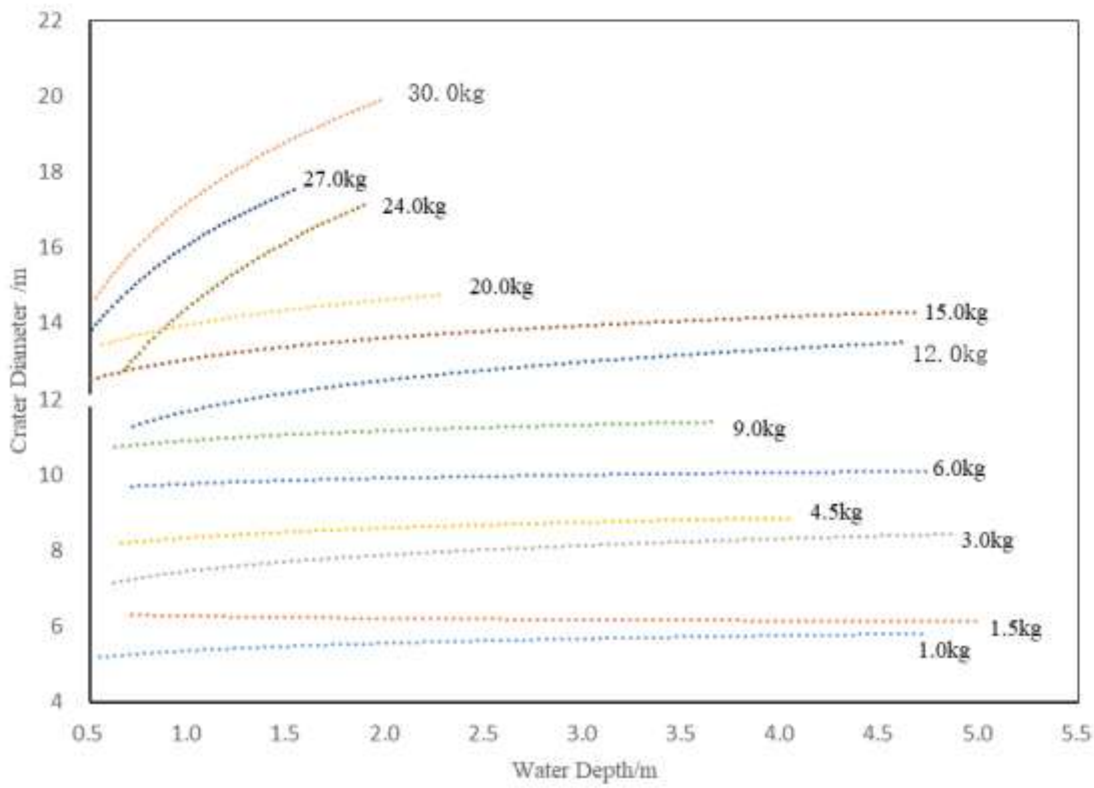

Fig 4. Relation between Measured blasting crater diameter and water depth below ice.

The relations between the scaled blasting crater radius and scaled ice cover thickness, the scaled water depth were developed using regression analysis. These relations are shown in trinomial (cross trinomial and pure trinomial) and binomial (cross binomial and pure binomial) forms in Equations (8) to (11):

$$Y = 3.2970 - 7.7716X_1 + 2.0904X_2 + 15.4095X_1^2 - 2.6299X_1X_2 - 0.6679X_2^2 - 8.7445X_1^3 + 1.7263X_1^2X_2 + 0.0054X_1X_2^2 + 0.1010X_2^3 \quad \textbf{[8]}$$

$$Y = 3.1993 - 6.1197X_1 + 1.5121X_2 + 10.0857X_1^2 - 0.8098X_2^2 - 5.1321X_1^3 + 0.1170X_2^3 \quad \textbf{[9]}$$

$$Y = 2.7515 - 1.0067X_1 + 0.4078X_2 + 0.9772X_1^2 - 0.3087X_1X_2 - 0.0264X_2^2 \quad \textbf{[10]}$$

$$Y = 2.7305 - 0.7480X_1 + 0.3225X_2 + 0.4232X_1^2 - 0.0560X_2^2 \quad \textbf{[11]}$$

3.3 Proposed formula and analysis of experiment results for blasting ice with explosive

The effectiveness assessment is described by the root mean square error and correlation coefficients, as shown in Equations (12)–(13).

$$RMSE = \sqrt{\frac{\sum_{i=1}^{n}[X(i) - Y(i)]^2}{n}} \quad \textbf{[12]}$$

$$r = \frac{n(\sum XY) - (\sum X)(\sum Y)}{\sqrt{[n\sum X^2 - (\sum X)^2][n\sum Y^2 - (\sum Y)^2]}} \quad \textbf{[13]}$$

where $RMSE$ = the root mean square error, r = the correlation coefficient, X = the measured data; Y = the forecasted data, and n = the total number of sample sequences. The smaller the coefficient $RMSE$ is, the smaller the difference between the predicted value and the measured value is. However, the closer the coefficient r is to 1, the closer the forecast value and the measured one are.

The root mean square error and correlation coefficients are compared between the forecasting results using Equations (6)–(11) and the measured ones, as shown in Table 2. Ignoring the impact of the water depth and only considering the relation between the blasting crater radius and the ice cover thickness, the root mean square errors of the trinomial Equation (6) and binomial Equation (7) are higher than that of Equation (8)–(11) which considered the impact of the water depth, while the correlation coefficients of Equations (6) and (7) are lower than that of Equation (8)–(11). The above results demonstrate that the impact of the water depth cannot be ignored in the impact factors of ice blasting on the Heilongjiang River. The root mean square errors and correlation coefficients of Equations (8) – (11) are shown in Table 2. The results shows that the evaluation values of the trinomial equations are better than that for the binomial equations, and the cross trinomial and cross binomial equations are better than the corresponding pure trinomial and pure binomial equations.

Table 2. Results Evaluation of different regression methods.

Conditions	Type of regression equation	Evaluation method	
		Root Mean Square Error	correlation coefficient
Relation between scaled blasting crater radius and scaled ice cover thickness	Pure binomial Equation (6)	0.8686	0.9087
	Pure binomial Equation (7)	0.8745	0.9073
Relation between scaled blasting crater radius, ice scaled thickness, and scaled water depth	Cross trinomial equations (8)	0.7577	0.9371
	Pure trinomial Equation (9)	0.7621	0.9311
	Cross binomial equations (10)	0.8294	0.9184
	Pure binomial equations (11)	0.8308	0.9180

Table 3. Relative errors between forecasted and measured blasting crater radius.

Relative error	Trinomial equations		Binomial equations	
	Cross trinomial Equation (8)	Pure trinomial Equation (9)	Cross binomial Equation (10)	Pure binomial Equation (11)
Average relative error	7.4	7.5	8.4	8.5
Max relative error	24.6	24.7	25.9	26.2
Min relative error	0.0	0.1	0.1	0.0

The relative errors from Equations (8) – (11) are shown in Table 3. Table 3 shows that the forecasting errors from the two trinomial equations are very close and no more than 7.5%, and the forecasting errors from the two binomial equations are very close and no more than 8.5%. For simplification purpose, the pure trinomial Equation (9) is used for the calculations of the blasting crater radius. Inserting the explosive weight, ice cover thickness, water depth, and blasting crater radius into Equation (9) and the following equation was obtained:

$$R_c = 3.20W^{1/3} - 6.12t + 1.51h_c + 10.09\frac{t^2}{W^{1/3}} - 0.81\frac{h_c^{\ 2}}{W^{1/3}} - 5.13\frac{t^3}{(W^{1/3})^2} + 0.12\frac{h_c^{\ 3}}{(W^{1/3})^2} \quad \textbf{[14]}$$

The forecasted blasting crater radius based on Equations (8) – (11) and the measured radius are compared in Fig.5 It can be seen that the forecasted values had similar trends as the measured values. The forecasted values based on the four equations were very close. The difference of the mean relative error based on the binomial and trinomial equations was within 1% from each other. To further simply the calculations, pure binomial Equation (11) was used in the calculations. Inserting the explosive weight, ice cover thickness, water depth and blasting crater radius into Equation (11) and the following equation was obtained:

$$R_c = 2.73W^{1/3} - 0.75t + 0.32h_c + 0.42\frac{t^2}{W^{1/3}} - 0.06\frac{h_c^{\ 2}}{W^{1/3}} \quad \textbf{[15]}$$

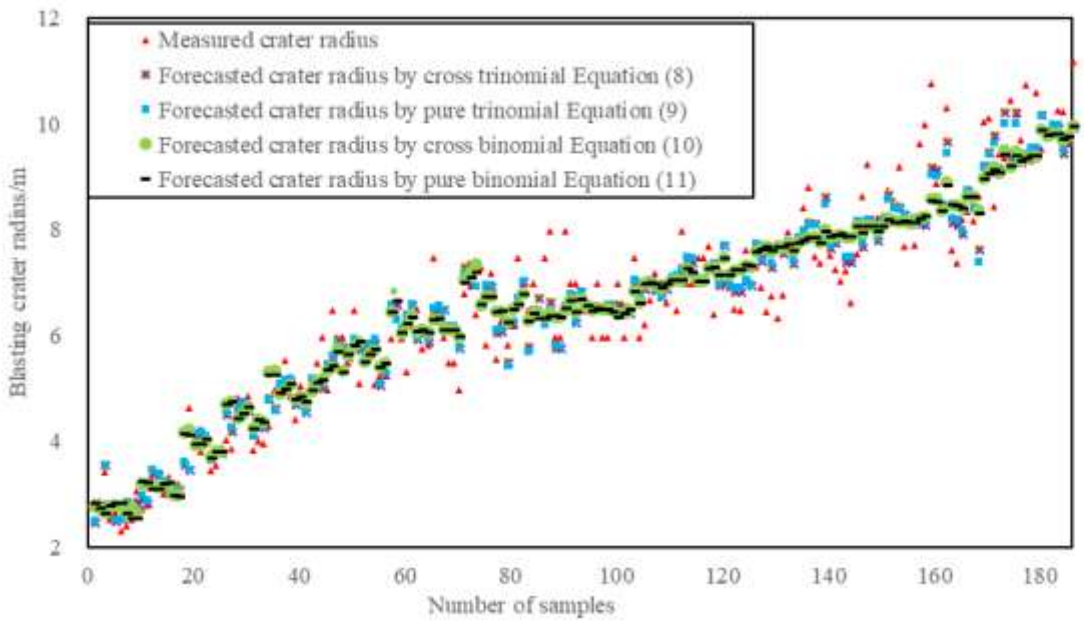

Fig 5. Scattered diagram of measured and forecasted blasting crater radius.

4. Conclusion

The Heilongjiang River is a natural river with wide and shallow river channel, thick ice cover and serves as the border of China and Russia. Ice blasting with explosive on the Heilongjiang River has some special characteristics. Ice blasting experiments and field observations have shown that when the type of the explosives are ignored, and the optimal principle recommended by USACE is adopted for the depth of the explosives below the ice cover, the blasting crater radius is affected not only by the explosive weight and ice cover thickness but also by the water depth. The equations are developed during this study to express the relations between the blasting crater radius and the ice cover thickness, explosive weight, and water depth below ice cover using the regression method. Based on analyses of the correlate coefficients, root mean square errors and relative errors by these equations, Equation (15) was proposed to describe the relations between the variables due to its small errors, strong correlations and simple format. The average relative error between the forecasted and measured values was no more than 8.5%. The proposed equation is applicable to not only natural rivers with thin ice cover but also shallow rivers with thick ice covers.

The proposed methods in this study were used for ice blasting in the Mohe reach of the upper Heilongjiang River in 2015 -2016 before breakup and successfully avoided breakup ice jams. Particularly, the precipitation during freeze up and before breakup was 51% and 74% higher than the annual average in 2015, respectively in 2016 the amount of precipitation in April was 77% higher than the multi-year average rainfall. Based on ice jam forecasting and field measures, the ice jam would potentially occur at the locations, where favorable conditions existed for the formation of ice jams. However, no ice jam occurred during breakup due to proactive ice blasting.

Acknowledgements
The authors are thankful for the financial support from the National Key Research & Development Plan of China (grant numbers 2017YFC0405103, 2017YFC0405704), IWHR Research & Development Support Program (grant numbers HY0145B642017, SKL2017CGS04, HY0145B912017), the Special Scientific Research Fund of Public Welfare Profession of China (grant numbers 201501025, 201301032) and the National Natural Science Foundation of China (grant number 51679263). The authors also appreciate the support from the Water Resources Department of Heilongjiang Province, the Support Centre of Flood Control and Drought Relief of Heilongjiang Province and the Mohe Hydrologic Administration during the ice blasting experiments.

References

(Beltaos S., 2008). River Ice Breakup. USA, Water Resource Publication, LLC., USA.
(Beltaos S., 1995). River ice jams. USA, Water Resource Publication, LLC., USA.
(Dai C. L., Yu C. G., Liao H. C., Zhang B. S., 2010). Survey and Forecast of River Ice. Beijing, China Water & Power Press., China. (In Chinese)
(Ding L. Q., He B. S., Yan X. G., 2010). New technology of breaking ice to ice prevention. Chinese Journal of flood control and Drought Relief, 2010, 2, 19-24. (In Chinese)
(Duan Y. S., Wang X. H., Liu S. B., 2003). Application of Blasting Technique to Against Ice Jam. Journal of Glaciology and Geocryology, 25(9), 250-226. (In Chinese)
(Guo X. L., Yang K. L., Fu H., Xia Q. F., Wang T., Yang S. H., 2017). Ice processes modeling during reverse water transfer of open canals: A case study. Journal of Hydro-environment Research, 17, 56-67.
(Liang X. Q., He B. S., Xie W. H., 2012). Experiment study on the blasting upon Thick Ice. Engineering Blasting, 18(2), 83-85. (In Chinese)
(Liang X. Q., Xiong F., Lu X. L., 2014). Experimental Research on Underwater Shock Wave Characteristic of Ice Blasting at Yellow River. Blasting, (4), 1-4. (In Chinese)
(Mellor M., 1987). Derivation of Guidelines for Blasting Floating Ice. Cold Regions Science and Technology, (13), 193-206.
(Shen H. T., 2003). Research on River Ice Processes, Progress and Missing Links. Journal of Cold Regions Engineering, (12), 135-142.
(Shen H., Knack I., 2015). Sediment transport in ice-covered channels. International Journal of Sediment Research, 30(1), 63-67.
(Shi R., Xu G. G., Liu D. R., Qin J., 2008). Underwater Test and Analysis for Explosion Energy of Explosives. Chinese Journal of Explosives & Propellants, 31(4), 1-5. (In Chinese)
(Sui J., Wang J, He Y., Krol F., 2010). Velocity profiles and incipient motion of frazil particles under ice cover, International Journal of Sediment Research, 25 (1), 39-51.
(Tong Z., Yang X. S., Xue P. X., 2012). Ice-Broken Explosion Mechanism of Yellow River// New blasting technology in China III. Beijing, Metallurgical Industry Press, 57-66. (In Chinese)
(United States Army Corps of Engineers, 1982). Breaking ice with explosives. Washington, DC, Cold Regions Research &Engineering Laboratory, USACE.
(United States Army Corps of Engineers, 2002). Ice Engineering, Engineering and Design. Washington, DC, Department of the Army, USACE.

(Wang J., Sui J. Y., Zhang H. Y., Chen P. P., Hirshfineld F., 2012). Mechanisms of ice accumulation in a river bend – an experimental study. International Journal of Sediment Research, 27(4), 521–537.
(Wang T., Yang K. L., Guo Y. X., 2008). Application of Artificial Neural Networks to Forecasting Ice Conditions of the Yellow River in the Inner Mongolia Reach. Journal of Hydrologic Engineering, 13(9), 811-816.
(Wang T., Yang K. L., Guo X. L., Fu, H., 2013). Freeze up water temperature forecast for the Yellow River using adaptive-networks-based fuzzy inference system. Proc., EWRI Word environment & water resources congress 2013(ASCE), Cincinnati, Ohio, USA, 2247-2260, 10.1061/9780784412947.221.
(Xia L. F., 2014). Research and Practice of Underwater Ice Jam Breaking by Manual-operated Blasting. Blasting, 31(2), 126-130. (In Chinese)
(Yu T. C., Wang X. F., Wang J. L., 2003). Underwater Shockwave Performance of Explosives, Energetic Materials, 11(4), 182-186. (In Chinese)
(Yin H. T., Yang X. H., Jiang M., Jin J. L., 2010). Experimental Research on Ice Breaking by Extended Blasting Cartridge under Ice. Engineering Blasting, 16(3),12-15. (In Chinese)

International Association for Hydro-Environment Engineering and Research

Supported by Spain Water and IWHR, China

24th IAHR International Symposium on Ice
Vladivostok, Russia, June 4 to 9, 2018

Scale effects in compressive strength of sea ice

Aleksey Marchenko[1,2], E. Karulin[3,2], M. Karulina[3,2], A. Sakharov[4,2], P. Chistyakov[4.2], D. Sodhi[5,2], A. Sliusarenko[6,2]

[1]The University Centre in Svalbard, Longyearbyen, Norway
[2]Sustainable Arctic Marine and Coastal Technology (SAMCoT), Centre for Research-based Innovations (CRI), Norwegian University of Science and Technology, Trondheim, Norway
P. O. Box 156 Longyearbyen, Norway
[3]Krylov State Research Centre, St.-Petersburg, Russia
[4]Moscow State University, Moscow, Russia
[5]Retired from Cold Regions Research Engineering Laboratory, Hanover, NH, USA
[6]Soft Engineering Co., Kiev, Ukrain
Aleksey.Marchenko@unis.no

Full-scale tests were conducted to determine compressive strength of in-situ ice beams by loading them horizontally over their entire thickness by a hydraulically operated loading platen with a capacity of exerting a maximum force of 60 tons (0.6 MN). The force and displacement signals from two hydraulic cylinders during ice compression were monitored and recorded at a sampling rate of 50 Hz. The tests were performed on sea ice in Spitsbergen region since 2013. The ice thickness during the tests ranged from 30 to 70 cm. Sea ice temperature and salinity were measured during and after each test. Small-scale, compressive-strength tests were performed on horizontal ice cores taken from the same ice. The ice strength from small-scale tests agrees reasonably well with existing data in the literature on ice strength. We found that the mean values of small-scale compressive strength and the full-scale compressive strength are in the same range of values for similar values of temperature and salinity averaged over the ice thickness. Uniaxial compressive strength obtained from full-scale tests with fixed-ends beams is greater by about two times the strength found from full-scale tests with short cantilever beams. Analysis of thin sections of ice is performed to analyze changes of the ice granular structure after the tests.

1. Introduction

Uniaxial compressive strength of ice is measured in a test by applying a load to an ice sample, which is not confined in transverse directions to that of the load. Compressive strength mainly depends on strain rate, temperature, salinity and structure of ice. Tests are usually performed at a strain rate of ~0.001 s^{-1}, because the compressive strength reaches its maximum at this strain rate (see, e.g., Timco and Weeks, 2010). Strain rates of the order 0.001 s^{-1} are also slightly above the strain rate separating the regimes of ductile and brittle modes of ice failure. Physical mechanism of the ductile-to-brittle transition is usually associated at a micro scale to the formation of wing cracks (Schulson and Duval, 2009). In brittle failure mode, the wing cracks are unstable and propagate according to LEFM. Productions of dislocations and displacements of grains are the physical mechanisms of ductile deformation and failure (Cole, 1995). Scale effect in ice strength is usually associated with presence of large-size cracks in a large sample and dependence of crack-growth criterion from large-size cracks. In full-scale experiments, spatial gradients of temperature, salinity and structure of ice samples also influence the failure scenario and thereby the ice strength.

Full-scale, uniaxial-compressive-strength tests were performed on sea ice during field works on drift ice in the Barents Sea by RV Mikhail Somov, organized by Artic shelf laboratory of AARI in 2003-2006. Results and description of these tests have not been published. A.Marchenko, E.Karulin and M.Karulina participated in these field works and observed the equipment and the experiments. In 2012 a similar rig was designed and constructed at UNIS, and since that time different full-scale tests were performed on land-fast ice of Ice Fjord and Van Mijen Fjord in Spitsbergen and on drift ice in the Barents Sea during the cruises with RV Lance. This research program includes full-scale-indentation tests (Karulin et al, 2014) and tensile-strength tests (Chistyakov et al., 2016). The rig was also used to perform fixed-ends-beam test (Marchenko et al, 2014) to determine compressive strength of ice (Sodhi, 1998).

Full-scale-indentation tests were performed in Canada (Croasdale, 1974; Croasdale et al, 1977), Japan (Tanaka et al., 1987; Sodhi et al, 1998), and Svalbard (Moslet, 2008; Karulin et al, 2014). In these tests, vertical indenters of cylindrical and flat shapes indented horizontally into an ice edge over the entire ice thickness. In "Nutcracker" test (Croasdale, 1974), the two loading legs having a diameter of 76 cm were hinged at the bottom and frozen into the ice at the surface of 5-m-deep water. Mean ice temperature and salinity averaged over the ice thickness were -12 C and 2 ppt. The legs could be pushed apart by three hydraulics rams, which were attached to the two legs at the top. The hydraulic rams were actuated by a gasoline-powered pump, which could supply fluid at a pressure of 70 MPa at various loading rates. The effective ice thickness near the legs was between 100 and 125 cm. Maximal ice pressure varied from 3.0 MPa to 6.1 MPa with a mean value of 4.7 MPa. The strain rate, calculated as the ratio of displacement rate to the diameter (v/D, D=76 cm), was in the range of 0.23×10^{-4} to 6.8×10^{-4} s^{-1} with a mean value of 2.62×10^{-4} s^{-1}. Representative loading rate in the full-scale experiment was 3 MPa/min. Uniaxial compressive strength, measured in the laboratory tests with loading rates varying from 16 to 33 MPa/min, were in the range of 0.93-3.83 MPa with a mean value of 2.07 MPa.

Full-scale tests with flat indenter were performed on freshwater lake ice (Croasdale et al, 1977). The flat indenter was 0.75 m wide and 1.0 m high and was pushed through the ice by means of four hydraulic rams acting against a reaction face 1.25 m wide and 1.0 m high. Ice surface temperature was in the range of -1.4 C and -17.8 C during the tests. The thickness of natural lake ice ranged from 74 to 99 cm. Three tests were performed with thin ice grown in test ponds and having a thickness in the range of 18-25 cm. Maximal ice pressure varied from 2.5 MPa to 4.95 MPa with a mean value of 3.55 MPa. The strain rate v/D varied from $0.68\text{x}10^{-4}\ s^{-1}$ to $32\text{x}10^{-4}\ s^{-1}$ with a mean value of $6\text{x}10^{-4}\ s^{-1}$. Two tests were performed with unconfined samples with the surface ice temperatures being in the range of –3.1 C and –3.3 C. Their stress under the compression was 0.94 MPa and 0.71 MPa at strain rates of $2.1\text{x}10^{-4}\ s^{-1}$ and $11\text{x}10^{-4}\ s^{-1}$.

In tests in Saroma Lagoon (Tanaka et al., 1987), a pile having a diameter of 54.5 cm and a height of 40 cm was pushed into ice by means of a hydraulic cylinder. Twelve tests were performed on the ice with thickness varying from 9.3 cm to 17 cm. Maximal ice pressure varied from 0.377 MPa to 11.5 MPa with a mean value of 2.4 MPa. The strain rate $v/4D$ varied from $0.87\text{x}10^{-4}\ s^{-1}$ to $66.5\text{x}10^{-4}\ s^{-1}$ with a mean value of $22.1\text{x}10^{-4}\ s^{-1}$. The ice temperature varied from -1.9 C to -5.2 C with a mean value of -3.02 C. Average ice salinity was 8 ppt. Distribution of ice pressure was investigated in the experiment using load cells embedded in the indenter.

In tests in Lake Notoro (Sodhi et al., 1998), the flat-segmented indenter was 1.5 m wide, with provisions to increase it to 3 m. The apparatus had a displacement control and a hydraulic servo-jack controlling the speed of indenter. Twenty-three tests were performed on sea ice with thickness ranging from 18.6 cm to 28.9 cm. Maximal ice pressures varied from 0.226 MPa to 2.84 MPa with a mean value of 0.85 MPa. Indentation speeds were 0.3, 3 and 30 mm s^{-1}. Ice failure was ductile at the indentation speed of 0.3 mm s^{-1}, and brittle at indentation speeds of 3 and 30 mm s^{-1}.

In the medium-scale ice-structure-interaction test (Moslet, 2008), the sea ice had a thickness in the range of 16-26 cm frozen in the test pool towed against a vertical, 0.655-m-diameter cylinder. Two experiments were performed in 2003 and 2004. In 2003, the maximal ice pressures of 0.173 MPa and 1.542 MPa were found, when the ice thickness, temperature and salinity were, respectively, 20 cm, -2.5 C, 10.7 ppt and 16-20 cm, -4 C, 7.1 ppt. The displacement rates of ice floes were 8 and 3.5 mm s^{-1}. In 2004, the maximal ice pressures of 0.15 MPa and 0.87 MPa were found, when the ice thickness, temperature and salinity were, respectively, 10 cm, -1.7^{o}C, 10.8 ppt and 16 cm, -4.3^{o}C, 8.1 ppt. The displacement rates of the floes were 8 and 6.2 mm s^{-1}. The average uniaxial compressive strength was 1.8 MPa.

In this present paper, full-scale tests on uniaxial compression of ice and edge indentation of ice sheet are described, and the test results are analyzed and compared with existing information on similar full-scale tests. The test results are compared with compression strength obtained from tests with fixed-ends beams and small scale tests on uniaxial compression of ice cores. All tests were performed on land fast ice in Svea Bay of the Van Mijen Fjord on the west coast of Spitsbergen and on the drift ice in a region east of Edgøya.

2. Experimental Procedure

The equipment for full-scale ice-strength tests has been designed and made under the support of SAMCoT project. The rig, shown in Fig. 1a, consists of a vertical semi-cylindrical or flat indenters connected to two horizontal hydraulic cylinders (Enerpack), each equipped with a displacement sensor and a load cell. Upper and down cylinders are A and B, respectively. Cylinder A is visible in Fig. 1a, whereas the cylinder B is underwater. The cylinders are connected to an electrical pump, powered by a three-phase 400-Volt generator. The stroke of a hydraulic cylinder is 37 cm, and it has a load capacity of 300 kN. The rig is mounted on a steel frame by blocks and tackles, which are used for lowering the indenter into a hole in an ice sheet. The rig, frame, electrical pump, field computer and generator are placed on three sledges and can easily be transported to different places in a program of field tests. It is powered by electrical engine working from two phase 220-V generator. Recorded during a test, the data include loads, stroke and oil pressure in each cylinder. The data are recorded at a sampling rate of 100 Hz on a hard disk of the field computer and also at a sampling rate of 50 Hz on a data logger CR6. The backup of data storage helps to avoid a loss of data in a cold environment.

To conduct a full-scale uniaxial compression (FSUC) test, the load is applied to vertical face of a cantilever beam, having a length of less than 1 m, by a flat indenter having a width of 60 cm and a height of 80 cm. In the full scale tests with fixed-ends beams, the load is applied in the middle of a beam by one of three ways: (a) horizontal force by a vertical cylindrical indenter of 15 cm in diameter and 80 cm in height (FSFEBH1) (Fig. 2a), (b) horizontal force by two vertical pipes of square cross-section mounted on the flat indenter (FSFEBH2) (Fig. 2b), or (c) by vertical force by an indenter being pushed down by a hydraulic cylinder mounted on the π-shape frame fixed to the ice by chains with anchors (FSFEBV) (Fig. 2c). The equipment shown in Fig. 2c is also used for flexural-strength tests with cantilever beams (Karulina et al, 2013; Marchenko et al, 2017). FSFEBV tests are similar to laboratory tests by Sodhi (1998) for an investigation of bearing capacity of floating ice sheets. The length of beams during fixed-ends-beam tests should be equal to, or longer than, six times the ice thickness and the beam width. During such tests with long beams the initial failure of a beam occurs by formation of one central crack and two root cracks (Fig. 2a,b), and then the beam fails by uniaxial compression in the middle around the loading points (white area in the front of flat indenter and between the loading points in Fig. 2b). FSFEBH1 and FSFEBH2 tests allow one to observe the beam failure during a test because the deformation of ice and propagation of cracks takes place in the horizontal plane. FSFEBH2 test helps to avoid indentation effects in the middle of the beam where maximal compressive stress is reached. In the full-scale indentation tests (FSI), the cylindrical indenter of 15 cm in diameter and 80 cm in height is pushed into an ice edge by two hydraulic cylinders in a horizontal direction (Fig. 3).

The full-scale tests were performed together with small-scale tests on uniaxial compression of ice cores in the field conditions since 2012 (Fig. 1b). Small-scale tests on uniaxial compression (SSUC) of ice cores were performed with the rig Kompis designed for the use in field conditions (Moslet, 2007). For small-scale tests, horizontal and vertical cores are taken from the ice with an (Kovacs) ice-coring auger, having an inner diameter of 7.25 cm. 15-cm-long samples were prepared with a two-disks saw having parallel blades. The load and displacement during a small - scale test were recorded at a sampling rate of 10 Hz in the field laptop connected to the rig

Kompis. Deformation of an ice cores was also measured with a strain sensor (Epsilon-Tech Averaging Axial Extensometer Model 3542RA2-050M-600M-ST) mounted at four pins on the sides of an ice sample (Fig. 1b), and the data were recorded on the data logger CR1000 at a sampling frequency of 50 Hz. Number of small-scale tests performed in each field expedition is usually much higher than the number of large-scale tests, because it takes a long time to prepare a large-scale sample. In SSUC tests, the boundary conditions at both ends of the ice cores are similar. The confinement at the core ends is related to ice friction with metal plates of the Kompis rig compressing a sample (Fig. 1b). In FSUC tests, the beam root had a radius of curvature to avoid stress concentration.

(a) (b)

Fig. 1. In-situ, full-scale, uniaxial-compression test (FSUC) (a) and small-scale, uniaxial-compression (SSUC) test (b).

Ice temperature during a full-scale test was measured with a thermistor string (GeoPrecision) placed in a blind 2-cm-diameter hole drilled close to the beam root (Fig. 1a). Distance between neighboring thermistors was 3-5 cm. Ice temperature in the small-scale tests was measured with a temperature probe immediately after each test. To obtain a salinity profile in natural ice and ice cores, ice samples were taken at different depths and delivered in plastic boxes to a warm place for melting. Later, salinity of melt water is measured with a (Toledo) salinity meter.

(a) (b) (c)

Fig. 2. Test with fixed-ends beams: horizontal loading with cylindrical indenter (FSFEBH1) on 16.04.2014 (a), horizontal two points loading with flat indenter (FSFEBH2) on 27.03.2017 (b) and vertical loading (FSFEBV) on 14.03.2013 (c).

(a) (b)

Fig. 3. Full-scale-indentation test (FSI). Initial position of a cylindrical indenter (a). Ice failure under an action of the indenter (b).

3. Results

Figures 4-8 show photographs of tests and plots of displacements and loads versus time during FSUC tests. Information on ice characteristics and tests results is listed in Table 1 since 2015; where h is the ice thickness, L and b are the beam length and width; T and S are the temperature and salinity averaged over the ice thickness. The strain rate is calculated using the following expression:

$$e_{FS} = v / L , \tag{1}$$

where v is the mean speed of indenter. During most of FSUC tests, brittle spalling of surface layer of ice was observed to take place but not at the bottom portion of an ice sheet.

In the test shown in Fig. 4, the beam failed when a vertical crack extended from the corner of the loaded face of the beam to the middle of the beam near the root. Total load didn't drop after the reaching of maximal value because of the resistance in the beam root. Figure 5 shows ductile failure of the beam with significant deformations in a part of the beam. Figures 6-8 show brittle failure of the beams accompanied by the spalling of the surface ice layer and formation of longitudinal cracks.

Tables 2 and 3 list mean values of the ice characteristics and tests results in SSUC tests performed with vertical and horizontal ice cores since 2013. Table 4 shows the ice characteristics and tests results in FSFEBV, FSFEBH1 and FSFEBH2 tests performed since 2012. Type of the test is indicated by the symbols v, h1 or h2. Compressive strength and strain rate are calculated with the formulae (Sodhi, 1998)

$$\sigma_{\mathrm{B}} = \frac{F \cdot L}{4bh^2 \beta (1-\beta)} , \; e = \frac{12hv}{L^2} , \tag{2}$$

where F is the maximum load applied on the beam, v is the mean speed of indenter. A value $\beta = 1/3$ is assumed from the condition that the central and root cracks extend about 2/3 of the ice thickness h. In our tests the cracks depths were different, but we assume that their mean value is about $(2/3)h$ and use $\beta = 1/3$ in formula (2).

(a) (b)

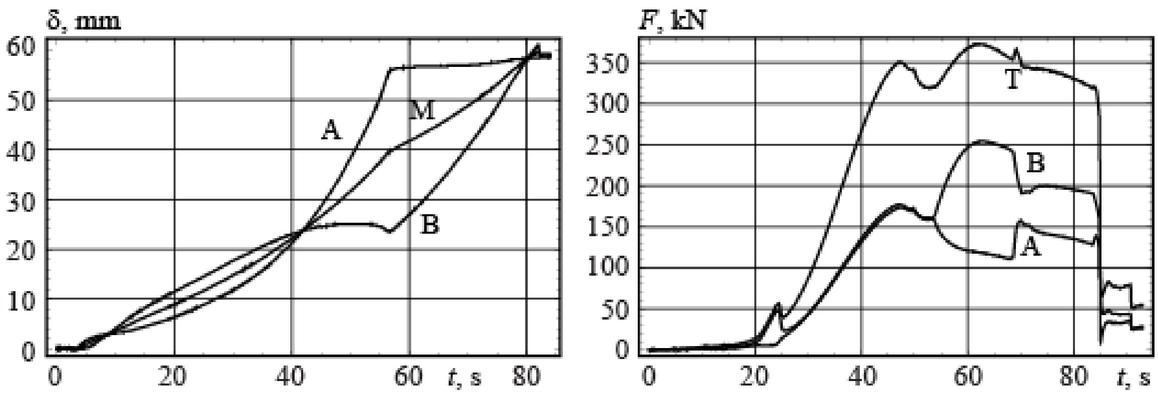

c) d)

Fig. 4. Photographs of ice beam during FSUC test on 03.03.2016 (a,b). Plots of the displacements and loads on the cylinders A and B versus the time (c,d). Lines M and T show plots of the mean displacement and the total load, respectively.

Table 5 lists ice characteristics and tests results in FSI tests performed since 2013. The indentation pressure and strain rate are calculated using the following expressions (Sanderson, 1998)

$$\sigma_{\mathrm{I}} = F_{\max} / (hD), \; e_{\mathrm{I}} = v / (2D), \quad (3)$$

where $F_{\max}$ is the maximum value of the total applied load, and v is the mean value of the indentation speed.

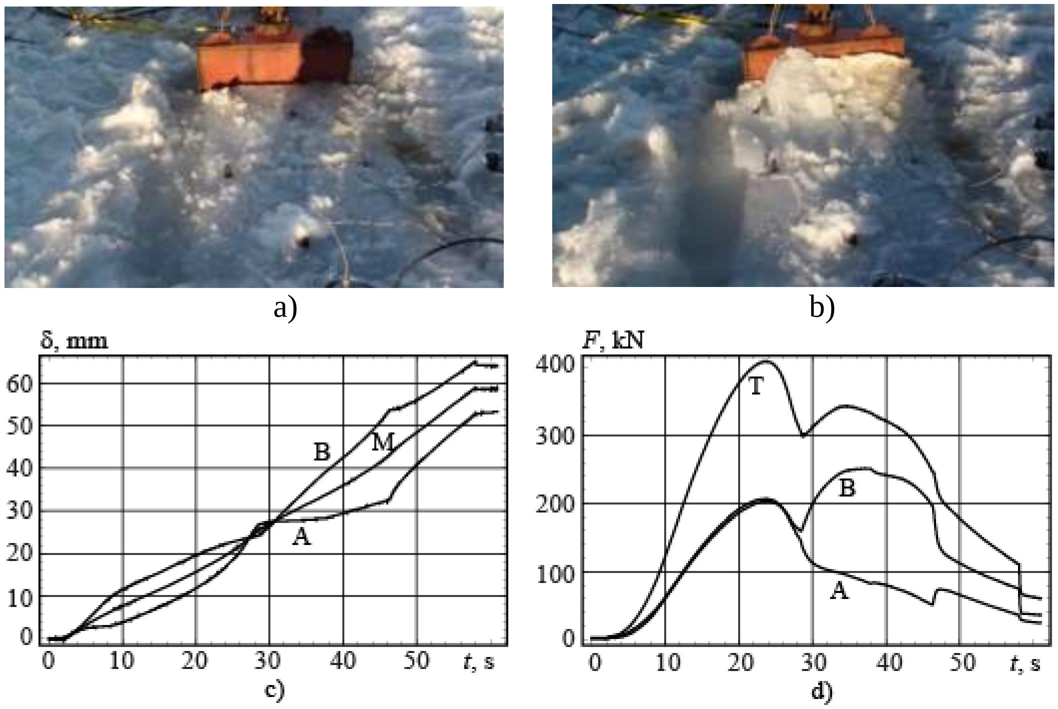

Fig. 5. Photographs of ice beam during FSUC test on 08.03.2016 (a,b). Plots of the displacements and loads on cylinders A and B versus time (c,d). Lines M and T show the mean displacement and the total load, respectively.

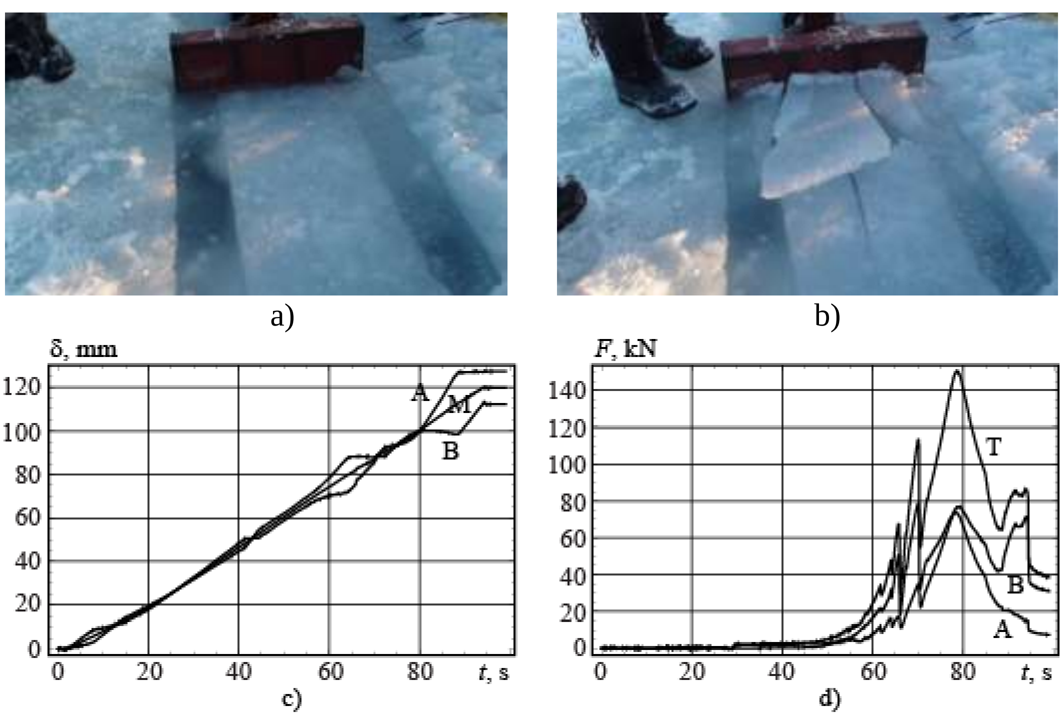

Fig. 6. Photographs of ice beam in FSUC test on 09.03.2016 (a,b). Plots of the displacements and loads on the cylinders A and B versus the time (c,d). Lines M and T show plots of the mean displacement and the total load, respectively.

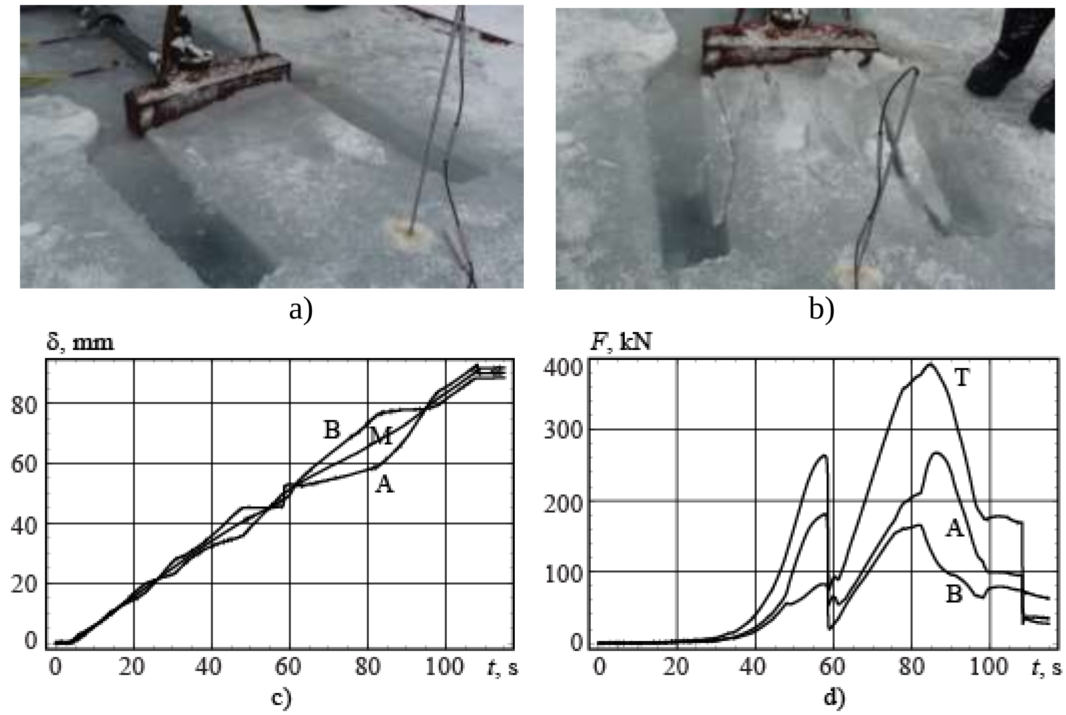

Fig. 7. Photographs of ice beam in FSUC test on 24.03.2017 (a,b). Plots of the displacements and loads on the cylinders A and B versus the time (c,d). Lines M and T show plots of the mean displacement and the total load, respectively.

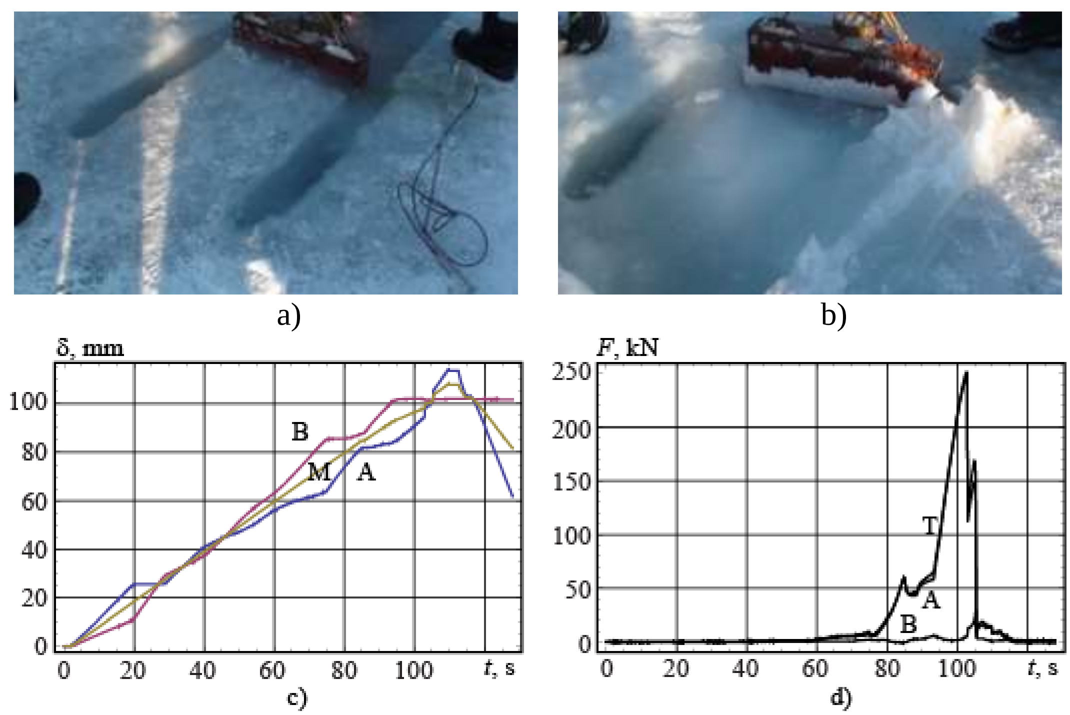

Fig. 8. Photographs of ice beam in FSUC test on 29.03.2017 (a,b). Plots of the displacements and loads on the cylinders A and B versus the time (c,d). Lines M and T show plots of the mean displacement and the total load, respectively.

Table 1. Results of full-scale, uniaxial-compression tests on ice.

N	Date	L,m	h,m	b,m	T,C	S,ppt	e_{FS}, s^{-1} ($\times 10^{-4}$)	σ_{FS},MPa
1	14.03.2015	1.41	0.71	0.71	-3.6	4.7	3.6	0.588
2	18.03.2015	0.80	0.73	0.50	-4.2	5.1	5.5	0.836
3	03.03.2016	1.00	0.58	0.60	-2.83	4.4	5.5	1.345
4	08.03.2016	1.00	0.60	0.63	-2.41	4.4	10	1.081
5	09.03.2016	0.81	0.58	0.40	-2.41	4.4	16	0.648
6	24.03.2017	0.80	0.55	0.59	-4.53	4.6	10	1.206
7	29.03.2017	0.80	0.58	0.60	-7.00	4.4	9.4	1.267

Table 2. Mean values of ice characteristics and uniaxial compressive strength in the tests with vertical ice cores

N	Date	T,C	S,ppt	e_{SSH}, s^{-1} ($\times 10^{-4}$)	σ_{SSV},MPa
1	13.03.2013	-9.6	7.8	n	2.25
1	02.04.2014	-5.4	4.94	n	0.84
2	17-18.03.2015	-2.76	5.38	7.0	0.97
3	08-09.03.2016	-3.3	4.04	7.2	4.85
4	28.03.2017	-11.5	3.59	6.95	8.31

Table 3. Mean values of ice characteristics and uniaxial compressive strength in the tests with horizontal ice cores

N	Date	T,C	S,ppt	e_{SSH}, s^{-1} ($\times 10^{-4}$)	σ_{SSH},MPa
1	02.04.2014	-7.6	4.3	n	0.58
2	08-09.03.2016	-2.4	4.53	6.4	1.2
3	28.03.2017	-9.6	4.12	n	3.89

Table 4. Results of uniaxial-compression tests performed on long, fixed-ends beams

N	Date	L,m	h,m	b,m	T,C	S,ppt	v,mm/s	e_B, s^{-1} ($\times 10^{-4}$)	σ_B,MPa
1v	26.03.2012	5.21	0.63	0.5	-4.5	5	n	n	2.1
2v	22.04.2012	2.09	0.23	0.65	-4.0	7	n	n	1.0
3v	22.04.2012	2.09	0.23	0.65	-4.0	7.5	n	n	1.5
4v	09.03.2013	7.00	0.73	0.72	-8.0	5.4	3	5.4	2.2
5v	14.03.2013	7.00	0.76	0.64	-8.0	5.4	2.80	5.2	2.2
6h1	26.03.2014	4.05	0.53	0.50	-8.0	4.0	0.90	2.8	4.33
7h1	03.04.2014	6.00	0.49	0.60	-8.0	4.0	2.10	3.4	1.43
8h2	27.03.2017	4.20	0.60	0.60	-6.5	5.14	0.87	3.5	2.92

Table 5. Results of indentation tests

N	Date	h,m	R	T,C	S,ppt	v,mm/s	e_I, s^{-1} ($\times 10^{-3}$)	σ_I,MPa
1	07.03.2013	0.65	0.23	-6.6	5-7	0.56	1.87	6.22
2	12.03.2013	0.73	0.21	-8.7	5-7	0.07	0.23	5.35
3tp	14.03.2013	0.18	0.83	-9.9	5-7	3.95	13.16	4.33
4tp	14.03.2013	0.18	0.83	-9.9	5-7	3.03	10.1	4.27
5BS	28.04.2013	0.39	0.38	-2.0	5.5	1.10	3.67	3.95
6BS	29.04.2013	0.50	0.30	-2.0	6.1	1.55	5.17	4.61
7BS	29.04.2013	0.53	0.28	-2.0	6.1	0.95	3.17	3.77
8BS	29.04.2013	0.50	0.30	-2.0	6.1	0.99	3.30	3.91
9	02.04.2014	0.43	0.35	-4.5	6.1	0.85/0.26	2.84/0.855	4.75/3.44
10	11.03.2015	0.72	0.20	-3.6	5.0	0.05	0.16	2.61
10'	11.03.2015	0.72	0.20	-3.6	5.0	0.37	1.23	4.63
11	18.03.2015	0.73	0.20	-3.5	5.7	0.35	1.16	3.88
12	02.03.2016	0.58	0.26	-2.8	4.38	0.75	2.50	4.76
12'	02.03.2016	0.58	0.26	-2.8	4.38	0.46	1.53	3.77
13	07.03.2016	0.59	0.25	-2.4	4.38	0.40	1.33	5.25
14	08.03.2016	0.59	0.25	-2.5	4.5	0.45	1.50	4.94
15	23.03.2017	0.69	0.22	-3.97	4.34	0.71	2.36	4.87
16	29.03.2017	0.56	0.27	-6.36	4.38	1.67	5.56	5.33

4. Discussion

The mean values of ice temperature, salinity, strain rate and strength in FSUC tests are -3.85 C, 4.57 ppt, $8.57 \mathrm{x} 10^{-4}\ \mathrm{s}^{-1}$ and 1 MPa, respectively. The mean values of ice temperature, salinity and strength in SSUC tests on horizontal samples are -6.5°C, 4.32 ppt and 1.89 MPa, respectively. The mean value of strain rates in SSUC tests on vertical and horizontal samples is $6.89 \mathrm{x} 10^{-4}\ \mathrm{s}^{-1}$. Thus the mean ice temperature is higher and the mean strain rate is lower in FSUC tests in comparison to those in SSUC tests, while the ice salinities are similar. Further, we compare FSUC and SSUC strengths with the formula of Timco and Frederking for the uniaxial compressive strength of horizontally loaded columnar ice (Timco and Weeks, 2010) and with the formula of Moslet for maximal strength in SSUC tests (Moslet, 2006)

$$\sigma_h = 37e^{0.22}(1-\sqrt{v_T / 270}),\ 10^{-7}\mathrm{s}^{-1} \le e \le 2\cdot 10^{-4}\mathrm{s}^{-1}, \tag{4}$$

$$\sigma_{h,\max} = 8(1-\sqrt{v_T / 700})^2,\ 7\cdot 10^{-4}\mathrm{s}^{-1} \le e \le 1\cdot 10^{-3}\mathrm{s}^{-1}, \tag{5}$$

where e is the strain rate, and v_T is the ice porosity. Instead of the porosity v_T, we use the following expression to obtain the liquid brine content (Frankenstein and Garner, 1967)

$$v_b = S\left(-\frac{49.185}{T} + 0.532\right),\ -0.5^\circ\mathrm{C} \ge T \ge -22.9^\circ\mathrm{C}. \tag{6}$$

The ratios of ice strength, as obtained by equation 3 for the same values of strain rates and liquid brine content as those found in ice samples, to measured values of FSUC and SSUC are defined as:

$$R_{FS} = \frac{\sigma_h}{\sigma_{FS}}, \; R_{SS} = \frac{\sigma_h}{\sigma_{SS}}. \tag{7}$$

The liquid brine contents are calculated using the data listed in Tables 1 and 3. The strain rates for the calculation of R_{FS} are taken from Table 1. Ratios R_{SS} are calculated using three values of σ_{SS} in Table 3 with two values of strain rates $6 \times 10^{-4}\ s^{-1}$ and $7 \times 10^{-4}\ s^{-1}$. Figure 9a shows values of R_{FS} and R_{SS} in a 3-D plot with respect to liquid brine content and strain rate. Values of σ_{FS} and σ_{SS} are compared with σ_h ($e_{SSH} = 7 \times 10^{-4}\ s^{-1}$) and $\sigma_{h,\max}$ in Fig. 9b. The mean value of R_{FS} is 4.2, and the mean value of R_{SS} is equal to 4.02 when $e_{SSH} = 6 \times 10^{-4}\ s^{-1}$, and 4.16 when $e_{SSH} = 7 \times 10^{-4}\ s^{-1}$. Scale effect is not discovered between measured values of FSUC and SSUC strength. Measured values of FSUC strength are smaller than maximum compressive strength measured in SSUC tests by Moslet (2006) by a factor of 4.2.

Figure 10a shows FSI strength to be higher than FSUC and FSFEB strengths. Indentation tests were performed at higher strain rates. Figure 10b shows that FSI strengths are within the range specified by formulas (4) and (5) for SSUC strengths σ_h (solid black lines in Fig. 10b) and $\sigma_{h,\max}$ (dashed line in Fig. 10b). Numbers in Fig. 10b show values of strain rate in $10^{-4}\ s^{-1}$. FSFEB tests show higher strength in comparison to those in FSUC tests within similar ranges of the liquid brine content and strain rate (Fig. 10b). Dependence of FSUC and FSFEB strength with respect to liquid brine content are approximated by a best-fit line (black and red lines in Fig. 10b)

$$\sigma_{FS} = 1.34 - 0.005 \cdot \nu_b, \; \sigma_B = 3.36 - 0.022 \cdot \nu_b, \tag{8}$$

where the units of σ_{FS} and σ_B are in MPa, and ν_b is in ppt.

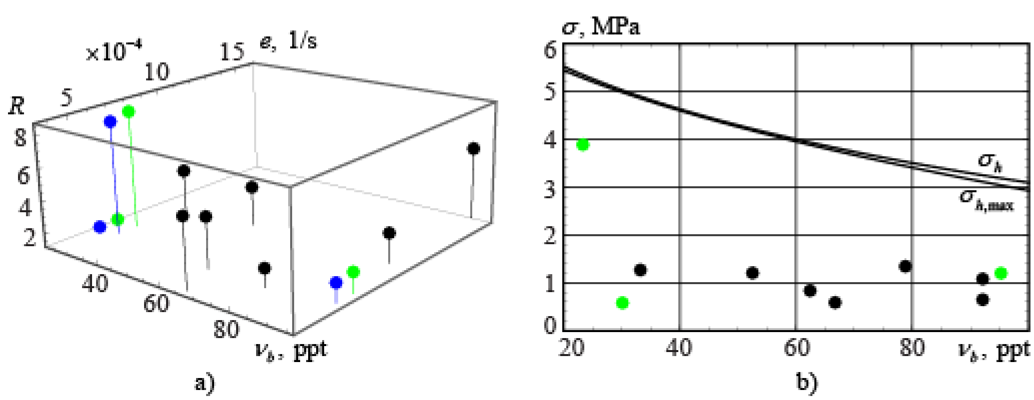

Fig. 9. Ratios R_{FS} (black point) and R_{SS} (blue and green points) versus the strain rate and liquid brine content (a). FSUC and SSUC strengths versus the liquid brine content (b). Blue and green points are calculated with strain rates equal to $6 \times 10^{-4}\ s^{-1}$ and $7 \times 10^{-4}\ s^{-1}$, respectively.

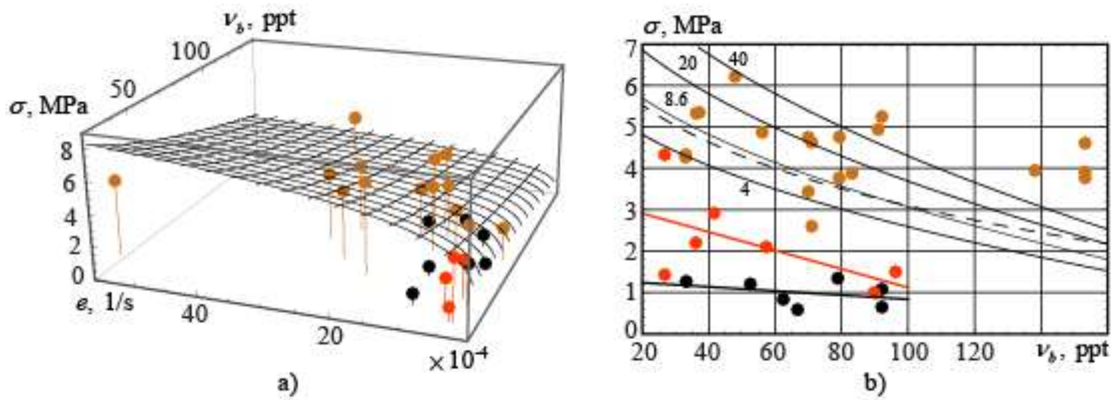

Fig. 10. FSUC (black points), FSFEB (red points) and FSI (brown points) strengths versus the liquid brine content and strain rate (a), and the same versus the liquid brine content (b).

Figure 11 shows results of FSI tests including the tests discussed in the Introduction. In all tests the strain rate was calculated according to the formula $v/2D$. "Nutcracker" tests were performed at a very low strain rates and on almost freshwater ice. In these tests the ice was frozen to the indentation pipe. The mean aspect ratio ($R = D/h$) equals 0.68. The mean aspect ratio in the Saroma Lagoon tests was around 4. In the Moslet's experiments the aspect ratio varied from 3.27 to 6.55. The aspect ratio in Spitsbergen tests (2013-2017) varies from 0.2 to 0.83 (Table 5). Figure 11b shows that FSI strength decreases with an increase of liquid brine content. This dependence is approximated by linear best-fit line:

$$\sigma_I = 5.36 - 0.016 \cdot \nu_b, \tag{9}$$

where σ_I is given in MPa, and ν_b is measured in ppt.

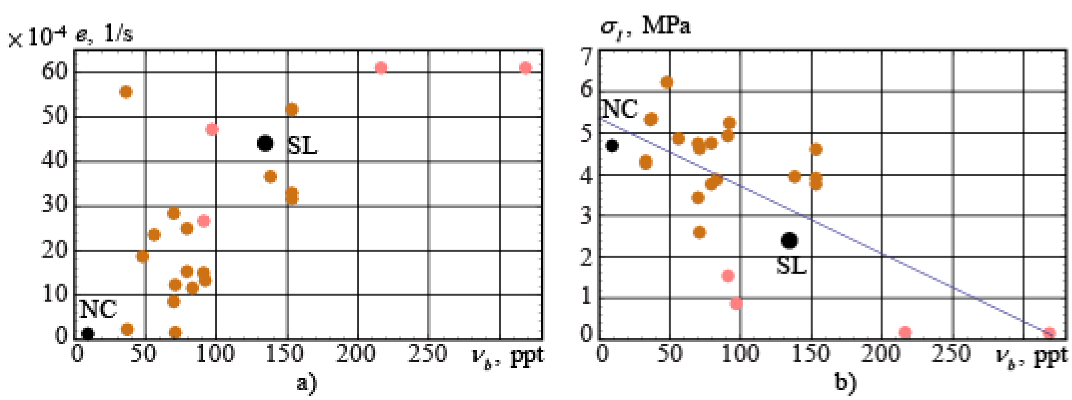

Fig. 11. Strain rates versus liquid brine content in FSI tests (a). FSI strength versus liquid brine content (b). NC -"Nutcracker" test (Croasdale, 1974) ; SL - Saroma Lagoon tests (Tanaka et al., 1987); Spitsbergen tests 2003, 2004 (Moslet, 2008) and Spitsbergen tests 2013-2017 (brown points),

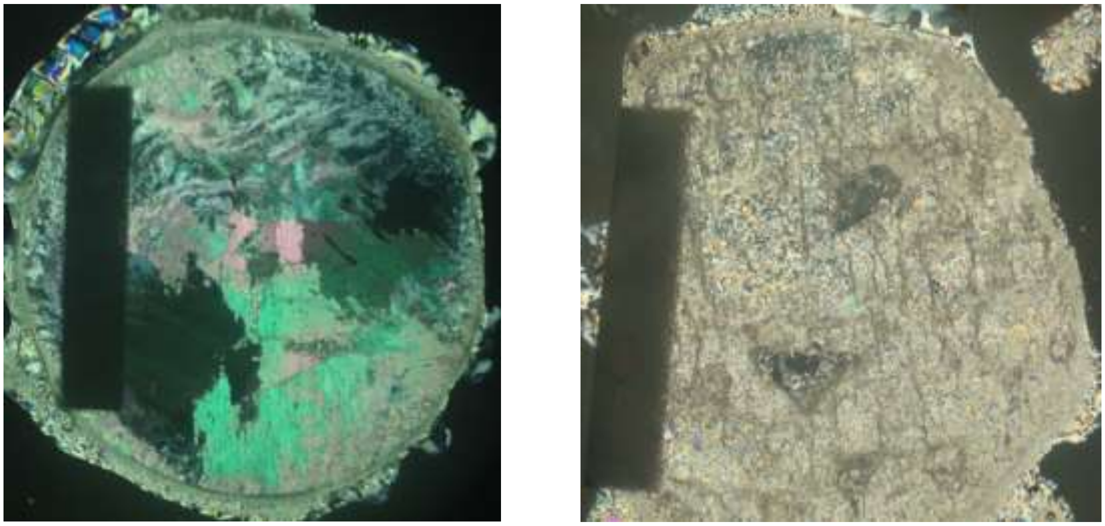

Fig. 12. Horizontal thin sections of natural ice (left panel) and of ice taken from compression zone of FSFEBH2 test (right panel), March 27, 2017.

Analysis of thin sections show a decrease of grain size in the compression zones of FSFEB tests and FSI tests. The left panel of Figure 12 shows horizontal thin section of natural sea ice at the location of field works on March 27, 2017. The right panel shows a horizontal thin section taken from the compression zone of the FSFEBH2 test visible in Fig. 2b as white triangular region in the front of flat indenter. Figure 13 shows a horizontal slab of ice taken in the front of cylindrical indenter. Semicircular surface belongs to the indenter-ice interface. Changes in granular structure of ice in the front of the indenter are visible as a matted region. Figure 14 shows thin sections taken from square regions 1 and 2 of Fig. 13. The left panel of Fig. 14 shows transition zone between natural ice (from the right) and deformed ice (to the left) with smaller grain sizes. The right panel shows compressed zone adjacent to the indentation surface. Semicircular zone of about 1 cm thickness extended along the indentation surface is visible in the right panel of Fig. 14. This zone is also visible near the semicircular edge surface of ice cut in Fig. 13.

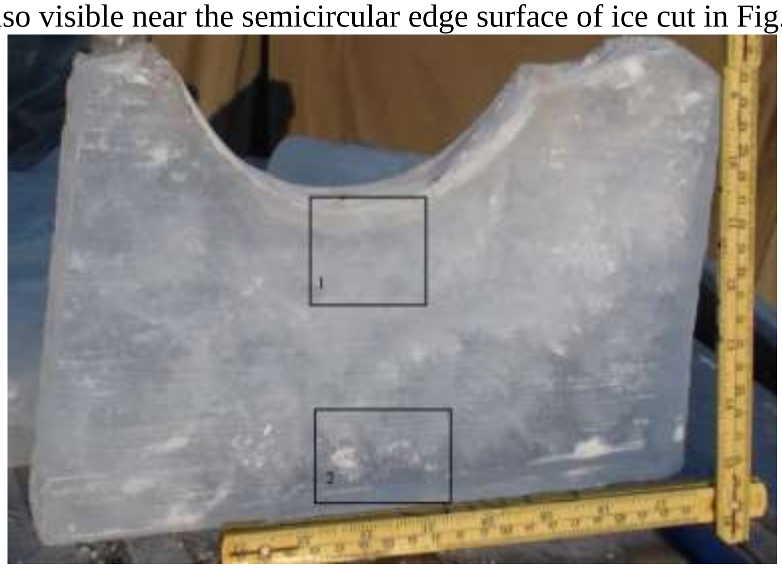

Fig. 13. Photograph of horizontal section of the compression zone near the indentation surface. Squares 1 and 2 point the locations of regions from where samples were taken for thin section analysis.

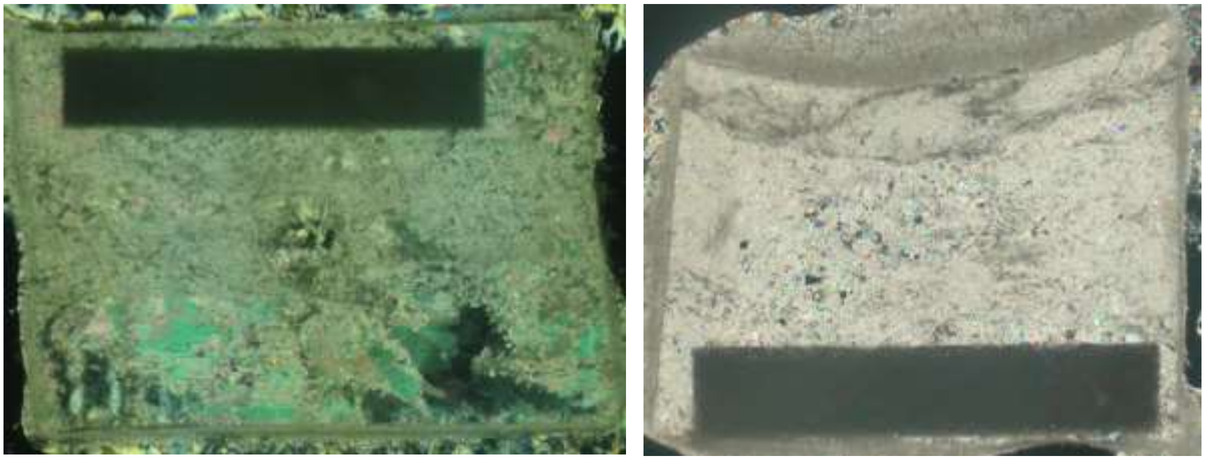

Fig. 14. Thin sections taken from square regions 1 and 2 shown in Fig. 13. Left panel: Transition zone between natural ice and compressed ice (square 2). Right panel: Compressed ice near the indentation surface (square 1).

5. Conclusions

Uniaxial compressive strength obtained from small-scale tests with ice cores and full scale tests with short cantilever beams are in the same range of values. The scale effect is not discovered in this case. Uniaxial compressive strength obtained from full-scale tests with fixed-ends beams is greater by about two times the strength found from full-scale tests with short cantilever beams. Analysis of thin sections shows a decrease in grain size in a compression zone of the full-scale test with fixed-ends beams. This effect is not observed in the full-scale tests with short cantilever beams, which usually split by macro cracks in several patterns without changes of their granular structure. Indentation pressures found from full-scale indentation tests are similar to maximal strength registered in small-scale uniaxial compression tests. Higher values of the indentation pressure in comparison to the full-scale, uniaxial-compression strength are attributed to the influence of lateral confinement of ice in the indentation tests.

Acknowledgments
The authors wish to acknowledge the support of the Research Council of Norway through the Centre for Sustainable Arctic Marine and Coastal Technology (SAMCoT) and AOCEC project of IntPart program.

References

Cole, D.M.,1995. A model for the anelastic straining of saline ice subjected to cyclic loading. *Philosophical Magazine* A, 72(1), 231-248.

Croasdale, K., R., I974. Crushing strength of Arctic Ice. Proceedings of a symposium on Beaufort Sea coast and shelf research. Reed, J.C. and Sater, J.E. (ed), Arlington, Virginia, Arctic Institute of North America, 377-399.

Croasdale, K., R., I977. Indentation tests to investigate ice pressures on vertical piers. J. Glaciology, V. 19, 81, 301-312.

Chistyakov, P., Karulin, E., Marchenko, A., Sakharov, A., Lishman, B., 2016. The tensile strength of saline and freshwater ice in field tests. *Proc. of the 23rd IAHR Symposium on Ice*, Ann Arbor, Michigan, paper 4872921.

Karulina, M., Karulin, E., Marchenko, A., 2013. Field investigations of first-year ice mechanical properties in North-West Barents Sea. POAC13-049, Espoo, Finland.

Karulin, E., Marchenko, A., Karulina, M., Chistyakov, P., Sakharov, A., Ervik, A., Sodhi, D., 2014. Field Indentation Tests of Vertical Semi-Cylinder on First-Year Ice. *Proc. of the 22th IAHR Symposium on Ice*, Singapore, paper 1125.

Marchenko, A., Karulin, E., Chistyakov, P., Sodhi, S., Karulina, M., Sakharov, A., 2014. Three dimensional fracture effects in tests with cantilever and fixed ends beams. Proc. of the 22th IAHR Symposium on Ice, Singapore, paper 1178.

Marchenko, A., Karulina, M., Karulin, E., Chistyakov, P., Sakharov, A., 2017. Flexural Strength of Ice Reconstructed from Field Tests with Cantilever Beams and Laboratory Tests with Beams and Disks. POAC17-177.

Moslet, P.O., 2007. Field testing of uniaxial compression strength of columnar sea ice.
Cold Regions Science and Technology, 48 (1), 1–14.

Moslet, P.O., 2008. Medium scale ice-structure interaction. *Cold Regions Science and Technology*, 54(2), 143-152.

Sanderson, T.J.O., 1998. Ice Mechanics. Risks to Offshore Structures. Graham & Trotman.

Schulson, EM., Duval, P , 2009. Creep and fracture of ice. Cambridge University Press, 401.

Sodhi, D.S., 1998. Vertical penetration of floating ice sheets. *International Journal of Solids and Structures*, 35 (31-32): 4275-4294.

Sodhi, D.S., Takeuchi, T., Nakazawa, N., Akagawa, S.,Kato, K., Kamesaki, K., Saka, K., Kurokawa, A., 1998. Medium-scale indentation tests on sea ice at various speeds. *Cold Regions Science and Technology*, 28, 161-182.

Tanaka, S., Sasaki, K., Saeki, H., 1987. The distribution of ice pressure acting on a pffshore circular pile. POAC-87, Fairbank, Alaska, V.1, 376-382.

Takeuchi, T., Masaki, T., Akagawa, S., Kawamura, M., Nakazawa, N., Terashima, T., Honda, H., Saeki, H., Hirayama, K., 1997. Medium-scale field indentation tests _MSFIT.: ice failure characteristics in ice/structure interactions. Proceedings, 7th International Offshore and Polar Engineering Conference, Honolulu, USA, Vol. II, pp. 376–382.

Timco, G.W., Weeks, W.F., 2010. A review of the engineering properties of sea ice. *Cold Regions Science and Technology*. 60, 107-129.

International Association for Hydro-Environment Engineering and Research

Supported by
Spain Water and IWHR, China

24th IAHR International Symposium on Ice
Vladivostok, Russia, June 4 to 9, 2018

Influence of the Water Temperature on Thermodynamic Consolidation of Ice Rubble

Aleksey Marchenko
[1]*The University Centre in Svalbard, Longyearbyen, Norway*
[2]*Sustainable Arctic Marine and Coastal Technology (SAMCoT), Centre for Research-based Innovations (CRI), Norwegian University of Science and Technology, Trondheim, Norway*
P.O.Box 156 Longyearbyen, Norway
Aleksey.Marchenko@unis.no

In the present paper the equations describing thermodynamic consolidation of ice rubble are formulated, model solutions are investigated and the time necessary for full consolidation of ice rubble is estimated depending on oceanic heat flux. Results of two laboratory experiments on thermodynamic consolidation of ice rubble submerged in sea water with different initial temperatures are also discussed in the paper. In the experiments cylindrical vessels filled with a mixture of ice rubble and water were insulated from the sides and from the bottom and placed in the cold room with temperature -5 C. Durations of the experiments were 12 hours and 15 hours. It was discovered that over the time of the experiments ice rubble submerged in the water with temperature above the freezing point consolidated faster than ice rubble submerged in the water at the freezing point.

1. Introduction

Ice ridges are formed due to the compression of ice floes. Ice blocks broken from the floe edges are pushed in the water below the surrounding ice and on the ice surface. Vertical sizes of ice ridges exceed the level ice thickness significantly and can reach in the Barents Sea 10-20 m (Marchenko et al., 2016). Thermodynamic consolidation influences the formation of consolidated layer inside ice ridges. It occurs due to several physical processes including atmosphere cooling (see, e.g., Høyland, 2002), release of cold reserves from submerged block (Hoyland and Liferov, 2005) and penetration of fresher water inside ridge keels (Shestov and Marchenko, 2016). The thickness of consolidated layer inside the first-year ice ridges is less than doubled thickness of level ice formed in similar weather conditions, while multiyear ice ridges can be fully consolidated (Høyland et al, 2008; Sudom et al., 2011).

The heating of ice rubble from below influence ice melt and rise up of melt water into the ice rubble. Melt water has lower salinity then sea water. Therefore a part of the melt water should be frozen inside the rubble with lower temperature. The model of this process was formulated by Marchenko et al (2016) in the case when ice rubble temperature is lower the water temperature below the rubble, i.e. when ice rubble drifts into a region with warm water. The rubble was considered as thermally insulated system which temperature increases due to the influx of melt water and thermodynamic equilibrium. It is evident that ice rubble temperature can't be higher the water temperature. Field observations show that ice rubble temperature is usually equals to the water temperature below the rubble (Shestov and Marchenko, 2014).

In the present paper a model of ice rubble consolidation is formulated in the case when ice rubble temperature is similar to the water temperature below the rubble. The oceanic heat flux to the rubble is taken into account in the model. The model is used to describe long term consolidation of multiyear ice ridges in the Arctic. Laboratory experiments are performed in the cold laboratory of UNIS to investigate the influence of melt water on the consolidation of ice rubble. Results of laboratory experiments are described and analyzed in the paper.

2. Long-term thermodynamic consolidation of ice ridges

Ice rubble is formed due to mechanical compression of floating ice. Submerged ice blocks form a keel, and ice blokes remaining above the water surface form a sail. Initially the ice rubble is a set of unfrozen ice blocks. In winter time the heat flux directed from the water into the air influences water freezing between submerged ice blocks. This process leads to the formation of consolidated layer (CL) extended from the air-water interface to the depth h_{cl}. The CL thickness h_{cl} increases with the time depending on the surface heat flux Q_s. The rubble below CL is not consolidated and it is called unconsolidated rubble (UR).

Amount of water trapped in UR between submerged blocks is characterized by macro-porosity p. The UR is extended up to the depth h_r. The depth h_r decreases with the time due to the melting of submerged ice blocks from below caused by ocean heat flux Q_w. Further we show that macro-porosity of UR decreases with the time due to the extrusion of sea water trapped inside UR by melt water formed at the bottom of UR. This process explains that multi-year ice ridges can be completely consolidated.

It is assumed that the temperature of UR equals to the freezing point of sea water, and the temperature of CL may have profile (Fig. 1a). Temperature of UR is determined by the sea water salinity (σ) according to the thermodynamic equilibrium

$$\sigma = \alpha T_f, \alpha = -0.0182, T_f > -8.2^\circ\mathrm{C}. \tag{1}$$

Growth of CL is described by the energy equation (Stefan law)

$$\rho_{si} p L_{si} \frac{dh_{cl}}{dt} = Q_{cl}, \tag{2}$$

where ρ_{si} is the sea density, L_{si} is the latent heat of sea ice, and Q_{cl} is the heat flux at the CL bottom.

Melting of UR from below is described by the energy equation

$$\rho_{si}(1-p)L_{si} \frac{dh_r}{dt} = -Q_w. \tag{3}$$

Amount of salts in unconsolidated rubble is equal to

$$S_{ur} = (h_r - h_{cl})[\sigma \rho_w p + \sigma_{si}\rho_{si}(1-p)], \tag{4}$$

where $h_r - h_{cl}$ is the thickness of UR, p is the macro-porosity of UR, ρ_w and ρ_{si} are the densities of water and ice, and σ_{si} is the salinity of submerged ice blocks. Salt content of UR is changed due to the salt fluxes at the bottom of CL and at the bottom of UR (Fig. 1b). The salt flux at the bottom of CL is a sum of two terms. The first term describes salt expulsion into the water below CL due to the water freezing ($F_{sw,cl}$) with further expulsion of the salt below UR due to the gravity mixing. Thus it is assumed that salt expulsion into the water below CL due to the water freezing at the boundary of CL and UR doesn't increase water salinity inside UR. The second term describes salt deflux from UR due to the incorporation of ice blocks into CL ($F_{si,cl}$)

$$F_{sw,cl} = -\rho_w p \sigma \frac{dh_{cl}}{dt}, \; F_{si,cl} = -\sigma_{si}\rho_{si}(1-p)\frac{dh_{cl}}{dt}. \tag{5}$$

The salt flux $F_{sw,cl}$ consists of two parts. The first part $F_{sw,cl,1} = -\rho_w p \sigma_{si} dh_{cl}/dt$ is the salt deflux due to the incorporation of liquid brine in the CL. The second part $F_{sw,cl,2} = -\rho_w p(\sigma - \sigma_{si}) dh_{cl}/dt$ is the salt deflux due to gravity mixing of dense water formed inside UR with sea water below UR.

The salt flux at the bottom of UR is a sum of two terms describing salt defluxes due to the discharge of water trapped inside UR ($F_{sw,ur}$), and due to the extrusion of sea water trapped inside UR by melt water formed at the bottom of UR due to the melting of ice blocks ($F_{si,ur}$)

$$F_{sw,ur} = \sigma \rho_w p \frac{dh_r}{dt}, \; F_{si,ur} = \rho_{si}(1-p)(\sigma - \sigma_{si})\frac{dh_r}{dt}. \tag{6}$$

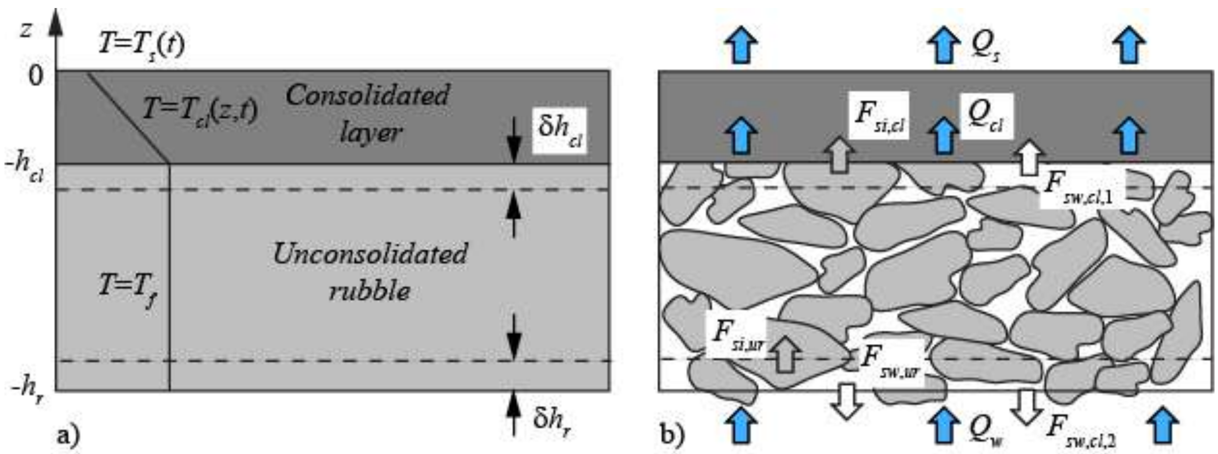

Figure 1. Schematic of ice rubble structure (a). Heat and salt fluxes through ice rubble (b).

The salt balance inside UR is described by the equation

$$\frac{dS_{ur}}{dt} = F_{sw,cl} + F_{si,cl} + F_{sw,ur} + F_{si,ur}. \tag{7}$$

Three equations (2), (3) and (7) are used for the calculation of three unknown functions $h_{cl}(t)$, $h_r(t)$ and $p(t)$.

Substituting equation (3) into equation (7) we find

$$\frac{1}{1-p}\frac{dp}{dt} = \frac{\kappa}{h_{ur}}\frac{dh_{ur}}{dt}, \; \kappa = \frac{\rho_{si}(\sigma - 2\sigma_{si})}{\sigma\rho_w - \sigma_{si}\rho_{si}}, \tag{8}$$

where $h_{ur} = h_r - h_{cl}$ is the thickness of UR. Integration of this equation leads to the formula

$$\frac{1-p_0}{1-p} = \left(\frac{h_{ur}}{h_{ur,0}}\right)^{\kappa}, \tag{9}$$

where p_0 and $h_{ur,0}$ are initial values of the macro-porosity and the thickness of UR.

The UR is completely consolidated when $p = 0$. The thickness of completely consolidated rubble equals

$$h_{ur,cc} = h_{ur,0}(1 - p_0)^{1/\kappa}. \tag{10}$$

The time to complete consolidation of UR is calculated from (8) when $Q_{cl} = 0$ and $Q_w = const$ as follows

$$t_{cc} = k_1 k_2 h_{ur,0} L_{si} \rho_w Q_w^{-1}, \; k_1 = \frac{\rho_{si}(\sigma\rho_w - \sigma_{si}\rho_{si})}{\rho_w[\sigma\rho_w - (\sigma - \sigma_{si})\rho_{si}]}, \; k_2 = (1 - p_0)[1 - (1 - p_0)^{(1-\kappa)/\kappa}]. \tag{11}$$

Assuming $\sigma = 35$ ppt, $\sigma_{si} = 5$ ppt, $\rho_w = 1020$ kg/m^3 and $\rho_{si} = 920$ kg/m^3 we find $\kappa = 0.74$ and $k_1 = 3.47$. Figure 2a shows the reduction of UR thickness to the moment of its complete consolidation depending on the initial macro-porosity. For example, the thickness of UR decreases to 0.62 of its initial thickness when the rubble is completely consolidated and its initial macro-porosity equals to 0.3. Figure 2b shows time to complete consolidation of UR versus the ocean heat flux. For example, UR with initial porosity 0.2 will be completely consolidated in 700 days when the ocean heat flux equals 10 W/m^2. Complete consolidation of the same UR occurs in 30 days when the ocean heat flux equals 300 W/m^2.

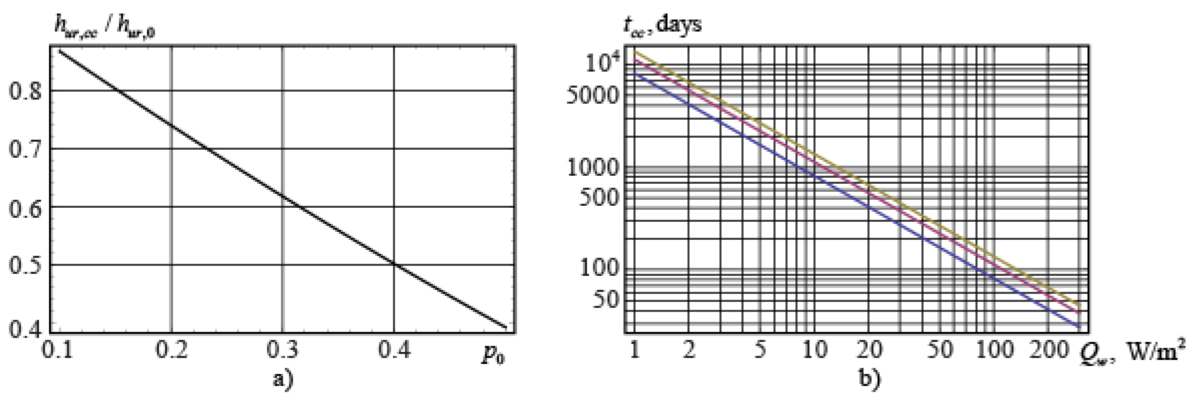

Figure 2. Ratio of the thickness of completely consolidated rubble to initial thickness of UR versus the initial macro-porosity of UR (a). Time to complete consolidation of ice rubble versus the ocean heat flux constructed with different values of initial macro-porosity of UR: $p_0 = 0.2$ (blue line), $p_0 = 0.3$ (pink line) and $p_0 = 0.4$ (mossy line) (b).

3. Experiments on thermodynamic consolidation of ice rubble

Laboratory experiments were performed to investigate the influence of upward heat flux on floating ice rubble. In the experiments sea water was added in two vessels partially filled by the same amount of ice rubble. The vessels were thermally insulated from below and from the sides by foam plastic and placed in the cold room. Initial sea water temperature was at the freezing point in one vessel and slightly above the freezing point in the other vessel. In the first vessel the ice rubble consolidated due to the cooling from the surface only. In the second vessel the consolidation occurred due to the surface cooling and due to the heat flux from the water which initial temperature was higher the initial temperature of the ice rubble. The experiment with two vessels was repeated twice.

During the experiments water and ice rubble temperature was registered with Fiber Bragg Grating temperature strings (http://www.aos-fiber.com/eng/Products.html) placed vertically in the middle of each vessel to monitor the air, rubble and water temperature. Each temperature string has 12 thermistors distributed with 1 cm distance between neighbor sensors. The FBG temperature measurement system's nominal resolution and accuracy in the experiment was 0.08^{o} C and 0.4^{o} C, respectively. The vessels have cylindrical shape with 20 cm diameter (19 cm at the bottom and 21 cm at the top) and 19 cm height.

Experiment 1

Vessel I (VI) was filled by broken ice (0.5 of the volume) and then the water with salinity of 32 ppt and temperature equal to the freezing point -1.7^{o}C was added to fill the rest of the volume. Similar vessel II (VII) was filled by broken ice (0.5 of the volume) and then the water with salinity of 32 ppt at the temperature 0.5^{o}C was added to fill the rest of the volume. The initial ice temperature in the vessels was around -2^{o}C. Each of the vessels was placed inside foam plastic block for the insulation from the sides and the bottom (Fig. 3a). Fiber Bragg Grating thermistor-strings with 12 thermistors were mounted in the both vessels. After that the room temperature was placed at -5^{o}C, and the temperature records were programmed for sampling frequency of 1 Hz.

a)

b)

Figure 3. (a) Two vessels filled by ice rubble and sea water in the cold laboratory. FBG temperature strings are mounted in the middle of the vessels to monitor vertical profiles of the air, rubble and water temperature. (b) Consolidated layers after the experiment 1.

Experiment 1 was run during 12 hours. CLs were formed in each vessel. After the experiment the CLs were taken out of the vessels by ice screws. The CL thickness was 8 cm in VI and 10 cm in VII (Fig. 3b). Amount of unconsolidated rubble below CL in VI was greater than in VII. Salinities of CLs were 8.73 ppt in VI and 8,45 ppt in VII. Salinities of unconsolidated rubble were 5.97 ppt in VI, and 7.26 in VII. Water salinities below the rubble were 39.4 in VI, and 37.9 ppt in VII.

Experiment 2

Vessels I and II were filled by broken ice with weights 1832 g and 1866 g respectively. Then sea water with the salinity of 34.2 ppt and the temperature of -1.7C was added to fill the rest of the volume in Vi and VII. The masses of water in VI and VII were 3479 g and 3790 g respectively.

The initial water temperatures were -1.7C in VI and 1.5C in VII. Fiber Bragg Grating thermistor-strings with 12 thermistors were mounted in the both vessels. After that the room temperature was placed at -5°C, and the temperature records were programmed for sampling frequency of 1 Hz.

Experiment 2 was run during 15 hours. During the experiment CLs were formed in each vessel. After the experiment the CLs were taken out of the vessels by ice screws. 2-3 ice pieces left below CL to the end of the experiment in VI. In VII no ice pieces left below CL to the end of the experiment. The weights of CLs were 2711 g in VI and 2839 g in VII. The weights of unfrozen water were 2463 in VI and 2745 in VII (weight is together with bucket). Amount of slush was higher in the bucket I. CL salinities were 7.8 ppt in VI and 7,9 ppt in VII. Total masses of ice and water decrease in VI on 322 g and in VII on 266 g because of surface evaporation.

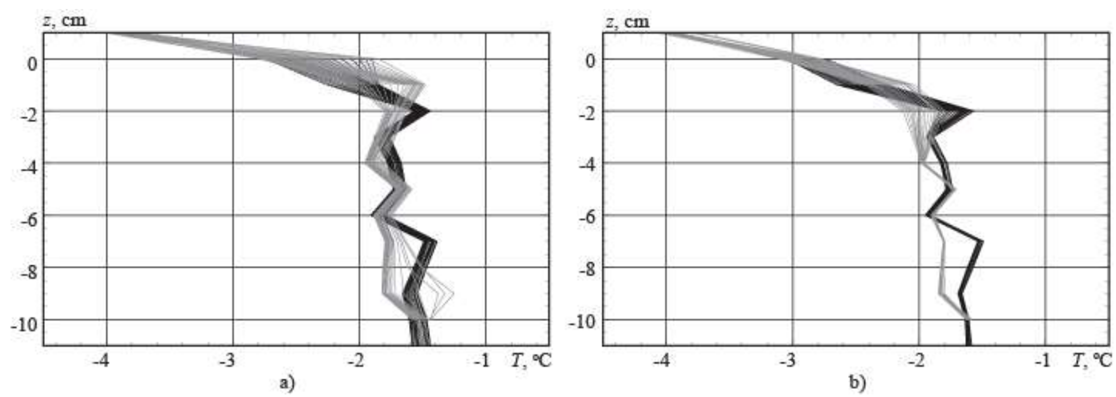

Figure 4. Vertical profiles of the temperature in VI (black lines) and VII (gray lines) constructed over each 0.3 h during first 6 hours (a) and during next 4.8 h (b) of the experiment 1.

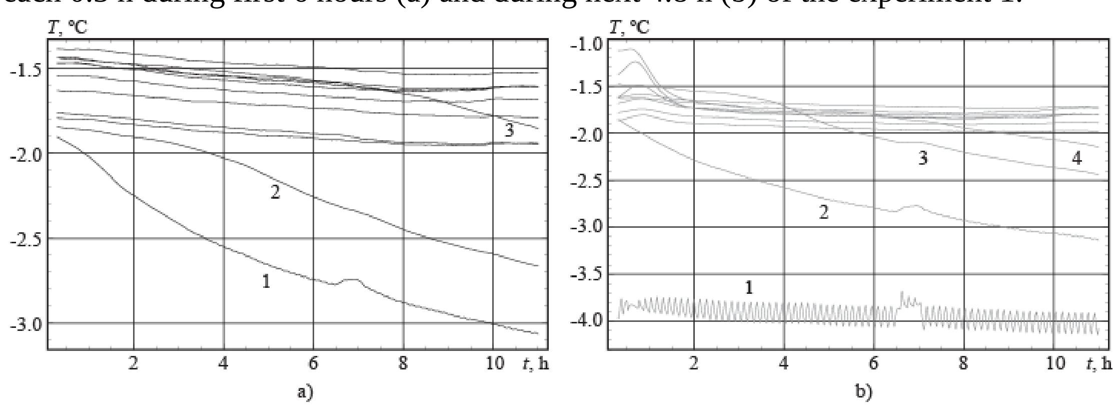

Figure 5. Experiment 1. Dependencies of the temperatures measured at different depth from the time inside VI (a) and VII (b).

All temperature records were processed using Moving Average operation over 0.5 h (1800 records) to exclude noise and influence of the room temperature oscillations caused by the fans work. Temperature profiles constructed with the recorded experimental data are shown in Fig. 4 and Fig. 6, and individual records of thermistors are shown in Fig. 5 and Fig. 7 versus the time. In experiment 1 two thermistors were above the ice surface in VI, and only one thermistor was above the water surface in VII. Records of these thermistors are shown by lines 1 and 2 in Fig. 5a, and by line 1 in Fig. 5b respectively. In experiment 2 the temperature strings were in similar positions in VI and VII. One can see that thermistors 1 (Fig. 5b, 7a and 7b) recorded temperature oscillations in the cold room caused by the fans.

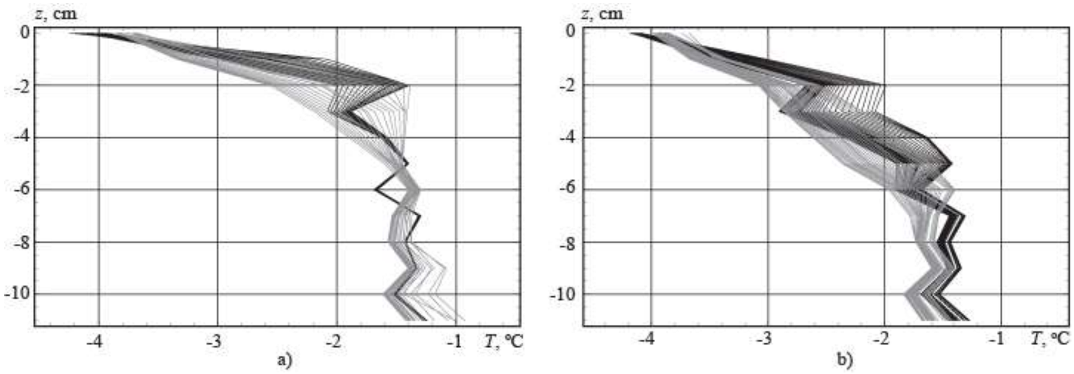

Figure 6. Vertical profiles of the temperature in VI (black lines) and VII (gray lines) constructed over each 0.3 h during first 6 hours (a) and during next 9 h (b) of the experiment 2.

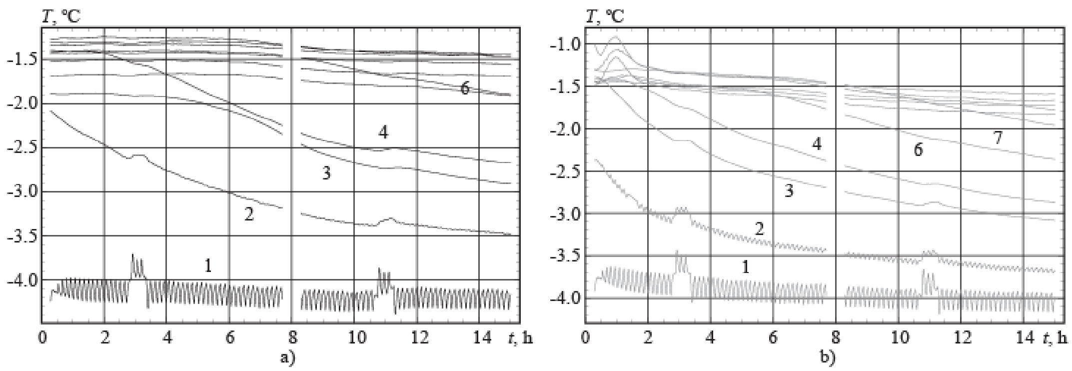

Figure 7. Dependencies of the temperatures measured at different depth from the time inside VI (a) and VII (b).

In both experiments 1 and 2 the temperatures of water and rubble inside 10 cm layer of VI and VII were almost similar in the beginning of the temperature record despite the initial temperatures of the water added in VII were higher the initial temperatures of the water added in VI. It is a result of a mixing of sea water with ice rubble placed in the vessels before to add the water. Figures 5b and 7b show local increase of the temperature in surface layers of VII during first two hours of both experiments 1 and 2. T can be explained by the freezing of overcooled melt water formed due to the mixing of ice rubble with sea water having initial temperature above the freezing point.

Figure 4b shows that ice rubble temperature was lower in VII than in VI in the end of the experiment 1. It explains larger thickness of CL in VII. Mean salinities of CLs in VI and VII were similar in this experiment. The experiment II was longer that experiment I, and final thicknesses of CLs in VI and VII were similar. Mean salinities of CLs in VI and VII were similar in this experiment as well. Temperature profiles in Fig. 7 demonstrate that quasi linear temperature gradient is extended on bigger depth in VII in comparison with VI. Linear temperature gradient characterizes dominant heat transfer by molecular heat diffusion in solids. In liquids the heat transfer is associated with convective mixing caused more or less constant temperature over the liquid volume. Figure 7 shows that amount of liquid brine trapped in permeable channels inside CL was greater in VI in comparison with VII in the experiment II. The liquid brine was leaking out of the channels when the CLs were taken out of the vessels after the experiment. Therefore the weight of CL taken from VI was smaller the weight of CL taken from VII.

4. Conclusions

Ocean heat flux to floating ice rubble influences the melting of the rubble and penetration of melt water inside the rubble. Mixing of melt water and sea water inside the rubble is a complex physical process which is accompanied by the formation of overcooled water, freeze bonds between submerged ice blocks and permeable channels filled with liquid brine inside the consolidated layer. As a result the consolidated layer inside the rubble is extended downward with higher rate in the presence of the ocean heat flux. In the same time the ocean heat flux increases melting rate of the rubble.

In the laboratory experiments the ice rubble mixed with sea water were placed into vessels insulated from below and from the sides. Therefore thermodynamic consolidation was accompanied by the increase of water salinity in the vessels that makes the boundary conditions different from the natural conditions in ocean. Nevertheless the laboratory experiments demonstrated the influence of a heat flux from warm water to ice rubble on the rubble consolidation due to the formation of melt water.

Acknowledgments

The author wish to acknowledge the support of the Research Council of Norway through the Center for Sustainable Arctic Marine and Coastal Technology (SAMCoT) and IntPart project Arctic Offshore and Coastal Engineering in Changing Climate (AOCEC).

References

Hoyland, K.V., 2002. Simulations of the consolidation process in first-year ice ridges. *Cold. Reg. Sci. Technol.*, 34, 143-158.

Hoyland, K.V., Liferov, P., 2005. On the initial phase of consolidation. *Cold Reg. Sci. Technol*. 41: 49–59.

Høyland, K. V., Barrault, S., Gerland, S., Goodwin, H., Nicolaus, M., Olsen, O.M., and Rinne,E., 2008. The consolidation in second and multiyear sea ice ridges Part 1: Measurements in early winter. 19th IAHR International Symposium on Ice, Vancouver, Canada, pp. 1231-1241.

Marchenko, A., Diansky, N., Fomin, V., Marchenko, A., Ksenofontova, D., 2016. Consolidation of Drifting Ice Rubble in the North-West Barents Sea. Proc. of the 23rd IAHR Symposium on Ice, Ann Arbor, Michigan, paper 4868538.

Marchenko, A.V., Diansky, N.A., Onishchenko, D.A., Chumakov, M.M., Nikitin, M.A., Fomin, V.V., Marchenko, N.A., 2016. Studies of ice drift and ridge consolidated layer evolution in the North-West Barents Sea. Proceedings of Hydrometcentre of Russia. V. 361, 229-258. (in Russian)

Shestov, A., and Marchenko, A., 2014. Properties of ice ridge keels and sea currents in their vicinity in the Barents Sea. Proc. of the 22th IAHR Symposium on Ice, Singapore, paper 1196.

Shestov, A.S., Marchenko, A.V., 2016. Thermodynamic consolidation of ice ridge keels in water at varying freezing points. *Cold Reg. Sci. Technol*, 121: 1-10.

Sudom, D., Timco, G., Sand, B., Fransson, L., 2011. Analysis of first-year and old ice ridge characteristics. POAC-11-164.

24th IAHR International Symposium on Ice
Vladivostok, Russia, June 4 to 9, 2018

Ice Regime of the HPP Tailrace when Winter Water Flow Passes the Spillway

N.S. Bakanovichus, A.A. Lyalina, I.N. Shatalina
JSC "Vedeneev VNIIG", 195220 Saint-Petersburg, Gzhatskaya, 21
bakanovichus@yandex.ru
anna_lyalina@inbox.ru
ishatalina@mail.ru

The ice regime is considered when flowing water through a power plant complex as part of a power plant + HPP-counter-regulator, when in winter it is necessary to use an operating surface spillway instead of the normal passage of water through turbines and water lines pass the flow of water. This can occur in the emergency condition of water lines. The situation that has arisen can be dangerous for the underlying HPP-counter-regulator, since it is possible to block its containment grating with a frazil ice as a result of a change in the ice regime of the lower tailrace of the overlying HPP.

1. The situation with the need to pass the flow of water through the operational spillways

The situation with the need to pass the flow of water through the operational spillways was created because of the accident of the hydroelectric unit at the HPP. Emergency condition of the power-generating water conducts has caused necessity to carry out annual winter drawdown through the spillway spans in order to empty the reservoir level for next year spring floods.

Change in the hydroelectric complex operating conditions caused the change in ice regime of the HPP tailrace. Water discharge via open channels of the operational spillway has lead to formation of a vast water-and-air cloud over the spillway. At negative air temperatures airborne water drops froze forming ice drops which fall to the flow. In addition to ice drops, flow temperature was decreased by melting of ice blocks breaking off from the ice-covered channels surface of the open spillway part. The temperature of flow in this case should decrease also due to more intensive heat transfer from water in air in compared to the mode through the closed water passage of HPP. The HPP tailrace had the form of one-arm channel where at the distance of 25 km a counter-regulatory power site was located.

2. The main purpose of the research

The main purpose of the research described was assessment of change in thermal and ice regime of the main HPP tailrace for quantity of frazil ice approaching the downstream counter-regulatory power site, taking into account the spray cloud, intensive heat exchange between the water flow and atmosphere, formation of ice drops, frazil ice and ice blocks breaking off from the ice-covered channels surface. When performing the calculations, possible frazil ice formation was considered in the flow path along the spillway due to aeration of the flow with large amount of cooled-off air (up to 85 % of the water flow).

3. Heat balance

Assessment of water temperature changes along the tailrace length for winter conditions of water discharge, bypassing the HPP power conduits and directly through the operational spillway was performed using the following equation of heat content change in the water flow:

$$c\rho Q\frac{dt}{d\tau} = q_{id} + q_{id,pt} + q_{ib} + q_{ib,pt} + q_{h,ex} \tag{1}$$

This represents heat content of water change per time unit, W/s, due tochange of heat content ice drops heating up to 0^0 C is q_{id} ; change of heat content ice drop-water phase transition is $q_{id,pt}$; change of heat content heating of ice blocks which fall in water up to 0^0C is q_{ib}; change of heat content ice blocks phase transition is $q_{ib,pt}$; heat exchange between water and air is $q_{h,ex}$.

q_{id} and $q_{id,pt}$ - are expressed as

$$q_{id} = \frac{c_i \rho_i Q_{id} t_{id}}{\tau} \quad \text{and} \quad q_{id,pt} = \frac{\sigma \rho_i Q_{id}}{\tau}, \tag{2}$$

a q_{ib} and $q_{ib,pt}$ - are expressed as

$$q_{ib} = \frac{\alpha_{ib}(t_{cr} - t) F_{ib} n_{ib} x}{\tau} \text{ и } q_{ib,pt} = \frac{\sigma \rho_i Q_{ib}}{\tau}. \tag{3}$$

The coefficient of heat transfer between water and particles of ice drops and ice blocks can be written as (W/m^2K)

$$\alpha_{ib} = \frac{\lambda_i 0{,}0693 Pe^{0,5}}{L}, \tag{4}$$

Where criterion Peclet is $Pe = \frac{vL}{a_i}$ and $L = \frac{W}{F}$ is the ratio of the volume of the ice block to the area of its surface, a_i is coefficient of temperature diffusivity (m^2/s), λ_i is coefficient of heat conduction, W/(m K).

The amount of heat expended on the heat exchange of water to air is defined as

$$q_{h,ex} = \frac{\alpha_{air-water}(\vartheta_e - t)bx}{\tau} \ . \tag{5}$$

Depending on the position of the zero isotherms and its distance from the HPP line, a different amount of frazil ice can approach the site of the counter-regulating HPP. Based on the results of calculations, for all variants of the location of zero isotherms in reservoir above the counter - regulating HPP line, the frazil ice discharge through the counter-regulating HPP was calculated. The discharge of frazil ice was determined by the formula:

$$Q_f = \frac{\alpha_1 (t - \vartheta_e) F_f}{\sigma \rho_f}, \tag{6}$$

Where α_1 is coefficient of heat transfer "water to air", W / (m2K); t is water temperature, K; ϑ_e is equivalent temperature of air, K; F_f is frazil ice producing area, taken from the zero isotherm section to the counter-regulating hydroelectric power station, m2; σ is specific latent heat of water crystallization, J / kg; ρ_f is frazil ice density, kg / m3.

4.Condition for calculation

Calculation was made for next condition:
Discharge of water in winter season was 1000 m^3/s;
Discharge flow of ice drops is taken from temperature of air (Tabl.1):

Table 1. Discharge flow of ice drops

Temperature of air,^{0}C	-35	-30	-25	-20	-15	-10	-5
Discharge of ice drop, m^3/s	3,72	3,70	3,69	3,67	3,65	3,62	3,53

Ice drops discharge calculations were based on field observations of dripping above the spillway. The cloud sizes thus obtained correspond to the measured ones. Calculations of drop trajectory parameters were performed for 0 to 90^0 trajectory range. After analysis of drop trajectory range, the following results were obtained: maximum values of flow flying distance, height and time of drops flight. The results obtained and their corresponding with field data shows that the assessment of precipitation rate produced by the water-and-air cloud is correct.

Discharge of ice blocks above water part of the operational spillway was 0,128m^3/s. Weather conditions of heat transfer water to air conform to south Siberia. On figure1 is shown change of average temperatures of air and water in tailrace. This data was obtained after the end of winter season.

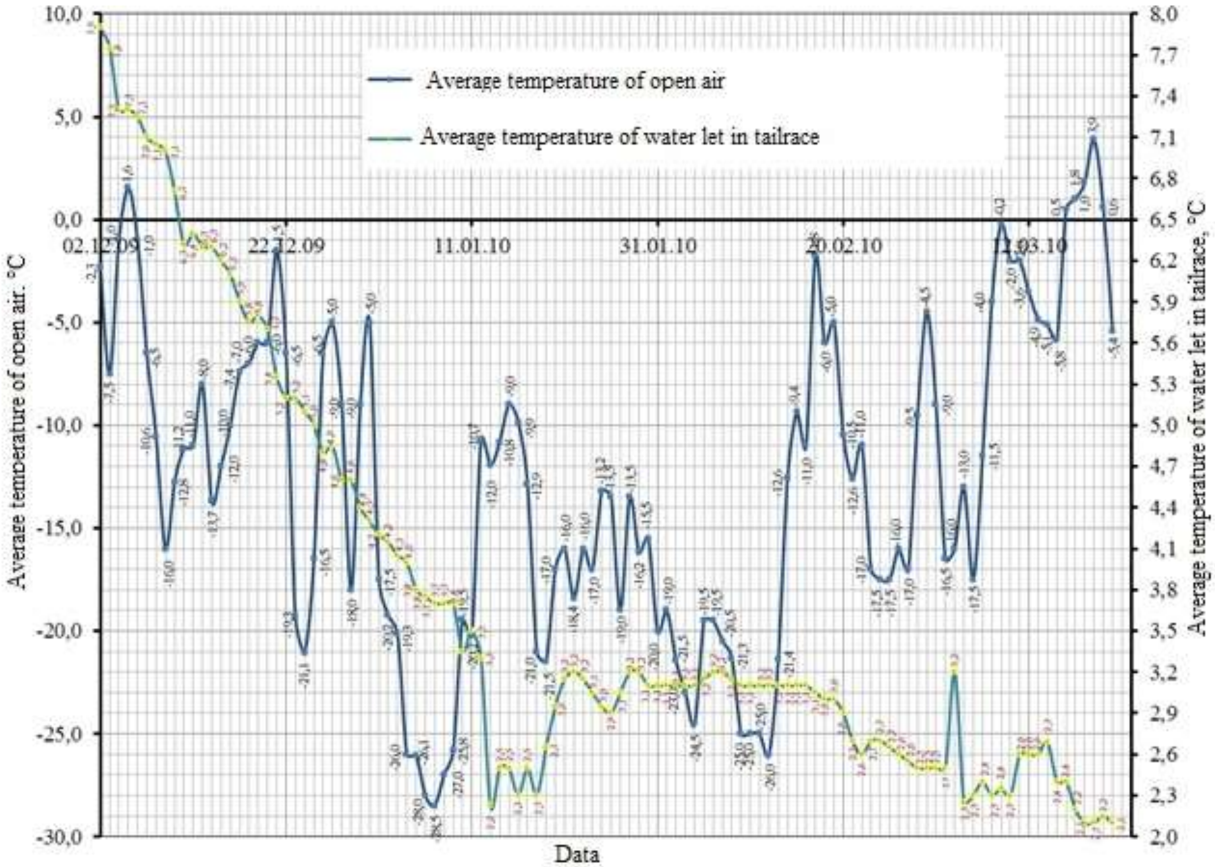

Fig. 1. Average temperatures of air and water in tailrace.

5. Result of calculation

Result of calculation discharge of frazil ice is in table 2 and on figure. 2. Calculation of the zero isotherm position in the tailraces (Table 2) shows that when the temperature of the discharge water is lowered, the zero isotherm is established inside the intermediate reservoir; this can lead to the formation of a frazil ice and the possible clogging of the containment gratings of the counter-regulatory hydroelectric power station (Table 2).

Table 2. Position of zero isotherm lower HPP (x_0, m), and calculation of discharge of frazil ice (Q_f , m^3/s)

$t_w{}^0C$	0,5		1,0		1,5		2,0	
$t_{air}, {}^0C$	x_0, m	Q_f	x_0, m	Q_f	x_0, m	Q_f	x_0, m	Q_f
October								
-5	-	-	-	-	-	-	-	-
-10	21400	0,06	-	-	-	-	-	-
-15	11200	0,48	-	-	-	-	-	-
-17,5	8200	0,70	-	-	-	-	-	-
November								
-5	-	-	-	-	-	-	-	-
-10	15300	0,32	-	-	-	-	-	-
-15	8600	0,79	-	-	-	-	-	-
-20	4800	1,27	16700	0,48	-	-	-	-
-25	2700	1,77	11900	1,oo	21600	0,18	-	-
-28,2	1800	2,09	9600	1,35	18100	0,54	-	-
December								
-5	21700	0,07	-	-	-	-	-	-
-10	12400	0,53	-	-	-	-	-	-
-15	7300	1,02	20500	0,2	-	-	-	-
-20	4300	1,52	14600	0,72	-	-	-	-
-25	2500	2,03	10,500	1,26	19100	0,45	-	-
29,8	1400	2,53	7800	1,80	15000	0,99	22400	0,16
January								
-5	20300	0,12	-	-	-	-	-	-
-10	11600	0,61	-	-	-	-	-	-
-15	6900	1,11	19400	0,29	-	-	-	-
-20	4100	1,62	13800	0,82	-	-	-	-
-25	2400	2,14	10100	1,37	18200	0,56	-	-
-30	1300	2,66	7500	1,93	14400	1,11	21300	0,30
-34,4	800	3,14	5700	2,47	11600	1,67	17600	0,85
February								
-5	-	-	-	-	-	-	-	-
-10	14300	0,38	-	-	-	-	-	-
-15	8100	0,86	23000	0,04	-	-	-	-
-20	4700	1,34	16000	0,55	-	-	-	-
-25	2600	1,85	11400	1,08	20800	0,26	-	-
-30	1400	2,40	8300	1,66	16000	0,84	23700	0,10
-32,3	1100	2,60	7300	1,89	14400	1,08	21600	0,25
March								
-5	-	-	-	-	-	-	-	-
-10	-	-	-	-	-	-	-	-
-15	13800	0,45	-	-	-	-	-	-
-20	6200	0,88	22000	0,09	-	-	-	-
-25	3300	1,33	15000	0,57	-	-	-	-
-27	2500	1,52	12900	0,78	-	-	-	-

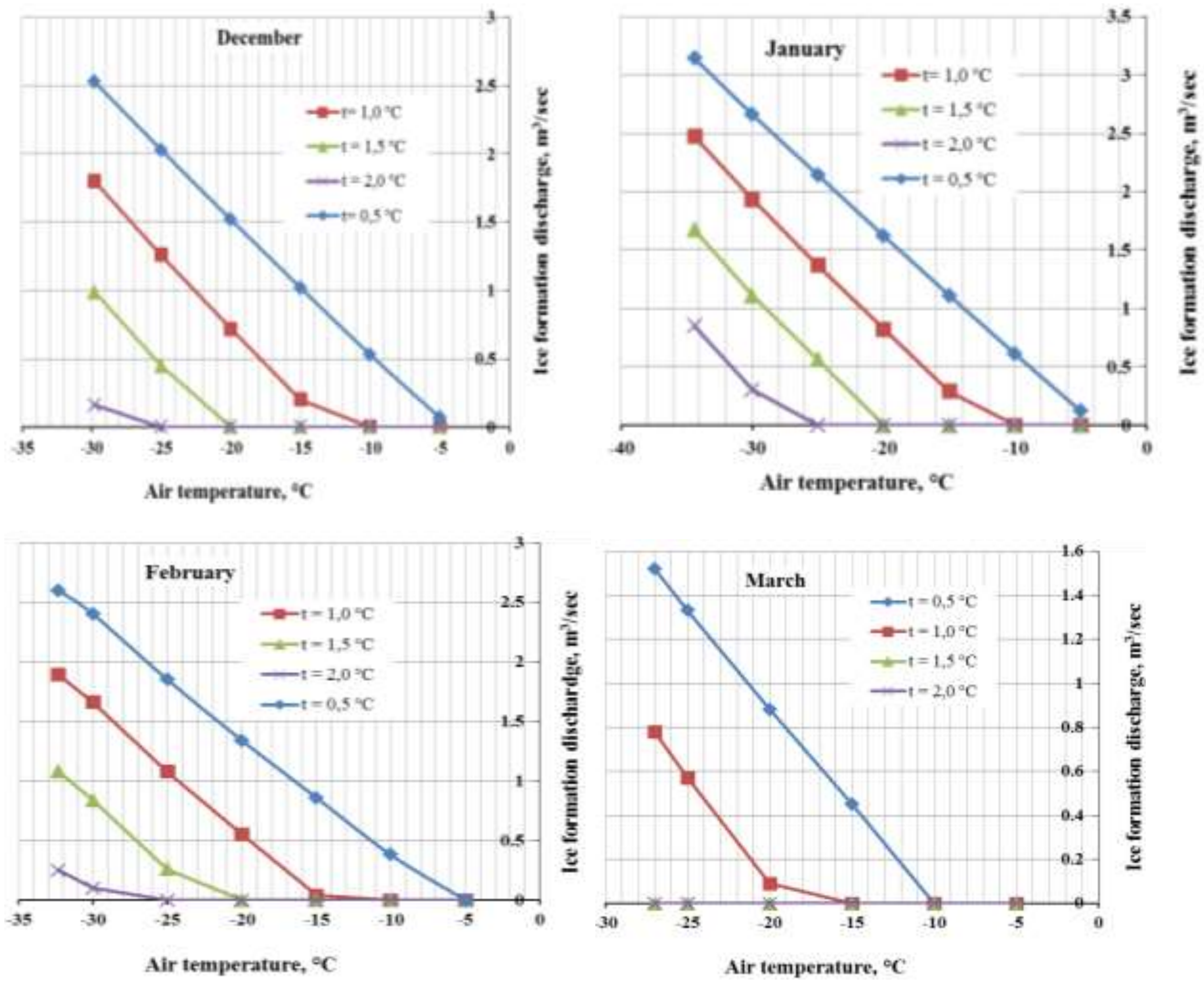

Fig. 2. Dependence of frazil ice discharge on air temperature (December-March).

5.Analyses results of calculation

In the time interval January-March, the temperature of run water can reach dangerous values of + 2^{0}C and lower, and accordingly the zero isotherm can be in reservoir upper of the counter-regulating hydroelectric power station, which causes formation of frazil ice.

In January at air temperatures from -34,4^{0}C to -25^{0}C at which the zero isotherm point can be higher than of the counter-regulating hydroelectric power station at the temperature of discharge water from the overlying HPP will be below +2,5^{0}C are dangerous. At temperatures air from -25 to -15^{0}C, temperatures discharge water below + 1,5^{0}C are dangerous. At temperatures air from -15 to -10^0 C, the temperatures discharge water below + 1,2^{0}C are dangerous. At temperatures air from -10 to -5^{0}C temperatures of discharge water below + 1^0 C are dangerous. At air temperatures below -5^{0}C, temperatures of discharge water below + 0,5^{0}C are dangerous.

In February at air temperatures from -32,2 to -25^{o}C at which the zero temperature will be in the higher reservoir of the counter-regulating HPP at a discharge water temperature below + 2^{0}C are dangerous. At air temperatures of -25 to -20^{0}C, discharge water temperatures below + 1,5^{0}C are dangerous. At air temperatures of -20 to -10^{0}C, discharge water temperatures below + 1^{0}C are hazardous. At air temperatures from -15 to -10^{0}C, discharge water temperatures below + 0.5 0^{0}C are dangerous.

In March, at air temperatures from -27 to -20^{0}C, at which the zero temperature will be in the higher reservoir of the counter-regulating hydroelectric power station at discharge water temperatures below 1,5^{0}C are dangerous. At air temperatures from -20 to -15^{0}C, discharge water temperatures below + 1^{0}C are dangerous. At air temperatures from -15 to -10^{0}C dangerous discharge water temperatures are below + 0,5^{0}C.

As calculations show in January-March, the water temperature under the influence of additional cooling can reach a dangerous interval of + 2^{0}C and lower, and, accordingly, initiate the processes of formation of frazil ice. Even if the minimum frazil ice discharge according to the calculations made is 0.1m3/s, this will be enough to completely block the grating of the HPP-counter regulator in less than 12 hours. With the maximum possible frazil ice discharge, the gratings will be clogged for 3-4 hours.

6.Comparison of calculation and field data

The observed water temperature conditions by the beginning of February (Fig. 1) show that the cooling of discharge water very closely approached dangerous temperature level. The water temperature was above the dangerous level by only 0,1^{0}C (see the field diagram on fig.1). Under these conditions, there was no accidental clogging of the hydropower plant's counter-regulators, since a sudden warming occurred in February. Only 0,1^{0}C in the water temperature separated the cascade from these two stations from the emergency situation.

Decrease in air temperature is observed until February 15 in the field conditions. The temperature of the discharged water is reduced to 3,0^{0}C. On February 15, the air temperature rises to 0^{0}C on March 3. During this time, the discharged water cools down to 2,1-2,2° C. Comparison of the calculated results with the field data makes it clear that the figures are close enough to a dangerous limit.

Concluding remarks

Imagine that February warming would not have happened. The temperature of the discharge water would fall below + 2^{0}C. This would cause a blockage of the counter-regulating grating and an emergency situation with the need to pass the flow through the counter-regulator vents. This situation would call into question the stability of structures in the alignment of the counter-regulating hydroelectric complex It becomes clear that, the analysis of the presented situation should be included in the compulsory calculations for estimating the icing

Analysis performed can be further used to assess facilities and structures for icing in hydroelectric complexes operated in difficult ice and thermal conditions.

International Association for Hydro-Environment Engineering and Research

Supported by Spain Water and IWHR, China

24th IAHR International Symposium on Ice

Vladivostok, Russia, June 4 to 9, 2018

In Situ Observation of Modelled Ice Drift Characteristics in the Bohai Sea, China

Yu Yan[1], Wei Gu[1,*], Ning Li[1]

[1] *Key Laboratory of Environmental Change and Natural Disaster of Ministry of Education, Faculty of Geographical Science, Beijing Normal University, Beijing 100875, China*

* *Author to whom any correspondence should be addressed*

yanyu@mail.bnu.edu.cn

weigu@bnu.edu.cn

ningli@bnu.edu.cn

In this study, we used polypropylene material with a density similar to that of Bohai Sea ice as modelled ice and carried out a free drift experiment of modelled ice in the open sea. The trajectories of isolated modelled ice, currents, and wind in the Bohai Sea during non-frozen and frozen periods were obtained. The results showed that the currents played a major role while the wind played a minor role in the free drift of isolated modelled ice when the wind was mild in the Bohai Sea. The modelled ice drift was significantly affected by the ocean current and wind based on the ice–current–wind relationship established by multiple linear regression, and the modelled ice velocity calculated by multiple linear regression was close to that of the in-situ observation. The modelled ice drift characteristics were shown to be close to that of the real sea ice, which indicated that the modelled ice could be used as a good substitute of real ice for in situ observations of free ice drift in the open sea, which helped solve time availability, safety and logistics problems related to *in situ* observation on real ice.

1 Introduction

Sea ice drift, a crucial part of oceanology studies, is a complex form of movement under the influence of a variety of forces, especially controlled by ocean currents and local wind. Synchronous observation of ice velocity, current velocity, and wind speed, is of great significance to identify ice drift characteristics (Simizu et al., 2014; Timmermans et al., 2011; Wu et al., 2005). At present, methods obtaining synchronous data mainly include the drifting buoy observations of multi-year ice in polar regions and experimental studies of modelled ice in indoor tanks.

The Bohai Sea is the southernmost seasonal frozen sea in the Northern Hemisphere. The frozen period is short in the Bohai Sea and the majority of the existing sea ice is drift ice, which is thin and easily breaks (Gu et al., 2013). However, an *in situ* buoy which is expensive and non-recyclable is not applicable to the Bohai Sea where is full of first-year ice. The research on sea ice drift in Bohai Sea mainly concentrated on non-contact measurements (Ji et al., 2013; Lang et al., 2014), such as satellite remote sensing observations and radar monitoring, in recent years. However, remote sensing and radar methods generally can only obtain information on sea ice drift but have difficulties in accessing the ice velocity, current velocity, and wind speed, simultaneously. Considering the limits mentioned above, we developed an *in situ* synchronous observation of ice–current–wind based on modelled ice to make novel solution. On the one hand, it could help to understand the characteristics of sea ice drift and provide key input parameters for the numerical simulation of sea ice drift. On the other hand, it solved the problems such as limited time for observations due to short frozen periods and high costs and safety of ice navigation.

In this paper, free drift experiments of modelled ice in the open sea in Liaodong Bay and Bohai Bay in the Bohai Sea were carried out during the non-frozen period. A comparative free drift experiment between modelled ice and real sea ice was conducted in the frozen period in Liaodong Bay.

2 Materials and methods

The mechanical properties, size, and shape of sea ice are quite varied, which can significantly affect the ice drift. The density is one of the most important mechanical properties. The density of sea ice in the Bohai Sea ranges from 0.74 g/cm^3 to 0.92 g/cm^3, with a common density of 0.85 g/cm^3 (Lin et al., 2010). Polypropylene with a density close to the sea ice in the Bohai Sea was used to model the isolated ice. Two thicknesses, 4.0 and 7.0 cm, were used to create different model ice. The shape of the modelled ice was selected based on common isolated sea ice (ellipse). In addition, for a modelled ice morphology close to that of real ice with a rough bottom, grooves were created to increase the roughness of polypropylene. The dimensions of the modelled ice used in the experiments are listed in Table 1; the design diagram and physical map of the modelled ice are shown in Fig. 1.

Table 1 Dimensions of modelled ice used in the experiment

No.	Density g/cm^3	Thickness cm	Shape (Ellipse) Major axis/cm	Minor axis/cm	Volume cm^3	Mass kg
A	0.91	4.0	200.0	150.0	9.43×10^4	85.77
B	0.81	7.0	200.0	150.0	1.65×10^5	133.60
C	0.91	7.0	200.0	150.0	1.65×10^5	150.09

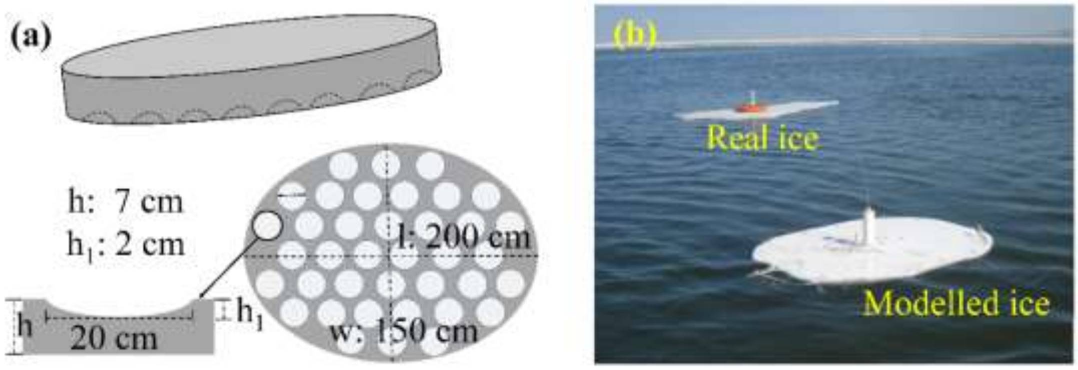

Fig. 1. Design diagram (a) and physical map (b) of the modelled ice.

To accurately determine the ice drift characteristics, simultaneous observations of ice-current-wind by an integrated observation system consisting of automatic identification system (AIS), ADCP, and weather station were indispensable. The trajectories of modelled ice were obtained by the AIS. During the experiments, the signal transmitter of the AIS was placed in the center of the modelled ice and the antenna was placed vertically, 0.50 m above the sea level. The AIS (ICOM, MAX-5000), which consisted of AIS transponder, receiving antenna, and computer, received the broadcasted signal and logged the trajectory of the modelled ice every minute on land. Then the ice velocity was calculated by the observation data from AIS. The sea surface wind data were measured by the weather station (Kestrel, NK 5500) placed on the power-off vessel following the modelled ice with 3.0 m height above the sea level every 1 min. Meteorological data on land were also measured by the weather station every 1 min.

3 Results and discussion

3.1 *Modelled ice drift characteristics and the relationship with current and wind*

The trajectories of the modelled ice in Bayuquan and Nanpaihe during the non-frozen period are shown in Fig. 2 and the vectors of the ice velocity, current velocity, and wind speed are shown in Fig. 3. In Bayuquan, the trajectories of the modelled ices A and B were close and the average velocity of A was slightly larger than B. Both A and B mainly drifted towards the southeast, with some movements in the south and southwest. The average current velocity in Bayuquan was slightly smaller than the modelled ice velocity. The current moved mostly toward the east, sometimes toward southeast and southwest. The wind speed was extremely small with light air forced during the observation period; west wind was predominant, followed by southeast and east wind. In Nanpaihe, the trajectories of the modelled ices A, B, and C were also close and the average velocity of modelled ice followed the decreasing order of A > B > C. The main drift direction of these three modelled ices was northeast and the secondary direction was north. The average current velocity in Nanpaihe was slightly larger than the modelled ice velocity and the main current direction was northeast, sometimes northwest. A gentle breeze was responsible for the wind speed of 5.19 ± 1.08 m/s; southwest wind was prevailing, followed by west wind.

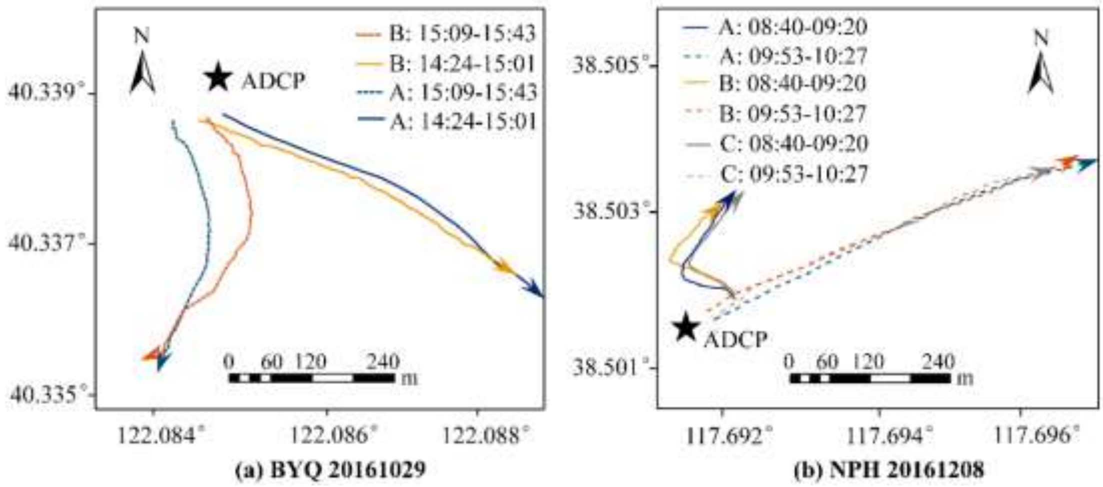

Fig. 2 Trajectories of modelled ices in Bayuquan (a) and Nanpaihe (b) during the non-frozen period.

The ice drift was consistent with the current velocity change, showing notable drift characteristics following the current flow (see Fig. 3). The velocity of the modelled ices A and B gradually decreased with decreasing current velocity during the experimental time in 29 October 2016 (Fig. 3a). Fig. 3b shows that the current direction reversed from 8:40 am to 9:20 am on 8 December 2016; the direction of the modelled ice drift also changed. The current velocity gradually increased from 9:53 to 10:27 am and the ice drift velocity also increased. Thus the current in the Bohai Sea played an important role in the modelled ice drift.

Although the wind was mild during the observation period, the wind also played a certain role in the modelled ice drift. When the direction of the wind and modelled ice were the same, the modelled ice drift was accelerated, forced by the wind. When the current direction was in conversion after 3:33 pm on 29 Oct. 2016 (Fig. 3a), the modelled ice velocity gradually increased under the action of the wind with the same direction in Bayuquan. When the wind direction was opposite to that of the modelled ice, however, the modelled ice velocity decelerated due to the wind. From 3:16 to 3:32 pm on 29 October 2016 (Fig. 3a), the ice drift velocity decreased and the direction then changed due to the increased opposite wind. The average velocity of the ocean currents (15.8 cm/s) from 11:03 to 11:07 am on 12 February 2017 was larger than before (Fig. 3c); however, the modelled ice velocity decreased due to the wind with opposite direction, which indicates that the wind with opposite direction decelerated the ice drift velocity. To sum up, the currents played a major role while the wind played a minor role in the free drift of isolated modelled ice in the Bohai Sea when the wind is mild.

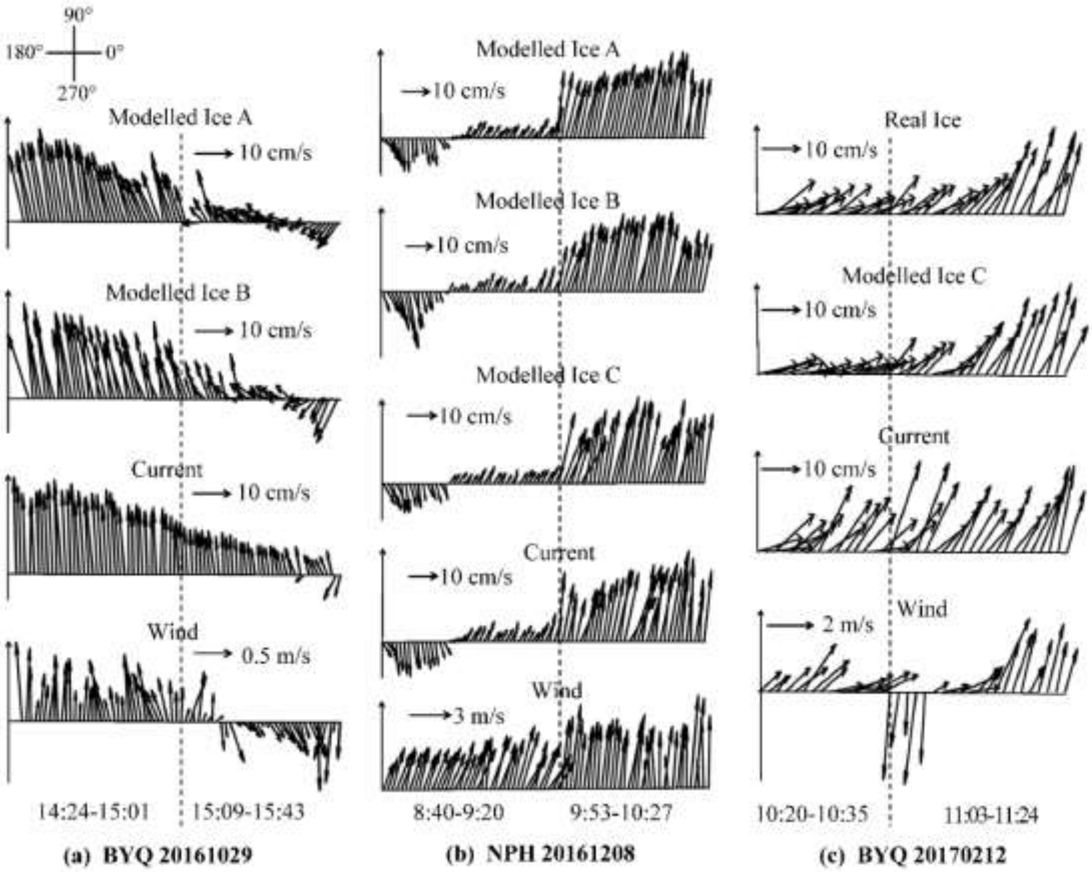

Figure 3 Vectors of the modelled ice velocity, current velocity, and wind speed in the Bohai Sea.

3.2 *Impact of current and wind on modelled ice drift*

To investigate the impact of current and wind on the modelled ice drift, multiple linear regression was employed. The time-varying isolated modelled ice velocity is balanced with the current and wind and the relationship between ice drift, currents, and wind can be described as follows (Lang et al., 2014; Li and Lu, 2006; Wu et al., 2005):

$$\begin{bmatrix} I_1 \\ I_2 \\ \vdots \\ I_n \end{bmatrix} = \begin{bmatrix} C_1 & W_1 & 1 \\ C_2 & W_2 & 1 \\ \vdots & \vdots & \vdots \\ C_n & W_n & 1 \end{bmatrix} \begin{bmatrix} a \\ b \\ c \end{bmatrix} , \quad \textbf{[1]}$$

$$\begin{bmatrix} a \\ b \\ c \end{bmatrix} = \begin{bmatrix} C_1 & W_1 & 1 \\ C_2 & W_2 & 1 \\ \vdots & \vdots & \vdots \\ C_n & W_n & 1 \end{bmatrix}^{-1} \begin{bmatrix} I_1 \\ I_2 \\ \vdots \\ I_n \end{bmatrix} , \quad \textbf{[2]}$$

where *I*, *C* and *W* are the ice velocity, current velocity and wind speed, respectively, and these three parameters are all complex numbers. *n* is the number of the sea ice drift vectors in the formula. The weighted coefficients of the current and wind of the modelled ice drift are *a* and *b*, respectively, while *c* is a constant. Multiple regression analysis provides the relationship among ice velocity (V_{ice}), current velocity (V_c), and wind speed (V_w) as follows:

$$V_{\text{ice-Bayuquan}} = 0.8560e^{i(-3.36°)}V_c + 0.0227e^{i(34.39°)}V_w - 0.0839e^{i(70.63°)} , \quad \textbf{[3]}$$

$$V_{\text{ice-Nanpaihe}} = 0.7688e^{i(-6.79°)}V_c + 0.0092e^{i(82.49°)}V_w + 0.0340e^{i(-40.58°)}\ , \qquad \textbf{[4]}$$

In Eq. (3) and (4), V_{ice} ,V_c, and V_w are vectors. The correlation coefficients R^2 of the equations are 0.73 and 0.85, with a 0.01-significance level in Bayuquan and Nanpaihe, respectively. The equations of the multiple linear regression reflected the relationship among ice drift velocity, current velocity, and wind speed well, indicating that the ice drift was significantly correlated with the current and wind. The current coefficients were much larger than the wind, indicating that the influence of the ocean current on the ice drift is more significant than that of wind. These results are in agreement with the result of previous studies (Lang et al., 2014; Li and Lu, 2006; Shi et al., 2016). In addition, the differences between the modelled ice drift and current directions in Bayuquan and Nanpaihe were –3.36° and –6.79°, respectively, while that between the modelled ice drift and wind directions were 34.39° and 82.49°.

To further explore the ice–current–wind relationship, the observed average current velocity and wind speed in Bayuquan on 29 October 2016 and Nanpaihe on 8 December 2016 were regarded as variables and substituted into the multiple regression equation. The calculated results are shown in Fig. 4. The ocean current played a leading role in the ice drift when the wind is mild, no matter in Bayuquan or Nanpaihe. The calculated modelled ice velocity in Bayuquan was close to the observed velocity, with a magnitude error of 10.33% and direction error of 6.21°. The direction of the ice velocity in Bayuquan slightly shifted from the synthetic interval of the vector of the current and wind with an acute angle (Fig. 4a). This suggests that the other factors, such as Coriolis force and pressure-gradient force has played a certain role in the free drift of isolated ice, especially in weak wind conditions, which is consistent with the findings of Fukamachi et al. (2011). The calculated modelled ice velocity in Nanpaihe was also close to the observed velocity, with a magnitude error of 12.05% and direction error of 4.78°. The direction of the ice velocity in Bayuquan was in the synthetic interval of the vector of the current and wind (Fig. 4b).

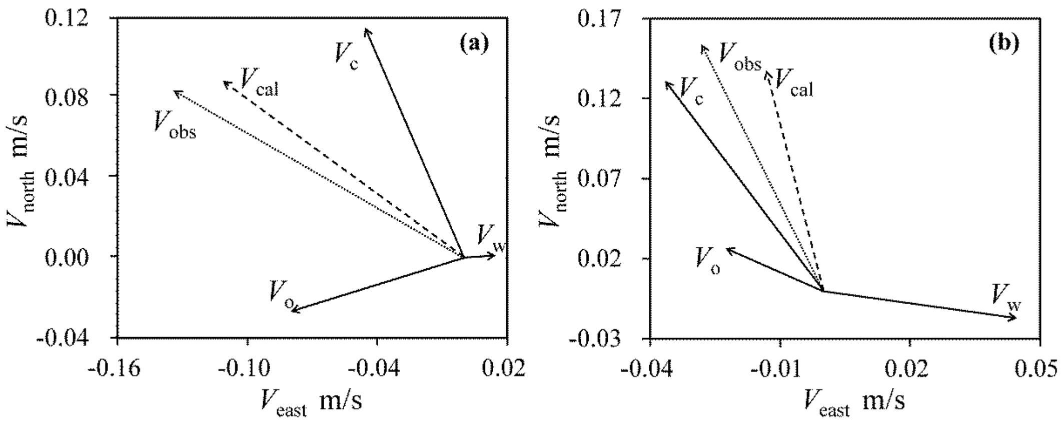

Fig. 4 Relationships among modelled ice, current, and wind in Bayuquan (a) and Nanpaihe (b). V_{cal} is the calculated modelled ice drift velocity based on the multiple linear regression model; V_{obs} is the observed modelled ice drift velocity; and V_c, V_w, and V_o are the current velocity, wind speed, and velocity influenced by other factors, respectively.

3.3 ***Comparison of the drift between modelled ice and real ice***

The comparative free drift experiment between modelled ice and real sea ice was carried out in the frozen period of 2016/17 in Liaodong Bay. Real sea ice (approximately 2 m × 1 m × 8 cm) was selected for the experiment (see Fig. 1b), which was close to the modelled ice C. The density of the real ice was 0.86 g/cm^3. The trajectories of modelled ice and real ice were close (see Fig. 5) and the average velocity of the modelled ice (15.11 ± 2.07 cm·s^{-1}) was slightly smaller than that of real ice (15.96 ± 2.16 cm·s^{-1}). The drift difference between the modelled ice and real ice was relatively large from 11:03 to 11:24 am (Fig. 5). During that period, the velocity of real ice (14.53 cm·s^{-1}) was larger than that of modelled ice (13.77 cm·s^{-1}) because of the decrease of real ice due to the melting process forced by the thermal factor. Both modelled and real ice drifted mainly towards the north, with some drifts toward the northeast. The average current velocity (14.54 cm·s^{-1}) was slightly smaller than the modelled and real ice velocity; the current mostly moved toward the north, sometimes toward the northeast. The wind speed was small (1.71 ± 0.53 m/s), with light breezes forced during the experimental period; south wind was predominant, followed by east and east wind.

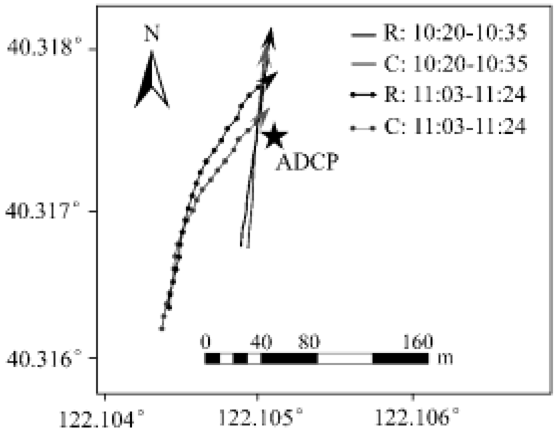

Fig. 5 Comparison of the trajectories of modelled ice C and real ice (R).

The ice–current–wind relationships of modelled and real ice drift were also established based on multiple regression. The results are as follows:

$$V_{\text{model-ice}} = 0.8078e^{i(9.28°)}V_c + 0.0102e^{i(11.31°)}V_w + 0.0224e^{i(50.98°)}, \quad \textbf{[5]}$$

$$V_{\text{real-ice}} = 0.8142e^{i(10.22°)}V_c + 0.0102e^{i(7.33°)}V_w + 0.0300e^{i(55.73°)}, \quad \textbf{[6]}$$

In Eq. (5) and (6), $V_{\text{model-ice}}$ and $V_{\text{real-ice}}$ are the modelled ice and real ice drift velocities, respectively. The correlation coefficients R^2 of the equations for modelled and real ice were 0.73 and 0.76, respectively. The ice–current–wind relationship of the modelled ice was close to that of the real ice, with a 0.01-significance level, indicating that both real and modelled ice were significantly influenced by current and wind. The trajectories, ice velocity, current coefficient, wind coefficient, and constant of modelled ice were similar to that of the real sea ice; hence, the real ice could be substituted by modelled ice for *in situ* observations of sea ice drift.

4 Conclusions

(1) The simultaneous acquisition of the ice velocity, current velocity, and wind speed helps to understand the ice drift characteristics in the Bohai Sea. When the wind was mild in the Bohai Sea, the current played a major role while the wind played a minor role in the free drift of isolated modelled ice.

(2) The modelled ice drift was significantly affected by the current and wind based on the ice–current–wind relationship using multiple linear regression. The magnitude error between the calculated and observed ice velocity was less than 12.05% and the velocity direction error was less than 6.21°. The ice velocity could be estimated using the observed current velocity and wind speed when the observed ice velocity was hard to obtain.

(3) The drift characteristics of modelled ice were similar to that of real sea ice; hence, the real ice could be substituted by modelled ice for *in situ* observations of sea ice drift.

References

Fukamachi Y, Ohshima K I, Mukai Y, et al. 2011. Sea-ice drift characteristics revealed by measurement of acoustic Doppler current profiler and ice-profiling sonar off Hokkaido in the Sea of Okhotsk. Annals of Glaciology, 52(57): 1–8

Gu Wei, Liu Chengyu, Yuan Shuai, et al. 2013. Spatial distribution characteristics of sea-ice-hazard risk in Bohai, China. Annals of Glaciology, 54(62): 73–79

Ji Shunying, Chen Xiaodong, Liu Yu, et al. 2013. A digital image technology and its application for the sea ice field observation in the Bohai Sea. Acta Oceanologica Sinica (in Chinese), 35(3): 119–127

Lang Wenhui, Wu Qing, Zhang Xi, et al. 2014. Sea ice drift tracking in the Bohai Sea using geostationary ocean color imagery. Journal of Applied Remote Sensing, 8(1): 083650

Li Zhijun, Lu Peng. 2006. Preliminary analysis of iceberg characteristics in the Antarctic Ocean. Journal of Dalian University of Technology (in Chinese), 46(3): 418–422

Lin Yebin, Xu Yingjun, Gu Wei, et al. 2010. Distribution of sea ice density and air porosity along the coast of the Bohai Sea. Resources Science (in Chinese), 32(3): 412–416

Shi Wenqi, Yuan Shuai, Xu Ning, et al. 2016. Analysis of floe velocity characteristics in small-scaled zone in offshore waters in the eastern coast of Liaodong Bay. Cold Regions Science and Technology, 126: 82–89

Simizu D, Ohshima K I, Ono J, et al. 2014. What drives the southward drift of sea ice in the Sea of Okhotsk? Progress in Oceanography, 126(SI): 33–43

Timmermans M, Proshutinsky A, Krishfield R A, et al. 2011. Surface freshening in the Arctic Ocean's Eurasian Basin: An apparent consequence of recent change in the wind-driven circulation. Journal of Geophysical Research: Oceans, 116: C00D03, doi:10.1029/2011JC006975

Wu Longtao, Wu Huiding, Li Wanbiao, et al. 2005. Sea ice drifts in response to winds and tide in the Bohai Sea. Acta Oceanologica Sinica (in Chinese), 27(5): 15–21

Anomalies of Bohai Sea Ice Cover and Potential Climate Driving Factors

Yu Yan[1], Wei Gu[1], Ning Li[1,*]

[1] *Key Laboratory of Environmental Change and Natural Disaster of Ministry of Education, Faculty of Geographical Science, Beijing Normal University, Beijing 100875, China*

** Author to whom any correspondence should be addressed*

yanyu@mail.bnu.edu.cn

weigu@bnu.edu.cn

ningli@bnu.edu.cn

Despite the backdrop of continuous global warming, sea ice extent has been found not to consistently decrease across the globe, and instead exhibit heterogeneous variability at middle to high latitudes. Continuous satellite monitoring of the Bohai Sea has shown that the sea ice cover area has increased slightly (1.55±1.13% yr^{-1}) from 1988 to 2015. The long-term average ice area (AIA) and maximum ice area (MIA) range from 0.40×10^4–2.00×10^4 km^2 and 0.78×10^4–3.55×104 km^2, covering 5.35–26.7% and 10.4–47.4% of the Bohai Sea, respectively. The detrended annual average ice area (AAIA) was further found to correlate with a slight decreasing mean ice-period average temperature (IAT, $r = -0.58$, $p < 0.01$) of 11 meteorological stations around the Bohai Sea as well as a mild increasing cumulative freezing degree days (*CFDD*, $r = 0.65$, $p < 0.01$). Correlation with decreasing Arctic Oscillation (AO) index ($r = -0.60$, $p < 0.01$) over the study period suggested AO as the primary large-scale climate factor for Bohai Sea ice. The results can provide important references for climate change and disaster monitoring and risk management.

1 Introduction

Sea ice cover has long been recognized as a sensitive and important indicator of the climate system in both global and regional observation and modelling studies (Vinnikov et al 1999, Bai et al 2011, Notz and Stroeve 2016). Due to the continuous global warming in recent decades (Vihma 2014), there has been a decline in ice extent in most polar and sub-polar frozen seas, including the Baltic Sea (Omstedt and Chen 2001), the sea of Okhotsk (Harada et al 2014), the Hudson Bay and the Canadian Archipelago (Cavalieri and Parkinson 2012). The Bohai Sea is a semi-enclosed sea located in North China, which is the southernmost frozen sea in the Northern Hemisphere. A better understanding of the variability of ice cover in this region is important for monitoring regional climate change (Gong et al 2007, Bai et al 2011). In addition, sea ice hazards in the Bohai Sea can severely affect aquaculture, marine transportation, offshore oil field operation and other economic activities in the Bohai Rim as a national economic hub of China (Gu et al 2013, Zhang et al 2016). And yet when managed properly, sea ice can also be desalinated to produce freshwater for agriculture or industry, and thus has the potential to help alleviate the severe fresh water shortage in the region as one of the most water-scarce areas in China (Liu et al 2013). Moreover, knowledge of the ice cover is necessary to decipher the sea ice contaminant pathways (Beattie et al 2014, Tovar-Sánchez et al 2010). Therefore, research on the long-term variability of sea ice cover can provide important references for climate change and disaster monitoring and risk management, assessing potential pollutants release, and estimating sea ice resources.

In the present study, the evolution of sea ice cover in the Bohai Sea during the winters of 1988–2015 was analyzed using satellite remote-sensing imagery, to elucidate the multidecadal variability in this peculiar mid-latitude frozen sea area. 640 satellite images of sea ice cover during the study period were analysed. Statistical methods such as correlation analysis and linear regression were used to explore the potential climate driving factors during this period.

2 Data

The evolution of sea ice cover was analyzed using a comprehensive series of remote-sensing data. We derived the sea ice cover using NOAA's Advanced Very High Resolution Radiometer (AVHRR) images with 1.1 km spatial resolution and NASA's Moderate Resolution Imaging Spectroradiometer (MODIS) images with 1.0 km spatial resolution. Images from these two sensors have been used to extract sea ice area in the Bohai Sea due to their high temporal resolution, moderate spatial resolution, multi spectral band and large-scale coverage. The AVHRR and MODIS data were downloaded from National Satellite Meteorology Center of CMA and NASA LAADS (Level 1 and Atmosphere Archive and Distribution System), respectively. More than 2500 images were downloaded for the entire study period.

Daily temperature was obtained from the website of the China Meteorological Data Sharing Service System (http://data.cma.cn/), including 11 meteorological stations around the Bohai Sea (figure 1). Daily data covering the entire ice period (1 December – 15 March) from 1988 to 2015 were obtained for these 11 stations. These data were subsequently used to calculate the cumulative freezing degree days (CFDD).

The monthly AO index, North Atlantic Oscillation (NAO) index and the Niño 3.4 region sea surface temperature anomaly index, which was used as a proxy of the El Niño–Southern Oscillation (ENSO) variability, from 1988 to 2015 was obtained from the NOAA/Climate Prediction Center (http://www.cpc.ncep.noaa.gov/). The North Pacific (NP) index were downloaded from National Center for Atmospheric Research (https://climatedataguide.ucar.edu/climate-data/north-pacific-np-index-trenberth-and-hurrell-monthly-and-winter). The monthly Pacific Decadal Oscillation (PDO) data were downloaded from the University of Washington/JISAO (http://research.jisao.washington.edu/pdo/). Correspondingly, annual circulation data were obtained by averaging the monthly data during the winter months (December–March).

3 Results and discussion

3.1 *Multidecadal variability of sea ice area in the Bohai Sea*

The evolution of the sea ice area in the Bohai Sea for the 1988–2015 period is shown in figure 1. As illustrated in the figure, the sea ice cover exhibit significant interannual change. The multidecadal (1988–2015) mean AAIA is 0.89×10^4 km^2, and the standard deviation is 0.36×10^4 km^2. In this study, winters with AAIA less than 0.53×10^4 km^2 (mean AAIA – 1 STD) were defined as mild winters, and those with AAIA greater than 1.25×10^4 km^2 (mean AAIA + 1 STD) were identified as harsh winters (Bai *et al* 2011). Figure 5 shows that, out of the 28 years, AAIA of 20 winters are bounded by the limits of mean AAIA ± 1 STD. The 1997/98, 2000/01, 2009/10, 2010/11 and 2012/13 winters experienced expanded ice cover above the 1.25×10^4 km^2 upper bound. In contrast, the 2001/02, 2006/07 and 2014/15 winters experienced reduced ice cover, with AAIAs below the 0.53×10^4 km^2 lower bound. Notably, the 2009/10 winter attained the maximum AAIA of 2.00×10^4 km^2, covering 26.7% of the whole Bohai Sea, whereas the 2014/15 winter had the minimum AAIA of 0.40×10^4 km^2 (a mere 5.35% coverage).

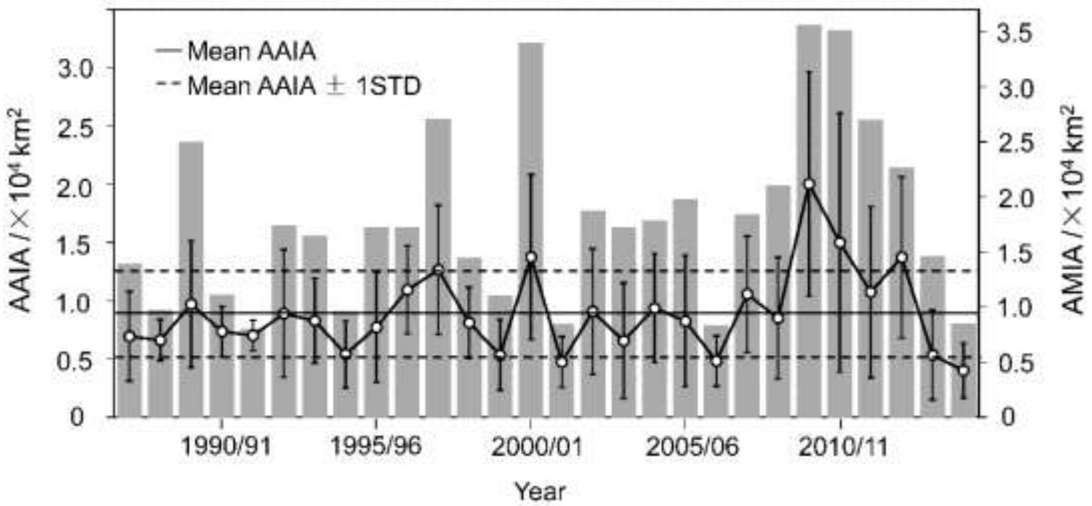

Fig. 1. Annual average ice area (AAIA) and the annual maximum ice area (AMIA) in the Bohai Sea for the 1988–2015 period. The solid line represents the mean value of AAIA, and the dotted lines correspond to mean AAIA ± 1 standard deviation (STD).

The variation of the AMIA is also presented in figure 5. Over the entire study period, the 2000/01, 2009/10 and 2010/11 winters attained AMIA greater than 3.00×10^4 km^2 and that of 1988/89, 1991/92, 1994/95, 2001/02, 2006/07 and 2014/15 winter was less than 1.00×10^4 km^2. The 2009/10 winter reached the maximum AMIA of 3.55×10^4 km^2 (47.4% coverage), whereas the 1991/92 winter attained the minimum AMIA of 0.80×10^4 km^2 (10.7% coverage). AMIAs of the remaining years were within the range of 1.00–3.00×10^4 km^2. A strong positive correlation ($r = 0.90$, $p < 0.01$) between AAIA and AMIA was also noted (not shown here for brevity). However, the ratio of AMIA/AAIA over the 28 years ranged from 1.14 to 2.73 (2.02 ± 0.39), indicating a large interannual variability.

3.2 *Seasonal cycle of sea ice cover in the Bohai Sea*

The seasonal cycle of ice extent in the Bohai Sea was derived from the WAIA averaged over the 1988–2015 period (figure 2). Overall, the seasonal cycle of average WAIA shows a single peak. The typical seasonal cycle of sea ice area in the Bohai Sea kicked off on an ice freeze-up date in early December. Afterwards, the ice growing phase lasted approximately 8 to 9 weeks until late January. The ice cover in the Bohai Sea reached the seasonal maximum around late January to early February. From mid-February to mid-March, the WAIA dropped rapidly, and the ice break-up phase lasted approximately 5 weeks. Notably, the ice growing phase (8 weeks) was considerably longer than the break-up phase (5 weeks) in the Bohai Sea, suggesting that the processes of sea ice formation and melting were not symmetrical. The different freezing and melting rates were closely related to the local temperature change rate, which were –0.08 °C/day and 0.19 °C/day during the sea ice freezing and melting phases, respectively, after averaged over the 28 years study period. Notably, Wang *et al* (2012) also reported the asymmetry of the seasonal ice cycle in the Great Lakes.

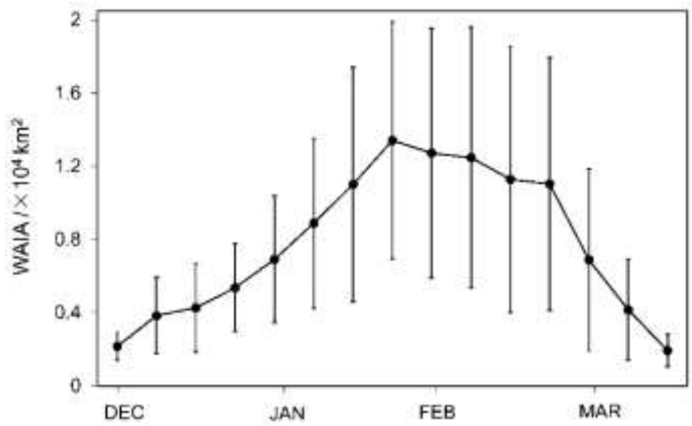

Fig. 2. Variation of the weekly average ice area (WAIA) in the Bohai Sea averaged over the 1988-2015 period with one standard deviation (indicated with the vertical bars).

The standard deviation associated with the average WAIA is also shown in figure 2, and the large interannual variability indicates that the local synoptic forcing such as surface air temperature and wind may play an essential role in ice conditions in the Bohai Sea. Wang et al (2012) found that the natural variability of ice cover in the Great Lakes was largely affected by the internal climate forcing. The predictability of sea ice cover by statistical or numerical models was generally poor due to the large STD, especially at the multidecadal time scales.

3.3 *Correlations between sea ice cover and climate factors*

The AAIA, the mean of the ice-period average temperature (IAT, defined as the average temperature for the ice period from December 1 to March 15 in the following year) of 11 meteorological stations around the Bohai Sea as well as the associated *CFDD*, and the AO index for the 1988–2015 period are shown in figure 3. The straight trend lines presented in the figure were obtained using the least squares fitting. The linear regression returns a slight overall increase of 1.38±1.00% yr^{-1} (R = 1.38, i.e., at a statistical significance of 80%), which is in parallel with the slight decrease in IAT (R = 0.74), the mild increase in *CFDD* (R = 1.04) and decreasing AO index (R = 1.74, i.e., at a statistical significance of 90 %).

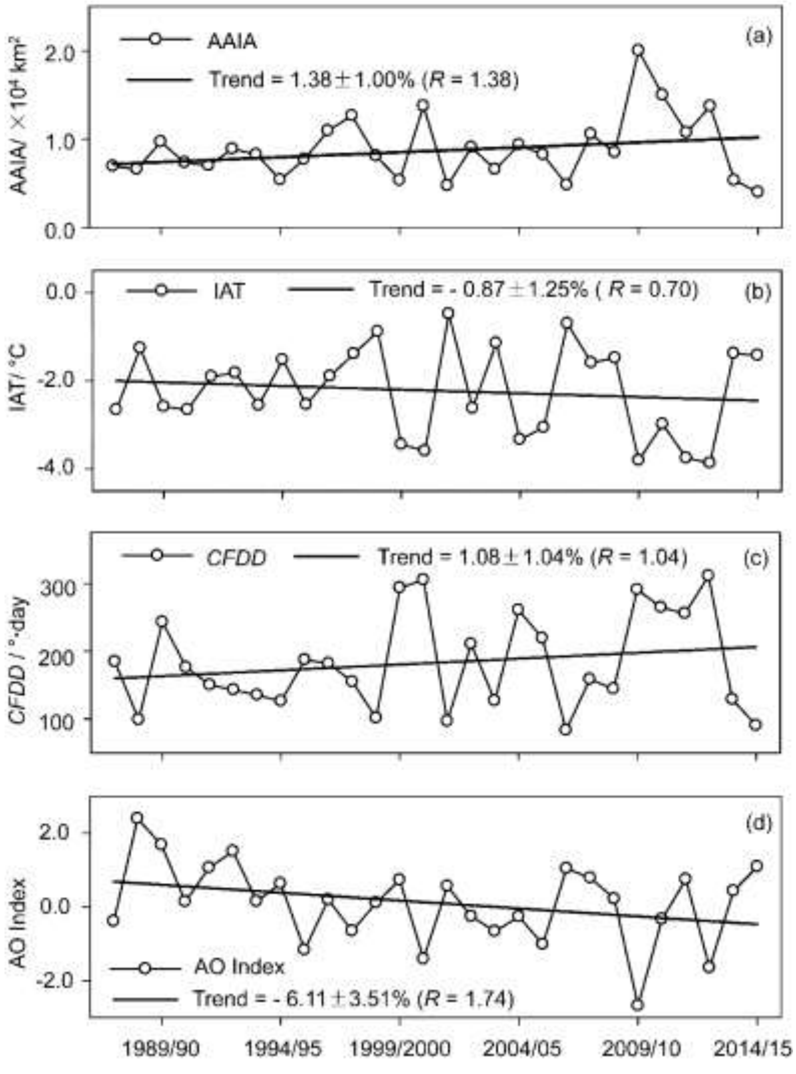

Fig. 3. Data points and multidecadal trends of (a) annual average ice area (AAIA), (b) the mean of the ice-period average temperature (IAT) of 11 meteorological stations around the Bohai Sea, (c) the associated cumulative freezing degree days (*CFDD*) and (d) AO index from 1988 to 2015.

A moderate negative correlation between the detrended time series of AAIA and the mean value of the IAT (r = –0.58, p < 0.01) of 11 meteorological stations around the Bohai Sea during the study period was shown in figure 4a, suggesting that the average sea ice condition in each year was closely related to the IAT. A moderate positive correlation (r = 0.65, p < 0.01) between the detrended time series of AAIA and *CFDD* is shown in figure 4c, which suggests that *CFDD* is another important climate factor for sea ice formation. Similar correlations were also found between AMIA and IAT/*CFDD* (see figures 4b&4d). This suggests that the local temperature is a controlling factor for the sea ice conditions in the Bohai Sea, which is consistent with the findings of Zhang *et al* (2016).

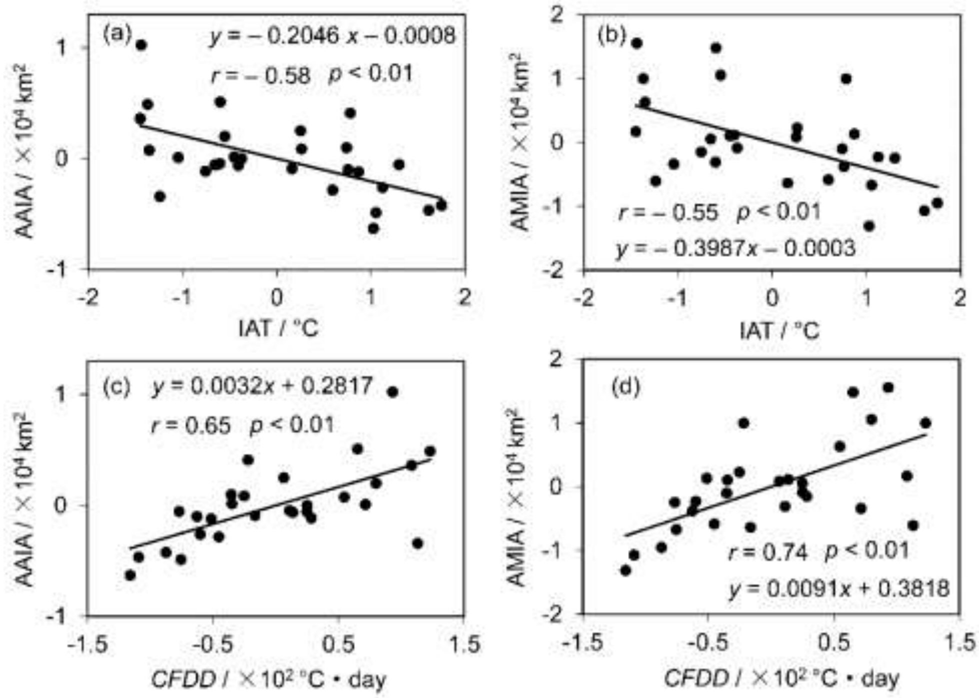

Fig. 4. Correlations between (a) annual average ice area (AAIA) and the mean ice-period average temperature (IAT) of 11 meteorological stations around the Bohai Sea, (b) annual maximum ice area (AMIA) and IAT, (c) AAIA and the associated *CFDD* and (d) AMIA and *CFDD* through detrended analysis.

As shown in figure 5, the Bohai Sea ice extent tended to be smaller in high-AO and NAO phases and larger in low-AO and NAO phases. The detrended Bohai Sea ice area exhibits moderate negative correlation with the AO index (r = –0.60, p < 0.01) and NAO index (r = –0.69, p < 0.01). During the negative phase of the AO, enhanced atmospheric pressure over the Arctic induced weaker westerly winds in the upper atmosphere, which allowed the cold air to reach further southern regions, resulting in colder winter in these regions (Bai *et al* 2011). At the same time, when the NAO index was in negative phase, the pressure difference was small, which decreased the storminess in the westerly wind belt and increased the zonal circulation and pushed large amounts of cold Arctic air to the south, resulting in significant cooling in Northeast Asia including the Bohai Sea (Bai *et al* 2011; Li *et al* 2013). Presumably due to the above mechanisms, the Bohai Sea usually experienced higher-than-normal ice cover during low AO and NAO winter. All harsh winters (1997/98, 2000/01, 2009/10, 2010/11 and 2012/13) occurred during the negative phase of AO and NAO. In the 2009/10 winter in particular, very strong negative AO and NAO occurred, resulting in the maximum ice extent over the entire study period.

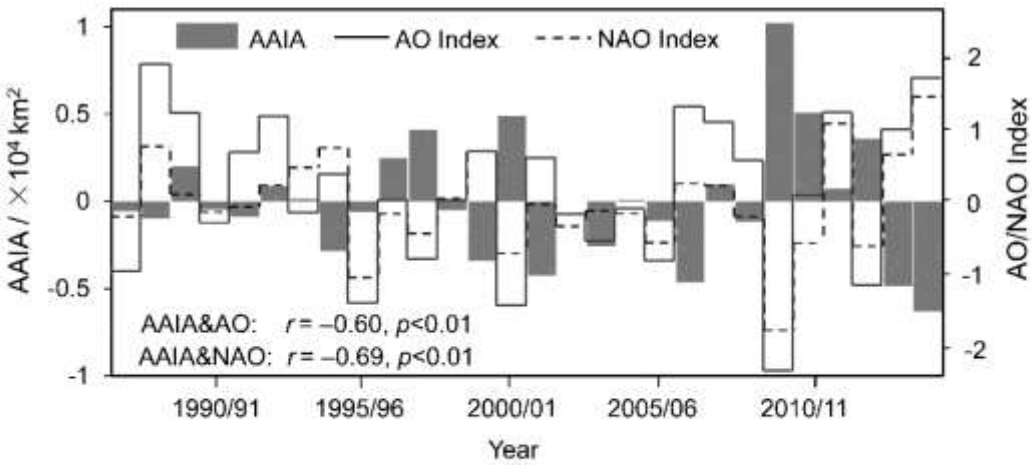

Fig. 5. Time series of detrended Bohai Sea annual average ice area (AAIA, bar) and December–March Arctic Oscillation (AO, solid line) and North Atlantic Oscillation (NAO, dashed line) index from 1988 to 2015

To estimate the impact of modes other than the AO and NAO on the evolution of sea ice area during 1988–2015, we assessed the correlation of sea ice extent to relevant large-scale climate factors such as ENSO, PDO and NP again using detrended time series (The relevant plots are not shown here for brevity). The detrended Niño 3.4 index exhibits a weak and insignificant correlation ($r = 0.10$, $p = 0.62$) with Bohai Sea ice area. Bai *et al* (2011) also reported that the influence of ENSO on the Bohai Sea ice was minimal. The correlations with detrended PDO ($r = –0.04$, $p = 0.82$) and NP ($r = –0.19$, $p = 0.34$) time series were also found to be weak and insignificant. The above correlation analysis suggests that AO and NAO appear to be the primary large-scale climate factors for Bohai Sea ice.

4 Conclusions

(1) Despite the backdrop of continuous global warming, the ice extent in the Bohai Sea exhibited a small overall increasing trend of 1.38±1.00% yr^{-1} during the study period (R = 1.38, i.e., at a statistical significance of 80%).

(2) The seasonal cycle of the ice extent in the Bohai Sea shows a single peak with longer freezing phase than melting phase. The different freezing and melting rates were closely related to the local temperature change rate, which were –0.08 °C/day and 0.19 °C/day during the freezing and melting phase, respectively.

(3) The detrended AAIA was further found to correlate with a slight decreasing mean ice-period average temperature (IAT, $r = –0.58$, $p < 0.01$) of 11 meteorological stations around the Bohai Sea as well as a mild increasing cumulative freezing degree days (*CFDD*, $r = 0.65$, $p < 0.01$). Correlation with decreasing Arctic Oscillation (AO) index ($r = –0.60$, $p < 0.01$) and North Atlantic Oscillation (NAO) index ($r = –0.69$, $p < 0.01$) over the study period suggested AO and NAO as the primary large-scale climate factors for Bohai Sea ice.

Acknowledgments

This study was financially supported by the National Natural Science Foundation of China (41571510) and the Fundamental Research Funds for the Central Universities (2014KJJCB02) and Project supported by State Key Laboratory of Earth Surface Processes and Resource Ecology (2013-ZY-06). The authors also appreciate the help of the members of the sea ice research group.

References

Bai X, Wang J, Liu Q, Wang D and Liu Y 2011 Severe ice conditions in the Bohai Sea, China, and mild ice conditions in the Great Lakes during the 2009/10 winter: links to El Nino and a strong negative Arctic Oscillation *J. Appl. Meteorol. Climatol.* **50** 1922–35

Beattie S A, Armstrong D, Chaulk A, Comte J, Gosselin M and Wang F Y 2014 Total and methylated mercury in Arctic multiyear sea ice *Environ. Sci. Technol.* **48** 5575–82

Cavalieri D J and Parkinson C L 2012 Arctic sea ice variability and trends, 1979-2010 *Cryosphere* **6** 881–89

Gong D Y, Kim S J and Ho C H 2007 Arctic oscillation and ice severity in the Bohai Sea, East Asia *Int. J. Climatol.* **27** 1287–302

Gu W, Liu C, Yuan S, Li N, Chao J, Li L and Xu Y 2013 Spatial distribution characteristics of sea-ice-hazard risk in Bohai, China *Ann. Glaciol.* **54** 73–79

Harada N, Katsuki K, Nakagawa M, Matsumoto A, Seki O, Addison J A, Finney B P and Sato M 2014 Holocene sea surface temperature and sea ice extent in the Okhotsk and Bering Seas *Prog. Oceanogr.* **126** 242–53

Liu C, Gu W, Chao J, Li L, Yuan S and Xu Y 2013 Spatio-temporal characteristics of the sea-ice volume of the Bohai Sea, China, in winter 2009/10 *Ann. Glaciol.* **54** 97–104

Notz D and Stroeve J 2016 Observed Arctic sea-ice loss directly follows anthropogenic CO_2 emission *Science* **354** 747–50

Omstedt A and Chen D 2001 Influence of atmospheric circulation on the maximum ice extent in the Baltic Sea *J. Geophys. Res. Oceans* **106** 4493–500

Tovar-Sánchez A, Duarte C M, Alonso J C, Lacorte S, Tauler R and Galbán-Malagón C 2010 Impacts of metals and nutrients released from melting multiyear Arctic sea ice *J. Geophys. Res. Oceans* **115** C07003

Vihma T 2014 Effects of Arctic sea ice decline on weather and climate: a review *Surv. Geophys.* **35** 1175–214

Vinnikov K Y, Robock A, Stouffer R J, Walsh J E, Parkinson C L, Cavalieri D J, Mitchell J F B, Garrett D and Zakharov V F 1999 Global warming and Northern Hemisphere sea ice extent *Science* **286** 1934–37

Wang J, Bai X, Hu H, Clites A, Colton M and Lofgren B 2012 Temporal and spatial variability of Great Lakes ice cover, 1973-2010 *J. Clim.* **25** 1318–29

Zhang N, Wu Y and Zhang Q 2016 Forecasting the evolution of the sea ice in the Liaodong Bay using meteorological data *Cold Reg. Sci. Technol.* **125** 21–30

24th IAHR International Symposium on Ice
Vladivostok, Russia, June 4 to 9, 2018

Predicting Ice Thickness for Engineering Applications

Robert Frederking
National Research Council Canada
Ottawa, Ontario K1A 0R6 Canada
Robert.frederking@nrc-cnrc.gc.ca

Many engineering problems require an estimate of ice thickness, either the maximum likely thickness or the thickness at some time during the winter. This can be for estimating ice forces on an offshore structure in the sea or a bridge pier in a river. Operation of icebreaking ships requires knowledge of ice thickness to establish the viability of transit to northern ports. Similarly, over-ice transportation on seas, lakes or rives depends on a knowledge of ice thickness. At some locations historical records can be used to estimate ice thicknesses, but with changing climate historical records have limited applicability. Having means for predicting ice growth during a winter is a helpful tool. In high Arctic regions it is assumed the primary factors affecting ice growth are air temperature and snow depth. Assessment of the equations against data from Arctic weather stations indicates that the incorporation of snow depth in terms of a mean annual snow depth is a simple means for improving their predictive capability. Modified equations including mean annual snow depth and freezing degree days as input parameters are proposed and tested against available data at two locations in the Canadian High Arctic; Resolute Bay in a marine coastal environment and Baker lake in an inland freshwater lake. These modified prediction equations are proposed for general application in the Arctic.

1. Introduction

An estimate of ice thickness is required for many engineering problems, either the maximum likely thickness over a winter or the thickness at some time during the winter. Having means for predicting ice growth during a winter is a useful tool.

Ice growth has been a classic problem in ice engineering. It was treated in the early literature (Stefan, 1891) in which a mathematical model of sea ice growth was developed and compared with measurement data from the Arctic. Many aspects of the physical processes involved in ice growth are known, as well as mathematical solutions. The challenge was and remains to make reasonable assumptions allowing an appropriate degree in simplification for the solution. Modern reviews of growth process of sea ice can be found in Leppäranta (1993) and freshwater ice in Ashton (2011) also have helpful discussions of simplifications. It has already been pointed out that many factors influence ice growth but two climatic factors, air temperature and precipitation in the form of snow generally are the most important, and information on them is generally available. There are differences between sea ice and fresh water ice growth. This paper will present simple and practical methods for predicting ice thickness based on the input data available. Assumptions and limitations will be spelled out. The methods will be illustrated with two examples, one for a sea ice marine site and the other for a freshwater lake.

2. Ice Growth

The ice growth process can be described as vertical heat conduction through a composite slab (ice and snow cover) with a phase change (freezing) at the bottom surface. Heat flux from the ocean beneath the ice cover, the influence of a snow cover, radiation to the ice surface or heat transfer from the ice surface to the atmosphere will be ignored. To grow an incremental thickness of ice Δh on the bottom surface of an ice cover, the latent heat of fusion so released has to be conducted through the ice sheet, away from the ice-water interface. The latent heat of this incremental thickness is given by $\lambda\ \rho\ \Delta h$ where λ is the latent heat of fusion of ice and ρ is the density of the ice. The amount of heat that can be conducted through the ice sheet is a function of conductivity of the ice sheet, k_i, the temperature gradient through the ice sheet, $\Delta T/h$, and the time, Δt. The ice sheet thickness is h, ΔT is the difference between the temperature at the top of the ice sheet T_s, usually takes as air temperature, and the temperature at the bottom, T_m, actually the freezing point of water. The balance between these two energy fluxes is given by

$$\lambda\ \rho\ \Delta h = k_i\ \Delta t\ \Delta T/h \qquad \textbf{[1]}$$

reformulating [1], integrating and solving for, h, the amount of ice grown over time $\int \partial t$ is

$$h\ = \{2(k_i\ /\ \lambda\ \rho) \int (T_s - T_m)\ \partial t\}^{1/2} \qquad \textbf{[2]}$$

The term $\int (T_s - T_m)\ \partial t$, with T_s the mean daily air temperature, time unit of days selected and summed over the time interval of interest, is accumulated freezing-degree-days, S.

$$S = \int (T_s - T_m)\ \partial t \qquad \textbf{[3]}$$

Substituting S into equation [2] and substituting usual properties for thermal and physical properties of ice we obtain the simple approximation of Stefan

$$h = 0.035\ (S)^{1/2} \qquad \textbf{[4]}$$

where h is in units of meters and S is °C-day. While the sign of S is negative, practice is to make it make positive in applications. Experience has shown that actual ice thicknesses are less than those predicted by equation [4]. Michel (1971) suggested a local conditions coefficient α that could be applied to equation [4] to make it more useful for engineering applications.

Sea ice growth in Arctic regions occurs under different conditions due to the high latitude; limited solar radiation during the principle growth period. Zubov (1945), made extensive measurements of ice thickness and climate in the Russian Arctic. Using his own measurements and noting those of Weyprecht (1879), also made in the Arctic, he proposed an empirical expression for predicting sea ice thickness

$$h^2 + 50h = 8\ S \qquad \textbf{[5]}$$

In Zubov's equation S is in units ºC-day and ice thickness h, cm. Zubov's and Weyprecht's data, together with Zubov's equation [5], and a modification of Stefan [4] with $\alpha = 0.7$ are plotted in Figure 1. The Zubov equation [5] is a good fit to the data. The Stefan equation, adjusted by applying a local conditions coefficient, $\alpha = 0.7$, provides a reasonable comparison to the data, but it tended to over-predict for thin ice and under-predict for thick ice.

While much focus has been on the ice properties and coefficients that go into equation [4], the accumulated freezing-degree-day term, S, also bears attention. Note: freezing-degree-day will be abbreviated f-d-d hereafter. Establishing the start for the accumulation of f-d-d is a question. In this paper the start is the day after which the accumulated f-d-d, as defined by S in equation [3] is consistently negative. At some locations the water may still be cooling at this time. Where it is available, counting from freeze-up is more representative. This is a more critical issue when predicting ice thickness during the early part of the winter than the maximum ice thickness.

Other investigators have looked into developing improved practical equations for predicting ice thickness from general environmental conditions. Sinha and Nakawo (1981) used detailed high-quality ice, snow and climatological measurements from Eclipse Sound in the Canadian High Arctic, to develop and test an ice thickness prediction model suitable for the conditions of the high Arctic. The equation developed was similar in form to Zubov's

$$h^2 + 2\ (k_i / k_s)\ h_s\ h = 2\ (k_i / \lambda\ \rho)\ \mathrm{S} \qquad \textbf{[6]}$$

They had frequent measurements of ice thickness, salinity, temperature profiles, snow thickness and density, as well as daily air temperatures. Using mean annual snow thickness and density, plus properties of sea ice from the literature, equation [6] made good predictions of ice thickness throughout the two winters for which they had data to test it. Note, that care always has to be paid to consistent units on both sides of the equation.

The draft of the new edition of ISO 19906 Arctic offshore structures (ISO, 2017) has an equation for predicting sea ice growth

$$h^2 - h_o^2 + m\,(h - h_o) = \omega\, S \qquad \textbf{[7]}$$

where h is the current ice thickness, h_o an initial ice thickness, and S in this case is the accumulated f-d-d between when h_o was determined and the time when the current ice thickness h is to be determined. The physical parameters of equation [7] are defined as $m = 2\,(k_i / k_s)\,h_s$ and $\omega = \beta\, 2\, k_\mathrm{i} / \lambda\, \rho$, essentially the same as in equation [6]. The only exception is the introduction of β, an empirical factor introduced to take into account local conditions, but not necessarily the same as α in equation [4]. If h_o is set to 0 it is seen that the ISO equation [7] is identical to the Sinha and Nakawo (1981) equation [6]. Some typical values of ice and snow physical properties are listed in Table 1. It should be noted these properties are all temperature and salinity dependent, some to a greater extent than others. For example, the latent heat of fusion of sea ice is quite dependent on its temperature and salinity. Similarly the conductivity of snow is very dependent on its density. Weeks (2010) provides a good review of snow and sea ice properties, including their temperature, salinity and density dependence.

Table 1. Physical properties of ice and snow.

Property	Units	Freshwater Ice	Sea Ice
density	kg/m3	917	900
Latent heat of fusion	kJ/kg	334	295
Conductivity of ice	W/(m ºC)	2.2	2.1
Conductivity of snow	W/(m ºC)	0.2	0.2

3. Examples of ice growth

There are 10 weather stations in the Canadian Arctic at which ice thickness and snow depths are systematically measured throughout the winter, plus the usual meteorological data. The predictive capability of equations [4] and [7] were tested against some of these measured data. Two stations have been selected for this purpose; Resolute (72º 42’ - N 94º 50’ W) where measurements are made in sea ice and Baker Lake (64º 19’ - N 96º 01’ W) in fresh water ice. At Resolute Bay measurements extend back to the late 1940s. The approach is to use f-d-d determined from air temperature measurements at the locations with properties for sea ice and freshwater ice from Table 1 to calculate an ice thickness. It will also be investigated how snow depth information can be used to improve the prediction of ice thickness.

Resolute Bay, Nunavut, Canada: Measured and predicted ice thicknesses together with snow depth for the winter 2005-06 is plotted in Figure 2. The α and β factors, noted on the figure, were adjusted to match the maximum ice thickness. The basic parameters and factors for the winter of 2005-06 and 2006-07 are summarized in Table 2. The winter 2005-06 had fewer f-d-d (8% less) than 2006-07, a greater snow depth (100% more), and not surprisingly, a lesser maximum ice thickness (12%). Based on f-d-d alone, the thickness should have been only about 4 % less. It is clear that the snow depth has a strong influence. The modified Stefan equation [4] has no direct means of incorporating snow depth, other than local conditions coefficient α. On the other hand, the ISO equation [7] has the possibility of including both the snow depth and, if known, the snow conductivity, while still providing some facility for local conditions with the factor β on the accumulated f-d-d term, *S*. It appears that with α of 0.75, equation [4] could have utility. The variability of β for just these two winters' factor brings into question the utility of equation [8].

Table 2. Ice growth parameters at Resolute Bay for winters of 2005-06 and 2006-07

Winter	FDD	Max Ice thickness (m)	Mean snow depth (m)	α factors	β factor
2005-06	4630	184	0.22	0.75	1.9
2006-07	4990	210	0.11	0.77	1.3

Next the entire Resolute Bay record in terms of maximum annual ice thickness, mean annual snow depth and accumulated f-d-d is plotted in Figure 3 to illustrate year-to-year variation.

Maximum annual ice thickness was examined in reference to accumulated f-d-d, *S*, and mean annual snow depth, h_s, and their influence shown by plotting them versus the measured maximum annual ice thickness in Figure 4. A stronger correlation to snow depth than f-d-d was seen. Some other Canadian Arctic station records were checked and generally similar relative influences were found. Based on this, a modified form of equation [7] was developed by inserting an empirical coefficient, γ, into the m term, since this is where snow depth comes into play. Thus a modified ISO equation was proposed

$$h^2 - h_o^2 + \gamma\, m\, (h - h_o) = \omega\, S \qquad \textbf{[8]}$$

with the empirical coefficient β set to 0.5. Based on the observed influence of snow depth, a modified equation [4] with a factor to include the influence of snow depth was also developed as

$$h = 0.037\ (1\text{-}h_s/h_{so})\ S^{1/2} \qquad \textbf{[9]}$$

where h_{so} is a normalizing snow depth selected to non-dimensionalize the snow depth, in this case h_{so} = 1 m. The results of the calculated maximum annual ice thickness using equations [8] and [9] are plotted in Figure 5. The predictions of the two equations are similar, with [8] coming closer to one to one slope on the linear regression than equation [9].

Baker Lake, Nunavut, Canada: The entire Baker Lake record in terms of maximum annual ice thickness, mean annual snow depth and annual accumulated f-d-d is plotted in Figure 6 to illustrate year-to-year variation. This site is a freshwater lake about 300 km inland from Hudson Bay, and has significantly less snow. Baker Lake has a slightly less severe winter with about 4500 °C-day versus about 5500 °C-day for Resolute Bay. Maximum annual ice thickness attained at Resolute Bay is less than at Baker Lake due to the difference in snow depth.

The relation between mean annual snow depth and f-d-d was examined versus maximum annual ice thickness. For snow depth a slight trend of increasing ice thickness with decreasing snow depth could be ascertained, but it was not significant. The relation to f-d-d was more pronounced. Calculated maximum annual ice thickness for all three prediction equations, [4], [8] and [9] are plotted in Figure 7. For the case of Baker Lake conditions the simple Stefan equation with $\alpha = 0.9$ provided the best prediction within the limited range of maximum annual f-d-d associated with this location. The parameters in equations [8] and [9] were adjusted to see if a better fit could be obtained, but the ones displayed on Figure 7 were the best that could be determined.

4. Summary and Conclusions

In the Canadian High Arctic, the amount of snow is a significant factor, in addition to winter severity (accumulated freezing degree days), in determining the maximum annual ice thickness in marine environments. Marine coastal sites in the Arctic generally have more snow than inland sites and consequently thinner ice, given comparable winter severity. The modified equations in this paper, [8] and [9], provide better utility for predicting maximum annual sea ice thickness by including weighing functions for snow thickness. Equation [8], with two local conditions factors should be useful for predicting ice thickness during the growth period. Future effects of climate change, including snowfall, on ice thickness can be evaluated with the aid of these equations. For engineering design purposes any apparent trends in ice thickness should also take into account the large annual variability, which is evident in the actual records and would likely persist or even increase in the future.

Acknowledgments

The support of the Arctic Program of the National Research Council is gratefully acknowledged

References

Ashton, G.D. 2011. River and lake ice thickening, thinning, and snow ice formation, Cold Regions Science and Technology, Vol. 68, pp. 3–19

ISO. 2017. ISO/FDIS 19906 Arctic offshore structures, International Organization for Standardization, Geneva

Leppäranta, M. 1993. A review of analytical models of sea ice growth, Atmosphere-ocean, Vol. 31, pp.123-138

Michel, B. 1971. Winter regime of rivers and lakes, Cold Regions Science and Engineering Monograph III-B1a. CRREL, Hanover, NH. April 139 pp.

Sinha, N.K. and Nakawo. M. 1981. Growth of first-year sea ice, Eclipse Sound Baffin Island, Canada, Canadian Geotechnical Journal, Vol. 18, pp. 17-23.

Stefan, J. 1891. Uber die Theorie der Eisbildung, insbesondere uber die Eisbildung im Polarmeere, Annalen der Physik und Chemie, 42, pp. 269-286.

Wayprecht, K. 1879. "Die Metamorphosen des Polareises" (The metamorphoses of polar Ice), Austro-Hungarian Arctic Expedition of 1872-74, 1879.

Weeks, W.F. 2010. On Sea Ice, University of Alaska Press, Fairbanks

Zubov. N.N. 1945. L’dy Arktiki [Arctic Ice]. Izdatel’stvo Glavsermorputi, Moscow. English Translation. 1963 by U.S. Naval Oceanographic Office and American Meteorological Society, San Diego, Calif.

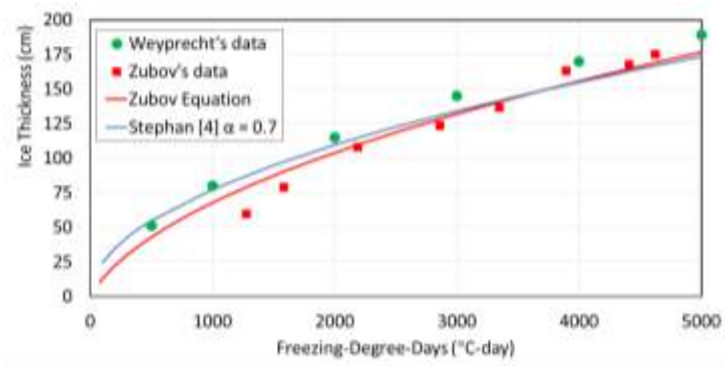

Fig. 1. Ice thickness as a function of freezing-degree-days from data and Zubov's equation.

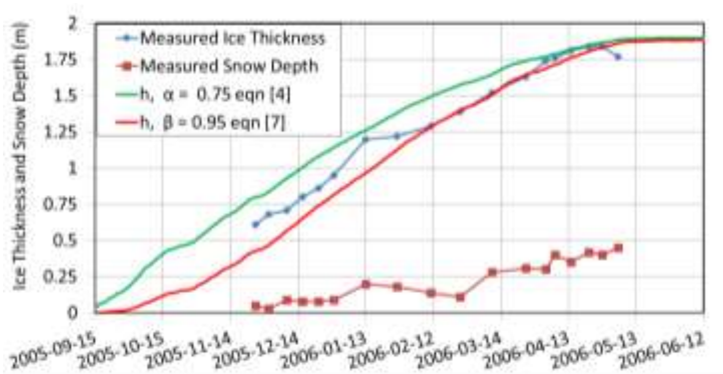

Fig. 2. Comparison of measured and predicted ice growth at Resolute Bay

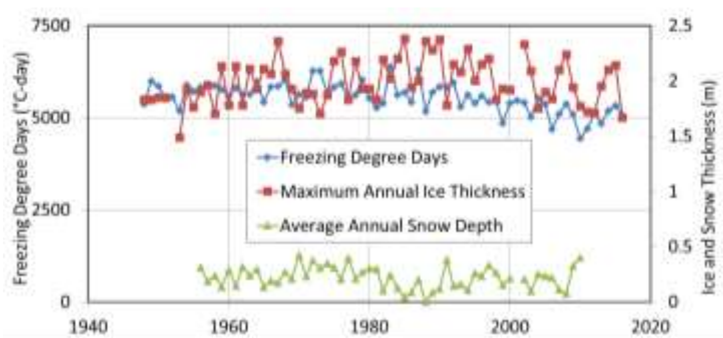

Fig. 3. Resolute Bay record of ice thickness, snow depth and freezing-degree-days

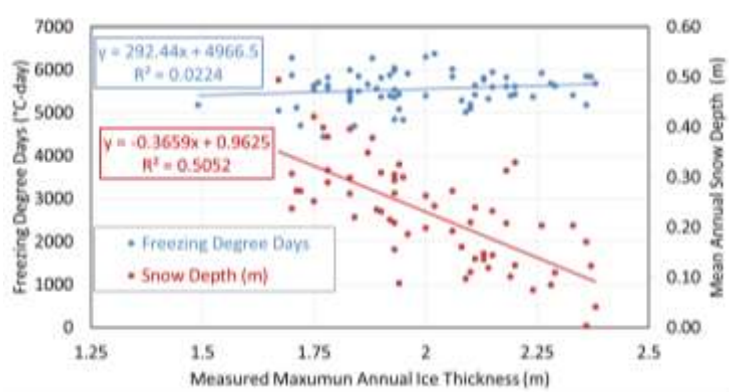

Fig. 4. Freezing-degree-days and mean annual snow depth trends at Resolute Bay

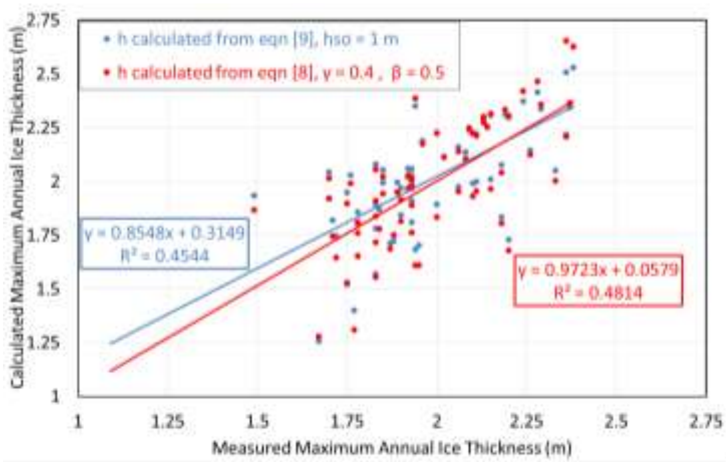

Fig. 5. Predictions of maximum annual ice thicknesses for Resolute Bay

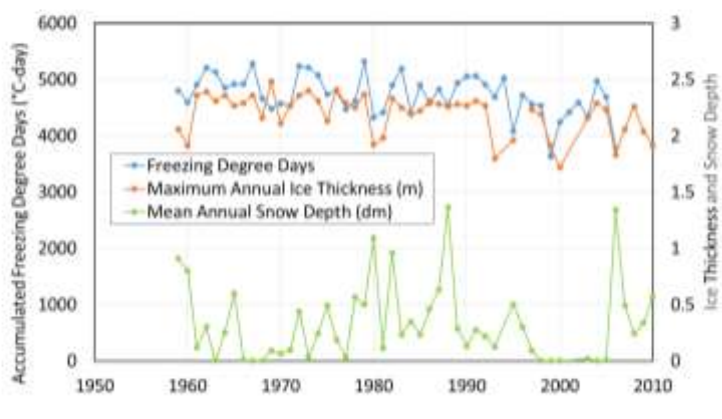

Fig. 6. Baker Lake record of ice thickness, snow depth and freezing-degree-days

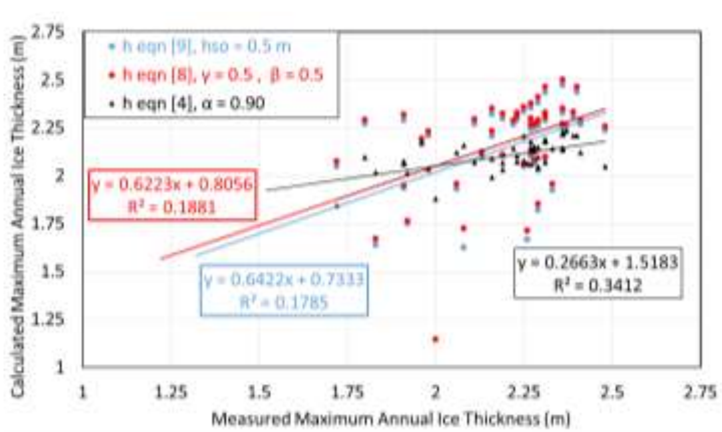

Fig. 7. Predictions of maximum annual ice thicknesses for Baker Lake

International Association for Hydro-Environment Engineering and Research

Supported by Spain Water and IWHR, China

24th IAHR International Symposium on Ice
Vladivostok, Russia, June 4 to 9, 2018

The Northernmost Airport Runway. How And Why Should We Perform Laser Scanning?

Nataliya A. Marchenko
The University Centre in Svalbard
Postbox 156. Longyearbyen, Norway, 9171, UNIS
natalym@unis.no

The runway of the northernmost airport (78^{o}N) in the Norwegian town of Longyearbyen suffers from large deformations due to permafrost degradation, which have increased during the past warm years. These deformations influence operational safety and significantly increase the cost of maintenance. The fast and precise assessment of the runway's current state and monitoring are vital for improvement and repairs. Laser scanning and mapping provide a new opportunity to quantify the visible deformations via 3D modelling, detect changes and determine the most sensitive places.
In autumn 2017, we performed a runway survey with a RIEGL VZ-1000 laser scanner and obtained point clouds with several mm resolution. Processing in RiScan and ArcGIS yielded a raster surface, contour lines and a set of profiles. An algorithm and optimal procedure were developed based on experience.

Keywords: laser scanning; runway; permafrost degradation; RIEGL VZ-1000.

Introduction

All Arctic infrastructures are subject to the impacts of harsh environmental conditions. Removing the natural surface cover activates the processes of permafrost degradation and erosion. This is especially visible in Longyearbyen (Spitsbergen, Norway), the northernmost town (78°N), a world leader in "global warming evidence" (Isaksen et al., 2016) and its airport runway. All plane passengers experience a bumpy landing, while airport employees work hard to maintain and improve the infrastructure. The location is shown in Fig. 1, and the photo (Fig.2) shows an overview of the airport and runway. This photo appears in an article that lists Longyearbyen/Svalbard airport as the most dangerous in Europe (ARTAI, 2015). The author is not alone - Longyearbyen airport is constantly featured in lists of the riskiest airports. Fortunately, no accidents have been caused by a bad runway surface. However, runway maintenance is very costly and the runway's condition is of key importance due to its connection with safety.

Fig. 1. Location of the Svalbard airport in the town Longyearbyen

Fig. 2. Photo of Svalbard Airport from the air (ARTAI, 2015)

The runway's degrading state can lead to increased risk of accidents with the potential for fatalities. Accident statistics show that 55% of the world's fatal aircraft accidents occurred during landing and take-off and accounted for 51% of all on-board fatalities. These accident statistics highlight the importance of addressing the risks associated with poor runway conditions, and implementing measures to reduce, mitigate or remove the risks altogether. Many countries make special efforts to improve runway safety (Federal Aviation Administration, 2018b). The Federal Aviation Administration in the United States Department of Transportation created a special portal on Runway and Taxiway Construction, including various standards and recommendations (Federal Aviation Administration, 2018a).

The first step towards runway optimization is identification of the weakest places, where repairing is the most urgent, and measurement of unevenness and change. The traditional way to make these observations, through a detailed survey and description, usually takes weeks of work for several persons with additional processing time. In this study, we test the applicability of a laser scanner, assuming that two specialists can cover the whole runway in several days. Our

previous experience demonstrated that this technique is much faster than others (Marchenko and Marchenko, 2017).
There are not many examples of a laser scanner being used for a runway survey. The exist study focus on methods and workflow. In the study by (Barbarella et al., 2017), a terrestrial laser scanner (TLS) was used to survey a stretch of a taxiway at an international airport. The authors designed the survey with the goal of defining the optimal parameters for the scans and the spacing between the TLS station points, combining high efficiency with data quality and accuracy. They implemented an algorithm for the semi-automatic extraction of the longitudinal and transversal profiles of the track from the digital elevation model (DEM). The algorithm allowed the verification of irregularities and the assessment of the severity of deviations from a linear trend, and seems to be suitable for obtaining an accurate reconstruction of the road surface. This surveying technique could improve the effectiveness of the measurements, and it could be used wherever pavement geometry cannot be assessed on discrete elements and a continuous approach is needed.
The paper by (Alhasan et al., 2017) describes algorithms for processing 3D stationary terrestrial laser scanning point clouds to obtain surface maps of point wise indices that characterize pavement roughness. Pavement roughness is a key parameter for controlling pavement construction processes and for assessing ride quality during the life of a pavement system.
In our study, the main focus was on deformations induced by frost heave and thaw settlement. The other important task was to find effective and time-saving techniques, given limited resources in the high Arctic.

1. Svalbard airport history and features

The Svalbard Airport is located northwest of the town Longyearbyen, on the island of Spitsbergen, at 78.24^{o} N. The runway is 2260 m long and 45 m wide, stretching in the east-west direction (Fig.4). South of the runway, a steep slope rises to an upland plateau called Platåfjellet, while on the north side the ground surface slopes gently down to Isfjorden. The climate is classified as an arctic desert characterized by low mean temperatures and low precipitation (180-200 mm annually). The average temperature is 6°C during the summer and -14°C during the winter. In the 1971-2000 Climate Normal period, the mean annual temperature was -5,9°C. In recent years, Svalbard has experienced higher temperatures. For 2000-2015, the mean annual temperature was 2,5°C higher than the Climate Normal, the mean winter temperature was 4,6°C higher, and the mean summer temperature was 1,4°C higher (Isaksen et al., 2016). Temperature fluctuations are more frequent during wintertime, and periods with -20°C to -30°C are not unusual. In addition to the low temperatures, strong winds have a significant cooling effect. The fluctuating temperatures also affect the snow cover, which varies between heavy wet snow during mild periods and ice cover during cold, dry periods. Strong winds also redistribute snow, which can act as an external load and insulator where it accumulates.
Another important consequence of the northern location is the polar night and midnight sun. The midnight sun lasts from the 20th of April until the 23rd of August, while the polar night lasts from the 26th of October to the 15th of February. While the polar night helps keep the ground temperature stable, the 24-hour sun during summer contributes to thawing. The change in the sun’s position further contributes to variation in the local surface temperature.
The permafrost in the area is approximately 250 meters thick and the annual temperature in the ground is – 5-6°C on the depth 10 m.

The ground beneath the airfield generally consists of well-graded moraine material, partly with low mechanical strength and with ice lenses up to 50 mm thick and a volumetric ice content of up to 70%. The active layer thickness varied between 50 and 100 cm. Borehole profiling showed that layers of silty clay and sandy, gravelly silt are present down to approximately 3 m depth. These materials were fully saturated when thawed and are very frost-susceptible. Further down, there is a 5 m thick layer of sandy gravel (of medium frost susceptibility) with ice lenses 10-20 mm and thin layers of silty sand and silty sandy clay. Bedrock was encountered at around 9-10 m depth.

Before the construction of the airport started in 1973, Luftfartsverket (The Norwegian Civil Aviation Authority) did preliminary investigations. They concluded that the ground did not have sufficient bearing capacity when thawed. The solution was then to construct an overburden thicker than the expected thaw depth. The expected thaw depth was set to 110 cm. The preliminary design work was deficient, most likely due to limited resources. No geotechnical survey or thermal analyses were done; only simple ground investigations and thaw depth measurements were conducted. The minimum overburden designed was too thin. Insulation of the runway and the installation of geotextiles were not considered. Given these choices, the runway already experienced problems from differential drawdown in 1975. Many experts have been involved in consulting to address these challenges since the airport opened.

Geotechnical investigations and temperature measurements were carried out in 1993 and 1994 (Barlindhaug, 1993; Barlindhaug, 1995). In 1994, Berdal Strømme compiled a report about the condition of the runway based on precision levelling and visual registration (Berdal Strømme 1994). Runway rehabilitation was performed in 1989, 2005, and regularly in recent years.

Many different runway construction alternatives have been considered over the years. Among them are to extend the polystyrene insulation to the whole runway area; to remove the entire structure and replace it; to raise the runway grade by adding a layer of insulation on top of the existing asphalt; and to add a bearing-layer of thaw stable mass (gravel fill) that would prevent the thawing front from reaching the ice-rich soil. All these actions require that the airport is closed for traffic for one summer or part of the season to complete the work. This is not an option since the community of Longyearbyen is dependent on air transportation for supplies and travel off Svalbard.

The only feasible solution is to overlay asphalt when needed. Even though this method is not a permanent solution, it was found to be the most cost and time-efficient method. The problem with this approach, in addition to not being permanent, is the unknown effect the increased asphalt layer has on the underlying soil (Instanes AS, 2005).

In practice, asphalt is added to the most problematic sections. This requires the constant identification of problem areas, where repair is already overdue. Such places are determined visually and by unevenness of vehicle movement. Thus, surveys that can reveal and map irregularities, characterizing them numerically, are necessary and in demand. The most effective way to perform such a survey is laser scanning.

2. Scanning field campaign in autumn 2017

In this survey, we used the high-resolution laser scanner RIEGL VZ-1000, giving a point cloud of surrounding objects and surfaces with 8 mm accuracy and 5 mm precision at a distance up to 1400 m in ideal conditions (Riegl, 2017). The time it takes to complete one scan depends on the chosen resolution, but is not much more than one hour.

During fieldwork in October 2017, we took 4 scans with a range of 360° on 12 October (numbers 1, 2, 3, 4 on Fig. 4). These scans took two hours. The scans were performed in daytime (10:30-12:20) in rather cold (2-3°C) and windy weather, but with sunshine. The surface was covered by rime. We placed the scanner in the middle of the runway at the distance 600 m between scan positions. Due to forecasted snow, we performed 3 other scans 16 October in the evening (16:30-18:00), when it was getting dark rapidly (numbers 5, 6, 7 on Fig. 4). We tried these scans with a 180° range, locating scanner at the side of runway, which took 1,5 hours. The surface was dry, and the weather was cold and windy. Due to traffic, we had limited and stressful time. One scan (number 6) was interrupted by an arriving plane.

Fig. 3. Scanning setup and procedure

Fig. 4. October 2017 scan positions

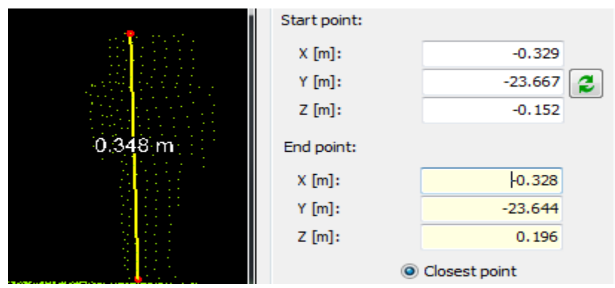

Fig. 5. Example of a point cloud showing zoom to a signal lamp and the possibility to measure distance and get coordinates in the Project coordinate system.

Fig. 6. Example of scanner performance on the relatively flat runway surface

We had no practice of scanning such a flat and extended object, as a runway. Nevertheless, the valuable data and experience was obtained. The data contains point clouds for seven scan positions, where each point has coordinates (XYZ) in the Project coordinate system, defined by the scanner during acquisition (Fig. 5). The distance between points increases tremendously as you move away from the device. It was several mm near the scanner (approximately up to 50 m) and several decimeters at distant locations in the surrounding hills (Fig. 6 and 7).

3. Data processing

The obtained point clouds were processed in RiScan software (Riegl, 2016). First, we combined all 7 scans using "multistation adjustment" tools. The combined data consisted of 8 644 278 points (Fig. 7). Next, we extracted the runway and reference buildings (Fig. 8), reducing the amount of points to 1 172 311.

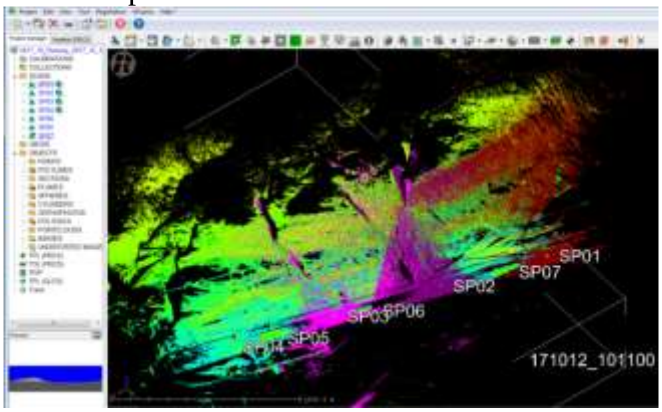

Fig. 7. All scans combined in the RiScan program into one point cloud

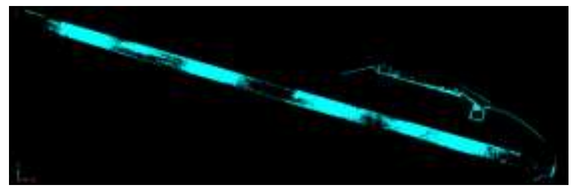

Fig. 8. Only runway and reference buildings in the point cloud

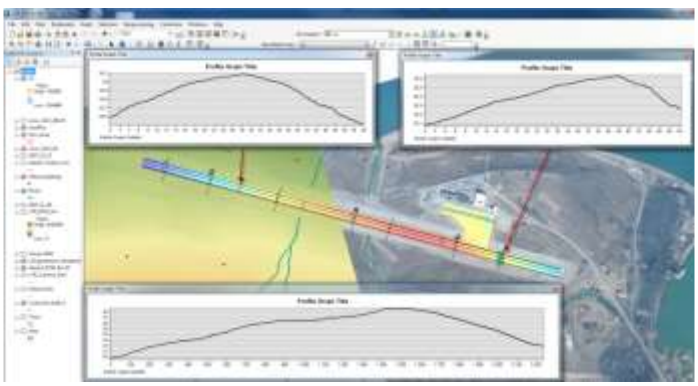

Fig. 9. Processing in ArcGIS with the DTM and aerial photo in the background. Longitudinal and transverse profiles are shown as a result

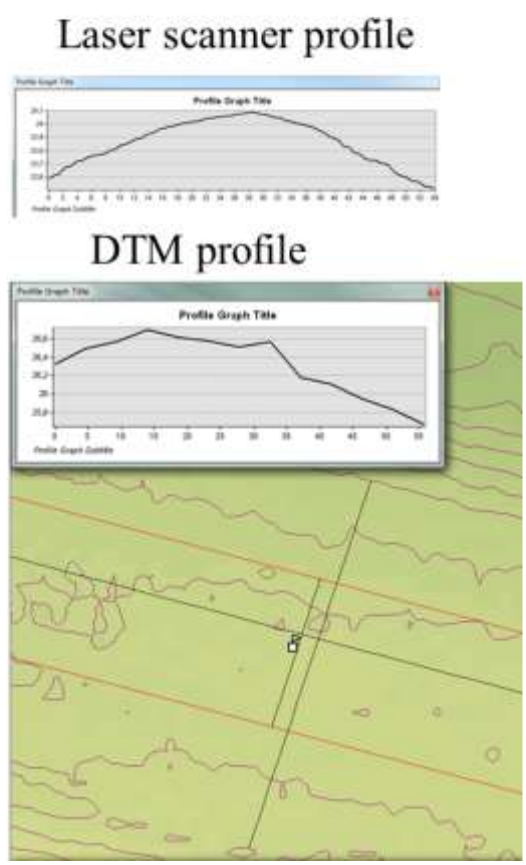

Fig. 10. Comparison of profiles derived from the DTM and Scanner data in the place of scan position 1.

Fig. 11. Point cloud with higher density, colored/painted by photos

Then we performed normalization and filtering (2,5D filter) with a determined distance between points of 0,5 m, and got a cloud of 270 078 points. We exported the data in .las format and opened it in ArcGIS software, where georeferencing, adjustment, and 3D analysis were performed. A raster surface and profiles were created via raster interpolation (Fig. 9).
Comparison of the obtained surface with an existing 5 m resolution digital terrain model (DTM) from the Norwegian Polar Institute shows that the surface created from the TLS scans looks much more natural and correct. The accuracy can be confirmed with simple in-situ measurements.

4. Lessons learned and future applications

We gained valuable experience of the scanning procedure, including knowledge of particularities and possible resolution in the given conditions. Part of this knowledge specifically concerns Arctic conditions, while some of the new expertise is common to all flat surfaces and runways and is widely applicable. The methodology is applicable for other work, like a survey of the roads in Longyearbyen, and can be used in other Arctic locations with permafrost.
Surprisingly, the rime on the runway surface did not decrease reflectance and did not degrade the image. However, a large decrease in resolution occurred as distance from the TLS increased. It was other but not pleasant finding. Reducing the scan step did not yield significant results. Increasing the horizontal resolution in relation to the vertical resolution, (to still have an acceptable acquisition time) as it recommended for flat horizontal surfaces, did not change the significantly the picture. We get a "good density" of points only closer than 50 m from the device. But it is necessary to understand what accuracy is really needed. In our example, to obtain a surface, we made thinning by using a 2.5D filter to gain points every 50 cm. We will have such a density at a distance of 150-200 meters. The point cloud with higher density, layered with photos acquired simultaneously during scanning, shows cracks on the runway surface and can be used to document the runway's current state (Fig. 11). Obtaining this higher density point cloud requires more acquisition time and shorter distances to the TLS.
Thus, data acquisition depends on data application. It is very important to discuss various techniques with practitioners, such as airport authorities, responsible for maintenance services, so they understand what results can be expected from different survey methodologies.
We plan to continue the investigation on the base of obtained experience and will perform one or two additional scanning sessions to obtain new point clouds and update the digital surface with changes that have occurred on the runway during the year. We hope to perform the following two scans: one in April-May, before thawing begins but when the ground is not covered by snow, to record maximal frost heave; and one in September, to document deformation that has occurred due to summer thawing.

Conclusions

The survey performed in autumn 2017 on the Svalbard airport runway with the laser scanner RIEGL VZ-1000, and with data processing in RiScan and ArcGIS, was efficient and yielded promising results. During several hours of fieldwork (7 scans for approximately 20 minutes each) and some weeks of processing (when time was mostly spent finding the best algorithm), we created a measurable and representative model of the runway (raster surface, contour lines and a set of profiles). The October 2017 surface can be compared with other images of the investigated surface to quantify visible deformation via 3D modelling.

Although laser scanning is widely used in various fields of science and engineering, terrestrial laser scanners are still very expensive and each application experience is unique and provides rich information for subsequent work. Despite the high cost, laser scanning is effective because it is fast and does not require many personnel. However, the data processing demands special software and skills. The obtained 3D point clouds and images can be measured and exported in different formats (with millions of points with XYZ coordinates) for visualization in common software (like ArcGIS, Matlab, Cloud Compare) in a reasonable time.

Laser scanning is a reliable, high-precision method for monitoring deformation of infrastructure and many other kinds of changes occurring on natural and man-made surfaces.

Acknowledgements

The author would like to thank the Longyearbyen airport Administration and employees for help during fieldwork, the company Artgeo for consulting with data processing, and colleagues at UNIS for supporting this study.

References

Alhasan, A., White, D.J., De Brabanter, K., 2017. Spatial pavement roughness from stationary laser scanning. International Journal of Pavement Engineering, 18(1): 83-96.

ARTAI, 2015. Os 5 aeroportos máis perigosos de Europa. ERDATI.

Barbarella, M., De Blasiis, M.R., Fiani, M., 2017. Terrestrial laser scanner for the analysis of airport pavement geometry. International Journal of Pavement Engineering: 1-15.

Barlindhaug, 1993. Geotechnical study contracted by Luftfartsverket

Barlindhaug, 1995. Svalbard airport runway distress investigation phase 2, site investigation and analysis.

Berdal Strømme 1994 Svalbard Lufthavn Longyear, Tilstandsregistrering.

Federal Aviation Administration, 2018a. Runway and Taxiway Construction. United States Department of Transport.

Federal Aviation Administration, 2018b. Runway Safety. United States Department of Transport.

Instanes AS, 2005. Longyearbyen airport survey.

Isaksen, K. et al., 2016. Recent warming on Spitsbergen—Influence of atmospheric circulation and sea ice cover. Journal of Geophysical Research: Atmospheres, 121(20): 11,913-11,931.

Marchenko, N., Marchenko, A., 2017. Investigation of large ice rubble field in the Barents Sea, Proceedings of the 24th International Conference on Port and Ocean Engineering under Arctic Conditions, Busan, Korea.

Riegl, 2016. RiSCAN PRO. Operating and Processing Software for RIEGL 3D Laser Scanners.

Riegl, 2017. Terrestrial Laser Scanning.

International Association for Hydro-Environment Engineering and Research
Supported by Spain Water and IWHR, China

24th IAHR International Symposium on Ice
Vladivostok, Russia, June 4 to 9, 2018

Sea Ice Observation and Comparison with Ice Maps during a Cruise in the Western Barents Sea in April 2017

Nataliya A. Marchenko
The University Centre in Svalbard
Postbox 156. Longyearbyen, Norway, 9171, UNIS
natalym@unis.no

Information about sea ice distribution and movement is very important for planning and existing offshore infrastructure and safe navigation. Several agencies provide sea ice maps which show various ice categories. For the Barents Sea the main sources of information are the Polarview.met.no (http://polarview.met.no/) portal by the Norwegian Meteorological Institute and the website of the Arctic and Antarctic Research Institute (Russia) (www.aari.ru). The first site provides ice charts daily (except weekends and holidays), showing ice concentration. The second site shows ice types (nilas, first year ice, old ice and fast ice) every third day. All these maps are based on ice analysis from satellite imagery. But what does the ice look like in reality? There is always some uncertainty about ice state, especially in the marginal zone, on the limit of spreading. That's why the observation of ice and ice chart analysis is valuable, especially in places where it can influence industrial and transportation activity.

The western part of the Barents Sea is a region of increasing activity – oil and gas exploration may increase in addition to traditional fishing.

During an expedition of the Arctic Technology Department of UNIS on the vessel MS Polarsyssel (22-30 April 2017), we crossed the "ice tongue" that stretches to Bear Island twice – once in the north and once in the south. On ice charts, this ice is shown as orange (7-9/10ths) and yellow (4-7/10ths). In the northern part, ice ridge morphology investigation, ice mechanical tests, and laser scanning of ice flows were performed at two sites. In the middle and southern part, time-lapse photography and films were used for comparison with ice chart information.

These investigations provided a realistic characterization of sea ice in the region and are a valuable addition to the long-term studies of sea ice in the region.

Introduction

The Arctic Technology Department of the University Centre in Svalbard (AT UNIS) regularly organizes study cruises on vessels to the western Barents Sea in the frame of the bachelor course AT-211 "Ice Mechanics, Loads on Structures and Instrumentation". The cruise is held between the end of April and beginning of May, based on the course schedule and assumed success of ice mechanical tests and oceanographic measurements. These cruises allow for the collection of interesting and valuable scientific data in an infrequently visited part of the Barents Sea. For example, in 2016, huge ice rubble was discovered near the north-east coast of Edge Island (Marchenko and Marchenko, 2017). Installation of buoys on the ice floes and icebergs allows for the investigation of ice drift (Marchenko and Marchenko, 2015). Researchers from different institutions like NTNU, C-Core, University College London, and Cambridge University often take part in the cruises.

The cruise schedule and route are dependent on ice, weather conditions and vessel capacity. For many years RV Lance was used. Having ice class 1A (ICE-1A: Strengthened for navigation in severe ice conditions), RV Lance went through ice 1 m thick and research stations were established quite far from the ice edge. Lance drifted in the Central Arctic basin in 2016-2017 and then retired from scientific expeditions. Thus, since 2017, AT UNIS uses the vessel MS Polarsyssel for scientific cruises. This firefighting vessel is used part of the year by the Governor of Svalbard for rescue operations and daily needs. Built in 2014, she has IMO: 9690949, Gross Tonnage: 4324, Deadweight: 3700 t, and Length Overall x Breadth Extreme: 88.5m × 18.3m. The vessel has ice class 1B, but due to the responsibility for preparedness for rescue missions it does not typically operate in ice. So, during our 2017 cruise, the marginal ice zone between Hopen and Bear Island was investigated (Fig. 1).

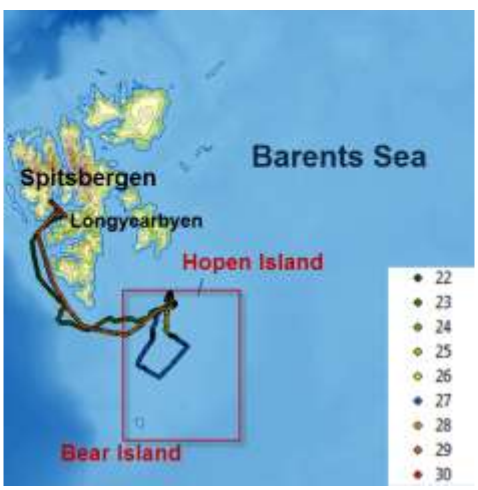

Fig. 1. a) Track of MS Polarsyssel (22-30 April – different point colors for each day); b) Working on an ice floe moored to the vessel (drone photo by Sebastian Sikora)

This cruise area is very interesting both from the scientific and practical point of view. The whole Barents Sea is a region of long-term human activity which has been thoroughly investigated for centuries (see overview by (Adrov, 2002). It is one of the fastest changing regions of the Arctic, and has experienced the strongest decline in winter sea-ice area in the Arctic in the last decades. The behavior of sea ice at its south-west limit is important for possible hydrocarbon exploration activities. In 1986, the Norwegian Oil and Gas Ministry offered licenses for operation in the area just south of Bear Island in the western Barents Sea, within the southern boundary of seasonal ice cover and iceberg drift at that time (Løset and Carstens, 1996). Thirty years later, the Ministry issued a report (Norwegian petroleum directorat, 2017) that stated that areas of the Barents Sea open for petroleum operations reach 74˚30'N and include drilling activities north of Bear Island. Thus, the area is still a focus of various investigations, including sea ice properties.

The ice regime of the Barents Sea has been studied since the middle of the last century, and the main features (variability of the ice edge, ice formation, concentration, and drift) and driving forces (wind, currents, wave and tidal processes) are known (Frolov et al., 2009; Mironov, 2004; Vinje and Kvambekk, 1991; Zubakin, 2006). A great volume of research is devoted to the drift of icebergs (Dmitriev and Nesterov, 2007; Keghouche et al., 2009; Løset and Carstens, 1996; Marchenko et al., 2010). As shown in (Buzin, 2009), based on data from 1955-2007, the boundary of old ice in the Barents Sea has two tongues: one stretching to Bear Island and the other along longitude 40^{o}E. However, actual observations of ice in the Bear Island region are scarce and particularly valuable.

1. Ice tongue stretching to Bear Island

The origin and content of ice near Bear Island has been investigated and discussed in the literature. For the period before rapid warming, the possibility of old ice observation near Bear Island at the end of the melting season was described by T. Vinje, who estimates old ice comprises 1% of the total number of ice observations during 1970-1981 (Vinje, 1985). According to data from Russian ice reconnaissance by air and ice chart archives, the propagation of old ice along Spitsbergen to more southern areas (Bear Island) is a more frequent phenomenon (Buzin, 2009). In some years, old ice extends in the western Barents Sea southward of 75^{o}N. Thus, old ice from the Central Arctic Basin can reach Bear Island in years with extreme ice extent. 2003 was the last cold year with ice extent close to the 1981-2010 average. With climate warming and sea ice area decline in the last decade, the seasonal ice boundary has retreated to the north considerably. However, the ice tongue stretching to Bear Island repeatedly appears in March-April. It is visible on satellite images and appears on ice maps even in the present warm period (Fig. 2).

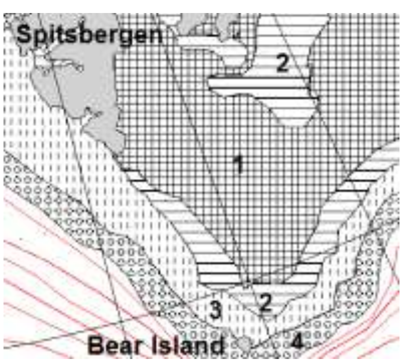

a) 3 April 2003

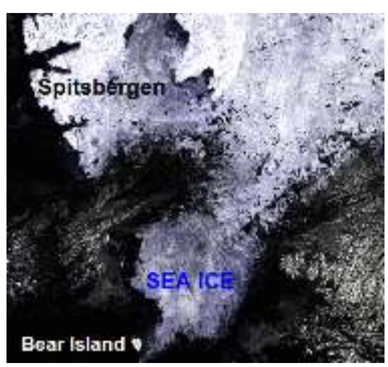

b)Apr 7, 2014 - Apr 15, 2014

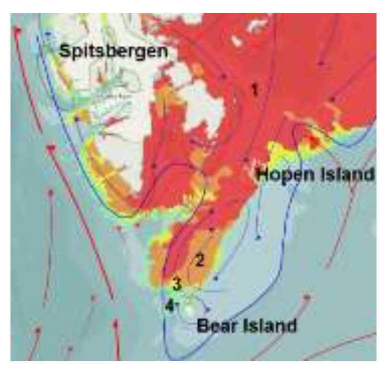

c)6 April 2018

Fig. 2. Ice tongue on sea ice maps (a, c) (Norwegian Meteorological Institute, 2018) and the satellite image (b) in different years during the days of maximum development. Ice categories on the map: 1 – very close drift ice (9/10-10/10), red zone; 2 – close drift ice (7/10-9/10), orange; 3 – open drift ice (4/10-7/10), yellow; and 4 – very open drift ice (1/10-4/10), green.

On the ice map from 6 April 2018, created in the BarentsWatch map service (BarentsWatch, 2018), sea currents and bottom topography are shown (Fig. 2c). The ice tongue is located in the relatively shallow waters of the Spitsbergen Banken, where depths are 30-40 meters. The ice tongue also follows the Arctic Water Stream, a sea current that runs along east Spitsbergen from the Arctic basin to Bear Island via Hopen Island (indicated by blue arrows on Fig. 2c). Depending on the synoptic situation, the ice tongue can be located to the east from the line connecting Hopen Island and Bear Island, as in 2014, 2015, and 2016, or more to the west as in 2013, 2017, and 2018. An analysis of the texture of satellite images (Marchenko et al., 2016) showed that in March 2015, extensive (2-10 km across) and large (500-2000 m across) ice fields were observed in the ice tongue, while in March 2016 this zone consisted of large ice fields and their fragments. Formation of the ice tongue occurred due to the movement of ice fields from zones with high ice compactness, which are characterized by the processes of compression and deformation of ice, leading to the hummocks drifting in the vicinity Bear Island. Average daily drift speed of ice fields is 12-15 cm/s. In 2015 and 2016 there were several periods of tongue presence lasting from 2 to 18 days. Strong, gusty wind (up to 22 m/s) inherent in polar mesocyclones forming under the influence of increased turbulence is one of the main factors driving the ice to Bear Island. Strengthening gusts will also cause an increase in the velocity of the near-surface current, and as a result the average daily drift velocity can reach 1.7 m/s.

Satellite imagery provides an overview of sea ice extent and movement, and allows for the investigation of the timing and location of the ice tongue. In 2017 we had the chance to cross the ice tongue and collect data in-situ that could be compared to air-borne measurements.

2. Sea ice survey at the end of April 2017

A study cruise of the Arctic Technology Department of UNIS started 22 April 2017 from Longyearbyen and headed to the southeast of Svalbard for sea ice investigation (Fig. 1).

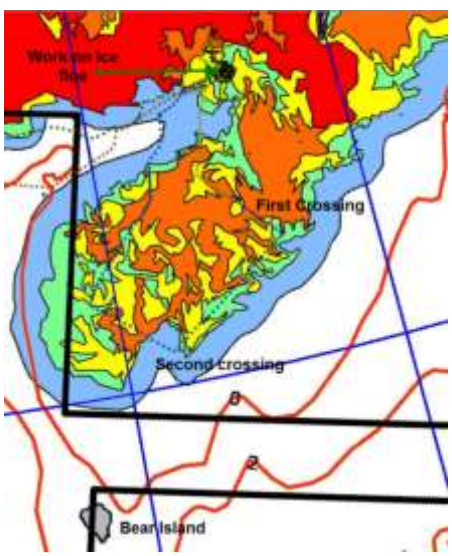

27 April 2017
(see color conventions on Fig. 2)

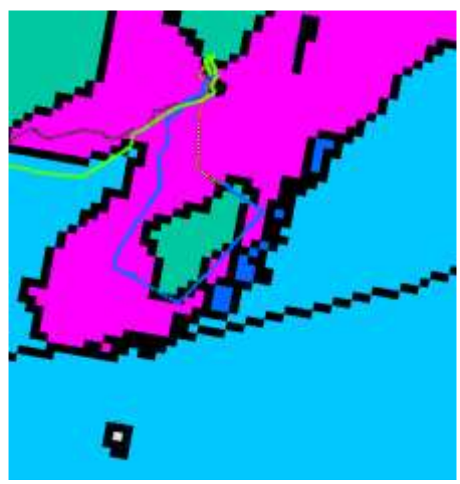

AARI map for 23-25 April. Blue – water, Dark blue – nilas, Pink area – young ice (10-30 cm), green area – one-year ice (30-200 cm). On the map 30.04-02.05, the whole tongue is shown in pink.

Fig. 3. Ship track while crossing the ice tongue overlaid on ice maps by (Norwegian Meteorological Institute, 2018) (a) and AARI (USIWO-ESIMO, 2014) (b)

On 23 April MS Polarsyssel went along the ice edge (red zone on ice map – Fig. 3a) to the east, observing ice state and looking for floes suitable for mooring. The broken ice field consisted of small (4-5 meters in diameter) angular ice floes and with dispersed larger ice floes of 20-30 meters. The space between the ice floes was almost completely filled by smaller, round ice pieces, less than a meter in diameter, and their debris. Large ice floes usually had a hummocky formation 1-2 m high, located near the sides, and a meltwater pond in the center. We aimed to investigate one of these ice floes and on 23 April (evening) we moored to a fairly typical floe. The group of AT-211 students, teachers and guest researchers worked two days (24-25 April) on the ice floe (Fig. 1b) doing ice mechanical tests, drilling and scanning. 26-27 April were devoted to sea ice observations while crossing the ice tongue and oceanographic measurements. Early on 28 April we sailed from the charted red zone to the green zone via the orange and yellow zones. Later on 28 April, the heavy storm began on our way back.

3. Typical ice floe morphology

A floe typical for the marginal zone was investigated 24-25 April, while it was moored to the ship (Fig. 1b and 4). The floe drifted during and after the investigation, following wind and making tidal loops, as is visible on the ship track (Fig. 3a) and the track of the buoy installed on the floe (Fig. 5b). Ice mechanical tests (which are not discussed in this paper) and floe dimension measurements were performed.

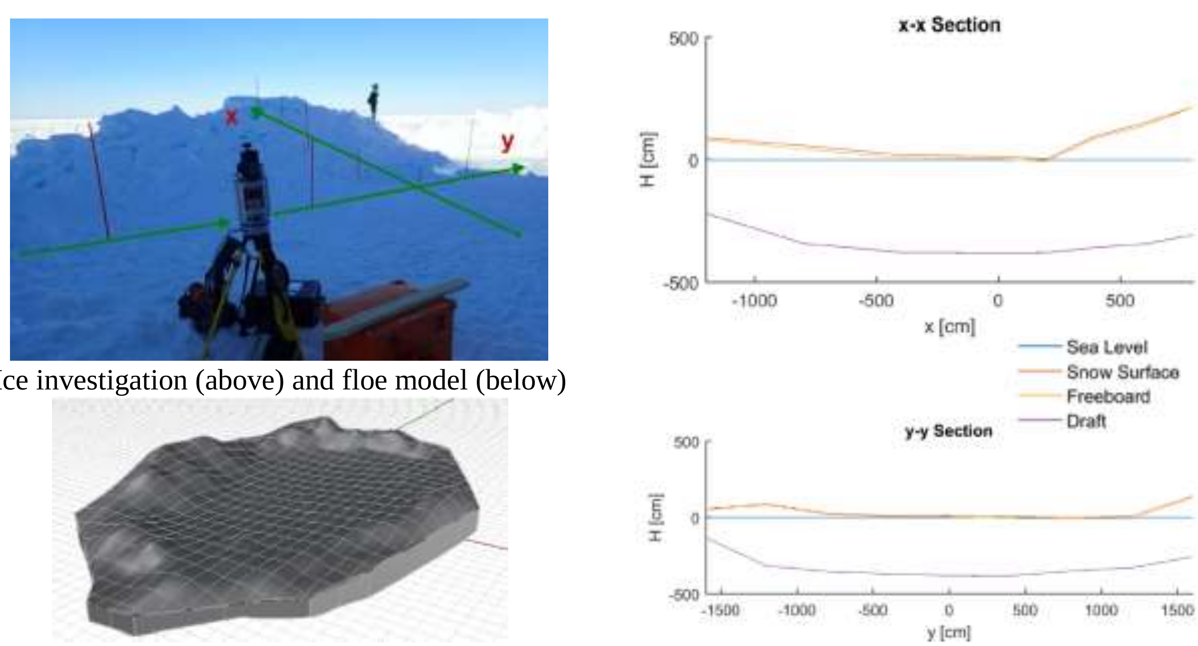

Fig. 4. Ice floe measurement and morphology

Characterizing the morphology of floes can be useful to estimate the mass and wind and water drag for drift patterns and impact load analysis of offshore structures. The geometry of the ice floe was profiled using a variety of techniques including systematic coring and laser scanning. Underwater multi-beam sonar profiling was attempted with an autonomous underwater vehicle (AUV), however problems with the sonar prevented the team from gathering any usable data. A thickness profile of the ice floe was obtained by using a Kovacs ice auger drill to measure depth along the x- and y-planes (Fig. 4). With this coring method, it was possible to measure the total ice thickness, draft, freeboard and snow depth at each drill site, which were marked by red poles (Fig. 4).

The above-water profile was constructed using a combination of freeboard measurements, 3D laser scan data and drone footage taken from above the ice floe. The drone footage was useful around the flow edges, where the laser scanner data was unusable due to shadows cast by the uneven surface. The ice floe profiles are presented in Fig. 4. The measured ice floe parameters were: length overall 43 m, breadth - 30 m, max draft – 3.82 m, max sail height – 2.16 m, water plane area – 934 m^2, submerged volume – 2655 m^3, and total ice volume – 3270 m^3.

Laser scanning with a RIEGL VZ1000 was also performed from the ship board to assess the ice field at the boundary of the red and orange zones (Fig. 5a)

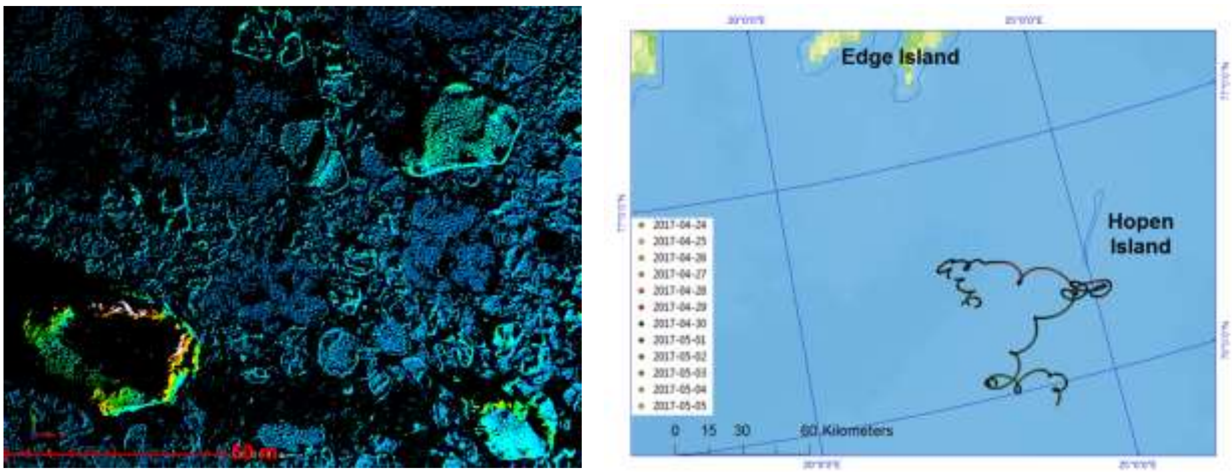

a) Ice field point cloud, showing individual ice floes

b) Ice floe movement (drifting buoy data) 24 April-5 May

Fig. 5. Ice field composition (a) and ice floe movement (b)

4. Ice tongue crossings

We crossed the ice tongue twice with a distance of 85 km between crossing lines in the transect in the northern part, close to the red zone, and the transect in the southern part, close to the destruction area (Fig. 6).

First crossing of the ice tongue at 75,8˚N

At the marginal zone (yellow on the ice map), there was mostly pancake ice less than 1 m in diameter not dense. The surface oscillated under the influence of light waves. The captain maintained a speed of approximately 7-8 knots. As we moved into the tongue, larger ice floes began to appear, which were fragments or melted ice floes similar to the one described above. The number of ice floes with hummocks increased as we moved toward the middle of the tongue. In the central part, the ice was composed of round floes 2-4 m in diameter and frequent ice floes 10-15 m in diameter (sometimes up to 20-25 m) with hummocks. These ice floes were smaller in size than the investigated ice floe, but had the same basic elements and morphology. The hummocks rose 1.5-2 m above the water. Some of the ice floes had a substantial underwater portion, significantly stretching beyond the surface dimensions. Expecting such floes to be more than 3 m thick and of considerable hardness, the captain lowered the speed to 2.5 knots.

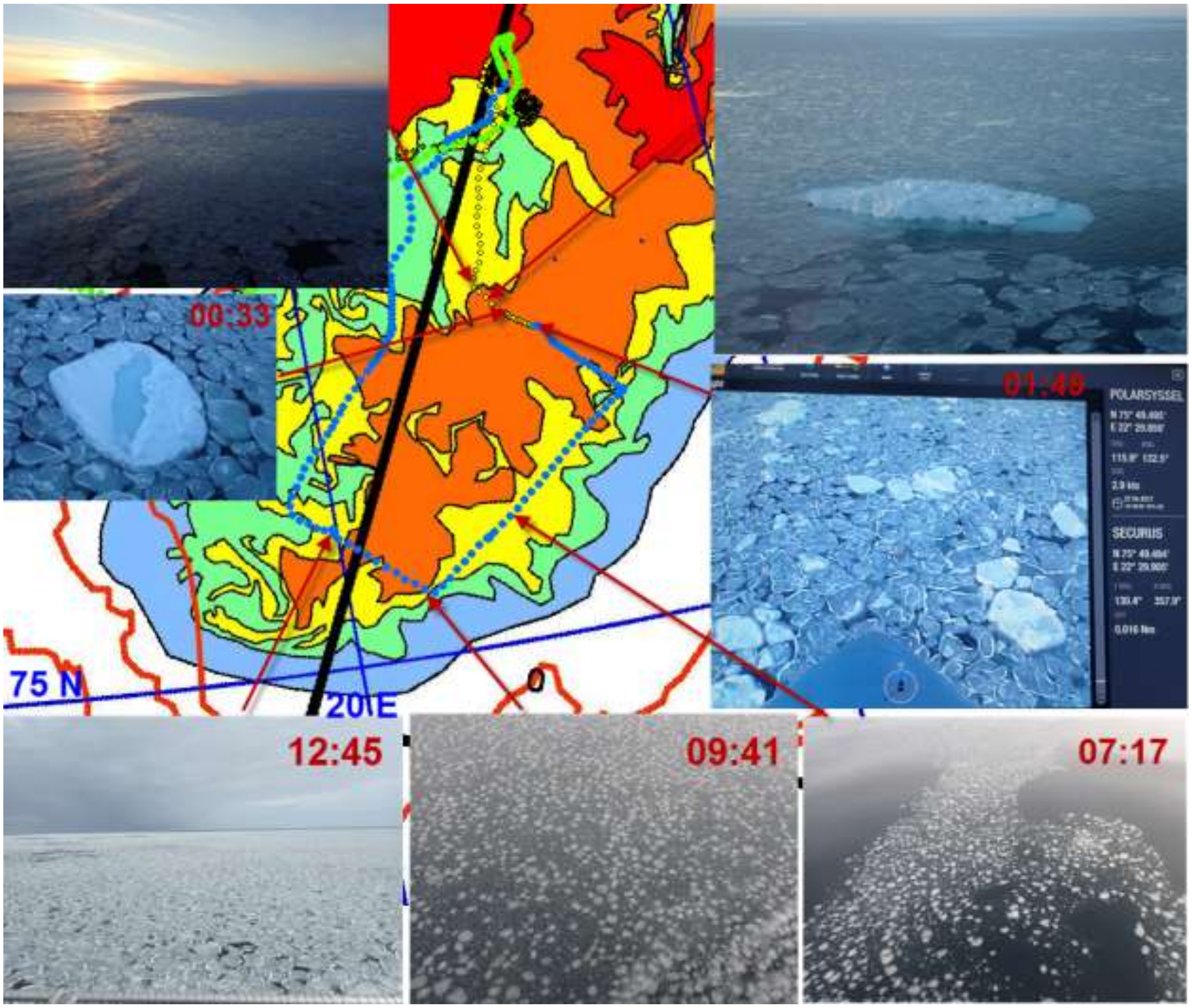

Fig. 6. Ice composition in the ice tongue indicated on the ice map for 27 May 2017. Polarsyssel track is shown by blue and yellow dots

Second crossing of the ice tongue at 75,3˚N

Our observations of the southern portion of the ice tongue are presented at the bottom of Fig. 6. There is a discrepancy between the zone boundary positions on the ice map and the observed ice conditions. There are three main zones characteristic of the tongue here: 1) Dense and thick pancake ice, fairly uniform in size with pronounced raised edges. This was observed in the yellow zone on the ice map (12:45 in Fig.6), but in fact the conditions were more in line with the orange zone category. The laser scanning showed that the pancakes had an oval shape 25-27 cm wide and 37-41 cm long. 2) Thin pancake ice (20 cm in diameter) amidst a dense slush, observed along the periphery of the first zone, corresponding to the yellow category on the ice map. 3) Bands of pancake ice with similar composition to the second zone were observed at the boundary with ice-free water. This corresponds to the green category.

According to the ice map by AARI (Fig. 3b), this ice belongs to the pink area – young ice (10-30 cm), and only in the central part of the northern transect could it be classified as dark green – one-year ice (30-200 cm).

5. Iceberg at 76,268°N

On 27 April at 22:00 we encountered an iceberg floating in ice free water (Fig. 7). The iceberg was visible from approximately 15 km away, as something huge and we slightly changed the course of the ship to observe it and potentially install a buoy. While approaching, it turned out that it was not that large, but was at least 10 m high above the water. The iceberg had a bizarre shape, was up to 20 m wide at the water surface, and had obviously a substantially wider submerged portion.

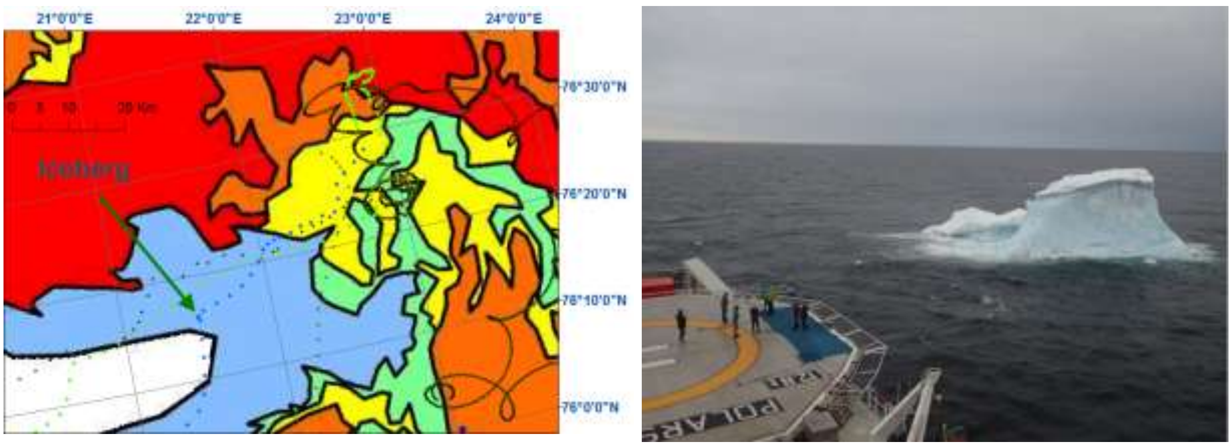

Fig. 7. Location (a) and appearance (b) of the iceberg. The deck of the ship is visible in the lower left corner (b)

Conclusion

Sea ice charts for the Barents Sea show ice categories in various colors, defined by ice concentration. The appearance of ice in zones of the same concentration can be different depending on place, time and ice state. Our observations in the marginal zone at the southern limits of ice extension in the western Barents Sea and at the ice tongue were used to define ice appearance in the various map color categories:

Red zone – Dense ice field consisting of small (4-5 m) angular ice floes, repeated larger floes (20-30 m) with hummocky formations (up to 2 m sail and 4 m draft) and smaller (less than 1 m) round pieces with their debris in between;

Orange zone in the northern part of the ice tongue – round floes (2-4 m) with frequent inclusions of ice floes (10-15 m, up to 25 m) containing hummocks (up to 2 m sail);

Yellow zone in the northern part of the ice tongue – similar to the orange zone by content, but with less ice coverage and less floes with hummocks;

Orange zone in the southern part of the ice tongue – dense and thick pancake ice, fairly uniform oval shape (25-27 cm wide and 37-41 cm long);

Yellow zone in the southern part of the ice tongue – thin pancake ice (20 cm in diameter) amidst dense slush;

Green peripheries of the ice tongue consist of ice strips tens to hundreds of meters wide with the same composition as the yellow zone, located within ice free water.

Icebergs (up to 10 m high) can be met in ice free water as far as 76°N.

These observations of sea ice can be useful for understanding of current processes of sea ice decline and possible risks for the various activities operating in the Barents Sea and the other Arctic regions.

Acknowledgments

The author would like to thank the “Polarsyssel survey team”: MS Polarsyssel crew, cruise leader Prof. Aleksey Marchenko, students on the AT-211 UNIS course, and guest researchers, as well as the SAMCoT and FIMA project (funded by the Research Council of Norway) and colleagues at UNIS for supporting this study.

References

Adrov, N.M., 2002. 1000- years of investigations of the Barents Sea. Part 1. From the beginning of millenium until the first half of XX, Murmansk.

BarentsWatch, 2018. Map service, Tromsø.

Buzin, I.V., 2009. On the Spreading of Old Ice In the Barents Sea. Int. J of Offshore and Polar Engineering, ISOPE, 19(4): 1-7.

Dmitriev, N.Y., Nesterov, A.V., 2007. Iceberg Drift In the Barents Sea According to the Observation Data And Simulation Results, The Seventeenth International Offshore and Polar Engineering Conference. International Society of Offshore and Polar Engineers, Lisbon, Portugal.

Frolov, I.E., Gudkovich, Z.M., Karklin, V.P., Kovalev, E.G., Smolyanitsky, V.M., 2009. Climate Change in Eurasian Arctic Shelf Seas. Centennial Ice Cover Observations.

Keghouche, I., Bertino, L., Lisæter, K.A., 2009. Parameterization of an Iceberg Drift Model in the Barents Sea. Journal of Atmospheric and Oceanic Technology, 26(10): 2216-2227.

Løset, S., Carstens, T., 1996. Sea ice and iceberg observations in the western Barents sea in 1987. Cold Regions Science and Technology, 24(4): 323-340.

Marchenko, A., Kulyakhtin, A., Eik, K., 2010. Icebergs drift in the Barents Sea: data analysis of ice tracking buoy and numerical simulations.

Marchenko, A.V. et al., 2016. Studies of ice drift and rifge consolidated layer evolution in the North-West Barents Sea. Proceedings of Hydrometcentre of Russia, 361: 229-258.

Marchenko, N., Marchenko, A., 2017. Investigation of large ice rubble field in the Barents Sea, Proceedings of the 24th International Conference on Port and Ocean Engineering under Arctic Conditions, Busan, Korea.

Marchenko, N.A., Marchenko, A.V., 2015. Sea currents and ice drift in western part of Barents Sea. A comparison of data from floating and fixed on ice buoys The 23rd Int. Conf. on Port and Ocean Eng. under Arctic Conditions (POAC 2015), Trondheim.

Mironov, E.U., 2004. Ice conditions in the Greenland and Barents seas and their long-term forecast. AARII, St. Petersburg.

Norwegian Meteorological Institute, 2018. Icechart and Ice information, Norwegian Ice Service - MET Norway.

Norwegian petroleum directorat, 2017. Geological assessment of petroleum resources in eastern parts of Barents Sea north 2017, Oslo.

USIWO-ESIMO, 2014. Uniform State System of information on conditions in the World Ocean. AARI, pp. English version of Russian site "Единая государственная система информации об обстановке в Мировом Океане".

Vinje, T., 1985. Drift, composition, morphology and distribution of the sea ice fields in the Barents Sea. Norsk Polarinstitrutt Skrifrer, 179C. NPI, Oslo, 26 pp.

Vinje, T., Kvambekk, A.S., 1991. Barents Sea Drift Ice Characteristics. Polar Research, 10(1): 59-68.

Zubakin, G.K., 2006. Ice formations of the seas of Western Arctic. AARI, St.Petersburg.

International Association for Hydro-Environment Engineering and Research
Supported by Spain Water and IWHR, China

24th IAHR International Symposium on Ice
Vladivostok, Russia, June 4 to 9, 2018

The Bottom Ice in the Northern Caspian Sea

P.I. Bukharitsin
professor of the Astrakhan State Technical University
Astrakhan, Russian Federation
e-mail: astrgo@mail.ru
A.P. Bukharitsin
graduate student of the Moscow University of Finance and Industry
Korolev, Russian Federation
E-mail:a.bukharitsin@gmail.com

The first regular study of sea ice in the Northern part of the Caspian started in the early 30s of the last century. Since then there was a lot of work done to define monthly ice edges, thickness distribution ice drift and ridging. Physical and chemical properties of ice such as strength, salinity and density were tested as well as properties of under-ice water with growing intensity since the first expeditions then. However, frazil ice as one of the most important ice types as one of the most important ice types in the area was not thoroughly studied. This work is one of the first ones that attempts to describe frazil ice formation process and estimate its effect on development of ice cover in the Northern Caspian Sea.

Introduction

The study of the ice cover of the freezing seas of Russia is acquiring now growing importance both for scientific and practical purposes. Ice cover hinders navigation, hampers to a considerable extent development of natural resources and construction of offshore structures, seafood production, etc. At the same time, ice can serve as a quay, an airfield or even a temporary protection dam. Development of reliable reference manuals, as well as improvement of existing methods and creation of new methods for forecasting natural processes and phenomena are not possible without considering the influence of the ice cover.

One of the most important characteristics of ice cover is the thickness of thermally grown level ice. The processes of natural (thermal) growth of ice, were investigated in detail by N.N. Zubov back in the 1930-ies and many others afterwards. His assessment of the severity of winters in terms of "the sum of freezing degree-days" was included in hundreds of regional design formulas that made it possible to calculate the maximum possible thickness of level ice. His empirically derived formula is still widely used operationally [1].

While it is difficult to observe ice growth processes in-situ the formulae are verified with regular instrumental measurements showing discrete results. It is even more difficult to estimate contribution of frazil ice into overall ice thickness growth near opening leads or polynyas, while it forms in the layer of supercooled water as thermal growth and frazil ice formation take place simultaneously.

Ice charts, as a rule, report stage of development that is visually defined with means of remote sensing not the thickness. The stages of the ice are shown with symbols and correspond to a certain thickness range. Considering the uncertainties with monitoring and defining ice types and their correspondence to ice thickness ranges there is only more questions arise in regards of early stages of ice development to accurately corelate them to thickness.

Frazil Ice Phenomena

Formation of the frazil ice in the Arctic seas was investigated by N.N. Zubov et al and many other researchers. However, the physics of the phenomenon itself, and, most importantly, the analytical form of its description, which makes it possible to quantify the fraction of frazil ice in its total thickness were proposed by E.I. Monakhov only in 1989. His work has shown that the content of the frazil ice averages 5-10% in the Arctic and Antarctic seas, but it may reach 30-50% and even 70-100% over local areas such as opening leads, polynyas, pre-coastal zones estuaries with fresh water inflow, [2].

Multiple break-ups of pre-coastal fast ice causing drift events, hummocking and formation of huge open water leads, and polynyas occur through winter ice seasons under influence of strong wind events. Wind direction variation through the season results in repetitive opening and closing of leads forming in one place and closing in the other. Under the influence of wind waves and negative air temperatures over opening waters of the leads, the entire water thickness is mixing with turbidity through the whole layer and is supercooled. Presence of a large number of nuclei of crystallization (the silt, sand lifted from the seabed and microscopic air bubbles) in the water column initiates intensive formation of frazil ice, which partially floats up to the surface of leads accumulating in form of slush, and subsequently freezes forming opaque ice cover (figure 1).

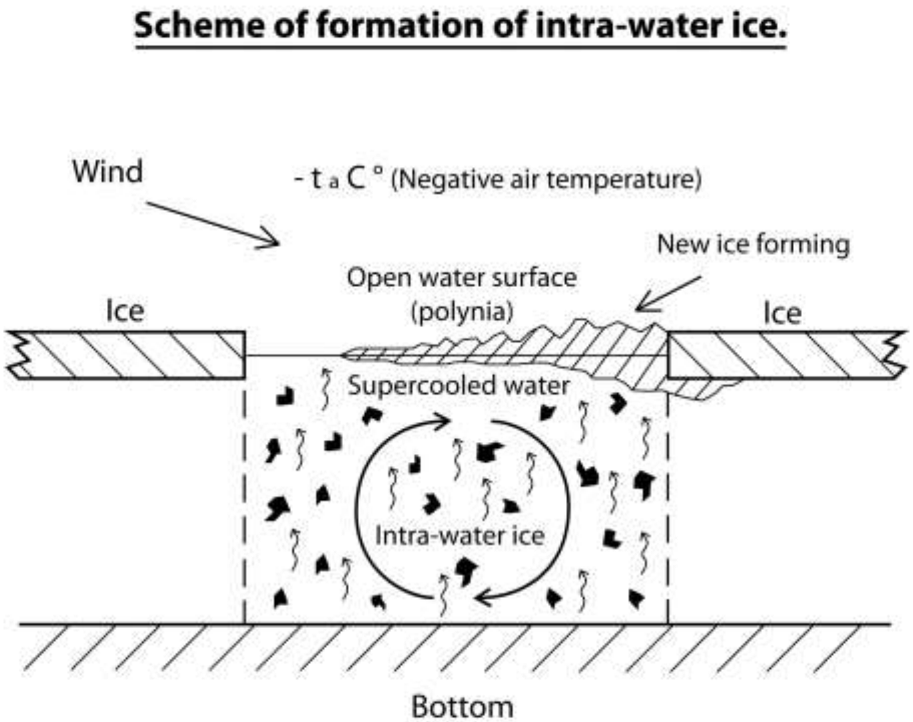

Fig. 1. Frazil ice formation in supercooled water under effect of wind chill due to wind and negative air temperature.

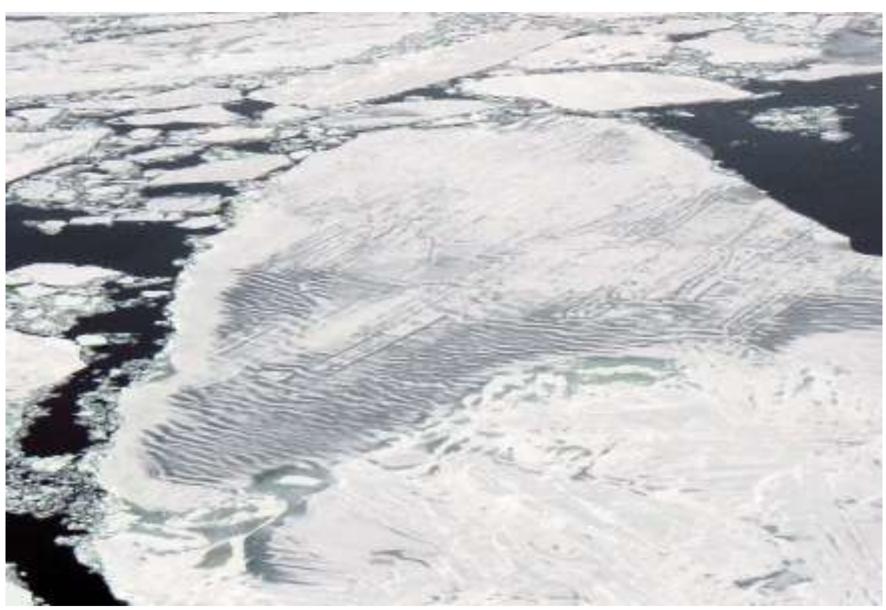

Fig. 2. Refrozen frazil ice with specific wavy surface as observed on a floe during aerial reconnaissance flight.

Due to the floating mass of frazil ice being very ductile during the freeze-up it often forms specific wavy surface under the influence of wind (figure 2). Some of the frazil ice is also partly drifted away by current and emerges underneath surrounding older ice. As it floats up it freezes to the bottom surface of ice around increasing the rate of its growth. When repeated many times, layered, porous and opaque ice is formed. Its total thickness may significantly exceed ambient thickness of thermally grown ice in the area. These processes are quite chaotic as they occur locally limited to the size of a polynya, or lead, with continuously changing dimensions and lifetime.

Frazil Ice Phenomena records in the Caspian

Analysis of more than 100 years archive records from the Caspian Sea has shown that, despite of almost no attention paid to the study of this phenomenon, the process of frazil ice formation was repeatedly observed by researchers particularly over ice covered shallow part of the Northern Caspian Sea. Works of F.I. Waller et al [1960-1990] showed that ice cover is forming and its thickness increases faster than can be predicted with Zubov's formula under the influence of negative air temperatures during the formation and development of ice cover in the shallow northern part of the Caspian Sea, because of rapid heat transfer.

The following are some of the cases indicating it:

In March 1953, while performing ice observations over reference profile in the mouth of Volga following significant drop of air temperature accompanied with strong wind and snowfall, intensive formation of frazil ice was observed over polynyas and cracks. It was in the form of opaque loose pieces of gray ice containing shells and pieces of algae (from the report).

In January 2002, during IB Captain Bukaev transit through Volga-Caspian Channel, the observers monitored the process of formation of frazil ice in over cooled water at slightly negative air temperature. It had form of ice crystals emerging on the surface and forming loose layer of primary ice forms with thickness ranging 2-5 cm and consisting of slightly frozen together crystals (from the report).

In 2016 formation of frazil ice was recorded with underwater camera in the central part of Ural Farrow during field work conducted there (Figure 3).

Fig. 3. Snapshot of frazil ice lifting to the surface of newly forming ice.

It should be noted that similar phenomena occur regularly in the lower part of Volga, after commissioning the Volga hydroelectric power station in 1959 Polynya downstream from the dam remaining open even during strong frosts acts as a generator of frazil ice, which is drifted downstream under existing ice in form of loose pieces with current. Sometimes cross-section of the river, is completely clogged with slush, which leads to formation of jams.

In-situ measurements

Thus, for example, for the identical sums of degrees of frost, the ice masses in one region of the sea may differ in thickness by a factor of almost two. The results of numerous instrumental measurements of the thickness of landfast and floating ice in the Northern Caspian showed that the minimum thickness of level ice was 45 cm while the maximum thickness reached 90 cm, which also indirectly confirmed contribution of frazil ice (figure 4).

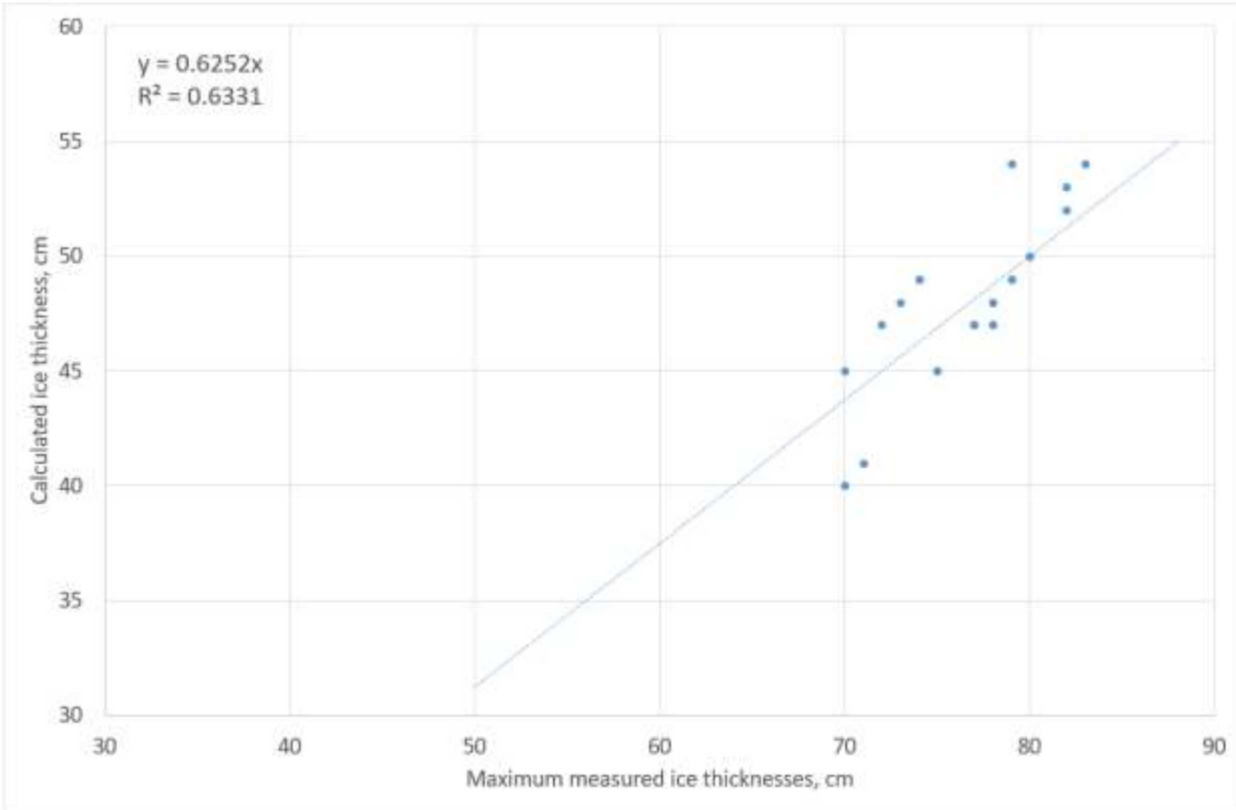

Fig. 4. Measured maximum ice thickness compared with calculated with FDD.

Open Water Leads

Thanks to satellite data becoming available during the later years possibility to monitor formation, development and extinction of the pre-coastal leads and polynya being one of the most important and changeable hydro-meteorological conditions during winter in the North Caspian. Air-borne ice reconnaissance missions of the earlier years did not provide such opportunity because of insufficient monitoring frequency and data incompleteness.

Locations, where polynyas and leads form and their development are determined with wind speed, direction and duration as well as under-ice water currents speed and direction. Satellite data helped to reveal that persisting seawards blowing winds result in leads opening between the landfast ice and drifting ice. They reach several hundred metres to tens of miles and more in width. Formation of these giant leads is facilitated with wind-drift currents, which result from wind drag over open water. Ice conditions may change rapidly with change of wind direction. Existing leads would collapse, while new ones will form at the windward side [3].

Conclusions

Analysis of ice charts compiled by UNOSIS and AARI in winter seasons 2013-2017 using satellite data showed high reliability and accuracy of such ice cover properties as the position of landfast and floating ice edges, polynyas and pre-coastal leads, compacted and open-pack ice zones, drift ice ccompactnes and ice floe sizes, and snow-cover on ice. However, one of the most important features, i.e. thermally accumulated ice thickness indicated on ice maps with respective symbols, does not correspond to the actual measured in-situ ice thickness.

Further study of frazil ice formation in the northern part of the Caspian Sea and its role in ice cover development will be undoubtedly be continued.

Acknowledgments

Authors would like to thank Sergey Vernyayev and Anton Sigitov from Iceman.kz for peer review, fruitful discussion and being a constructive opponent to the ideas laid out in this article.

References

1. Zubov N.N. Some characteristic sea ice // M.: Izd-in Gidromet. committee USSR and RSFSR, 1932. 44 s.

2. Monahov E.I. The Conditions of the shaping BOTTOM ice // Abstract to thesises on competition degree candidate of the geographical sciences. L.: 1989. 23 s.

3. Buharicin.P.I. Influence salt dome on processes of the formation lida in North Kaspian // Material of the 24th International Conference on Port and Ocean Engineering under Frctic Conditions POAC,2017. Busan, Korea, june 11-16, 2017. – p.1-11.

4. Buharicin.P.I., Ayazbayev E.Kh. Use of satellite data in mapping northern Caspian ice cover // Material 22nd IAHR International Symposium on Ice, 11-15 August 2014, Singapore. – p.119-126.

International Association for Hydro-Environment Engineering and Research
Supported by Spain Water and IWHR, China

24th IAHR International Symposium on Ice
Vladivostok, Russia, June 4 to 9, 2018

Strain-controlled cyclic compression of sea ice

Anne-Niekolai Heijkoop
Delft University of Technology (TU Delft)
Stevinweg 1, 2628 CN Delft, Netherlands
University Centre in Svalbard (UNIS)
P.O. Box 156, N-9171 Longyearbyen, Norway
niekheijkoop@gmail.com
Torodd Skjerve Nord
Sustainable Arctic Marine and Coastal Technology (SAMCoT)
Norwegian University of Science and Technology
7491 Trondheim, Norway
torodd.nord@ntnu.no
Knut Vilhelm Høyland
Sustainable Arctic Marine and Coastal Technology (SAMCoT)
Norwegian University of Science and Technology
7491 Trondheim, Norway
knut.hoyland@ntnu.no

This paper details the setup and results of an experimental campaign to investigate the constitutive behaviour of sea ice under cyclic compression. The ice samples were laboratory prepared sea ice, retrieved from horizontal cores with porosities ranging from 22-34 ppt and salinities ranging from 2-4. The displacement-controlled amplitude (10-100 μm) with a frequency ($10^{-1} – 10^{-4}$ Hz) was applied after an initial compression of 1 MPa for regular tests and 0.2 MPa for observation tests. All tests were performed at a temperature of -10 ℃. The slow varying relaxation contribution of the measured strain was removed by a high-pass filter, enabling to extract the anelastic strain component at the frequency of interest. The experiments resulted in a reproducible compressive cyclic straining test, of which the hysteresis loops show the anelastic behaviour of the material at the tested frequency. The anelastic strains were compared with a model for stress-controlled experiments.

1. Introduction

The frequency-dependent behaviour of sea ice is important for the understanding of ice-structure interaction and wave-ice interaction. The rheological properties of sea ice are complex and depend on many factors, such as the microstructure of the ice, the salinity, temperature and porosity. In addition, sea ice behaviour subjected to a load depends on the amplitude, duration and frequency. Model developments started by Glen (1955) that relate stress exerted on the ice to the creep behaviour of the ice. The equations are primarily empirical, and a fundamental mechanistic description of the relationship between the two parameters (i.e. stress and strain) remains elusive. It was only until the late nineties that a study towards the cyclic loading response of sea ice was conducted (David M. Cole, 1995). The experimental results of this campaign were presented by Cole and Durell (1995) which supported the model framework laid down by Cole (1995). This model relates the cyclic stress exerted on ice to the resulting, stress-controlled, deformation of ice, based on the microstructure of the ice. The fundamental physical phenomenon is the dislocation relaxation. These efforts were preceded by the findings of Mellor and Cole (1981)on the cyclic loading of ice.

This works further improves the understanding of the frequency-dependent behaviour of sea ice. To broaden the applicability of the model, a displacement-controlled, opposite to the established stress-controlled method, is developed. Therefore, a reproducible experimental campaign is designed and conducted, in which laboratory prepared sea ice is displacement controlled, cyclically compressed. The results of the experiments are compared to the developed model.

2. Theory

A major cause for viscous and anelastic deformation in ice is the plane glide motion of dislocations, which is defined by Hondoh (2000) as: “the motion on a plane (glide plane) parallel to both the Burgers vector and the dislocation line”. A dislocation is “a boundary lone of a region where part of the crystal has been displaced relative to another part” (John W Glen, 1974). The magnitude and direction of the lattice distortion, resulting from a dislocation in a crystal lattice, is represented by the Burgers vector, i.e. the material above the plane moves relative to the material below by an amount equal to the Burgers vector.

The number of dislocations in a material is called the dislocation density. It is expressed as the total dislocation length per unit volume. The units of the dislocation density are mm of dislocation per cubic mm. The dislocation densities of carefully solidified metal crystals are found close to 103 mm^{-2} and for heavily deformed metals at an order of 109 to 109 mm^{-2} (Callister, 2001). For the deformation of ice, only the mobile dislocation density, thus the dislocations that move, are considered. For laboratory prepared saline ice this is in the order of 108 mm^{-2}. However, note that this value is the value that is found by either X-ray topography, cyclic tests or a stress relaxation test (D.M. Cole, 1998).

Cole (1995) used experimental results to derive the loss and storage compliance of the sea ice dislocation relaxation, respectively D_2^d and D_1^d at -10°C. The grain boundary relaxation is implemented as well, thus D_2^{gb} and D_1^{gb} and both relaxation mechanisms are expected to operate simultaneously, such that the loss compliance D_2 and the storage compliance D_1 are:

$$D_1 = D_1^{gb} + D_1^d \quad \textbf{[1]}$$

$$D_2 = D_2^{gb} + D_2^{d} \quad \textbf{[2]}$$

in which the individual contributions are described in Eqs. 3-6, for which the constants are given in Table 2. The strain, ε, is calculated as a function of the storage and loss compliance in Eq. 8, for a sinusoidal given stress history, Eq. 7, in which σ_0 is the stress amplitude and ω the radial frequency.

$$D_1^{d}(\omega) = D_u^{d} + \delta D^{d}\left(1 - \frac{2}{\pi}\tan^{-1}[\exp(\alpha^{d} s^{d})]\right) \quad \textbf{[3]}$$

$$D_1^{gb}(\omega) = D_u^{gb} + \delta D^{gb}\left(1 - \frac{2}{\pi}\tan^{-1}[\exp(\alpha^{gb} s^{gb})]\right), \quad \textbf{[4]}$$

$$D_2^{d}(\omega) = \alpha^{d}\delta D^{d}\frac{1}{\exp(\alpha^{d}s^{d}) + \exp(-\alpha^{d}s^{d})} \quad \textbf{[5]}$$

$$D_2^{gb}(\omega) = \alpha^{gb}\delta D^{gb}\frac{1}{\exp(\alpha^{gb}s^{gb}) + \exp(-\alpha^{gb}s^{gb})} \quad \textbf{[6]}$$

$$\sigma = \sigma_0 \sin(\omega t) \quad \textbf{[7]}$$

$$\varepsilon = \sigma_0(D_1 \sin(\omega t) - D_2 \cos(\omega t)) \quad \textbf{[8]}$$

The experiments by Cole and Durell (1995) were conducted by employing a sinusoidal load oscillating about zero on cylindrical milled, laboratory grown saline ice. The cyclic stress amplitude remained below 0.8 MPa, the frequency ranged from 10^{-3} to 1 Hz. The influence of stress history and a significant frequency effect were important results from this research. However, while the developed equations successfully predict the ice deformation based on a certain (cyclic) stress, Eq. 7, exerted on the ice, it is not yet confirmed, whether they can be applied to the inverse relationship, i.e. predict the resulting stress when a certain strain is applied.

3. Setup of experiments and data comparison

The experiments were conducted in the cold laboratories at the University Centre in Svalbard, Norway. Cylindrical specimens with a length of 175 mm were cut from a 75 mm diameter drilled horizontal and vertical cores of laboratory grown sea ice. The ice was made from a mix of ¼ filtered local sea water (retrieved from Adventfjorden, Svalbard) and ¾ tap water (retrieved from a local meltwater lake) with a bulk salinity of 8 ppt in a tank with heated walls. The temperature in the cold laboratory during growth varied between -20°C and -15°C. The specimens were wrapped in plastic bags and stored in -20°C until compression tests were performed. The specimens were fastened in the clamp system, by applying a layer of fresh water, fifteen hours before the compression tests started to equilibrate to the -10°C desired test temperature.

The clamped specimen was instrumented with an external strain sensor and a load transducer was placed on top. The loading frame, has a nonlinear stiffness upward to 109 kN/mm. The bottom plate is displacement controlled with a stepper engine. The loading frame is instrumented with a load transducer, of which the value is read in the same software as the stepper engine is controlled.

The stepper engine is controlled through an open loop control system. For a typical cyclic experiment, shown in Fig. 3, a constant strain rate (10^{-3} s^{-1}) is applied until a set force corresponding to a stress of 1.0 MPa is reached after which a sinusoidal displacement is superposed with a defined amplitude and frequency. The experimental parameters that varied are: the set force (initiating the cyclic displacement), the double amplitude, the frequency and the number of cycles. As shown in Fig. 2, two types of experiments were executed in which a series of experiments with high initial load and varying amplitude was alternated with an experiment with a low initial load and amplitude, the so-called observation test.

Fig. 1. Clamped ice specimen in loading frame, with installed strain sensor and load cell

To assess the stiffness and compliance of the frame, the cyclic tests were also carried out using an aluminum specimen. The aluminum specimen is a 175 mm tall tube. An important assumption is that the specimen responds linear in the same range of force applied as on the ice specimen.

After the cyclic compression tests, the specimens were characterized by measuring their density, salinity and by preparing thin sections. The density was measured using the hydrostatic weighing method in paraffin. The salinity was measured with a conductivity meter. The thin sections were prepared at $-20°C$ from horizontal and vertical slices of the specimen. The slice was then planed down to a thickness of less than 1 mm. The force and strain recorded with the external sensors were used to analyze the compliances and moduli of the ice.

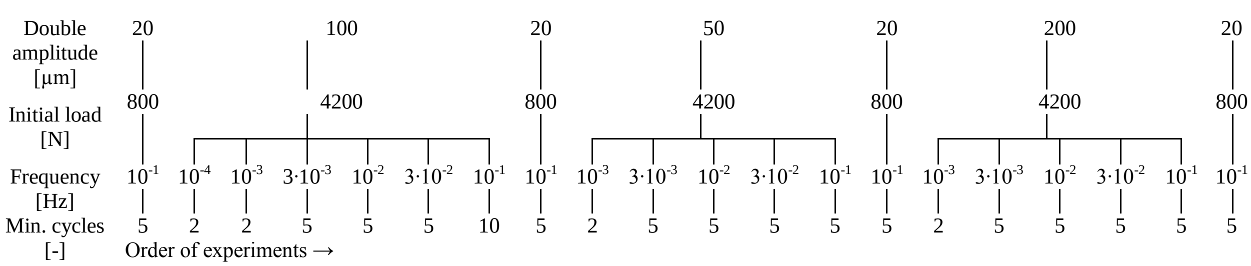

Fig. 2. Test matrix for cyclic compression experiments on specimens from the horizontal cores

The stress and especially the strain signal contained instrumental noise, which was reduced by using a third order Butterworth type filter with a low pass frequency. Slower trends in the stress and strain signals were filtered with a high pass filter. The focus of this work lies with the response of the material to the controlled frequencies. Therefore, the low pass filter frequency was scaled with the loading frequency. The scale factor was determined by visually assessment of the resulting filtered signal.

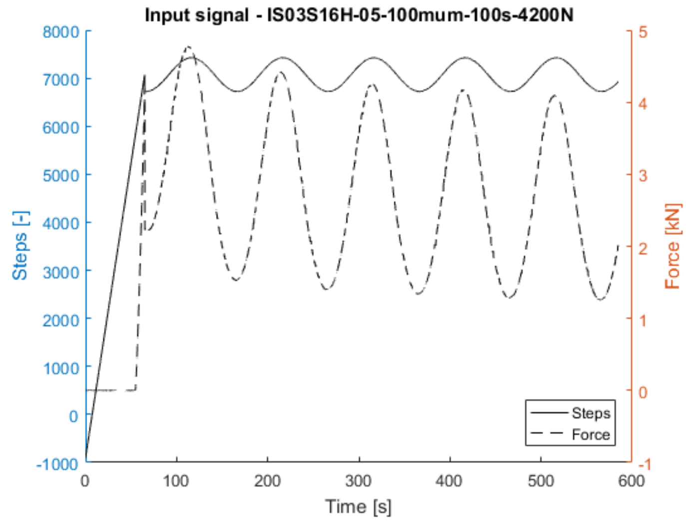

Fig. 3. Controller input signal and measured force

Each loop of the filtered cyclic data was analyzed separately, i.e. the width (ε_w) and height (σ_h) of each loop was determined at respectively the mean stress and mean strain. The stress and strain amplitude (σ_0 and ε_0) were measured from the time series. Subsequently the loss and storage compliance were calculated, respectively D_2 and D_1, using Eqs. 9-10, where the loss modulus, M_2, is determined in Eq. 12.

$$D_2 = \frac{\varepsilon_w}{\sigma_0} \qquad \textbf{[9]}$$

$$D_1 = \sqrt{\left(\frac{D_2 \sigma_0}{M_2 \varepsilon_0}\right)^2 - (D_2)^2} \qquad \textbf{[10]}$$

$$M_2 = \frac{\sigma_h}{\varepsilon_0} \qquad \textbf{[11]}$$

The effective modulus was determined from the tangent to the curve at the point of the mean stress. Since each loop passes the mean stress twice, the mean of the tangents was determined to be the effective modulus of the whole loop.

4. Results

4.1 Individual specimen

The temperature of the cold lab, the density and salinity of the specimen was measured. The porosities were computed. The specimen characteristics are listed in Table 1.

Two thin sections of the specimen are presented in Fig. 4. The direction of the grains, thus the basal planes are oriented vertical. The basal dislocations have the largest influence on the orientation factor. The c-axes of the specimens were unaligned. The grain sizes are in the order for which the model was validated.

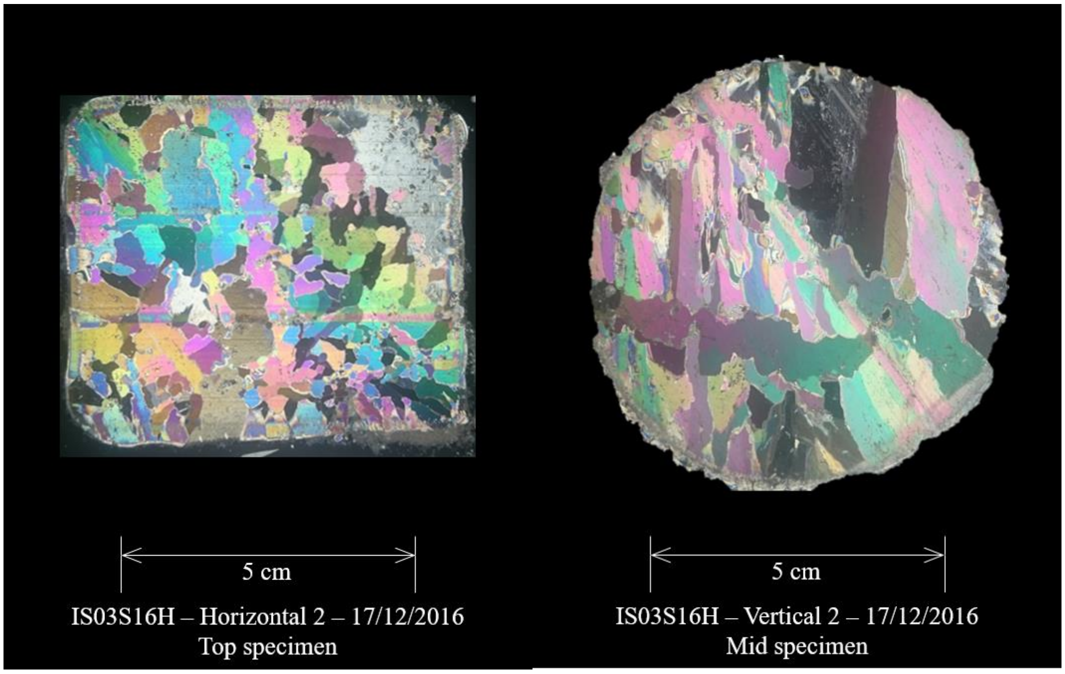

Fig. 4. Horizontal (l) and vertical (r) thin sections of horizontal specimen IS03S16H

Table 1. IS03S16H Specimen characteristics

Specimen		IS03S16H
Density	$[kg/m^3]$	903.2
Salinity	$[-]$	2.6
Air porosity	[%]	2.0
Brine porosity	[%]	1.4
Total porosity	[%]	3.4

4.2 Cyclic compression tests

The result of a typical cyclic compression experiment is shown in Fig. 5. The stress and strain are noise filtered. The strain shows a slow increase during the test. This may be explained by the applied zero-frequency component of the haversine. The stress is slowly decreasing over time, showing stress relaxation. The stress relaxation is explained by the compression of the specimen.

The stress-strain curve is plotted in Fig. 6. The loop width and height are clearly visible and can be estimated to obtain the dynamic compliances.

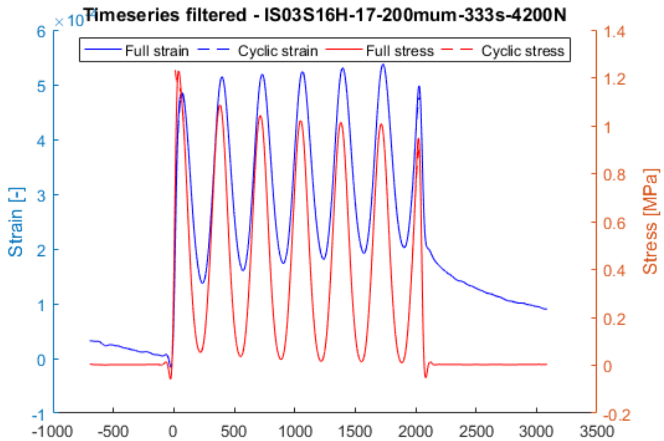

Fig. 5. Noise filtered stress and strain time series for experiment IS03S16H-17

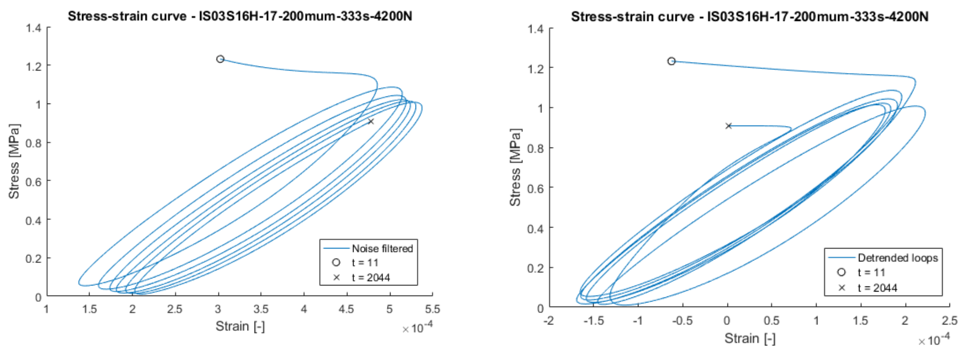

Fig. 6. Noise filtered (l) and high pass filtered (r) loops for experiment IS03S16H-17

The loss and storage compliance, measured for all experiments on sample IS03S16H, as a function of the frequency are plotted in Fig. 7. In the figure, the loss compliance and storage of each loop of the experiments are plotted in the same graph. Model predictions of the loss compliance were carried out using Eqs. 1-11 with input specimen specific parameters and constants from Cole (1995) (Table 2).

Table 2. Specimen specific parameters

Symbol	Name	Value	Unit
T	Temperature	-10	℃
α^d	Peak broadening factor dislocation relaxation	0.53	$-$
K^d	Stress restoring term	0.07	Pa
δD^d	Strength of dislocation relaxation	1.4×10^{-9}	Pa^{-1}
α^{gb}	Peak broadening factor grain boundary relaxation	0.6	$-$
B_0/K^{gb}	Pre-exponential term	8×10^{-28}	s^{-1}
Q^d	Activation energy dislocation relaxation	eV	eV
b	Burgers vector	4.52×10^{-9}	[−]
E_U	Elastic modulus ice	9.0	GPa
B_0	Constant in drag term	1.205×10^{-9}	Pa s
Q	Activation energy grain boundary	1.32	eV
k	Boltzmann constant	8.617×10^{-5}	$\mathrm{eV\,K}^{-1}$

The loss compliance model prediction shows the same trend and magnitude as the experimental data points. The storage compliance resembles the data points for all the amplitudes. The model storage compliance is higher than the data points, especially for higher frequencies.

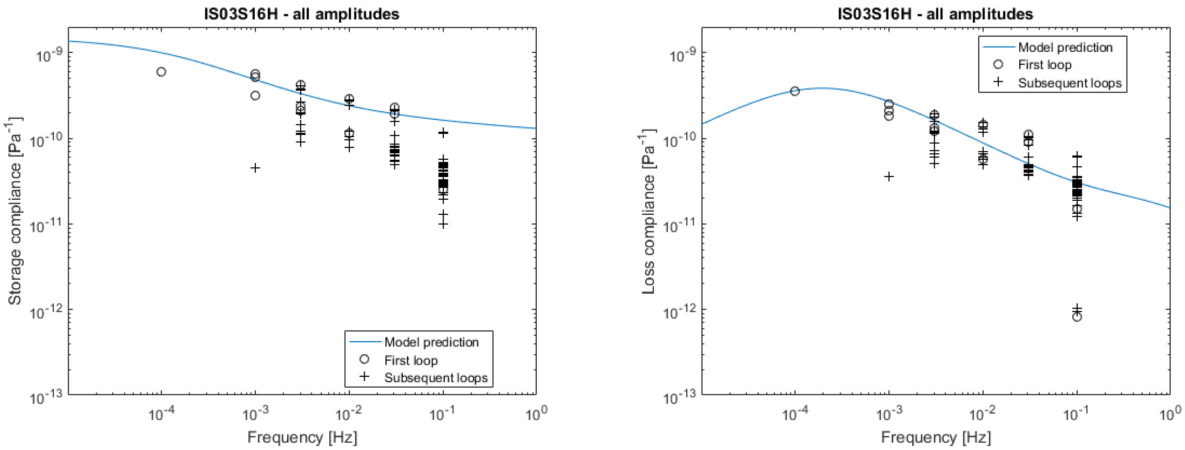

Fig. 7. Measured storage (l) and loss (r) compliances for all experiments on specimen IS03S16H and model prediction

5. Discussion

The displacement profiles applied and measured, defined from the test matrix, were visible and could be analyzed limited by low amplitudes and large amplitudes combined with a high frequency. The external strain sensor used, was not able to identify the strain when the double amplitude was smaller than 50 μm, even after applying filters. For the upper limit, the specimen would not relax fast enough to maintain a load; thus, the specimen was released every cycle. The compressive experiments include stress relaxation of the specimen, which must be either subtracted or filtered, to analyse the steady state behaviour. For an easier assessment of the steady state behaviour cyclic compression-tension experiments can be conducted. With these experiments, the viscous deformation may also easily be identified.

Another observed phenomenon in the applied displacement profile is the ‘mode switch jump’, where the steps jumped to another value when the constant loading switched to the cyclic loading. The time offset of the cyclic signal was shifting with the current control system, since the time between the start of movement of the plates and the contact with the specimen was not specified.

The low pass frequency filter performed well to reduce noise from the cyclic part of the tests. However, the low pass frequency filter could not handle sudden changes, such as mode switches or tests where the upper plate lost contact with the specimen. To build confidence in the analysis method, the high-pass filter was applied to simulated stress and strain time histories, obtained by using the model of Cole and Dempsey (2001). The simulated data contained of a compressive stress signal and the strain response, separated into elastic, anelastic and viscous components. By applying the high pass filter to the total strain component, the following remarks can be made:

The hysteresis visible in the stress-strain curves is caused only by the anelastic component. The shift of the loops to the right is caused by the creep and the shift downwards by the stress relaxation. The filtered loop width acts as an asymptotic loop width for the unfiltered loop width when these values compared per subsequent loop. The slow varying relaxation contribution of the measured strain was removed by a high-pass filter, enabling to extract the anelastic strain component at the frequency of interest.

The self-deformation of the frame is not well known for the applied low stresses. To circumvent the self-deformation influencing the strain measurements only strain in the specimen itself was measured, which was the focus of this work. To allow for a better controlled strain input the control system can be expanded such that the measured deformation can be used as a new input, providing a closed feedback loop.

The end caps were a valuable piece of new equipment for compression tests under low stresses. The end caps provided a proper alignment of the specimen, relatively independent of the quality of the cuts. Another advantage is that within a reasonable range the operational height between the plates of the frame remained the same, contributing to the reproducibility of each test. Detrimental was the fastening system, a variable height of fresh water ice between the specimen and the specimen. The interference of this additional joining between the specimen and the end caps is not known. Another disadvantage of the fastening system is the removal of the specimen from the end caps. A significant amount of height of specimen is lost when cut from the end caps.

Two load cells were used to measure the applied force, one built into the frame and one external load cell. The built-in load cell was precise enough to identify the steps of the engine. The signal of the external load cell showed some noise, but the level of the noise was low enough to interpret the results.

A significant amount of noise was visible in the signal measured by the external strain sensor. The noise proved to be too large to analyze the observation test. However, for larger amplitudes the used sensor provided reliable results.

6. Conclusions

A successful experimental campaign on the cyclic straining of laboratory prepared sea ice was designed and conducted. A complete description of the experimental campaign is included in the work resulting in a reproducible method.

The high pass filter method successfully reduces the total strain response to a steady state strain response, where the loop width per frequency of interest can be compared to each other.

The modelled steady-state response to a stress history or strain history matched well with the experimental observations, for both the individual experiments as the frequency dependence of the storage and loss compliance.

Acknowledgments
The authors wish to acknowledge the support of the Research Council of Norway through the Centre for Research-based Innovation, SAMCoT, and the support of the SAMCoT partners.

The authors would also like to thank Dr. David Cole. He lectured at UNIS for two weeks about the model on which this work was based. During and long after this period, the topic was discussed and both our interest and knowledge on the model were greatly improved.

References
Callister Jr., W.D., 2001. Fundamentals of Materials Science and Engineering. John Wiley & Sons, Inc., Phoenix, USA.

Cole, D.M., 1995. A model for the anelastic straining of saline ice subjected to cyclic loading. Philosophical Magazine A, 72 (1), 231-248.

Cole, D.M., 1998. Modeling the cyclic loading response of sea ice. Int. J. Solids Struct., 35 (97), 4067–4075.

Cole, D.M., and Dempsey, J.P., 2001. Influence of scale on the constitutive behavior of sea ice. IUTAM Symposium on Scaling Laws in Ice Mechanics and Ice Dynamics, Fairbanks, Alaska, 251–264.

Cole, D.M., and Durell, G.G., 1995. The cyclic loading of saline ice. Philosophical Magazine A, 72 (1), 209-229.

Glen, J.W., 1955. The creep of polycrystalline Ice. Proc. of the Royal Society A: Mathematical, Physical and Engineering Sciences, 228(1175), 519–538

Glen, J.W., 1974. The physics of ice. Corps of Engineers, U.S. Army, Cold Regions Research and Engineering Laboratory. Hanover, New Hampshire, USA.

Hondoh, T., 2000. Nature and behavior of dislocations in ice, Physics of Ice Core Records, 3-24.

Mellor, M., and Cole, D.M., 1981. Cyclic loading and fatigue in ice, Cold Regions Science and Technology, 4, 41-53

24th IAHR International Symposium on Ice
Vladivostok, Russia, June 4 to 9, 2018

Application of Neural Network Model for Ice Jam Forecasting in the Heilongjiang River

Xinlei Guo[1], Tao Wang [1], Hui Fu [1], Yongxin Guo [1], Li Jiazheng[1]
1. State Key Laboratory of Simulation and Regulation of Water Cycle in River Basin, China Institute of Water Resources and Hydropower Research, Beijing, China

Abstract: The forecast of ice jams and its break-up is crucial to prevent possible flooding in cold region. Current breakup ice jam forecasting methods are largely based on conventional statistical analyses or past experience. New forecasting technologies are urgently needed for ice flood management. In this paper, an ice jam forecasting model was established based on the neural network theory and used for ice jam forecasting in the upper Heilongjiang River (Amur River), where ice floods occur frequently. The model based on the neural network clustering method had an accuracy rate of 85%, which was significantly higher than the 62% accuracy rate of the conventional statistical method for breakup ice jam forecasting. The model had a forecast period of 10 days with a maximum error of 2 days and forecast qualified rate of 100% for breakup date forecasting. The forecast on the breakup ice jam, which was released 24 days ahead, provides the accurate results for the breakup date and the occurrence of breakup ice jams in the spring of 2017.

Key words: River ice; breakup; Ice jam; Forecast; Neural network; Heilongjiang River

1. Background

Ice jams occurring in rivers of cold region can cause severe ice flooding problems. According to the definition of ice jam suggested by Shen et al. (1995), the surface ice jams will be formed as a large amount of floating ice pieces are blocked by ice covers in the downstream river reach, and consequently the free surface level of the river is elevated. The surface ice jams can be generated during freezeup or breakup period. Further, the frazil ice jams can be formed when enough frail-ice particles are built-up under ice cover before and during freezeup. As for the two types of the ice jams during freezeup, much efforts has been devoted to understand its physical mechanism and to develop a rational theoretical model accordingly. Shen et al. (1991, 1995) suggested a one-dimensional model which simulates frazil ice accumulation and transportation process. Yet the impact of real three dimensional flow characteristics beneath ice cover and complex geometry boundary cannot be incorporated in such simplified model. Shen et al. (1993, 2010) further presented a two-dimensional model, which is applied to simulate ice transport and ice jam formation during Clair River freezeup (Kolersk and Shen 2015). Fu et al. (2015, 2017) studied the correlation between safe discharge and water level of an inverted siphon for preventing ice jam formation with a physical model using real ice.

Artificial neural network models are also developed to predict ice condition in field as there are not enough field data and boundary information available for theoretical modelling. For instance, the Heilongjiang River, the border river of China and Russia, locates in the northern part of China. Only limited data of the geometry of the river and its flow condition can be obtained in China territory. Moreover, for meandering river, such as Yellow River, its natural flow passage is flexible to some extent due to erosion and scouring. So it is difficult to apply and verify the rigid mathematical model in the situations above. It is well known that neural network theory is an alternative for modelling complex nonlinear physical process without directly solving governing partial equations. In addition the noise present in input and output of the network is processed without pronounced loss of accuracy due to distributed processing feature of the network. Therefore with advantage of the neural network, there are many practical application of neural network theory in recent years. ASCE (2000a, b) presented a set of practical applications related in hydrological forecasting, including forecasting of water levels, sedimentation, flooding, rainfall, and surface runoff (Chau 2006; Dawson et al. 2006; Riad et al. 2004). With the advancement of river ice research, the artificial neural network has shown the potentiality for modeling the behavior of complex nonlinear processes of ice jam formation for its advantage of overcoming the limitations of conventional forecasting methods. Chen et al. (2004) used conventional BP neural network to predict ice-run and freezeup during winter. Wang et al. (2012, 2014) developed neural fuzzy model for forecasting ice-run and freezeup dates, which has been used in the Yellow River and South-North Water Transfer Projects.

In general, breakup ice jams occurring during periods of thaw can be classified into thermal breakup and mechanical breakup. During the thermal breakup process, the ice cover gradually deteriorates and melts in region with insignificant movement by natural thermal effects. The river flow remains relatively steady during the spring breakup period. No ice jams can be produced by accumulation of large floating ice blocks. Mechanical breakup is produced by hydraulic forces caused by changes of river flow and its surface level. Ice blocks are transported downstream of the river until transport capacity of the river is exceeded. After the blocks are obstructed by the ice covers, the ice jams will be produced. Consequently, the river flow is backed up and its surface can be raised rapidly causing risk of downstream flooding. The ice jams can break up in short time, say several hours. When ice jams break suddenly, severe flooding can also happen downstream. Therefore, ice jam forecasting for river breakup is critical in preventing or alleviating ice jam and flooding hazards. Roughly, the formation and development of ice jams during breakup can be affected by multiple factors including air and water temperature, wind speed and direction, river flow feature, and weather condition, etc.

Currently there are few established mathematical models for simulating and forecasting breakup ice jams process. Beltos (1984, 2008, 1993, 1995) described and analyzed the physical process of ice accumulation, ice jam formation, and ice jam breach during breakup. Beltos (1990) also defined the onset of the breakup as the time when sustained ice movement occurs in a particular site, and formulated an empirical method for forecasting the breakup occurring based on the boundary constraints of the river plane geometry. Dai et al. (2010) performed ice jam forecasting on the Heilongjiang River using statistical methods and empirical equations. The conventional artificial neural network is also applied for forecasting onset of breakup. Wang et al. (2008, 2009, and 2013) performed the forecast of the Yellow River breakup date and water temperature change during winter based on the neural network theory. Mahabir et al. (2006, 2007) applied the neural network theory to predict breakup and flooding after ice jam release on the Athabasca River. As the mechanical breakup is still not well understood and limitation of field information, the breakup forecasting techniques are much empirical and site-specific.

This paper reports a neural network model using Back Propagation (BP) to simulate ice jam occurrence based on of the mechanism of the ice jam evaluations. The model has been applied to forecast breakup ice jam occurrence and breakup date in the Mohe County reach of the Heilongjiang River, where the frequent damaging ice jams occur.

2. Neural Network Model for Ice jam Forecasting

Ice forecasting modeling based on BP neural network theory involves two processes: learning process of historical ice conditions and forecasting process, as shown in Fig. 1. The learning process of the network includes forward information transmitting procedure and backward error correction procedure. The procedure that the input information is transmitted from the input layer to the output layer through hidden layers is referred to forward information transmitting.

If the actual output of the network does not meet expected errors, the error in the output is feedback from the output layer to the input layer in the reversed direction in order to correct the connection weights at the neuron nodes on each of the layers. This procedure is referred to backward error correction transmitting. These iterative procedures are performed until the output error in the model satisfies the required accuracy or maximum number of iterations has been reached and the learning process ends.

After the steps described above, the algorithm is developed and trained to map an input vector to an output vector between which the error is minimized, and then the network model using weight coefficients and thresholds based on the historical data learning process is applied to ice jam forecasting.

The majority of the artificial neural network applications in water engineering involves the application of the BP model, which is found superior over conventional statistical and stochastic methods in continuous flow series forecasting (Alp 2006). Yet the iterative procedures of the neural network are sensitive to the selected initial weight values and the networks are sometimes trapped by the local error minima during the training stage, which could prevent the network training from reaching the global minimum error in BP neural network model based on the Gradient Descent algorithm proposed by Maier (2000). The methods, such as Newtons algorithm, Levenberg-Marquardt algorithm, stochastic gradient algorithms, and simulated annealing, may overcome this problem of training a number of networks starting with different initial weights, and help the networks escape local minima.

To deal with this problem, the Levenberg-Marquardt algorithm is used to improve the BP neural network models. Wang (2008) successfully applied a BP neural network model improved by the Levenberg-Marquardt algorithm to forecast the beginning date of ice run, freeze up and break up in the Yellow River. This algorithm is an iterative technique that locates the minimum of a multivariate function that is expressed as the sum of squares of a nonlinear real-valued function, and the minimum sum of squares error can be obtained by using the square error instead of the mean square error. Therefore, the Levenberg-Marquardt algorithm can be considered as a hybrid between the classical Newton and steepest descent algorithms. It has been proven that the Levenberg-Marquardt algorithm converges more quickly than the Gradient Descent method (Wang, 2014).

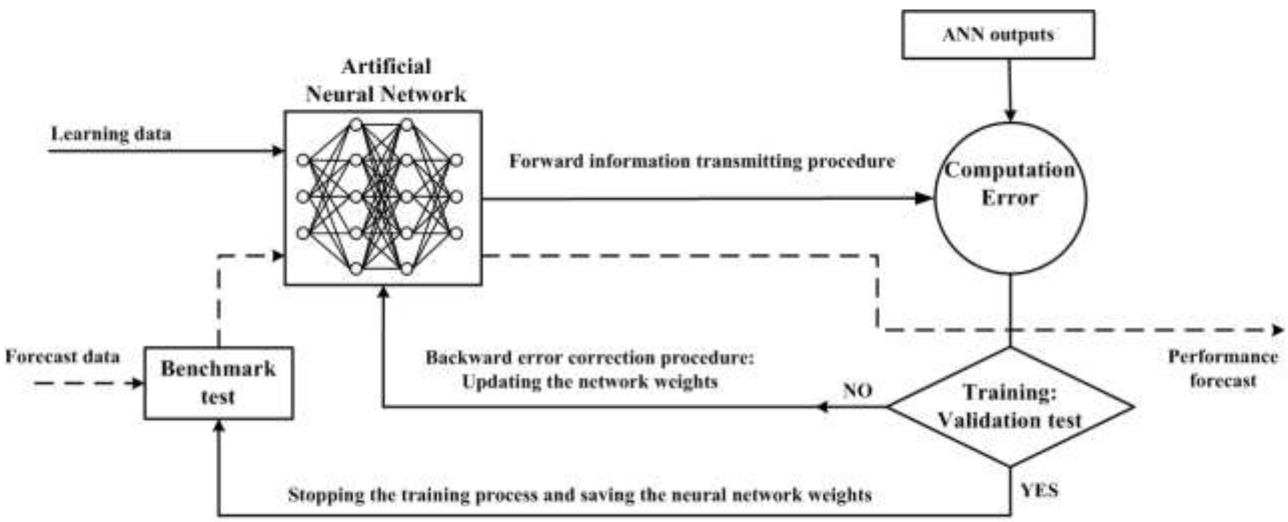

Fig. 1. Forecast procedure of the Neural Network.

When the occurrence of an ice jam is forecasted by neural network model based on its learning process of the historical hydrological data, meteorological data and so on, the output is in the form of whether an ice jam would occur or not. This corresponds to an output value of 1 or 0. The training process of the network model is a process of network clustering. That is to say it groups the data based on similar properties. When a neural network is trained for classification or clustering, each output is assigned a class label and the probability of an output result into that class can be determined. Neural networks can establish non-linear decision map which can better determine class or clustering processes. Ice jam forecast can be performed based on the nonlinear learning and computation processes of the neural network clustering method. Since breakup ice jams often occur at the beginning period of the breakup, the form period of ice jam forecasting is known through forecasting the breakup date.

An ice jam forecast model based analyzing the forecast impact factors is expressed as

$$D_{jam} = f\left(P_{bf}, P_{df}, P_{bb}, T_{df}, T_{bb}, Q, H_{1}, H_{snow}, H_{ice} \cdots\cdots V_{cs}\right) \qquad \textbf{[1]}$$

Where D_{jam} = the occurrence condition of ice jams; P_{bf} = precipitation prior to freezeup, mm; P_{df} = precipitation during the freezeup period, mm; P_{bb} = precipitation prior to breakup, mm; T_{df} = accumulated negative air temperature during the freezeup period, °C; T_{bb} =change of temperature prior to breakup, °C; Q = volumetric discharge, m^3/s; H_1 = water level during freezeup, m; H_{ice} =ice cover thickness, m; H_{snow} = snow depth on the ice cover, m; and V_{cs} = water channel storage, m^3.

In order to eliminate the influence of the different dimensions of all the factors during the neural network training and forecasting, and to avoid the neural network unit saturating, these factors are expressed in non-dimensional form as the following:

$$y_i = \frac{z_i - z_{\min}}{z_{\max} - z_{\min}} \alpha + \beta \qquad \textbf{[2]}$$

Where z_i and y_i = original and standardized parameters, respectively; $z_{\max}$ and $z_{\min}$ = the maximum and minimum values of z_i, respectively; α is a coefficient in [0, 1], and $\beta = (1 - \alpha)/2$, so the network input units y_i is the range of [0.05 0.95].

3. Controlling factors for breakup jam formation on Heilongjiang River

Ice covers of Heilongjiang River are typically very thick and strong with heavy snow on the top. Based on the records since the 1950s, ice jams occur on almost yearly basis in certain reaches of the Heilongjiang River. On average, significant ice jam events occur every 3 years. The ice jam phenomenon in the Heilongjiang River are so prominent that it is crucial to conduct detailed ice jam observation and forecasting for preventing possible flooding in this region. A reliable ice jam forecasting system of Heilongjiang River can provide an effective tool to assist with ice jam removal and flooding disaster prevention. The jams usually occurred during spring breakup period. Main reasons of breakup ice jam occurrence include the following:

(1) Geographical location and river flow direction

The river location and flow direction are the dominating factors on the reversed breakup and lead to ice jam formation in the Heilongjiang River. The Argun River and the Shilka River are two large tributaries of the Heilongjiang River, which are the headstreams of Heilongjiang River. Both rivers flow from southwest to northwest, as shown in Fig. 2, and from the low latitude to the high latitude with a 700km distance difference. This condition causes breakup to occur in the upstream reach and tributaries usually breaks up before the downstream reach. The ice cover in the downstream reach becomes a natural obstacle to the ice discharge and causes jam formation.

Fig. 2. River Locations and Flow Direction of the Heilongjiang River.

(2)River geometry and topography characteristics

Topography and river characteristics play an important role of ice jam formation. The upper reach of the Heilongjiang River flows through the Greater Xinggan Mountains with high mountains, valleys, and plains alternating on the river banks. Under the radiation and thermal effects of the sun, the plains receives more heat than the valleys, and the sunny reach of the mountains receives more heat than the shady one, resulting in variations in ice melting at different locations along the river, which may cause ice jam by the ice blocks. The upper reach of the Heilongjiang River is a typical mountainous river with steep channel bottom, variations in the channel width, and irregular bank lines. The river meanders like L, S, or Ω routes, and even has more than 90 degree bends, as shown in Fig. 3. Some river reaches are narrow and meandering with connecting center islands, many diversions and bifurcations as shown in Fig. 3. The channel width and depth change significantly along the river. All these channel characteristics and its flow capacity provide favorable hydraulic conditions for easy ice jam formation.

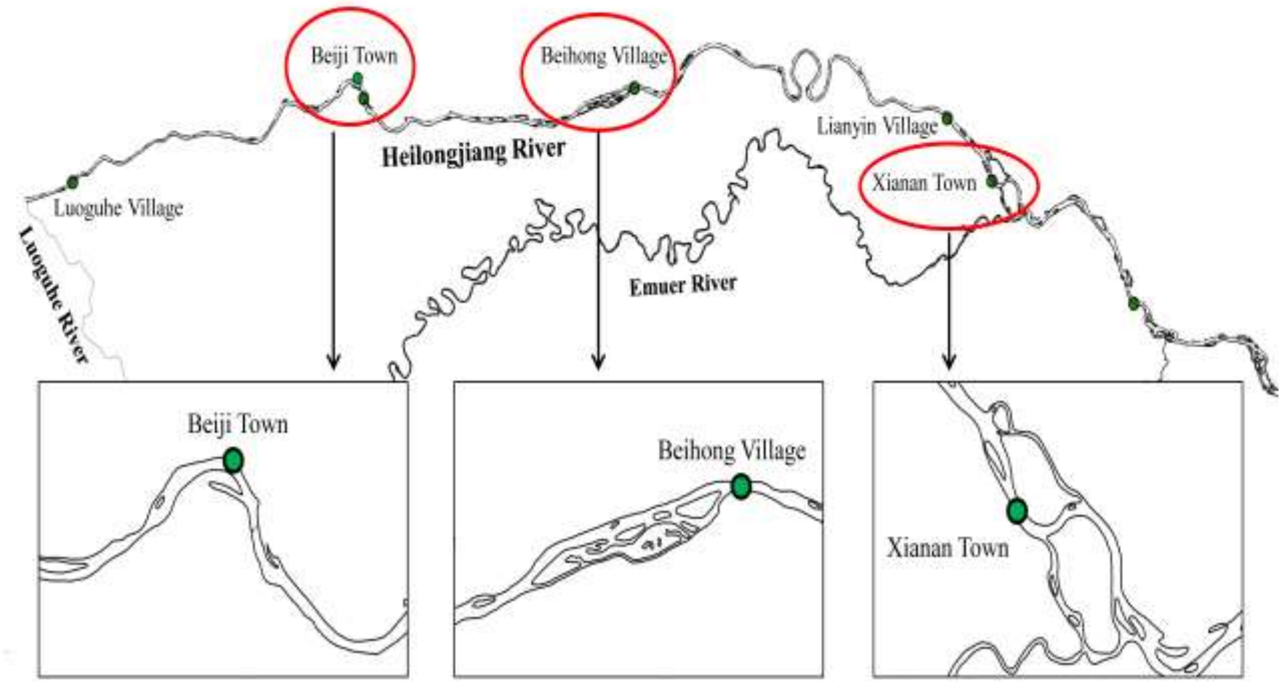

Fig. 3. Location Map of Mohe reach, Heilongjiang River.

(3) Hydrological and meteorological factors
Hydrometeorological factors directly influence the formation of ice jam. The main factors in the Heilongjiang River basin include the winter and spring air temperature, water storage capacity of the channel, precipitation during the freezeup period and before breakup, evaporation, snow cover thickness, and ice cover thickness. When these unfavorable hydrometeorological conditions or combinations of unfavorable hydrometeorological conditions occur, mechanical breakup of the Heilongjiang River could happen and lead to ice jam formation. For example, rapid rise of air temperature coupled with rainfall or snowfall during early spring will cause a rapid increase in river discharge due to snowmelt runoff and precipitation. This process then leads to mechanical breakup and breakup ice jam formation the Heilongjiang River.

The Heilongjiang River is located in a remote region. The number of hydrologic stations in this region is far below the national average. Since the Heilongjiang River is the border of China and Russia, the river cross sections and flow rates cannot be directly measured, which results in severely deficient field information including meteorological data, hydrographic data and river geometry. This study used neural network modeling to forecast ice jam formation in the Mohe reach. The hydrological data for the model input was obtained mainly from the Beiji Gaging Station in Mohe County. Daily average precipitation and air temperature data for Mohe County were from the China Meteorological Administration. The forecast factors included:

- Precipitation (snowfall and rainfall) before freezeup, mm;
- Precipitation (snowfall and rainfall) during freezeup, mm;
- Precipitation (snowfall and rainfall) before breakup, mm;
- Accumulative negative temperature during freezeup, ℃;

- Air temperature change before breakeup, ℃;
- Thickness of ice cover, m; and
- Date when the air temperature goes above zero degrees, month/date.

Breakup Ice jam forecasting

The ice jam forecasting model based on the Levenberg-Marquardt BP neural network clustering method includes 3 layers, an input layer, a hidden layer, and an output layer. The Sigmoid function is used as the transfer function in the hidden layer. The Logarithm function is employed as the transfer function for the output layer, which defined the network output value to a range between 0 and 1. The adaptive learning rate, whose values change from 0 to 1, is used throughout the simulations. In this study, the Hydrological and meteorological data measured from 1957 through 2002 are used for training the networks and those from 2003through 2015 for forecasting the ice jam.

For comparison, the forecast results of the statistical analysis model are presented to test the accuracy of the forecasting results from the neural network model. The current ice jam forecasting statistical model of the Heilongjiang River is based on the probability statistical method. The occurrence probability P is calculated based on Equations (3) and (4) below:

$$P_{total} = P_1 + P_2 + P_3 + \cdots\cdots P_n \quad \textbf{[3]}$$

$$P_{average} = P_{total} / n \quad \textbf{[4]}$$

Where n = Number of forecast factors, P_n = Probability of No. nth factor, P_{total} =Sum of the probabilities, and $P_{average}$ =Average probability of the No. n impacting factors.

The occurrence probabilities of the ice jam impacting factors between 1990 and 2015, as the same as the above forecast factors, are analyzed and the average probability is about 45%. Therefore 45 percent is used as the criterion for ice jam occurrence.

Comparison with the ice jam forecast results based on the neural network clustering method and probability method is summarized in Table 1. It shows that the forecast result of the neural network model in ice jam occurrence is accurate for 11 of the 13 years from 2003 to 2015, resulting in an accuracy rates of 85%, while the statistical model was accurate for 8 years, resulting in an accuracy rate of 62%. These results suggest an obvious advantage of the neural network model over the conventional statistical model. Both models forecast shows that breakup ice jam would occur in 2015 because of the fact that the precipitation during freezeup and before breakup was 51% and 74% higher than the annual average, respectively. However, ice breaking measures with explosives before breakup were implemented in Mohe reach of the upper Heilongjiang River where potential ice jam risk would occur based on ice jam forecasting, which prevented ice jam formation and ice flooding from occurring in 2015(Liu and Wang, 2017).

Table 1. Results comparison between neural network method and statistical method.

Year	Measured of Ice jams	Neural Network Method		Statistical Method	
		Forecasted Result	Pass (Y/N)	Forecasted Result	Pass (Y/N)
2003	No ice jam	No ice jam	Y	Ice jam occurrence	N
2004	Ice jam occurrence	Ice jam occurrence	Y	Ice jam occurrence	Y
2005	No ice jam	No ice jam	Y	No ice jam	Y
2006	No ice jam	Ice jam occurrence	N	No ice jam	Y
2007	No ice jam	No ice jam	Y	No ice jam	Y
2008	No ice jam	No ice jam	Y	No ice jam	Y
2009	Ice jam occurrence	Ice jam occurrence	Y	Ice jam occurrence	Y
2010	Ice jam occurrence	Ice jam occurrence	Y	No ice jam	N
2011	No ice jam	No ice jam	Y	Ice jam occurrence	N
2012	No ice jam	No ice jam	Y	No ice jam	Y
2013	Ice jam occurrence	Ice jam occurrence	Y	Ice jam occurrence	Y
2014	No ice jam	No ice jam	Y	Ice jam occurrence	N
2015	No ice jam	Ice jam occurrence	N	Ice jam occurrence	N

4. Breakup Date Forecasting

Breakup ice jams occurrence usually occur 1-2 days after the breakup. The beginning date of breakup ice jam can be estimated based on the forecasted breakup date, which provides valuable time for agencies to take preventive measures in advance to prevent and mitigate ice dam formation and potential ice flood disaster. The BP neural network model based on the Levenberg-Marquardt algorithm is used to forecast the breakup date. Data from the 49-year period from 1957 through 2003 were used as learning data, and then the model was used to forecast the breakup date from 2004 through 2015. The forecasting results are summarized in Table 2 below. The average forecast period of the model was 10 days and the maximum error was 2 days. Based on the *Hydrological Forecasting Standards* (GB/T 22482-2008) (see Table 3), this forecast results have high accuracy with the measured and meet the requirements of the national standards.

This forecasting model was used for ice jam forecasting of the Mohe reach in 2017. Based on long-term forecast of hydrometeorological information of the upper Heilongjiang River published by the China Meteorological Administration, the breakup ice jam condition forecast was released on April 1, 2017 ahead, that there would not be ice jams during breakup, and the breakup date was estimated to be April 28. In fact, the breakup date in the headstream Luogu villages in Mohe reach was April 28, and the breakup date was April 24 in Beiji town of Mohe reach which is 40km away from the upper Luogu Villages (Fig. 3). Moreover, no ice jam or ice jam flooding occurred in this Mohe reach. The actual breakup date on the Luogu Villages reach matched the forecasting result perfectly. In the Beiji town reach, the experiments for breaking ice cover with explosives were conducted on 9-12 April (Liu and Wang, 2017), which resulted in an earlier breakup than the Luogu villages reach and the breakup date was 4 days earlier than the forecasted date. This ice jam forecast in 2017 had a forecast period of over 24 days. According to the Hydrological Forecasting Standards in China (GB/T 22482-2008), the allowed error is 7 days for a forecast period of 15 days. Therefore, the forecasting error was significantly smaller than the allowed value and the forecasting results were in good agreement with the measured values.

Table 2. Results of river breakup date forecasting.

Year	Measured Date (Month-Date)	Forecasted Date (Month/Date)	Error (days)	Forecast period (days)	Pass (Y/N)
2004	04-28	04/27	-1	8	Y
2005	05-02	04/30	-2	12	Y
2006	05-01	05/01	0	11	Y
2007	04-26	04/26	0	6	Y
2008	05-02	05/02	0	12	Y
2009	04-14	04/15	1	/	Y
2010	05-02	05/02	0	12	Y
2011	04-25	04/25	0	5	Y
2012	04-30	05/01	1	10	Y
2013	05-01	04/30	-1	11	Y
2014	04-29	04/29	0	9	Y
2015	04-27	04/27	0	7	Y

Table 3. Allowed error based on *Hydrological Forecasting Standards* (GB/T 22482-2008).

Forecast period (days)	<2	3～5	6～10	11～13	14～15	>15
Allowed error	1	2	3	4	5	7

5. Conclusion

Cold regions suffers from severe ice flooding from ice jams in spring. Forecast of ice jam occurring are keys to ice flooding prevention and mitigation. The mechanism of breakup ice jam formation and development is very complex and not understood completely. Ice jams form and break quickly, which imposes difficulty for field observation and measurements as well as forecasting. The advantages of the neural network method include the following: (1) it has strong approximation capability for complex nonlinear mapping relations, the robustness and fault toleration; and (2) it has strong adaptive capability of handling obscure and incomplete data. Due to these reasons, the neural network method is considered to be an excellent tool for ice jam forecast, which is a complex nonlinear phenomenon and impacted by many different factors. This paper presents an ice jam neural network forecast model that is developed for natural rivers in the cold regions. Conclusions from this study include the following:

(1) Based on field investigations and theoretical analyses of historical ice jam data on the Heilongjiang River, it is found that the main causes of ice jam occurrence on the upper reach of the Heilongjiang River are mechanical and thermal effects as well as hydraulic and geometric characteristics of the river. With analyzing the ice jam occurrence as well as available hydrometeorological data, it is found that important factors that affect river breakup and ice jam forecast include the precipitation before freezeup, precipitation during freezeup, precipitation before breakup, air temperature during freezeup, air temperature change before breakup, water level change before breakup, and thickness of the ice.

(2) The neural networking clustering method can forecast of ice jam for the Mohe reach of the Heilongjiang River. The model grouped the parameters related to ice jam occurrence through the neural learning procedure of the network and completed ice jam forecasting. The forecast accuracy rates are 85% for the neural network model and 62% for statistical model, respectively. It was apparent that the neural network clustering method had advantages over the conventional statistical method.

(3) The neural network model can predict the beginning date of ice jam occurrence by forecasting breakup date. The maximum error in the forecasting results for the 12-year period from 2004 to 2015 is 2 day under the condition of the 10-days average forecasting period in the Mohe reach. The forecast results are in good agreement with the measured values and meet the national standards.

(4) The neural network model accurately forecasted the breakup date and ice jam condition of the Mohe reach in 2017, which provided reliable data for agencies to implement little measures on ice disaster prevention and mitigation, and, as a result, a significant amount of economical and human resources was saved.

Acknowledgements
The authors are thankful for the financial support from National Key Research & Development Plan of China (2017YFC0405103, 2017YFC0405704), IWHR Research & Development Support Program (HY0145B642017, SKL2017CGS04, HY0145B912017) and the National Natural Science Foundation of China (51679263). The authors also appreciate the support from the Heilongjiang Hydrologic Bureau and the National Meteorological Administration in providing hydrological and meteorological data.

References

(Alp, M., and Cigizoglu H. K. 2007). “Suspended sediment load simulation by two artificial neural network methods using hydrometeorological data.” Environ. Modell. Software, 22 (1), 2-13.

(ASCE.2000a). “Artificial neural networks in hydrology. I.” J. Hydrol. Eng., 5(2), 115–123.

ASCE. (2000b). “Artificial neural networks in hydrology. II.” J. Hydrol. Eng., 5(2), 124–132.

(Beltaos, S.1984). “A conceptual model of river ice breakup.” Can. J. Civ. Eng., 17(2), 173-183.

(Beltaos, S. 1990). “Fracture and breakup of river ice cover.” Can. J. Civ. Eng., 17 (2), 173–183.

(Beltaos, S. 1993). “Numerical computation of river ice jams.” Can. J. Civ. Eng., 20(1), 88-89.

(Beltaos, S. 2008). “Progress in the study and management of river ice jams.” Cold Reg. Sci. Technol., (51), 2-19.

(Beltaos, S. 1995). River ice jams. Water Resource Publication, LLC., USA.

(Chau, K. W. 2006). “Particle swarm optimization training algorithm for ANNs in stage prediction of Shing Mun River.” J. Hydrol., 329(3-4), 363-367.

(Chen, S. Y., and Ji, H. L. 2004). “Fuzzy optimization neural network BP approach for ice forecast.” J. Hydraul. Eng., 36(6), 114-118(in Chinese).

(Cigizoglu, H. K. 2005). “Application of the generalized regression neural networks to intermittent flow forecasting and estimation.” J. Hydrol. Eng., 10(4), 336-341.

(Dai, C. L., Yu, C. G., Liao, H. C., and Zhang, B. S. 2010). Survey and Forecast of River Ice. China Water & Power Press, Beijing, China (in Chinese).

(Dawson, C. W., Abrahart, R. J., Shamseldin, A. Y., and Wilby, R. L.2006). “Flood estimation at ungauged sites using artificial neural networks.” J. Hydrol., 319(1-4), 391-409.

(Fu, H, Guo, X. L., Yang, K. L., and Wang, T. 2017). “Ice accumulation and thickness distribution before inverted siphon.” J. Hydrodyn. (Ser. B), 29(1), 840-846.

(Fu, H., Yang, K. L., Guo, X. L., Guo, Y. X., and Wang, T. 2015). “Safe operation of inverted siphon during ice period.” J. Hydrodyn. (Ser. B), 27(2), 204-209.

(Kolerski, T., and Shen, H. T. 2015). “Possible Effects of the 1984 St. Clair River Ice Jam on Bed Changes.” Can. J. Civil Eng., (12), 696-703.

(Lal, A. M, and Shen, H. T. 1991). “Mathematical-model for river ice processes.” J. Hydrol. Eng., 117, 851-867.

(Liu, Z. P., Wang, T., Guo, X. L., and Fu, H. 2017). “Breaking ice with explosive in Heilongjiang River.” J. Hydraul. Eng., 48(3), 253-260(in Chinese).

(Mahabir, C. Hicks, F, and Fayek, A. R. 2006). “Neuro-fuzzy river ice breakup forecasting system”. Cold Reg. Sci. Technol., (46), 100-112.

(Mahabir, C., Hicks, F. E., and Fayek, A. R. 2007). “Transferability of a neuro-fuzzy river ice jam flood forecasting model.” Cold Reg. Sci. Technol., (48), 188–201.

(Maier, H. R., and Dandy, G. C. 2000). "Neural network for the prediction and forecasting of water resources variable: a review of modeling issues and applications." Environ. Modell. Software, 15, 101-124.

(Ministry of Water Resources of the People's Republic of China 2008). Hydrographic forecast standard GB/T. 22482-2008. China Water Power Press, Beijing, China (in Chinese).

(Riad, S., Mania, J., Bouchaou, L., and Najjar, Y. 2004). "Rainfall-runoff model using an artificial neural networks approach." Math. Comput. Model, 40(7-8), 839-846.

(Shen, H. T., Chen, Y. C., and Wake, A. 1993). "Lagrangian Discrete Parcel Simulation of Two Dimensional River Ice Dynamics." Int. J. Offshore Polar Eng., 3 (4), 328-332.

(Shen, H. T. 2010). "Mathematical Modeling of River Ice Processes." Cold Reg. Sci. Technol., 62(1), 3-13.

(Shen, H. T, Wang, D. S., and Lal, A. M. 1995). "Numerical Simulation of River Ice Processes." J. Cold Reg. Eng., 9(3), 107-118.

(Wang, T. 2014). Ice Condition Forecast, China Water & Power Press, Beijing, China (in Chinese).

(Wang, T., Yang, K. L., Guo, X. L., and Fu, H. 2012). "Appication of Adaptive-Network-Based Fuzzy Inference System to ice condition forecast." J. Hydraul. Eng., 43(1), 112-117(in Chinese).

(Wang, T., and Yang, K. L. 2009). "Ice forecast by artificial neural networks in the Middle Route of the South to North Water Diversion Project." J. Hydraul. Eng., 40(11), 1403-1408 (in Chinese).

(Wang, T., Yang, K. L., Guo, X. L., and Fu, H. 2013). "Freeze up water temperature forecast for the Yellow River using adaptive-networks-based fuzzy inference system." Proc., EWRI Word environment & water resources congress 2013, ASCE, Cincinnati, Ohio, USA, 2247-2260.

(Wang, T., Yang, K. L., and Guo, Y. X. 2008). "Application of Artificial Neural Networks to Forecasting Ice Conditions of the Yellow River in the Inner Mongolia Reach." J. Hydrol. Eng., 13(9), 811-816.

International Association for Hydro-Environment Engineering and Research

Supported by Spain Water and IWHR, China

24th IAHR International Symposium on Ice
Vladivostok, Russia, June 4 to 9, 2018

Two Applications of a Cross-Correlation Based Ice Drift Tracking Algorithm; Ship-Based Marine Radar Images and Camera Images from a Fixed Structure

Ilija Samardžija
Sustainable Arctic Marine and Coastal Technology (SAMCoT)
Norwegian University of Science and Technology
Høgskoleringen 7A, 7491 Trondheim, Norway
ilija.samardzija@ntnu.no

Cross-correlation function can be used to estimate the sea ice drift velocity from a pair of sequential images of an ice surface. The approach is established in scientific literature and mostly used for calculating the velocity field of ice drift from satellite imagery. Traditionally, disadvantages of the approach are large computational requirements and inability to account for the rotational motion of the ice field. When used on a smaller spatial and temporal scale to estimate the global ice drift, inability to capture the rotational motion is not crucial since the assumption of translational motion of the ice field does not impair the estimate of the global ice drift. This paper presents an ice drift tracking algorithm that is based on cross-correlation between subsequent marine radar frames that captures ice features surrounding a ship. Computational requirements are not an issue in this use and few days of ice drift is calculated in matters of minutes. The algorithm can produce a real-time ice drift measurements that are valuable information in ice management operations. One potential usage of the results is shown where using the estimated ice drift velocity, the drift of the channels produced in ice management operations is estimated. The same cross-correlation approach can be implemented on camera images. An example of ice drift estimate using the camera images from Norströmsgrund lighthouse is given.

1. Introduction

Sea ice motion is driven by the wind and, to a lesser degree, the ocean currents. Some of the first ice drift observations are made by Nansen (1902), where it is reported that motion of the vessel *Fram*, drifting with the ice across Arctic Basin, was about 2% of the surface wind speed. Since the pioneering findings by Nansen, much research has been done in the field of ice motion, spanning scales (spatial and temporal) from local (usually important for ice engineering problems) to mesoscale (geophysical problems). There is considerable amount of literature on ice drift phenomena. For a of detailed review of this topic, interested reader is referred to Leppäranta (2011).

The algorithm described in this paper was developed independently by the author for purpose of ice drift velocity tracking from marine radar images. However, usage of the same method (based on two-dimensional cross-correlation of two images) can be found in literature. Early development of the approach can be traced back to Leese et al. (1971), where cross-correlation is used in conjunction with satellite imagery for tracking cloud motion. Ninnis et al. (1986) uses the method for estimating the ice drift from radiometer images of the Beaufort Sea. Fily and Rothrock (1987) improve the efficiency of the method by estimating the ice motion subsequently from low to high-resolution images. Furthermore, known to the author of this paper, first studies of ice drift with use of cross-correlation method in conjunction with land based radar images are reported by Tabata (1975).

Ice drift velocity is crucial information during ice management operations (Eik, 2008). As noted in Moran et al. (2004), real time drift direction information is especially important for successful ice management operation. Haugen et al. (2011) give a comprehensive overview of ice intelligence for ice management operations. Methods for estimating the ice drift include satellite imagery, drift buoys, visual observation and subsurface systems. Deploying ice drifters (GPS trackers or radar mirroring devices) on ice is time-consuming and potentially hazardous operation. Another obvious drawback is that the ice drifters need to be redeployed multiple times during the operation. Satellite imagery gives an excellent spatial coverage, but time between acquisitions does not allow real time ice drift measurement. Subsurface systems, such as ADCP, usually do not give real time information.

This paper describes a cross-correlation based ice tracking algorithm implemented on subsequent marine radar images and camera images. Apart from the above mentioned pioneering work by Tabata (1975), marine radar usage for ice drift estimation can be found in works by Sun et al. (2004) and Karvonen et al. (2010). Other than cross-correlation based methods, object tracking methods are also available, where automated algorithms find distinct features and follow them to obtain ice drift velocity (Karvonen, 2013, 2016).

In this paper, only the global average ice drift velocity in vicinity of vessel (radius of 3 nm for radar images) is estimated. This is the key information in ice management and some potential application in connection with ice management is discussed later. For camera images obtained at Norströmsgrund lighthouse the ice drift velocity is estimated in the vicinity of the lighthouse. This measurement gives a new information that can be valuable in studies about ice-structure interaction.

2. Methods

2.1 Georeferencing of marine radar images

The goal is to make an estimate of ice drift velocity relative to the Earth. In order to do so, the two images that are being compared need to be georeferenced. This has been done for the marine radar images, as the ship is moving and if the images were not georeferenced the obtained ice drift velocity would be relative to the ship.

Georeferencing is done for each pair of images that are later used for tracking the average ice drift in time step defined by two moments when the radar images were obtained. It is done by plotting first and second image on a map with a rectangle with fixated georeferenced boundaries. The boundaries of the rectangle are calculated from the boundaries of the two images that are being compared. Each radar image has latitudinal and longitudinal boundaries. These are:

$$\begin{aligned} \lambda &= \lambda_S \ \lambda_N \\ \phi &= \phi_W \ \phi_E \end{aligned} \quad . \qquad \textbf{[1]}$$

where λ_{lim} are the latitudinal boundaries with south boundary λ_S and north boundary λ_N , while ϕ_{lim} are the longitudinal boundaries with west boundary ϕ_W and east boundary ϕ_E . Georeferenced boundaries of fixed square can be calculated as follows:

$$\begin{aligned} \lambda_R &= \frac{\lambda_{\mathrm{lim},0} + \lambda_{\mathrm{lim},1}}{2} \\ \phi_R &= \frac{\phi_{\mathrm{lim},0} + \phi_{\mathrm{lim},1}}{2} \end{aligned} \quad , \qquad \textbf{[2]}$$

where indices “0” and “1” indicate the first and the second radar image. The procedure is schematically shown on the Fig. 1.

When ship moves non-significantly, the calculation of the drift is easily done since the two radar scans cover almost the same area. In case that the ship moves fast, it might leave the area of the first scan by the time the second scan is obtained and then there is no common area covered that can be compared. However, this problem can be compensated by taking a smaller time step between two scans. The author experienced that in case that the ship has arrived to the boundary of first image the calculation can still be done, as there is enough overlapping area. For example, if the ship is moving relatively fast through the ice (e.g. 10 kts) and the radar range is three nautical miles, the time between scans (time for ship to come to the edge of the first radar scan) will be 1100 s. This is enough time to capture even small ice movement. Further details about this analysis is not given here, but it is important to understand that there is a balance between ship speed, ice drift speed, radar range and time step that can be adjusted for best results.

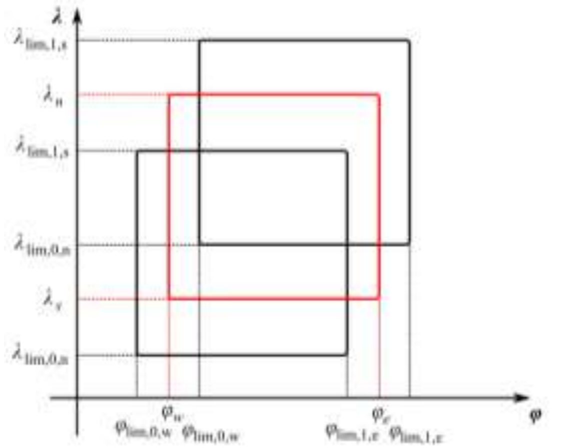

Fig. 1. Schematic illustration for calculating the georeferenced boundaries of fixed rectangle**.**

2.2 Projective transformation of camera images

When implementing the algorithm on camera images, georeferencing is not necessary if the camera is mounted on a bottom fixed platform. However, in order to get an orthonormal top view of the ice surface from a camera image, projective transformation needs to be done. Planar projective transformation is defined as the following linear transformation (Hartley & Zisserman, 2003):

$$\begin{pmatrix} \mathbf{x}_1' \\ \mathbf{x}_2' \\ \mathbf{x}_3' \end{pmatrix} = \begin{bmatrix} h_{11} & h_{12} & h_{13} \\ h_{12} & h_{22} & h_{23} \\ h_{13} & h_{23} & h_{33} \end{bmatrix} \begin{pmatrix} \mathbf{x}_1 \\ \mathbf{x}_2 \\ \mathbf{x}_3 \end{pmatrix}, \qquad \textbf{[3]}$$

or in more concise form:

$$\mathbf{x}' = \mathbf{H}\mathbf{x}\ , \qquad \textbf{[4]}$$

where $\mathbf{x}'$ are the coordinates of three points in the 2D world plane on surface of ice, $\mathbf{x}$ are the coordinates on the image plane and $\mathbf{H}$ is the projective transformation matrix.

The projective transformation matrix, $\mathbf{H}$, can be obtained by placing a rectangular object of known dimensions on the ice surface (usually a plate with a checkerboard pattern). Later in this paper, ice drift tracking algorithm was used to estimate the drift velocity using the camera images that was mounted on the offshore lighthouse Norströmsgrund. When the measurement campaign was planned, this usage of camera images was not anticipated and rectangular object required for calibration was not placed on the ice surface. There are other methods to calculate the projective transformation matrix that use known angles, two equal unknown angles or known length ratios (Liebowitz & Zisserman, 1998). These inputs were approximately estimated from the videos and projective transformation was performed. An example of transformation is shown in Fig. 2. This approximate projective transformation causes error with an overall factor for the drift velocity and a factor between orthogonal components of the velocity (x and y directions). These two factors are unknown. For one event, where ice is drifting predominantly in one direction, the relative velocity can be very well captured.

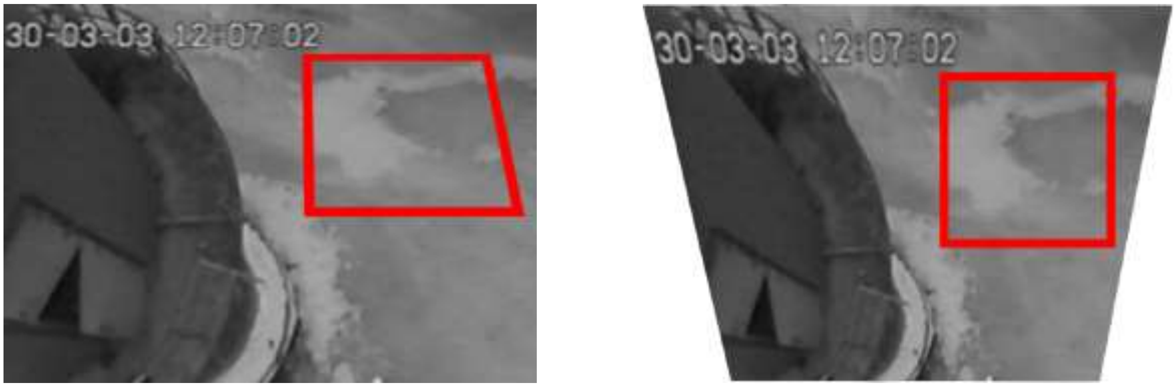

Fig. 2. Example of projective transformation of camera images. Left: the original image with perspective distortion of the ice surface. Right: the transformed image that gives orthonormal top view of the ice surface. Red rectangle is drawn for better visualization of the projective distortion.

2.3 Ice drift tracking algorithm

Once the images are pre-processed, the implementation of the cross-correlation ice drift tracking algorithm can be done. Before starting the description in mathematical terms, I give the explanation in simple words: subsection of one of the images is taken and moved around on top of the other image until the best possible overlap is found. Once we know where we have to move the image to get this overlap, we can estimate the drift velocity.

To compare a pair of frames, bivariate (Pearson) correlation coefficient is used. Note that that more advanced methods, such as using fast Fourier Transform (FFT) and phase correlations, are available. However, with computing power available today, a robust approach using bivariate correlation coefficient is sufficiently effective for our purpose.

Bivariate correlation coefficient is a measure of linear relationship of two variables. In concise form, it reads:

$$\rho\left(I(t), I(t+\Delta t)\right) = \frac{\mathrm{cov}\left(I(t), I(t+\Delta t)\right)}{\sigma_{I(t)}\sigma_{I(t+\Delta t)}} . \qquad \textbf{[5]}$$

When comparing two grayscale images, input matrices give information about the light intensity of pixels. $I(t)$ is the matrix of the first image (or subsection of image in our case), $I(t+\Delta t)$ is the matrix of the second image that was taken after time step Δt. $\mu_{I(t)}$ and $\mu_{I(t+\Delta t)}$ are the mean light intensities of the images. $I(t)_{ij}$ and $I(t+\Delta t)_{ij}$ represent the accompanying pixels of the two images. *cov* is the covariance. $\sigma_{I(t)}$ and $\sigma_{I(t+\Delta t)}$ are standard deviations of the two compared images. When identical images are compared, bivariate correlation coefficient will be equal to one. Coefficients closer to zero will indicate that images are more different.

Fig. 3 on the left side shows an overlay sketch of two compared images. The more transparent object represents an ice field that has moved in northwest direction. We can take a subsection (marked with rectangle on the Fig. 3) from two radar images to compare them using bivariate coefficient. If the location of subsections is the same for both frames, the two images that are being compared would be as shown on the right side of the Fig. 3. It is easy to imagine that correlation coefficient will be close to zero. However, if we move subsection area of the second image as shown on the Fig. 4, the correlation coefficient will be closer to one.

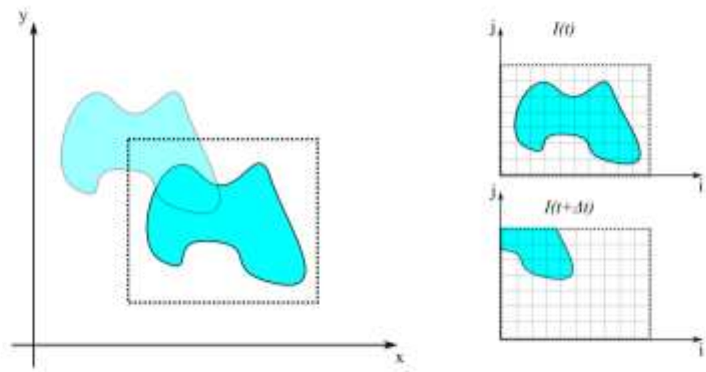

Fig. 3. Left: sketch of an overlay of two radar images for which ice feature has drifted in the northwest direction (transparent object). Left: extracted subsections of the two images where the location of subsections identical. Correlation of the two extracted images will be low for this case.

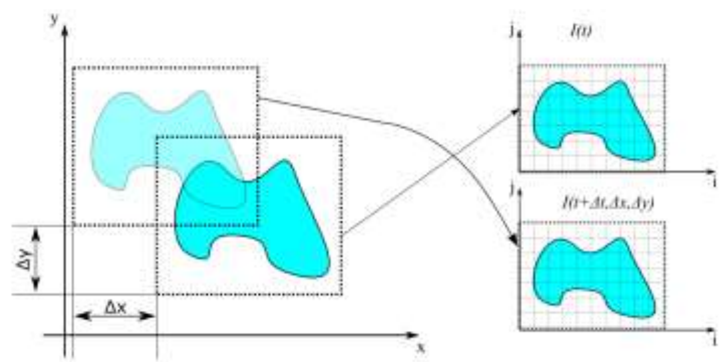

Fig. 4. Left: sketch of an overlay of two radar images for which ice feature has drifted in the northwest direction (transparent object). Left: extracted subsections of the two images where the location of subsection is moved for the second image. Correlation of the two extracted images will be high for this case.

We can move the subsection of the second image around the subsection of the first image in bounds defined horizontally $-\Delta X, +\Delta X$ and vertically $-\Delta Y, +\Delta Y$. By repeating the calculation, we will get a matrix of correlation coefficients $\rho\ I\ t\ , I\ t+\Delta t, \Delta x, \Delta y$. Example of one such matrix is shown on the Fig. 5. The location of maximum correlation coefficient is proportional to the vector of ice field displacement. Let the location of maximum correlation coefficient be $\Delta x_{\max}$ and $\Delta y_{\max}$, velocity vector can be given as:

$$v = v\left(\frac{a}{\Delta t}\Delta x_{\max}, \frac{a}{\Delta t}\Delta y_{\max}\right), \qquad \textbf{[6]}$$

where a is the ratio that translates displacement from pixels to meters.

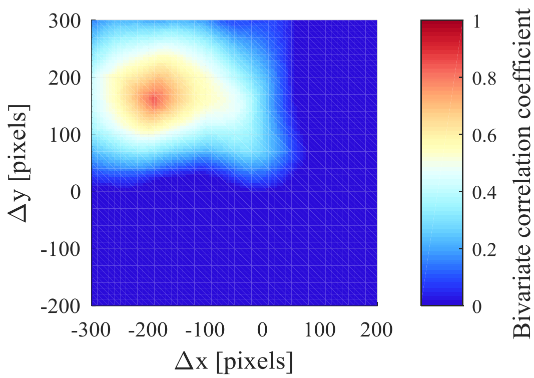

Fig. 5. Correlation coefficient $\rho\left(I(t), I(t+\Delta t, \Delta x, \Delta y)\right)$ for the example shown on the Fig. **3**, where the feature has moved in the northwest direction.

3. Results

3.1 Marine radar

In March 2017, Statoil conducted Station Keeping Trials (SKT) in the Gulf of Bothnia (Liferov et al., 2018). The main goal of the campaign was to collect data relevant for station-keeping and ice management operations. Various instruments were utilized to collect the data, but relevant to this paper are the marine radar, ice drifter GPS buoys and Acoustic Doppler Current Profiler (ADCP). Radar images that are used in this paper were recorded from the Magne Viking ship that was anchored and almost stationary (some movement did occur as the ship interacted with ice). Another ship, Tor Viking, was performing physical ice management by breaking the ice in front of the anchored ship to reduce the ice pressure. GPS buoys and ADCP measurements of ice drift were used to validate the obtained results. GPS buoys were deployed on solid ice floes. They were equipped with a GPS instrument that recorded the position of the buoy. This way, the instrumentation gave us the measurement for the ice drift of a single ice floe. Please note that this may occasionally differ from the global ice drift. ADCP instruments were deployed under the ice surface. They were anchored together with an Ice Profiling Sonar (IPS) on a single anchor line. The IPS instrument was recording the draft of the ice for a single location. ADCP was measuring the water current profile and the drift of the ice for a single location. More details about the ADCP and IPS and their measurements during the SKT can be found in Teigen et al. (2018).

Fig. 6 shows comparison of the drift speed measurements from ADCP and drift buoys to the estimates obtained with the algorithm. Time, Δt, between two images for each estimate was 26.5 minutes. On few occasions, there were interruptions in radar scanning, caused by the personnel on board. One of more pronounced interruptions can be seen on March 7th, approximately from 15:00 until 18:00. For this period, drift estimates were not made. Also, note that the drift buoy signal had some interruptions in measurements. For example, this can be noticed on the Fig. 6 where the drift buoy signal has sharp discontinuities, such as around 18:00 on March 7th. ADCP instrument gave more reliable and continuous measurement. The Lagrangian nature of ADCP measurement makes it more compatible for comparison of the algorithm results. The algorithm produces Eulerian velocity for one time step, as it tracks the same field. If a ship is drifting along with the ice, the ice drift signal produced with the algorithm will be Eulerian as well. However, if the ship is stationary (as in the case analyzed here), the signal of the drift estimate will be Lagrangian, since the drift was measured for a fixed location.

Visual examination of the algorithm result on the Fig. 6 shows that the algorithm is capable of estimating the global ice drift speed with a good accuracy. Some discrepancies did occur, but most of them can be explained by the fact that drift buoy was placed on a single ice floe that can have somewhat different local velocity from the global ice field velocity. This is especially noticeable before midnight on March 10.

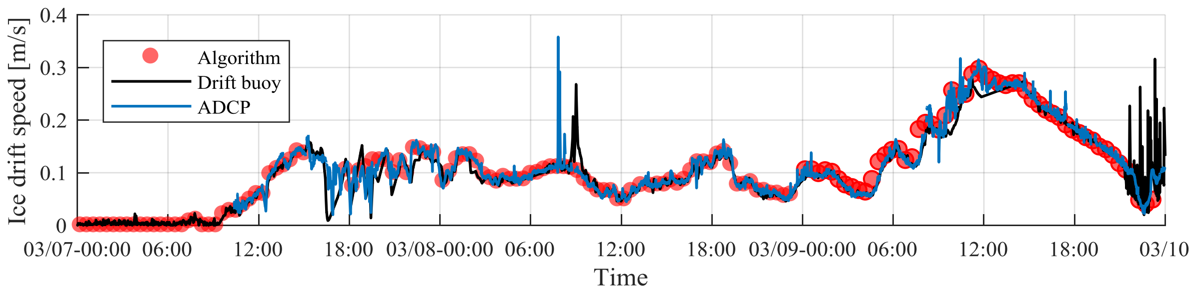

Fig. 6. Comparison of the algorithm's ice drift speed estimates to the measurements.

Using the estimated ice drift velocity, we can make an estimate of the open water channels drift. This is done by placing points on the track of the ship and applying the estimated ice drift velocity on these points. An example of such calculation is given in Fig. 7, where the drift of channels is estimated for the three days of drift that was estimated above. Since the algorithm can give a real time measurement of the ice drift, it is also possible to make an estimate of the channel drift in real time.

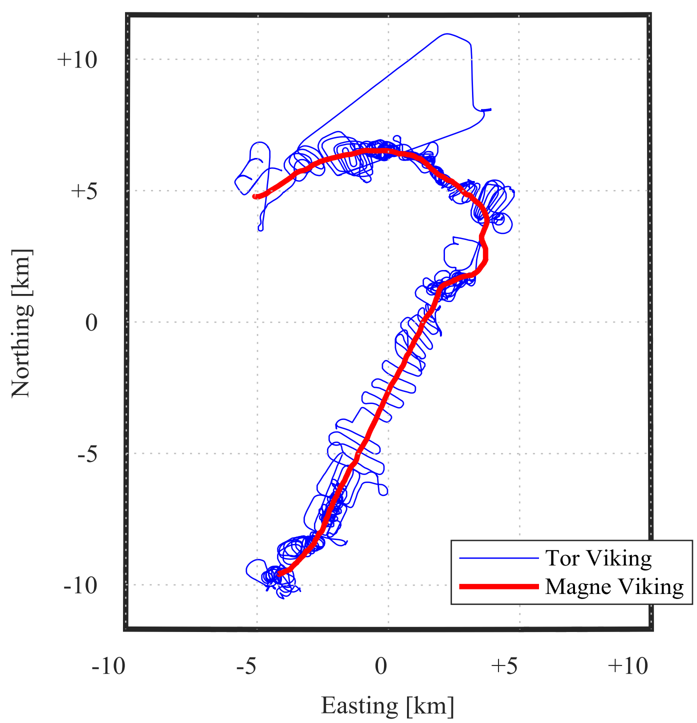

Fig. 7. Drift estimation of the channels left behind the anchored ship (Magne Viking) and the ice managing ship (Tor Viking).

3.2 Camera

During the LOLEIF/STRICE project, full-scale measurements were taken at the Norströmsgrund lighthouse in order to enhance understanding of the ice-structure interaction phenomena (Schwarz & Jochmann, 2001). During this campaign, only measurements of the ice drift are the manual estimates by the personnel monitoring the measurements at the actual lighthouse. Time between these estimates was usually several hours. More details about the manual drift estimation technique is given in Jochmann and Schwarz (2000). The lighthouse was equipped with several cameras that were recording the ice surface in the near vicinity of the structure. Example of one frame form the camera videos is shown already in the section about the projective transformation of camera images (Fig. 2). These frames can be used with the drift tracking algorithm to estimate a continuous signal of ice drift velocity near the structure.

Fig. 8 presents an example of estimated ice drift speed for one event that has occurred on March 17th, 2003. In this example, ice drift was estimated every 7 seconds, but the time between two frames was set to 21 seconds. In the same figure, plot of the total horizontal load is given (measured with load panels instrumented on the lighthouse).

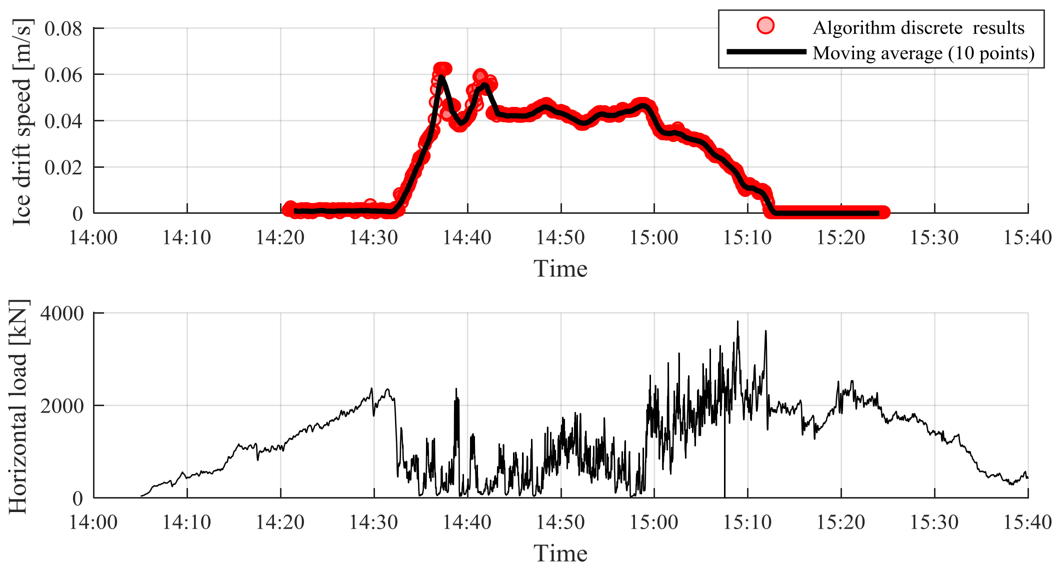

Fig. 8. Top: Ice drift speed estimated using algorithm on camera images. For parts where estimate is not given the ice was stationary. Note that the two distinct peaks happened when pieces of the ice floe broke off and drifted with higher speed. Bottom: Horizontal ice load measured by load panels on the lighthouse.

4. Summary and conclusion

This paper has presented a robust and simple algorithm for obtaining global ice drift measurements from surface images of sea ice. Examples for two different applications of the algorithm are shown. First application was using the images from ship based marine radar. Estimates were made for three days. Spatial scale was in order of several nautical miles (range of the radar was three nautical miles). Second application was with camera images recorded from a fixed offshore structure. Estimates were made for one hour during which the ice field has started drifting for some time and eventually stopped. Spatial scale, in this example, was in order of several meters around the lighthouse.

Efficiency of the algorithm was not discussed. However, in my experience, a poorly optimized MATLAB script of the algorithm performs the calculations quickly. Three days of ice drift would be calculated in several minutes when estimates were done using the radar images.

As mentioned in the introduction section, the essence of the method is not novel and more advanced methods are available in literature. Some of them are used on satellite imagery, where images are divided in many pieces and velocity vector field is calculated by estimating the drift in each of the subsections. For this use it is sensible to use more efficient method. However, for estimating only the global drift, the robust method described here is sufficient.

The method could be used in future full-scale measurement campaigns. Using a simple camera on an offshore structure can reveal new insights about the ice drift near the structure. This is an inexpensive method, but gives a valuable information. Marine radar could be mounted on an offshore structure as well. This would be more expensive, but additional information about the ice drift in the far field can be gained.

Example of application with radar images was given for an anchored ship that was located in the same area for three days. Application on radar images obtained from a moving ship is not given in this paper. The author has made some attempts to do this using the radar images from the ice managing ship that was often in motion. When ice management was done in limited area, implementation was fairly simple and accurate, as long as the georeferencing of the radar images was done correctly. As mentioned in the section about georeferencing of the radar images, when ship moves out of the area in short time it is more challenging to get two radar images that overlap the same georeferenced area. In this case, reduction of the time step between the two images that are compared would help to get a scan of same area. However, since the ice drift has smaller magnitude for a smaller time step, the relative error would increase. Given the ship speed and the ice drift speed, radar range and time step that can be adjusted for best results.

Acknowledgements

Support to the SKT project was provided by Statoil ASA and Statoil Greenland AS. I am grateful for their support. I wish to acknowledge the support of the Research Council of Norway through the Centre of Research-based Innovation, SAMCoT, and the support of the SAMCoT partners. I would like to thank the coordinators of the LOLEIF and STRICE teams, Dr. Joachim Schwarz and Dr. Walter L. Kühnlein for collecting the full-scale data for Norströmsgrund lighthouse. I would also like to thank the crew of Tor Viking for making my time at the icebreaker unforgettable. Finally, I would like to thank my supervisor Knut V. Høyland for appreciating the importance of this work and encouraging me along the way.

References

Eik, K. (2008). Review of experiences within ice and iceberg management. *The Journal of Navigation*, *61*(4), 557-572.

Fily, M., and Rothrock, D. A. (1987). Sea ice tracking by nested correlations. *IEEE Transactions on Geoscience and Remote Sensing, GE-25*(5), 570-580.

Haugen, J., Imsland, L., Loset, S., and Skjetne, R. (2011). Ice observer system for ice management operations. Proc. 21st International Offshore and Polar Engineering Conference, ISOPE, Maui, HI, United states.

Jochmann, P., and Schwarz, J. (2000). Ice force measurements at lighthouse Norströmsgrund-Winter 2000. LOLEIF Report.

Karvonen, J. (2013). Tracking the motion of recognizable sea-ice objects from coastal radar image sequences. *Annals of Glaciology, 54*(62), 41-49.

Karvonen, J. (2016). Virtual radar ice buoys-a method for measuring fine-scale sea ice drift. *Cryosphere*, *10*(1), 29-42.

Karvonen, J., Heiler, I., and Haapala, J. (2010). Ice drift information retrieval from radar time series. Proc. 20th IAHR Symposium on Ice, Lahti, Finland.

Leese, J. A., Novak, C. S., and Clark, B. B. (1971). An Automated Technique for Obtaining Cloud Motion from Geosynchronous Satellite Data Using Cross Correlation. *Journal of Applied Meteorology, 10*(1), 118-132.

Leppäranta, M. (2011). *The drift of sea ice*: Springer Science & Business Media.

Liebowitz, D., and Zisserman, A. (1998). Metric rectification for perspective images of planes. Proc. Proceedings 1998 IEEE Computer Society Conference on Computer Vision and Pattern Recognition, Los Alamitos, CA, USA.

Liferov, P., McKeever, T., Scibilia, F., Teigen, S. H., Kjøl, A., Almkvist, E. and Lindvall, J. K. (2018). Station-keeping trials in ice: Project overview. Proc 37th International Conference on Ocean, Offshore and Arctic Engineering, OMAE, Madrid, Spain.

Moran, K., Backman, J., and Farrell, J. W. (2004). Deepwater drilling in the Arctic Ocean's permanent sea ice. *Proceedings of the Integrated Ocean Drilling Program, 302*, 13.

Nansen, F. (1902). *The oceanography of the north polar basin*: Longmans, Green, and Company.

Ninnis, R., Emery, W., and Collins, M. (1986). Automated extraction of pack ice motion from advanced very high resolution radiometer imagery. *Journal of Geophysical Research: Oceans*, *91*(C9), 10725-10734.

Schwarz, J., and Jochmann, P. (2001). Ice force measurements within the LOLEIF-project. Proc. Proc. 16rd International Conference on Port and Ocean Engineering under Arctic Conditions, POAC, Ottawa, Ontario, Canada.

Sun, H.-q., Shen, Y.-m., and Qiu, D.-h. (2004). Measuring sea ice drift via cross-correlation of radar ice images. *Journal of Hydrodynamics, 16*(6), 716-720.

Tabata, T. (1975). Sea-ice reconnaissance by radar. *Journal of Glaciology, 15*(73), 215-224.

Teigen, S. H., Lindvall, J.K., Samardzija, I., and Hansen, R. I. (2018). Station-keeping trials in ice: Ice and Metocean Conditions. Proc 37th International Conference on Ocean, Offshore and Arctic Engineering, OMAE, Madrid, Spain.

Probabilistic Assessment of Ice Environment and Ridge Loads for the Norströmsgrund Lighthouse

Ilija Samardžija[1], Knut V. Høyland[1], Bernt J. Leira[2], Arvid Næss[3]
[1] Sustainable Arctic Marine and Coastal Technology (SAMCoT)
Norwegian University of Science and Technology, Høgskoleringen 7A, 7491 Trondheim, Norway
ilija.samardzija@ntnu.no
[2] Department of Marine Technology Norwegian University of Science and Technology
Otto Nielsens veg 10, Marine Technology Centre, 7491 Trondheim, Norway
[3] Centre for Ships and Ocean Structures (CeSOS) Norwegian University of Science and Technology
Otto Nielsens veg 10, Marine Technology Centre, 7491 Trondheim, Norway

Structural reliability analysis requires statistical distribution of the loads. One such case is ice load calculation for offshore structures. Ice-structure interaction is a highly stochastic phenomenon due to the natural variability of sea ice (aleatory uncertainties) and lack of knowledge about the processes that are taking place and long-term data needed for ice load calculation (epistemic uncertainties). Ice ridges are typically the ice features that govern the quasi-static ice load calculations in areas without icebergs. This is the case for Gulf of Bothnia, where Norströmsgrund lighthouse is located. This paper investigates how to utilize a Monte Carlo simulation for probabilistic assessment of ice environment and ice loads on the Norströmsgrund lighthouse. Information found in literature about sea ice growth, ridge formation and ice drift in Gulf of Bothnia (and in general) are used to simulate the ice environment parameters (e.g., ice ridge frequency of occurrence, ridge keel depth, consolidated layer thickness). Simple and generally accepted load models are used to avoid involving additional uncertainties that arise with more advanced models. The final result of the simulation is the probability distribution of the ridge horizontal load acting on Norströmsgrund lighthouse, from which loads with specific return period can be extracted (e.g., 100-year load).

1. Introduction

Modelling an uncertain phenomenon can be fully described only by using a probabilistic approach, where one needs to capture both aleatory uncertainties of the natural variability and epistemic uncertainties inherited by the lack of knowledge. Using a deterministic approach often results in excessively conservative design and overlook of important information. In order to analyze the reliability of an offshore structure it is necessary to assess the probability distributions of the extreme loads. For a structure located in ice-infested waters, sea ice will most likely govern the extreme horizontal loads. In areas where icebergs are not present, ice ridges are expected to govern the loads. Sea ice has a large natural variability spanning small and large spatial and temporal scales. Uncertainties in describing the ice-structure interaction are immense. Phenomena of ice-structure interaction has been researched extensively in the past couple of decades. However, there are gaps in knowledge that are still puzzling scientists and engineers. Examples of these difficulties are given by Jordaan (2015), where the author points out some of the issues concerning the mechanical behavior of ice, full-scale data analysis and crude idealizations of ice features in load models. This paper examines how a Monte Carlo simulation (MCS) can be utilized to simulate individual ice ridge loading events on the Norströmsgrund lighthouse. By simulating many seasons, a set of annual maximum loads is created from which statistical conclusions can be made.

The need for probabilistic treatment of ice loads acknowledged by the ISO 19906 Arctic offshore structures standard. A summary about the design methodology given in the ISO 19906 can be found in Thomas et al. (2011). The standard uses the limit states design approach and specifies that characteristic ice loads with associated annual exceedance probability shall be determined and used in load combinations. The action (load) factors in the load combination are calibrated in order to meet the required reliability targets. Background of the calibration for the ice loads factors, that itself is done using a probabilistic approach, can be found in the report made by C-CORE (2010) and summarized in Fuglem et al. (2011); Maes and Thomas (2011).

The accuracy of parameters and types of input probability distributions greatly depends on the quality and quantity of available data. In this work, we use readily available sources to establish statistical distributions for the needed input parameters. The accuracy of the adopted statistical distribution types and parameters is secondary in this paper and the methods are the primary focus. Some of the assumptions are too simplistic and several important correlations are neglected. This is done deliberately to make a simplistic probabilistic model that will lay a foundation for a more advanced model that will be developed in our future studies. This way, it will be possible to evaluate the implications of including more subtle details of the ice-structure interaction phenomena.

In the following few paragraphs, we try to give a short literature review in a chronological order and regarding the field of probabilistic ice loads assessment. To the authors knowledge, the first attempt to make a probabilistic ice-structure interaction analysis was done by Bercha et al. (1978). Another pioneering attempt was done by Wheeler (1981), where a MCS is used to estimate the ice load statistical distribution for a conical offshore structure. From the same period, it is worth mentioning the work by Jordaan (1983), where the author emphasizes the importance of probabilistic methodologies for decision-making in risk and safety assessment for arctic offshore projects. A comprehensive ice-structure MCS with a sensitivity analysis is given in Vivatrat and Slomski (1983, 1984). Dunwoody (1991) performs an MCS of ice loads, but makes a questionable claim that the probability distributions of the ice feature characteristics must be from the log-normal family (in our experience, a lognormal type of distribution can have a good fit around the mean value, but the heavy tail of the distribution usually causes overestimation of the loads). Nessim and Jordaan (1991); Nevel (1991) are two landmark papers that show the state-of-the art (at the time) of the probabilistic ice load assessment. These two landmark papers conclude the initial development in the field. In the view of the authors of this paper, the initial period is followed by two distinct periods.

The first period is marked by somewhat reduced interest in the field and mostly scattered publications without noticeable structured progress. The period ends with introduction of the ISO 19906 draft version in the year 2007. Kato (1992) proposes a MCS based system for evaluating the ice loads for various ice features and offshore structure types. He later gives more specified examples of how this system can be used (two publications mentioned below). Comfort et al. (1998) use a MCS to analyze the influence of the limit-stress and limit-force loading scenarios. Kato (1998) performs a MCS of ice loads on a caisson structure for offshore Sakhalin. A comprehensive MCS of the ice loads for the Confederation Bridge is described by Brown et al. (2001), where they elaborately discuss the implications of choice of the parent distribution to the extreme loads. Specifically, it is described how usage of a lognormal distribution can lead to overestimates of the extreme loads. Spencer and Masterson (2002) perform a MCS for a multi-legged offshore platform interacting with first-year ice ridges. Timco and Frederking (2004) utilize a MCS to make a probabilistic analysis of the seasonal ice loads that can have operational applications, unlike the most of the publications where extreme loads were analyzed. Kato (2006) performs a MCS of first-year ridge loads with some sensitivity analysis and concludes that the consolidated layer thickness and the encounter rate of ridges are the most dominating input parameters for the resulting probability distribution of ice loads. Finally, it is worth noting the publication of Bercha et al. (2006), where the reliability of offshore structures in Arctic is addressed in general.

After the provision of the ISO 19906, one can track more structured development in the field, where particular authors (or groups) develop their approach through several publications. All of the publications address the issues and possibilities of implementing the probabilistic framework in connection to the ISO 19906. First in the series of publications is work done by Cammaert et al. (2008), where several important aspects of ice loads probabilistic assessments are discussed (e.g., the importance of including the correlations between the relevant parameters, seasonal variation of the parameters, influence of climate change on ice loads and model uncertainty). Onishchenko (2009) presents an analytical approach to the problem, unlike the most of the publications mentioned here, where MCS simulation technique is the primary method of choice. Eik and Gudmestad (2010) shows an example of how a probabilistic analysis can contribute to assessment of the iceberg design loads and the efficiency of the various components of iceberg management. Fuglem et al. (2015) give another publication addressing the iceberg design loads, where also the companion wave loads are considered. Jordaan et al. (2011) show an interesting possibility of simulating the ice environment development during a winter seasons in the Caspian Sea. Wang et al. (2011) make a comparison of the First-Order Reliability Method (FORM) and the MCS in scope of probabilistic ice loads analysis. Walter et al. (2013) describes how an ice environmental model can be developed using the contour methodology. Bekker et al. (2012) analyze ice data from Gulf of Bothnia and describes a method of developing a probabilistic ice environment model. Interesting result in this study are the nomograms showing the inner-seasonal development of the ice parameters probability distributions. More work on the topic of probabilistic ice loads assessment by the same leading author can be found in Bekker et al. (2013a); Bekker et al. (2013b); Bekker et al. (2009). Thijssen and Fuglem (2015) give a probabilistic treatment of the ice loads for seasonal operations. Several publications are addressing the issues concerning with multi-year sea ice, Fuglem et al. (2014b); Thijssen et al. (2016); Thijssen et al. (2015). Most recent publication by Charlebois et al. (2018) uses a probabilistic model for ice forces on a caisson structure in Beaufort Sea. Finally, we list the remaining publications that are discussing issues of risk and structural reliability for offshore arctic structures in general and in connection to the ISO 19906: Fuglem et al. (2014a); Fuglem et al. (2011); McKenna et al. (2014); Moslet et al. (2011); Thijssen et al. (2014); Thomas (2014, 2015); Thomas et al. (2011).

Probabilistic ice loads assessment using a MCS can be performed in various ways, mostly depending on the ice-structure interaction considered, as well as the quality and quantity of available data. Even for a same problem of interest and identical data available, one can take different paths in order to evaluate the probability distribution of the ice loads. The work presented here does not represent any significant advancement in the field, but shows an example of a probabilistic assessment of ice environment and ridge loads. The methodology presented here will serve as a base case study for further development of a probabilistic ice loads model that we intend to develop in our future research.

2. Methods

2.1 First-year ridge load calculation formulae

Formulation given in ISO 19906 (section *A.8.2.4.5.1 First-year ridges*) is used to estimate the horizontal ridge load for the individual events. Upper bound estimate for FY ridges horizontal global load, F_R, can be done by separately taking into account contribution from consolidated layer and keel rubble load component (Eq. [1]). We assume that there is enough forcing in the surrounding ice so that the ridge is always failing against the structure (limit stress). This is a conservative assumption, as some of the strongest ridges might not fail against the structure. For further details on limiting mechanisms, see Croasdale (2009); Timco et al. (2017). Total ice ridge load can be estimated as follows:

$$F_R = F_C + F_K , \qquad \textbf{[1]}$$

where F_C is the load component due to the ridge consolidated layer and F_K is the load component due to the keel rubble of the ridge.

Ice load from consolidated component can be estimated using the formulation for the ice crushing global load calculation, same to that of level ice. Other than the ice crushing failure mode, there are other failure modes for the consolidated layer and ice ridge in general, such as splitting, shearing (plug failure) and spine failure (Timco et al., 2000). However, these are considered to result in less severe loads compared to the crushing failure mode (Bjerkås & Bonnemaire, 2004). The level ice (or consolidated layer) load in case of crushing failure can be estimated as:

$$F_C = F_G = p_G\, w\, h, \qquad [2]$$

where p_G is the average ice pressure over the nominal contact area; w is the width of the of the contact area (structure width – 7.2 m in our case); h is the level ice thickness.

Equation for estimating the upper bound global average ice pressure given in ISO 19906 is based on the work by Kärnä and Qu (2006). The expression reads:

$$p_G = C_R \left(\frac{h}{h_1}\right)^n \left(\frac{w}{h}\right)^m \qquad \begin{array}{l} m = -0.16 \\ n = -0.5 + h/5 \quad h < 1\text{m} \;; n = -0.3 \quad h \geq 1\text{m} \end{array}, \qquad [3]$$

where p_G is the global average ice pressure, in megapascals; h is the level ice thickness, in meters; h_1 is a reference thickness of 1 m; m and n is are empirical coefficients; C_R is the ice strength coefficient, in megapascals.

The adopted model for the load component of keel rubble is based on the approach used in soil mechanics for estimating the passive failure of granular material. The formulae are based on work of Dolgopolov et al. (1975), with modifications by Kärnä and Nykänen (2004):

$$F_K = \mu\, h_k\, w \left(\frac{h_k\, \mu_\phi\, \gamma_e}{2} + 2c\right)\left(1 + \frac{h_k}{6w}\right), \qquad [4]$$

$$\mu_\phi = \tan\left(45° + \frac{\phi}{2}\right), \qquad [5]$$

where h_k is the rubble thickness measured from bottom of consolidated layer; μ_ϕ is the passive pressure coefficient; ϕ is the angle of internal friction; c is the apparent keel cohesion (average value over the keel volume); γ_e is the effective buoyancy. The effective buoyancy is calculated as follows:

$$\gamma_e = (1 - e)(\rho_w - \rho_i)\, g, \qquad [6]$$

where e is the keel macroporosity; ρ_w is the water density (1005 kg/m^3 – deterministic value in our simulation); ρ_i is the ice density (910 kg/m^3 – deterministic value in our simulation).

2.2 Monte Carlo simulation

Monte Carlo simulation is performed for 1,000,000 seasons, with number of ridge-structure interaction events set to 1200 for each season. The number of events (interaction rate) is a key component in probabilistic analysis. The number is estimated by taking into account average season duration, percentage of time when ice is failing in crushing mode and mean ice drift speed when ice is crushing as given in Kärnä and Qu (2006), as well as the ice ridge occurrence frequency as given in Lewis et al. (1993). This rough estimate is too simplistic and uncoupled from the statistical distributions of ice parameters. This issue is discussed further in the discussion section of this paper.

To reflect the seasonal variability of winter severity we use data about the maximum level ice thickness. The idea is that the ice thickness will be proportional in some way to the maximum level ice thickness throughout a season. The maximum annual level ice thickness is modeled using a normal distribution with a mean of 0.72 m and a standard deviation of 0.12 m. The parameters of the distribution are based on data from Kemi measurement station and we assume that this is a good representative for Northern Bay of Bothnia (Ronkainen, 2013). Note that this location is further north from our location and in landfast ice zone. Therefore, this statistics might somewhat overestimate the ice thickness.

Simulation of one season starts by generating a maximum level ice thickness for that season from the distribution described above. Assuming that a ridge interaction event can occur at any point in time during the season with equal probability, we generate interaction times for all of the N number of events. Interaction times, t_n, are given in normalized values of season length. Knowing the interaction time, we can estimate the level ice for the given event. This is done using a normalized ice growth curve that was developed based on the average ice growth trend obtained from Saloranta (2000), where average ice growth of seasons 1979-90 for a location in Gulf of Bothnia is given. It is assumed that ice grows in similar manner in our location as well. Similar type of ice growth curve was also used in probabilistic ice loads assessment by Timco and Frederking (2004) for a structure in Beaufort Sea. The normalized ice growth equation adopted here is approximate and used as an example to point out the importance of inner-seasonal ice thickness variation in probabilistic simulation. The equation can be expressed as:

$$\begin{aligned} h_n(t_n) &= \sqrt{\frac{t_n}{0.8}} \qquad \text{for} \quad 0 \le t_n \le 0.8, \\ h_n(t_n) &= 5 - 5t_n \qquad \text{for} \quad 0.8 < t_n \le 1, \end{aligned} \qquad \textbf{[7]}$$

where h_n is the normalized ice thickness and t_n is the normalized time of ridge interaction in the given winter season. Graphical illustration of the Eq. [7] is shown in Fig. 1. The approach assumes that the ice is growing to its maximum thickness in the first 80% of the season proportional to square root of time. In addition to the field measurements and numerical simulations (Saloranta, 2000), this assumption is supported by analytical ice growth models (Leppäranta, 1993; Stefan, 1891). In summary, for a given season's maximum ice thickness, normalized time of ridge interaction and assuming the above described ice growth nature, level ice thickness for an event will have the following value:

$$h_{LI,i} = h_{y,AM} \times h_n(t_n), \qquad \textbf{[8]}$$

where $h_{y,AM}$ is the simulated maximum level ice thickness (annual maximum – AM).

We have established a method for generating the surrounding level ice thickness for events, but we need the consolidated layer thickness. ISO 19906 recommends that in absence of data, the consolidated layer thickness can be assumed to be twice as the surrounding ice. Immediately after a ridging event, the surrounding level ice will have a certain thickness, while the consolidated layer is about to develop from the loose rubble. The consolidated layer will grow with a faster rate than the nearby level ice because only the voids in the rubble need to be frozen. Based on the field measurements reported in literature, it can be deducted that the ratio between consolidated layer and level ice will not get greater than two (FY ridges). We assume that age of a ridge (time since it was created) when the ridge is hitting the structure completely random. Thereby, the ratio between the consolidated layer and the level ice will be random too. It is assumed that this ratio for a given ridge interaction event has a uniform distribution with bounds [1, 2]. In summary, after simulating level ice thickness, we multiply it with a randomly simulated ratio to get the consolidated layer thickness. Fig. 2 illustrates the input level ice annual maximum (AM) level ice thickness and the results of the ice thicknesses simulation (level ice thickness for a given event (GAE), consolidated layer thickness for a given event and annual maximum consolidated layer thickness).

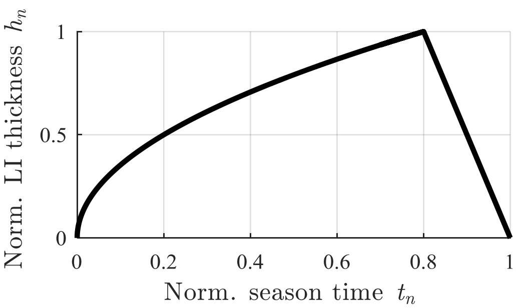

Fig. 1. Eq. [7] – Normalized ice growth function.

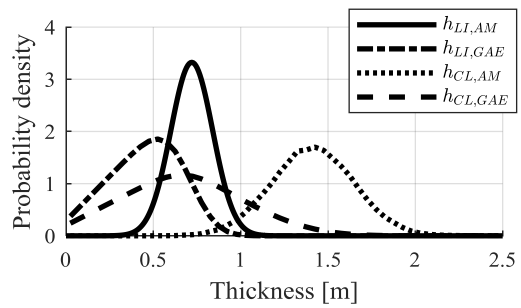

Fig. 2. Ice thicknesses probability distributions.

Next step is to simulate the strength coefficient C_R. ISO 19906 instructs that PDF should be estimated for this parameter when probabilistic approach is used. Unfortunately, no guidance is given on how to establish this probability distribution. Only the characteristic values with a certain return period are given. In our probabilistic simulation, we need distributions with probabilities for a given event (parent distributions). ISO 19906 recommends characteristic value of the strength coefficient with 100-year return period for Baltic Sea (1.8 MPa). Figure 10 in paper by Kärnä and Masterson (2011) summarizes the results from an extreme value analysis of both local and global ice pressures that was previously performed by Kärnä and Qu (2005); Kärnä et al. (2006). The figure shows how ice strength coefficient varies with the return period. Line from the figure that corresponds to the global pressure is recreated in the Fig. 3 (dashed line). Using these results, we can read the ratio between the characteristic values with 100-year and 1-year return periods. From this, we calculate that the characteristic value associated with 1-year is 1.2 MPa. We assume that the parent distribution of strength coefficient can be described with a two-parameter Weibull distribution. By knowing the average number of events per season n, we know that the probability (in the parent distribution) of the 1-year event is equal to $1/n$ and for the 100-year event it is equal to $1/100 \times n$. This gives us enough information to calibrate the shape parameter α (1.234) and the scale parameter β (0.245) of the assumed

Weibull distribution. Full line in Fig. 3 shows how this artificially created distribution gives us variation of the strength coefficient with the return period. When comparing this to the original variation as given in Kärnä and Masterson (2011), one can see that characteristic values for 1-year and 100-year return period are equal (these were our calibration points), and for the rest it is reasonably accurate. Fig. 4 illustrates the given an event (GAE) distribution of the adopted Weibull distribution for the strength coefficient with the above stated parameters and the resulting annual maximum (AM) distribution given the number of events per season.

It is important to note that the above-mentioned recommendations for the strength coefficient are valid for level ice, but we use it for consolidated layer. Due to the higher homogeneity of level ice thickness in comparison to the consolidated layer and possibly the same relation in local strength properties, one would expect that level ice would give higher global loads than the consolidated layer of a same average thickness. In our simulations, we neglect this effect. For further details on this topic, reader is referred to the discussions on the subject given in Høyland (2007); Høyland et al. (2000); Shafrova and Høyland (2008).

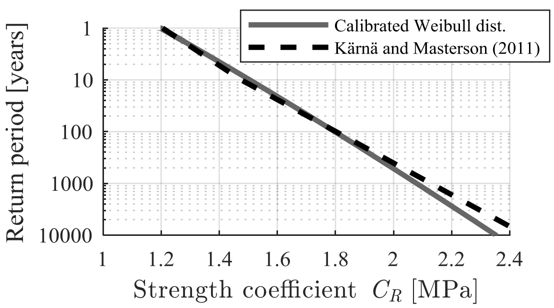

Fig. 3. Characteristic values for associated return periods of strength parameter.

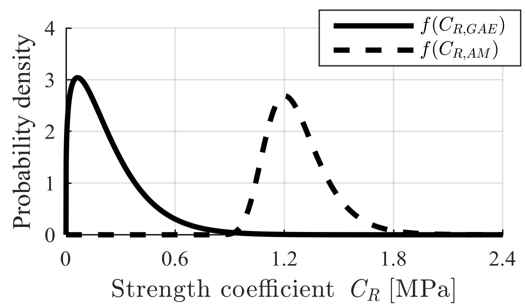

Fig. 4. Given an event (GAE) and annual maximum (AM) PDF of the strength coefficient C_R .

Having established the simulation methodology for both ice thickness and strength coefficient (for a given event in a given season), we can now simulate the consolidated layer component of the total ridge load. To complete the total ridge load simulation, we need to simulate the rubble component. No correlation between the parameters of the consolidated layer and parameters of the rubble is assumed. Implications of this assumption is discussed later in the text. The following parameters are used for describing the probability distributions of the parameters needed for the rubble load component. Uniform distributions (with bounds given in brackets) are used for keel macroporosity [20 % – 40 %], apparent cohesion [5 kPa – 7 kPa] and angle of friction [$20^\circ - 40^\circ$]. The bounds are adopted from the recommendations given in the ISO 19906. The most important parameter, the keel depth, is modelled using an exponential distribution. The exponential type of distribution for this parameter was used because previous studies show considerable evidence that ridge keel depths obey this type of distribution (Wadhams & Davy, 1986). The only parameter of the distribution, the mean, was calculated using the mean sail height measured by helicopter-borne laser profiling (Lewis et al., 1993) and multiplied by the ratio of maximum keel depth to maximum sail height (Strub-Klein & Sudom, 2012). This calculation gives us a mean keel depth of 4.2 m. We use this approach in absence of upward looking sonar data for the Baltic Sea, which would be the best source of data for this parameter. The used exponential distribution is shifted by 2 m and with a mean of 2.2 m. Note that it is assumed that any ridge deeper than the water depth cannot approach the structure.

3. Results and discussion

Fig. 5 summarizes the results of the MCS performed in this paper. It shows the probability distribution of total horizontal ridge load, as well as the probability distributions two load components (consolidated layer and rubble). The characteristic loads with 100-year and 10000-year return periods are 11.7 MN and 16.1 MN, respectively. It is interesting to note that the design line load for the Norströmsgrund lighthouse was 2.2 MN/m (Bjerkås & Nord, 2016). This means that the design ice load was 15.84 MN.

The rubble load component does not increase significantly with higher return periods because of the depth limitations. Although the consolidated layer gives higher loads for a same return period when the two components are analyzed independently, the rubble component still contributes significantly to the total load. For 54% of the maximum annual load events, the rubble component was higher than the consolidated layer component. Further clues about the importance of rubble can be seen on Fig. 6 with a bivariate distribution of consolidated layer thickness and keel depth for the events of annual maximum loads. It can be seen that there are two concentrations of these events. One is located towards the limiting water depth and modal consolidated layer thickness (0.68 m). Second is located towards the minimum value of keel depth as previously defined in the keel distribution (2 m) and close to the modal maximum annual consolidated layer thickness (1.41 m).

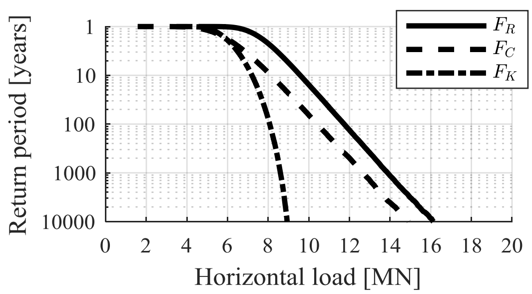

Fig. 5. Probability of exceedance for ridge loads and its components given in terms of return periods.

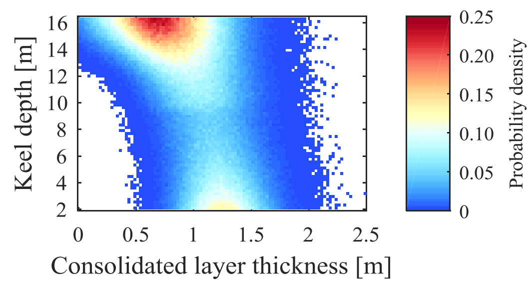

Fig. 6. Bivariate probability distribution for the annual extreme loads.

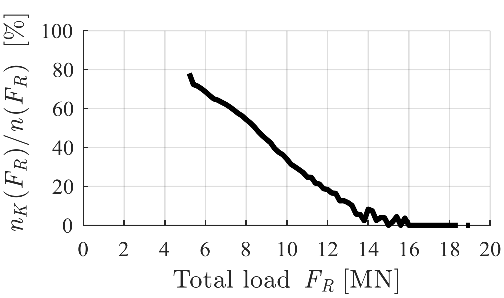

Fig. 7. Percentage of annual extreme events where rubble gives a higher load than the consolidated layer.

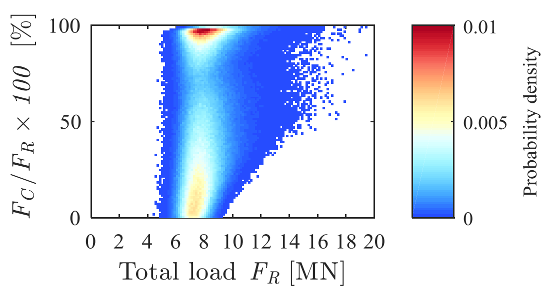

Fig. 8. Consolidated layer load component contribution to the total load.

To give a complete description, we need to show the relative importance of the two load components. First, we subsample all of the annual extreme events in intervals of 0.2 MN of the total load F_R. In each of these intervals there will be a certain number of extreme events $n \; F_R$. For each interval, we count the extreme load events where the rubble load was the dominating component $n_K \; F_R$ (contributing to the total load with more than 50%). By dividing

$n_K\left(F_R\right)/n\left(F_R\right)$ we get the percentage of the extreme events that were dominated by rubble load for each interval (Fig. 7). It can be seen that more events are dominated by consolidated layer component as the total load increases. This is caused by the assumption that the consolidated layer probability distribution varies from year to year, while the keel depth has the same probability distribution for all years. This means that for those years where the consolidated layer thickness is small, the keel rubble is governing the loads. This still does not mean that the rubble is not important for the higher extreme loads. We can see this on Fig. 8 that illustrates the probability distribution of the annual maximum load events with respect both to the total load F_R and the consolidated layer contribution to the total load $F_C/F_R \times 100$. Although for the higher total loads the consolidated layer component contribution is usually higher than 50%, the rubble component is often contributing with a significant percentage.

4. Conclusion and outlook

The approach described is aimed at development of probabilistic assessment of ice environment and ice ridge loads. Case study was performed using a Monte Carlo simulation for the Norströmsgrund lighthouse. This structure was chosen for the case study because a great deal of knowledge about the full scale ice-structure interaction originates from the measurements done on this structure. Still, it was not a trivial task to setup the simulation. Difficulties arise when probability distributions of relevant parameters need to be established. For example, the strength coefficient is an empirical parameter. Therefore, only full-scale measurements can serve as a basis for establishing the probability distribution of the parameter. A method to back-calculate the parent distribution of this coefficient is proposed in this paper. In addition, a way to simulate the consolidated layer thickness for the individual events is described.

We emphasize the importance of establishing the probability distribution in accordance to what is simulated. Adopting a probability distribution from data of annual extremes when simulating individual events is one example where a crude error can be made. More subtle errors are made when distributions are based on data that comes from field measurements at the end of the season, while the simulation is performed throughout a season. This error is present in this paper, where we take measurements of ridge sails that represent the state at one point in time and we use the same distribution for all the seasons and throughout a season. Having same ridge keel depth statistics for all season will not cause a big error. However, assumption that the ridges are statistically equally deep throughout a season will cause overestimated keel depths early in the season because it can be expected that level ice thickness and keel depths are positively correlated (i.e., deep keels are produced towards the end of the season when level ice is sufficiently thick) (Amundrud et al., 2004; Hopkins, 1998).

Another error is hidden in the assumption of uniform distribution of interaction times in the season. To a smaller extent, this is not true due to the fact that ice mobility can change during the season. To a larger extend, a more subtle effect influences the distribution of the number of events in different parts of a season. Ridge statistics is commonly obtained from Upward Looking Sonar instruments and Rayleigh criterion is used to identify the individual ridges. Thresholds used in Rayleigh criterion will influence the number of ridges (Ekeberg et al., 2015). Early in the season the number of ridges identified by the method will be much smaller due to the fact that most of the ridges are below the threshold. Appropriate way to account for this would be to use a keel depth probability distribution that develops throughout a season and number of events that must be coupled to the used probability distribution of keel depths (and thereby also developing throughout a season). One way to do this is to quantify the correlation of level ice and ridge keel depth statistics and then simulate ridges accordingly to the surrounding level ice. We hope that this will be possible in our future research. Furthermore, we will explore the possibilities of simulating the consolidation of rubble more accurately by taking the physics of the phenomena into account. Among other details of ice-structure interaction that were not included in our simulation and not discussed here, we highlight the importance of including the limiting scenarios in the simulation (limit-stress and limit force).

The presented case study clearly has some limitations. The first is the limited data on which the probability distributions of the input parameters were established. The second is negligence of important correlations, such as level ice and keel depth correlation. The third is rather simplified treatment of interaction rate. The final, forth, is the negligence of some of the important aspects of ice-structure interaction, such as limiting scenarios. Furthermore, sensitivity analysis was not performed and this is the main reason why the results need to be interpreted with caution. It is easy to expect that characteristic loads would change with adjusted input parameters, but more importantly, the qualitative conclusions about the relative contributions of the two load components could completely alter with adjusted relative weights between inputs related to the consolidated layer and to the keel rubble. Despite the limitations of our method, the approach shows some important aspects of probabilistic assessment of ice loads and ice environment and provides a framework for further improvements. We have shown how relative importance of consolidated layer and rubble in ridge loads calculations can be analyzed. This is one example of how probabilistic analysis can be beneficial in enhancing our understanding of ice-structure interaction and possibly give us guidance about what should be the focus of future studies in ice engineering and/or future full-scale measurements.

Let us end this paper by concluding that a better treatment of strength coefficient, C_R, need to be made. This parameter contains a great deal of aleatory uncertainty owing to the natural variability of ice environment. This part of the uncertainty is not fully quantified yet. In addition, there is epistemic uncertainty built into this parameter as well, as we still cannot fully understand the ice-structure interaction phenomena. Increasing the reliability of offshore structures in arctic areas can be done most effectively with a better characterization of ice-structure interaction. In example of ridge loads, this would be reflected in better description of the strength coefficient uncertainty by quantifying the aleatory and reducing the epistemic part of the uncertainty that are combined in this coefficient. It is our recommendation that this can be best done by comprehensive long-term full-scale measurements of ice-structure interaction.

Acknowledgements

The authors wish to acknowledge the support of the Research Council of Norway through the Centre of Research-based Innovation, SAMCoT, and the support of the SAMCoT partners. This work has been carried out within the NTNU Oceans Pilot project "Risk, reliability and ice data in arctic marine environment".

References

Amundrud, T. L., Melling, H., and Ingram, R. G. (2004). Geometrical constraints on the evolution of ridged sea ice. *Journal of Geophysical Research, 109*(C6), 12 pp.

Bekker, A. T., Sabodash, O. A., and Kovalenko, R. G. (2013a). Modeling and analysis of probabilistic distributions of ice loads on lighthouse structures in the Gulf of Bothnia. Proc. 23rd International Offshore and Polar Engineering Conference. International Society of Offshore and Polar Engineers, Anchorage, Alaska, USA.

Bekker, A. T., Sabodash, O. A., and Kovalenko, R. G. (2013b). Probabilistic modeling of extreme value distributions of ice loads on "Molikpaq" platform for Sakhalin-II project. Proc. 32nd International Conference on Ocean, Offshore and Arctic Engineering, OMAE Nantes, France.

Bekker, A. T., Sabodash, O. A., Kovalenko, R. G., and Rusakov, D. S. (2012). Probabilistic modeling of ice environment from lighthouses zone in the Gulf of Bothnia. Proc. 22nd International Offshore and Polar Engineering Conference, ISOPE, Rhodes, Greece.

Bekker, A. T., Sabodash, O. A., Seliverstov, V. I., Koff, G. L., and Pipko, E. N. (2009). Estimation of Limit Ice Loads On Engineering Offshore Structures In the Sea of Okhotsk. Proc. 9th International Offshore and Polar Engineering Conference, Osaka, Japan.

Bercha, F. G., Danys, J. V., and Rokne, J. G. (1978). Probabilistic ice-structure interaction theory. *5th IAHR Symposium on Ice, v*(1), 77-95.

Bercha, F. G., Gudmestad, O. T., Nevel, D., Foschi, R., Sliggers, F., and Nikitina, N. (2006). Reliability of arctic offshore installations. Proc. 7th International Conference and Exhibition on Performance of Ships and Structures in Ice, ICETECH, Banff, AB, Canada.

Bjerkås, M., and Bonnemaire, B. (2004). Ice ridge-structure interaction Part II: Loads from firstyear ice ridges and their surrounding ice sheets. Proc. 17th IAHR Symposium on Ice, St. Petersburg, Russia.

Bjerkås, M., and Nord, T. S. (2016). Ice action on Swedish lighthouses revisited. Proc. 23rd IAHR Symposium on Ice, Ann Arbor, Michigan, USA.

Brown, T. G., Jordaan, I. J., and Croasdale, K. R. (2001). A probabilistic approach to analysis of ice loads for the Confederation Bridge. *Canadian Journal of Civil Engineering, 28*(4), 562-573.

C-CORE. (2010). Calibration of action factors for ISO 19906 Arctic offshore structures.

Cammaert, A. B., Trumars, J., and Eide, L. I. (2008). A probabilistic approach to design ice loads for an Arctic jack-up drilling platform. Proc. 27th International Conference on Offshore Mechanics and Arctic Engineering, OMAE, Berlin, Germany.

Charlebois, L., Frederking, R., Timco, G. W., Watson, D., and Richard, M. (2018). Evaluation of pack ice pressure approaches and engineering implications for offshore structure design. *Cold Regions Science and Technology, 149*, 71-82.

Comfort, G., Singh, S., and Dinovitzer, A. (1998). Limit-force ice loads and their significance to offshore structures in the Beaufort Sea. *International Journal of Offshore and Polar Engineering, 8*(1), 16-21.

Croasdale, K. R. (2009). Limit force ice loads - An update. Proc. 20th International Conference on Port and Ocean Engineering under Arctic Conditions, POAC, Lulea, Sweden.

Dolgopolov, Y. V., Afanasiev, V. P., Koren'kov, V. A., and Panfilov, D. F. (1975). Effect of hummocked ice on the piers of marine hydraulic structures. Proc. 3rd IAHR Symposium on Ice Problems, Hanover, W Ger.

Dunwoody, A. B. (1991). Reliability against drifting ice. An adjunct to Monte Carlo simulation. *Journal of Offshore Mechanics and Arctic Engineering, 113*(3), 253-259.

Eik, K., and Gudmestad, O. T. (2010). Iceberg management and impact on design of offshore structures. *Cold Regions Science and Technology, 63*(1-2), 15-28.

Ekeberg, O.-C., Høyland, K., and Hansen, E. (2015). Ice ridge keel geometry and shape derived from one year of upward looking sonar data in the Fram Strait. *Cold Regions Science and Technology, 109*, 78-86.

Fuglem, M., Richard, M., and King, T. (2014a). An implementation of ISO 19906 formulae for global sea ice loads within a probabilistic framework. Proc. Arctic Technology Conference, Houston, TX, United states.

Fuglem, M., Richard, M., and Thijssen, J. (2014b). Challenges Implementing ISO 19906 for Probabilistic Assessment of Multi-year Sea Ice Loads on Sloping Structures. Proc. 11th International Conference and Exhibition on Ships and Structures in Ice, Alberta, Canada.

Fuglem, M., Stuckey, P., and Jordaan, I. (2011). Probabilistic ice loads assessments for arctic regions: Inputs for calibration of ISO 19906. Proc. Arctic Technology Conference, Houston, TX, United states.

Fuglem, M., Stuckey, P., and Suwan, S. (2015). Estimating iceberg-wave companion loads using probabilistic methods. Proc. 34th International Conference on Ocean, Offshore and Arctic Engineering, OMAE, St. John's, NL, Canada.

Hopkins, M. A. (1998). Four stages of pressure ridging. *Journal of Geophysical Research, 103*(C10), 21883-21891.

Høyland, K. V. (2007). Morphology and small-scale strength of ridges in the North-western Barents Sea. *Cold Regions Science and Technology, 48*(3), 169-187.

Høyland, K. V., Kjestveit, G., Heinonen, J., and Määttänen, M. (2000). LOLEIF ridge experiments at Marjaniemi; The size and strength of the consolidated layer. Proc. 15th IAHR Symposium on Ice, Gdansk, Poland.

ISO 19906. (2010). Arctic offshore structures. *Petroleum and natural gas industries*.

Jordaan, I. (1983). Risk and Safety Assessment for Arctic Offshore Projects. Proc. 2nd Massachusetts Institute of Technology Sea Grant College Program Lecture and Seminar.

Jordaan, I. (2015). Some issues in ice mechanics. Proc. 34th International Conference on Ocean, Offshore and Arctic Engineering, OMAE, St. John's, NL, Canada.

Jordaan, I., Stuckey, P., Bruce, J., Croasdale, K., and Verlaan, P. (2011). Probabilistic modelling of the ice environment in the northeast Caspian sea and associated structural loads. Proc. 21st International Conference on Port and Ocean Engineering under Arctic Conditions, POAC, Montreal, QC, Canada.

Kärnä, T., and Masterson, D. M. (2011). Data for crushing formula. Proc. 21st International Conference on Port and Ocean Engineering under Arctic Conditions, POAC, Montreal, QC, Canada.

Kärnä, T., and Nykänen, E. (2004). An approach for ridge load determination in probabilistic design. Proc. 17th IAHR Symposium on Ice, Saint Petersburg, Russia.

Kärnä, T., and Qu, Y. (2005). Analysis of the Size Effect in Ice Crushing – edition 2. In: VTT Technical Research Centre of Finland, Internal Rep. No. RTE-IR-6/2005, Version.

Kärnä, T., and Qu, Y. (2006). Extended Baltic model of global ice forces. Proc. 18th IAHR Symposium on Ice, Sapporo, Japan.

Kärnä, T., Qu, Y., and Yue, Q. (2006). An extreme value analysis of local ice pressures. Proc. 7th International Conference and Exhibition on Performance of Ships and Structures in Ice, ICETECH Banff, AB, Canada.

Kato, K. (1992). Design ice force estimating system. Proc. 2nd International Offshore and Polar Engineering Conference, San Francisco, CA, USA.

Kato, K. (1998). Trial calculation of design ice loads on an arctic structure for offshore Sakhalin. Proc. 8th International Offshore and Polar Engineering Conference, Montreal, Canada.

Kato, K. (2006). Morphology of a first-year ridge and its influences on design ice load in the Sea of Okhotsk. Proc. 18th IAHR Symposium on Ice, Sapporo, Japan.

Leppäranta, M. (1993). A review of analytical models of sea‐ice growth. *Atmosphere-Ocean, 31*(1), 123-138.

Lewis, J. E., Lepparanta, M., and Granberg, H. B. (1993). Statistical properties of sea ice surface topography in the Baltic Sea. *Tellus, Series A (Dynamic Meteorology and Oceanography), 45A*(2), 127-142.

Maes, M. A., and Thomas, G. A. N. (2011). Risk-based calibration of action factors in the new ISO 19906 Arctic Offshore Structures Standard. Proc. Arctic Technology Conference, Houston, TX, United states.

McKenna, R., Fuglem, M., and Croocker, G. (2014). Uncertainty in 100 and 10,000 Year Ice Loads on Offshore Structures. Proc. 11th International Conference and Exhibition on Ships and Structures in Ice, Alberta, Canada.

Moslet, P. O., Gudmestad, O. T., Sildnes, T., and Saebo, E. (2011). The new ISO19906 standard and related arctic activities at DNV. Proc. 21st International Conference on Port and Ocean Engineering under Arctic Conditions, POAC, Montreal, QC, Canada.

Nessim, M., and Jordaan, I. (1991). The Selection of Design Ice Loads and Design Ice Features for Fixed Structures in the Beaufort Sea. In *Ice-Structure Interaction* (pp. 483-506): Springer.

Nevel, D. E. (1991). Probabilistic Ice Forces on Offshore Structures. In *Ice-Structure Interaction* (pp. 541-557): Springer.

Onishchenko, D. A. (2009). Analytical approach to the calculation of the design values of the loads associated with discrete ice features. Proc. 20th International Conference on Port and Ocean Engineering under Arctic Conditions, POAC, Lulea, Sweden.

Ronkainen, I. (2013). *Long-term changes in Baltic Sea ice conditions.* (Master thesis). University of Helsinki, Helsinki, Finland.

Saloranta, T. M. (2000). Modeling the evolution of snow, snow ice and ice in the Baltic Sea. *Tellus, 52A*, 93-108.

Shafrova, S., and Høyland, K. V. (2008). Morphology and 2D spatial strength distribution in two Arctic first-year sea ice ridges. *Cold Regions Science and Technology, 51*(1), 38-55.

Spencer, P., and Masterson, D. (2002). A Monte-Carlo simulator for calculating ice loads on multi-legged offshore structures. Proc. 16th IAHR Symposium on Ice, Dunedin, New Zealand.

Stefan, J. (1891). Über die Theorie der Eisbildung, insbesondere über die Eisbildung im Polarmeere. *Annalen der Physik, 278*(2), 269-286.

Strub-Klein, L., and Sudom, D. (2012). A comprehensive analysis of the morphology of first-year sea ice ridges. *Cold Regions Science and Technology, 82*, 94-109.

Thijssen, J., and Fuglem, M. (2015). Methodology to evaluate sea ice loads for seasonal operations. Proc. 34th International Conference on Ocean, Offshore and Arctic Engineering, OMAE, St. John's, NL, Canada.

Thijssen, J., Fuglem, M., and Croasdale, K. (2016). Probabilistic Assessment of Multi-Year Sea Ice Loads on Upward Sloping Arctic Structures. Proc. Arctic Technology Conference, St. John's, Newfoundland and Labrador, Canada.

Thijssen, J., Fuglem, M., Muggeridge, K., Morrison, T., and Spencer, P. (2015). Update on Probabilistic Assessment of Multi-year Sea Ice Loads on Vertical-faced Structures. Proc. Arctic Technology Conference, Copenhagen, Denmark.

Thijssen, J., Fuglem, M., Richard, M., and King, T. (2014). Implementation of ISO 19906 for probabilistic assessment of global sea ice loads on offshore structures encountering first-year sea ice. Proc. OCEANS 2014, Piscataway, NJ, USA.

Thomas, G. A. N. (2014). Design method for ISO 19906 Arctic offshore structures. Proc. Arctic Technology Conference, Houston, TX, United states.

Thomas, G. A. N. (2015). Risk and reliability in the design of arctic offshore structures. Proc. 23rd International Conference on Port and Ocean Engineering under Arctic Conditions, POAC, Trondheim, Norway.

Thomas, G. A. N., Bercha, F. G., and Jordaan, I. (2011). Reliability, limit states and action factors for ISO 19906. Proc. Arctic Technology Conference, Houston, TX, United states.

Timco, G. W., Croasdale, K., and Wright, B. (2000). An overview of first-year sea ice ridges. NRC Report HYD-TR-047. Ottawa, Ont., Canada.

Timco, G. W., and Frederking, R. (2004). Probabilistic analysis of seasonal ice loads on the Molikpaq. Proc. 17th IAHR Symposium on Ice, Saint Petersburg, Russia.

Timco, G. W., Sudom, D., Frederking, R., Barker, A., and Wright, B. D. (2017). A critical review of Arctic pack ice driving forces: New sources of data. *Cold Regions Science and Technology, 138*, 1-17.

Vivatrat, V., and Slomski, S. (1983). A Probabilistic Basis for Selecting Design Ice Pressures and Ice Loads for Arctic Offshore Structures. Proc. 15th Offshore Technology Conference, Houston, TX, USA.

Vivatrat, V., and Slomski, S. (1984). Probabilistic selection of ice loads and pressures. *Journal of waterway, port, coastal, and ocean engineering, 110*(4), 375-391.

Wadhams, P., and Davy, T. (1986). On the spacing and draft distributions for pressure ridge keels. *Journal of Geophysical Research, 91*(C9), 10-697.

Walter, E. L., Stole-Hentschel, S., and Moslet, P. O. (2013). Estimating characteristic load effects on floating structures in ice. Proc. 32nd International Conference on Ocean, Offshore and Arctic Engineering, OMAE, Nantes, France.

Wang, B., Basu, R., Jha, A., and Winterstein, S. (2011). Reliability analysis of ice loads on arctic offshore structures. Proc. 21st International Conference on Port and Ocean Engineering under Arctic Conditions, POAC, Montreal, QC, Canada.

Wheeler, J. D. (1981). Probabilistic force calculations for structures in ice-covered seas. *Engineering Structures, 3*(1), 45-51.

24th IAHR International Symposium on Ice
Vladivostok, Russia, June 4 to 9, 2018

The Influence of Ice Response to the Peak Ice Load on Ship's Bow Shoulder

Mikko Kotilainen*, Mikko Suominen*, Pentti Kujala*
*Department of Mechanical Engineering, Aalto University**
Tietotie 1C, Espoo, Finland
mikko.kotilainen@aalto.fi
mikko.suominen@aalto.fi
pentti.kujala@aalto.fi

The interest in arctic sea routes and natural resources poses a challenge to the ship building industry. The ice-induced loads on ship hull need to be understood. These loads include multiple uncertainties. In addition to the mechanical properties of ice varying a lot (Timco and Weeks, 2010), also the ship-ice contact geometry is constantly changing (Daley, 1991) as the ship navigates through ice. This paper analyses stereo camera photos in order to examine what the ice response is as the peak ice load occurred on ship's bow shoulder. Weibull distributions are fitted to loads in each ice response mode, after which the distribution predictions are compared. The results suggest that the ice response mode influences the measured peak ice load. Hence by knowing the ice response mode in addition to other influencing covariates, ice loads could be predicted more accurately. The low loads are predicted in condition where the ice seems to break more easily, whereas high loads are predicted with rotating ice floes, crushing of ice and when ice floes are pushed on top of other ice.

1. Introduction

The factors affecting the ship-encountered ice loads include multiple uncertainties. The uncertainties including ice properties (Timco and Weeks 2010), the ship-ice contact geometry (Daley 1991), and the modes at which the ice fails all vary a lot. In addition to those uncertainties, if the load is measured only on one frame, the measured peak load is uncertain in the sense that the peak could have occurred on the frame before, and the force experienced by the frame is due to pushing or rotating the broken ice piece. On the other hand, the load seen by the frame could also be the initial crushing of the ice piece, breaking on the next frame to cause the peak load. This paper studies what the loading condition is on ship's bow shoulder and the corresponding ice loads when the peak load occurs on a particular frame.

Because the icebreaking process is not well understood, a multitude of full-scale experimental studies has been conducted over several decades. Multiple studies have compared ice loads and ice pressures to the conditions (see e.g. Glen and Blount 1984; St John et al. 1990, 1995; Kotisalo and Kujala 1999; Frederking 2000; Hänninen et al. 2001; Leira et al. 2009; Matsuzawa et al. 2010; Kotilainen et al. 2017, 2018). Others have studied the maximum ice loads in time windows of certain length (e.g. Kujala et al. 2007), the highest local ice pressures (e.g. Jordaan et al. 1993) and the distribution for the ice loads (e.g. Suominen and Kujala 2010; Suyuthi et al. 2012a, 2012b, Wei). Kotilainen et al. (2017) showed that if loads on one frame are studied as a function of ice and operational conditions (ship speed and ice thickness); a hierarchical Bayesian model can be used to predict the load distribution in different conditions.

This paper introduces two new methods to reduce the uncertainty of the measured ice load. First, we study loads on three adjacent frames (#113, #112.5 and #112 in Fig. **2**) to make sure that the highest peak ice load (peak load from here on) occurs on a certain frame. If the measurements were taken from only one or two adjacent frames, this could not be known with certainty. Figure 1 illustrates this problem. If only frames #112.5 and #112 were instrumented, we would not be able to know if the highest peak load occurred on one of the previous frames and has moved on the middle frame as the ship is moving in the ice. By studying also the third frame, we can find out if the peak load occurred on the middle frame. If the peak load occurs on the middle frame, something interesting has happened with the ship-ice contact, i.e., ice has either broken or moved. The second way to reduce the uncertainty is to observe what happens when the peak load occurs on the middle frame. A stereo camera was mounted above the three instrumented frames and by synchronizing the frame timestamps with the stereo camera timestamps, we can look at the camera photo to see what happens to the ice at the time when the peak load occurred.

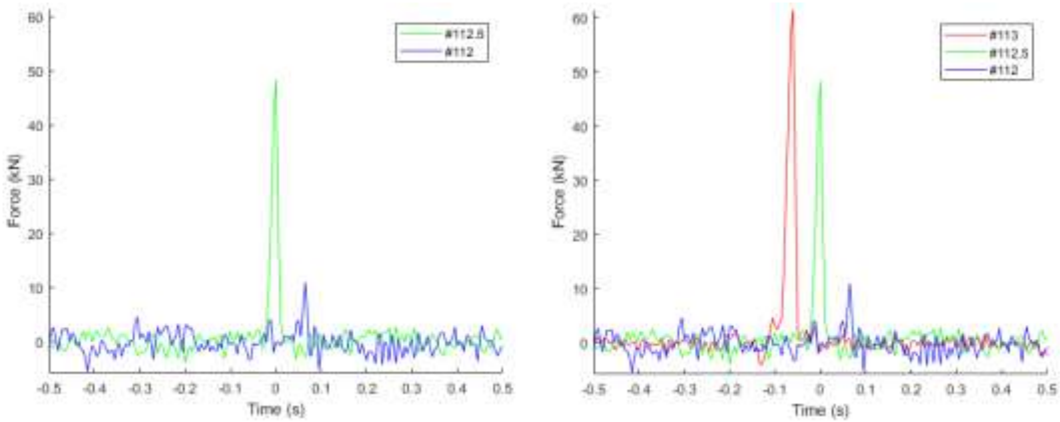

Fig. 1. Problem of identifying peak loads with only two instrumented frames. The load moves from one frame to the next as the ship moves in ice.

2. Measurements

2.1 Ship and instrumentation

The loads were measured onboard the polar supply and research vessel S.A. Agulhas II in the Baltic Sea during an ice trial during spring 2012. The ship was built to Polar Class PC5 and the hull strength is in accordance with DNV ICE-10. The ship's main dimensions are presented in **Table 1**.

Table 1. Ship's main dimensions.

Length, bpp.	121.8 m
Breadth moulded	21.7 m
Draught, design	7.65 m
Corresponding deadweight	5000 t
Speed, service	14.0 kn

The ship is powered by a diesel electric propulsion system consisting of four diesel generators, each producing 3 MW. Two 4.5 MW electric motors provide power for two controllable pitch propellers. Additionally there are two bow thrusters and one stern thruster for fine maneuvering. The ice loads in this paper refer to the ice-induced force measured on the transverse frames using shear strain gauges with a sampling frequency of 200 Hz. Fig. **3** shows the instrumented nine frames: two at the bow (#134.5-#134), three at the bow shoulder (#113-#112) and four at the aft shoulder (#41-#39.5). The shear force acting between the sensors is determined from the force-strain ratio by measuring the difference between shear strains on the upper and lower parts of the frame (Suominen et al. 2017). In addition, the strains occurring in the hull plating were measured with one-directional strain gauges (two at the bow shoulder).

The studied frames are the three adjacent frames on bow shoulder (#113, #112.5 and #112). A stereo camera system, taking pictures with a frequency of 3 Hz, was mounted above those frames (Kulovesi and Lehtiranta, 2014). The ship speed was measured by the ship's GPS.

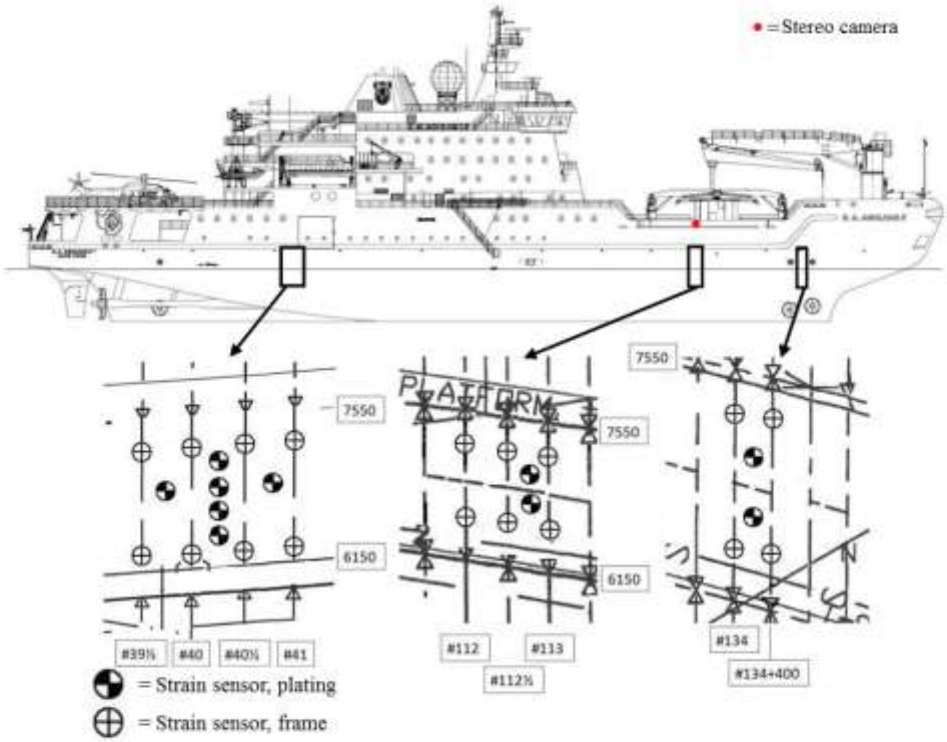

Fig. 2. Ship and instrumentation.

2.2 Voyage

The voyage started on 19th of March 2012 from Rauma. Due to a mild winter, the ice covered only the northern part of the Bothnian Bay. The ship arrived in the icy waters in the morning of March 21st and returned to open waters for the night. A similar procedure was done on the 22nd of March. Figure 3 shows the map illustrating first day ice trial voyage and the ice concentrations (Suominen, et al. 2013). The measurements were ongoing while the ship was in ice and a total of 24 hours of data was collected.

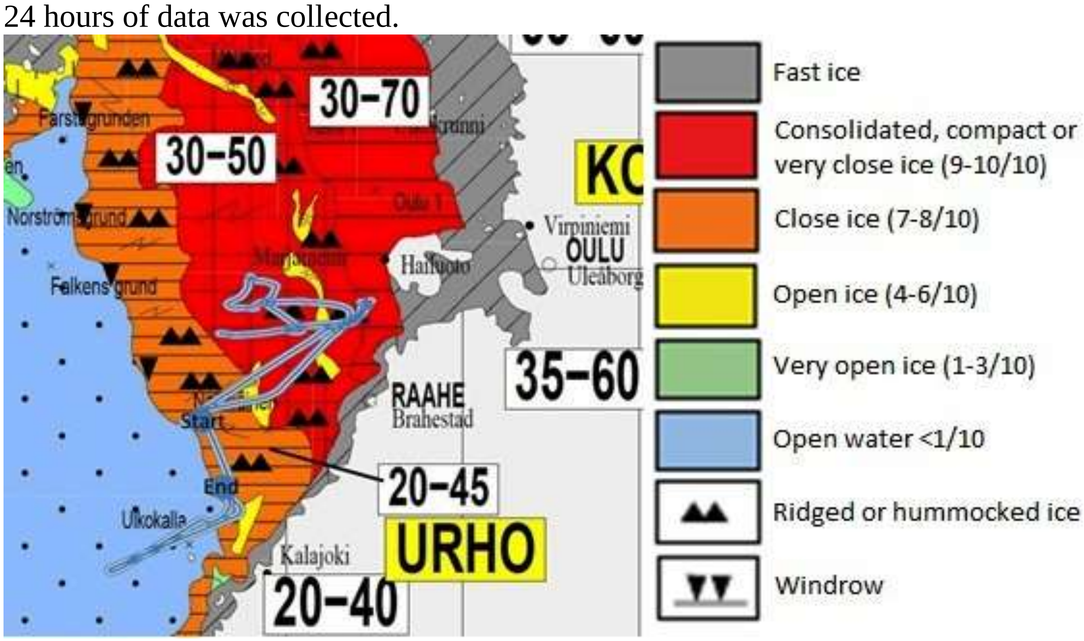

Fig. 3. Ice concentration and ship route on March 21 (Suominen et al. 2013).

3. Data processing

3.1 Peak load identification

The frame spacing is 40 cm, meaning that if we assume the ice floe is fixed on its place, the time it takes the ship to move 40 cm, is the time that the ice load moves from one frame to the next. As mentioned in section 2.1, three frames are instrumented at the bow shoulder. Because three adjacent frames are instrumented, it is possible to determine the cases where peak ice load occurs on the middle frame. The determining factor is that the peak load on the second frame is higher than the peaks on either the first or the third frame. The procedure is explained in more detail below.

The loads on the middle frame are identified applying a threshold (here 20 kN) and a Rayleigh separator (here 0.5). The forces below the threshold are discarded as noise, and the maximum forces are then identified. The Rayleigh separator compares the minimum force between two maximum force peaks. If the minimum is lower than the separator times the lower of the load peaks, the loads are considered to be separate. Otherwise, they are considered as one, continuous, load (Kotilainen et al. 2017).

Now we can examine the ice loading process of the middle frame in more detail. First, there is the approaching stage, where the force starts growing but the observed frame is not yet in in contact with the ice. On this stage, the experienced forces are due to reflections from other frames where the ice is in contact. After this, there is the contact stage when the contact spot moves into the observed frame panel. The ice crushes against the panel until the load peaks and starts declining (Kotilainen et al. 2017). This declining stage will be explained in a moment, but first, we will analyze what happened when the load peaked. This declining load could be caused by multiple reasons:

1. the ice could have failed by bending or shearing,
2. the ice piece could have moved, or
3. the contact spot could have moved to the next frame as the ship advanced in the ice.

After this, the ice load starts declining in the disengaging stage where the broken ice piece is pushed away and the load decreases.

However, the force on middle frame could happen in three situations:

a) the peak load occurs in the previous frame, and what middle frame sees is the disengaging stage that has moved onto middle frame,
b) the peak load occurs on middle frame, or
c) the first contact occurs on middle frame, but the contact spot moves to the next frame where the peak load occurs.

If only one frame is instrumented, we cannot distinguish between these situations. In order to identify which situation it is, adjacent frames need to be studied. The situation a) can be identified by studying the previous frame #113. If the force on #113 is higher than on #112.5, it is considered to be situation a), otherwise it is either b) or c). Similarly, the situation c) can be identified by studying the forces on the next frame #112. If the force on #112 is higher than on #112.5, the situation is considered to be of type c), otherwise it is either a) or b). We are interested of situation b), so therefore the force on #112.5 must be higher than the forces on #113 and #112. Next, we need to choose the length of the time window where the forces are compared in order to identify the type b) situations.

The time window is selected so that the ship has moved double the frame spacing (80cm) backward or forward (for a total time window of 160cm). In order to obtain this time window, ship speed is taken at the moment the load peaked on #112.5. After that we can calculate how long it takes for the ship to move 80 cm. For example, if the ship speed was 4m/s, the time window would be $\frac{0.8m}{4m/s} = 0.2s$ backward and forward. Within this time window, the load amplitude on #112.5 must be higher than the maximum of either #113 or #112. This constraint was satisfied in 852 loads. We study only the loads that satisfy this condition, so that we can say that at that moment the ice either broke or moved and we know the peak load associated with that event. Next, we measure the corresponding ice response mode.

3.2 Ice response modes

The reason we want to identify the instants where the peak load occurred on #112.5 is that the stereo camera was mounted above those frames. Because both the peak loads and stereo camera photos have time stamps, they can be synchronized. The initial synchronization was done using a wristwatch to adjust the clocks at the start of both days. The difference in the timestamps is assumed to change slowly. This allows the difference to be updated at each clear event, such as when the ice floe turns in the observed frame. The synchronization allows us to study the stereo camera photos at these instants to determine what happened to the ice as the peak load occurred. This is done by identifying from stereo camera photos different ice response modes that describe how the ice reacts as the peak load occurs in the middle frame.

The identified ice response modes for the events are:

1. Identification difficult
2. Tiny floes
3. Floe bounces from underwater
4. Broken floe pushed horizontally
5. Rotated broken floe pushed vertically
6. Radial crack propagates in floe
7. Circumferential crack propagates in floe
8. Both radial and circumferential cracks
9. Rotated floe splits in two pieces
10. Broken floe rotates into vertical orientation
11. Large floe pushed
12. Broken floe pushed on top of another ice floe

The categorizing allows us to study how each ice response mode influences the peak ice load on frame #112.5. Below, each ice response mode is illustrated with an example situation of four photos (time difference between the photos is 1/3 seconds) and the measured loads. The photos are selected so that the peak load occurs on the third photo. In the measured forces, dashed lines indicates the time window where the forces are compared.

1. Identification difficult

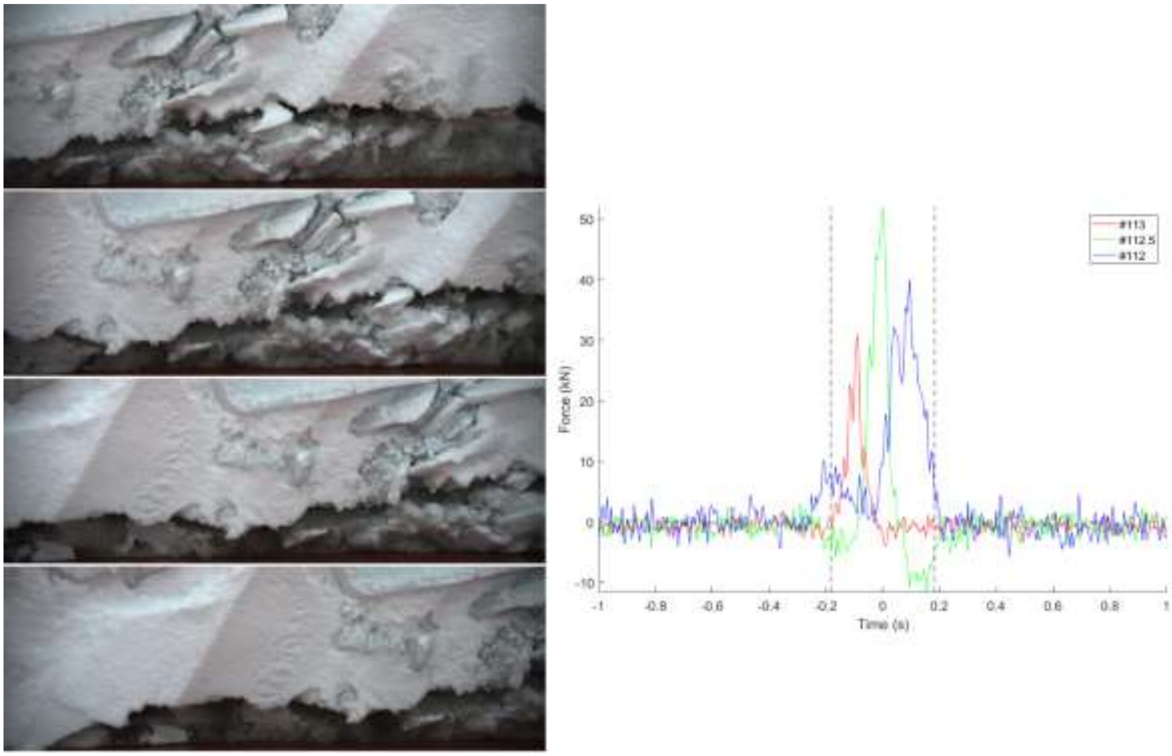

Fig. 4. Due to multiple irregularly shaped ice pieces on the frame, it is difficult to identify the event that causes the load to peak.

2. Tiny floes

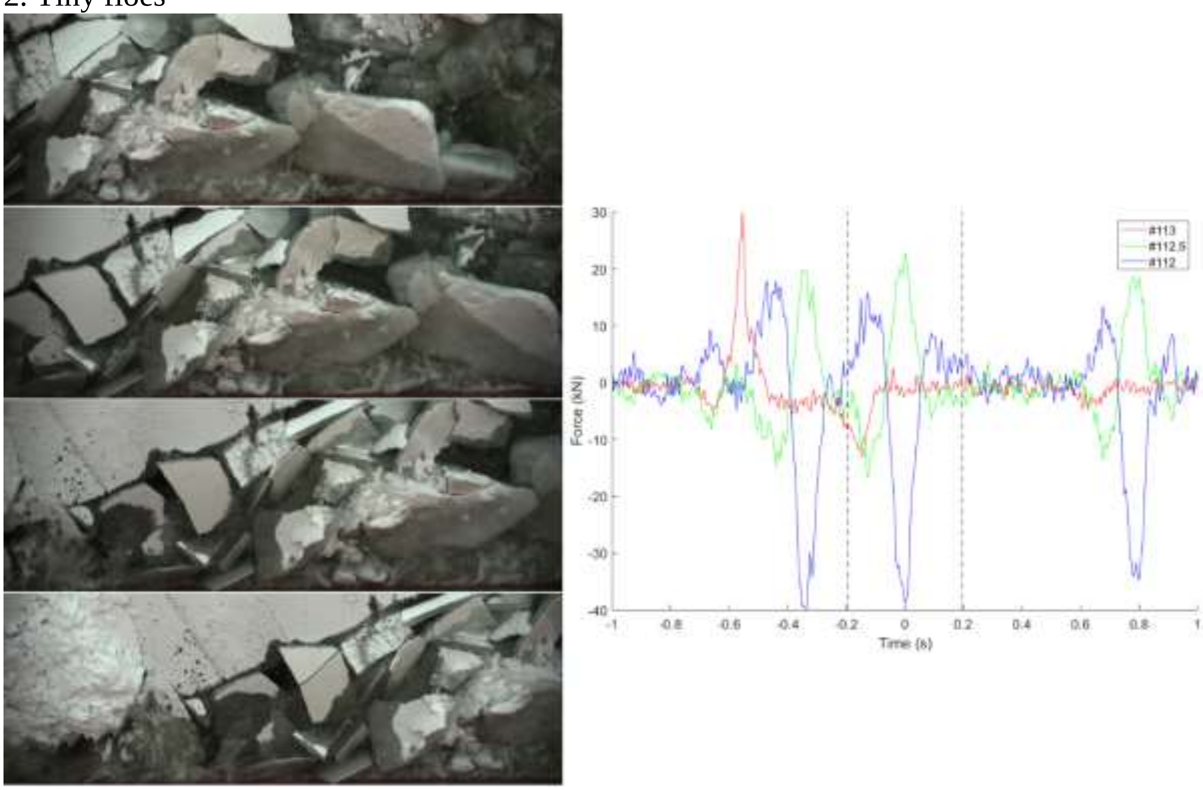

Fig. 5. Multiple tiny floes in contact with the frame.

3. Floe bounces from underwater

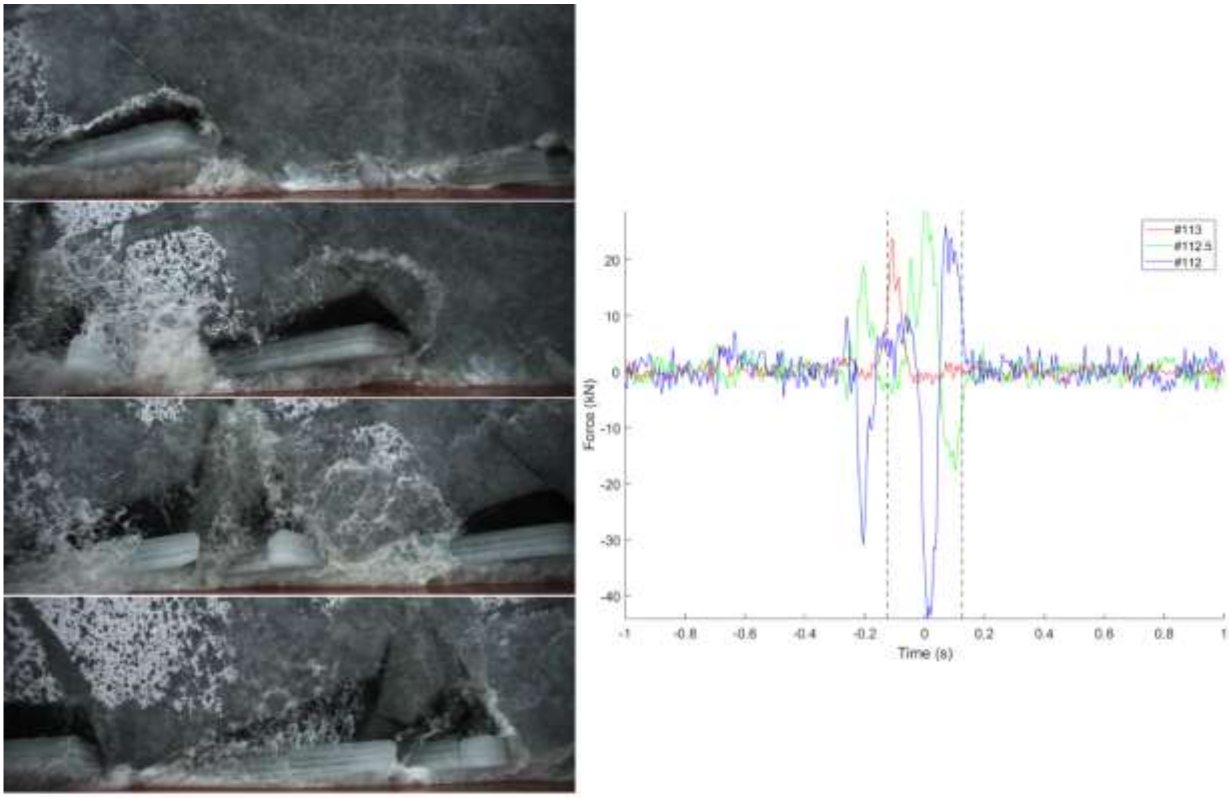

Fig. 6. A floe submerged by the ship bounces from underneath the ship.

4. Broken floe pushed horizontally

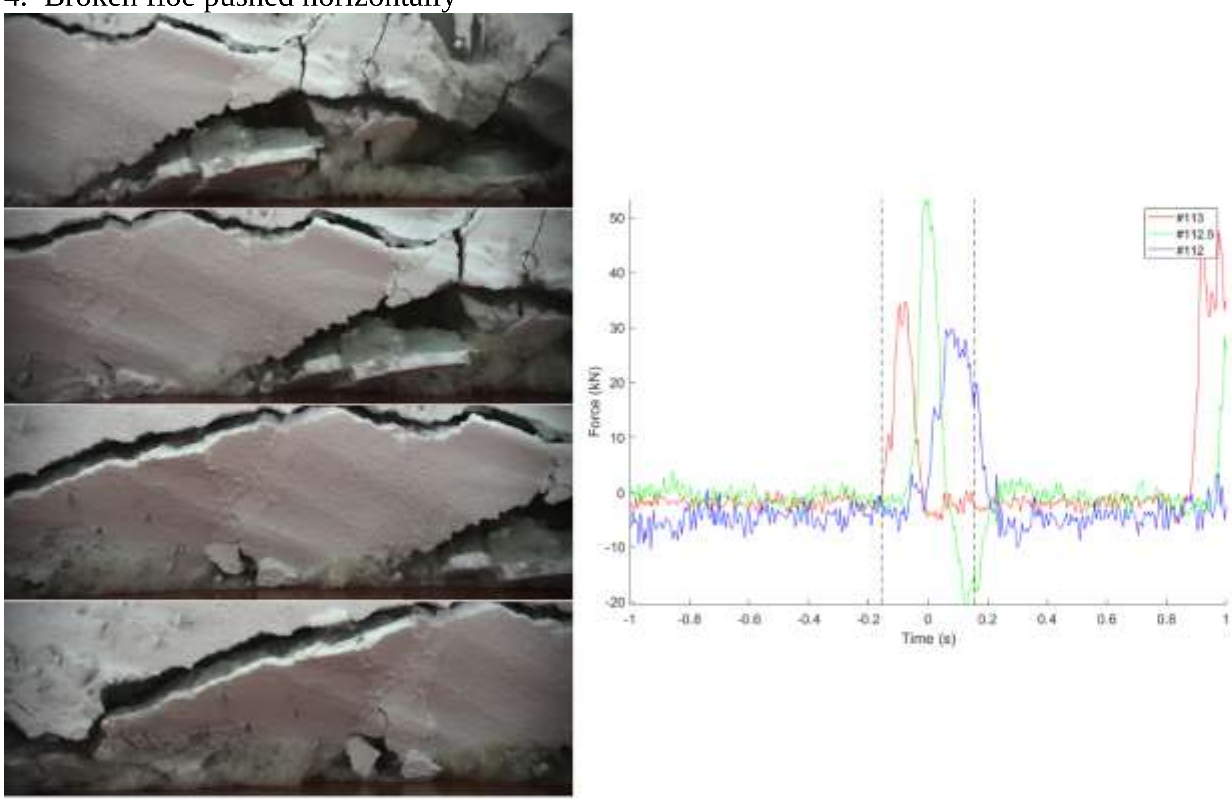

Fig. 7. Ship pushes a broken floe in the horizontal plane.

5. Rotated, broken floe pushed vertically

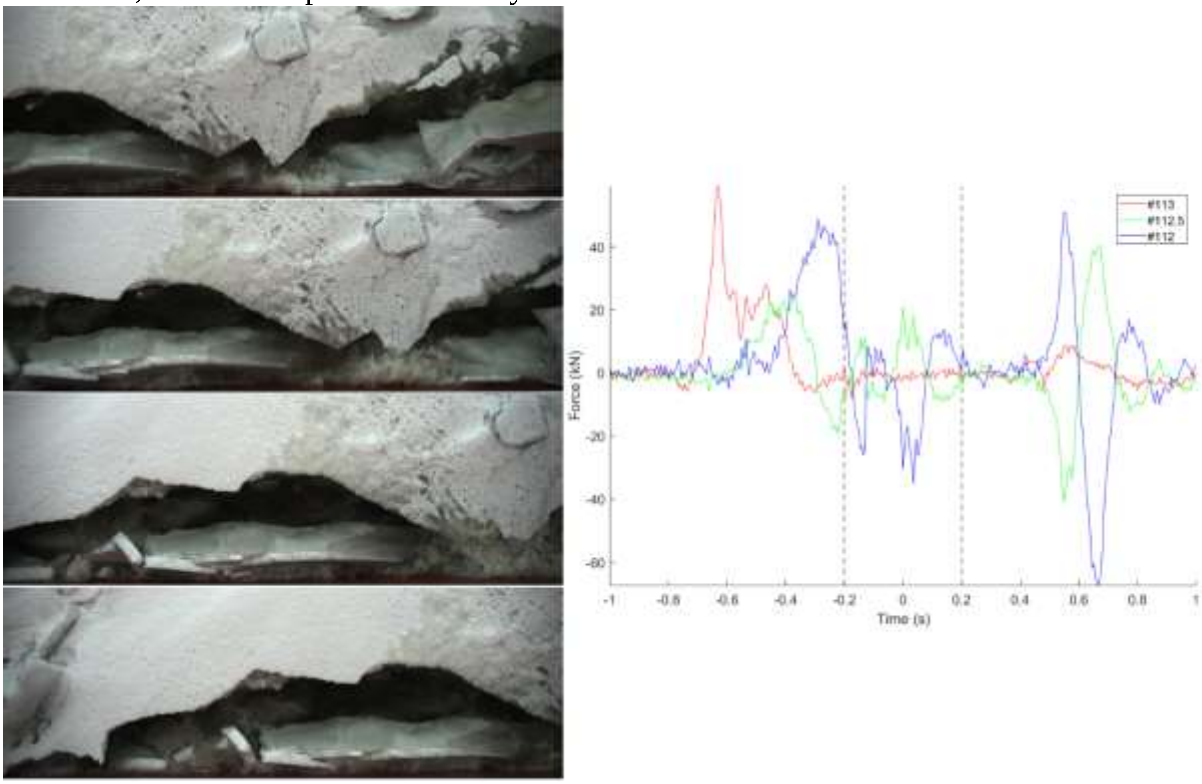

Fig. 8. Ship pushes a rotated, broken floe.

6. Radial crack propagation in ice

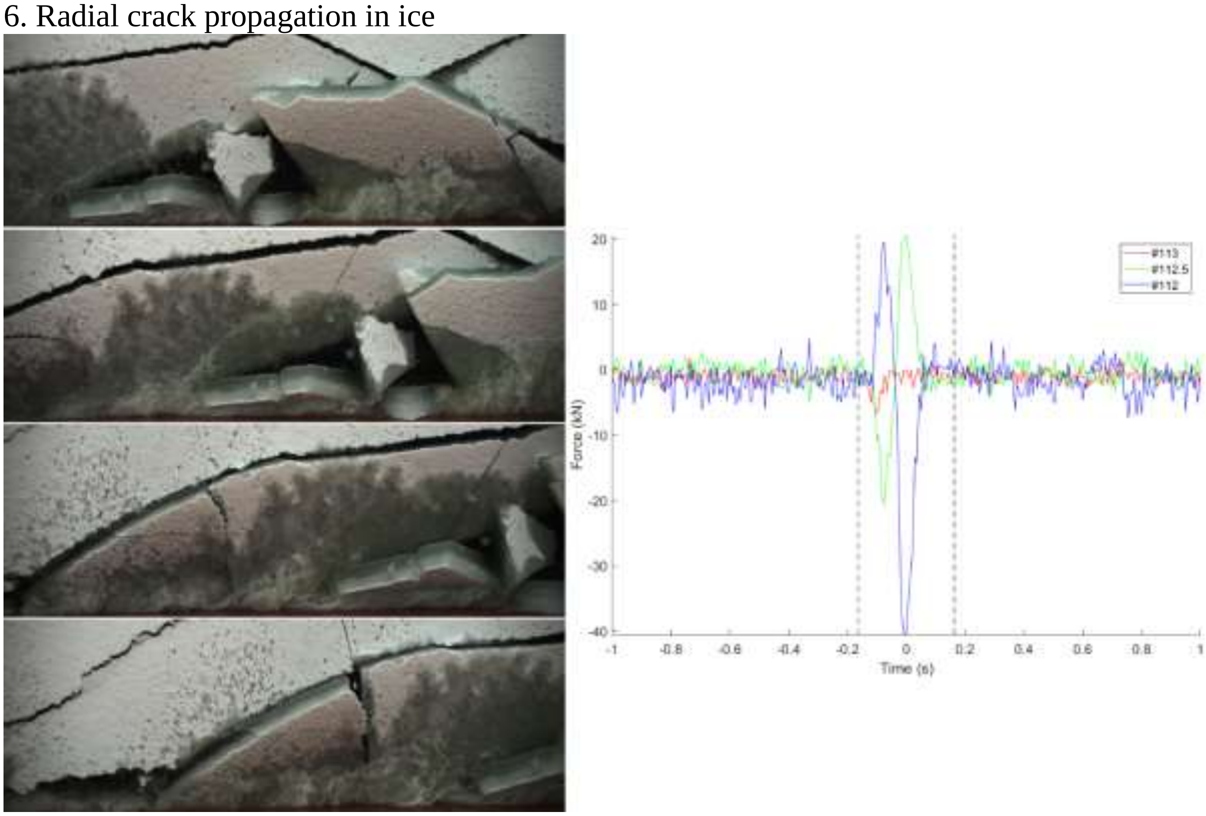

Fig. 9. A visible radial crack propagates in ice.

7. Circumferential crack propagation in ice

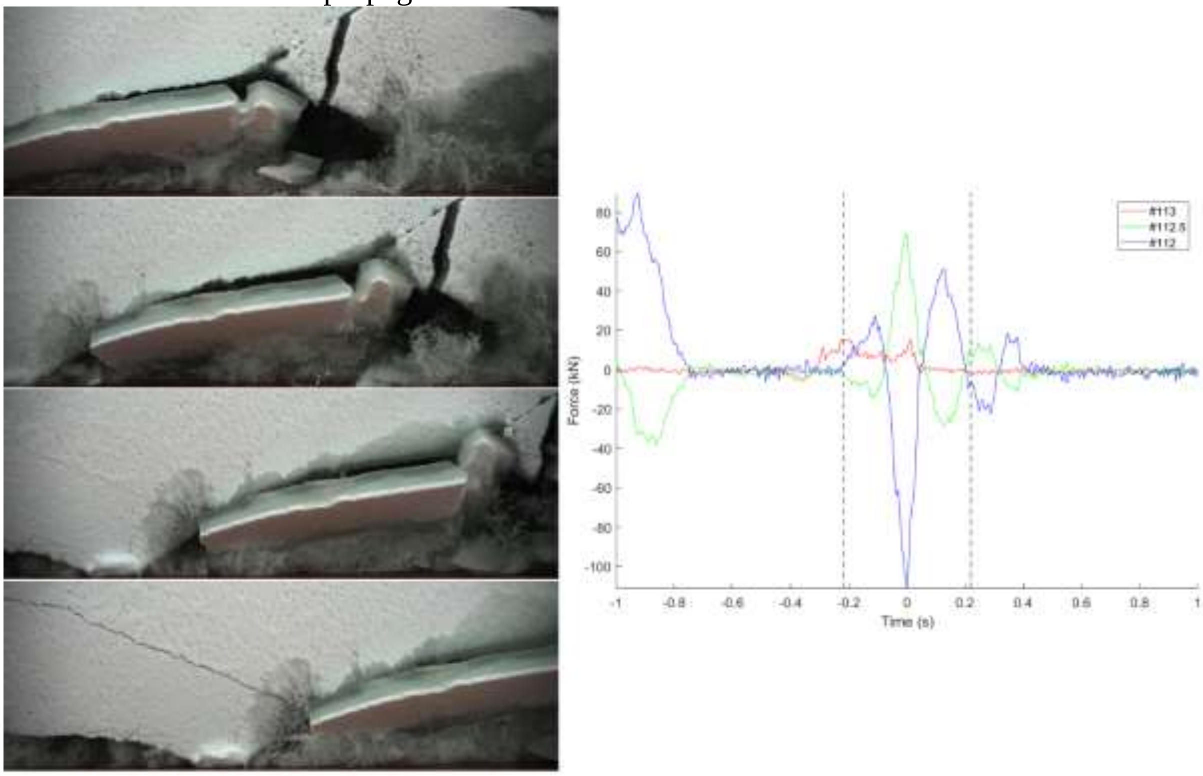

Fig. 10. A visible radial crack propagates in ice.

8. Both radial and circumferential cracks in ice

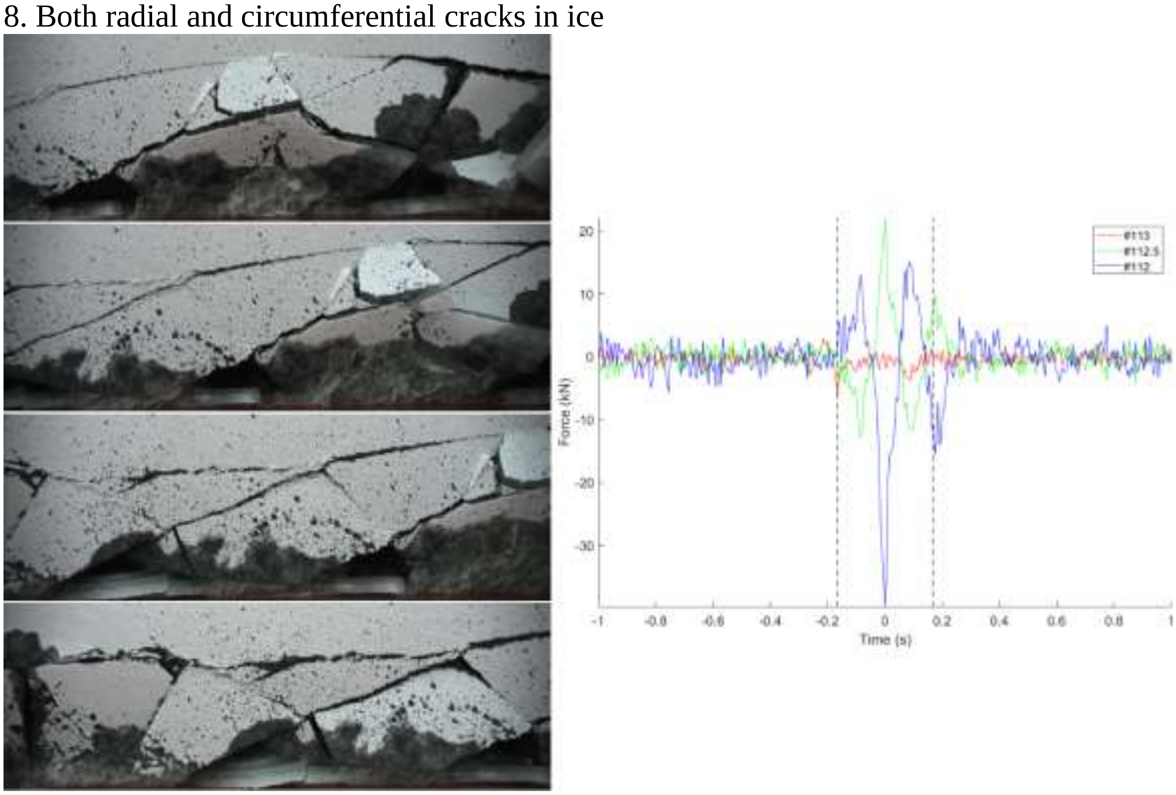

Fig. 11. Both radial and circumferential cracks propagate in floe, difficult to identify what causes the load to decrease.

9. Rotated floe splits in two pieces

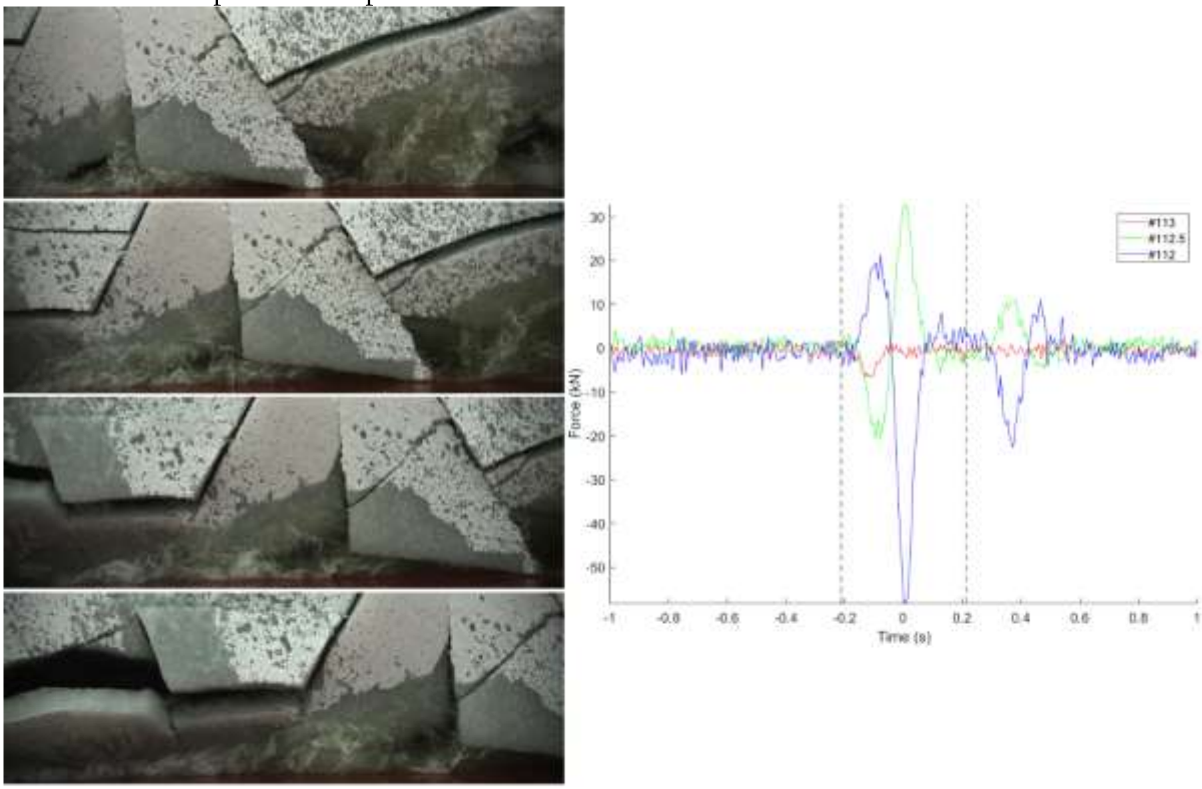

Fig. 12. Rotated floe splits in two or more pieces.

10. Broken floe rotates into vertical orientation

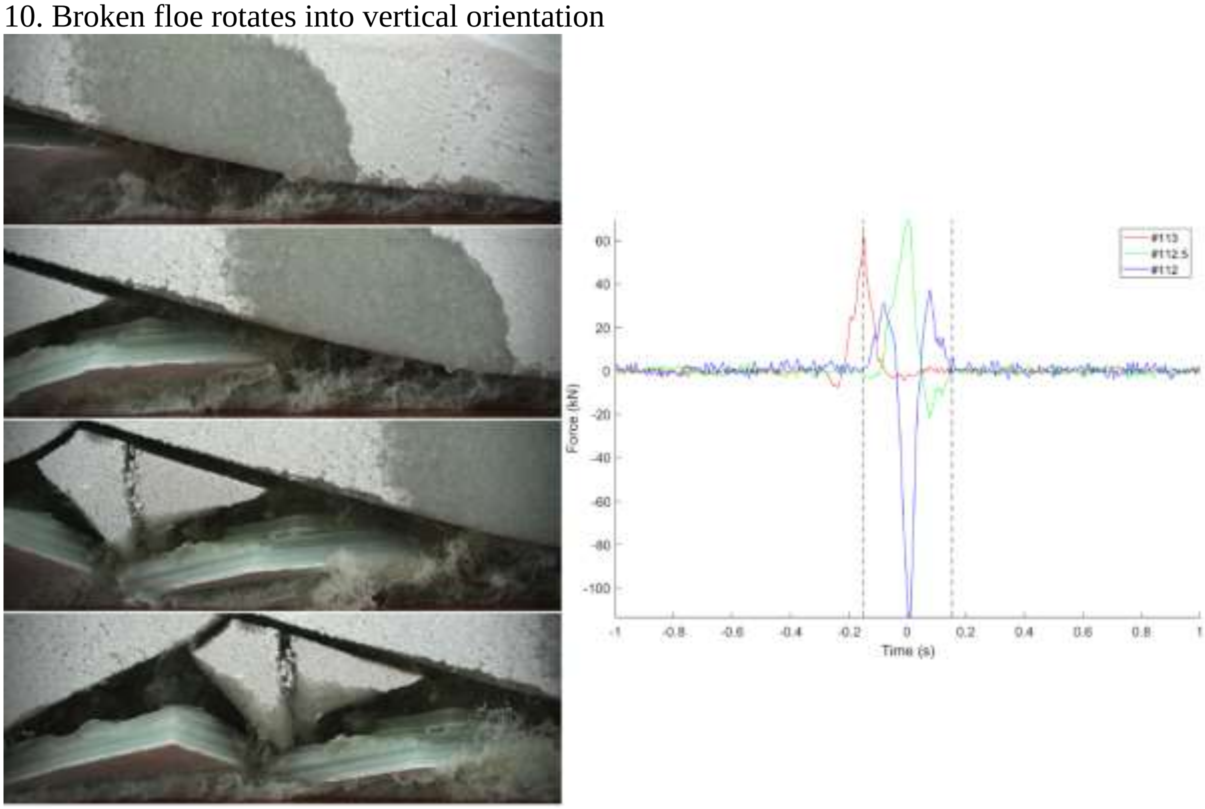

Fig. 13. An already broken floe rotates into vertical orientation.

11. Large floe pushed

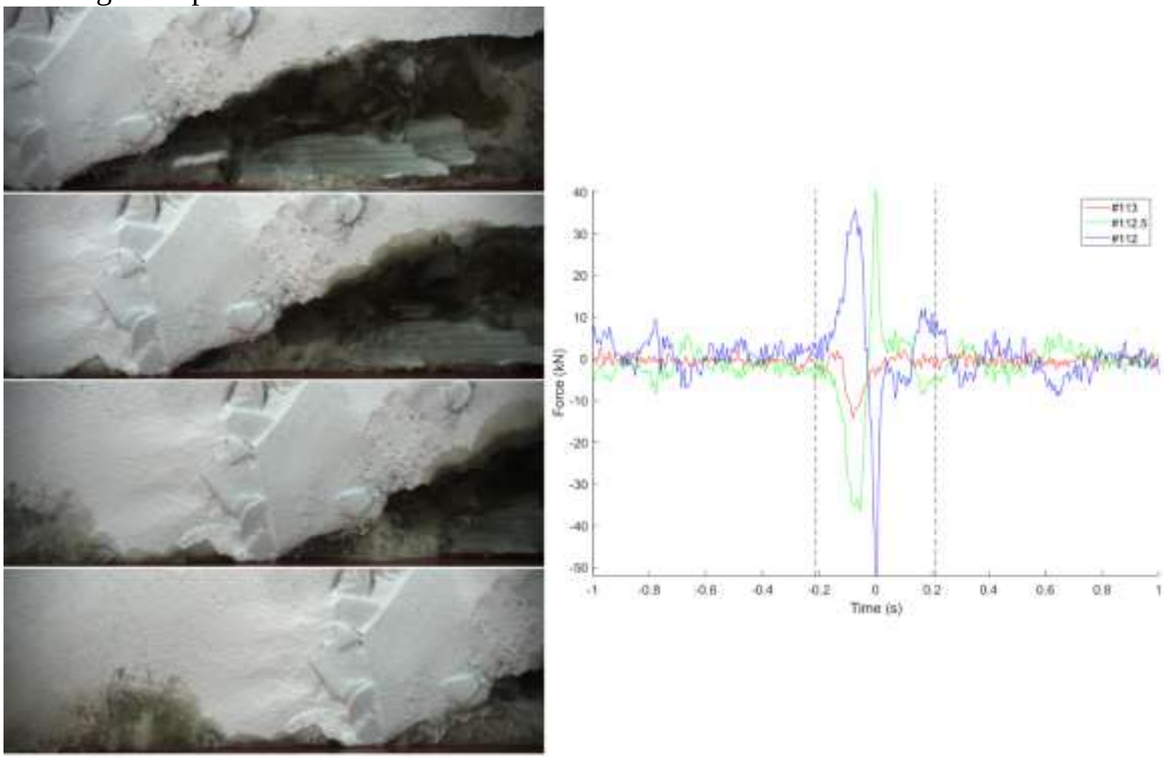

Fig. 14. The pushed floe is larger than the camera can capture. The floe does not split into smaller pieces by visible crack propagation or bending failure. Instead, in most cases crushing failure is observed.

12. Broken floe pushed on top of another ice floe

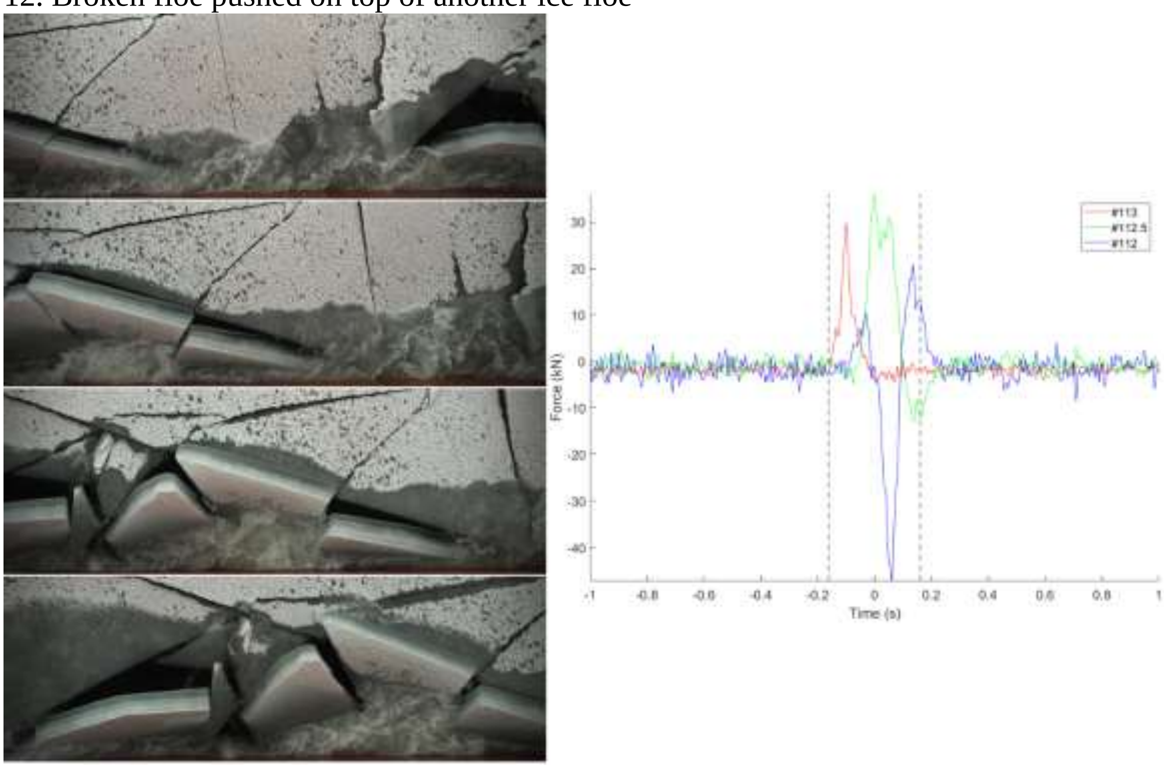

Fig. 15. Ship pushes an already broken floe on top of another ice floe.

4. Results

Fig. 16 shows the measured loads in each ice response mode. In order to get a better sense of the amount of small ice loads in each mode, a little jitter is added to the x-axis.

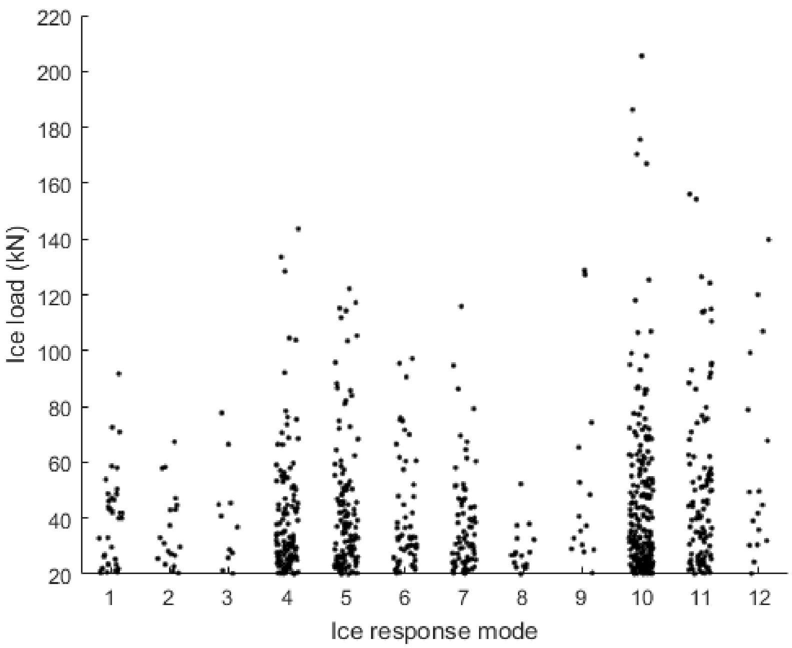

Fig. 16. Measured ice loads in each response mode. A little jitter is added to x-axis to better show all the ice loads.

The highest ice loads occur in response mode 10, where the ice floe rotates into vertical orientation. However, the large variation in loads within a mode indicates that the ice loads cannot be predicted on the loading condition alone, but rather that there are more factors affecting the ice load. In order to get a better insight of how the different conditions affect the ice loads, shows the load means and standard deviations in different conditions.

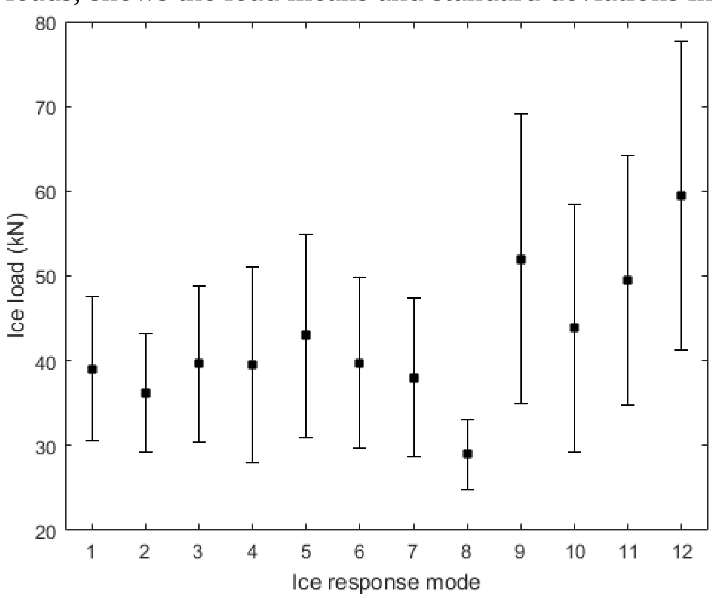

Fig. 17. Load mean ± one standard deviation in each ice response mode.

The highest mean loads are observed in response modes 9, 11 and especially 12 where a floe is pushed on top of another ice floe. The lowest loads are observed in mode 8, where both radial and circumferential cracks visually propagate. However, as the load distribution is far from Gaussian, means and standard deviations might not be the best parameters to estimate. Previous studies have shown that Weibull-distribution fits the measured ice loads well in many situations (see e.g. Suominen and Kujala 2010; Suyuthi et al. 2012a, 2012b; Kotilainen et al. 2017, 2018). Thus, Weibull distributions were fitted on the measured loads in each response mode to get the Weibull parameters and graphically check if the Weibull distribution fits the loads well. Figure 18 shows the fits in the same axis, whereas Table 3 shows fitted Weibull-distribution parameters together with a threshold-exceeding load corresponding to the 99% quantile. The Weibull distribution seems to fit the observed loads adequately in all modes. A higher scale means higher loads in general, whereas a lower shape allows for more extreme loads. The highest loads (99% quantile) are predicted in modes 5, 9, 10, 11 and 12. Note that the load corresponding to threshold exceedance subtracts the threshold from the load, so that the measured 99% quantile for the load would be the sum of the threshold-exceeding load and the threshold.

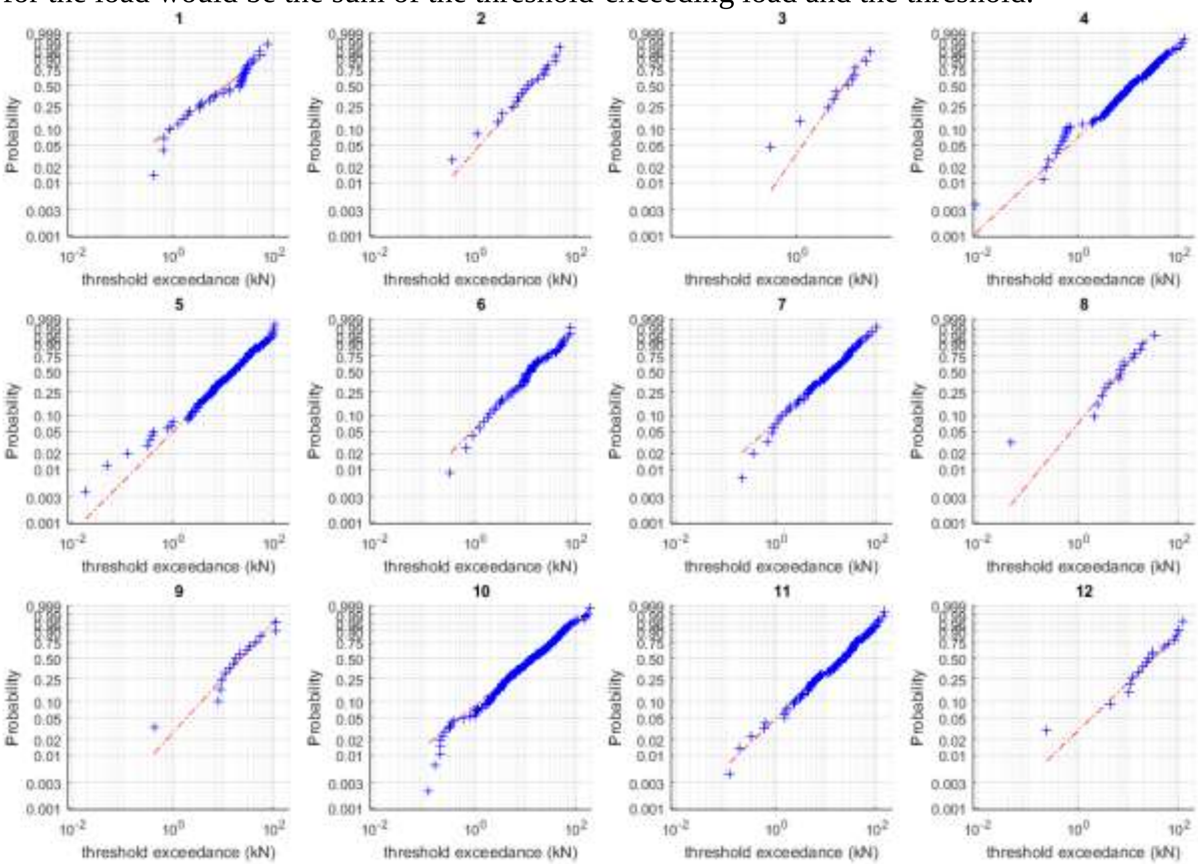

Fig. 18. Weibull fits for the threshold exceeding part of the load.

Table 2. The estimated Weibull parameters together with the 99% quantile for the threshold-exceeding load for different ice response modes

Ice response mode	1	2	3	4	5	6	7	8	9	10	11	12
Scale	18.7	16.7	19.0	17.8	22.0	19.5	17.6	9.2	31.6	21.7	28.7	39.5
Shape	0.96	1.09	0.92	0.84	0.91	0.97	0.95	1.07	0.98	0.84	0.94	1.00
99% quantile (kN)	92	68	99	110	118	94	88	38	151	133	145	181

In addition to the load measurements, we studied how the ship speeds were distributed in each loading condition. This way we can study if the speed affects the loading condition. Figure 19 shows the ship speeds (m/s) in each loading condition together with the average speed of the condition. Speeds are lower in tougher conditions, e.g. where a large floe is pushed (11), and higher in easier conditions e.g. where a floe jumps from underwater (3).

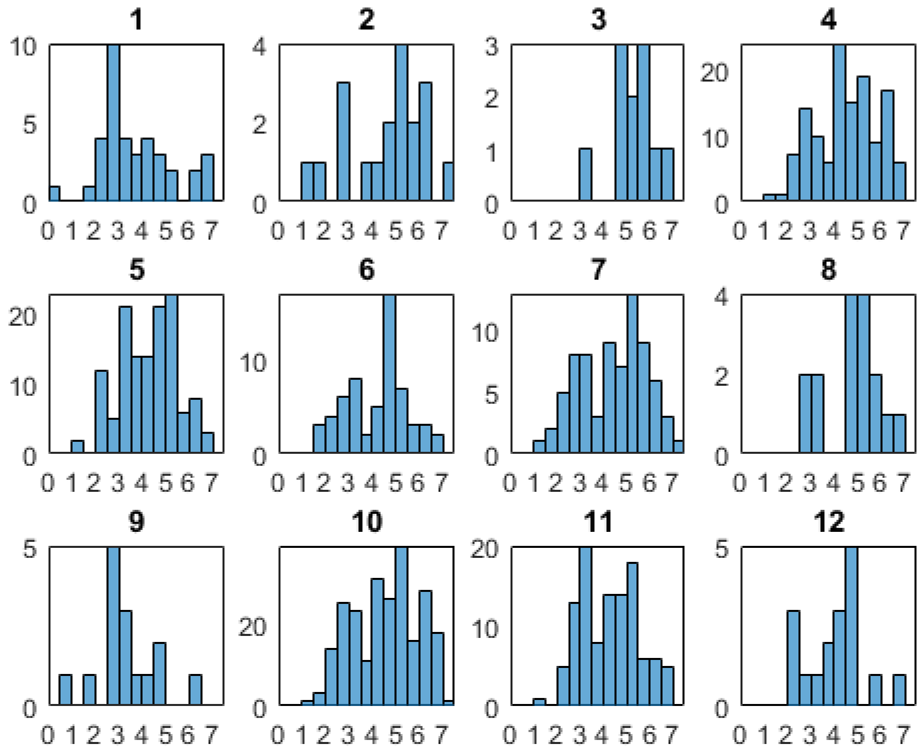

Fig. 19. The measured speed (in m/s) in each ice response mode.

5. Discussion

The measurements include many uncertainties. The time synchronization of two different measurement systems can be difficult. However, we can synchronize the system multiple times using clear loading events such as when an ice floe rotates on the frame. As the difference between measurement timestamps changes slowly, we can update the difference at each clear event. To better identify these events, we can locate the frame from the photos where multiple events occur. There are also other problems when identifying the loading condition. In some photos it is difficult to tell what is going on at the frame as multiple events are happening there. For example, multiple ice pieces can be near the frame rotating, being pushed and broken. In addition, in some photos it was difficult to differentiate whether the floe in the vertical orientation was being rotated or not. Moreover, the amount of sunlight was low at the end of the second day. This lead to discarding of 66 loading cases. In addition, the measured forces on the outer frames #113 and #112 are less accurate than on the middle frame #112.5, as the measurement is more certain if the adjacent frames are instrumented.

The time window was determined by the distance that the ship moves within a certain period. This assumes two things. First, the ship speed does not change when the ice piece has moved from frame #113 to #112. This is true to a high accuracy, as the ship has a lot of inertia and the speeds were in general high so it does not take a long time for the ship to move 80 cm. The

second assumption is that the ice floe does not move parallel to the ship's motion. This assumption is more problematic. Assuming that the ice sheet is initially still is acceptable, as ice sheet movement compared to the ship speed is negligible. However, small ice floes can be accelerated quickly in the contact with the ship due to friction. This leads to the ice pieces moving from one frame to the next slower than it takes for the ship to move one frame spacing. Thus, we selected a larger time window (of 160cm compared to 80cm) to compare the forces in.
The results are affected by the geometry of the studied frame. The loads on the frame #112 are generally higher and the breaking mode could be different there. The studied frames are located at the bow shoulder where the parallel part of the ship begins. The choice of studying the loads that peak on the middle frame likely affect the observed loading conditions, compared to the bow frames, where flare angle is lower, and frame #112, where the parallel part of the ship starts.

This analysis has ignored multiple covariates that affect the ice loads. For some of the covariates the measurement was simply not possible to make such as for ice shearing and bending strengths. As these strengths depend on the ice microstructure, they will vary a lot even in ice samples collected from nearby locations. It is not possible to first measure these properties and afterwards drive through that ice with the ship and measure what kind of ice loads occurred. On the other hand, some of the measured covariates are ignored as well. For example, ship speed and ice thickness are believed to influence the ice load but are ignored in this analysis. The only explanatory covariate for measured load is the loading condition, i.e. how the ice piece moved or failed when the peak load occurred. Due to missing all these covariates, measured load peaks within a response mode vary a lot. Despite that, we can observe some evidence of how the different loading conditions influence the measured peak loads.

The highest loads are predicted in ice response modes 5, 9, 10, 11 and 12. Modes 5, 9 and 10 include the rotated floes. Sometimes in these observations, it is difficult to distinguish if the floe rotated at the moment the peak load occurred. In mode 11 a large floe is pushed and usually crushing of ice is observed. Because crushing of ice causes higher forces than bending, this makes sense. In mode 12 floe is being pushed on top of another floe. This could be explained by the quick change in floe's potential energy and the friction. The lowest loads are predicted in response mode 8, where both radial and circumferential cracks are visible. This response mode could indicate, that the ice is broken more easily. However, one should note that the estimated Weibull parameters are quite uncertain in response modes where only few loads were measured, and hence, the 99% quantile is quite uncertain. In addition, the load is likely affected by other covariates as well, such as ice thickness and the ice floe size.

In the future studies, the method could be improved by including all the explanatory covariates that are believed to affect the ice loads, such as the ship speed and ice thickness in addition to the loading condition. It would be also possible to measure something related to the specific loading condition. For example, the sizes of pushed or rotated ice floes could be measured from the photo. This would provide further information of the conditions at which the load occurred, thus decreasing the uncertainty of the loading condition further. In addition, the method could be refined further to study how the ice response modes could be identified from the force signals.

Acknowledgement
The authors would like to thank the Lloyd’s Register Foundation for funding the Joint Center of Excellence for Arctic Shipping and Operations which enabled this paper. The Lloyd's Register Foundation supports the advancement of engineering-related education, and funds research and development that enhances the safety of life at sea, on land, and in the air. The additional funding from the Academy of Finland through the Antload project is gratefully acknowledged, in addition to the funding from Tekes (the Finnish Funding Agency for Technology and Innovation) through PSRV project (project partners Aalto University, University of Oulu, University of Stellenbosch, Aker Arctic, Rolls-Royce, STX Finland, Wärtsilä, DNV, and the Department of Environmental Affairs of South Africa).

References

Daley CG. 1991. Ice edge contact - a brittle failure process model. Acta Polytechnica Scandinavica Mechanical Engineering Series, 100.

Frederking R. 2000. Local Ice Pressures from the Louis S. St Laurent 1994 North Pole Transit. National Research Council Report HYD-CR-054. Ottawa: Canadian Hydraulics Centre.

Glen IF, Blount H. 1984. Measurements of ice impact pressures and loads onboard CCGS Louis S. St. Laurent. In Proceedings of the 3rd Offshore Mechanics and Arctic Engineering Symposium, vol. III. ASME, New Orleans, LA. p. 246-252.

Hänninen S, Lensu M, Riska K. 2001. Analysis of the Ice Load Measurements During USCGC Healy Ice Trials, Spring 2000. Helsinki University of Technology.

Jordaan IJ, Maes MA, Brown PW, Hermans IP. 1993. Probabilistic analysis of local ice pressures. Journal of Offshore Mechanics and Arctic Engineering, 115(1), 83-89.

Kotilainen M, Vanhatalo J, Suominen M, Kujala P. 2017. Predicting ice-induced load amplitudes on ship bow conditional on ice thickness and ship speed in the Baltic Sea. Cold Regions Science and Technology 135:116-126.

Kotilainen M, Vanhatalo J, Suominen M, Kujala P. 2018. Predicting local ice loads on ship bow as a function of ice and operational conditions in the Southern Sea. Ship Technology Research (in press).

Kotisalo K, Kujala P. 1999. Ice load measurements onboard MT Uikku during the Arcdev voyage. In: Tuhkuri J, Riska K, editors. POAC’99. Proceedings of the 15th International Conference on Port and Ocean Engineering under Arctic Conditions; Aug 23-27; Espoo, Finland. Vol. 3. p. 974-987.

Kujala P, Valkonen J, Suominen M. 2007. Maximum ice induced loads on ships in the Baltic Sea. In Proc. 10th International Symposium on Practical Design of Ships and Other Floating Structures PRADS. p. 1278-1286.

Kulovesi J, Lehtiranta J. 2014. Level Ice Thickness Measurement Using Ship-Based Semi-Automatic Computer Vision. 22nd IAHR International Symposium on ICE; Aug 11-15; Singapore, China. p. 111-118.

Leira B, Børsheim L, Espeland Ø, Amdahl J. 2009. Ice-load estimation for a ship hull based on continuous response monitoring. Proceedings of the Institution of Mechanical Engineers, Part M: Journal of Engineering for the Maritime Environment, 223(4):529-540.

Matsuzawa T, Takimoto T, Shimoda H, Wako D. 2010. Five-Year Observations of Ship Hull Ice Load in the Southern Sea of Okhotsk. 20th IAHR International Symposium on Ice; Jun 14-18; Lahti, Finland.

St John JW, Daley C, Blount H. 1990. Ice loads and ship response to ice - summer 1982/winter 1983 test program, Report No. SSC-329.

St John JW, Minnick PV. 1995. Ice load impact study on the National Science Foundation's Research Vessel Nathaniel B. Palmer, Report No. SSC-376, Washington, DC: Ship Structural Committee.

Suominen M, Kujala P. 2010. Analysis of short-term ice load measurements on board MS Kemira during the winters 1987 and 1988. Tech. rep. Aalto University, School of Science and Technology, Department of Applied Mechanics, Espoo, Finland.

Suominen M, Karhunen J, Bekker A, Kujala P, Elo M, von Boch und Polach R, Enlund H, Saarinen S. 2013. Full-Scale Measurements on Board PSRV S.A. Agulhas II in the Baltic Sea. Proceedings of the 22nd International Conference on Port and Ocean Engineering under Arctic Conditions, Espoo, Finland.

Suominen M, Kujala P, Romanoff J, Remes H. 2017. Influence of load length on short-term ice load statistics in full-scale. Marine Structures.52:153-172.

Suyuthi A, Leira B, Riska K. 2012a. Short term extreme statistics of local ice loads on ship hulls. Cold Regions Science and Technology 82:130–143.

Suyuthi A, Leira B, Riska K. 2012b. Statistics of local ice load peaks on ship hulls. Structural Safety. 40:1-10.

Timco GW, Weeks WF. 2010. A review of the engineering properties of sea ice. Cold Regions Science and Technology. 60(2):107-129.

International Association for Hydro-Environment Engineering and Research
Supported by Spain Water and IWHR, China

24th IAHR International Symposium on Ice
Vladivostok, Russia, June 4 to 9, 2018

Hysteretic behavior of freshwater ice under cyclic loading: preliminary results

Andrii Murdza, Erland M. Schulson, Carl E. Renshaw
Ice Research Laboratory, Thayer School of Engineering, Dartmouth College
Hanover, NH 03755 USA
Andrii.Murdza.th@dartmouth.edu
Erland.M.Schulson@dartmouth.edu
Carl.E.Renshaw@dartmouth.edu

Flexural experiments were conducted on freshwater columnar-grained S2 ice loaded normal to the columns to determine the hysteretic behavior under reversed cyclic loading at different temperatures, amplitudes and displacement rates. The ice was loaded in four-point bending.

Two series of experiments were conducted. In the first, the applied stress amplitude was held constant during the test. For these tests temperature was varied from -3°C to -25°C; the displacement rate was also varied, from 0.001 to 0.5 mm/s. In the second series of tests samples were subjected for cycling at different stress amplitudes, varied from 0.7 MPa to 2.1 MPa, while keeping the displacement rate and temperature constant, 0.1 mm/s and -10°C respectively.

These experiments show that energy dissipated during cycling increases with decrease of displacement rate and increase of temperature and stress amplitude. Internal friction increases with an increase of temperature and decrease of displacement rate and is independent of the stress amplitude.

1. Introduction

It was reported earlier (Iliescu et al., 2017) that the flexural strength of freshwater columnar-grained S2 ice may be increased by about a factor of two upon subjecting the material to cycles of fully reversed, up/down bending. This behavior is rather surprising and, to be better understood, requires further investigation. Therefore, to gain insight into the observed phenomenon, albeit indirectly, it was decided to consider hysteretic behavior.

Amplitude and rate-dependent energy loss is a well-known phenomenon in metals and alloys, originating in internal friction that leads to nonlinear energy dissipation. Internal friction can be described by hysteresis. Reported here are results from a series of experiments that were conducted to study internal-friction behavior of freshwater ice. Similar experiments on freshwater ice are described by Cole (1990) and Weber & Nixon (1996a).

Movements of dislocations influence internal friction. We suppose, that the strengthening of ice during cycling (Iliescu et al., 2017) is a result of dislocation nucleation and interaction. Therefore, a study of internal friction may allow us to investigate dislocation effects on ice behavior upon repeated loading.

2. Experimental Procedure

The ice we studied was produced in the laboratory. Tap-water was frozen unidirectionally, top down, in the manner described elsewhere (Iliescu & Schulson, 2002). This procedure produced bubble-free, columnar-grained ice that possessed the S2 growth texture in which the c-axes were confined more or less to the horizontal plane of the ice, but randomly oriented within that plane. The average column diameter was 4.4±0.7 mm and the length exceeded 50 mm. From such material, we cut and then milled thin plates of dimensions ~13 mm in thickness (parallel to the long axis of the grains), ~75 mm in width and ~300 mm in length. We flexed the plates up and down under 4-point loading, using a servo-hydraulic loading system to which we attached special apparatus designed and built on site; a detailed description of this apparatus with photos is given in (Iliescu et al., 2017). The distance L between the outer pair of loading cylinders was set by the geometry of the apparatus to be L=254 mm; the spacing between the inner pair was 127 mm; the diameter of the cylinders was 12.7 mm. The loading induced bending stresses, both tensile and compressive, that acted in the across-column direction.

In performing the experiments, the hydraulic actuator was displaced symmetrically under displacement control with respect to the neutral axis of the plate. The resulting displacement of the top surface of the plate was measured using a calibrated LVDT gauge. The actuator's travel was load-limited in both directions (up and down) by an imposed load-limit that corresponded to the desired outer-fiber maximum stress. More specifically, loading was controlled using a FlexTest-40 controller that allowed the actuator, before changing its direction of motion, to slow down momentarily as the load approached the prescribed limit. In other words, the actuator was displaced at the prescribed rate until the load-limit was reached at which point displacement was reversed at the same rate. Although most tests were performed at an outer-fiber center-point displacement rate of 0.1 mm/s, the cycle period varied from 4 to ~ 11 s and depended on the load-limit. Higher loads took longer to reach the limit.

Two series of experiments were performed. In the first, a stress amplitude of 0.7 MPa was applied and held constant. These tests were performed at three temperatures: -3°C, -10°C and -25°C; the outer-fiber center-point displacement rate was also varied, from 0.001 to 0.5 mm/s. About 200 cycles of the 0.7 MPa stress amplitude were applied prior to testing, to avoid short-time effects in the ice behavior and to stabilize hysteresis loops. However, no difference was registered during pre-loading. Samples were allowed to equilibrate to the test temperature for about 24 hours before testing.

In the second series of tests samples were subjected to cycling at different stress amplitudes, from 0.7 MPa to 2.1 MPa, while keeping the outer-fiber center-point displacement rate and temperature constant, at 0.1 mm/s and -10°C respectively. The highest stress level of 2.1 MPa is significantly greater than the flexural strength of non-cycled freshwater ice. In order to reach such high stress levels and to be able to cycle ice "safely" there (i.e., without fracturing), the following strengthening procedure was used: specimens were cycled for about 100 times at six levels of progressively higher stress amplitude, from ~±1.0 MPa to ~±2.2 MPa (see Iliescu et.al., 2017 for details).

Hysteretic behavior was analyzed through stress-strain loops to determine the effect of temperature, stress amplitude and outer-fiber center-point displacement rate. All strains and stresses are outer-fiber values.

The internal friction ϕ during cycling can be calculated based on the following approach suggested by Nowick & Berry (1972):

$$\tan\phi = \frac{\Delta W}{2\pi W} \qquad \textbf{[1]}$$

where ΔW is the energy per unit volume dissipated during a cycle (or the area enclosed by a stress-strain loop) and W is the maximum stored energy per unit volume during a cycle (area beneath the loading curve of a hysteresis loop). Numerical integration of unfiltered stress-strain data was implemented to calculate ΔW and W.

3. Results

3.1 *Effect **of Rate***

A set of tests at outer-fiber center-point displacement rates of 0.001 mm/s, 0.01 mm/s, 0.1 mm/s and 0.5 mm/s was used to explore the effect of the loading displacement rate on outer-fiber stress-strain hysteresis. Data were obtained for three different temperatures of -3°C, -10°C and -25°C and are listed in ***Table 1***. The sample was loaded for 10 cycles of equal stress amplitude of 0.7 MPa at each displacement rate except at the lowest rate 0.001 mm/s. At the lowest rate only four cycles were applied, due to the time constraint (period was ~ 10 min). ***Fig. 1*** demonstrates the effect of displacement rate on stress-strain behavior at -10°C**.** As can be seen from this figure and from ***Table 1***, greater energy dissipation is observed for lower loading rate. For the outer-fiber center-point displacement rates of 0.5 mm/s the behavior of the testing machine was not ideal as a great degree of load overshoot was obtained at the beginning. After some technical manipulations, we were able to produce loading with the desired constant load amplitude; however, the loading cycle could have a slightly different shape (as may be seen on the figure) and sometimes the load became uncontrolled for a while, leading to premature failure of the sample. Besides, sampling frequency was limited and, for the highest displacement rate of 0.5 mm/s, was not high enough for an accurate computation of dissipated energy during the loop. Consequently, results obtained at the displacement rate of 0.5 mm/s might be somewhat inaccurate. A few attempts to cycle the specimen at displacement rates of 1 mm/s were made; unfortunately, none of them was successful since samples broke due to the reasons mentioned above.

3.2 *Effect* ***of Temperature***

Fig. 2 shows the results of the loading at the outer-fiber center-point displacement rate of 0.1 mm/s. As can be seen, at -3°C the curve becomes strongly nonlinear owing to an increase in inelastic strain. At -25°C the stress-strain curve behaves almost elastically. ***Fig. 2*** and data in ***Table 1*** show greater dissipated energy as temperature increases. It can be noted that there is a more significant difference between -3°C and -10°C than between -10°C and -25°C.

3.3 *Effect* ***of Stress Amplitude***

Fig. 3 shows the results of an experiment in which the load was applied at an outer-fiber center-point displacement rate of 0.1 mm/s and at the temperature -10°C. The specimen received pre-testing as described in Section 2, followed by 10 cycles each of $\sigma_{\max}$ = ±0.7, ±1, ±1.3, ±1.5, ±1.7, ±1.9, ±2.1 MPa. Energy dissipated during the loop increases as stress amplitude increases; however, the maximum stored energy during a cycle also increases. It appears that internal friction is independent of the stress amplitude for the described testing conditions, as shown in **Fig. 4**. Whether internal friction is independent of stress amplitude at other temperatures for S2 ice is not known (more below).

4. Discussion

Total strain during the deformation caused by an applied external stress consists of elastic and inelastic components. Barring contributions from cracking, of which none was detected in these tests, inelastic strain may be viewed as a combination of plastic and anelastic components. Anelastic strain is ultimately fully recovered after removal of a transient load; plastic strain, conversely, is irreversible. Plastic strain (or sometimes termed dislocation strain) can be explained by the motion of dislocations (Granato & Lücke, 1956b).

According to Granato & Lücke (1956b), energy loss (at least in cold metals) during the deformation where dislocation-induced strain occurs, may be separated into two types: dynamic and static loss. Dynamic loss ϕ_i is usually observed in high megacycle range: it is frequency dependent and stress amplitude independent and is attributed to the phase lag between applied external stress and damped motion. Static or hysteretic loss ϕ_h is characterized by low frequencies and is proportional to the area confined by the stress-strain loop. Static loss is frequency independent and stress amplitude dependent.

On the one hand, there is an evidence of static loss in our results. As reported in (Granato & Lücke, 1956a), the dependence of ϕ_h on the strain amplitude ε_0 (total strain at maximum outer-fiber stress) should be described by a straight line in the form $\log(\varepsilon_0 \tan\phi_h)$ versus $1/\varepsilon_0$. Our experimental data follow linear dependency which is shown in ***Fig. 5***. It is important to mention, that ϕ_h should be calculated as $\phi - \phi_i$, but since ϕ_i cannot be obtained due to the limitation of data, ϕ is used instead. However, as mentioned in (Cole, 1990), this inaccuracy would not greatly affect the form of the results.

On the other hand, we suggest that there is a strong evidence of dynamic loss in our results. The internal friction as a function of frequency for different temperatures shown in ***Fig. 6***. The trend for all temperatures is that the internal friction of ice decreases with an increase in frequency, i.e. internal friction is frequency dependent. Besides, as was already mentioned, internal friction does not depend on stress amplitude (**Fig. 4**). Hence, both trends on **Fig. 4** and ***Fig. 6*** show the evidence of dynamic loss. To conclude, we might have obtained a mixture of dynamic and static losses since features of both arise.

One important thing to note is a difference in our results from those of Cole (1990) and Weber & Nixon (1996a). Based on our experimental data (**Fig. 4**), internal friction does not depend on stress amplitude, whereas in both of the works mentioned internal friction increases when stress amplitude rises. So, why in our experiments internal friction is independent of stress amplitude? To explain this discrepancy we will refer to the work done by Vassoille et al. (1978) on single crystals of ice. They reported that in the high-temperature range, internal friction becomes amplitude dependent. However, based on Figure 2 in their paper, we may clearly distinguish amplitude dependency only at temperatures -5.5°C and higher at strain amplitudes beyond $3*10^{-4}$. All the tests in Weber & Nixon (1996a) were conducted at -5°C which may explain why they observed strain amplitude dependency. Of the experiments by Cole (1990), unfortunately we did not find information about the testing temperature of corresponding experiments and therefore cannot make a fair statement regarding discrepancy in the results. Besides, Nowick & Berry (1972) mention that in metals the damping may not become amplitude dependent until the strain amplitude exceeds $10^{-5} – 10^{-4}$. In our experiments strain variation was from 1 to $5*10^{-4}$, which perhaps, is not enough for the activation of strain dependency.

The internal friction as a function of frequency for different temperatures is depicted in ***Fig. 6***. This trend compares favorably with the results of Weber & Nixon (1996a) who also studied the behavior of columnar S2 ice. The only difference is in the absolute values of internal friction. Our values of $\tan\phi$ are lower by about a factor of three. Our sense is that the difference is probably a reflection of the difference in experimental conditions. The experiments of Weber & Nixon (1996a) were conducted on samples with a notch so that extra energy dissipation during the cycle might have come from the crack opening. Unfortunately, information regarding the orientation of grains relative to the loading direction is not presented in their paper. However, based on the previous work (Weber & Nixon, 1996b), we might assume that the orientation was the same as in our tests. The experiments of Weber & Nixon (1996a) and Cole (1990) conducted on granular ice show the same trend of internal friction-frequency records up to 0.1 Hz; at higher loading frequencies, internal friction levels off. This difference in internal friction behavior might depend on the orientation of grains, since in granular ice grain orientation is random. As is well known (Schulson & Duval, 2009), the primary mechanism of plastic deformation of ice is through the basal slip. Absolute values of internal friction obtained by Cole (1990) are substantially greater than our values. A possible reason for the difference again may be referred to the test conditions (leaving grain orientation aside at this point), i.e. four-point bending versus uniaxial loading. In the case of uniaxial loading, greater volume of material is subjected to the highest stress and, hence, higher degree of dislocation initiation occurs. Consequently, one would expect greater internal friction for the uniaxial test setup. Besides, in four-point bending, material is stressed biaxially with an effective stress between one-third and one-half of the maximum outer-fiber stress, as discussed in Iliescu et al. (2017). As a result, effective stress for our experiments is lower than obtained by Cole (1990) and may have an impact on the internal friction. It is also worth noting that temperature has an influence on the internal friction, though it is substantially less than frequency.

To sum up, internal friction as a function of stress amplitude at different temperatures remains unclear for our experimental setup. More work is needed to explore whether temperature influences dependency between internal friction and stress amplitude for columnar freshwater S2 ice loaded in the described above manner.

5. Conclusions

We conclude, that energy dissipated during cycling increases with decrease of displacement rate and increase of temperature and stress amplitude. Internal friction increases with an increase of temperature and decrease of displacement rate and is independent of the stress amplitude.

Acknowledgements

This work was supported by the US Department of the Interior-Bureau of Safety and Environmental Enforcement (BSEE), contract no. E16PC00005.

References

Cole, D. M. (1990). Reversed direct-stress testing of ice: Initial experimental results and analysis. *Cold Regions Science and Technology*, *18*(3), 303–321.

Granato, A., & Lücke, K. (1956a). Application of dislocation theory to internal friction phenomena at high frequencies. *Journal of Applied Physics*, *27*(7), 789–805.

Granato, A., & Lücke, K. (1956b). Theory of mechanical damping due to dislocations. *Journal of Applied Physics*, *27*(6), 583–593.

Iliescu, D., Murdza, A., Schulson, E. M., & Renshaw, C. E. (2017). Strengthening ice through cyclic loading. *Journal of Glaciology*, *63*(240), 663–669.

Iliescu, D., & Schulson, E. M. (2002). Brittle compressive failure of ice: Monotonic versus cyclic loading. *Acta Materialia*, *50*(8), 2163–2172.

Nowick, A. S., & Berry, B. S. (1972). *Anelastic Relaxation in Crystalline Solids*. New York and London: Academic Press.

Schulson, E. M., & Duval, P. (2009). *Creep and fracture of ice*. Cambridge University Press, Cambridge.

Vassoille, R., Maï, C., & Perez, J. (1978). Inelastic Behaviour of Ice Ih Single Crystals in the Low-Frequency Range Due to Dislocations. *Journal of Glaciology, 21*(85), 375–384.

Weber, L. J., & Nixon, W. A. (1996a). Hysteretic Behavior in Ice Under Fatigue Loading. *Proc. 15th OMAE*, Florence, Italy, 75-82.

Weber, L. J., & Nixon, W. A. (1996b). Fracture toughness of freshwater ice – Part I: Experimental technique and results. *Journal of Offshore Mechanics and Arctic Engineering*, 118(2), 135–140.

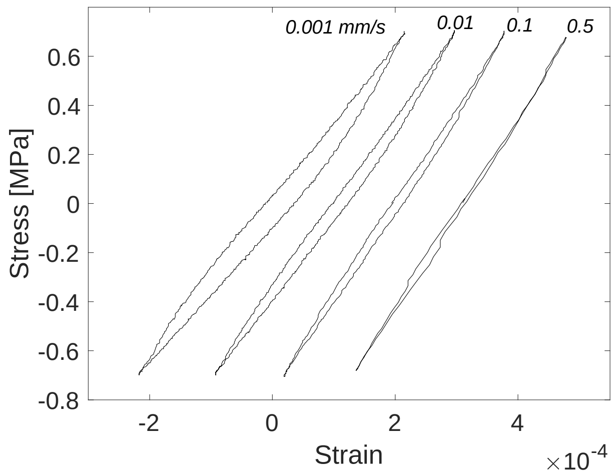

Fig. 1. Stress-strain records for hysteretic loops obtained through different displacement rates at temperature -10°C.

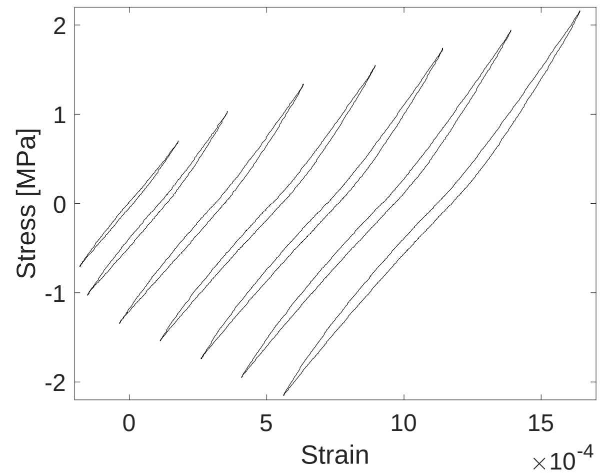

Fig. 3. Stress-strain records for hysteretic loops obtained through different applied external stress amplitudes at the displacement rate 0.1 mm/s and temperature -10°C.

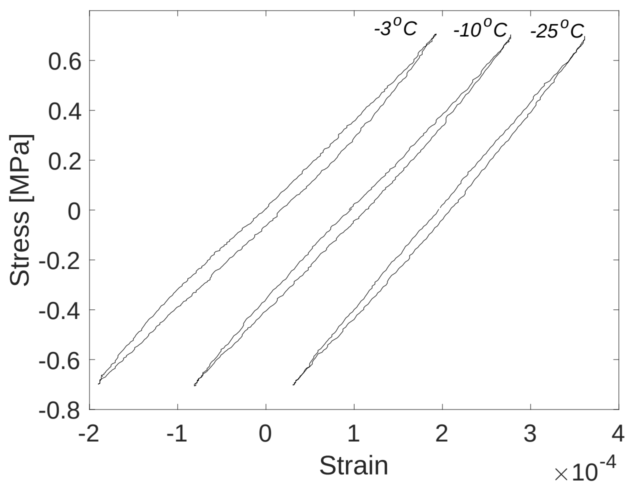

Fig. 2. Stress-strain records for hysteretic loops obtained through different temperatures at the displacement rate 0.1 mm/s.

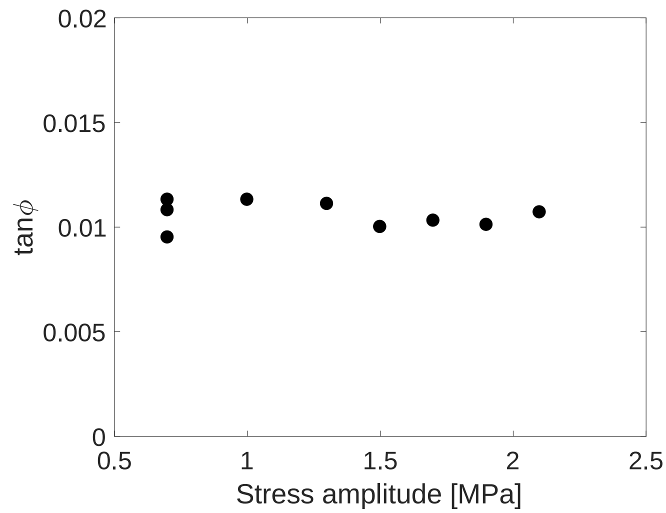

Fig. 4. Internal friction as a function of stress amplitude for the data shown in Figure 3.

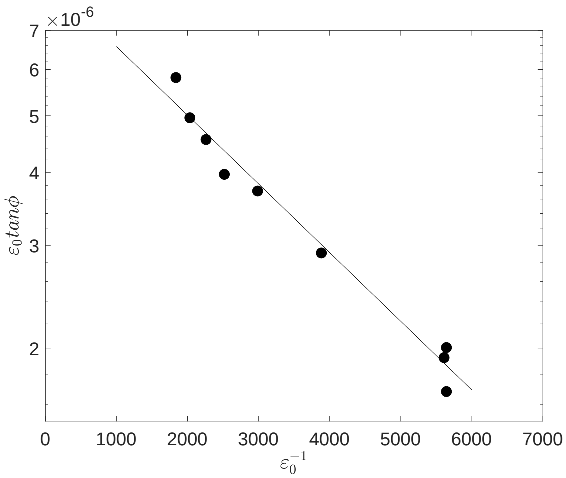

Fig. 5. A Granato-Lucke plot for the data shown in Figure 3.

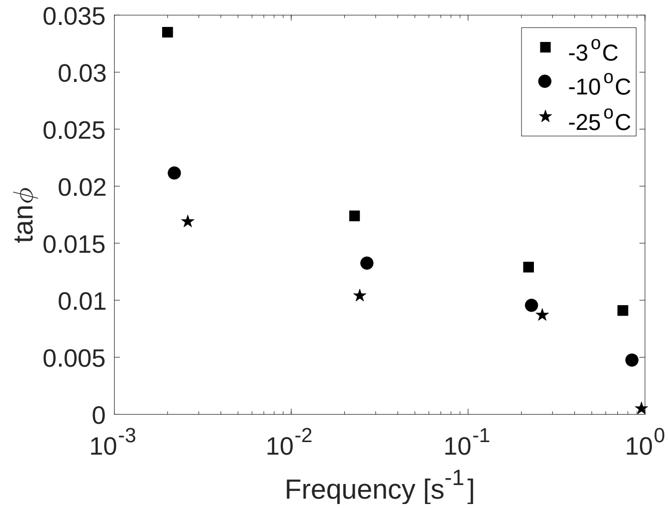

Fig. 6. Internal friction as a function of frequency for different temperatures and displacement rate of 0.1 mm/s.

Table 1. Data from cyclic loading experiments.

#	Temperature (°C)	Displacement Rate (mm/s)	Frequency (Hz)	Stress Amplitude (MPa)	Strain Amplitude ε_0 $\times 10^{-4}$	Dissipated Energy per loop per unit volume ΔW (J/m^3)	tan ϕ $\times 10^{-3}$
1	-10	0.5	0.85	0.7	1.8	6.8	4.7
2	-10	0.1	0.23	0.7	1.8	15.2	9.5
3	-10	0.01	0.027	0.7	1.9	22.9	13.2
4	-10	0.001	0.0022	0.7	2.2	41.3	21.1
5	-3	0.5	0.75	0.7	1.8	13.3	9.1
6	-3	0.1	0.22	0.7	1.9	22.3	12.9
7	-3	0.01	0.023	0.7	2.1	32.6	17.4
8	-3	0.001	0.002	0.7	2.5	78.7	33.5
9	-25	0.5	0.95	0.7	1.6	0.6	0.5
10	-25	0.1	0.26	0.7	1.7	12.7	8.7
11	-25	0.01	0.024	0.7	1.8	16.3	10.4
12	-25	0.001	0.0026	0.7	2.0	29.1	16.9
13	-10	0.1	0.19	1.0	2.6	36.8	11.3
14	-10	0.1	0.15	1.3	3.3	61.9	11.1
15	-10	0.1	0.12	1.5	4.0	74.7	10.0
16	-10	0.1	0.11	1.7	4.4	97.7	10.3
17	-10	0.1	0.10	1.9	4.9	120.2	10.1
18	-10	0.1	0.09	2.1	5.4	155.2	10.7
19	-10	0.1	0.24	0.7	1.8	17.2	10.8
20	-10	0.1	0.25	0.7	1.8	18	11.3

International Association for Hydro-Environment Engineering and Research
Supported by Spain Water and IWHR, China

24th IAHR International Symposium on Ice
Vladivostok, Russia, June 4 to 9, 2018

The Physical Characteristics of Consolidated Saline Ice: Results from Ice Tank Experiments

Mark Shortt, Peter Sammonds and Eleanor Bailey
Institute for Risk and Disaster Reduction, University College London, London, UK
C-CORE, St. John's, NL, Canada
mark.shortt.12@ucl.ac.uk

We present results from consolidation experiments on saline ice conducted at the Hamburgische Schiffbau-Versuchsanstalt (HSVA) Large Ice Model Basin (LIMB) in Hamburg, Germany. The aim was to investigate the strength and physical characteristics of freeze-bonds developed in a range of conditions encountered in rafted and ridged sea ice, by employing: 1) free floating ice compared with submerged ice and, 2) the presence or absence of a liquid layer. Stacks of two 1m^2 blocks of saline ice were used: 1) free-floating and submerged beneath the water surface and, 2) with a 3 mm liquid layer and with direct contact between the ice blocks. There were a total of four experiments, each left to consolidate for five days, during which the temperature and salinity evolutions were measured. By the end of the consolidation period the two direct contact experiments had consolidated sufficiently for full cored samples to be taken. Conversely, those experiments that contained a liquid layer were too weak to survive coring, despite an apparent freezing of the brine within the layer deduced via salinity measurements. Cored samples from each experiment were taken, from which salinity profiles were determined. The compressive strengths of samples from the direct contact experiments were also measured and compared to level ice. Both consolidated samples were weaker in compression than the level ice. The sample from the submerged experiment was considerably weaker than the sample from free-floating ice. The observations from the two liquid layer experiments support the necessity to distinguish between thermodynamic and full mechanical consolidation.

1. Introduction

Ridging and rafting are features that arise in regions of compression/shear in the Arctic sea ice cover. Ridge keels and rafted layers both comprise pieces of saline ice separated by liquid sea water which gradually freezes, resulting in bonding between constituent ice pieces and an overall strengthening of the feature in a process known as consolidation. When subjected to wind shear and/or ocean currents, these consolidated features may exert considerable loads on offshore structures or pose hazards to vessels operating in the region. From an engineering perspective, it is therefore necessary that the physical and mechanical behaviour of rafted and ridged sea ice are well characterized throughout the consolidation procedure. Of particular importance are the mechanical properties of the freeze bonds (F.B.s) that form between constituent ice pieces during consolidation as it has been suggested that F.B. strength governs the initial strength of consolidated ice rubble [*Ettema & Urroz* (1989)]. This paper details four experiments conducted to investigate the effect of two factors on the consolidation process: 1) free-floating vs. submersion beneath the water surface and, 2) a 3mm liquid layer vs. direct contact between the ice blocks. These conditions were chosen to cover a range of conditions encountered in rafted layers and ridge keels.

2. Experimental Methodology

2.1 Ice Tank Properties

The experiments were conducted over a four-week period at the Hamburgische Schiffbau-Versuchsanstalt (HSVA) Large Ice Model Basin (LIMB) in Hamburg, Germany, which has dimensions: 78 m x 10 m x 2.5 m and contains NaCl-doped water with a spatially varying salinity ranging between 6-8 ppt. These range of values are considerably lower than typically encountered in Arctic seas, but had the advantage of increasing the freezing temperature, thus expediting the consolidation process. Adjacent to the ice tank lies a cold room containing storage facilities and apparatus to prepare samples and investigate the mechanical and crystallographic properties of the ice. The structure of natural S-type sea ice was replicated by using ‘artificial full scale ice’, which was grown to a level thickness of approximately 15 cm before the experiments were conducted. The nominal air temperature was approximately -10°C for the duration of the experiments.

2.2 Direct Contact Experiments

The methodology was based on similar consolidation experiments described in *Bailey* (2011). The same lateral dimensions (1 m x 1 m) were used to provide a direct comparison to the results obtained in *Bailey* (2011) and to enable a sufficiently large area for a number of cored samples to be extracted for analyses. Four $1m^2$ blocks were cut from the level ice side-by-side such that a 4 m x 1 m channel was created, after which the blocks were manually stacked. To measure the temperature profiles of the ice blocks over the consolidation period, temperature strings, each containing four Resistance Temperature Detectors (RTDs), were frozen into the centre of each ice block. For the submerged experiment, weights were added on top in addition to a metal framework, which prevented lateral movement of the blocks beneath the waterline. A layer of polystyrene was added between the blocks and the framework to further insulate the experiment from the atmosphere and to prevent conduction between the ice and metal. A summary of the experimental arrangements for the two direct contact experiments is shown in Figure 1.

2.3 Liquid Layer Experiments
Following the completion of the direct contact experiments, the 3 mm liquid layer experiments were prepared. By this time, the level ice had reached a thickness of approximately 25 cm. The experimental set-up closely followed the direct contact experiments shown in Figure 1, but with two necessary alterations. Firstly, to provide the gap for the liquid layer, 3 mm thick Perspex spacers were frozen onto the surface of the lower ice blocks prior to assembly. Due to issues with the logging, the RTD strings could not be used in these experiments. The temperature evolution of the liquid layers was monitored using individual K-type thermocouples. For the submerged experiment, metal framework, polystyrene insulation and weights were added, as per the direct contact methodology.

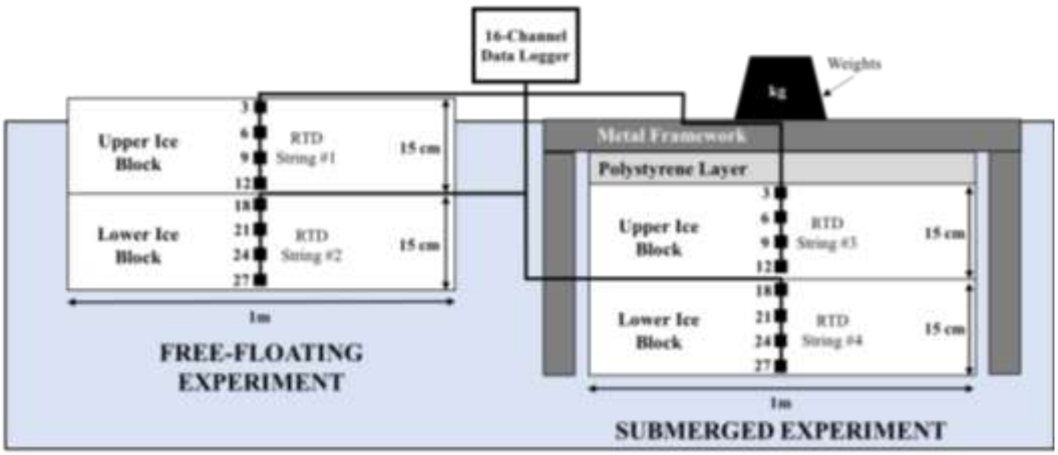

Fig. 1. Experimental arrangements for the free-floating and submerged experiments in direct contact. The liquid layer experiments followed the same basic arrangement, but with the changes described in-text. The numbers next to each RTD represents the depth in centimetres from the top surface of the upper ice block.

3. Results

3.1 Consolidation Time
Each experiment was left to consolidate for approximately five days. The state of consolidation was monitored using a combination of coring and drilling through the upper ice blocks to the F.B. layers. All cores were extracted using a 7 cm diameter auger. The extent of the consolidation was primarily deduced from the resistance experienced when drilling and the physical state of the subsequent cores. This was further investigated by drilling through to the F.B. layer and extracting brine using a pipette. The F.B. layer was considered fully frozen when brine could no longer be extracted. This was done for the two free-floating experiments, but was not possible in the submerged experiments.

The salinity of the brine measured in the liquid layers of both free-floating experiments increased over the initial consolidation period. At the beginning of the experiments, the salinities were the same as the surrounding water. After approximately one day, the salinities of both F.B. layers had increased to around 18 ppt. After 36 hours, it was no longer possible to extract brine from the F.B. layer in the free-floating direct contact experiment. For the free-floating liquid layer experiment, brine could no longer be extracted after 96 hours. After five days, the direct contact experiments had consolidated sufficiently for full cored samples to be taken. However, after the same amount of time, no cores from the liquid layer experiments remained intact, indicating that consolidation had not been reached.

3.2 Temperature Evolutions

Due to the previously mentioned issues with the logging, only the first 1600 minutes of the consolidation phase was measured. Furthermore, the temperature data over this time period was intermittent as the software crashed multiple times. Temperature profiles at different times over the first 1600 minutes of consolidation are shown in Figure 2. It should be noted that three of the RTD probes measured anomalously low temperature readings. This originated from instrumental error, as these RTDs were calibrated three months earlier than the others. These anomalous temperature readings are not shown in the plots in Figure 2. The temperature evolutions measured by the thermocouples in the liquid layer experiments are plotted in Figure 3.

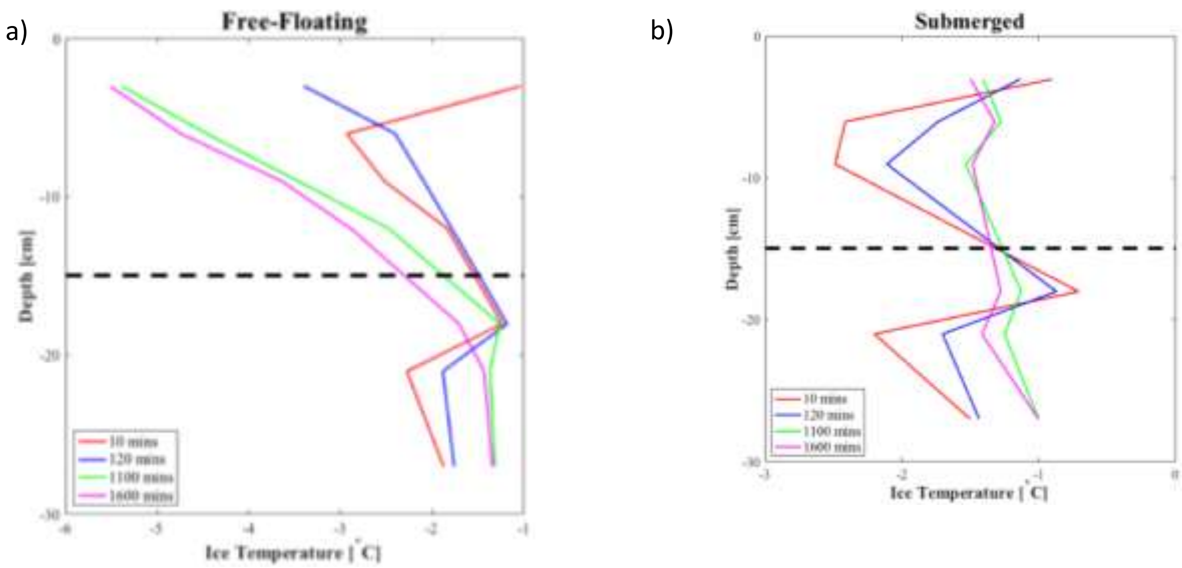

Fig. 2. Temperature profiles at different times over the first 1600 minutes of the consolidation period for a) free-floating direct contact experiment and b) submerged direct contact experiment. The black dotted line denotes the approximate location of the F.B. layer.

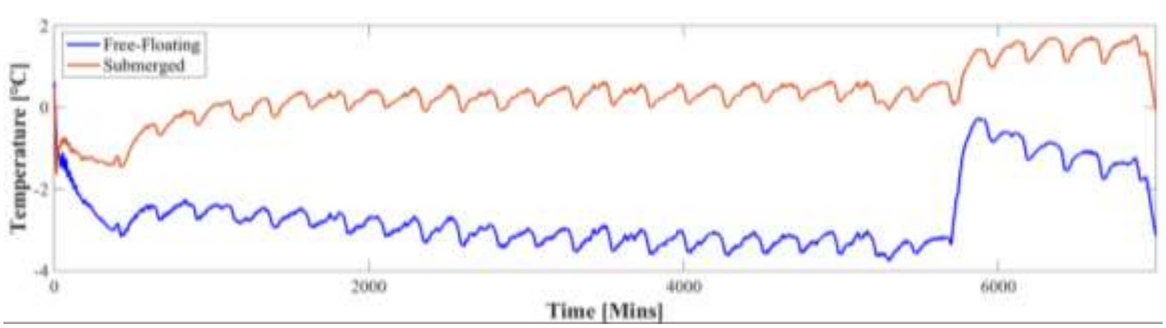

Fig. 3. Temperature evolution in time of the 3mm liquid layers in the two liquid layer experiments. The increase in temperatures measured just prior to 6000 minutes is due to a corresponding increase in the air temperature.

As shown in Figure 2, the temperature profiles in both the free-floating and direct contact experiments gradually become more linear as heat is redistributed throughout the thickness of the two ice blocks. However, 1600 minutes was not enough time for the temperature profiles to become fully linear. The free-floating experiments decrease in temperature at a faster rate than the submerged experiments due to exposure to the colder atmosphere, resulting in a greater amount heat conduction away from the ice compared to the submerged experiments. The temperature measured in the liquid layer of the submerged experiment remained at around the freezing point of the tank water, which ranged between -0.3°C and -0.5°C, depending on the exact salinity. This suggests that the liquid layer did not fully freeze over the consolidation period, supporting the observations that were made when coring.

3.3 Salinity Profiles

Salinity profiles were taken of the level ice and each consolidation experiment. It should be noted that even though the liquid layer experiments had not fully consolidated, it was still possible to take salinity profiles. Cores were cut into sections and melted down in plastic containers, and the salinity of the resulting brine measured using a salinity meter. The results are plotted in Figure 4.

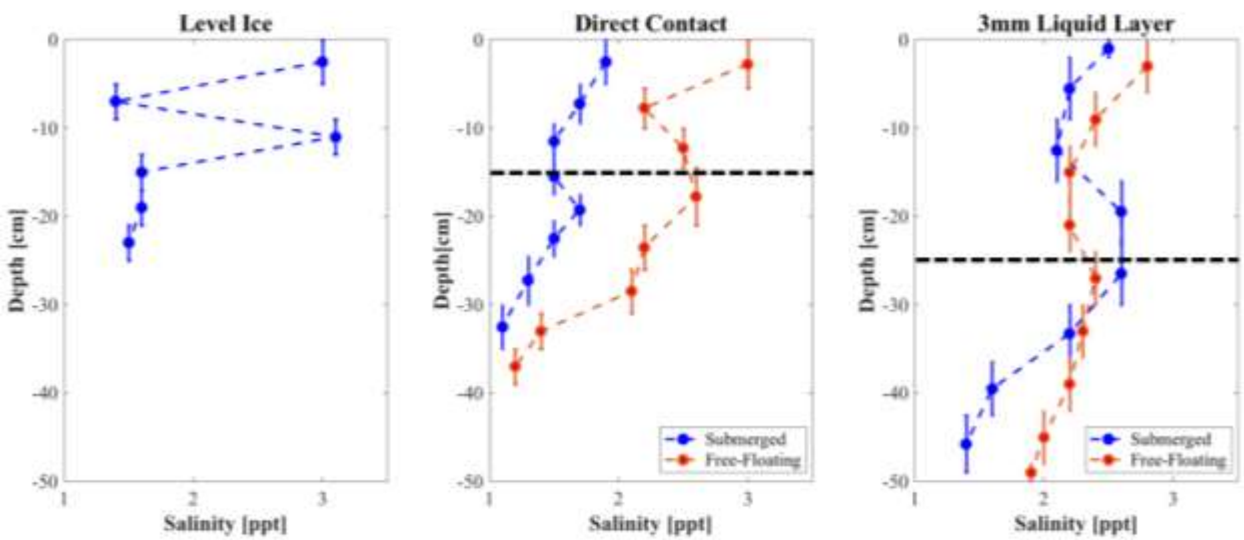

Fig. 4. Salinity profiles of the level ice and two direct contact experiments. The dotted black lines indicate the approximate positions of the F.B. layers. The vertical error bars denote the thickness of each section of the core

The salinity profile of the level ice differs from the expected C-shape typical of young sea ice, which has been attributed to brine drainage from sections of the core during extraction, transportation and preparation. This is supported by observing the salinity profiles from each experiment, which all exhibit approximately C-shaped distributions in the upper ice blocks. In each consolidation experiment, there is a peak in salinity at the approximate locations of the F.B. layers, which is consistent with the observations from drilling. The salinity in the lower ice block in each experiment gradually decreases with thickness in a relatively linear fashion. In theory, the salinity at the bottom of the lower ice block should exhibit a peak from newly formed, more saline ice. This disparity has been attributed to brine drainage from the lower sections of the cores during extraction.

3.4 Ice Structure

Any cores that remained intact were imaged under lighting provided by a polariscope. This gave an indication of the position and structure of the F.B. layer and any other visible features present in the samples. Photographs of typical intact cores from the two direct contact experiments are shown in Figure 5. There was an obvious 1cm thick layer in the free-floating sample (Figure 5a), which we believe corresponds to the F.B. layer. For the submerged ice (Figure 5b), the exact position and structure of the F.B. layer was ambiguous, due to the presence of an approximately 7cm thick high porosity band towards the centre of samples.

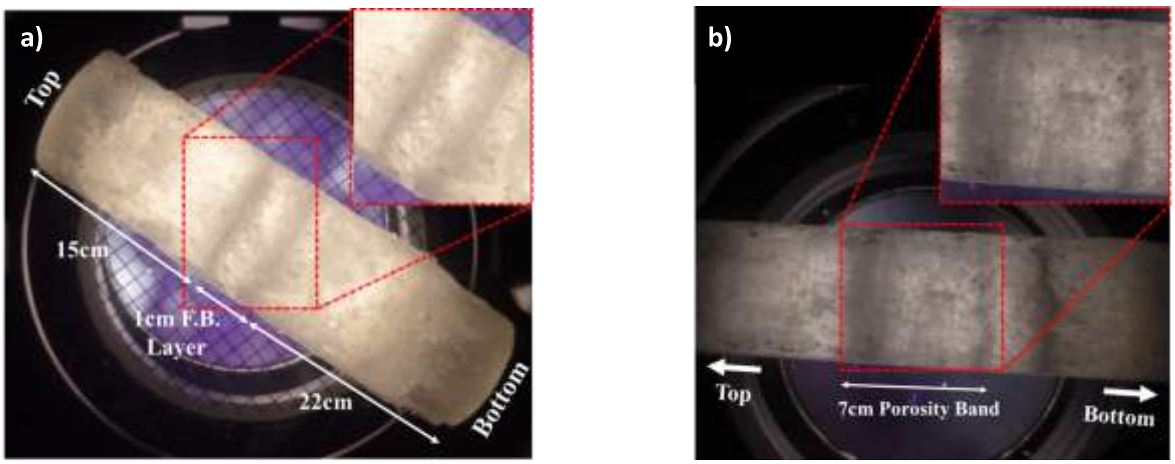

Fig. 5. Samples illuminated under polariscope from a) free-floating direct contact experiment and b) submerged direct contact experiment.

3.5 Compressive Strengths

The compressive strengths of the consolidated floes in the direct contact experiments were measured and compared to level ice using a 10 kN uniaxial load frame situated in the cold room. Due to the relatively low maximum load that could be applied by the uniaxial frame, the cored samples were cut to a smaller square cross-sectional area of 4 cm x 4 cm using a band-saw. The samples were orientated such that the F.B. layer was perpendicular to the loading axis. All tests were performed at a constant loading rate of approximately 5 mms^{-1}. Three compression tests were conducted – one for the level ice and each of the direct contact experiments. Relevant parameters for each sample tested under compression are given in Table 1.

Table 1. Parameters for the uniaxial compression tests: air temperature (T_{air}), ice temperature during test (T_{ice}), bulk ice salinity (S_{bulk}), maximum load (F_{max}) and compressive strength (σ)

	Length [cm]	T_{air} *[°C]*	T_{ice} *[°C]*	S_{bulk} *[ppt]*	F_{max} *[kN]*	σ *[MPa]*
Level Ice	10	-8.0	-6.6	-	4.65	2.91
Free-Floating	10	-11.2	-4.2	1.3	2.78	1.74
Submerged	13	-8.9	-10.5	-	1.11	0.70

The level ice was strongest, with a measured strength of σ_{level} = 2.91 MPa. The free-floating direct contact sample was next strongest, but was 60% the strength of the level ice. Despite possessing a lower ice temperature, the submerged direct contact sample was considerable weaker: 24% the strength of the level ice, and 40% the strength of the free-floating sample.

4. Discussion

The initial thickness of the ice blocks in the liquid layer experiments were approximately 10 cm thicker than in the direct contact experiments, which acted to increase the time for heat diffusion through the thickness of the ice blocks. Additionally, the presence of a thicker liquid layer meant a greater amount of total heat transfer to the surrounding ice would have been required for full freezing. Increased consolidation time with liquid layer size has been observed in previous thermodynamic models [*Bailey et al.* (2010)] and in the laboratory [*Bailey et al.* (2012)].

Increased salinity of the F.B. layer over the initial consolidation period has been previously documented [*Marchenko & Chenot* (2009), *Bailey et al.* (2012)] and results from both brine drainage from the upper block and salt rejection during freezing. The salinity of the liquid layer can provide an indication of the state of consolidation. *Bailey et al.* (2012) distinguish between thermodynamic consolidation: where the ice has physically bonded, and mechanical consolidation: where the F.B. strength stabilises and the salinity of the layer becomes constant. Using these definitions, it may be concluded that after 96 hours the free-floating liquid layer experiment may have thermodynamically consolidated, since no brine could be extracted from the liquid layer. However, after five days the F.B.s were too weak to survive coring, suggesting that the strength had not yet stabilised, and thus mechanical consolidation had not been reached.

The F.B. layer in the free-floating experiment in direct contact measured approximately 1cm, which was thicker than expected. *Bailey* (2011) also found a thicker F.B. layer (around 2 cm for an anticipated 3mm liquid layer) in the similar HSVA consolidation experiments which was attributed to the twisting of thermistor cables within the liquid layer, which acted to increase the gap above the anticipated 3mm thickness. It is possible that something similar may have occurred in the direct contact experiments. Indeed, the cables for the lower RTD strings were attached to Perspex and frozen onto the top surface of the lower ice blocks prior to assembly, which may have acted to increase the thickness of the gap between the two ice blocks. The high porosity band present in the submerged direct contact samples probably corresponds to a 7-8 cm thick brine porous layer at the base of the level ice, which was revealed when taking vertical thin sections.

The free-floating direct contact experiment was essentially a rafted ice set-up, and thus it is suitable to compare the strength result to previous studies on the compressive strength of rafted sea ice. *Jizu et al.* (1991) note that the strength of rafted ice is considered to be 10-20% weaker than level ice, which is still proportionately stronger than measured in this experiment. However, *Poplin & Wang* (1994) found the average compressive strength of vertically orientated rafted sea ice to be approximately 40% the strength measured for landfast sea ice. The submerged ice was considerably weaker in compression than the other two types of ice. This was true even though the ice temperature under testing was several degrees colder than the other two samples. The low compressive strength may be due to the presence of the high porosity band that constituted a large proportion of the sample. The compressive strength of columnar saline ice is found to decrease with increasing total porosity [e.g. *Moslet* (2007)]. It is interesting to note the different failure mechanisms of the samples under compression. The level and free-floating samples exhibited multiple axial splitting, typical of saline ice loaded vertically under unconfined uniaxial compression at high strain rates [e.g. *Kuehn & Schulson* (1994), *Sammonds et al.* (1998)]. In contrast, the submerged ice failed catastrophically within the top section of the sample, above some point in the high porosity layer. The different failure mode observed in the submerged sample may have occurred because the microstructure within the porosity band was different from the surrounding columnar level ice.

5. Conclusions

Consolidation experiments were performed at the HSVA LIMB to investigate the effect the effect of an atmospheric heat flux and liquid layer on the consolidation of two $1m^2$ blocks of saline ice. The physical and mechanical properties of the ice in each experiment were measured and compared to level ice. After five days, the experiments in direct contact had mechanically consolidated, but the liquid layer experiments had not, despite reaching a state of apparent thermodynamic consolidation in the case of the free-floating experiment.

Acknowledgements

The work described in this publication was supported by the European Community's Horizon 2020 Research and Innovation Programme through the grant to HYDRALAB-PLUS, Contract no. 654110. The authors would like to thank the Hamburg Ship Model Basin (HSVA), especially the ice tank crew, for the hospitality, technical and scientific support and the professional execution of the test programme in the Research Infrastructure ARCTECLAB. We would like to thank Sally Scourfield for providing the opportunity to conduct these experiments and Ben Lishman, Aleksey Marchenko and Samantha Buzzard for their assistance over the experimental period.

References

Bailey, E., D. L. Feltham, P. R. Sammonds, 2010, A model for the consolidation of rafted sea ice, Journal of Geophysical Research, 115.

Bailey, E., 2011, The consolidation of rafted sea ice, PhD thesis, University College London

Bailey, E., Sammonds, P., Feltham, D.L., 2012, The consolidation and bond strength of rafted sea ice, Cold Regions Science and Technology, 83-84, 37-48.

Ettema, R., Urroz, G. E., 1989, On internal friction and cohesion in unconsolidated ice rubble, Cold Regions Science and Technology 16, 237-247.

Jizu, X., S. Qingzeng, S. An, F. Yunlin, L. Tongkui, 1991, Sea Ice Engineering in China, Journal of Coastal Research, 7(3), 759-770.

Kuehn, G. A., Schulson, E. M., 1994, The mechanical properties of saline ice under uniaxial compression, annals of glaciology, 19, 39-48.

Marchenko, A., Chenot, C., 2009. Relegation of ice blocks in the water and on the air. In: Proc. of the 20th Int. Conf. on Port and Ocean Eng. under Arctic Conditions (POAC), Luleå, Sweden. Vol. POAC09-67.

Moslet, P. O., 2007, Field testing of uniaxial compression strength of columnar sea ice, Cold Regions Science and Technology, 48(1), 1-14.

Poplin, J. P., A. T. Wang, 1994, Mechanical properties of rafted annual sea ice, Cold Regions Science and Technology, 23, 41-67.

Sammonds, P. R., Murrell, S. A. F., Rist, M. A., 1998, Fracture of multiyear sea ice, Journal of Geophysical Research, 103(21), 795–721, 815.

International Association for Hydro-Environment Engineering and Research

Supported by Spain Water and IWHR, China

24th IAHR International Symposium on Ice
Vladivostok, Russia, June 4 to 9, 2018

Field Observation of Ice Flow in the Abashiri River

Yu INAMI [1), Hiroshi YOKOYAMA [1), Hiroki YABE [1), Shunichi MAEDA [1) and Yasuhiro YOSHIKAWA [2)

[1) Civil Engineering Research Institute for Cold Region
1-3-1-34 Hiragishi, Toyohira Ward, Sapporo, Japan, 062-8602
inami-y@ceri.go.jp
yokoyama-h22ab@ceri.go.jp
yabe-h@ceri.go.jp
maeda-s22ae@ceri.go.jp
[2) Kitami Institute of Technology,
165 Koencho, Kitami, Japan, 090-8507
yoshi@mail.kitami-it.ac.jp

On midwinter, ice cover and anchor ice occur in rivers in cold regions. Therefore, river in cold region has problems of uncertain H-Q curve and collision to the dike by ice sheet. In addition, ice jam affects the water-intake and ice jam causes a rise in water level. However, actual phenomenon is not observed enough and there is less knowledge.

It is the first-class river that the Abashiri River flows into the Sea of Okhotsk. In Abashiri River, special bank installed downstream deteriorate multiply by ice sheet collision and salt damage. The authors had performed field observation in order to clarify the ice flow condition in the Abashiri River. In addition, we had done 2 dimensional-unsteady flow numerical calculation.

This calculation indicated that it is likely to be a source of river ice because velocity is low and easy to stagnate at the lake. And it was revealed that it is conceivable that the risk of rising water level will increase, such as ice jam because the river ice is flushed when it floods.

1.Introduction

In the rivers in cold regions, ice cover, ice sheets, and anchor ice form and ice flow in the rivers occur during the severe cold season (Photo 1). Such ice-related river conditions cause problems including low accuracy of the HQ curve and collision of ice against embankments. Ice jams affect water intake, and water level increase occurs because of decreased river discharge capacity from ice jams. However, river ice related phenomena have not been sufficiently observed, and knowledge of river ice has been insufficient.[1, 2, 3)]

The Abashiri River in Abashiri City of Hokkaido is a Class A river that flows into the Sea of Okhotsk (Figs. 1, 2). Compound deterioration from ice collision, salt damage, and frost damage, of the special embankment at the lower reaches of the Abashiri River has been reported. The Abashiri River has Lake Abashiri between KP 7.4 and KP 18.0. The elevation of the lake surface is about 0m. When the tide water level at the river mouth exceeds the water level of the lake, reverse flow occurs. Therefore, the flow regime of the Abashiri River is complex under the influence of the tide. Ice sheet is a type of suspended material, and the ice sheets are carried by the flowing river water and collide against the bank revetment. To understand the movement of ice sheets, it is necessary to examine the relationship between the flow regime and the flow of ice sheets. Furthermore, the relationship between the flow regime and formation and melting of river ice has been pointed out. Yoshikawa et al. reported that the river ice tends to form in a river section where the bed gradient is small, flow velocity is low, the water depth is great, and river width is narrow. Because at such location, stagnation and jamming of river ice tend to occur. In light of the above, it is understood that clarification of the flow regime of the Abashiri River is necessary for elucidation of a series of process from formation of ice sheets to flowing down of the ice sheets to collision of ice sheets against the revetment.

To clarify the flow regime and ice flow of the Abashiri River, the authors conducted an onsite observation using a fixed-point camera and an acoustic Doppler current profiler (ADCP). The timings of freezing and melting were investigated by examining the movies taken using the fixed-point camera and the meteorological data. The flow velocity of the river ice was also investigated using the velocity data obtained using the ADCP. To understand the spatiotemporal flow regime of a river section between the river mouth (KP 0) to Hongo Water Level Observation Station (KP 21.7), which includes Lake Abashiri, a reproduction calculation for the flow field and the formation and melting of ice sheets was done by using the one-dimensional unsteady flow calculation (CERl1D).

Photo 1. Ice sheet at the Abashiri river

2.Onsite observation

2-1.Outline of the Abashiri River

The Abashiri River is a class A river, which originates in Mt. Ahoro of the Akan Mountain Range, flows northward and into Sea of Okhotsk (Fig 1, 2). The river has Lake Abashiri at the section from about KP 7.4 to KP 18.0. At the high tide, the seawater flows back into the lake, because the elevation of the lake surface is 0m. The basic data for the Abashiri River and Lake Abashiri are shown in Table 1. For the Abashiri River, damages that are specific to the rivers in cold regions have been reported; they include intrusion of river ice into the pollution control fences and compound deterioration from ice collision, salt damage, and frost damage of the special embankment at the lower reaches.

Fig. 1. Locations of Abashiri River and Vladivostok

Fig. 2. Location of Abashiri River (details)

Table 1. The basic data for the Abashiri River and Lake Abashiri

Abashiri River	
Length	115 km
Basin	1380 km^2
Average discharge	13.96 m^3/s
Lake Abashiri	
Catchment area	32.28 km^2
Max depth	16.8 m
Average depth	6.1 m
Surface elevation	0 m

Photo 2. Video camera (KP 3.1, right bank)

2-2.Outline of the onsite observation

Studies and knowledge on the ice flowing down the river have been insufficient. However, clarification of amounts of river ice that flow down the river and identification of the location where the river ice is formed are of engineering importance. To understand the behavior of river ice that flows down a river, we installed a video camera with infrared lighting (WV-SPW631LJ, Panasonic) on the right bank, at KP 3.1, of the Abashiri River (Photo 2). The period for movie shooting was from 13:00PM on February 24 to 10:47AM, May 24, 2017.

2-3.Results and discussion

The time varying flow condition of river ice will be discussed by using the movies taken by the fixed-point camera. The daily cycle of river ice was determined by using the movies taken from 13:00 PM, February 24 to 24:00 PM, February 25. The air temperature and the snowfall condition (with/without) are shown in Fig 3. The air temperature data used were from Abashiri Meteorological Observatory. The river was not frozen at 13:00PM on February 24, when movie shooting started. Flow of river ice was not observed at this time. Snow started falling at 13:17 PM, and ice flowing down the river was observed at 14:00 PM. Snowfall intensity became low around 16:30 PM. However, the flowing ice was continuously observed. The river froze over at 00:30 AM, February 25. The air temperature rose to 0.7 at 12:00 PM, February 25. The river ice started to melt around 13:30 PM. The river water did not freeze again during that day. In light of the above, it was understood that the river ice is formed with the decrease in the air temperature and the river water freezes. Ice melting starts when the air temperature rises during the day. It was suggested that falling snow is the source of river ice and flow of river ice starts some time after the start of snowfall.

The examination result is shown based on the movies taken on March 4. Thin ice layer was seen around 2:00 AM, and ice sheets flowing down the river were seen around 8:00 AM. During this time, snowfall was not recorded. It was suggested that the thin ice layers formed in the reaches upstream from the observation point developed into ice sheets while they were flowing down the river. The flow of ice sheets stopped around 14:00PM. The air temperature at this time was low; therefore, it was thought that the absence of ice sheets at the observation point was not because the ice melted away, but because the ice sheets formed upstream from the observation point had all flowed down. When snow started to fall at 16:00 PM, ice sheets started to flow down again. The second flow of ice sheets was thought to be from snowfall.

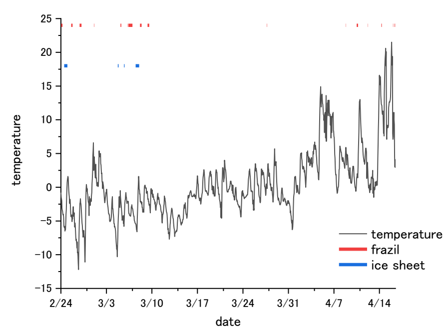

Fig. 3. Air temperature and snowfall

3.Reproduction calculation

3-1.Governing equation

For the calculation model, the one-dimensional river variation calculation model proposed by Yoshikawa et al. was used. This model consists of calculations treating the river flow, river ice flow, river water temperature, the formation and melting of ice sheet, and breaking of river ice. River ice is roughly categorized into two types: a hard ice sheet and frazil ice underlying the ice sheet. In this calculation model, however, river ice is categorized into a fixed hard ice sheet and flowing ice (including broken ice sheet). Generation of frazil ice from decreasing air temperature and from snowfall, ice formation from frazil ice and melting, and salinity intrusion are not considered in this model.

3-1-1.Flow calculation

The one-dimensional river ice change calculation model proposed by Yoshikawa et.al[1, 2, 3)] was used. For calculating the flow, the equation of continuity and equation of motion were used. The increase and decrease in the river discharge in relation to the formation and melting of ice sheets and the increase and decrease in the amount of flowing river ice were considered by using the equation of continuity. The calculation was done in the explicit difference method, in which the dependent variables are spatially arranged in a staggered pattern and the leap-frog time scheme was used.

For calculating river water flow, the equation of continuity [1] and the equation of motion [2] were used. For river ice flow, the equation of continuity [3] and the equation of motion [4] were used.

$$\frac{\partial A_w}{\partial t} + \frac{\partial Q_w}{\partial x} + \frac{\rho_i}{\rho_w}\frac{\partial A_{is}}{\partial t} = 0 \qquad [1]$$

$$\frac{\partial Q_w}{\partial t} + \frac{\partial}{\partial x}\left(\frac{Q_w^2}{A_w}\right) + gA_w\frac{\partial}{\partial x}\left(z + h_w + \frac{\rho_i}{\rho_w}\left(h_{is} + h_{if}\right)\right) + \frac{gn_b^2 u_w^2 S_w}{R_w^{1/3}} + \frac{\rho_i}{\rho_w}\frac{gn_i^2 u_i^2 S_i}{R_i^{1/3}} = 0 \qquad [2]$$

$$\frac{\partial A_{if}}{\partial t} + \frac{\partial Q_{if}}{\partial x} - \frac{\partial A_{is}}{\partial t} = 0 \qquad [3]$$

$$\frac{\partial Q_{if}}{\partial t} + \frac{\partial}{\partial x}\left(\frac{Q_{if}^2}{A_{if}}\right) + gA_{if}\frac{\partial}{\partial x}\left(z + h_w + \left(h_{is} + h_{if}\right)\right) - \frac{gn_i^2 u_i^2 S_i}{R_i^{1/3}} = 0 \qquad [4]$$

Where, A (m^2): flow area of the river water, area of flowing river ice, and area of ice sheet; Q (m3/sec): discharge and amount of flowing river ice; z (m): riverbed elevation; h (m): thickness; n ($sec/^{1/3}$): Manning's roughness coefficient; u (m/sec): velocity in the longitudinal direction of the river; S (m): wetted perimeter; R (m): hydraulic radius; ρ_w (kg/m^3): 999.8 was given as the density of water; ρ_i (kg/m^3): 917.4 was given as the density of ice. t (sec): time; x (m): distance; g (m/sec^2): gravitational acceleration of 9.8. The subscript w (water) represents the value regarding river water; *is* (ice sheet) represents the value regarding ice sheet; *if* (ice flow) represents the value regarding flowing ice; and i (ice) represents the value regarding ice, which is expressed as $h_i = h_{is} + h_{if}$.

3-2.Result

3-2-1. Comparison between the value measured onsite and the calculated value

For the boundary conditions, the discharge at the Hongo point (KP 21.7) was used as that for the upstream end and the water level at Abashiri Port (KP 0) was used as that for the lower stream end. The measured discharge data at Hongo had not been published at the time of data analysis; therefore, the authors used the HQ equation for converting the water level data at Hongo into discharge. For the water level at Abashiri Port, the values published by the Meteorological

Agency were used. The water level data and the river channel data used in this calculation employ the Tokyo Peil (T. P.) as 0m. The water levels measured at Hongo and the calculated values are shown in Fig 4. From this figure, the peak water level does not reach to the measured value; however, the normal time water level, the water level during the flooding from 11:00AM to 12:00PM on February 4, and the water level during the flooding from 11:00AM to 12:00PM on February 21 were reproduced satisfactorily. The mean square error for these values was 0.054m. In light of the above, the given discharge is said to be appropriate.

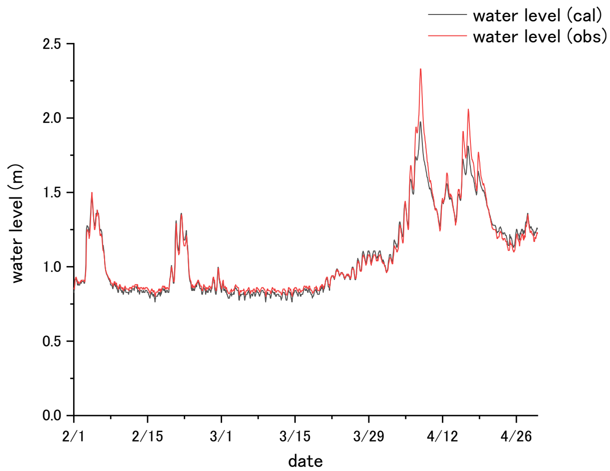

Fig. 4. Measured and calculated water levels at Hongo

3-2-2.Spatial flow regime

The spatial flow regime of the area subject to the calculation is shown in Fig 5. The water level of Lake Abashiri was constant at roughly 0m during the period subject to the calculation. In the part of the Abashiri River immediately downstream from the lake to Abashiri Port, which has the downstream end of the calculation section, was under the influence of tides in Abashiri Port, which had been set as the boundary condition for the downstream end. This section is also under the influence of the changes in the discharge at Hongo point, which was the boundary condition of the upstream end of the calculation section. In the part of the river upstream from the lake where the water level is nearly constant, the influence from the sea tide is very small. The discharge in this part changes with the changes in discharge at the Hongo point which was the upstream-end boundary condition. The spatial velocity regime of the area subject to the calculation is shown in Fig 6. The flow velocity in Lake Abashiri was about 0m/sec during the period subject to the calculation. Therefore, it is thought that Lake Abashiri has a long residence time. This tendency is similar at the flood. In the part downstream from the lake, the high flow velocities were observed in the section from KP 1.8 to KP 2.0, at KP 2.7, and KP 3.6. These three locations are narrow sections. High flow velocities were also observed at KP 6.4, which is a bend. In the numerical calculation, the water level of Abashiri Port did not exceed the water level of Lake Abashiri; therefore, reverse flow did not occur. However, flow of river ice from the downstream to the upstream of the video camera was observed several times.

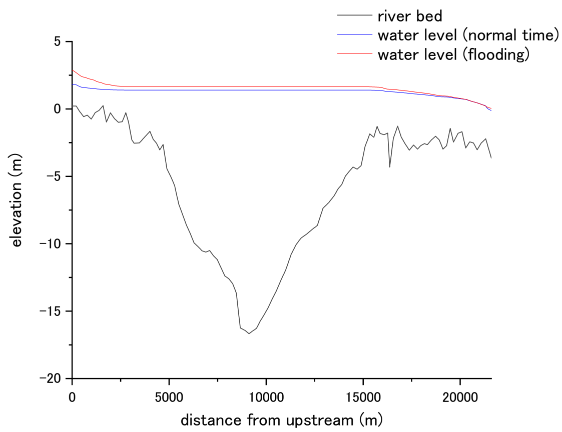

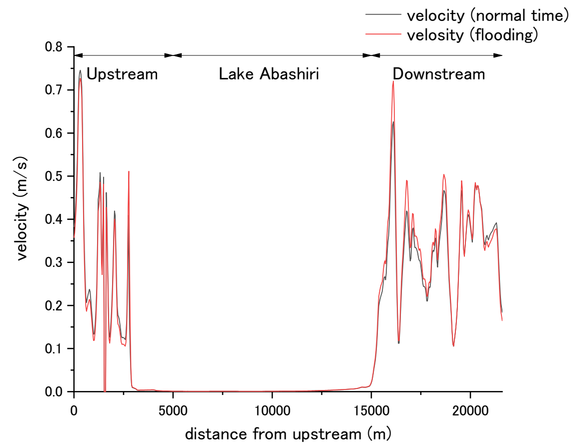

Fig 5. The longitudinal profile of water level at normal time and that at flooding

Fig 6. The longitudinal profile of water flow velocity at normal time and that at flooding

4.Discussion

4-1. Comparison between the flow velocity of ice sheet and the flow velocity of river water determined from the movies

The flow velocity of ice sheets, which was determined from the movies and the flow velocity of the river water determined from the numerical calculation were compared. In Fig 7, it was found that the calculation underestimated the flow velocity. The reasons for this underestimation was thought to be the following: the calculated values were the values averaged in the direction of the water depth, the flow velocity of ice sheet was the flow velocity of river water in the surface layer, and the wind drove the flow velocity of ice sheet greatly. The correlation coefficient for the observed flow velocity of ice sheet and the calculated flow velocity of the river water was 0.657.

4-2. Sensitivity analysis for the ice thickness

The calculation results for formation and melting of ice sheet are shown in Fig 8. It is understood that the ice sheet is not easily formed in the part upstream from Lake Abashiri. The river width in this section is narrow; however, the riverbed gradient is great and the flow velocity is relatively high, which prevents ice sheet from forming easily. In contrast, ice sheets were observed to form in Lake Abashiri. In the lake, the flow velocity is low and the water tends to stagnate, which promoted formation of ice sheets. In the river section downstream from Lake Abashiri, where, similar to the conditions in the section upstream from the lake, the river width was narrow and the flow velocity was relatively high; however, ice sheets were seen to form. The examination in this study is an Eulerian examination, in which formation and melting of ice sheet at one location are examined in relation to the changes in the conditions including air temperature and water temperature. It is not a Lagrangian examination, in which a given flowing ice sheet is followed from its formation to melting. Therefore, that existence of ice sheets flowing down in the downstream section from the lake does not directly indicates that the ice sheets formed in the lake are flowing down. However, the flow velocity vector is from the lake toward Abashiri Port. In light of this, it can be thought that the ice sheets formed in the lake were flowing into the river section downstream from the lake.

A river ice sheet level and water level in the Lake Abashiri are equal after the flood because river ice in Lake Abashiri flowed down with the flood. From these, it is the situation that water level rising and ice jam occur easily at the flood, There is a danger that the water level will rise further.

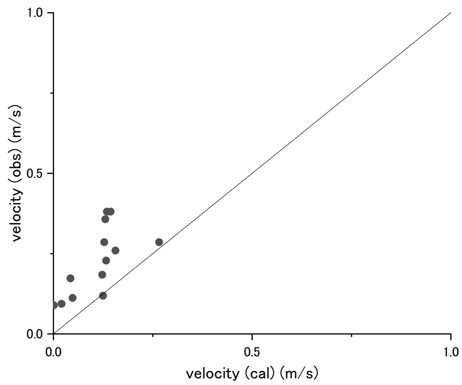

Fig 7. Comparison between the ice sheet velocity and flow velocity

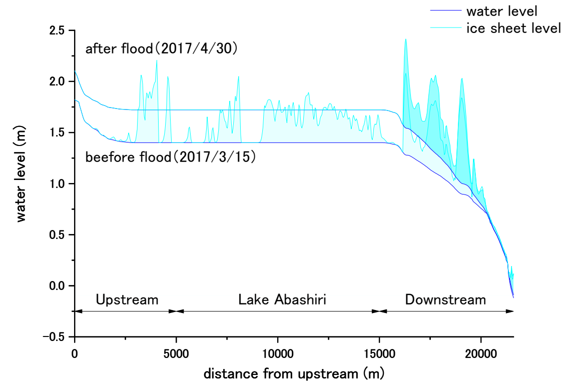

Fig 8. The longitudinal profiles of riverbed elevation, water level, and river ice surface

5.Conclusion

- As the temperature decreases, river ice is formed and frozen. It is shown that ice melting begins with rising temperature during the day. It was also suggested that snowfall is a source of river ice and flow of river ice begins after snowfall.
- It is likely to be a source of river ice because velocity is low and easy to stagnate at the lake.
- It is conceivable that the risk of rising water level will increase, such as ice jam because the river ice is flushed when it floods.
- The mending part is likely to clog the ice sheet and ice sheet forms.
- By Eulerian analyzing the ice sheet formation and flowing down, it was possible to grasp the spatial characteristics in the research area.

References

Yoshikawa Y., Watanabe Y., Hayakawa H. and Hirai Y. (2011). A Study of Ice Break and Ice Flow during River Ice Breakup, *Journal of Hydraulic Engineers*, Vol.67, No.4, pp.I_1075-I_1080 (in Japanese)

Yoshikawa Y., Watanabe Y., Hayakawa H. and Hirai Y. (2012). The Phenomenon of Breakup in a Frozen River and Development of a Practical Formula for Ice Sheet Thickness Calculation, *Journal of Hydraulic Engineers*, Vol.68, No.1, pp.21-34 (in Japanese)

Yoshikawa Y., Kuroda Y., Abe T., Toyabe T., Park H. and Oshima K. (2016). Study on the ice-jam occurrence based on hydraulic experimentation, *Proceedings of the 23rd IAHR International Symposium on Ice*

Shimizu Y., Fujita M., Hirano M., Yamada T. (1997). Calculation of Density Current in Abashiri Lake and Abashiri River, *Journal of Japan Society of Hydrology & Water Resources*, Vol.10, No.1, pp.44-55 (in Japanese)

Liu L, Li H and Shen H. T. (2006). A Two-Dimensional Comprehensive River Ice Model, *Proceedings of the 18th IAHR International Symposium on Ice*

Yoshikawa Y., Yasuda H., Watanabe Y. (2007). Impact of a Mesh Structure on Salinity Intrusion in Abashiri River, Vol.13, pp.7-12 (in Japanese)

Flow Resistance of Breakup Ice Jams

Lin Fan[1] , Zeyu Mao[2], and Hung Tao Shen[3]
[1] *Development Research Center, Ministry of Water Resources*
Haidian, Yuyuantan S Rd, Beijing,China
l-fan11@tsinghua.org.cn
[2] *Department of Hydraulic Engineering, Tsinghua Universityб Beijing, China*
maozeyu@mail.tsinghua.edu.cn
[3] *Department of Civil and Environmental Engineering, Clarkson University*
Potsdam, NY 13699-5710, USA
htshen@clarkson.edu

Empirical methods have been used for calculating the flow resistance of river ice jams. The friction coefficient or Manning's coefficient has been suggested to vary linearly with the jam thickness or the ratio of jam thickness to flow depth. This study exams the flow resistance due to the seepage flow through the jam and the resistance due to the shear stress on the undersurface of the jam. It shows that the resistance due to the seepage flow is an important part of the flow resistance, especially for the portion of the jam where the thickness is very large, such as the part near the jam toe.

1. Introduction

Surface ice jams are usually accompanied by a rapid water level rise due to the blockage effect resulting from the thickness and hydraulic resistance of surface ice floe accumulations. Due to the difficulty in obtaining the jam thickness profiles in the field the calibration of ice jam model parameters often relies on the observed water levels. Since the water surface profile is affected by both the jam thickness and the flow resistance, it is possible to reproduce the observed water surface profile even if the predicted jam thickness profile is in error (Healy and Hicks, 1999). This shows the need of a better understanding on the flow resistance of ice jams.

Based on field data, Nezhikhovskiy (1964) related Manning's roughness coefficient n_i to the flow depth under the jam and the jam thickness for ice covers formed by accumulations of ice floes, dense slush, or loose slush. Beltaos (1993) developed an equation for the composite friction factor, f_o, for channel flow with an ice jam with f_o varies linearly with the ratio of ice jam thickness, t_j, and the depth of flow under the jam, H, as $f_0 = 0.39 \sim 0.56\left(\frac{t_j}{H}\right)$. Shen et al. (2000) assumed the Manning's coefficient of the jam varies linearly with the jam thickness between a minimum value for a single layer juxtaposed cover and a maximum value for a large jam thickness in a dynamic ice jam model. Applications of the model showed good agreement with field data (Shen 2010). This study examines components of the head loss of jams to gain a better understanding on the hydraulic resistance of ice jams.

2. Effect of Roughness on Jam thickness

In this section the effect of flow resistance of ice jam on the jam profile will be discussed using the January 1986 Thames River ice jam data (Beltaos 1993). The water surface and ice jam profiles are calculated using the method of ICEJAM (Flato and Gerard 1986), which solves the coupled flow and jam equations for jam thickness and water level. This approach has been adopted in HEC-RAS (Brunner 2010). Figure 1a shows simulated water surface and jam profiles using a bed Manning's coefficient n_b = 0.025 (Beltaos 1993) with three different jam roughness formulations:

Case 1 - Constant jam roughness: The ice jam Manning's coefficient n_i = 0.06 as given in HEC-RAS Example 14 (Brunner 2010) is used. The simulated result does not match with the observed data.

Case 2 - Nezhikovsky's formula: The equations given in Brunner (2010), based on Nezhikhovskiy (1964), are used for the ice jam roughness. The simulation result compares reasonably well with the data except for the jam toe.

Case 3 - Variable roughness along the jam: The jam Manning's coefficient along the channel is calibrated to match the observed jam and water surface profiles.

Figure 1b summarizes the jam Manning's coefficient used in these three cases, which shows the jam resistance coefficient should vary with the thickness in order to accurately describe the jam and water surface profiles. The result from Case 3 shows that the Manning's coefficient can be assumed to vary linearly between a minimum and maximum values as proposed by Shen et al. (2000).

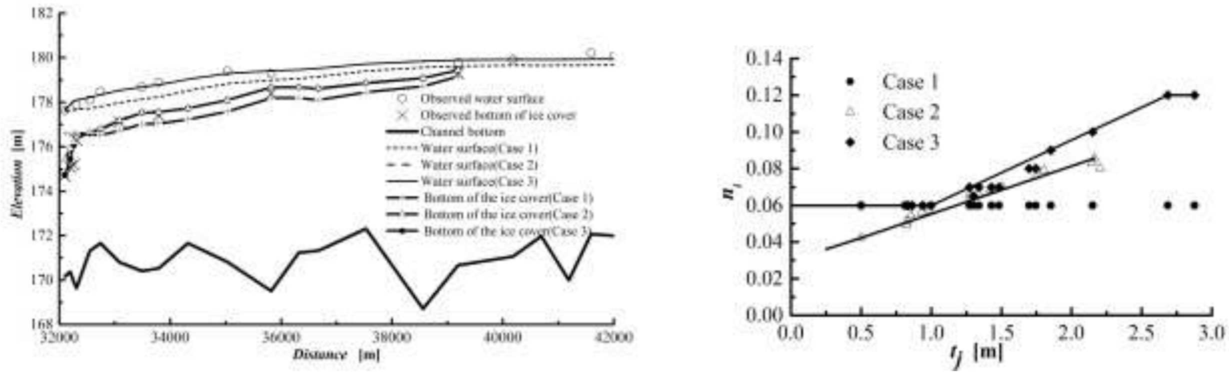

Fig. 1. a) Comparison of model output with observed data for three different jam roughness formulations; b) The variation of the ice roughness with ice jam thickness for all three cases

3. Head Loss in an Ice Jam Reach

In an ice jammed channel reach, the total energy loss consists of those due to the bed shear stress, the shear stress on the undersurface of the jam, and the energy loss due to the seepage flow through the jam. The total friction slope, S_f, between two cross sections can be expressed as:

$$S_f = S_{fb} + S_{fi1} + S_{fi2} = P_b\tau_b + P_{i1}\tau_{i1} + D_t \ / \ \rho g\overline{A} \qquad \textbf{[1]}$$

in which, S_{fb}, S_{fi1} and S_{fi2} are friction slopes correspond to the bed resistance, resistance due to the undersurface roughness of the jam, and the resistance due to the seepage flow through the jam, respectively; ρ = water density; $\overline{A}$ = average flow area under the jam between two cross sections; P_b and τ_b = bed wetted perimeter and shear stress, respectively; P_{i1} and τ_{i1} = ice cover wetted perimeter and shear stress, respectively; and D_t = seepage drag on ice particles in the jam.

Head Loss Due to the Seepage Flow

The friction slope S_{fi2} for a jam element of unit length with a submerged cross section area A_j, which contains N ice particles, can be expressed as:

$$S_{fi2} = \frac{D_t}{\rho g\overline{A}} = \frac{ND}{\rho g\overline{A}} \qquad \textbf{[2]}$$

in which, $N = 1\text{-}n \ A_j / \ \beta d_s^3$ (Bear 2013); n = porosity; d_s = a measure of particle size; g = gravity; $D = C_D \frac{\rho v^2}{2}\alpha d_s^2$, water drag on a particle; C_D = drag coefficient; $v = q/n$, seepage velocity; q = apparent velocity; αd_s^2 = cross-section area of a particle normal to flow; $d_s \approx 2t_i$; α and β = a shape factors. The drag coefficient can be expressed as (Bear 2013):

$$C_D = \frac{2n\lambda}{\alpha Re} + \frac{2n\lambda C_1}{\alpha} \qquad \textbf{[3]}$$

in which, λ is a factor representing the effect of neighboring particles, and $C_1 \approx 1.0$, is a constant varies slightly for different media (Venkataraman and Rao 1998).

The apparent velocity q can be related to the hydraulic gradient as (Bear 2013, Beltaos 1999):

$$S_f = b\frac{1-n}{gn^3 d_s}q^2\left(\frac{a(1+n)}{b\,\mathrm{Re}}+1\right) \qquad \textbf{[4]}$$

in which, a and b are shape factors; $Re{=}qd_s/\upsilon_f$ and υ_f = kinematic viscosity. Since flow through ice jams is fully turbulent, the Reynolds number is very large, in the order of 10^4 (Beltaos 1999), while $\frac{a\;1+n}{b}$ is in the order of 100 and λ is in the order of 10 (Bear 2013), the first term in Eqs. 3 and 4 can be neglected. Eq. 4 can be written as:

$$q = \mu\sqrt{S_f} \qquad \textbf{[5]}$$

where, $\mu{=}\sqrt{\gamma\frac{n^3}{(1-n)}gd_s}$ is the seepage coefficient and $\gamma{=}\frac{1}{b}=\frac{4}{3\beta}$.

Combining Eqs. 1 to 5, the friction slope S_{fi2} can be expressed as:

$$S_{fi2} = \xi S_f\frac{A_j}{\overline{A}} \qquad \textbf{[6]}$$

in which, $\xi = 1-n\;\;\kappa\mu^2/ngd_s$, A_j = submerged cross-section area of the ice jam, $\kappa = C_1\lambda/\beta$, $\lambda \approx 3\pi$ (Bear 2013). For wide river channels, Eq. 6 can be simplified to:

$$S_{fi2} = \xi\frac{\rho_i}{\rho}\frac{t_j}{H}S_f \qquad \textbf{[7]}$$

Head Loss Due to the Undersurface Roughness of the Jam

The first term of Eq. 1 gives:

$$S_{fb} = P_b\tau_b/\rho g\overline{A} = A_b S_f/\overline{A} \qquad \textbf{[8]}$$

in which, $\tau_b = \rho g R_b S_f$; A_b = the flow area associated with river bed, $A_b = \frac{1}{2}\left(\frac{n_b}{n_c}\right)^{1/2}$; n_b = bed Manning's coefficient; and n_c = composite Manning's coefficient. Hence, the friction slope contributed by the shear stress on the bottom surface of the jam can be calculated from:

$$S_{fi1}{=}S_f - S_{fb} - S_{fi2} \qquad \textbf{[9]}$$

4. Case Studies

Three cases are used to analyze energy loss of ice jams. These cases are:

1. Jam in a uniform channel

An idealized ice jam formed at the transition from a steep reach to a flat reach in a rectangular uniform channel is simulated (Shen et al. 2008). The simulated jam with a downstream boundary water level of 18 m and an inflow discharge of 3000 m^3/s is shown in Figure 3.

2. Thames River ice jam

The 1986 Thames River ice jam, which is simulated in Section 3. The Case 3 simulated result shown in Figures 1 will be used.

3. Matapedia River ice jam

An ice jam was observed in the Matapedia River in April, 1986. The simulated result of Beltaos and Burrell (2008) using the RIVJAM model as shown in Fig. 4 will be used.

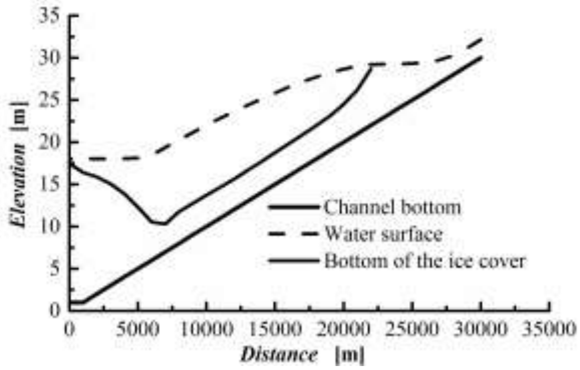

Fig. 2. Model result for a jam in a rectangular uniform channel

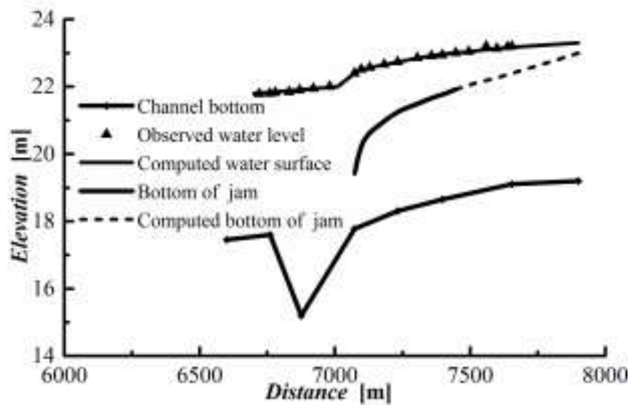

Fig. 3. Matapedia river ice jam simulated by RIVJAM

4.1 Head loss

Substituting the water depth and velocity of each cross section calculated from the ice jam model results, the total head loss along the jam is determined. Using the total loss value with Eqs. 7 and 9, with C_1 = 1.0 and $\lambda = 3\pi$, the loss caused by seepage flow in ice jams and shear stresses along the jam undersurface can be obtained.

1. Uniform channel jam

The flow discharge in this channel is approximately 3000m^3/s. The seepage coefficient, μ , is taken as 1.0m/s, and the thickness of ice block, t_i, in the jam is 0.5m. Assuming a porosity, n, of 0.4, the dimensionless coefficient, γ , is 1.67, and the value of the shape factor of particle β is taken as 0.78. The ratio between the friction slope of seepage flow, S_{fi2}, and the total friction slope, S_f, is given in Fig. 4, which shows clearly that the ratio increases with the ratio of the thickness of the jam to the flow depth to a maximum value of 56%.

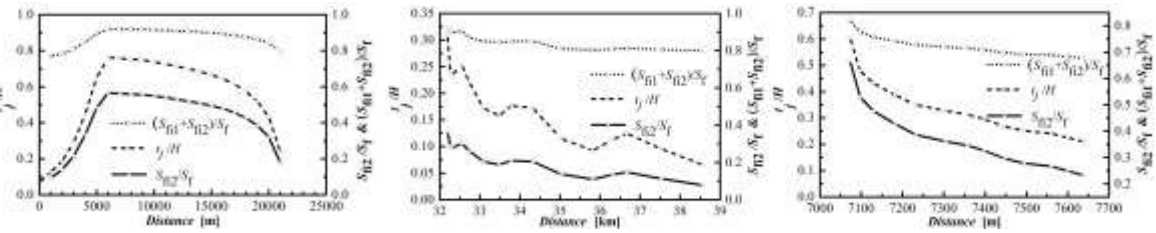

Fig. 4. Variation of friction slopes along the jam in the uniform channel, Thames River, and Matapedia River

2. Thames River jam

The flow discharge was approximately 290m^3/s, while the seepage coefficient, μ , is 0.6m/s, and the thickness of ice block, t_i, in the jam was 0.2m (Beltaos 1993). The value of the shape factor of particles, β, is about 0.8. The ratio of friction slope of seepage flow in ice jam and total friction slope is shown in Fig. 4, which shows clearly that the ratio increases with the jam thickness to water depth ratio. The maximum value of S_{fi2} is about 38% of the total energy loss.

3. Matapedia River jam

In this case, the flow discharge was approximately 140m^3/s, μ = 1.5m/s, d_s = 1.2m, and porosity n = 0.4 (Beltaos and Burrell 2008). The value of the shape factor β is about 0.75. Figure 7 shows that the ratio between the friction slope of seepage flow and the total friction slope increases with the jam thickness to water depth ratio to a maximum of about 66%.

All three cases discussed above showed that the head loss due to the seepage flow through the jam becomes a dominating part of the total loss when approaching the jam toe region.

4.2 Relationship between f_i and t_j/H

To explain why the resistance coefficient of ice jam increases with its thickness, the relationship between the ice jam friction factor f_i and t_j/H is examined in this section.

The friction factor of the jam can be calculated from the shear stress on the undersurface of the jam, τ_{i1}, and the seepage drag, D_t. The shear stress τ_{i1} can be calculated from the energy slope S_{fi1} and the flow depth under the jam controlled by τ_{i1}. Using the shear stress on the undersurface of the ice cover τ_{i1} in conjunction with the drag force on the seepage flow, D_t, the ice jam friction factor in Eq. 1 can be described as:

$$f_i = f_{i1} + f_{i2} = \frac{8}{\rho V^2}(\tau_{i1} + \tau_{i2}) = \frac{8}{\rho V^2}(\tau_{i1} + \frac{D_t}{B}) \qquad \textbf{[10]}$$

in which, V = velocity under the jam; B = channel width; and $\tau_{i1} = \rho g H S_{fi1}$. Using Eqs. 2 to 4 and $C_D = \dfrac{2n\lambda C_1}{\alpha}$, Eq. 10 gives:

$$f_i = \frac{8gHS_{fi1}}{V^2} + \frac{8\kappa(1-n)\rho_i t_j}{\rho d_s n}\left(\frac{q}{V}\right)^2 \qquad \textbf{[11]}$$

Figure 5 shows the relationship between f_i and t_j/H for all three cases.

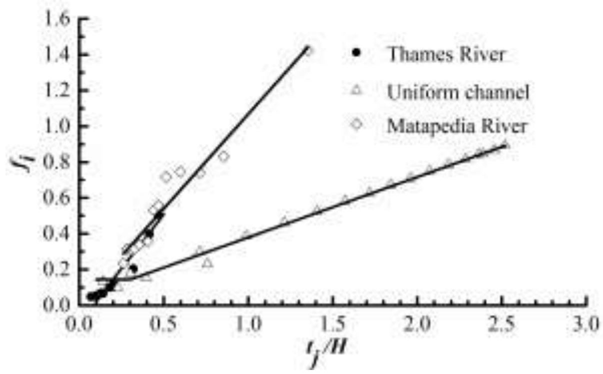

Fig. 5. Ice jam friction factor f_i versus t_j/H

4.3 Relationship between n_i and t_j

Using the value of f_i calculated in Figure 5, Manning's coefficient of the jam, n_i , can be obtained from the relationship $f_i^{1/2} = n_i \sqrt{8g} / R_i^{1/6}$. Figure 6 shows the jam Manning's n_i versus t_j and t_j/H. This figure showed that jam Manning's coefficients vary linearly with either the jam thickness or the ratio t_j/H, but limited by a minimum value corresponding to the roughness of the juxtapose ice cover from a single layer ice floe accumulation.

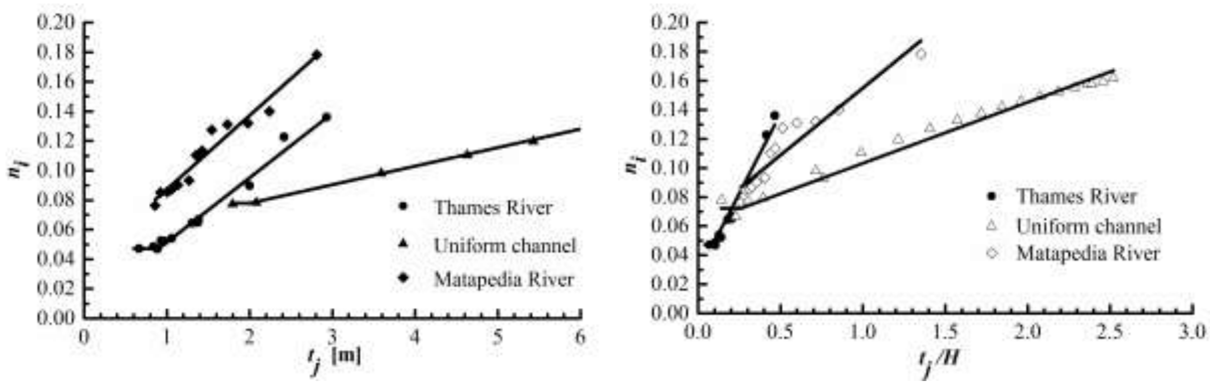

Fig. 6. Manning n_i versus t_j and t_j/H for uniform channel, Thames River and Matapedia River Ice Jams

6. Conclusions

Flow resistance is an important parameter affecting the flow condition associated with an ice jam as well as the jam thickness. Empirical flow resistance equations are often used in ice jam models. These equations consider the jam resistance coefficient varies with the jam thickness with little theoretical explanation. Through a detailed analysis of the seepage flow resistance and the resistance due to the undersurface roughness of jams, this study showed that the seepage flow resistance increases with the jam thickness and the resistance due to the undersurface roughness of the jam remains relatively constant. Moreover, the relative contribution of the resistance due to the undersurface roughness decreases in comparison with the seepage flow resistance when the jam thickness increases. The seepage flow resistance is a dominating part of the jam resistance excepted for a portion of the jam near its head, where the jam thickness is small with negligible seepage flow. The analysis also showed that the total jam resistance in terms of the friction factor or Manning's coefficient could be approximated by a linear function of the jam thickness or the ratio of jam thickness to the flow depth under the jam, but limited by a minimum value corresponding to the juxtaposed ice accumulation.

Acknowledgements
This study was conducted during the first author's visits at Nanyang Technological University and Clarkson University under the support of Tsinghua University.

References

Beltaos, S., 1993. Numerical computation of river ice jams, Canadian Journal of CivilEngineering, 20(1), 88-99.

Beltaos, S., 1999. Flow through the voids of breakup ice jams, Canadian Journal of Civil Engineering, 26(2), 177-185.

Beltaos, S., 2001. Hydraulic roughness of breakup ice jams, Journal of Hydraulic Engineering, ASCE, 127(8), 650-656.

Beltaos, S., Burrell, B. C., 2008. Ice-jam Measurements versus model predictions: A case study, Matapedia River, Proceedings, 19th IAHR Ice Symposium, Vancouver, Canada, 335-346.

Bear, J., 2013. Dynamics of fluids in porous media, Courier Corporation.

Flato, G. M., Gerard, R., 1986. Calculation of ice jam profiles, Proceedings, 4th Workshop on River Ice, Montreal, Canada, Paper C-3.

Healy, D., and Hicks, F., 1999. Comparison of ICEJAM and RIVJAM ice jam profile models, Journal of Cold Regions Engineering, ASCE, 3(4), 180-198.

Nezikhovsky, R.A., 1964. Coefficients of roughness of bottom surface on slush-ice cover, Soviet Hydrology, AGU, 127-150.

Shen, H. T., Su J., and Liu, L., 2000. SPH simulation of river ice dynamics, Journal of Computational Physics, 165(2), 752-770.

Shen, H. T., 2010. Mathematical modeling of river ice processes, Cold Regions Science and Technology, 62(1), 3-13.

Shen, H. T., Gao, L. and Kolerski, T., 2008. Dynamics of Ice Jam Formation and Release, Journal of Coastal Research, S52: 25-32.

Venkataraman, P., Rao, P. R. M., 1998. Darcian, transitional, and turbulent flow through porous media, Journal of Hydraulic Engineering, ASCE, 124(8), 840-846.

International Association for Hydro-Environment Engineering and Research
Supported by Spain Water and IWHR, China

24th IAHR International Symposium on Ice
Vladivostok, Russia, June 4 to 9, 2018

Ice Investigations to Support the Design and Operation of "Prirazlomnaya" Platform

M. Karulina
Krylov State Research Centre
44 Moskovskoye shosse, St. etersburg, 196158 Russia
marina@EK17106.spb.edu

Offshore ice-resistant fixed platform "*Prirazlomnaya*" was installed in the southeast part of the Barents Sea, and offloading of oil produced at this platform has been carried out since 2014. This is the first major project on drilling, production, storage and offloading of oil in the Arctic implemented in Russia that was preceded by several years of theoretical and experimental investigations. Platform ice-resistant block has square shape in plan with chamfered corners and inclined sides intended to decrease global ice loads acting on the platform. Extended sides with length at waterline of about 107 m result in rather rapid formation of ice pile-ups in front of the platform that in their turn define the level of ice loads acting on the platform. Moreover, ice pile-ups hinder normal operation of complex that includes the platform itself, shuttle tankers for oil offloading, supply and ice management vessels as well as vessels on duty for salvage and rescue operations. The paper reviews main fields of ice studies performed by Krylov State Research Centre, Russia, between 1996 and 2017, including 1) analysis of environmental conditions at the oil field in winter period; 2) investigation of *Prirazlomnaya* interaction with drifting ice features and determination of ice loads; 3) study the conditions and mechanisms governing ice buildup accumulation in front of the platform and the behaviour of these buildups as ice conditions change; 4) development of ice management measures intended to eliminate ice buildups and mitigate the intensity of their accumulation. Some of the proposed methods to deal with ice pile-ups were implemented in practice during several expeditions to the area of "*Prirazlomnaya*" site in 2014-2018. The results of investigations and expeditions are given in the paper.

1. Introduction

West Arctic waters, including the Barents Sea, the Pechora Sea and the Kara Sea are one of the most promising in terms of expected oil & gas resources. One of the major oil fields in this area, *Prirazlomnoye*, discovered in 1989, is located in the southern part of the Pechora Sea, at the south-eastern periphery of the Barents Sea, 60 km offshore (Figure 1, left). *Prirazlomnoye* is the first-ever Russian project of oil development on the Arctic shelf. To this effect, a unique fixed ice-resistant marine platform, *Prirazlomnaya*, was designed in CDB RUBIN and built in Russia. This platform, installed at its site in 2011, performs the entire scope of technological operations: drilling, production and storage of oil, as well as preparation and offloading of ready product (Figure 1, right). Natural water depth at the location of *Prirazlomnaya* platform is 19.2 m. To prevent foundation scouring, this platform is surrounded by a protective stone berm of 35.5 m width and 2.5 m. Thus, actual water depth near the platform is 16.7 m. The platform block has square shape in plan with chamfered corners and inclined sides with slope angle 58°. The platform width at waterline is about 107 m.

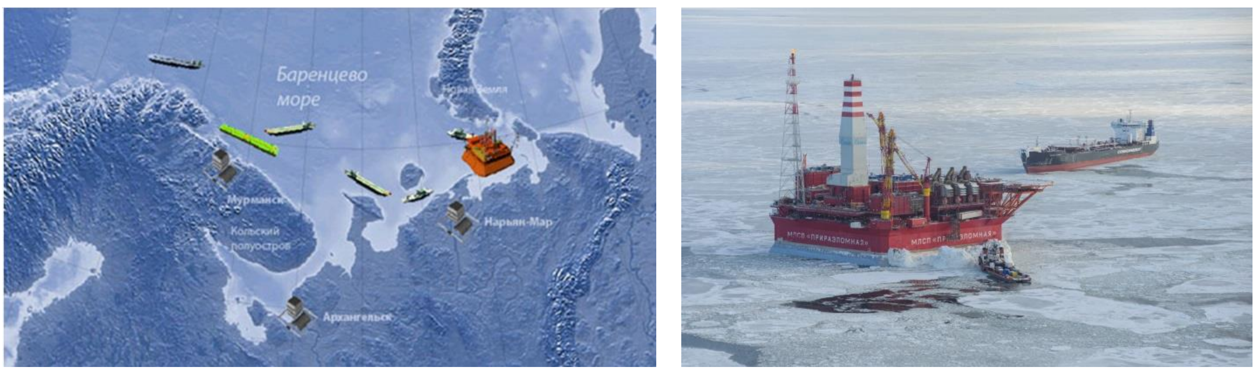

Fig. 1. Location of *Prirazlomnaya* platform and general view of the platform.

Oil offloading from *Prirazlomnaya* goes all year round, including the ice period, by means of two ice-going shuttle tankers *Kirill Lavrov* and *Mikhail Ulyanov*. These ships of about 260 m length were built at Admiralty Shipyards as per the design of Aker Finnyards. Supply of technological materials and stores to the platform, as well as ice management operations and safe approach of shuttle tanker, is ensured by multi-purpose ice-breaking support vessels of Moss 828 design (*Vladislav Strizhov* and *Yury Topchev*). Besides, *Murman* multi-purpose emergency & rescue vessel is on duty around the platform, to address various emergencies (fire, explosion, spill of oil products, etc.) and evacuate personnel if required.

The necessity to ensure efficient and safe all-year-round operation of the technological complex required extensive studies of how its elements operate in ice conditions. Starting with 1996, a number of theoretical and model studies involving Krylov Centre were performed at the design stage of *Prirazlomnaya* platform. Once the platform was installed at its intended operation site, new challenges appeared, and have to be solved to ensure operation of the platform in ice conditions, so this work is still underway.

This paper reviews main fields of ice studies performed by Krylov Centre between 1996 and 2017, including:

- Analysis of environmental conditions at the oil field;
- Investigation of *Prirazlomnaya* interaction with ice formations and determination of ice loads;
- Study of the laws governing ice buildup accumulation in front of the platform and the behavior of these buildups as ice conditions change;
- Development of ice management measures intended to eliminate ice buildups and mitigate the intensity of their accumulation.

2. Analysis of Environmental Conditions at *Prirazlomnoye* Oil Field

The information on natural processes in the intended operation area of *Prirazlomnaya* platform over 30-year period was accumulated and analyzed by the experts of Arctic & Antarctic Research Institute (AARI) at the platform development stage. Besides, AARI numerically simulated ice drift in this area. This analysis has shown that key factors influencing ice drift trajectories near the platform are **tidal currents** and **wind**.

Tidal currents in the Pechora Sea are rather strong and, usually, semi-diurnal, i.e. tidal wave completes its full movement cycle in two directions in approximately 12-hour period. In still weather, direction, speed and phase of this periodical ice drift component practically coincide with those of tidal wave. The observations have shown the inception of compression zones in ice at the initial phase of its tide-induced drift.

Still weather is observed during 25% of winter time. Without wind, ice trajectories are nearly elliptic (Dmitriyev et al., 2004). The long axis of the ellipse can be up to 8000 m in length, but it could also reduce down to 1 km, and the period of ice flow passage via the opposite points of its trajectory varies between 4 and 8 hours, depending on superposition of various tidal current harmonics. Average period of passing via the extreme points of the ellipse is 6 hours.

In case of strong winds (14-15 m/s and more) aerodynamic forces become prevalent, and the ice drifts in the direction of wind with slight deviations due to tidal currents. At the wind speeds of 3-12 m/s, ice drift trajectories are complex, featuring short-time loops with respect to long-term periods of ice drift at extremely low speeds and drift direction variation from 90° to 180°. Due to varying wind directions and speeds, in combination with various conditions of tidal currents, ice drift trajectories could be the most bizarre (Figure 2) (Dmitriyev et al., 2004).

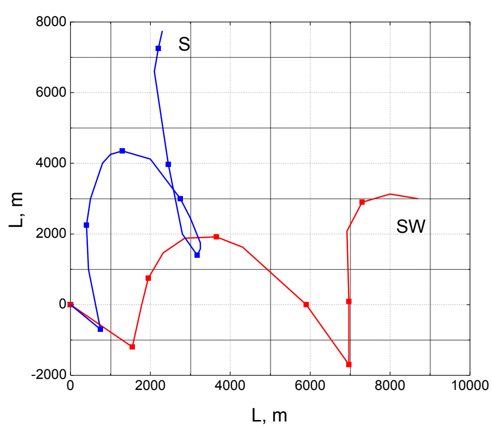

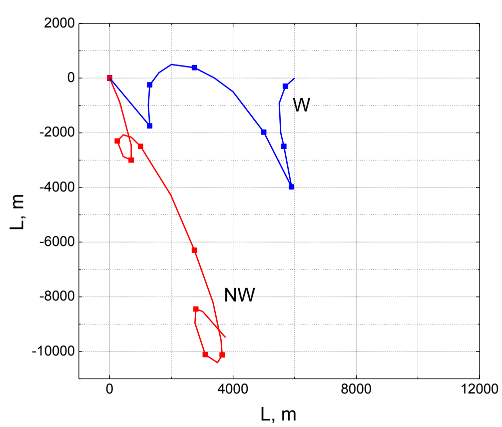

Fig. 2. Ice drift trajectories over 24-hour period with weak (6-7 m/s) winds of different directions.

The parameters of ice formations used in the studies performed at the design stage of *Prirazlomnaya* platform were based on the generalized findings of AARII expeditions in the Pechora Sea. Average thickness of level ice (of thermal origin) in the area of *Prirazlomnaya* is 0.68 m, level ice thickness of 100-year occurrence is assumed as 1.6 m. Uniaxial compression strength of level ice is taken as 1.4 MPa, its bending strength being taken as 0.6 MPa. Keel depth of ridge (100-year occurrence) was taken as 22.5 m, its consolidated layer thickness being 3.5 m.

Weather data analysis has shown that there is always probability of ice drift from all directions. At the same time, there are prevailing ice drift directions NW – SE and SE – NW in the site. This outcome was used when solution about the platform orientation was accepted.

3. Ice Load Assessment Based on Ice Model Tests

In 1996, to determine global ice loads on *Prirazlomnaya* platform, a series of model studies was performed in Ice Basin of KSRC. Model scale was about 1:60. Ice action of both level ice and ridges on the platform model was investigated for different drift directions. In the tests the model was towed in immovable model ice sheet.

The model tests have shown that the platform interaction with level ice drifting perpendicularly to the inclined side generally corresponded to the Croasdale scheme (Croasdale et al, 1994) adopted in ISO (2010). The cyclic nature of ice load which can be seen from a typical time history of horizontal ice force (Figure 3) corresponds to ice buildups evolution in front of the platform. Each cycle begins with ice force increasing due to ice pile-ups growth and has the force drop at the end when the ice pile-ups collapse. It can be seen that the maximal value of ice force is growing from cycle to cycle because the pile-ups size increases, too. Based on the model studies, Marchenko and Karulin (2005) proposed analytical model for determination of ice loads and ice pile-ups size.

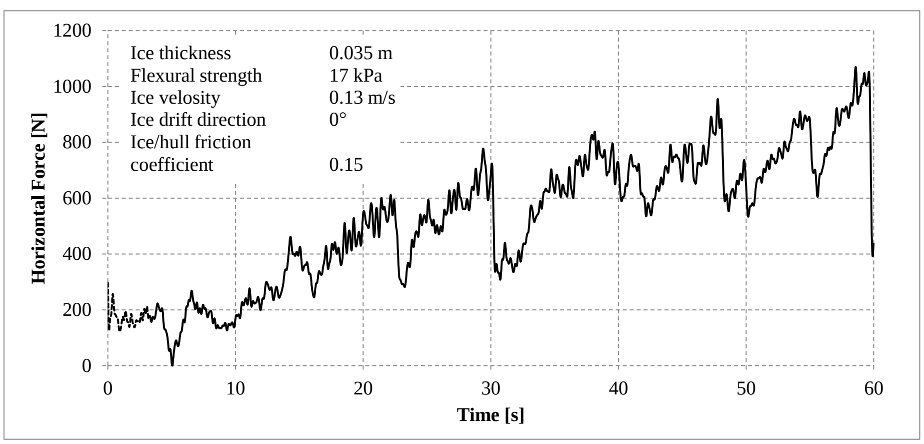

Fig. 3. Experimental time history of horizontal ice-induced force.

The model tests have made it possible to study the effect on ice load of a number of factors that are not considered in the Croasdale scheme, in particular, the underwater accumulation of ice, the variation of velocity and the ice drift angle. One of the main difficulties with model testing in Ice Basin was the impossibility to accurately reproduce specified strength properties of ice in accordance with modeling scale. Therefore, construction of multi-factor regression models was implemented in the processing of test data for determination of global ice loads (Alexeev et al., 1998). Design values of global ice loads subsequently used in the stability analysis of this gravity-based structure were taken as per model test data. Global horizontal ice-induced force of 100-year occurrence was taken as about 400 MN. This load corresponded to the first year ridge action upon the platform.

One of the advantages of model experiment is that it yields assessments of other ice load components that are hard to determine theoretically. In particular, measurements of yawing moment (moment about the vertical axis passing through the center of the structure) made it possible to assess eccentricity of total horizontal ice force application. Eccentricity is defined here as non-dimensional arm of yawing moment:

$$\overline{l_z} = \frac{a}{B_{wl}} = \frac{M_z/F_H}{B_{wl}},$$

where a is arm of yawing moment, M_z is yawing moment, F_H is horizontal force, B_{wl} is waterline width of the structure.

Figure 4 schematically illustrates the cause of eccentricity in case of ice drifting perpendicularly to the platform side. It is non-uniform distribution of ice load induced by ice due to non-uniformity of ice sheet itself, non-simultaneity of ice failure processes, of ice block turnings, etc. If the ice drifts at a certain angle to the platform, this eccentricity of total horizontal ice force is also due to the asymmetry of the problem. Load eccentricity as a factor to be taken into account in stability assessments of wide structures installed on the ground was pointed out by a number of experts (Jefferies and Wright, 1988; Lengkeek and Besseling, 2013).

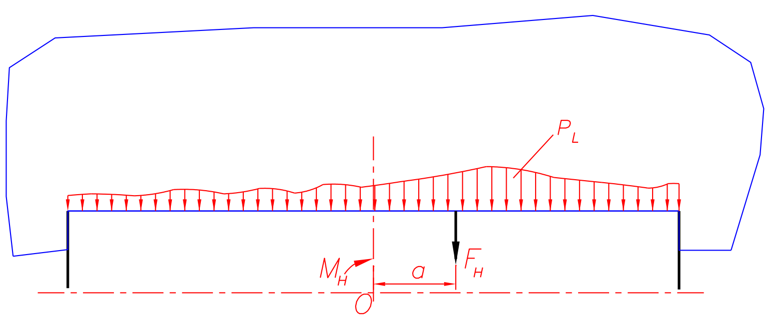

Fig. 4. Scheme of ice load distribution resulting in eccentricity of ice force application

The ice model tests of *Prirazlomnaya* platform have shown that eccentricity of maximal horizontal ice force ranged from 1% to 4.6% in case of ice drifting perpendicularly to the platform side, and for the horizontal ice force, 62% of the maximum value, the eccentricity of the load application was more than 12% of the platform width.

4. Studies of Ice Rubble Buildups in Front of the Platform

Formation specifics of ice rubble buildups in front of wide platforms

Analysis of ice conditions at Prirazlomnoye oil field, as well as of the platform shape, has shown that considerable stationary ice rubble buildups are highly likely to accumulate in front of the platform. Therefore, already at the design stage of *Prirazlomnaya*, this issue became a subject of dedicated studies, including model tests in Ice Basin.

The first step of those studies was to analyze operation experience of wide platforms installed on the shelf of freezing seas. This analysis was based on full-scale observation data for three platforms used in the 1980s for wildcat drilling in the Sea of Beaufort. These structures were installed at different depths, directly onto the seabed or onto an artificial berm:

- Caisson Retained Island (CRI) – octogonal concrete barrier of maximum width 117 m;
- Single Steel Drilling Caisson (SSDC) – 163-m tanker retrofitted for wildcat drilling;
- *Molikpaq*–105-m wide octogonal steel structure.

During the first CRI-based drilling at Tarsuit-N44 site, a large buildup of drifting ice rubble was formed around the platform, becoming several hundred meters long by the end of that winter (Sayed et al., 1986). This ice buildup rested on the seabed and was used to protect CRI against direct exposure to drifting multi-year ice. However, *Prirazlomnaya*, due to its functional purpose, must not have stationary buildups staying near it for a long time, so this experience cannot be used.

At the Amerk field with water depth 26 m, the berm at CRI location made actual depth at equal to 9 m. Early that winter, a buildup began to accumulate gradually expanding in all directions (Neth et al., 1983). The layout of its formation and growth is shown in Figure 5.

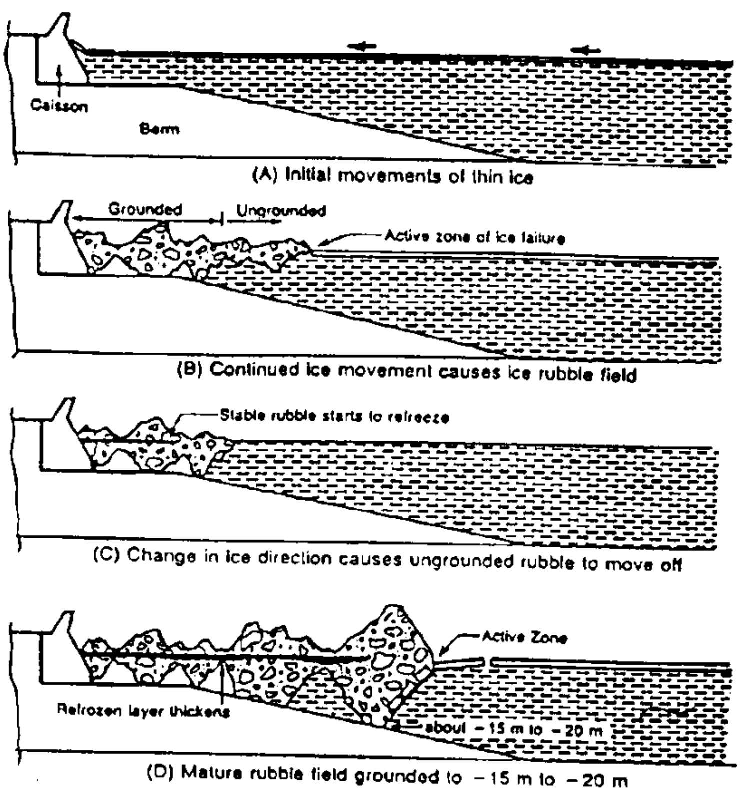

Fig. 5. Generation and growth of ice rubble buildup in front of the platform.

With each change of ice drift direction, rubble buildups with loose or no fastening to the seabed were snapping off and going away, diminishing the buildup. The observations have shown that the outer edge of that buildup never remained for a long time in zones with water depths exceeding 16-19 m.

Similar observations over SSDC platform operation have shown that the outer edge of ice buildup seldom reaches water areas with depth exceeding 18-20 m.

When using the *Molikpaq* platform in Tarsuit P45 and Amauligak I65 sites, the water depth was 19.6 m taking into account the berm (Neth et al., 1983). Grounded ice buildups were formed only when the ice drift vector was perpendicular to the wide side of the platform. When the ice drift direction was changed, they were demolished. Ice drift along the diagonal of the platform did not lead to any ice buildups.

Analysis of the available data led to conclusion that the most important external factor responsible for generation of a stationary ice buildup resting at the seabed was water depth at the platform location. If this depth is less than 16 m, there appear stationary ice buildups resting firmly on the seabed. At the depths of 19-20 m typical for *Prirazlomnaya* platform site, there appear stationary buildups that can be carried away if ice drift direction changes by ca. 90°.

Model studies of ice buildups formation and behavior in case of drift direction change
The model studies performed in 2000 were intended to investigate the laws of ice buildups formation and behaviour in case of drift direction change. The scale factor was the same as in previous experiments. Each test included measurements of target parameters: ice thickness, speed and duration of unidirectional drift. After each test run, profiles of above-water and underwater buildups (Figure 6) were measured carefully. To simulate the changes in ice drift direction, a part of ice sheet with buildup in front of the platform was cut off from the remaining sheet (Figure 6), the platform model with seabed simulator and buildup was turned by required angle (the angle of drift direction change), and then the model was towed in this position.

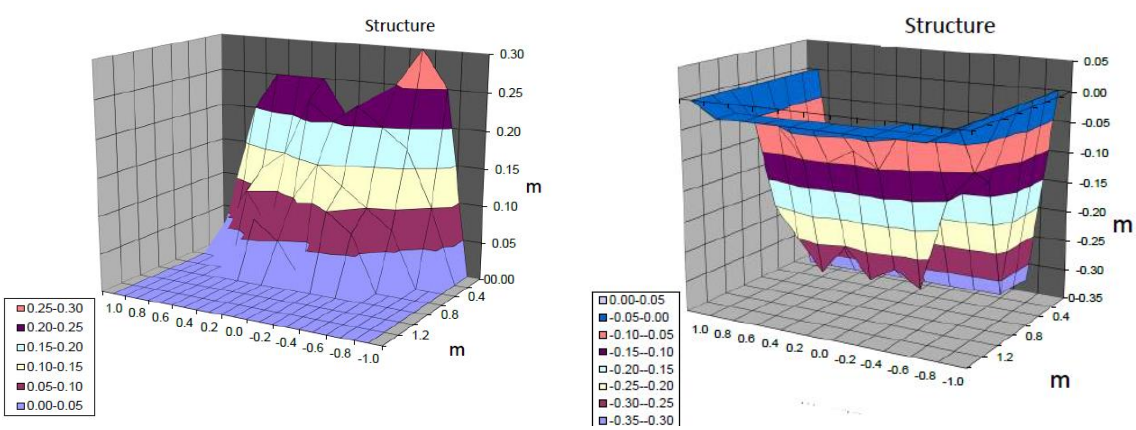

Fig. 6. Profiles of above-water and underwater buildups after test run.

Fig. 7. View of buildup in front of the platform after removal of surrounding ice sheet.

The model studies have shown that:

- If ice drifts perpendicular to the wide side, the initial stage of buildup formation and growth is unsteady: ice rubble accumulation is accompanied by periodical collapses of ice sheet, increase in size of underwater ice accumulation, which quickly reaches the bottom.
- If the model is installed diagonally, ice buildups appear neither above water or underwater, all ice pieces being carried away to the channel behind the platform. Taking into account this result, the platform was positioned so as its diagonal coincides with a line of dominant ice drift directions at the *Prirazlonnoye* oil field.
- The studies on dynamic friction coefficient between ice and model surface has shown that increase of this parameter from 0.15 to 0.40 results in qualitative changes of the interaction picture because sliding of ice pieces along the platform surface becomes worse. This peculiarity was taken into account in making design solutions: at waterline area the platform has stainless steel belt.
- Broken ice area had a compacted ice zone forming a "false bow" with drifting broken ice flowing around it (Figure 8). These ice accumulations were easily carried away as ice drift direction changed.

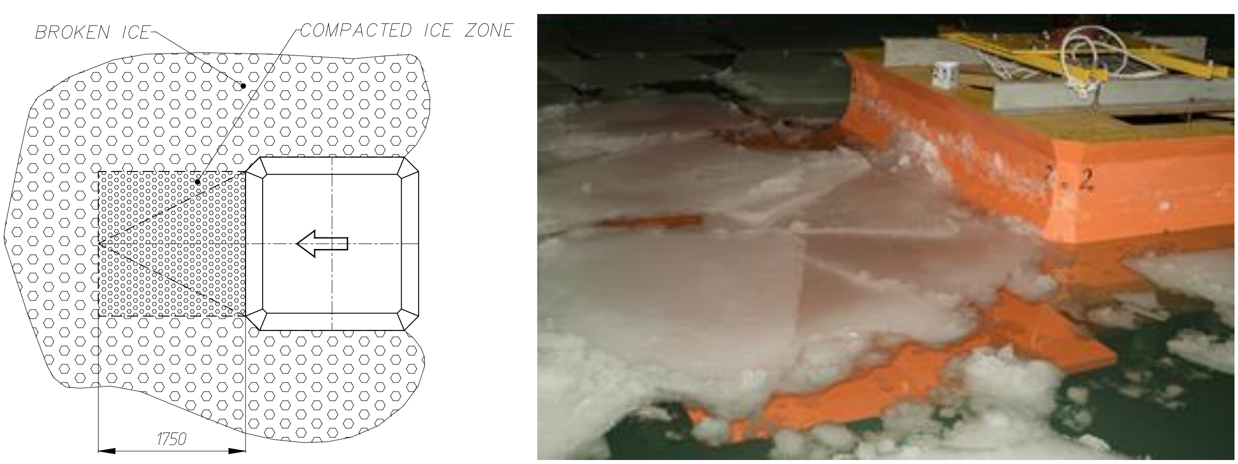

Fig. 8. Formation of compacted ice zone in front of the platform in broken ice field.

Generalization of these experimental studies led to analytical assessments of buildup size variation depending on unidirectional drift duration of ice with different thickness. Calculations have shown (Figure 9) that at ice thickness of 0.5 m a buildup of considerable size might appear in rather a short time, within half an hour. These analytical assessments were confirmed by full-scale observations of *Prirazlomnya* crew. The photo and dimensions of buildups in front of the platform in Figure 10 were obtained in winter 2015 in 0.5-0.7 m thick drifting ice.

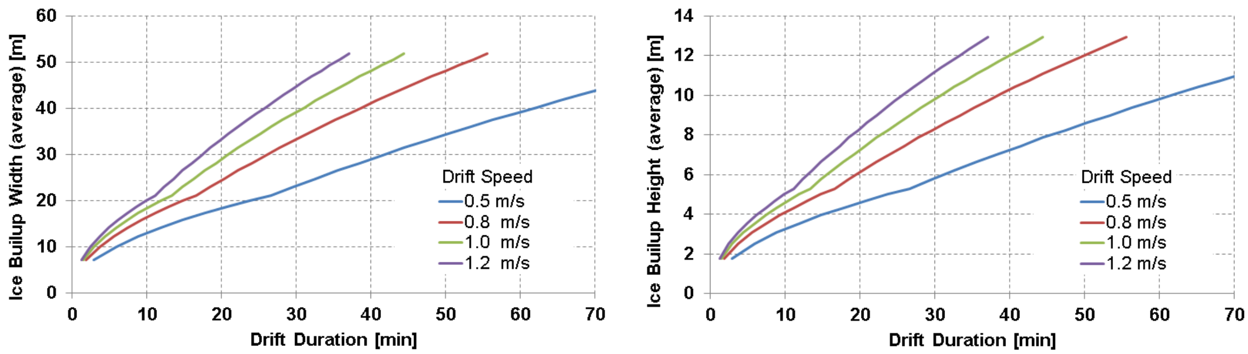

Fig. 9. Growth of ice buildup width and height: frontal drift. Ice thickness is 0.5 m.

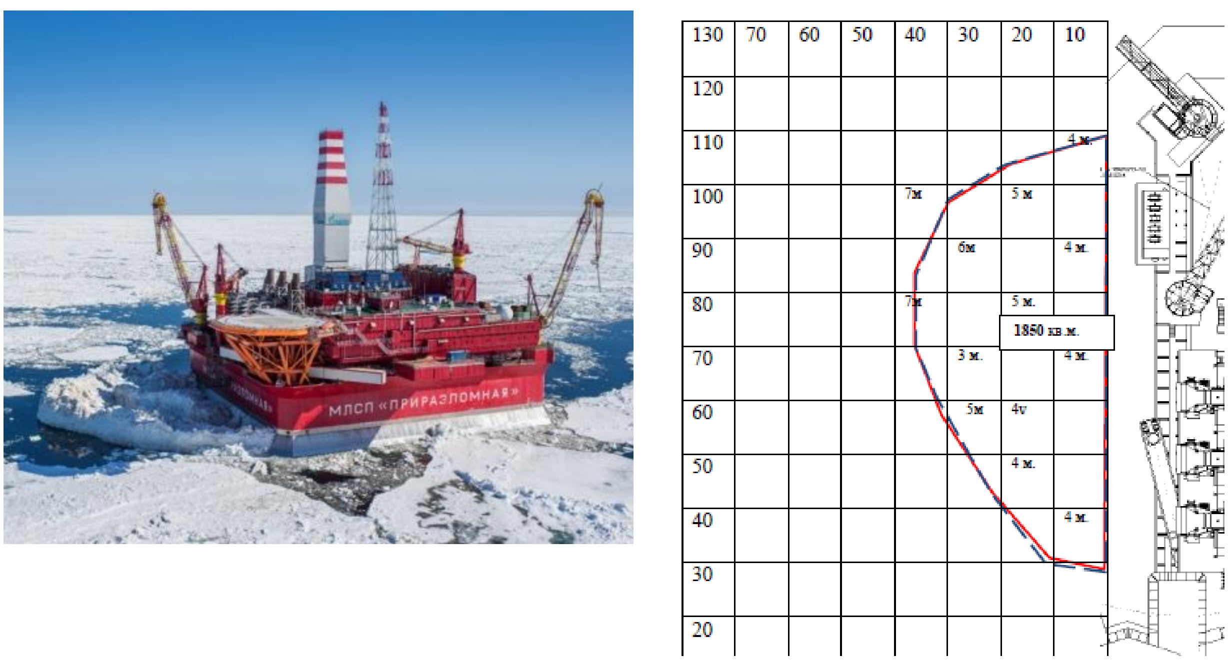

Fig. 10. Ice buildup in front of the platform in full-scale conditions. The figures in the diagram (right) are buildup heights above sea level (in meters).

The experimental studies have identified the main factors contributing to formation of considerable ice buildups, as well as the conditions of buildup displacements in case of ice drift direction change. Considerable ice buildups are formed by level ice and ridges drifting for a long time (approximately 0.5 hours and more) unidirectionally and perpendicularly to the long side of the platform.

Ice buildups can be displaced by the change in drift directions under the following conditions:

- Ice drift direction changes by nearly 90°
- Buildup does not touch the seabed (i.e. floats) or only has loose fastening to the ground
- Platform sides are rather smooth, without various appendages that would hinder sliding of ice floes
- Buildup is not frozen to the platform.

The last factor was studied on a full-scale platform and was not observed. On the whole, model test results were confirmed by full-scale observations over formation and behavior of buildups near the platform, performed by the expedition aboard *Vladislav Strizhov* vessel in 2016.

5. Ice Management (IM) Operations near *Prirazlomnaya* Platform

After *Prirazlomnaya* was installed at its site and commissioned, there came up a number of new ice-related challenges to solve. Ice buildups forming in front of the platform not only affect global ice loads but also complicate or make impossible supply operations, personnel evacuation, emergency & rescue activities. Also, there is danger for the tanker under loading, as well as for other ships: stamoukha might get off the seabed and hit the ship

Main tasks of IM operations for icebreakers and ice-breaking supply ships operating near *Prirazlomnaya* platform were formulated so as to eliminate or mitigate these adverse effects, and namely: 1) hinder formation of new ice buildups near the platform; and 2) diminish or eliminate ice buildups that already exist. Efficiency and practicability of the IM measures developed to accomplish these tasks were assessed both by model tests and in full-scale conditions. The most important of these measures will be discussed below.

Formation of ice "barriers" in front of the platform

To prevent formation of considerable ice buildups in close proximity to the platform, IM ships can make artificial ice "barriers" in front of its wide frontal side. In this case, drifting ice cover will break into pieces at the boundary of this "barrier", or a "false bow" made of ice, and these pieces, thanks to streamlined shape of the "barrier", will bypass both the barrier and the platform.

This scenario was identified during full-scale observations over ice interaction at *Prirazlomnaya* platform. There was a case when an ice floe with streamlined shape, drifting perpendicularly to the long side of the platform, stopped near it and stayed there for quite a long time (approximately 0.5 hours), so that other drifting ice pieces, unable to reach the surface of the platform, bypassed this ice floe in the horizontal. However, this scenario could not be reproduced in the model tests due to specifics of scaled modeling (model ice is too thin and its Young's modulus is too low): instead, there was observed a rafting scenario, when artificial triangular ice floe went under the continuous ice sheet (Figure 11). In full-scale conditions, this rafting scenario takes place when ice is of small thickness, up to approximately 0.5 m. At higher thicknesses, ice layers are unlikely to go far under each other without breaking.

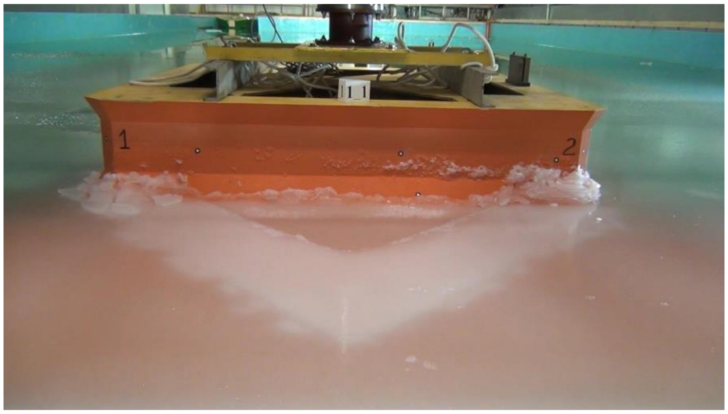

Fig. 11. Triangular ice floe going under continuous ice sheet.

It has to be noted that this “ice barrier” in front of the platform is quite unstable: its shape can vary constantly, and a slight change in ice drift direction might carry away the barrier itself. In view of this, and also to comply with safety requirements for ships operating near the platform, IM ships did not make any artificial ice barriers in front of *Prirazlomnaya*.

Effect of channels in level ice upon ice buildup formation

Experimental studies of the channel efficiency in front of *Prirazlomnaya* to diminish the size of buildups were performed in Ice Basin still at the design stage of this platform, in early 2000s (Yamschikov et al., 2016b). Figure 12 illustrates a ridge drifting towards the platform and managed by an ice-breaking vessel: a) ice buildups in front of the platform after interaction with an intact ridge; b) ice-breaking vessel passing through a ridge; c) ice buildup in front of the platform after interaction with a managed ridge. It is clear that buildups near the platform are considerably smaller if there is a channel in front of the platform:

a) b) c)

Fig. 12. Ice buildup management in front of *Prirazlomnaya* platform

This result was taken into account, and in 2014 various layouts of ice channels were developed, with follow-up model studies of their respective efficiencies. Some tested layouts are given in Figure 13. Channel variants studied in these investigations were 21 m and 32 m wide, with different orientation of their axes with respect to the platform. Besides certain test runs included simulation of compression effects, i.e. closings of channel edges.

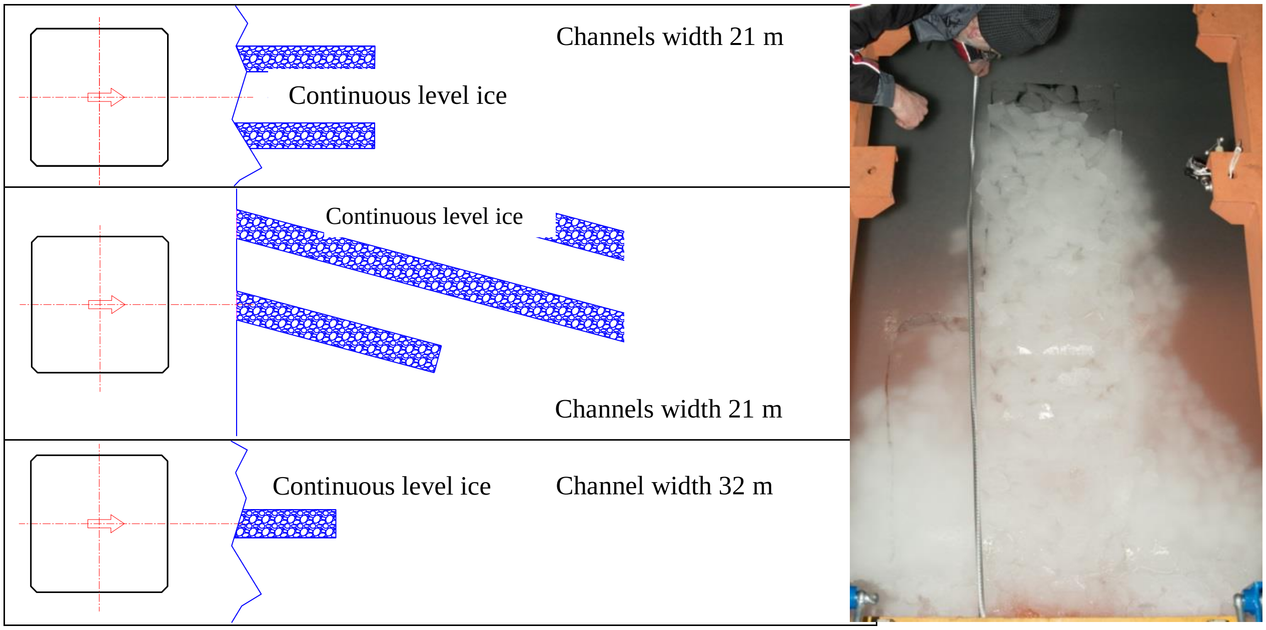

Fig. 13. Some channel configurations studied in the model tests

The results of these studies have shown that narrow (21 m) channels of various configurations, as well as a wide channel near the platform side do not have any significant effect upon formation intensity of ice buildups. Several channels closed by compression proved ineffective either.

A channel at the middle of the platform side (with width equal to approximately 1/3 of the side's width) enabled considerable reduction of ice buildup formation intensity: the majority of ice pieces was falling into the channel and drifted in it (Figure 13, right). Underwater ice buildups were accumulating at the edges of this channel, reaching the surface of the berm only after considerable time. Here, ice was not fastened to the berm as securely as in previous cases. It means that in full-scale conditions this IM scenario may lead to ice buildup displacement due to drift direction change.

Despite the positive results obtained for the latter scenario, channel creation near the real platform, with drifting ice incoming, is quite risky because the ship could be hit against the platform. Laying the channels at considerable distance from the platform is ineffective due to ice compression zones and frequent changes of ice drift direction. As a result, this IM technique was not tried out in full-scale conditions.

Management of ice sheets near the platform by means of IM vessels
As demonstrated above, drifting broken fields ice usually do not form considerable buildups that would reach the berm and rest firmly on the seabed in front of the platform. To use this effect, it is necessary to make extensive areas of managed ice, and this task is hard to accomplish for IM ships operating near the platform because ice drift direction changes frequently and ice management activities must be performed in strict accordance with safety requirements, to prevent IM ships from colliding with each other and from being hit against the platform.

Development of methods for eliminating ice buildups near the platform

Feasibility analysis of IM operations, as well as try-out maneuvers performed in winter navigation of 2014/2015, have shown that multi-purpose ice-breaking ships currently available cannot fully prevent formation of ice buildups, so it became necessary to develop measures and tools for breaking stable ice rubble buildups that appear near *Prirazlomnaya*. To this effect, more than 10 methods – mechanic, hydraulic and pneumatic – were suggested. In real practice, the following methods were applied:

- gradual breaking of ice buildup by the hull of IM ship;
- washout of the underwater buildup by propeller jets;
- use of an excavator installed and fixed on the deck of IM ship.

The first two methods proved ineffective because ice buildups resting firmly on the seabed have quite dense underwater parts, clearly too strong to break for currently available tools.

Conversely, use of excavator proved quite effective and enabled complete and sufficiently fast removal of ice rubble buildups (Yamschikov et al., 2016a). The physics of this method is quite simple: a buildup that rests firmly on the seabed will float if its above-water portion is partially removed. This portion is not consolidated, so it can be decreased easily enough if ice pieces from its surface are shoveled into water. That is exactly what happened when this method was tried out in March 2016: after 13-hour work of the excavator, the buildup that initially had its above-water part 8 m height (on an average) floated up and split. The ice blocks thrown by the excavator into water were carried away by propeller jets, and the split buildup itself was carried away by current.

6. Conclusion

Efficient operation of technological complex on *Prirazlomnaya* oil field in ice conditions is largely due to comprehensive theoretical and experimental studies performed at its design and operation stages. Yearly expeditions that started in winter 2015/2016 are intended to study operational challenges of the platform in winter and have already yielded valuable information for comparing theoretical and model tests results against full-scale observation data. These expeditions became a unique opportunity for trying out a number of technical solutions intended to improve operation of all the elements in the technological complex of *Prirazlomnaya*: the platform itself, shuttle tankers and ice-breaking support vessels.

Acknowledgments

Some of the studies were carried out in cooperation with CDB "Rubin" and LLC Gazprom Neft Shelf.

References

Alexeev, Yu., Karulin, E., Karulina, M., and Sutulo S., 1998. A method for predicting ice loads on structures based on model test data. Proc 14th IAHR Symposium on Ice, Potsdam, New York, v.1, pp.497-502.

Croasdale, K. R., Cammaert, A. B., Metge, M., 1994. A method for the calculation of sheet ice loads on sloping structures. Proc 12th IAHR Symposium on Ice, Trondheim, Norway.

Dmitriev, N.E., Zubakin, G.K., Bokov, V.N., Voinov, G.N., 2004. The intra-day variability of wind, ice drift and current in the Pechora Sea. AARI Transactions, Vol. 449, pp. 24-42

ISO19906, 2010. Petroleum and natural gas industries - Arctic offshore structures.

Jefferies, M.G., and Wright, W.H. 1988. Dynamic response of Molikpaq to ice-structure interaction. proc. of 7th conference OMAE, Houston, pp.201-220.

Lengkeek, H.J., and Besseling F., 2013. Combined translational and rotational sliding of gravity based structures loaded by ice. Proc. of the 22nd Int. Conference on Port and Ocean Engineering under Arctic Conditions, Espoo, Finland

Marchenko, A.V., and Karulin, E.B., 2005. A Method for Calculation of Ice Loads on Wide Structure from Drifting Ice. KSRC Transactions, Issue 24 (308), pp.27-41.

Neth V.W. et al., 1983. Design, construction and monitoring of the Tarsuit relief ice pad, Proc. of the 22nd Int. Conference on Port and Ocean Engineering under Arctic Conditions

Sayed, M., Frederking, R.M.W. and Croasdale, K.R. 1986. Ice Stress Measurements in a Rubble Field Surrounding a Caisson-Retained Island. Proc. of 1st International Conference on Ice Technology, pp. 255-262, Boston, Mass., USA

Yamschikov, D., Pronyashkin, A., Karulin, E., 2016a. Development of ice management techniques in support of Prirazlomnaya ice-resistant platform operation. KSRC Transactions, Issue 92 (376), pp.129-148.

Yamschikov, D., Pronyashkin, A., Karulina, M., 2016b. Ice management efficiency assessment based on model tests in Ice Basin. KSRC Transactions, Issue 93 (377), pp.43-56.

24th IAHR International Symposium on Ice
Vladivostok, Russia, June 4 to 9, 2018

Experimental study on ice jam under completely ice-covered river

Hiroshi YOKOYAMA[1], Yasuhiro YOSHIKAWA[2], Hiroki YABE[1], Kenji TAKAHASHI[3], Satoshi KONISHI[4]

[1]Civil Engineering Research Institute for Cold Region,
1-3-1-34 Hiragishi, Sapporo, Hokkaido, 0628602, Japan
[2] Kitami institute of technology, Koen-cho 165, Kitami, Hokkaido, Japan
[3] Asahikawa Development and Construction Department, Hokkaido Regional Development Bureau, MLIT, 1-3-3-15 Miyamae, Asahikawa, Hokkaido,0788513, Japan
[4] Abashiri Development and Construction Department, Hokkaido Regional Development Bureau, MLIT, 2-6-1 Shinmachi, Abashiri, Hokkaido, 0938544, Japan
yokoyama-h22ab@ceri.go.jp

We aim to clarify ice jam mechanism under completely ice-covered river by model experiments. It had been investigated that conditions of occurrence of ice jam depended on river width, change of water. However, researches about mechanism of ice jam under completely ice-covered river caused by ice inflow from upstream has not been conducted.
The experiments were conducted by channel that was simplified actual ice-covered river on a scale of 1/100. The test channel had four sections with different width and longitudinal slope. Ice plates model made by polypropylene (specific gravity was same to real ice) were fed from upstream of the channel. We conducted experiments with different river discharge, intake flux of ice, and size of ice plates. We performed two types of ice jam by setting different completely ice-covered section: One was set at sudden expansion (Run C1). The other was set at sudden contraction (Run C2).
In Run C2, required time for ice jam was longer with larger discharge, smaller ice plates, or larger intake flux of ice. These trends were previously confirmed in ice jam experiments under non-completely ice covered river. But in Run C1, relation between required times for ice jam and discharge or intake flux was not clear if ice plates were smaller. Longitudinal changes of channel width and bed slope differed in Run C1 and C2 and seemed to affect ice jam progress. We suggested some points for modeling these phenomena.

1. Introduction

An ice jam possibly brings about the following troubles: a sudden rise in the river water level; flooding; damage to river structures from ice floes on a tidal wave running up along a frozen river (Abe et.al, 2012); and a failure in water intake due to inlet clogging. As extreme climatic phenomena including heavy rainfall/snowfall are expected to occur more frequently under the influence of the global warming, comprehension of the mechanism of the development of a river ice jam in a cold region and improvement of a technology to predict the time and place of occurrence of those phenomena are inevitable to investigate both facilities and measures for reducing damage.

Many researches have been attempted to clarify the mechanism of the development of an ice jam in various studies. For example, a field observation of river ice jams was conducted and investigated the mechanism of ice jam occurrence (Yoshikawa et.al, 2012). On the basis of ice jam hydraulic experiments, Yoshikawa et al. proposed an “ice jam scale” with consideration of changes in the river width in addition to the Froude number for river ice, and proved that an ice jam was likely to occur when the ice jam scale was higher (Yoshikawa et.al, 2016).

However, it is not still clear that the mechanism and evaluation of development of ice jam caused by river ice flowing into a completely ice-covered section. In this study, we carried out a hydraulic model experiment on the inflow of river ice into a completely ice-covered section, and figured out conditions of ice jam development by using the ice jam formation scale.

2. Ice jam hydraulic experiment

(1) Outline of the experiment

We conducted hydraulic model experiment, referring the conditions of ice jam observed in the Shokotsu River in February, 2010. From the result of non-uniform flow calculation based on the flow rate of $14m^3/s$ prior to the development of an ice jam and transverse data derived from the ice jam sections from KP11 section (11km upstream from river mouth) to KP20 section (20km upstream end from river mouth) in the actual river, the following values were acquired: the minimum, mean and maximum widths of water surface were 21.3m, 40.8m, and 82.0m, and the minimum and maximum bed slopes were 1/769 and 1/125, respectively. For the sake of convenience of the hydraulic experiment, the model was built on a scale of 1/100, with a channel width of 0.2m as minimum, 0.4m as a mean, and 0.8m as a maximum, whereas the minimum gradient was set to be level and the maximum gradient at 1/120. On the basis of these parameters, the channel width and the stream gradient were combined arbitrarily to build the structure of the experimental channel.

The experimental channel consisted of the following four 2m-long sections from downstream: Site 1 (0.8m width, LEVEL), Site 2 (0.2m width, 1/120 gradient), Site 3 (0.4m width, LEVEL), and Site 4 (0.2m wide, 1/120 gradient). The plan view of the channel is illustrated in **Figure 1**.

In consideration of the 1/100 model scale, two sizes of square shape ice plates were prepared, namely 0.04m side and 0.08m side, of which the thickness was set uniformly at 0.006m, by reference to the maximum outside dimension (approx. 4m) and thickness (approx. 0.6m) of ice plates piled up after the development of an ice jam in the actual river channel. Ice plate models were made of polypropylene, which held the same specific gravity (=0.9) as that of ice plates in the actual river. To make the velocity of ice plate models discernible, 0.04m side ice plate models were stamped with 0.02m red circle in diameter and 0.08m side ice plate models were stamped with a 0.04m red circle in diameter on the both sides of each model, respectively. The surface of the completely ice-covered section was covered totally with polypropylene (0.006m thick).

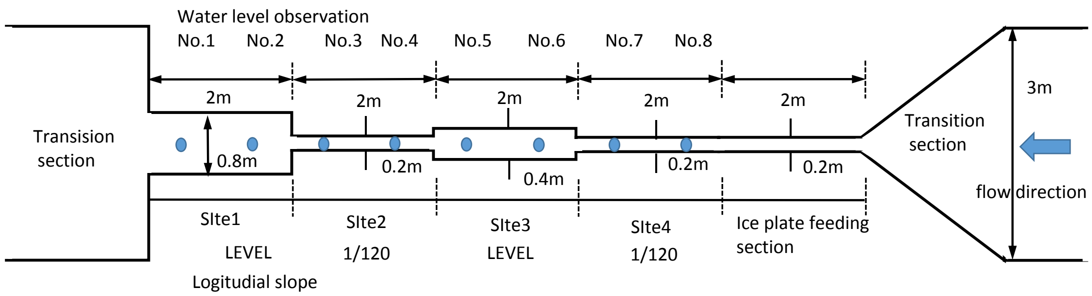

Fig. 1. Plan view of ice jam experiments channel

Table 1. Conditions of ice jam experiments

Case #	River discharge $Q_w(m^3/s)$	Ice plate flux q_{ice} (m^3/s)	Ice plate size a_i(m)	Completely frozen ice area
C1-1	0.0042	0.0006	0.08	Site 1
C1-2	0.0042	0.0006	0.04	Site 1
C1-3	0.0042	0.0003	0.08	Site 1
C1-4	0.0042	0.0003	0.04	Site 1
C1-5	0.0035	0.0006	0.08	Site 1
C1-6	0.0035	0.0006	0.04	Site 1
C1-7	0.0035	0.0003	0.08	Site 1
C1-8	0.0035	0.0003	0.04	Site 1
C1-9	0.0028	0.0006	0.08	Site 1
C1-10	0.0028	0.0006	0.04	Site 1
C1-11	0.0028	0.0003	0.08	Site 1
C1-12	0.0028	0.0003	0.04	Site 1

Case #	River discharge $Q_w(m^3/s)$	Ice plate flux (m^3s^{-1})	Ice plate size a_i(m)	Completely frozen ice area
C2-1	0.0042	0.0006	0.08	Site 2
C2-2	0.0042	0.0006	0.04	Site 2
C2-3	0.0042	0.0003	0.08	Site 2
C2-4	0.0042	0.0003	0.04	Site 2
C2-5	0.0035	0.0006	0.08	Site 2
C2-6	0.0035	0.0006	0.04	Site 2
C2-7	0.0035	0.0003	0.08	Site 2
C2-8	0.0035	0.0003	0.04	Site 2
C2-9	0.0028	0.0006	0.08	Site 2
C2-10	0.0028	0.0006	0.04	Site 2
C2-11	0.0028	0.0003	0.08	Site 2
C2-12	0.0028	0.0003	0.04	Site 2

Table 2. Measuring instruments used in the experiments

Items	Facilities' names, company, specs
Water level	Pressure sensor (ATM1ST, Koshin Denki Kogyo,) Logger unit(NR-600, Keyence)
Water temperature	Mercurial thermometer (1 degree Celsius intervals)
Vertical photography	digital single-lens reflex (Mark II, Canon), 24mm prime-lens, 1920×1080 pixels
Laterally photography	Digital video camera recorder (GZ-EX350, JVC Kenwood), 1920×1080 pixels

A total of 24 cases listed in **Table 1** were examined in the experiment. As for the placement of a completely ice-covered section within the channel, two scenarios were drawn up. A completely ice-covered section was assigned to Site 1 for the C1 series and to Site 2 for the C2 series. In the C1 series, a sudden expansion in the lower reaches was completely ice-covered whereas the C2 series contained a sudden contraction in the lower reaches, which was completely ice-covered. By reference to the maximum flow rate of 286m^3/s at the time of ice jam development, the experimental river discharges were set with three cases: 0.0028m^3/s as a standard, 0.0035m^3/s and 0.0042m^3/s. The amount of ice plates was given two cases of 0.0006m^3/s and 0.0003m^3/s according to the rate of 60m^3/s observed before the development of an ice jam. An ice jam occurred upstream from the completely ice-covered sections in all cases but C2-4.

The specifications of ice plate measuring instruments are listed in **Table 2**. To record a temporal sequence of longitudinal water levels within the channel, a piezo tubes was installed on the channel bottom at eight points from No. 1 to No. 8 shown in **Figure 1**, at a 0.5m point from the downstream end of Site 1 and at intervals of 1m from the upper reaches. The piezo tubes were connected to a pressure sensor by conveyance pipes, and voltage values from the pressure sensor was obtained through a data logger. By preliminarily applying a relational formula between voltage and water level, the water level was measured every 0.01 second. To record the velocity and number of ice plate models within the channel, two digital cameras were fixed above the channel and dynamic images began to be taken simultaneously from the start of the experiment. In addition, a camcorder was installed on the flank of the channel and began to be activated simultaneously from the start of the experiment to confirm the stagnation of ice plates within a 0.5m range upstream from the completely ice-covers section. To conduct the particle tracking velocimetry (PTV) method for evaluating the velocity of ice plate models, PC Software (Dipp Flow, products of Ditect Co.ltd.) was employed.

(2) Attenuation rate of ice plate velocity

The attenuation rate of the velocity of ice plate movement due to the occurrence of an ice jam was examined, by following the method proposed by Yoshikawa et al., 2016.

The attenuation rate of the ice plate velocity, λ, is expressed with the following equation Eq. [1].

$$\lambda = \frac{u_i}{u_{w0}} = \frac{1}{1+S_{ij}} \quad \textbf{[1]}$$

where, u_i (m/s): the ice plate velocity after the development of an ice jam, and u_{w0}(m/s): the flow velocity right before the development of an ice jam. The ice plate velocity right before the development an ice jam is equal to the flow velocity. They freely flow down, where u_i=u_{w0}, and therefore λ= 1. When ice jam entirely settles into shape, u_i= 0 and thus λ= 0.

$u_i$was obtained by the measurement of PTV method within a 0.5m range upstream from the completely ice-covered section was used as the mean velocity of ice plate movement.

u_{w0} was calculated as cross-sectional averaged velocity before occurrence of ice jam. Water depth was obtained from water level data (1 second averaged) right before the start of ice plate feeding (No.3 and No.4 in Site 2 for the C1 series and No.5 and No.6 in Site 3 for the C2 series).

The ice jam scale, S_{ij}, presenting the dimension of an ice jam, treats accumulated ice plates as a group. It is expressed with the following equation Eq. [2], which is based on the equilibrium moment of force on a group of ice plates.

$$S_{ij} = \frac{1}{F_{ri}\sqrt{\frac{B_2}{B_1}}\sqrt{\frac{C_D}{2}\left(\frac{H_i}{L_i}\right)^2 + C_f\left(\frac{H_i}{L_i}\right) + \frac{C_D}{2}}} \quad \textbf{[2]}$$

The Froude number for river ice, F_{ri}, which is related to the ice plate velocity and thickness, is expressed with the following equation Eq.[3].

$$F_{ri} = \frac{u_i}{\sqrt{\left(\frac{\rho_w-\rho_i}{\rho_w}\right)gH_i}} \quad \textbf{[3]}$$

where, B_1 (m): the mean channel width at a place of ice jam development, B_2(m): the channel width downstream from an ice jam, L_i(m): the length of an accumulated ice plate group, H_i(m) (m): the mean thickness of an accumulated ice plate group, u_i(m/s): the mean velocity of ice plates flowing, ρ_i(kg/m^3): the ice density, ρ_w(kg/m^3): the water density, C_D: the drag coefficient of an ice plate group, C_f: the surface friction coefficient of an ice plate group, C_L: the lift force coefficient of an ice plate group, and g (m/s^2): the gravitational acceleration. This study followed the past studies6) and employed the following parameters: g=9.8m/s^2, C_D= 0.4, C_f= 1.0, C_L= 0.4, ρ_i=917kg/m^3 and ρ_w=1000kg/m^3.
The length of an ice plate group, L_i was given 0.5m, equal to the length of the section analyzed with the PTV method.
The mean thickness of an accumulated ice plate group, H_i(m) was calculated as Eq.[4].

$$H_i = \frac{N_i \times a_i^2}{L_i \times B_1} \qquad \textbf{[4]}$$

where, N_i: the number of ice plates stagnating within a 0.5m range upstream from the completely ice-covered section. It was figured out from image data at one second intervals. a_i(m): side of ice plates

3. Experimental results and discussion
(1) Development process of an ice jam
It has been pointed out in past studies that an ice jam forms in the early stage where the river discharge is low, the amount of ice plates is large and the size of ice plates is large.2) The characteristic behaviors of ice plates stagnating upstream from the completely ice-covered section were compared severally for both the C1 series and the C2 series.
Figure 2 illustrates the temporal changes in the velocity of ice plates flowing and the number of ice plate stagnating within a 0.5m range upstream from the ice-covered section for both the C1 series and the C2 series. By setting C1-9 and C2-9 (the flow rate: 0.0028 m^3/s, the amount of ice plates provided: 0.0006 m^3/s, and the size of ice plates: 0.08m) as a reference case where an ice jam is most likely to occur, the behaviors of ice plates with different flow rates and different amounts and sizes of ice plates were compared.
To begin with, the C1 series is inspected by comparing C1-1, C1-5 and C1-9 of different flow rates. In comparison with C1-9 of the 0.0028m^3/s flow rate, the velocities of ice plates flowing in C1-5 of 0.0035m^3/s and C1-1 of 0.0042 m^3/s were low and reached nearly zero at an early time. When C1-9 with the amount of ice plates at 0.0006 m^3/s and C-11 at 0.0003m^3/s are compared, no difference was found between them in the time when the ice plate velocity reached nearly zero. Likewise, in comparison between C1-9 and C1-10, the velocity of ice plates reached nearly zero at an early time in C1-10, which contained a smaller size of ice plates. Thus, as far as the C1 series was concerned, no relation of ice jam formation was detected with the flow rate and the amount and size of ice plates.
Meanwhile, in the C2 series, C2-9 with the flow rate of 0.0028m^3/s, C2-5 of 0.0035m^3/s, and C2-1 of 0.0042m^3/s decreased the velocity of ice plates to nearly zero in order of time. The number of ice plates stagnating increased as the flow rate rose, and the development of an ice jam tended to delay as the flow rate increased. When C2-9 with the amount of ice plates at 0.0006m^3/s was compared with C2-11 at 0.0003m^3/s, the velocity of ice plates flowing in C2-9 was attenuated earlier and at the same time the number of ice plates stagnating increased. More ice plates

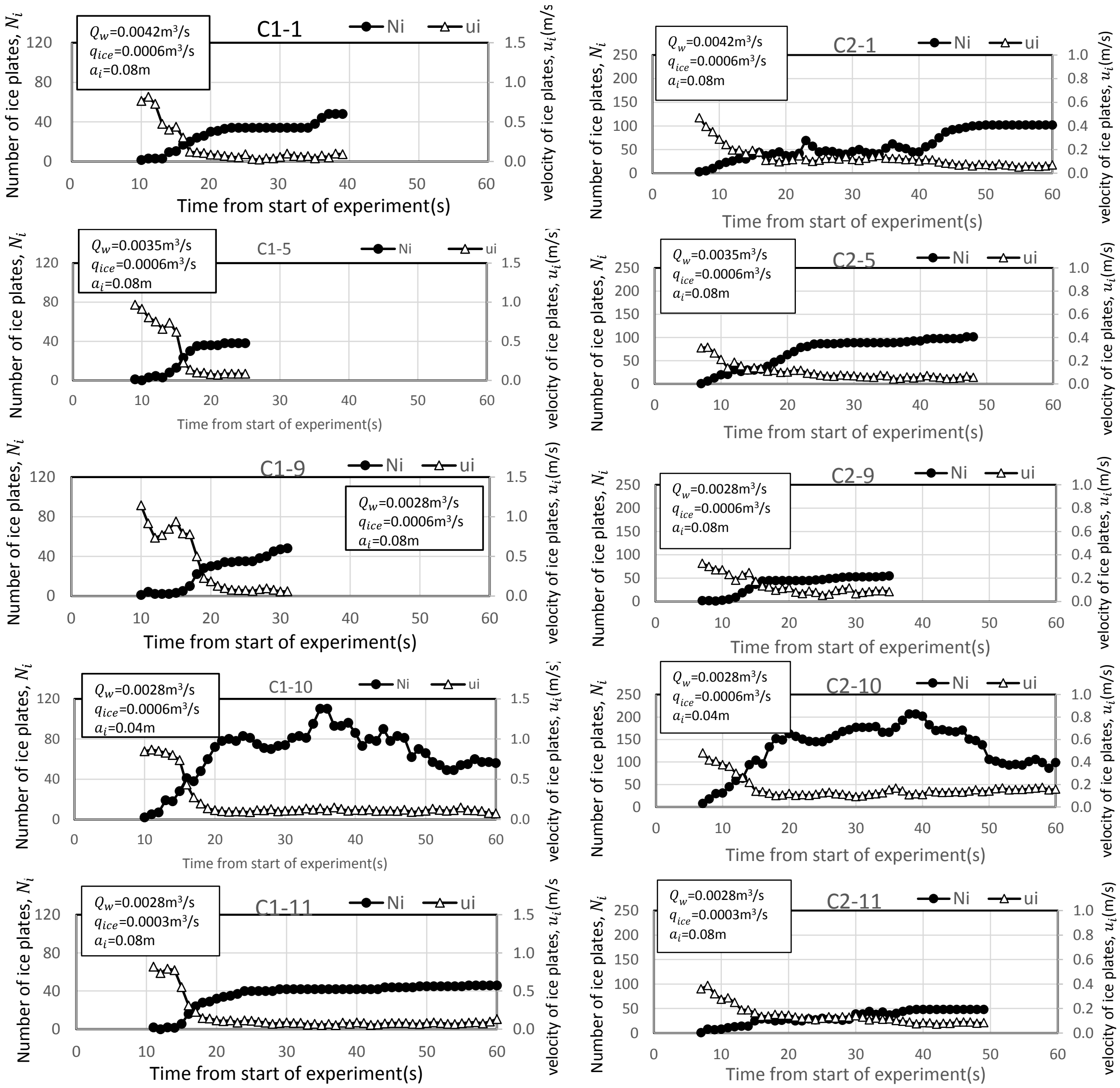

Fig. 2. Results of experiments (Number of ice plates and mean velocity of ice plates)

seemed to stagnate as the amount of ice plates increased. Regarding the size of ice plates, the number of ice plates stagnating in C2-10 with the 0.04m size was turned to be unstable, therefore making it difficult to distinguish their properties.

As stated so far, some effects of the flow rate and the amount of ice plates on ice jam occurrence were observed in the C2 series where the completely ice-covered section was suddenly contracted. Yet, in the context of the size of ice plates, no clear difference was found in the both series. In the C1 series where the completely ice-covered section was suddenly expanded, the development of an ice jam was not able to be related with the flow rate, the amount of ice plates or the size of ice plates.

(2) Investigation of ice jam scale

The attenuation rate of the ice plate velocity, λ, was compared between theoretical values and experimental values. The result is demonstrated in **Figure 3**. There, theoretical values of λ, in

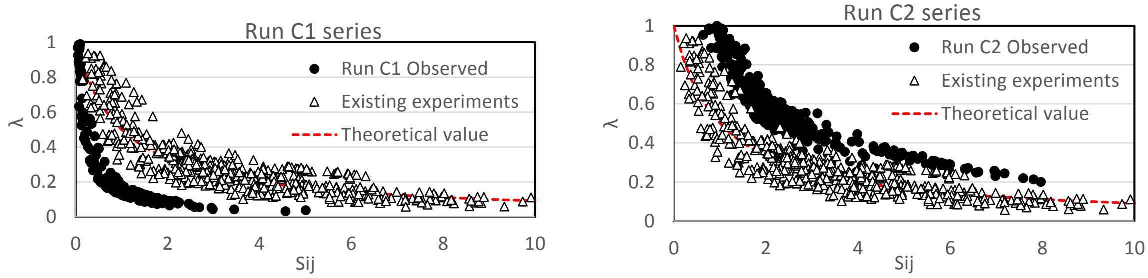

(1) Run C1 series (2) Run C2 series

Fig. 3. Comparison of relation of λ and S_{ij} with this experiments and existing experiments

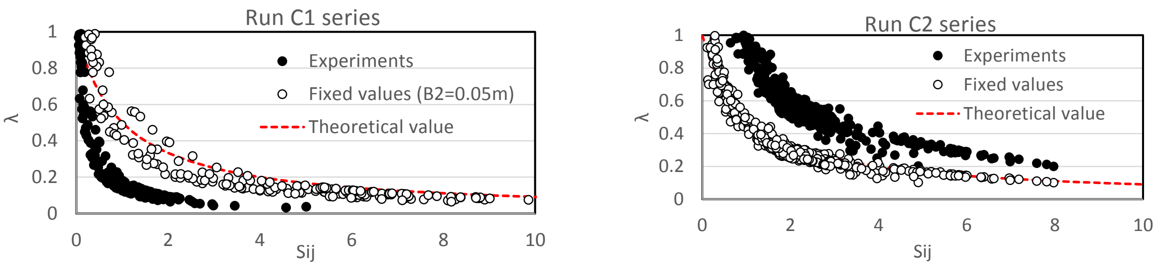

(1) Run C1 series (2) Run C2 series

Fig. 4. Comparison of relation of λ and S_{ij} with observed and fixed values

relation to S_{ij} derived from Eq. [1], are plotted as red dot line. Any data assuming u_i>u_{w0} were excluded because λ do not exceeds 1.0 in theory. Existing experimental results of ice jam development with changes in the river width (Yoshikawa Et.al, 2016) are plotted included. The existing experimental results seemed to agree with the theoretical values fairly well.

According to **Figure 3(a)**, the relation of λ and S_{ij} in the case of the C1 series substantially differed between the experimental values and the theoretical values, where the experimental values of λ were smaller than the theoretical values for the same S_{ij}. This means that attenuation of the ice plate velocity obtained from the experiment is larger than that obtained from the theoretical value as the stagnation of ice plates advances.

Also in the case of the C2 series, as **Figure 3(b)** demonstrates, the relation of λ and S_{ij} was considerably different between the experimental values and the theoretical values. Contrary to the C1 series, the experimental values of λ were larger than the theoretical values for the same S_{ij}. This means that attenuation of the ice plate velocity obtained from the experiment is smaller than that obtained from the theoretical value as the stagnation of ice plates advances.

(3) Investigation of fixed value of ice jam scale

As a next, we fixed some calculation of S_{ij}. Concerning the C1 series, the downstream channel width, B_2, on the ice jam scale of Eq. [2], was calibrated by trial and error, and the adjusted downstream channel width, B_2', which closely approximated the theoretical value, was obtained. The result is shown in **Figure 4(a)**. When the adjusted value was set at B_2'=0.05m, which was 1/16 of the original downstream channel width, B_2=0.8m, the experimental values generally agreed with the theoretical values.

As for the C2 series, it was assumed that a dead water zone appeared immediately upstream from the narrowing channel section, possibly affecting the velocity of ice plates flowing. We fixed Thus, u_{w0}, which would estimate λ was adjusted rather than applying B_2'. To figure out u_{w0}, the mean flow rate not in the originally defined upstream total cross section (0.4m channel width) but in the effective 0.2m-wide section excluding the dead water zone was calculated, and the relation between λ and S_{ij} was reexamined. The result is shown in **Figure 4(b)**. The relation between λ and S_{ij} came to closely approximate the theoretical value. Although the consequence of channel width reduction is reflected in Eq. [2], it is necessary to take account of the cross-sectional dead water zone in evaluating the velocity of ice plates flowing before ice jam development.

(4) Examination on differences in the river width ratio of the completely ice-covered section
As stated above, concerning the attenuation rate of the velocity of ice plates flowing in the C1 series, the experimental value generally agreed with the theoretical value, by replacing the original downstream channel width, B_2=0.8m, with its 1/16 value, B_2'=0.05m. The reason for this outcome is examined from the viewpoint of ice plate stagnation.
The discussion given so far is still in the stage of inferences at the moment. Thus, it is hoped to thoroughly investigate the mechanism of ice plate stagnation in future experiments under various conditions.

4. Conclusion
The findings in this study are summarized below.
(1) In the cases (C1 series) where the completely ice-covered section expanded, the relation between λ and S_{ij} differed from that of the theoretical formula. The observed value exhibited the stagnation of ice plates more noticeably than the theoretical value. In this experiment, the experimental value generally agreed with the theoretical value on the assumption that the channel width in downstream cross section reduced to a tenth of the actual width or narrower.
(2) In the cases (C2 series) where the completely ice-covered section contracted, the relation between attenuation rate, λ, and ice jam scale, S_{ij}, generally agreed with the existing theoretical formula, by properly evaluating the ice plate velocity right before ice jam development.
(3) Reasons why the relation between λ and S_{ij} differed from the theoretical formula were examined in the C1 series. One of the reasons may be attributed to the flow promoting the stagnation of ice plates in the sectional transition area to the completely ice-covered section, which possibly led to different conditions for ice jam development from those explained by the conventional λ and S_{ij} relation.
As our future task, we will carry out in-depth surveys on the mechanism of ice plate stagnation in the sectional transition area and thoroughly sort out the relation between λ and S_{ij}.

Acknowledgment
This work was supported by JSPS KAKENHI Grant Number JP18K04361.

References
Abe, T., Yoshikawa, Y., Hirai, Y., 2012: Measuring the River Ice Floe Sizes Broken by 2011 Tohoku Pacific-Coast Earthquake Tsunami, Proceedings of the 21st IAHR International Symposium on Ice
Yoshikawa, Y., Watanabe, Y., Hayakawa, H. and Hirai, Y., 2012: Field observation of a river ice jam in the Shokotsu River in February 2010. Proceedings of the 21th IAHR International Symposium on Ice, Dalian, China, pp. 105–117
Yoshikawa, Y., Kuroda, Y., Abe, T., Toyabe, T., Park, H., Oshima, K., 2016: Study on the ice-jam occurrence based on hydraulic experimentation, Proceedings of the 23rd IAHR International Symposium on Ice

International Association for Hydro-Environment Engineering and Research

Supported by Spain Water and IWHR, China

24th IAHR International Symposium on Ice
Vladivostok, Russia, June 4 to 9, 2018

Proposed Simplified Ice-Jam Numerical Model for Ie-Covered Rivers

Yasuhiro Yoshikawa[1] Hotaek Park[2] Kazuhiro Oshima[3] Hiroshi Yokoyama[4]
[1]*Kitami institute of technology, Kitami, Hokkaido, Japan*
[2]*JAMSTEC, Yokosuka, Kanagawa, Japan*
[3]*Institute for Environmental Sciences, Aomori, Japan*
[4]*Civil Engineering Research Institute for Cold Region, Sapporo, Hokkaido, Japan*
yoshi@mail.kitami-it.ac.jp

The purpose of this study was to construct a simple ice-jam numerical model, with a low calculation load, that can be incorporated into a global-scale model. By attempting to reproduce ice-jam phenomena occurring in actual rivers, the proposed model was evaluated and its issues were clarified.

This model comprises equations for river water flow, river ice flow, formation and melting of ice sheets, and water temperature. For calculating the river ice flow rate, a river flow deposition equation was proposed.

In addition, we demonstrated that as this model does not consider river ice fracture events, the reproducibility of water levels was low in locations where the river ice area was calculated to be smaller than the actual area. Finally, important parameters in the model were discussed.

1. Introduction

In the case of cold-region rivers, river ice flows downstream where it becomes blocked in river channels and causes ice jams, which can cause sudden spikes in water level. Disasters due to ice jams occur in countries with temperatures below freezing, such as USA, Canada, China, and Russia. There are reports of ice jams in Hokkaido (Hara et al., 1994), Japan that caused human casualties and sudden spikes (Shen et al., 2003) in water levels. For the future, it is necessary to understand the manner in which the frequency and scale of ice-jam disasters will change according to climate change.

Regarding the impact of climate change on rivers in cold regions, previous research includes the impact (Hotaek et al., 2016) of snow accumulation on river ice thickness and the impact (Hotaek et al., 2017) of air temperature on river water temperature. However, it has been noted (Tokuda et al., 2017) that there is a need for a global-scale numerical model for evaluating climate change that can reproduce the ice-jam phenomenon. An existing one-dimensional, unsteady flow numerical model (Yoshikawa, et al., 2014a) that uses different ice block sizes is based on the dynamic wave method, which targets ice-jam phenomena caused by the deposition of ice sheets in narrow, constricted areas. To easily integrate this model into a global-scale numerical model, it is preferable to simplify the basic equations and for the equations to be within the range of the reproduced phenomena. However, this type of simple ice-jam model has not yet been constructed.

The purpose of this study was to construct a simple ice-jam model, with a low calculative load, that could be incorporated into a global-scale numerical model and to evaluate and clarify issues related to the proposed numerical model by reproducing ice-jam phenomena occurring in actual rivers.

2. Construction of a simple ice-jam numerical model

The proposed numerical model comprises equations for river water flow, river ice flow, formation and melting of fixed ice sheets, and river water temperature. To decrease the calculation load and produce a simplified model, a simple equation was used for the basic formula, and the cross-section of the river ice was considered to be rectangular. A conceptual diagram is shown in Figure-1. River ice can be broadly categorized into hard ice sheets (ones fixed are ice sheets and ones flowing downstream are ice floes), soft frazil ice, and snow accumulated on ice sheets or frazil ice.

The proposed numerical model refers to river ice as a mixture of hard ice floes flowing downstream and frazil ice flowing downstream.

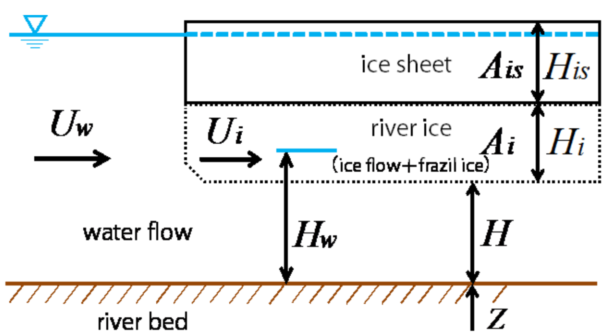

Fig. 1. Conceptual diagram of the proposed ice-jam numerical model

(1) Flow of river ice

The basic model used a continuity equation based on the kinematic-wave method and Manning's mean velocity equation. The right hand side of the consecutive equation, Eq. [1], expresses the change in the flow area for river ice gaps caused by changes in downstream flowing river ice. The kinematic-wave method has constraints that restrict its application in the cases in which the slope is small or the cases in which there are outstanding diffusion terms (Kure, Yamada, 2009).

$$\frac{\partial A_w}{\partial t} + \frac{\partial Q_w}{\partial x} = \lambda_i \frac{\rho_i}{\rho_w} \frac{\partial A_i}{\partial t} \quad \textbf{[1]}$$

$$Q_w = A_w U_w \quad \textbf{[2]}$$

$$U_w = \frac{1}{n} R^{\frac{2}{3}} I^{\frac{1}{2}} \quad \textbf{[3]}$$

Where, $A_w(\mathrm{m}^2)$ is the flow area, i.e., the combined value of the areas where only water flows and areas where the river ice gap locations flow; $A_i(\mathrm{m}^2)$ is the cross-sectional area of the river ice, which includes the areas of both the ice and the gaps added together; $Q_w(\mathrm{m}^3/s)$ is the river ice volumetric flow rate; λ_i : is the river ice gap rate applied as 0.4; $\rho_w(\mathrm{kg/m}^3)$ is the water density and is set at 1,000 ; $\rho_i(\mathrm{kg/m}^3)$ is the ice density and is set at 917; $t(\mathrm{s})$ is the time; $x(\mathrm{m})$ is the distance; $U_w(\mathrm{m/s})$ is the water flow rate of a river in the vertical direction; $n(\mathrm{s/m}^{1/3})$ is Manning's coefficient of roughness; $R(\mathrm{m})$ is the diameter depth calculated considering the wetted perimeter of the river ice.

Water surface incline, *I*, is an important factor in the proposed model because the water level and the water surface incline change owing to the presence of river ice, and changes in the flow rate also cause changes in the river ice flow rate. Water level is obtained from the river bed height + water depth where only water flows + ice sheets and river ice draft depth of ice sheets under river ice. Definitively, A_w obtained from Eq. [1] is divided by river width, *B*, to obtain the water depth, H_w, with the consideration of the gaps in the river ice, and with riverbed height, *Z*, water level, H_w, is calculated according to Eq. [4]. The water surface incline is calculated from the differences in water levels.

$$H_z = Z + H_w + \frac{\rho_i}{\rho_w}\left((1-\lambda_i)H_i + H_{is}\right) \quad \textbf{[4]}$$

(2) Flow of river ice

The basic equation uses consecutive Eqs. [5] and [7] as the downstream flowing river ice deposition equation (Yoshikawa et al., 2016). Equation [7] considers river ice as blocks of ice in ice aggregates, and it is derived based on the assumption that the force rotation moment acting on the ice blocks is zero.

$$(1-\lambda_i)\frac{\partial A_i}{\partial t} + \frac{\partial Q_i}{\partial x} = 0 \quad \textbf{[5]}$$

$$Q_i = A_i U_i \quad \textbf{[6]}$$

$$U_i = U_w - \sqrt{\frac{\frac{B_i}{B_d}\left(\frac{\rho_w - \rho_i}{\rho_w}\right) g H_i}{\frac{C_D}{2}\left(\frac{H_i}{L_i}\right)^2 + C_f\left(\frac{H_i}{L_i}\right) + \frac{C_L}{2}}} \quad \textbf{[7]}$$

Where, $Q_i(\mathrm{m^3/s})$ is the downstream flowing ice deposition flow quantity; $U_i(\mathrm{m/s})$ is the river ice rate in the river's vertical direction; $B_i(\mathrm{m})$ is the width of the ice blocks; $B_d(\mathrm{m})$ is the width of the river flowing downstream; $g(\mathrm{m/s^2})$ is the acceleration of gravity, which is 9.8 ; $H_i(\mathrm{m})$ is the river ice thickness in the vertical direction of the ice bock; $L_i(\mathrm{m})$ is length of the ice block in the river's vertical direction; C_D is the profile drag coefficient; C_f is the friction resistance coefficient; and C_L is the uplift force coefficient.

(3) Ice sheet form melting

For the calculation of the formation and melting of ice sheets we use the following formula (Yoshikawa et al., 2014b) derived from the heat balance equation:

$$H_{is} = H'_{is} - \left(\frac{65.2}{10^5}\right) \alpha \frac{T_a}{H'_{is}} - \left(\frac{45.8}{10^2}\right) \beta^{4/5} T_w H^{1/3} \quad \textbf{[8]}$$

Where $H_{is}(\mathrm{m})$ is the ice sheet thickness, $H'_{is}(\mathrm{m})$ is the ice sheet thickness before Δt, $H(\mathrm{m})$ is the water depth where only water flows. T_a(°C) is the air temperature (mean daily value), and T_w(°C) is the water temperature (mean daily value). For example, when Δt = 1 hour, the unit-converted values divided by 24, i.e., T_a/24 and T_w/24 become the input values. As an initial condition, we set $H'_{is}(\mathrm{m})$ = 1 mm, which is indicated as an appropriate value in a previous study (Yoshikawa et al., 2014b). α expresses the extent of the ice sheet formation in relation to temperature; the ice sheet extent increases with temperature. This unit is dimensionless, we apply coefficient a that is based on a correlation equation (Yoshikawa et al., 2014b) based on the features of the river channel and coefficient $\beta = U_w/H^{2/3}$. When there is river ice deposited downstream, this ice is melted using a melting term, which is the third term from the right of formula [8].

(4) River water temperature

The basic formula uses the following formula, which ignores the dispersion term based on the formula presented in a previous study (Yoshikawa et al., 2010), from which the suitability of formulas in which the dispersion term is ignored was confirmed (Hotaek et al., 2017) in global-scale calculation models and the suitability of the calculation results was determined.

$$\rho_w C_P \frac{\partial(A_w T_w)}{\partial t} + \rho_w C_P \frac{\partial(Q_w T_w)}{\partial x} = -(1-N)B\phi_{wa} - NB\phi_w \quad \textbf{[9]}$$

$$\phi_{wa} = h_{wa}\left(\widehat{T_w} - T_a\right) \quad \textbf{[10]}$$

$$\phi_w = C_{wi} \frac{{U_w}^{0.8}}{H^{0.2}} \left(\widehat{T_w} - T_f\right) \quad \textbf{[11]}$$

Where $C_P(\mathrm{kJ/(kg\ °C)})$ is the water specific heat; in this case the applied value is 4.2. N is the horizontal freezing ratio, i.e., the ratio of the river ice width in relation to the water surface width, whose value is obtained using the same formulas proposed in a previous study (Yoshikawa et al., 2010). $\phi_{wa}(\mathrm{W/m^2})$ is the thermal flux between the atmosphere and the river water. $h_{wa}(\mathrm{W/(m^2\ °C)})$ is the water surface heat exchange coefficient; here we apply a value of

20. $C_{wi}((\mathrm{W\,S^{0.8}})/(°\mathrm{C\,m^{2.6}})) = 1622$. T_f(°C) is the river ice bottom surface temperature at 0. $\widehat{T_w}$(°C) is the water temperature after Δt, this is treated here as an unknown.

3. Recalculation of ice jams

We attempted to apply this calculation model to actual rivers and reproduce the ice-jam phenomenon. Based on field observations of the ice jams in the actual river, it is not possible to determine when the deposited river ice flowed downstream. Therefore, we may not reach precise conclusions solely based on these observations. In addition, it is difficult to predict, beforehand, where the ice jams will occur, but as we were successful in measuring the vertical water level, which was captured on camera, and in observing (Yoshikawa et al., 2012) the river ice deposits in ice jams occurring in Shokotsu River, we attempted to reproduce the ice-jam phenomenon based on this observation data.

(1) Field Observation

In the Shokotsu River, located in eastern Hokkaido, the water-level measurement, camera capture, and river ice area measurement after ice jams occurred were performed in the locations shown in Figure-2.

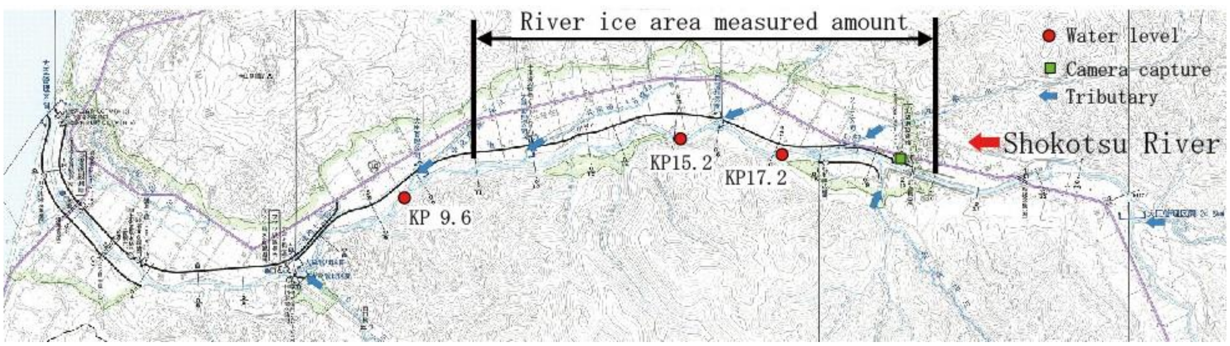

Fig. 2. Location of the field observation sites along Shokotsu River
(KP: distance in km from the river mouth)

Camera capture was performed at a location that was situated 19.3 km away from the river mouth, and this was taken as a thaw event occurring at the tip of the ice jams. Owing to an increase in water flows from upstream, water flows on to the top of the river ice surface, and, following this, the river ice itself is carried by the water flows. After 10 s, thawing begins, and within one hour, river ice flowing downstream is confirmed.

The river ice measurement after the ice jam occurred was conducted between March 28 and March 31 in 2010 in the section between KP11 and KP20 (46 sections, every 200 m). An example is shown in Figure-3. We used GPS and total station measurements, and we measured the quantity of deposited river ice at the change point and the quantity of accumulated snow at the change point depending on the river bathymetry. We measured only the deposited river ice. The river ice area when the ice jams occurred were based on the deposited left bank and right bank river ice, and the area directly linking the left and right banks, and surrounding areas were considered as the estimated river ice area. This value is obtained after adding the estimated river ice area and the measured river ice area.

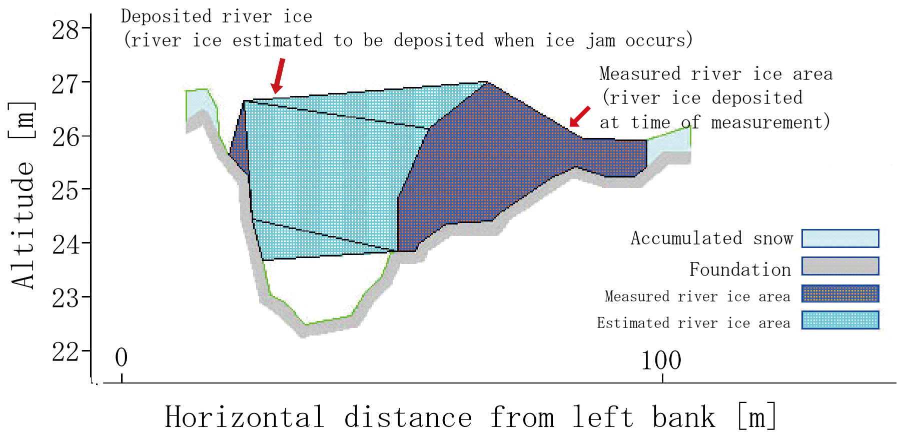

Fig. **3**. Example of a cross-section diagram of river ice area after ice jams occurred (KP 15.2) March 28–31, 2010)

(2) Calculation conditions

The calculation interval was the 22.6-km section from the point 2 km away from the river mouth to the point that was 24.6 km away, and this was calculated for the 110-day period from December 1, 2009, 13:00 to March 21, 2010, 13:00. The cross-section interval Δx = 200 m for the time interval Δt under the CFL conditions was successively obtained as the courant number 0.1.

The applied river channel conditions were the river bed height and river width. A varied flow calculation using the measurement data from November 2007 was performed to determine the river width and the flow area. This wetted area was divided by the river width, and the mean river bed height was calculated from the mean water depth and the water level. For the flow volume, the drought water-discharge was applied. As an initial condition, we applied a water depth based on the varied flow calculation.

As a boundary condition, the flow volume and the river ice thickness at the upstream tip were applied along with the water level at the downstream tip. The applied mean river ice thickness was observed to be 30 cm based on field observations (Yoshikawa et al., 2012) after the ice jams occurred during the river ice downstream period, obtained from the results of camera capture during the thaw . For the water temperature, the observation data after flowing from the upstream tip to the tributary were applied. For the air temperature, the observation data from the point that was located 19.8 km away from the river mouth were applied.

(3) River ice area and water level

The observed and calculated values of the river ice area during the river ice area observation period shown in Figure-2 are presented in Figure-4. The diagram shows the calculation results when the river ice flows were not considered.

In Figure-4, we can see that the calculation results, considering the river ice flows, have higher river ice areas than the calculation results when the river ice flows are ignored and that there is high reproducibility of the river ice area while considering the river ice flows. The calculated values of river ice areas while considering river ice flows were smaller than those based on the observed values, and the mean absolute error between the calculated values and observed values was 73 m^3. In particular, in downstream, where the river ice area was larger than upstream, the error between the observed and the calculated values was large. From the results of the field

observations (Yoshikawa et al., 2012), comparing upstream to downstream, the relative river width is smaller at the ice jams source. Consequently, we consider that the river ice was deposited upstream. The calculated value of the downstream river ice area is smaller than the observed value probably because the river ice quantity supplied from upstream was small.
Regarding the observed and calculated values of the water level, the upstream point between regions where the ice jams occurred (KP17.2) is shown in Figure-5. The downstream point between regions where ice jams occurred (KP15.2) is shown in Figure-6, and the points (KP9.6) where the ice jams did not occur are shown in Figure-7. The mean absolute errors for the calculated and the observed values are shown in the same diagram. At KP15.2, which is close to the point of origin of the ice jams, the mean absolute error is larger than those at KP9.6 and KP17.2.

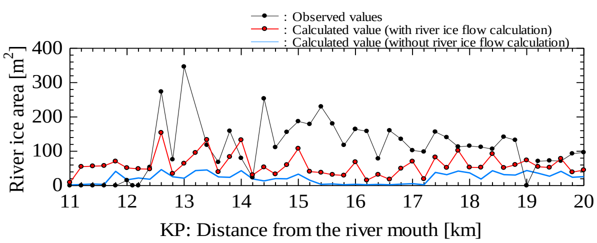

Fig. 4. Observed and calculated values of the river ice area in the intervals where ice jams occur.

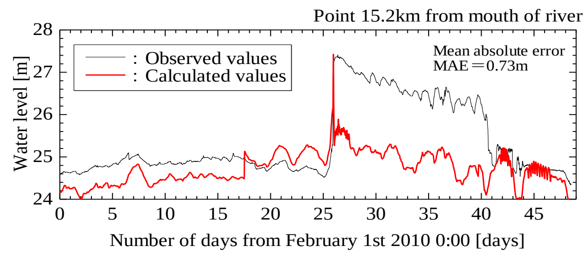

Fig. 6. Water level observed and calculated value (KP15.2).

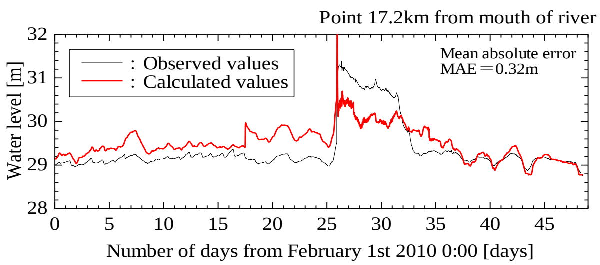

Fig. **5**. Water level observed and calculated values (KP17.2).

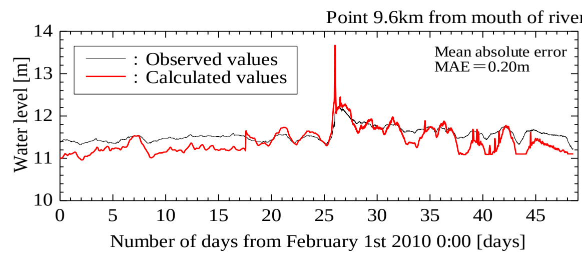

Fig. 7. Water level observed and calculated value (KP9.6)

Camera capture confirmed the occurrence of the ice-jam phenomenon on February 26, 2010. From Figure-5, we can observe that the water level at the point where the ice jams occurred reproduces the calculated value. However, we look at the water level at the downstream point (KP15.2) between the regions where ice jams with a large mean absolute error between the observed and calculated values of the river ice area occur(Figure-6). The phenomenon peak, when the ice jam formation continued and the water level increased, was not reproduced. In the point (KP9.6) where ice jams did not occur, the water level variation cannot be reproduced by the calculated values.

(4) Evaluation of the proposed calculation model and issues
This calculation model can express river ice downstream deposit phenomena based on a simple formula. At points where the river ice area is smaller than the actual area, the water level has low reproducibility. The calculated river ice area may be low because of breakage and the downward

flow of river ice from upstream. Moreover, most of the river ice flows downstream. However, the present calculation model does not consider the river ice breakage. In terms of calculation precision, while using a calculation model that considers breakage, it is considered that the error margin for the calculated values before February 26, 2010, when the ice jams occurred, would be the same as those in this calculation, and would consequently decrease. From Figures-5, 6, and 7, the mean absolute errors for KP17.2, KP15.2, and KP9.6, were 0.36 m, 0.38 m, and 0.20 m, respectively, before February 26, while after that, they became 0.28 m, 1.14 m, and 0.20 m, respectively. In particular, there is a large error margin in KP15.2 from February 26 onwards. Considering breakage, the river ice quantity flowing downstream and the precision in the water level increase estimate would be expected to increase. It is possible that this calculation model can be applied to cases in which the quantity of river ice from upstream is unknown.

Important parameters in this calculation model include the ice block length, L_i, the ice block width, B_i, the profile drag coefficient, C_D, the friction resistance coefficient, C_f, and the uplift coefficient, C_L. In this investigation, using trial and error, one-tenth of the river width B of this section was used and for the various coefficients, values from the existing research (Yoshikawa et al., 2016) were applied. However, a method for setting these values based on actual observations is required.

4. Conclusion

In this study, we attempted to construct a simple ice-jam calculation model with a small calculative load that could be incorporated into a global-scale calculation model and to reproduce the ice-jam phenomena occurring in actual rivers. This calculation model is based on a simple formula, but it is capable of expressing river downstream deposition phenomena. At points where the calculated river ice area was lower than the actual area, reproducibility was low probably because our model does not consider river ice breakage. Important parameters in this calculation model are L_i, B_i, C_D, C_f, and C_L.

In this study, the basic formula is simplified by treating aggregates of river ice as a single ice block. Thus, the present model is applicable not only to river ice but also to other drifting objects in the river.

Acknowledgments

This work was supported by JSPS KAKENHI Grant Number JP18K04361 and JP17H01870. We would like to express our gratitude for this.

References

Hara, F., et al., 1994. Research into the Sudden Increase in Discharge of River Water Due to Ice Jam. Proceedings of Cold Region Technology Conference, 10th, pp.462-470.

Hotaek Park et al., 2016. Quantification of Warming Climate-Induced Changes in Terrestrial Arctic River Ice Thickness and Phenology. Journal of Climate, Vol.29, No.5, pp.1733-1754.

Hotaek Park et al., 2017. Warming Water in Arctic Terrestrial Rivers under Climate Change. Journal of Hydrometeorology, Vol.18, No.7, pp.1983-1995.

Kure,S., Tadashi, Yamada, 2009. Theoretical derivation of the conceptual rainfall-runoff models. Journal of Japan Society of Hydrology and Water Resources, Vol.22, No.5, pp.386-400.

Shen,H.T., Liu,L., 2003. Shokotsu River ice jam formation. Cold Regions Science and Technology, 37, pp.35-49.
Tokuda, D., et al., 2017. Development of a global river temperature model considering river ice. Japan Society of Hydrology and Water Resources 2017 Research Workshop, pp.32-33.
Yoshikawa, Y., et al., 2010. Consideration of one-dimensional water temperature calculation model in an ice-covered river, JSCE, 65th, pp.409-410.
Yoshikawa, Y., et al., 2012. Field observation of a river ice jam in the shokotsu river in february 2010. Proceedings of The 21th IAHR International Symposium on Ice, pp.105-117.
Yoshikawa, Y., et al., 2014a. One-dimensional mixture river ice calculation and ice jam simulation. Journal of JSCE, Ser. B1(Hydraulic Engineering), Vol.70, No.4, pp.I_679-I_684.
Yoshikawa, Y., et al., 2014b. A simple equation for ice sheet thickness and ice formation/breakup prediction, Journal of JSCE, Vol.2, pp.203-213.
Yoshikawa, Y., et al., 2016. Study on the Ice-jam Occurrence based on Hydraulic Experimentation. Proceedings of The 23rd IAHR International Symposium on Ice, Ann Arbor, Michigan.

International Association for Hydro-Environment Engineering and Research
Supported by Spain Water and IWHR, China

24th IAHR International Symposium on Ice
Vladivostok, Russia, June 4 to 9, 2018

Birefringence in Ice Crystals. Principles and Application in Sea Ice Microstructure Studies

Aleksey Shestov[1, 2]
[1]The University Centre in Svalbard (UNIS), Longyearbyen, Norway
[2]Sustainable Arctic Marine and Coastal Technology (SAMCoT), Centre for Research-based Innovations (CRI), Norwegian University of Science and Technology (NTNU), Trondheim, Norway
UNIS, Pb. 156, 9171 Longyearbyen, Norway
aleksey.shestov@unis.no

This article addresses the optical reasoning of the widely used method of thin sectioning to study the microstructure of the sea ice. The application of the method in education and research is briefly discussed. Birefringence is the crucial property of ice crystal which is utilized in this method to distinguish ice grains, their size, geometrical and optical orientation. Principles of the optical phenomena are explained, and retardation of ordinary and extraordinary rays relative to each other is calculated. Based on retardation, spectral intensity function introduced by ice crystal to incident ray is obtained, and as a result, the formation of the color of the individual crystal is explained. Using spectral intensity function, the distinguishability measure of the individual crystal is formulated, and optimal geometrical thickness of thin section sample is advised. In the end, few practical aspects for observation of the thin section samples in the laboratory, as resulted from the optical reasoning, are given. The article is believed to be of interest both for research and teaching process.

1. Introduction

As for the last few decades and for now ice mechanics research is continued to be actively driven by the engineering applications. Sustainable Arctic Marine and Coastal Technology (SAMCoT) project is a live example of such development, where the need for quantitative models on ice mechanical behavior is formulated. And such models are being developed for predictive purposes in engineering projects planned in ice-covered waters where structures or vessels will undergo a different range of failure modes and level of ice loads. Cole (2001) addressed the aspects of ice microstructure influence on its mechanical properties and admitted that, frequently, generalized continuum model had been employed because of the difficulty in developing entirely mechanistic models of complex failure processes in ice. Instead, some of the terms in the models could be empirically associated with microphysical processes. That is why the microstructure analysis of ice has become the inalienable part of studies of mechanical properties of ice. Such analysis involves characterization of ice column by ice grains sizes and orientation of the c-(optical) axis of individual ice grains. Known microstructure characterization of the sample ice provides insights into basic ice properties and growth process, and as a result into microphysical processes, which in turn contributes into generalized models. The traditional way of performing microstructure characterization of ice is to accomplish many thin sections of the sample along the ice column depth. For each thin section, a substantial number of c-axis determinations are required to complete the crystal-fabric analysis. Procedures involved in the fabric study, laboratory techniques and methods of preparing thin sections are discussed by Langway (1958), while no optical reasoning behind it is given. The current paper intends to touch upon the optical property, birefringence, which makes individual ice grains visible and distinct from each other, observed in cross-polarized light on universal stage (Figure 1a). The author understands that a number of textbooks are available on the subject of optical crystallography, but he finds that a discussion on this topic in the context of ice, in particular, is needed. After years of teaching the microstructure of ice in the laboratory, the author is currently pursuing microstructure characterization of sea ice in large-scale fracture experiments. The work towards sensitivity of fracture parameters to the orientation of the columnar ice (as, e.g., in Dempsey et al. (1992)) is being prepared. Basics of birefringence are introduced, and calculation examples for ice crystals are shown in the paper. The paper is considered to be an attempt to give a somewhat detailed explanation on the optical physics which makes fabric analysis possible, but by no means should it be regarded as a complete summary of the topic. It is thought to be useful for researchers using microstructure analysis of ice and in the teaching process.

2. Birefringence

Birefringence is a phenomenon in anisotropic molecularly ordered transparent medium, when a ray of light is splitting into two components, both linearly polarized (further using term polarization is always related to the polarization of electric field) and planes of polarization are perpendicular to each other. In general, if incident ray falls along the normal to the surface of birefringent media, one ray (o- ordinary ray) continues to propagate strait, while the second ray (e- extraordinary ray) deviates. The nature of the phenomenon is related to the fact that passing through the media alternating electrical field of the ray of light causes electrons to oscillate. Due to anisotropy in the lattice of material, it can be easier for rays with one orientation of polarization compared to rays with another orientation of polarization. As a result, such different rays experience different phase speed of light in the media.

From the definition of refraction index, phase speed of light in the media, v, is inversely proportional to the refraction index, n. The solution of Maxwell's equations finds that ($n = \sqrt{\varepsilon\mu}$, ε - is the relative electric permittivity and μ - is the relative magnetic permeability; in visual range of light frequencies, the relative magnetic permeability of many related materials is very near 1)

$$v = \frac{c}{\sqrt{\varepsilon\mu}} = \frac{c}{n}; \quad \mu \to 1; \quad n = \sqrt{\varepsilon} \tag{1}$$

where c - is the speed of light in vacuum. Relative electrical permittivity shows by what factor the force of interaction of two charges is weaker in the media compare to the vacuum. For isotropic medium relative electrical permittivity is a scalar value. In anisotropic materials relative electrical permittivity is a tensor value, what means that property depends on the direction sample is probed. As a consequence, index of refraction (Eq.(1)) is a tensor value (Figure 1b). Most of the birefringent materials are uniaxial crystals, where the only direction ($n_\zeta \neq n_\eta = n_\theta$) governs the optical anisotropy in the material, while all directions perpendicular to that are optically isotropic. This direction is called optical axis (c-axis in ice) of the crystal. Another type of crystals is biaxial crystals ($n_\zeta \neq n_\eta \neq n_\theta$), which are not considered further since natural ice (Ih - hexagonal ice) has a uniaxial structure of the crystal (Pauling, 1935).

The schematic illustration of the laboratory set up to study the microstructure of ice using thin section samples on the universal stage (e.g., Langway (1958)) is shown below together with a detailed look into the crystal, and its refractive index tensor ellipsoid (Figure 1). Once incident ray of light enters the birefringent media, it splits into two component o-ray and e-ray. E-ray gets linearly polarized in the plane of the incident ray and optical axis. O-ray gets linearly polarized in the plane perpendicular to the plane of polarization of e-ray. These two rays experience different refraction indexes, n_o and n_e, defined by refraction index ellipsoid tensor and its orientation to the direction of the incident ray of light. The refraction index of o-ray does not depend on the orientation $n_o = n_\eta = n_\theta$, while refraction index of e-ray depends on the angle between the optical axis and incident ray $n_e = n_\zeta \div n_\eta$ (particular value is defined from projection of tensor ellipsoid on the plane perpendicular to the incident ray (Figure 1)). As a result, o-ray and e-ray passing geometrical crystal with different phase speeds. Uniaxial birefringence

$$\Delta n = n_e - n_o \tag{2}$$

is classified as positive when o-ray is faster than e-ray. Ih ice has a positive birefringence. In case of an arbitrarily oriented optical axis of the crystal, ordinary and extraordinary rays are geometrically split and follow different optical paths. In case when optical axis is perpendicular to the incident ray, two rays follow the same optical path and exhibit maximum possible birefringence value $\Delta n = n_\zeta - n_\eta$. In the case when the optical axis and incident ray are parallel no birefringence occurs $\Delta n = 0$. Refraction indexes of o- and e- ray in Ih ice are spectrally dependent, though their difference is almost independent and about the value $\Delta n = n_\xi - n_\eta = 0.0015$ (Ehringhaus (1917) after Petrenko and Whitworth (2002)).

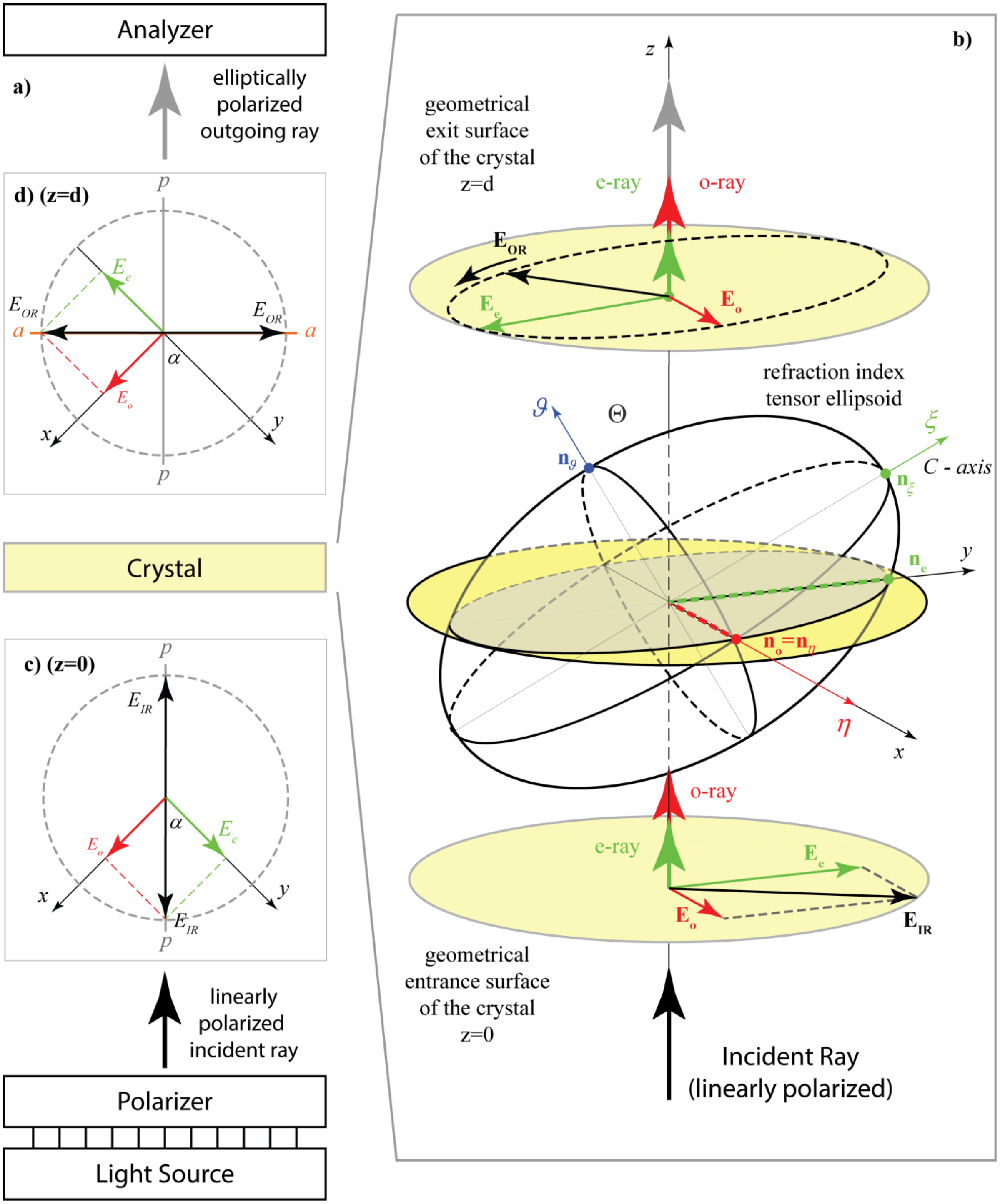

Fig. 1. Schematic illustration of set up of thin sectioning method for ice microstructure investigations (a). Refraction index tensor ellipsoid of the crystal (b). Separated incident ray into o- and e- rays at the entrance surface of the crystal z=0 (c). Retarded e- ray compared to o-ray and new polarization of outgoing ray at the exit surface of the crystal z=d (c) ($\Theta = 0$, α=45°).

3. Retardation

The linearly polarized light wave of the incident ray splits into two linearly polarized waves of o-ray and e-ray as soon as incident ray enters crystal. The planes of polarizations were discussed and shown above (Figure 1b). The amplitudes of the electric field of waves, E_o and E_e respectively, fulfill the following expression $E_o^{\,2} + E_e^{\,2} = E_{IR}^{\,2}$, where E_{IR} is the amplitude of electrical field of incident ray wave (Figure 1c). Inside the crystal, o- and e- ray waves propagate independently, and both are retarded compared to the speed of light in vacuum. As discussed above, in positively birefringent materials, o-ray passes faster through the sample than e-ray, phase speeds of two rays are defined by Eq.(1). Utilizing the wave equation and the fact that frequency of light wave does not change as it moves from air to crystal, one can find that retardation appears in the reduction of the wavelength of light in crystal, λ_c, compared to the wavelength of light in vacuum, λ, $\lambda_c = \lambda / n$. The corresponding electric field waves of o- and e-rays inside the crystal in respective planes of polarization can be written as follows:

$$E_o = E_{IR}\,\mathrm{Sin}\,\alpha\,\mathrm{Cos}(\frac{2\pi}{\lambda}\left[ct + n_o z\right]), \quad E_e = E_{IR}\,\mathrm{Cos}\,\alpha\,\mathrm{Cos}(\frac{2\pi}{\lambda}\left[ct + n_e z\right]), \tag{3}$$

where α is the angle between polarization planes of the incident ray and e-ray, c is the speed of light in vacuum, t is time, and z is distance through the crystal thickness from 0 to d, so that d is the thickness of the crystal (Figure 1b). The term retardation for the birefringent material is related to the relative retardation of e-ray to o-ray and expressed as a phase difference between two waves at the exit surface of the crystal (z=d):

$$\delta = \Delta\varphi\big|_{z=d} = \frac{2\pi}{\lambda}\Delta n d\,. \tag{4}$$

At the entrance surface of the crystal (z=0) retardation is zero, as both o-ray and e-ray are excited by the same incident ray. Retardation will cause a change of polarization of outgoing ray compared to linear polarization of incident ray (Figure 1b). In general, that will be an elliptical polarization. Note that retardation depends on birefringence parameter, the thickness of the sample and it is spectral dependent. Birefringence depends on the angle Θ the c-axis sticks out of the sample plane (Figure 1b). The thickness of the sample can be adjusted, but it is the same for the whole spectrum. Once the sample is prepared, angle Θ and thickness are constant, and wavelength only affects the retardation parameter. The fact that retardation is spectral dependent is the crucial point. The polarization of every spectral component in outgoing ray will be elliptical in general but different from each other. Both orientations of main axes and values of semi-major and semi-minor axes will be different (Figure 2). Since further such outgoing ray going through the analyzer which allows only one direction of the electric field of each spectral component to go through, different spectrum components will be seen of different intensity. This is how individual crystal in thin section sample obtains its color. Mathematically the linearly polarized oscillating electric field of the specific spectral component of outgoing ray, E_{OR}, is expressed through the sum of projections of o- and e-ray on the allowed direction of the analyzer (Figures 1, 2). Utilizing Eq.(3), it can be written as follows:

$$E_{OR} = E_e\,\mathrm{Sin}\,\alpha - E_o\,\mathrm{Cos}\,\alpha = E_{IR}\,\mathrm{Sin}(2\alpha)\,\mathrm{Sin}(\frac{\delta}{2})\,\mathrm{Sin}\left(\frac{2\pi}{\lambda}\left[ct - \frac{(n_o + n_e)d}{2}\right]\right). \tag{5}$$

4. Intensity

Intensity is a scalar value quantitatively characterizing the power carrying by wave along the propagating direction. The spectral intensity or power spectral density (PSD) describes the intensity present in the wave as a function of wavelength, per unit wavelength. The intensity of the monochromatic linearly polarized optical wave is proportional to the amplitude of electric field, $I_{OR} : |E_{OR}|$. After analyzer electrical field of the outgoing ray will oscillate in the plane of the allowed direction of the analyzer and incident ray direction. As discussed above, retardation (different polarizations of different spectral components) will result in that amplitudes of thr electric field of different spectral components will be different (Figure 2a). The system crystal-analyzer will introduce PSD to the incident light coming through it. Further, for simplicity, we assume that that spectral intensity of incident ray, $I_{IR} : |E_{IR}|$, is equivalent ($E_{IR}(\lambda) = E_{IR}, \lambda \in [\lambda_{blue}, \lambda_{red}]$). This allows us to obtain only the effect of crystal-analyzer on the formation of the color seen. Using Eq.(5), the relative spectral intensity of outgoing ray, $I(\lambda)=I_{OR}(\lambda)/I_{IR}$, as it is seen after analyzer can be expressed as follows:

$$I(\lambda) = \mathrm{Sin}^2(2\alpha)\,\mathrm{Sin}^2(\frac{\delta}{2}). \tag{6}$$

Two independent parameters are affecting the intensity: spectrally dependent retardation (Eq.(4)), $\delta=\delta(\lambda)$, and the angle between c-axis projection and polarizer allowed direction, α. Maximum of intensity occurs under the condition of α=45° and at the wavelength λ_{max} at which the retardation is an odd number of π:

$$\delta(\lambda_{max}) = \pi(2k+1),\ k = 0,1,2,3... \quad \Rightarrow \quad \lambda_{max} = \frac{2\Delta n d}{2k+1} \tag{7}$$

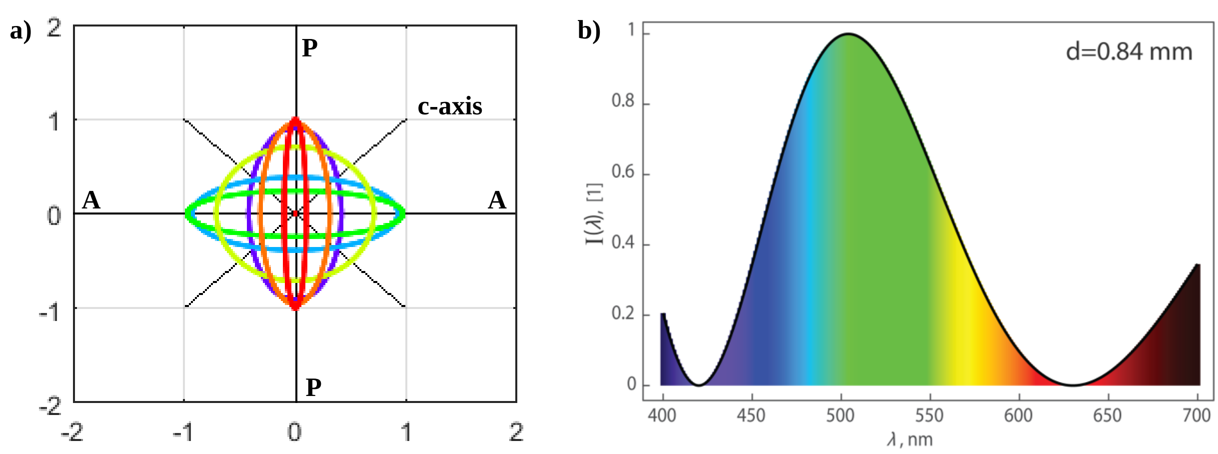

Fig. 2. Resulting polarizations of the electric field of the different spectral component of the outgoing ray from the crystal (a) and PSD function of the outgoing ray as seen after analyzer (b). Electric field space (a) and relative spectral intensity (b) are normalized to the electric field amplitude, E_{OR}/E_{IR}, and spectral intensity, I_{OR}/I_{IR}, of incident ray respectively. $\Theta = 0$, α=45°,

$\Delta n = n_\zeta - n_\eta = 0.0015$, and $\mathrm{d{=}0.84mm}$. P-P allowed direction of the polarizer. A-A allowed direction of the analyzer.

The resulting polarization of the electrical field of different spectral components of the outgoing ray after crystal and their intensities as seen after analyzer are shown below (Figure 2). The example is shown for conditions when c-axis is in the plane of the sample ($\Theta = 0$; as a result birefringence (Eq.(2)) is maximum $\Delta n = n_\zeta - n_\eta = 0.0015$ (Figure 1b)), and oriented in that plane according to maximum possible intensity ($\alpha{=}45°$), and thickness of the crystal $\mathrm{d{=}0.84mm}$. One can see that under shown conditions individual crystal will be seen in green part of the spectra after analyzer. Retardation (Eq.(4)) governs the spectral range at which individual crystal is seen, while the orientation of c-axis' projection in the plane of the sample, angle α, regulates its brightness: maximum possible ($\mathrm{I}(\lambda_{\max}){=}1$) at 45° and totally dark ($\mathrm{I}(\lambda){=}0,\ \lambda \in [\lambda_{blue}, \lambda_{red}]$) at 0° or 90°. Thus, the color of the crystal seen after analyzer is governed by the thickness of the sample d and the angle Θ, angle of the c-axis out of the sample plane, which defines birefringence (Eq.(2), Figure 1b). As in the example above (Figure 2), we continue to consider the situation when c-axis in the plane ($\Theta = 0$). In particular, such situation corresponds to S2 ice observed at horizontal thin section: c-axes of all individual grains are in the sample plane but oriented differently in this plane. In such situation color of the individual crystal depends only on the thickness of the sample. In the example above (Figure 2), the thickness $\mathrm{d{=}0.84mm}$ was chosen not randomly and will be addressed below.

Note that due to the discreteness of the condition in Eq.(7), there can be different situations of the fulfillment of the condition, depending on the sample thickness d. First, none of the visual range spectral components fulfill the condition; second, the only spectral component fulfills the condition (e.g., Figure 2b); and third, two or more spectral components fulfill the condition. Fulfilling the condition leads to the situation that relative intensity of this spectral component reaches maximum possible value under given orientation of the crystal, $I(\lambda_{\max}) = \mathrm{Sin}^2(2\alpha)$. In any case, for any thickness of the sample, there always will be a PSD function forming the visible color of individual crystal. Due to the condition in Eq.(7) this color can be more (single narrow peak) or less (two or more peaks; single broad peak; no peaks at all) distinct. To characterize color distinguishability a distinguishability measure, D, of PSD function was proposed as follows:

$$D(d) = \left[1 - \int_{\lambda_{blue}}^{\lambda_{red}} I(\lambda)\, d\lambda \,/\, (I^{\max} \Delta\lambda) \right], \qquad (8)$$

where $\Delta\lambda = \lambda_{red} - \lambda_{blue}$ - the length of the visible range of electromagnetic spectra, and λ_{blue} and λ_{red} its respective boundaries; $I^{\max} = \max(I(\lambda));\ \lambda \in [\lambda_{blue}, \lambda_{red}]$ is the maximum intensity over the whole visual spectra at the specific thickness of the sample. Measure D evaluates only the shape of PSD function: $\mathrm{D} \to 1$ - there are one or several infinitely narrow peaks, which give a distinct color, $\mathrm{D} \to 0$ - PSD function flattens, and there is no color. To describe the overall quality of resulting picture of crystal seen after polarizer, quality function, $Q(d) = D(d) I^{\max}(d)$, was proposed combining distinguishability with a maximum value of spectral intensity. All three parameters, Q, D and $\mathrm{I}^{\max}$, are plotted together showing the quality of thin section within the range of thickness, d, from 0 to 2 mm (Figure 3a). Usually, depending on different parameters in the laboratory, less than 1 mm thin section thickness can be achieved. Thickness $d=0.84\text{mm}$, chosen in the example above, corresponds to the second highest peak on the distinguishability curve (Figure 3a). Thickness ranges $d<0.13\text{ mm}$ and $0.24<d<0.40\text{ mm}$ correspond to the situation when none of the spectral components of the visible range of light fulfills the condition of Eq.(7). This causes the sharp drop in maximum intensity and distinguishability at d=0.34 mm. Thickness $0.13<d<0.24\text{ mm}$ corresponds to the situation when the only spectral component fulfills the condition (Eq.(7), k=0); since k=0, spectral intensities of the whole visible range are close to $I(\lambda_{max})=1$. As a result PSD function is rather flat. At thickness $d>0.40\text{ mm}$, spectrum starts to fulfill the condition (Eq.(7), k=1), and half peak shape of PDS forms. The highest peak of quality at d=0.37 mm is due to half shape of PSD function, which gives good distinguishability and high values of spectral intensity (Figure 3b). Peaks at 0.84 mm, 1.35 mm and 1.71 mm correspond to PSD function shape of one, two and three full peaks correspondingly, though of reduced spectral intensity values.

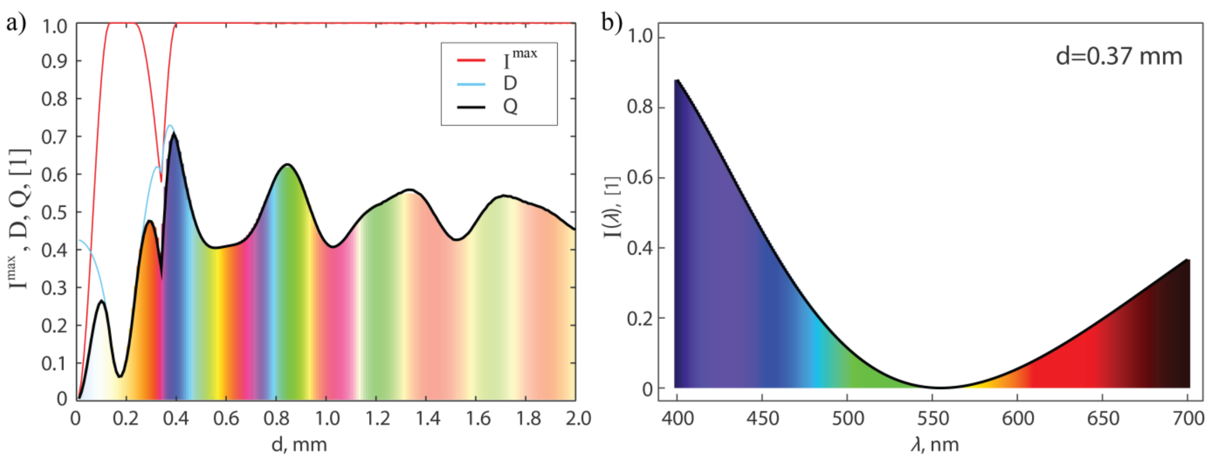

Fig. 3. The maximum spectral intensity, I^{max}, distinguishability measure, D ,and quality function, Q, against the thickness of the sample, d ($\Theta=0$; $\alpha=45°$) (averaging PSD function for every particular depth, seen color of the sample is constructed and shown under quality function curve) (a). PSD function of the outgoing ray as seen after analyzer at d=0.37 mm (b).

5. Conclusions

The optical reasoning behind the thin sectioning technique of ice microstructure investigation (e.g. (Dempsey and Langhorne, 2012) is given. Birefringence of ice crystal and the mechanism of formation of the spectral intensity function due to retardation in the crystal were explained. The spectral intensity function of the outgoing ray observed after the analyzer was calculated. The appearance of colors of individual crystals, seen in thin section, is governed by calculated spectral intensity function. Proposed procedures of fabric studies (Hill and Lasca, 1971; Langway, 1958) becomes more demonstrative if understand the optical reasoning of the birefringence. For example, from Eq.(6) it is clear that there are four orientations (either along polarize or analyzer) of c-axis, when the crystal is observed dark; and four orientations (45° to polarizer and analyzer), when the intensity of individual crystal is maximum. The calculations were made under the assumption that PSD function of incident ray is constant (all spectral components of intensity are equivalent), in reality, the shape of outgoing ray PSD function would adjust accordingly affecting the distinguishability measure. Though the maximum peaks of the spectral intensity and the quality function would remain at the same wavelength and the same thickness of the sample respectively. The constructed quality function gives some practical reasoning to choose the thickness of the thin section sample: two best results are observed at d=0.37 mm and d=0.84 mm, and they are seen in blue (Figure 3b) and green (Figure 2b) range of spectra respectively. Though both are practically possible, the one which is thinner can sometimes be challenging to achieve, as many factors in the laboratory are affecting the good practice of thin section preparation. The thicker one is almost always possible to perform. Until now always the situation with perpendicular oriented polarizer and analyzer was considered. As it followed from the calculation and observed in the laboratory, rotation of analyzer causes the color of individual crystals to change to its complementary color ($\delta(\lambda^{*}_{\max}) = 2\pi k;\ k = 1, 2, 3...$) when orientations of polarizer and analyzer are aligned. That is why S2 ice thin sections are seen in green (red – complementary to green) range of spectra (d=0.84 mm) or in blue (yellow – complementary to blue) range of spectra (d=0.37 mm). Below examples of corresponding S2 sea ice horizontal thin sections are shown (Figure 4).

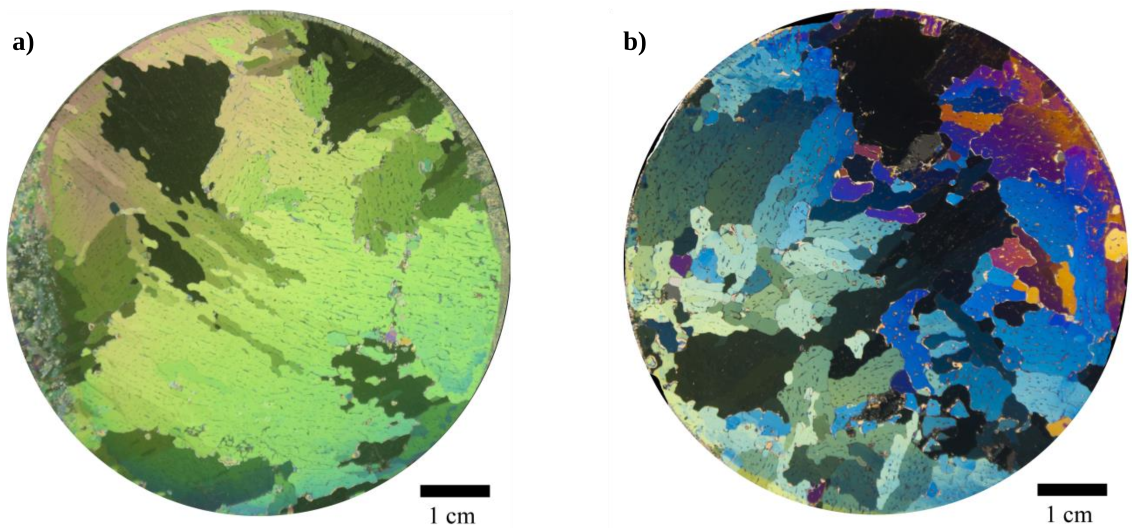

Fig. 4. Horizontal thin sections of sea ice from Van Mien Fjord, Spitsbergen. Depth: 31 cm (a) and 11 cm (b) (core: 12 February 2015).

There are few practical implementations for observations in the lab can be formulated based on the discussion above and results of the paper:

- there is no sense to make sample thinner than d=0.37 mm, it will reduce its quality
- rotating the sample on the universal stage causes a periodical change in intensity at individual crystals seen, but no change in spectral range (color) they are seen,
- rotating the analyzer causes a periodical change in spectral range crystal seen between two colors which are complementary to each other (see above),
- S1 ice individual crystals will be seen in different colors and of different intensity,
- S2 ice individual crystals will exhibit the same color, but the different intensity,
- S3 ice individual crystals will be seen in the same color and the same intensity.

Though this paper does not bring more knowledge on the microstructure of ice itself, it offers a more in-depth description of the optical reasoning behind the method used for ice microstructure investigations and gives practical advice for choosing the thickness of the thin section and explains the results seen on the universal stage. This is believed to be useful both for research and teaching process.

References

Cole, D.M., 2001. The microstructure of ice and its influence on mechanical properties. Engineering Fracture Mechanics, 68(17): 1797-1822.

Dempsey, D.E. and Langhorne, P.J., 2012. Geometric properties of platelet ice crystals. Cold Regions Science and Technology, 78(0): 1-13.

Dempsey, J.P., Wei, Y. and Defranco, S.J., 1992. Notch sensitivity and brittleness in fracture testing of S2 columnar freshwater ice. International Journal of Fracture, 53(2): 101-120.

Ehringhaus, A., 1917. Beitrage zur Kenntnis der dispersion der doppelbrechung einiger kristalle. Georg-August-Universitat zu Gottingen.

Hill, J.R. and Lasca, N.P., 1971. An Improved Method for Determining Ice Fabrics. Journal of Glaciology, 10(58): 133-138.

Langway, C.C.J., 1958. Ice Fabrice and Universal Stage. U. S. Army Snow Ice and Permafrost Research Establishment.

Pauling, L., 1935. The Structure and Entropy of Ice and of Other Crystals with Some Randomness of Atomic Arrangement. Journal of the American Chemical Society, 57(12): 2680-2684.

Petrenko, V.F. and Whitworth, R.W., 2002. Physics of Ice. Oxford University Press, Oxford, 392 pp.

International Association for Hydro-Environment Engineering and Research
Supported by Spain Water and IWHR, China

24th IAHR International Symposium on Ice
Vladivostok, Russia, June 4 to 9, 2018

Experimental Study on Uniaxial Compressive Strength Features of Wuliangsu Lake Ice

Li Zhijun, Xu Zijun, Wang Qingkai
State Key Laboratory of Coastal and Offshore Engineering
Dalian University of Technology, Dalian 116024, China;
lizhijun@dlut.edu.cn; xuzijun@mail.dlut.edu.cn; dlutwqk@163.com
Li Guoyu
State Key Laboratory of Frozen Soil Engineering, Northwest Institute of Ecology and Environmental Resources, Chinese Academy of Sciences, Lanzhou 730000, China
Guoyuli@lzb.ac.cn

In order to accumulate the uniaxial compressive strength of thermal growth fresh water ice, we chose the columnar ice from Wuliangsu Lake where is a kind of furiotile lake beside the Yellow River to be the test samples. The samples were loaded in the directions vertical to the ice surface and parallel to the ice surface under different displacement speeds at -2ºC, -5ºC, -7ºC, -10ºC and -15ºC by electronic universal test machine with strict temperature control and displacement speed control. The influence of strain rate, loading direction and temperature on the uniaxial compressive strength were studied. The tests find that the uniaxial compressive strengths vary with the strain rates and temperatures. At a certain temperature, the strength increases to a peak value first, then reduces, and finally tends to smooth with the increase of strain rate and the ice samples include three failure forms: bulging failure, shear failure and splitting failure. In the range of the test temperature, the ice strength decreases with the increase of test temperature. The uniaxial compressive strength can be fitted into a surface with temperature and strain rate. The strength loaded in the direction vertical to the ice surface is larger than that parallel to the ice surface. The peak uniaxial compressive strength loaded in the direction vertical to the ice surface is 2.1 times as large as the strength loaded in the direction parallel to the ice surface. The strain rate at the peak strength increases with ice temperature decreasing, and logarithmic function can be used to express the variation of peak strength with ice temperature.

Background

Ice, as a natural phenomenon in the cold region, not only has a beneficial side to human life, but also has a negative side to human activities and causes many kinds of disasters. Therefore, scholars in China and foreign countries have carried out a long term study of fresh water ice. However, the behavior of ice is related to its growth environment, the engineering behavior of ice is regional, and the mechanical behavior of the Yellow River ice has certain characteristics. There are mainly two kinds of frozen forms in the Yellow River because of the river dynamic, one is the ice caused by thermal, the so-called “horizontal freezing”, one is the ice caused by thermal and dynamic, the so-called “vertical freezing”. These two kinds of frozen river ice increase thickness at the bottom by the thermal, there may also have the dynamic to carry the ice flowers to increase the ice thickness. The different ice formations cause differences in ice crystals and ice mechanical behaviors. In recent years, Chinese scholars have done research on the uniaxial compressive strength of river ice with dynamic factors (Wang et al, 2016). Before collecting ice samples, because it is difficult to judge the pure thermal growth ice (columnar ice) in the river, there are few reports on the mechanical properties of columnar ice. Foreign scholars paid attention to the engineering mechanical properties of fresh water ice in the last century. In recent years, they have shifted the focus to the effect of ice crystal on constitutive relation on micro scale (Iliescu and Baker, 2007), and the response of ice to climate change on macro scale (Murfitt and Brown, 2017). Most of the ice samples studied were based on natural ice (Jones, 2007), which did not take care the effect of ice crystals. Only Cole (2001) used columnar ice samples and considered the effect of the columnar crystalline grain size. However, the uniaxial compressive strength of the pure thermal growth ice is short of achievement in China. With the advance of the construction of “The Belt and Road” and the basic construction of the plateau cold regions and the arid and semi-arid areas, water conservancy and traffic engineering will inevitably increase the demand for the mechanical properties of ice in the future. Dalian University of Technology cooperated with Chinese Inner Mongolia Agricultural University, Finnish University of Helsinki and some other units, chose Ningxia-Inner Mongolia reach in the Yellow River and Wuliangsu Lake in the 2015-2016, 2016-2017 and 2017-2018 winter, carried out a comprehensive investigation of the natural resource environment and ecology. The contents of the investigation included the process of ice growth and decay, the ice temperature, the transmission of light in ice, the mechanical properties of ice, and the velocity of radar wave transfer in ice. The columnar ice compressive strength in this paper is part of the mechanical properties of ice in this comprehensive investigation.

The uniaxial compressive strength of the ice is influenced by the ice crystal structure, the size of the test samples (Li et al, 2013), the loading direction, the strain rate, the temperature, the porosity (Li et al, 2011a) and the rigidity of the test machine. Based on the observed ice crystal structure and the size and loading direction of the ice samples, this paper determines how to make the ice billets into the samples, and then carries out the tests. Using the obtained experimental data, the paper analyses the influence of ice sample temperature, loading strain rate and loading direction on ice uniaxial compressive strength and the relationship between the uniaxial compressive strength and the experimental factors under different experimental conditions were analyzed. They are useful for the accumulation of uniaxial compressive strength characteristics of columnar ice, and for a perfect uniaxial compressive constitutive relation of columnar ice in the future.

Preparation of tested ice samples

The thickness of the ice was 40-43cm and the ice billets were taken to prepare the tested ice samples in January 2016. The ice billet was a rectangular block with a length of 60cm, a width of 40cm and a thickness of the whole ice. The cut ice billets were packed with insulated foam boxes and shipped them back to the low temperature laboratory at Dalian University of Technology when the air was cold. According to the suggestions on the test method of ice mechanical properties (Schwarz et al, 1981), two types of standard samples of 7.0cm×7.0cm×17.5cm were prepared with electric chain saw and sawing machine according to the loading direction: vertical to the ice surface (Type-A) and parallel to the ice surface (Type-B).

Before the test, the crystals of the ice were observed. It is a typical columnar ice. Therefore, its mechanical properties are anisotropic. Its average density is $0.913 g/cm^3$, which is lower than that of the ideal fresh ice due to bubbles in the ice (Li et al, 2011b).

Test instrument

The loading equipment is the CSS-44100 electronic universal test machine made in China, which is made up of computer system combined with main engine, accessories and the EDC120 digital controller produced by German DOLI electronic company. For the purpose of a local low temperature test environment, we installed a low temperature test box between the beam and the base plate of the test machine. The box is cooled by a BF200 cooling bath. In order to ensure the accuracy of the temperature control in the box, the Pt 1000 temperature sensor was installed inside the box, and the temperature in the box was strictly controlled by the SR253 temperature controller. The temperature measuring precision of Pt 1000 temperature sensor can reach 0.1 °C, and the resolution is 0.01 °C. At the same time, the air convective duct and light are also installed in the boxs to make the temperature field uniform in the box and observe the failure of the sample through the vacuum insulated glass window. In addition, in order to block the temperature exchange between test box inside and outside, we used bakelite material to replace the steel pressure testing machine for connecting rod and replaced the upper and lower pressure heads of the steel with the nylon material. At the same time, an automatic leveling device is installed at the nylon head to ensure that the upper and lower ends of the ice samples are in full contact with the pressure head during the compressive process (Wang et al, 2016). Before the test, the sample was kept in a uniform temperature box for over 24h.

Analysis of test results

The ability of material to resist failure under external force is called strength. However, it is difficult to observe the internal damage of ice in the loading process and measure the stress of the point. Therefore, the ultimate stress of the test is taken as the uniaxial compressive strength of an ice sample. They were divided into two types of samples according to loading direction vertical to ice surface (Type-A) and parallel to ice surface (Type-B), and they were tested at -2ºC, -5ºC, -7ºC, -10ºC and -15ºC. 10 groups of tests were carried out and a total of 340 samples were loaded, 295 samples were successful and obtained the effective loading process curves. The strain rate range of two types of samples was between $3\times10^{-7}s^{-1}$ to $2\times10^{-2}s^{-1}$.

The effective tested strength data were placed in a double logarithmic coordinate system with a transversal coordinate as a strain rate and a longitudinal coordinate as a strength. According to Wang et al (2016), the relationship between ice strength and strain rate divides the strain rate range into ductile zone, transition zone and brittle zone. The brittle failure and ductile failure of ice are explained by the mechanism of crack propagation. Meanwhile, the strain rate range is partitioned by using view of Wang et al (2016). As an example of A type samples under -5 ºC, Figure 1 shows that the failure form of ice is ductile failure, and it is a ductile zone when the strain rate is less than $3\times10^{-5}s^{-1}$; the failure form of ice is ductile failure and brittle failure and it is a transition zone at a strain rate of $3\times10^{-5}s^{-1}$ to $6.5\times10^{-5}s^{-1}$; the failure form of ice is brittle failure and it is a brittle zone when the strain rate is more than $6.5\times10^{-5}s^{-1}$. Cole (2001) considers that in the strain rate of 10^{-2} s^{-1} to $10^{-1}s^{-1}$, the uniaxial compressive strength of ice is independent of strain. Hence, the region of the strain rate from 10^{-2} s^{-1} to $10^{-1}s^{-1}$ is called the stable zone.

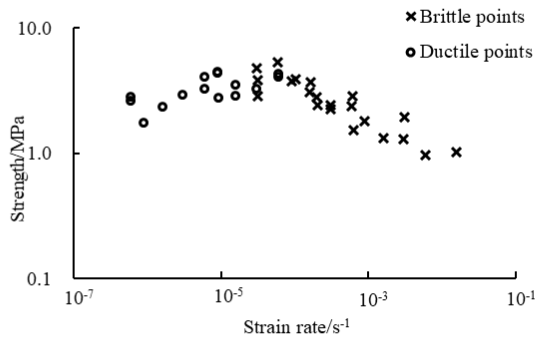

Fig. 1. The relationship between strength and strain rate at -5ºC of the Type-A samples

1. Relationship among the uniaxial compressive strength, strain rate and temperature

Draw the test data (-2ºC, -5ºC, -7ºC, -10ºC and -15ºC) in the way of Figure 1; according to Wang et al (2016) and Figure 1, four subsections of ductile zone, transition zone, brittle zone and stable zone are fitted; then integrate. The relationship between the uniaxial compressive strength and the strain rate under a certain temperature is Eq. [1].

$$\sigma = k\dot{\varepsilon}^{b} \qquad \textbf{[1]}$$

Where: σ is strength (MPa); $\dot{\varepsilon}$ is strain rate (s^{-1}); k and b are coefficients which are related to strain rate. Table 1 corresponds to the fitted coefficients in different zones of Figure 2.

Table 1. Fitted coefficients *k* and *b* for Eq. [1]

Type of samples	Temperature /ºC	Ductile zone *k*	Ductile zone *b*	Transition zone *k*	Transition zone *b*	Brittle zone *k*	Brittle zone *b*	Stable zone *k*	Stable zone *b*
Type-A	-2	16.7706	0.1633	14.5395	0.1553	0.1007	-0.3706	0.5549	0
	-5	23.5670	0.1633	20.6293	0.1553	0.1311	-0.3706	0.7223	0
	-7	26.7030	0.1633	23.4572	0.1553	0.1444	-0.3706	0.7956	0
	-10	30.4843	0.1633	26.8793	0.1553	0.1600	-0.3706	0.8816	0
	-15	35.4371	0.1633	31.3797	0.1553	0.1798	-0.3706	0.9906	0
Type-B	-2	5.0692	0.1502	3.4325	0.1010	0.2367	-0.2493	0.7460	0
	-5	7.1852	0.1502	4.8715	0.1010	0.3144	-0.2493	0.9910	0
	-7	8.1671	0.1502	5.5398	0.1010	0.3490	-0.2493	1.1000	0
	-10	9.3549	0.1502	6.3487	0.1010	0.3898	-0.2493	1.2286	0
	-15	10.9164	0.1502	7.4125	0.1010	0.4420	-0.2493	1.3931	0

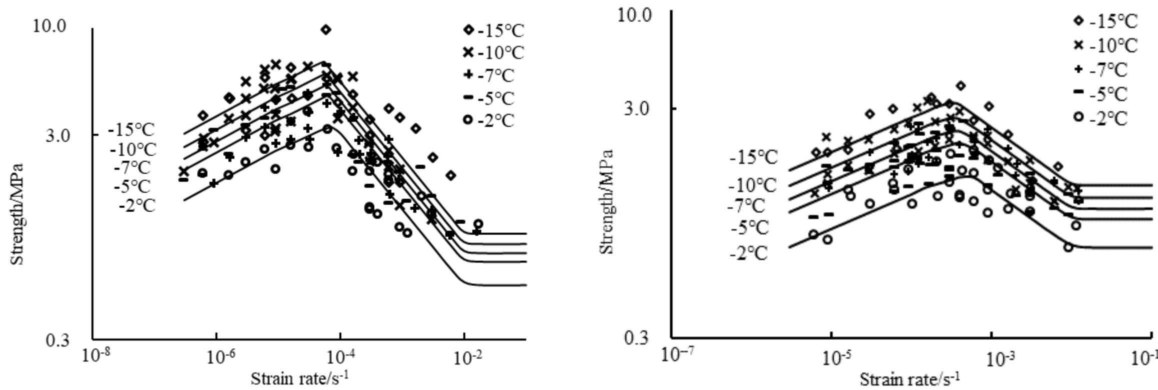

(a) Type-A Samples (b) Type-B Samples

Fig. 2. Relationships of the compressive strength with the strain rate in different temperatures

From the experimental data and curves in Figure 2, we can see that the experimental uniaxial compressive strength of the ice has a certain range of dispersion, and some test strengths intersect with the test strengths of adjacent temperatures. Combined with Figure 1, it is found that the strength of the ice increases gradually at the same strain rate both in Type-A and Type-B.

In order to combine the effect of temperature and strain rate on the ice uniaxial compressive strength, Wang et al (2016) established the relationship among strength and temperature in the wide range of strain rate. The similar relationship among sea ice strength and porosity changes in the wide range of strain rate was also established in Li et al (2011a). This method was also used to establish the statistical relationship curve surface among the fresh columnar ice uniaxial compressive strength and strain rate, temperature in Eq. [2]. It is more intuitive to show the influence of temperature (-2ºC~-15ºC) and strain rate ($3\times10^{-7}s^{-1}$~$2\times10^{-2}s^{-1}$) on the fresh columnar ice uniaxial compressive strength.

$$\sigma = a\dot{\varepsilon}^b|T|^c \qquad \textbf{[2]}$$

Where: σ is strength (MPa); $\dot{\varepsilon}$ is strain rate (s^{-1}); T is temperature (ºC); *a, b* and *c* are coefficients which are related to strain rate and temperature, they are shown in Table 1.

In Wang et al (2016), this equation is only used to fit the surface of ductile zone and brittle zone. In this paper, the points of transition zone were fitted with this function and got a satisfactory result.

Table 2. Fitted coefficients *a, b, c* and correlation coefficient *r* for Eq. [2]

Type of samples	Failure behaviors	Fitted coefficients and correlation coefficient			
		a	*b*	*c*	*r*
Type-A	Ductile zone	12.9651	0.1633	0.3713	0.8447
	Transition zone	11.1588	0.1553	0.3818	0.8642
	Brittle zone	0.0825	-0.3706	0.2876	0.9423
	Stable zone	0.4546	0	0.2876	1.0000
Type-B	Ductile zone	3.8935	0.1502	0.3807	0.8399
	Transition zone	2.6338	0.1010	0.3821	0.8290
	Brittle zone	0.1909	-0.2493	0.3100	0.9101
	Stable zone	0.6017	0	0.3100	1.0000

At the same temperature, with the increase of the strain rate, the strength of the ice has experienced three kinds of development. First, the strength increases with the increase of the strain rate and reaches the peak value, it corresponds to the ductile failure, then the strength decreases with the increase of the strain rate, it corresponds to the brittle failure, finally the strength tends to be stable and keeps constant, it corresponds to the rigid failure. The peak uniaxial compressive strength occurs between the ductile failure and the brittle failure, which occurs in the ductile-brittle transition zone. In the design of ice resistant vertical structures, the peak uniaxial compressive strength is the scientific basis to support the design strength. The test results show that the strain rate of peak uniaxial compressive increases with the increase of ice temperature (Table 3). It shows that the ice brittleness is less obvious with the increase of ice temperature. The relationship between them can be expressed in exponential relationship.

Table 3. The strain rate at the peak uniaxial compressive strength in two loading directions

Temperature/ºC	-2	-5	-7	-10	-15
Strain rate of Type-A/s^{-1}	7.0×10^{-5}	6.5×10^{-5}	6.0×10^{-5}	5.8×10^{-5}	5.5×10^{-5}
Strain rate of Type-B/s^{-1}	4.0×10^{-4}	3.8×10^{-4}	3.5×10^{-4}	3.3×10^{-4}	3.0×10^{-4}

The fitting result of samples in Type-A is：

$$\dot{\varepsilon}_{cp} = 7.0854 \times 10^{-5} e^{-0.018|T|} \qquad r=0.9604 \qquad \textbf{[3]}$$

The fitting result of samples in Type-B is：

$$\dot{\varepsilon}_{cp} = 4.1807 \times 10^{-4} e^{-0.023|T|} \qquad r=0.9918 \qquad \textbf{[4]}$$

Where: $\dot{\varepsilon}_{cp}$ is the strain rate at the peak uniaxial compressive strength (s^{-1}); T is temperature (ºC).

2. Relationships between peak uniaxial compressive strength and temperature

In Figure 2, the peak value of each curve is defined as the peak uniaxial compressive strength corresponding to the ice temperature. The relationship between peak uniaxial compressive strength and ice temperature is established, as shown in Figure 3. In addition, the ratio of peak uniaxial compressive strength between Type-A and Type-B is calculated (Table 4).

Table 4. The peak uniaxial compressive strength in two loading directions and their ratio

Temperature/ºC	-2	-5	-7	-10	-15
Peak strength of Type-A/MPa	3.2907	4.6156	5.1835	5.9397	6.8411
Peak strength of Type-B/MPa	1.5575	2.2104	2.4800	2.8338	3.2671
Ratio	2.113	2.088	2.090	2.096	2.094

In the past, the relationship between peak uniaxial compressive strength and temperature was fitted by linear function. In Li et al. (2013), it is pointed out that the linear function is not able to meet the physical fact that the ice peak strength tends to be 0 when the temperature is close to freezing point. Therefore, based on the viewpoint of Wang et al (2016), the logarithmic function is used to fit the relationship between them, that is to say, under the same loading direction, the relationship between peak uniaxial compressive strength and temperature is:

$$\sigma_{cp} = E\ln(|T|) + F \qquad \textbf{[5]}$$

Where: σ_{cp} is the peak uniaxial compressive strength (MPa); T is temperature (ºC); E and F are coefficients.

The fitting result of samples in Type-A is：

$$\sigma_{cp} = 1.7435\ln(|T|) + 1.9455 \qquad r=0.9936 \qquad \textbf{[6]}$$

The fitting result of samples in Type-B is：

$$\sigma_{cp} = 0.8386\ln(|T|) + 0.9169 \qquad r=0.9946 \qquad \textbf{[7]}$$

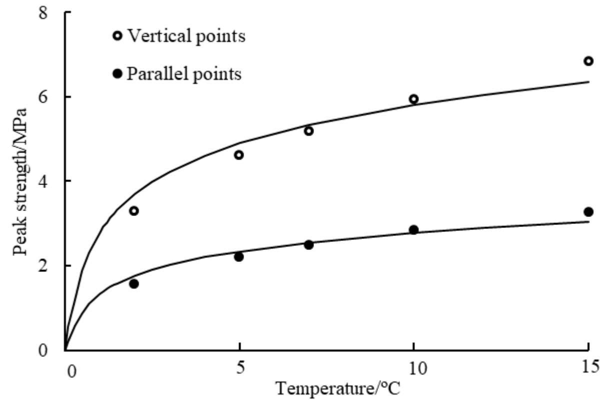

Fig. 3. The relation curves of peak uniaxial compressive strength and temperature

Figure 3 shows the statistical relationship of Eq. [6] and Eq. [7]. They show that the uniaxial compressive strength of the columnar ice increases with the decrease of ice temperature gradually. According to Wang et al (2016), Eq. [6] and Eq. [7] can be applied to the ice temperature below -30ºC. This temperature can cover the temperature range of fresh water ice in most parts of the north of China. The pure thermal growth Wuliangsu Lake ice is columnar structure and its mechanical properties are anisotropic. The test results also confirm that the strength of the loading direction vertical to ice surface is greater than that of the loading direction parallel to ice surface. Table 3 indicates that the ratio of the peak strength of Type-A and Type-B is about 2.1 times.

Conclusions

The uniaxial compressive strength of the columnar ice from Wuliangsu Lake is influenced by temperature and strain rate. For the two different loading directions, the relationships among the uniaxial compressive strength with strain rate and temperature were obtained.

In the test temperature range, the peak compressive strength of the columnar ice from Wuliangsu Lake increases with the decrease of temperature, and a logarithmic function is better for the relationship.

The uniaxial compressive strength of ice samples which are loaded in direction vertical to ice surface(Type-A) is about 2.1 times of the uniaxial compressive strength of ice samples which are loaded in direction parallel to ice surface (Type-B).

Acknowledgements

This work was supported by the Global Change Research Program of China (2015CB953901) (51639003, 51579028) and the National Natural Science Foundation of China.

References

Cole D M, 2001. The microstructure of ice and its influence on mechanical properties. Engineering Fracture Mechanics, 68(17-18): 1797-1822.

Iliescu D, Baker I, 2007. The structure and mechanical properties of river and lake ice. Cold Regions Science and Technology, 48: 202–217.

Jones S J, 2007. A review of the strength of iceberg and other freshwater ice and the effect of temperature. Cold Regions Science and Technology, 48: 202–217.

Li Z J, Zhang L M, Lu P, et al, 2011a. Experimental study on the effect of porosity on the uniaxial compressive strength of sea ice in Bohai Sea. Science China Technological Sciences, 54(9): 2429-2436.

Li Z J, Huang W F, Jia Q, et al, 2011b. Distributions of crystals and gas bubbles in reservoir ice during growth period. Water Science and Engineering, 4(2):204-211.

Li Z J, Zhou Q, Wang E L, et al, 2013. Experimental study on the loading mode effects on the ice uniaxial compressive strength. Journal of Hydraulic Engineering, 44(9): 1037-1043. (in Chinese)

Murfitt J, Brown LC, 2017. Lake ice and temperature trends for Ontario and Manitoba: 2001 to 2014. Hydrological Processes. 31:3596–3609.

Schwarz J, Frederking R, Gavrillo V, et al, 1981. Standardized testing methods for measuring mechanical properties of ice. Cold Regions Science and Technology, 4(3): 245-253.

Wang Q K, Zhang B S, Deng Y, et al, 2016. Study on test of uniaxial compressive strength of ice in Yellow River and its influencing factors. Water Resources and Hydropower Engineering, 47(9): 90-94. (in Chinese)

International Association for Hydro-Environment Engineering and Research
Supported by Spain Water and IWHR, China

24th IAHR International Symposium on Ice
Vladivostok, Russia, June 4 to 9, 2018

A Brittle Failure Simulation of Level Ice Using a Fully Lagrangian Particle Method Based on Continuum Mechanics

Di Ren, Jong-Chun Park
Dept. of Naval Architecture & Ocean Engineering, Pusan National University
63-2 Busandaehak-ro, Geumjeong-gu, Busan 46241, Korea
jcpark@pnu.edu

A meshless Lagrangian method based on the moving particle semi-implicit (MPS) method is employed on the basis of continuum mechanics and applied to simulate ice fracture problems in this study. Ice can be considered as homogeneous isotropic elastic material before the fracture happened. When failure occurs, the connection between particles will be cut off. This process only occurs when fractures develop between two particles. The location and direction of fractures are calculated according to the maximum tensile stress theory. The developed method is adopted to solve the ice failure for three-point bending test and the wedge level ice test problems, and the simulated results are validated by comparing with the experimental results conducted in an ice tank.

KEY WORDS: MPS (Moving Particle Semi-implicit) method; Brittle fracture; 3-point bending problem; Level ice; Ice breaking

1. Introduction

As technology and environment change, the rate of development in the Arctic region has been increasing year by year. As a result, the needs for icebreaker are also emphasized, and no transportation would not play a replaceable role instead of it. In the design of an icebreaker and its construction process, the ice load is always one of the most important factors. In recent days, furthermore, the emergence of multi-functional icebreakers such as LNG icebreakers has further raised the requirements for the accuracy of ice loading assessment and prediction. Ice fracture plays a dominant role in the prediction of ice loads.

In order to simulate this process, many researchers choose a discrete element method (DEM) to simulate the ice fracture problems (Lepparanta et al., 1990; Hansen and Løset, 1999; Selvadurai and Sepehr, 1999; Polojarvi and Tuhkuri, 2009; Ji et al., 2013). The advantage of DEM is that it can make a better expression of the behavioral characteristics of discontinuous material (André et al., 2012). However, since the scale of a computational domain for the problem to be solved is much larger than that of ice particles in natural environment, it seems preferable the ice should be modeled to represent the behavioral characteristics of a continuous material on a macroscopic scale.

In the present study, a moving particle semi-implicit (MPS) method which is a meshless Lagrangian method, has been developed on the basis of continuum mechanics and applied to simulate the ice fracture problems. It is assumed that ice is a homogeneous isotropic elastic material before the fracture happened. When failure occurs, the connection between particles will be cut off. This process only occurs when fractures develop between two particles. The location and direction of fractures are calculated according to the maximum tensile stress theory. The developed method is adopted to solve the ice failure for three-point bending tests and the ice breaking around a wedge advancing the level ice test problems. The simulation results are validated by comparing with the experiments conducted in an ice tank.

2. Numerical Method

The momentum conservation equation for structure can be expressed as:

$$\frac{D\vec{u}}{Dt} = \frac{1}{\rho}\nabla\cdot\left(\lambda tr\left(\varepsilon\right) + 2\mu\varepsilon\right) + \vec{f} + \vec{g} \qquad \textbf{[1]}$$

where, ρ, t, $\vec{u}$, ε, $\vec{f}$, $\vec{g}$ indicate the density of fluid, time, velocity vector, strain tensor, external force and the gravity acceleration, respectively. And the Lame's constants λ and μ can be calculated by Young's modulus E and Poisson ratio ν as:

$$\lambda = \frac{E\nu}{\left(1+\nu\right)\left(1-2\nu\right)} \quad \mu = \frac{E}{2\left(1+\nu\right)} \qquad \textbf{[2]}$$

Additionally, the angular momentum conservation equation is introduced as:

$$I\frac{D\vec{\omega}}{Dt} = \vec{r}\times\vec{f}_{shear} \qquad \textbf{[3]}$$

where, I , $\vec{\omega}$, $\vec{r}$, $\vec{f}_{shear}$ indicate the moment of inertia, angular velocity, position vector and shear force, respectively.

An improved MPS-based model (Hwang et al., 2014; 2016) is employed to discretize the governing equations numerically. Eq. [1] can be organized into the following form:

$$\frac{D\vec{u}}{Dt} = \frac{\lambda}{\rho}\nabla \cdot tr\left(\varepsilon\right)\left[I\right] + \frac{2\mu}{\rho}\nabla \cdot \varepsilon + \vec{f} + \vec{g} \qquad \textbf{[4]}$$

By taking into account the relative distance change of the neighboring particles with respect to the target particle, the volume strain is calculated as:

$$\left\langle tr\left(\varepsilon\right)\right\rangle_i = \frac{d}{n_i}\sum_{j\neq i}\frac{\left|\vec{r}_j - \vec{r}_i\right| - \left|\vec{r}_j^{\,0} - \vec{r}_i^{\,0}\right|}{\left|\vec{r}_j^{\,0} - \vec{r}_i^{\,0}\right|} w\left(\left|\vec{r}_j^{\,0} - \vec{r}_i^{\,0}\right|\right) \qquad \textbf{[5]}$$

where $\vec{r}^{\,0}$ indicate the initial position vector and d is the number of dimensions.

After that, the first term on the RHS of Eq. [4] is considered by the following equation:

$$\lambda\nabla \cdot tr\left(\varepsilon\right) = \lambda\frac{d}{n_i}\sum_{j\neq i}\frac{\left[tr\left(\varepsilon\right)_j + tr\left(\varepsilon\right)_i\right]}{\left|\vec{r}_j^{\,0} - \vec{r}_i^{\,0}\right|^2}\left(\vec{r}_j - \vec{r}_i\right) w\left(\left|\vec{r}_j^{\,0} - \vec{r}_i^{\,0}\right|\right) \qquad \textbf{[6]}$$

And the second term on the RHS of Eq. [4] can be discretized as below:

$$\left\langle 2\mu\left(\nabla^2\delta\vec{r}\right)\right\rangle_i = 4\mu\frac{d}{\rho_s n_i}\sum_{j\neq i}\frac{\left(\vec{r}_j - \vec{r}_i\right) - 0.5\left[R_j\left(\vec{r}_j^{\,0} - \vec{r}_i^{\,0}\right) + R_i\left(\vec{r}_j^{\,0} - \vec{r}_i^{\,0}\right)\right]}{\left|\vec{r}_j^{\,0} - \vec{r}_i^{\,0}\right|^2} w\left(\left|\vec{r}_j^{\,0} - \vec{r}_i^{\,0}\right|\right) \qquad \textbf{[7]}$$

where R is the rotational matrix calculated from the rotational angle of each particle.

Similarly, the angular acceleration of structure particles calculated by Eq. [5] can be discretized as:

$$\left\langle I\frac{D\vec{\omega}}{Dt}\right\rangle_i^n = -2\mu\frac{d}{n_i}\sum_{j\neq i}R_i\left(\vec{r}_j^{\,0} - \vec{r}_i^{\,0}\right)\times\frac{\left(\vec{r}_j^{\,n} - \vec{r}_i^{\,n}\right) - \frac{1}{2}\left[R_j\left(\vec{r}_j^{\,0} - \vec{r}_i^{\,0}\right) + R_i\left(\vec{r}_j^{\,0} - \vec{r}_i^{\,0}\right)\right]}{\left|\vec{r}_j^{\,0} - \vec{r}_i^{\,0}\right|^2} w\left(\left|\vec{r}_j^{\,0} - \vec{r}_i^{\,0}\right|\right) \qquad \textbf{[8]}$$

For more detail description on the MPS-based model, refer to Hwang et al. (2014; 2016).

In the present study, the 6th-order weight function, w, was used in Eq. [5] to [8]:

$$w = \begin{cases} \left(1 - \dfrac{r}{r_e}\right)^3\left(1 + \dfrac{r}{r_e}\right)^3 & 0 \le r \le r_e \\ 0 & r > r_e \end{cases} \qquad \textbf{[9]}$$

In order to consider the brittle failure of ice, the maximum normal stress criterion is used for a failure criteria of brittle fracture (Juvinall & Marshek, 2006), i.e. a brittle material will fail when the first principal stress, σ_1, exceeds the uniaxial tensile strength of the material, σ_f, as:

$$\sigma_1 \geq \sigma_f \quad \textbf{[10]}$$

When a particle i is judged that the crack occurs locally, a spring-like relationship will be disconnected with the neighboring particle j which is located opposite to the crack. In the numerical process, the following 3 conditions to decide whether to disconnect the inter-particle link:

$$\begin{aligned} &\langle \sigma_1 \rangle_i \geq \sigma_f \\ &\langle \sigma_1 \rangle_j \geq \sigma_f \\ &\left(\langle \nabla \sigma_1 \rangle_i \cdot \hat{n}_i \right)\left(\langle \nabla \sigma_1 \rangle_j \cdot \hat{n}_j \right) < 0 \end{aligned} \quad \textbf{[11]}$$

3. Numerical Simulation

Firstly, the simulation of three-point bending tests is performed using the present method. **Figure 1** shows the initial set-up condition of three-point bending test.

For providing the validation data, a series of experiments for three-point bending tests with ice beam made of fresh water was independently conducted in a cold room at Korea Maritime and Ocean University. The material properties calculated from the experiments for the different cases are summarized in **Table 1**. The Young's modulus and yield stress from the experiments were used as material properties of ice in the simulation. And the yield strain is compared with the simulation results as verification. The error averaged is about 7%.

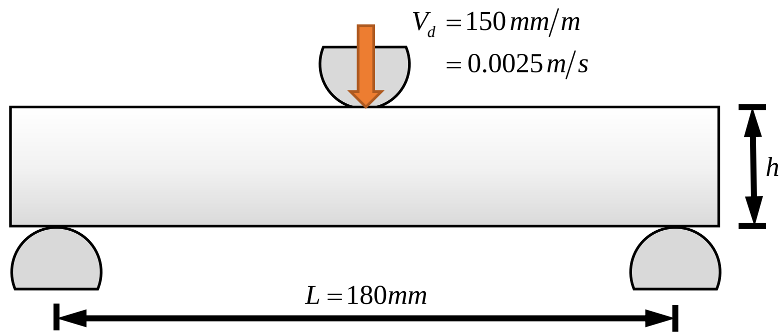

Fig. 1. Initial set-up condition of three-point bending test.

Table 1. Material properties for different cases.

Exp. No.	$E(MPa)$	$\sigma_f\ (MPa)$	$\varepsilon_f^{\exp}$	$\varepsilon_f^{\text{simulation}}$	Error
01	270.08	1.14	0.0042	0.0045	7.1%
02	209.82	0.68	0.0032	0.0035	8.5%
03	183.88	1.23	0.0067	0.0071	6.1%
04	137.30	0.99	0.0072	0.0077	7.0%
05	98.78	0.78	0.0079	0.0084	6.3%

Next, the present method is applied to a wedge-ice interaction simulation. The initial setup is illustrated in **Figure 2**. It is assumed that a wedge-shaped bow is advancing forward at a constant speed of about 1.2 knot to the level ice. Before fracture, the level ice is considered as a continuous material with ice properties, and only buoyancy is reflected as fluid force. Independently, the experiment in an ice tank was conducted at the Korea Research Institute of Ships & Ocean Engineering (KRISO). The size of level ice used in the experiment was 32 meters long and 6 meters wide, but to save the simulation time, both length and width of the level-ice was reduced to 3 meters in the simulation. **Figure 3** shows a snapshot of simulation. As the wedge advances, it can be seen that small and large ice fragments broken in the rear by the interaction with the level ice are reasonably simulated. The time-history of ice-load acting on the bow is depicted in **Figure 4**. The time average of the load is about 4.14N, which corresponds to around one-fifth of the experimental result 21.83N.

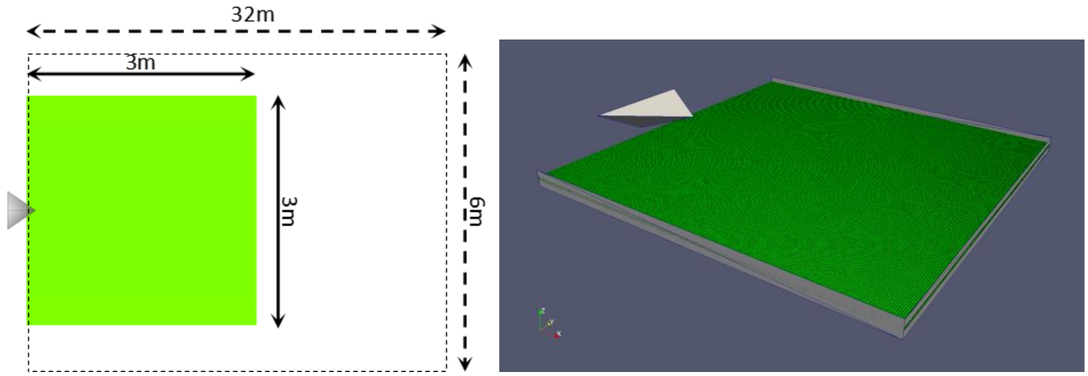

Fig. 2. Initial setup for wedge-ice interaction simulation.

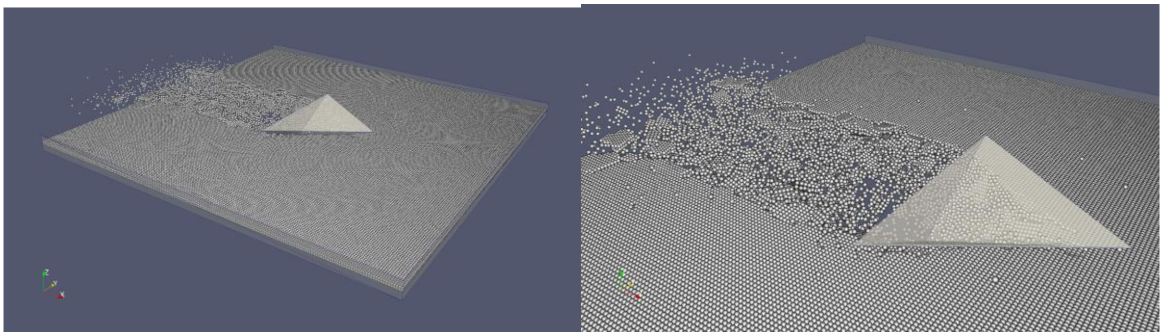

Fig. 3. Overall (left) and enlarged (right) view of snapshot from simulation at t=3sec,.

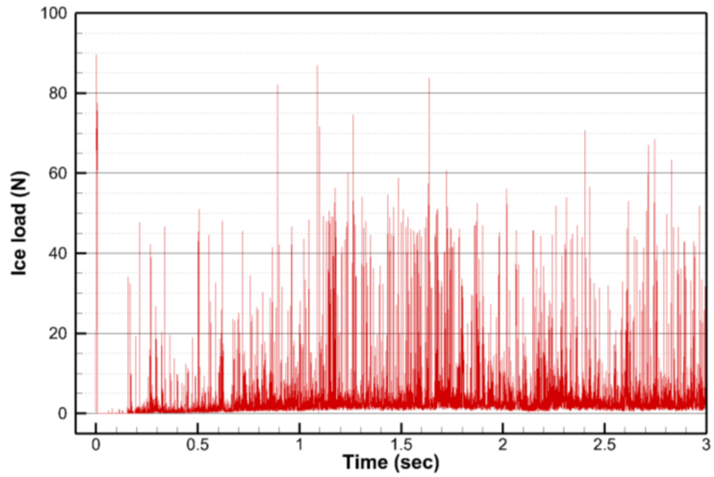

Fig. 4. Time history of ice loads on wedge.

4. Conclusions

In this study, a Lagrangian particle method had been developed and applied to simulate the ice fracture problems, such as the ice failure for 3-point bending tests and ice breaking around a wedge advancing the level ice. In 3-point bending test, the present method shows a good consistency with experiments. And for wedge-icebreaking simulation, the fracture mode seems to be reasonably simulated. However, the ice load on the wedge is still not sufficient compared to the experiment, therefore various improvements of the present method should be required in near future.

Acknowledgments

This work was supported by the IT R&D program of MOTIE/KEIT. [10060329, Development of numerical simulator for environmental load on ship and offshore in polar region]

References

André, D., Iordanoff, I., Charles, J. L., & Néauport, J., 2012. Discrete element method to simulate continuous material by using the cohesive beam model. Computer Methods in Applied Mechanics and Engineering, 213, 113-125.

Hansen, E.H., Løset, S., 1999. Modelling floating offshore units moored in broken ice: model description. Cold Regions Science and Technology, 29, 97–106.

Hwang, S.C., Khayyer, A., Gotoh, H., & Park, J.C., 2014. Development of a fully lagrangian MPS-based coupled method for simulation of fluid–structure interaction problems. Journal of Fluids and Structures, 50, pp. 497-511.

Hwang, S.C., Park, J.C., Gotoh, H., Khayyer, A., & Kang, K.J., 2016. Numerical Simulation of Sloshing Flows with Elastic Baffles by Using a Particle-based Fluid–Structure Interaction Analysis Method. Ocean Engineering, 118, pp. 227-241.

Ji, S., Li, Z., Li, C., Shang, J., 2013. Discrete Element Modeling of Ice Loads on Ship Hulls in Broken Ice Fields. Acta Oceanologica Sinica, 32(11), 50-58.

Juvinall, R. C., & Marshek, K. M., 2006. Fundamentals of machine component design (Vol. 83). John Wiley & Sons: New York.

Lepparanta, M., Lensu, M., Lu, Q.M., 1990. Shear flow of sea ice in the Marginal Ice Zone with collision rheology. Geophysica, 25(1–2), 57–74.

Polojarvi, A., Tuhkuri, J., 2009. 3D discrete numerical modelling of ridge keek punch through tests. Cold Regions Science and Technology, 56, 18–29.

Selvadurai, A.P.S., Sepehr, K., 1999. Two-dimensional discrete element simulations of ice-structure interaction. International Journal of Solids and Structures, 36, 4919–4940.

International Association for Hydro-Environment Engineering and Research
Supported by Spain Water and IWHR, China

24th IAHR International Symposium on Ice
Vladivostok, Russia, June 4 to 9, 2018

Hazards originating from increased voyages in new areas of the Arctic

Magne-Petter Sollid[2], Ove T. Gudmestad[1,2], Knut-Espen Solberg[1]
[1]*University of Stavanger, Norway*
[2]*University of Tromsø, The Arctic University, Norway*

As the ice cover of the Arctic is retracing, Arctic is being opened for more shipping and voyages, however, the hazards relating to voyages in new areas of the Arctic should be noted. The increased activities relate to transport along the Northern Sea Route, in particular associated with transport of liquefied gas from Russian plants to the Far East, to increased research activities conducted by many countries and organizations, and not at leased by increased cruise ship activities.

The increased shipping activities involve areas where previously ships did not pass and unchartered waters which pose severe risks to shipping with danger of grounding and subsequent leakages. Grounding is caused by lack of reliable and undated sea charts with a particular hazard caused by unnoticed underwater rocks and also to moving sandbanks.

According to the Norwegian Maritime Administrations accident statistics database (Norwegian Maritime Authority, 2017), there were 14 registered accidents involving passenger vessels in the Spitsbergen area in the period from 1981 to 2014. Of these accidents, 12 were due to grounding. When glaciers are retracting, the open waters are not chartered, therefore ships bringing passengers close to the glaciers pose exceptional risks to the passengers.

Cruise activities close to glaciers also exposes ships to interaction with glacial ice and ships without structural strengthening may be holed due to collision with glacial ice. In other areas, accidents have occurred recently; two vessels were dented by ice in the Chukchi Sea in 2012. A tanker was holed in September 2013, which created a real danger of an ecological disaster from fuel leakage which lasted for several days.

The paper will discuss hazards for ship voyages in the Arctic and suggest mitigating measure by which the risk of grounding and interaction with ice is considerably reduced.

1. Introduction.

Svalbard is an archipelago situated in the northern part of the Barents Sea north of the Norwegian mainland. The islands in the group are situated from 74^0 to 84^0 northern latitude and from 10^0 to 35^0 eastern longitude. The whole region of the Barents Sea surrounding the archipelago ranges from 74^0 to 90^0 northern latitude and from 00^0 to 35^0 eastern longitude. The region is characterized by its remoteness, harsh weather conditions, low temperature, winds and sea ice. The seafloor varies between the Deep Ocean, shallow coastal areas and fjords.

2. Development of passenger traffic in the Svalbard area.

Marine traffic in the area is growing due to increased tourism. In the period from 1997 to 2014, the number of passenger visiting Longyearbyen with overseas ships increased from 15.400 to 42.000 and the number of passengers traveling on expedition cruises around the archipelago is about 10.000 yearly since 2008 [1]. The marine traffic due to passenger vessels is characterized as overseas cruises, expedition cruises and day-trip cruises, see Table 1. The number of overseas cruise ships arriving to Svalbard is increasing, and in 2014 23 ships arrived a total of 33 times. The number of persons onboard these cruises varies from 370 on the smallest to about 8.000 on the largest with a passenger to crew ratio of about 3. The expedition cruises have a different operational set up as they plan for expedition tourism around the archipelago using the local ports as starting points for their voyages. These are of smaller size, and in 2014 there were 35 cruise ships operating, doing about 202 expeditions in the archipelago. The number persons on board are ranging from less than 10 to 2.000 with a passenger crew ratio of 1 to 2. The day-cruise ships are smaller vessels taking up 100 passengers and with a passenger crew ratio to 6 -7. In 2014 there were 3 ships operating on a daily basis from the port of Longyearbyen.

Table 1: Numbers for passenger vessel traffic on Svalbard: NoS = Number of Ships, PoC = Ports of Call, PoB = Persons onboard, PtC = Passenger to Crew ratio, ToP = Total of Persons per season, DoT = Day of Trip, GT = Gross Tonnage, LOA = Length Overall, Dra = Draught [1, 2]

	NoS	PoC	PoB	PtC	ToP	DoT	GT	LOA	Dra
Overseas-cruise	23	33	370-8000	3	50351	1-2			
Expedition-cruise	35	202	10-2000	1-2	20131	5-14	140-8400	40-120	3,2-7
Day-cruise	2-4	300-400	10-100	5-7	16047	1	135-340	28-50	3,2-3,8

3. Navigational accidents

Navigating in the Polar Regions and around the Spitsbergen area involves many challenges that impose a higher risk to personal life and the environment than in other maritime environments. As an example (see Figure 1), on June 1st 2014, a small day cruise ship grounded on the reef at the inlet to Ymerbukta in Isfjorden. The hull was perforated in the forepeak and extra pumps were supplied to stabilize the ship. About 40 passengers, all ages, were rescued by two helicopters and flown back to Longyearbyen - a rescue operation that lasted approximately 3 hours. The weather this day was perfect for a day-cruise trip; high-pressure and sunshine, light breeze wind and no waves. Different meteorological conditions could have had a severe impact on the emergency response and evacuation during this accident.

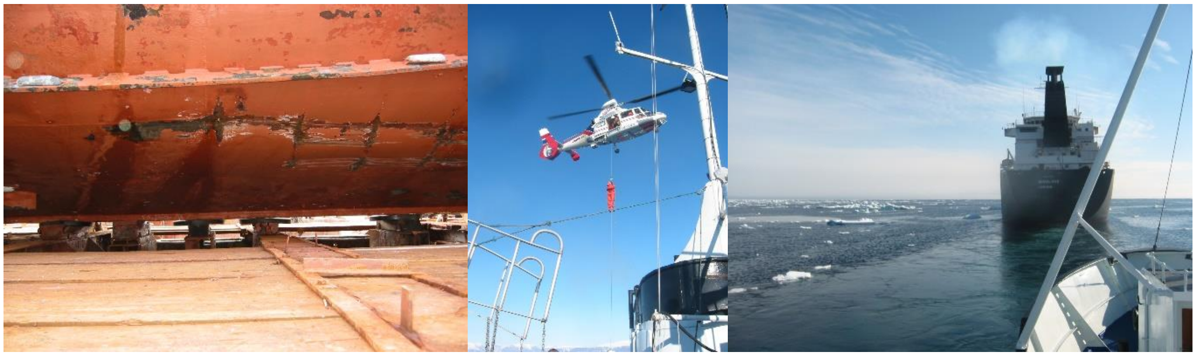

Fig. 1. Left - damages on hull from grounding. Middle – evacuation of passenger. Right – towing of passenger ship to port of Longyearbyen.

According to the Norwegian Maritime Administration's accidental statistics database [3], there are 67 registered accidents in the Svalbard archipelago region from 1981 to 2017. 19 accidents were registered with passenger vessels and 17 were registered as groundings, see table 2 below.

Table 2. There are 67 entries in the SDU north of 73^0 N in the period from 1981 to 2017 (occupational hazards, environment and leakage are excluded)

	Type of accident						
Type of vessel	**Grounding**	**Capsizing**	**Harsh environment**	**Collision**	**Fire/ explosion**	**Machinery**	**Total**
Fishing vessel 15-24 m		2				1	3
Fishing vessel > 24 m	15	2	2	10	5	2	36
Freight vessel	2						2
Passenger	17			1	1		19
Others	7						7

Underreporting of maritime accidents to vessel accident databases is a fact and the performance of the reporting to the Norwegian Maritime Administration is about 65 % [4]. For this analysis of passenger traffic in the Svalbard area - the accidental statistics of NMA [3] was compared and supplemented with statistics from the Joint Rescue Coordination Centre Northern Norway [5], IHS Fairplay, and reports from the Norwegian Coastal Administration [6] and also with news from various national and local media. It was then found that in the period from 1981 to 2017, there have been 25 groundings with passenger ships in the area. Finding data for the oldest events is difficult. There are no grounding events registered to overseas passenger cruise ships and a summary of the findings are listed in table 3 below.

Table 3: Numbers for accidents with passenger ships on Svalbard. 1 = number of grounding accidents, 2 = number of different vessels subject to accident, 3 = average age at time of accident, 4 = average number of persons on board at accident, 5 = number of vessel evacuated, 6 = numbers of vessel with towing assistance.

Type	1. accident	2. vessels	3. age	4. POB	5. evac	6. towed
Day-cruise	3	2	53	29	3	2
Expeditions	20	14	48	81 (n=10)	3(n=14)	5(n=11)

It must be underlined, however, that the Russian Cruise Ship Maxim Gorgy on 21st June 1989 rammed a small iceberg east of Spitzbergen, the main island of the Svalbard Archipelago. Some passengers went into the lifeboats and some went onto the ice-. All were rescued by the Norwegian Coast Guard vessel "Senja". An accident with a large cruise liner represents the ultimate disaster scenario for the Arctic, whether the accident is due to ice interaction, groundings or other reason.

The same number of accidents as registered for Svalbard is also reflected in other areas of the Arctic. In the period from 1990 to 2012 there were 499 registered grounding accidents of total 788 registered accidents north of 60 degrees in Greenland [7]. 85 of these grounding accidents were with passenger ships whereas cargo ships formed 188 of the grounding accidents. Ship groundings in general account for about one third of the total commercial ship accidents worldwide [8]. In Norwegian waters groundings accounted for 45 % of the total ship accidents [9], in the Gulf of Finland 48 % were grounding accidents [10] and 47 % of all accidents involving Greek registered ships over 100 GT were due to groundings [11]. The numbers of groundings are the figures most national summaries of maritime accidental highlight – groundings are the major accidents in the maritime transportation sector.

4. Causation of groundings in the Arctic

Errors in nautical charts due to old soundings or non-surveyed areas are common causes of groundings [8]. Sailing into unchartered waters is a navigational violation rather than an error as it is expected that navigators are aware of the lack of surveying. The immediate causation of a powered grounding accidents also lies in the failure of passage planning, piloting, inadequate bridge team management, assumptions and complacency.

Understanding the human factors that are underlying major shipping accidents is of key importance to improve the understanding of risk and management of mitigating measures to prevent new accidents. Studies estimate that around 80 % of causes in marine accidents are attributable to human factors [12]. Casual factors for groundings have been studied by Macrae [12] and it was found that the major triggering factors for groundings are insufficient planning (30.3 %), insufficient interpretation (18.2%), and insufficient communication (15.2%). The common findings were that all groundings are the cause of deficits of planning in combination with a communication or a ship location problem. The analysis further revealed that route failure planning was due to wrong interpretation of plans (18.1%), absent plans (27.3%) and incomplete plans (54.6%). The reason for incomplete and absent plans arose from cognitive bias (illusion of control, over-reliance on personal experience) or poor working conditions. Constructing adequate and detailed plans is the requirement of every marine voyage, and as such, it can be said that 81.9% of the planning failures were due to personal violations. Interpretation failures are considered to be related to the lack of plan and it was found that these failures either could be decision errors regarding the vessel heading (33.3%) or faulty diagnoses of the vessels position limits (66.6%).

It is likely to assume that the probability of ship groundings will increase when operating in the polar areas. In addition to lack of chartering, the harsh environment and the remote area of the Arctic impose elevated levels of risk due to both the increased probability of occurrences and more severe consequences.

Additional sources of hazards due to operating in polar areas are listed in the Polar Code. Leveling effects on the risk of grounding are listed below (Table 4).

Table 4: Leveling (increased) effects of grounding risk in the Arctic. Effects are listed due to increased probability and increased severity of consequences.

Effect	**Leveled prob. of grounding**	**Leveled consequence of grounding**
Ice, as it may affect: hull structure, machinery systems, navigation, working environment, maintenance and emergency preparedness and safety equipment systems	- Broken ice, floes and slush can result in clogging of rudders giving reduced steering capability. - Bergy-bits and growlers initiating rapid and unplanned maneuver.	- Lowering of lifeboats onto ice not possible. - Damage to lifeboats and rafts if maneuvering in ice.
Topside icing: reduction of stability and equipment functionality	- Additional heeling factor reducing maneuverability.	- Affecting probability of capsizing in combination with flooding. - Grounding due to changed maneuverability. - Grounding due to changed heeling factor
Low temperature, as it affects: working environment, human performance, maintenance end EPPR tasks, survival time and safety equipment.	- Increased probability of flu and colds leading to sick-leaves of key personnel. - Demotivation, leading to complacency. - General increase in probability of human errors	- Increased probability of hypothermia. - Malfunction of survival equipment - Reduced time to rescue and survival - Grounding
Extended periods of darkness as it may affect navigation and human performance.	- Navigation errors due to reduced visibility. - Increased probability of human error due to depressions and reduced functionality	- Reduced visibility leading to grounding - Increase challenges to emergency response as Search and Rescue, recovery of persons.
High latitude, as it may affect: navigation systems, communication systems and quality of ice imagery information	- Magnetic compass useless due lack of horizontal component of magnetic field. - Gyro unstable north of 85N - Difficulties for receiving weather information and emergency communication	- Grounding - Emergency communication
Remoteness and lack of hydrographic data, navigational aids and seamarks. Limited SAR facilities and emergency response.	- Few, missing and damaged AtoN Aids to Navigation - Position fixing difficult due mistaken identification of shore features. - Increased risk of grounding	- Grounding - Escalating consequences due to reduced SAR
Lack of crew experience with potential for human error.	- Risk of navigational mistakes, violation and complacency as not understanding the environment	- Grounding
Rapidly changing weather conditions with potential of escalating incidents.	- Navigational failure	- Grounding

5. Hydrographic charting and aids to navigation in the Arctic

Cruise ships are from time to time navigating close to glaciers as a part of delivering expedition and adventure experiences to their passengers. Increased contribution to the probability of grounding is first of all the quality of the hydrographic charting. The arctic areas have in general poor charting but as the glacier retracts new un-surveyed areas emerge.

Establishing a reliable geospatial database described within a consistent reference system is of decisive significance when it comes to safe navigation. Most Arctic sea maps are either of poor quality and many areas are not surveyed at all. This can be seen in light of the relative limited marine traffic in the Arctic compared with other areas and it is also due to the cost and risk of survey operations due to the harsh environments and remoteness. Compulsory carriage of ECDIS onboard all ships above 500 GT is coming to an end in 2018. But the combination of modern charting technology together with accurate positioning from the Global Navigation Satellite System (GNSS) is not any guarantee for safe navigation as the electronic chart quality is not better than the technology used for the hydrographic charting and methods to compile them. Further on, one is totally dependent on GNSS coverage to use the electronic charts.

Also, in many Arctic locations, tide and current predictions have never been calculated and for many other locations, tide and current predictions have not been measured since the early 1950s when only a few days of data were collected. Accurate predictions require at least 30 days of continuous data collection.

Safety of navigation relay heavily on Aids to Navigation (AToN) which can be categorized by short-range and long-range aids. Short-range aids to navigation include fixed/floating buoys, landmarks with lights, spars and leading lights and marks. Long-range aids to navigation include shore-based radio direction finding and satellite-based positioning. AToN also include safety and navigation information messaging via broadcasting. In the Arctic, AToN are unavailable due to the limited traffic, cost of installation and maintenance and harsh conditions.

6. Mitigating measures for grounding in the Polar Regions.

Navigators onboard a vessel are fully dependent on information and tools as up-to-date charts, latest depth information, tidal information and aids to navigation, to undertake a safe journey. In many of the new emerging trafficked Arctic areas, many of these tools are out-of-date or unavailable. It will take decades before the Arctic oceans have been fully surveyed and charted. Finding mitigating measures and reliable solutions to avoid grounding in the meanwhile is of high importance.

One mitigating measure to avoid groundings can be the use of an "underwater radar" – or namely a forward-looking sonar (FLS), Figure 2. Today, this technology is mature and robust and is used by fishing boats and by underwater vehicles for obstacle avoidance. Forward looking sonars are advertised with ranges from 1000 to 3000 meters, dependent on the operating conditions. Several cruise ships, *The World* and *Lindblad*, for example, are already using this technology for expedition cruises [13]. There are also limitations in using such system – such as requiring high user intervention and competence. Another bridge system, putting more workload on the navigators, are also mentioned.

Use of Virtual Aids to Navigation (VAToN) is another solution that can be suitable for navigation in remote and polar areas. VAToN is a digital information object in full compliance with standard AToN and does not require any physical infrastructure. This digital object is promulgated by another service provider and the information can be presented on electronic navigational charts. This digital information presented on an onboard navigation system such as the Electronic-Chart-Display-and-Information-System-ECDIS (ECDIS) can be either static or dynamic – i.e. its characteristics can change in space and time in accordance with the vessel specifications. It can also be permanent, temporary or momentary in duration with respect to indication of a hazard to navigation.

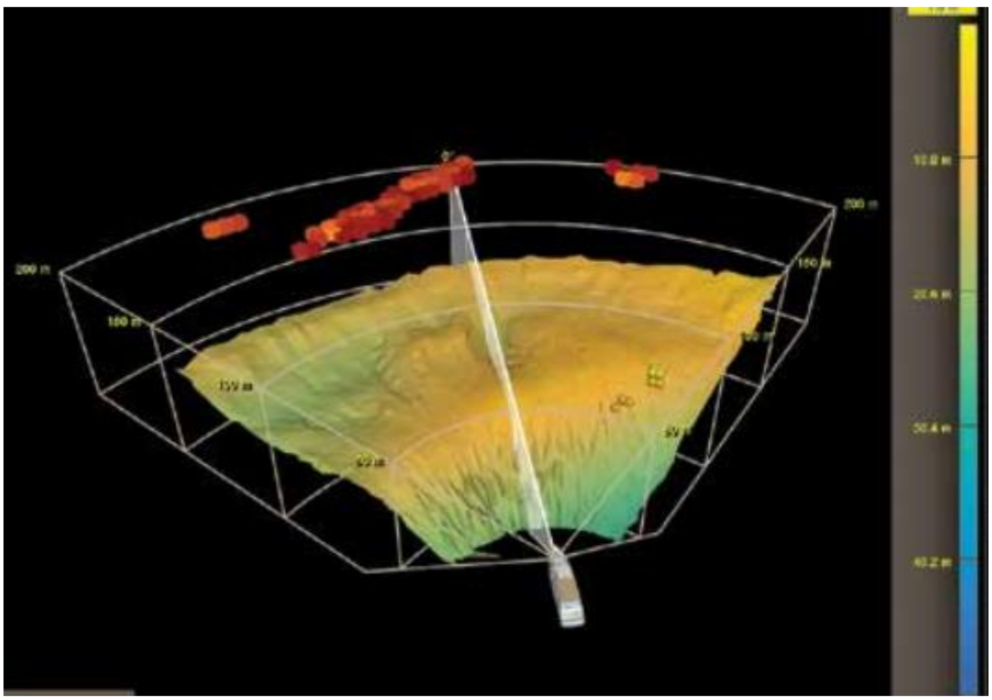

Fig. 2. Picture of forward looking sonar [13]

In several groundings accidents such as M/V Clipper Adventure, M/V Costa Concordia, M/V Rena and M/V Exxon Valdez - a forward looking sonar could have provided a 2 to 3 minutes warning to the navigator or a VAToN placed in front of the respective reefs where the grounding occurred, could have contributed significantly to avoid these accidents [14]

Olex is another hydrographic system that is widely used in the Norwegian fishing fleet and has also, for instance, been used by the Norwegian "Hurtigruten". Olex is a seafloor mapping system, Figure 3 that interfaces with single and multibeam echo sounders where depths are collected and merged into a central depth database that can be shared among ships. For instance, if a ship navigates in arctic fjords close to a glacier – they can record depth data while they go and share these depth data with the next ship coming in.

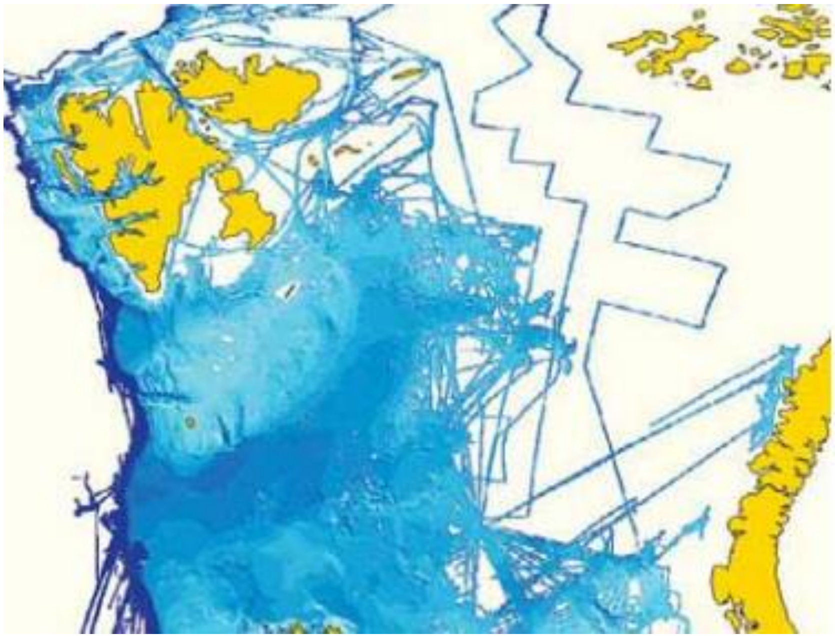

Fig. 3. Olex depth data in the Barents Sea collected from echo sounders on Norwegian fishing fleet [15]

7. References

1. Sysselmannen på Svalbard, *Reiselivsstatistikk for Svalbard*. 2014: Longyearbyen.
2. Kystverket, *Polarlostjeneste på Svalbard*. 2007: Ålesund.
3. Norwegian Maritime Administration, *Accidents 1981-2015*, N.M. Administration, Editor. 2017: Haugeusund.
4. Hassel, M., B.E. Asbjørnslett, and L.P. Hole, *Underreporting of maritime accidents to vessel accident databases.* Accident Analysis & Prevention, 2011. **43**(6): p. 2053-2063.
5. Joint Rescue Coordination Centre Northern Norway. *Reported groundings in the Svalbard region. Unpublished* 2018.
6. Norwegian Coastal Administration, *Weekly reports from Coastal Administration's emergency team.* 2011-2018.
7. DNV GL, *Marine environmental risk assessment - Greenland*. 2015, DNV GL: Høvik. http://naalakkersuisut.gl/~/media/Nanoq/Files/Attached%20Files/Miljoe/Rapport/Risikoanalyse%20for%20havmiljomrdet%20i%20og%20omkring%20Grnland%202015.pdf
8. Mazaheri, A., J. Montewka, and P. Kujala, *Modeling the risk of ship grounding - A literature review from a risk management perspective*. WMU Journal of Maritime Affairs, Volume 13, Issue 2, pp 269 - 297, 2014.
9. DNV-GL, *Analyse av ulykkestatistikken for norske farvann de siste 30 årene*. Sjøsikkerhetsanalysen 2014, DNV GL. p. 67. http://www.kystverket.no/contentassets/f056df3c875140aa98ef49a25cc082c6/2_ulykkesanalyse.pdf
10. Kujala, P., M. Hänninen, T. Arola and J. Ylitalo, *Analysis of the marine traffic safety in the Gulf of Finland*. Reliability Engineering and Sysyem safety, 2013. 1349-1357.
11. Samuelides, M.S., N. Ventikos, and I.C. Gemelos, *Survey on grounding incidents: Statistical analysis and risk assessment*. Ships and Offshore Structures, Vol. 4. 2009. 55-68.

12. Macrae, C., *Human factors at sea: Common patterns of error in groundings and collisions*. Maritime Policy and Management. Vol. 36. 2009. 21-38.
13. Russel, I., *Forward-Looking Sonar for navigation*, In: *Seaways*. 2015, Nautical Institute. http://www.nautinst.org/filemanager/root/site_assets/the_navigator/navinspire/navinspire/pages_from_seaways_-_jun15.pdf
14. Wright, R.G. and C.M. Zimmerman, *Vector data extraction from forward-looking sonar imagery for hydrographic survey and hazard to navigation detection*. *OCEANS'15 MTS/IEEE Washington*. 2015. IEEE.
15. Lyubin, P.A., et al., *Megabenthos of the Barents Sea*. In: Biological – Geological Seabed Mapping and Monitoring in the Barents Sea, Norwegian-Russian workshop HAV5, ed.: Jørgensen, L.L. N.A. Anisimova and A. B. Storeng, Chapter: 1.2, Publisher: IMR-PINRO, 2011.

24th IAHR International Symposium on Ice
Vladivostok, Russia, June 4 to 9, 2018

Observations of Ice Bottom Morphology and Flow Velocities under Ice

Xiaowei Cao[1], Peng Lu[1], Baosen Zhang[2], Guoyu Li[3], Zhijun LI[1]
1. State Key Laboratory of Coastal and Offshore Engineering, Dalian University of Technology
2. Yellow River Institute of Hydraulic Research, Yellow River Conservancy Commission
3. State Key Laboratory of Frozen Soil Engineering, Cold and Arid Regions Environmental and Engineering Research Institute, Chinese Academy of Sciences
1. 2 Linggong Road, Dalian, Liaoning, China. 116023
2. 45 Shunhe Road, Zhengzhou, Henan, China, 450003
3. No.320, West Donggang Rd, Lanzhou, Gansu, China. 730000
hdcxw@mail.dlut.edu.cn, lupeng@dlut.edu.cn, 976129493@qq.com,guoyuli@lzb.ac.cn, lizhijun@dlut.edu.cn

The sea ice draft is an important part of global water circulation, and it produces major impacts on the global climate change and polar region navigation. The river ice draft also produces major impacts on the river ice flood and engineering disaster prevention. The ice bottom morphology has an important influence on the flow field and velocity under ice. In order to study this relationship, the ice bottom morphology in the range of 10 m × 10 m and vertically flow velocities distribution under ice were measured in the Yellow River. The ice bottom morphology was measured via ground penetrating radar (GPR) technology and traditional borehole measurements. Applying high-frequency GPR (200 MHz) enables detailed surveying of variation in ice thickness, and get the ice bottom morphology. Using the borehole data to calculate radar propagation velocity in the ice enables improve the accuracy of GPR measurement results. The vertically flow velocities distribution under ice measured with an acoustic Doppler current profiler (ADCP) were survey from 6 boreholes. Using the data of GPR and ADCP enables discussing the influence of ice bottom morphology on the flow field and velocity under ice.

1. Introduction

Arctic sea ice, an important component of the climate system, has received extensive attention recently. The variation of Arctic sea ice represents a significant indicator of changes in the climate system such as global change and polar amplification. To some extent, the observation and climate modeling suggests that sea ice can itself be an agent of climate change (Mysak et al., 1990, Deser et al., 2000). Sea ice draft plays an important role in studying and researching the Arctic sea ice (Rothrock et al., 1999). Information on ice draft in the river is particularly essential for modern society in many respects, for example, ice jam flood (Beltaos et al. 2008). It analyses ice-induced scour and erosion in ice engineering (Prowse, 2001). Ice bottom morphology has a profound influence on the flow field and velocity.

It has always been difficult to quickly and accurately measure ice thickness. (Laxon et al., 2003). Much efforts have been put in the past to investigate and develop techniques to measure ice thickness. On the large scale, the remote sensing (Tamura et al., 2007), radar (Zhao, 2008) and carrier sonar (Rothrock et al., 1999) has been widely used. On the small scale, mooring sonar and ultrasonic detection technology achieved the progress of continuous observation, but the accuracy is only ±1 cm (Richtermenge et al. 2006). Drilling is the most effective means of ice thickness measurement, but it is inefficient and difficult to achieve continuous measurement of the ice bottom morphology. The ground penetrating radar (PAR) serves as a very useful non-invasive method for ice thickness measurement, which has the advantages of fast, efficient, continuous and real-time. In addition, this method has been applied to determine the Arctic (Wang et al., 2007) and river ice thickness (Kämäri et al., 2017, Cao et al., 2016).

Acoustic Doppler Current Profiler (ADCP) is the velocity sonar with under water acoustic Doppler principle (Brumley et al., 1991). It is primarily used to remotely measure the water velocity in a wide range and monitor sea (Gartner et al., 2004) and river (Kämäri et al., 2017).

2. The study site and method

2.1 Study site

The Yellow River is the second largest river in China, with a total length of 5400 km (Ke et al., 2000). The site of this measurement is a meandering river that located in the upper of the Yellow River, in the Inner Mongolia (Fig. 1). The river width and the average ice thickness is about 200 m and about 53.6 cm respectively. The two positions (A and B) with 10 square meters, were chosen to measure the ice bottom morphology and flow velocities under ice (Fig 1). The upstream and downstream flow velocities under ice were measured by ADCP. The ice thickness of A and B was measured by GPR.

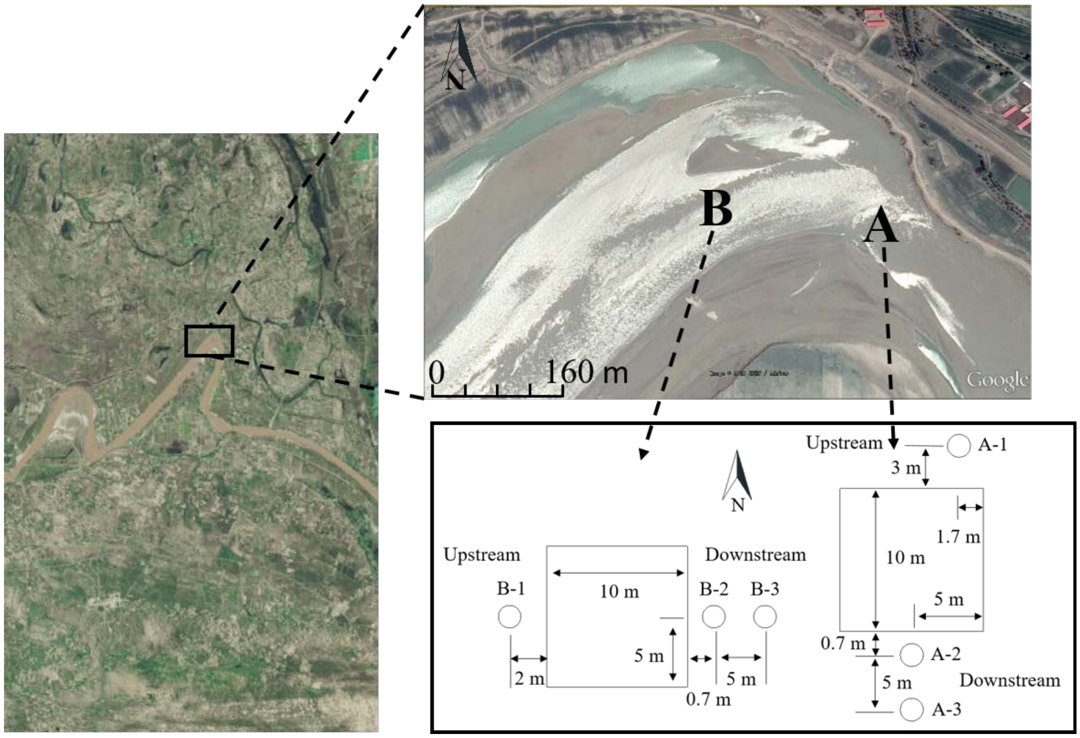

Fig. 1. Study site

2.2 Ice thickness measurements with GPR

GPR in this study is a RIS-K2 ground penetrating radar produced by IDS, Italy. The maximum measurable ice thickness and resolution were determined by the radar antenna frequency. Previous study has shown that the antenna frequency of 200 MHz has higher resolution for ice thickness than other frequencies, the number is about 1 m (Sun et al., 2003). According to the average ice thickness of this place, the antenna of 200 MHz was used to measure the ice thickness. The width of the GPR was 40 cm, and the measurement interval is 1 m.

The basic principle of GPR is that electromagnetic waves reflect or scatter back to the receiver from interfaces between materials with different electrical properties. The time that the electromagnetic wave through the ice can be obtained from the radar image. Therefore, the accuracy of the GPR was determined by the velocity of electromagnetic wave in ice. The velocity of the electromagnetic wave can be expressed as follows (Annan, 2009).

$$v=\frac{c}{\sqrt{\varepsilon_r}} \quad \textbf{[1]}$$

Thereof, c represents the light speed, ε_r is the relative permittivity.

Considering the relative permittivity of ice is influenced by possible cracks, bubbles, and impurities within the ice layer, it is difficult to directly measure the concrete figure in the field. Therefore, according to the pervious study in 2015-2016 winter (Cao et al., 2016), the velocity of the electromagnetic wave can be calculated by the radar and ice thickness that can be measured at 10 meandering positions. Half of them were used to calculate the velocity of the electromagnetic wave by the equation [2].

$$v=2D/t \quad \textbf{[2]}$$

In the equation above, D is the ice thickness measured by drilling. The t is the time for electromagnetic wave to pass through a layer and return to the antenna (the two-way travel time), which was recorded by the GPR antennas. The specific calculation results are presented in Table 1.

Table 1. Velocity of the electromagnetic wave in ice

No.	D (cm)	t (ns)	v (cm/ns)	Average of v (cm/ns)
1	51.60	6.99	14.76	
2	58.10	7.38	15.75	
3	52.00	6.80	15.29	15.27
4	60.90	8.00	15.23	
6	56.10	7.33	15.31	

The average velocity of the electromagnetic wave is approximately 15.27 cm/ns. Based on this number and the time obtained from the radar image, the ice thickness can be calculated by the equation [2]. The remaining 5 positions are used to verify average velocity (Fig. 2). It can be seen from the figure 2 that the R^2 is as high as 0.97. Hence, this method is possible and practical.

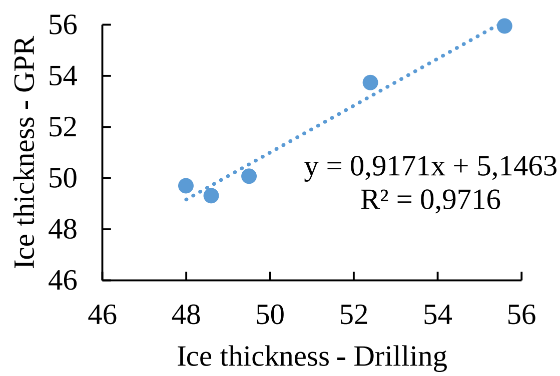

Fig. 2. Comparison the ice thickness between the radar and drilling

2.3 The measurement of flow velocities under ice

Workhorse Rio Grande (four 1.2 MHz velocity transducers) was used to measure flow velocities under ice. The measurement accuracy of the sensor was ±0.25%. The resolution was 0.001 m/s, and unit size was 10 cm.

The flow velocities of upstream and downstream of each area (A and B) under ice were measured, and specific measurement positions were A-1, B-1, A-2, A-3, B-2, B-3 (Fig. 1). Water depths of the ADCP were 50 cm for the A upstream and 40 cm for the A downstream, 20 cm for B.

3. Results

3.1 Ice bottom morphology

Fig. 3 clearly reveals the radar image of the partial area of A and B regions as well as the air-ice-water interface. The time extracted from the radar image, the average velocity and formula [2] can be used to obtain the ice thickness distribution in the A and B regions.

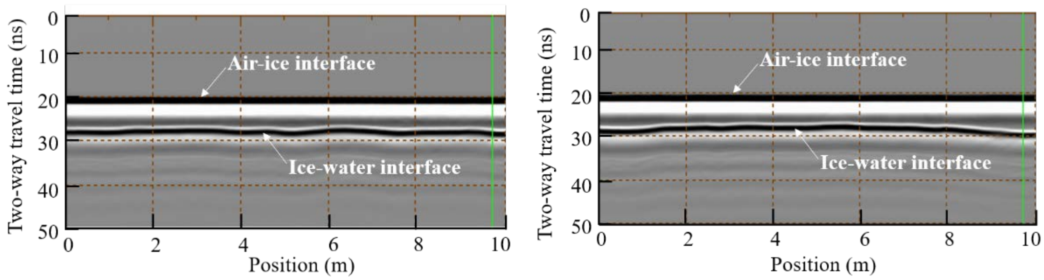

Fig. 3. Radar image of partial area A and B

Fig. 4 demonstrates ice bottom morphology. From the Fig. 4, the ice thickness of the area A was from 52.86 cm to 66.08 cm, and the average was 58.99 cm. The ice thickness of the area B was from 50.85 cm to 86.12 cm, and the average was 56.55 cm.

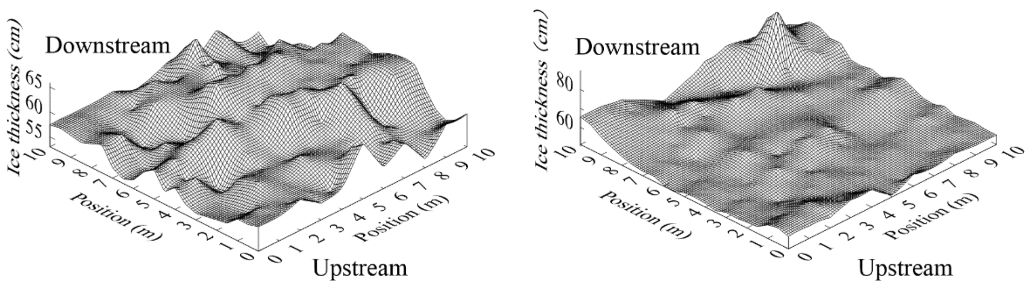

Fig. 4. Ice bottom morphology of A and B

3.2 Flow velocities under ice

Fig. 5 shows flow velocities under ice. The average flow velocities under the area A were about 0.86 m/s on the upstream and 0.76 m/s on the downstream. The fastest flow occurs at about 1.2 meters, 0.89 m/s on the upstream and 0.85 m/s on the downstream. For the area B, the average flow velocities under ice was about 0.028 m/s on the upstream and 0.013 m/s on the downstream. The fast flow occurs at about 1.14 m, 0.053 m/s on the upstream and 0.0022 m/s on the downstream.

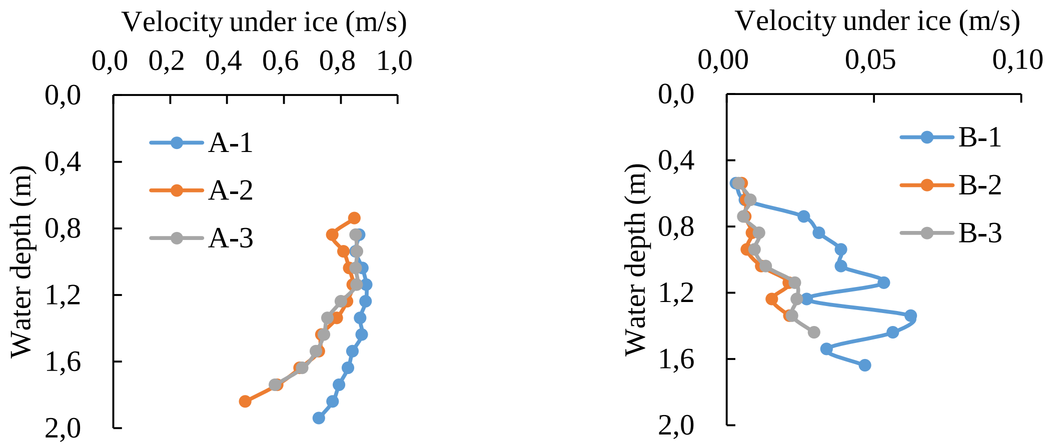

Fig. 5. Flow velocities under ice of area A and B

4. Discussion and Conclusion

4.1 Ice bottom roughness

In order to better describe the ice bottom patterns in area A and B, different profiles were chose to calculate the amplitude roughness. Three sections were chose in parallel flow direction and vertical flow direction respectively, 1 m, 5 m and 9 m. The ice thickness distribution of these profiles was shown in Fig. 6.

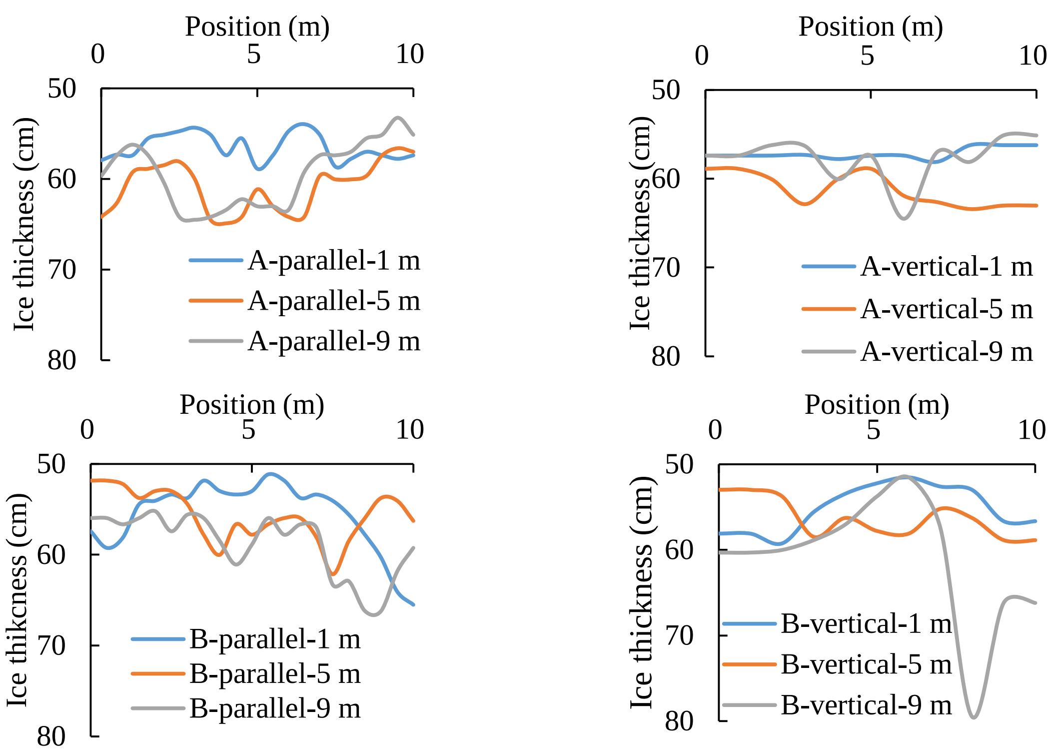

Fig. 6. Ice thickness of different profiles

The roughness of a surface can be quantified as the variance of its elevation around its mean value (Andreas et al. 1993). Defining the elevation of a line of a N points at any point j with z_{xj} (with x being the ice thickness), the roughness variance is defined as sum of the squares of deviations from its mean value$\langle z_x \rangle$,

$$\sigma_x^2 = \frac{1}{N} \sum_{j=1}^{N} \left(z_{xj} - \langle z_x \rangle\right)^2 \qquad \textbf{[3]}$$

The specific calculation results were shown in the following table 2.

Table 2. Different ice bottom roughness

Position		Roughness σ_x (cm) A	B
Parallel	1 m	2.17	15.42
	5 m	7.22	34.07
	9 m	12.43	11.94
Vertical	1 m	0.38	10.69
	5 m	3.24	29.02
	9 m	6.38	63.04

From the results of the ice bottom roughness, It can be clearly seen in both areas that the parallel flow direction roughness of the outside of the curve is higher that of inside of the curve. It can be caused by the accumulation of ice floes. Due to the scouring of the water flow, the ice bottom morphology of the inside of the curve was relative smooth.

4.2 Flow velocities under ice

The specific flow velocities in the Fig. 5 were close to zero. Therefore, it can be judged that the area B was located in the river beach and there was no ware flow. The ice growth of the area B was not mainly affected by the water flow.

For the area A, the average flow velocity was reduced (0.86 to 0.76 m/s) after passing through the ice bottom. From this study, the ice cover have an impact on the flow field under the ice. Due to the lack of measurement data, it is impossible to perform in-depth analysis. The next step will be to measure the ice bottom morphology and flow velocities at different freezing periods, and analysis of the intrinsic links.

Acknowledgments

This research was supported by the Global Change Research Programme of China (2015CB953900), National Natural Science Foundation of China (51579028) and the Open Foundation of the State Key Laboratory of Frozen Soil Engineering (SKLFSE201604).

References

Mysak, L. A., Manak, D. K., and Marsden, R. F., 1990. Sea-ice anomalies observed in the Greenland and Labrador seas during 1901-1984 and their relation to an interdecadal Arctic climate cycle. Climate Dynamics, 5(2), 111-133.

Deser, C., Walsh, J. E., and Timlin, M. S., 2000. Arctic sea ice variability in the context of recent atmospheric circulation trends. Journal of Climate, 13(3), 617--633.

Rothrock, D. A., Yu, Y., and Maykut, G. A., 1999. Thinning of the arctic sea‐ice cover. Geophysical Research Letters, 26(23), 3469-3472.

Beltaos, S., 2008. Progress in the study and management of river ice jams. Cold Regions Science and Technology, 51(1), 2-19.

Prowse, T. D., 2001. River-ice ecology :Ⅰhydrologic, geomorphic, and water-quality aspects. Journal of Cold Regions Engineering, 15(1), 1-16.

Laxon, S., Peacock, N., and Smith, D., 2003. High interannual variability of sea ice thickness in the arctic region. Nature, 425(6961), 947-950.

Tamura, T., Ohshima, K. I., Markus, T., Cavalieri, D. J., Nihashi, S., and Hirasawa, N., 2007. Estimation of thin ice thickness and detection of fast ice from SSM I data in the Antarctic Ocean. Journal of Atmospheric & Oceanic Technology, 24(10), 431-443.

Zhao B. G., 2008. Study on ice monitoring and forecasting with radar of ice area projects point in Liaodong Bay Bohai Sea. Dalian Maritime University (in Chinese).

Richtermenge, J. A., Perovich, D. K., Elder, B. C., Claffey, K., Rigor, I., and Ortmeyer, M, 2006. Ice mass-balance buoys: a tool for measuring and attributing changes in the thickness of the arctic sea-ice cover. Annals of Glaciology, 44(44), 205-210(6).

Wang, B. B., Sun, B., Tian, G., Guo, J. X., and Wang, D. L., 2007. The application of the 3D GPR method to measuring the depth of arctic summer sea ice and analyzing its underside morphology. Geophysical & Geochemical Exploration.

Kämäri, M., Alho, P., Colpaert, A., and Lotsari, E., 2017. Spatial variation of river-ice thickness in a meandering river. Cold Regions Science and Technology, 137, 17-29.

Cao X. W., Li C. J., Yan X. F., Wu Y. F. and Li Z. J., 2017. Measuring Ice Thickness around the Curve and Piers in the Yellow River with Ground Penetrating Radar. South-to-North Water Transfers and Water Science & Technology, 14(6), 91-95.

Brumley, B. H., Cabrera, R. G., Deines, K. L., and Terray, E. A., 1991. Performance of a broad-band Acoustic Doppler Current Profiler. IEEE Journal of Oceanic Engineering, 16(4), 402-407. Lotsari, E., Kasvi, E., Kämäri, M., and Alho, P., 2017. The effects of ice cover on flow characteristics in a subarctic meandering river. Earth Surface Processes & Landforms, 42(8).

Gartner, J. W., 2004. Estimating suspended solids concentrations from backscatter intensity measured by Acoustic Doppler Current Profiler in San Francisco bay, California. Marine Geology, 211(3–4), 169-187.

Sujuan, K. E., Guangqi, L. U., and Ren, Z., 2000. Study on mechanism of ice jam formation in bayangaole section of yellow river. Journal of Hydraulic Engineering, 31(7), 0066-0070.

Sun B., Wen J. H., 2003. Sea ice thickness measurement and its underside morphology analysis using radar penetration in the Arctic Ocean. Science in China, 46(11):1151-1160.

Annan, A. P., 2009. Chapter 1. Electromagnetic Principles of Ground Penetrating Radar. Ground Penetrating Radar. Elsevier Science & Technology.

Andreas, E. L., Lange, M. A., Ackley, S. F., and Wadhams, P., 1993. Roughness of Weddell Sea ice and estimates of the air-ice drag coefficient. Journal of Geophysical Research Oceans,98(C7), 12439-12452.

International Association for Hydro-Environment Engineering and Research
Supported by Spain Water and IWHR, China

24th IAHR International Symposium on Ice
Vladivostok, Russia, June 4 to 9, 2018

Dissipation Rates of the Turbulent Kinetic Energy under Ice Cover of Lake Baikal

Georgiy Kirillin[1*], Ilya Aslamov[2], Vladimir Kozlov[3], Nikolay Granin[2]
[1]Leibniz-Institute of Freshwater Ecology and Inland Fisheries (IGB), Berlin, Germany
[2]Department of Hydrology and Hydrophysics, Limnological Institute, Siberian Branch of Russian Academy of Sciences, Irkutsk, Russia
[3]Institute for System Dynamics and Control Theory, Siberian Branch of Russian Academy of Science, Irkutsk, Russia
** kirillin@igb-berlin.de*

Ice cover on polar and temperate lakes creates seasonally developing boundary layer at the ice base with specific features: fixed temperature at the solid boundary and stable density stratification beneath. Turbulent transport in the boundary layer determine the ice growth and melting conditions at the ice-water interface, especially in large lakes and marginal seas, where large-scale water circulation can produce highly variable mixing conditions. Since the boundary mixing under ice is difficult to measure, existing models of ice cover dynamics usually neglect or parameterize it in a very simplistic form. We present first detailed observations on mixing under ice of Lake Baikal, obtained with the help of advanced acoustic methods. The dissipation rate of the turbulent kinetic energy (TKE) was derived from spectra of velocity fluctuations at a single point under ice, and from correlations (structure functions) of current velocities along vertical profiles in the boundary layer. The range of the dissipation rate variability covered 2 orders of magnitude. Intensity of mixing was closely connected to mean speeds of the under-ice currents, the latter being of geostrophic origin and having lake-wide scales. Turbulence directly affected heat flux at the ice-water interface and, by this, the ice growth and melting rate. To quantify these effects, we develop a parameterization of the water-ice heat flux based on the Kolmogorov microscale involving the dissipation rate of TKE. The parameterization describes well the thickness of the viscous sub-layer at the ice base, and the conductive heat flux across it, determined from the fine-scale temperature measurements in the boundary layer. The parameterization can be implemented in coupled lake-ice models, which typically use TKE dissipation rate as a prognostic variable.

1. Introduction.

Seasonal formation of ice cover is an essential feature of polar seas and surface waters. The demand on a better quantitative description of the formation, evolution, and decay of the seasonal ice, as a function of external forcing, has grown recently because of large-scale trends to shortening of the ice season and decrease of the arctic sea ice extent. Closure of the global mass budget of the arctic seasonal ice is a complex problem, related, apart from the atmospheric and terrestrial heat sources, to the heat upward heat transport stored in the Arctic Ocean. An important role in the upward heat transport is played by the storage of the solar radiation in the under-ice water and the advective transport by the under-ice currents. Lake Baikal is the lake most closely resembling the Arctic Ocean with regard to the seasonal ice dynamics.

In order to reveal the major factors governing the ice-water heat flux in lakes, we analyze the outcomes from a field campaign held on Lake Baikal (Russia), which is the deepest and the most voluminous lake on earth. Among other great lakes of the world Lake Baikal reveals the longest ice-covered period and the most steady ice cover, occupying the entire lake for 3-5 months of the year. This feature is conditioned by the unique pattern of lake-atmosphere interaction in winter, characterized by a strong surface cooling under influence of the Siberian atmospheric pressure maximum. Consequently, ice regime plays a crucial role in hydrodynamics and ecosystem functioning of the lake. The complex nearly-geostrophic circulation pattern exists in the large water volume under ice throughout the winter. In this regard, the dynamics of Lake Baikal under ice shares many typical features of polar seas. During one ice season, ice structure as well as ice and snow cover thicknesses vary significantly over the lake that allows carrying out a wide range of ice-related field studies.

2. Study site and methods.

The field study was performed in the southern part of Lake Baikal in January-March 2017. Two autonomous stations were installed in the vicinity of a quasi-stationary longshore current, regularly observed during ice cover period (Fig. 1). Station 1 was installed 4.5 km from the lake shore at the point with maximum speeds of the under-ice currents; the initial ice thickness was 23 cm. Station 2 was located 3.5 km to the north from station 2; the initial ice thickness was 24 cm. Each station registered temperature at 30 vertical levels distributed within the ice cover, the water boundary layer, and the air above the ice. The distance between temperature sensors was 5 cm within the ice and 10-50 cm in water and in the atmosphere. Three sensors of the short-wave solar radiation registered the vertical radiation decay within the air-ice-water system. Ice thickness was registered by a 330-kHz echo-sounder, deployed upward-looking at a fixed distance from the ice surface. Two-dimensional electromagnetic current meters "INFINITY-EM" ("JFE Advantech Co., Ltd.") were used to measure the current velocities: (velocity range ± 5 m/s, resolution 0.02 cm/s, accuracy ± 1 cm/s. The current meters were positioned at a distance of 1 m from the surface of the ice cover. Four additional current meters were deployed at Station 1 at distances 0.6, 0.8 and 1.4 m from the ice surface.

Fig. 1. Ice conditions in Southern Baikal on (A) 9 February and (B) 12 April 2017 and locations of the autonomous measurement stations.

Detailed characteristics of turbulent mixing in the under-ice boundary layer were obtained with the help of the high-resolution Doppler flow rate meter HR Aquadopp (Nortek AS, Norway). The profiler was deployed for 48 hours successively at each of the two stations. The values of short-period fluctuations of the flow velocity were used to calculate dissipation rate of the kinetic energy of turbulence (TKE) based on the Kolmogorov's hypothesis on the self-similarity of the velocity structure functions (see Wiles et al. 2006 for the method description). In addition, the detailed profiles of mean currents, obtained with a time interval of 2 s and a spatial resolution of 15 mm, served to verify long-term point measurements by electromagnetic recorders, demonstrating good agreement (Fig. 2).

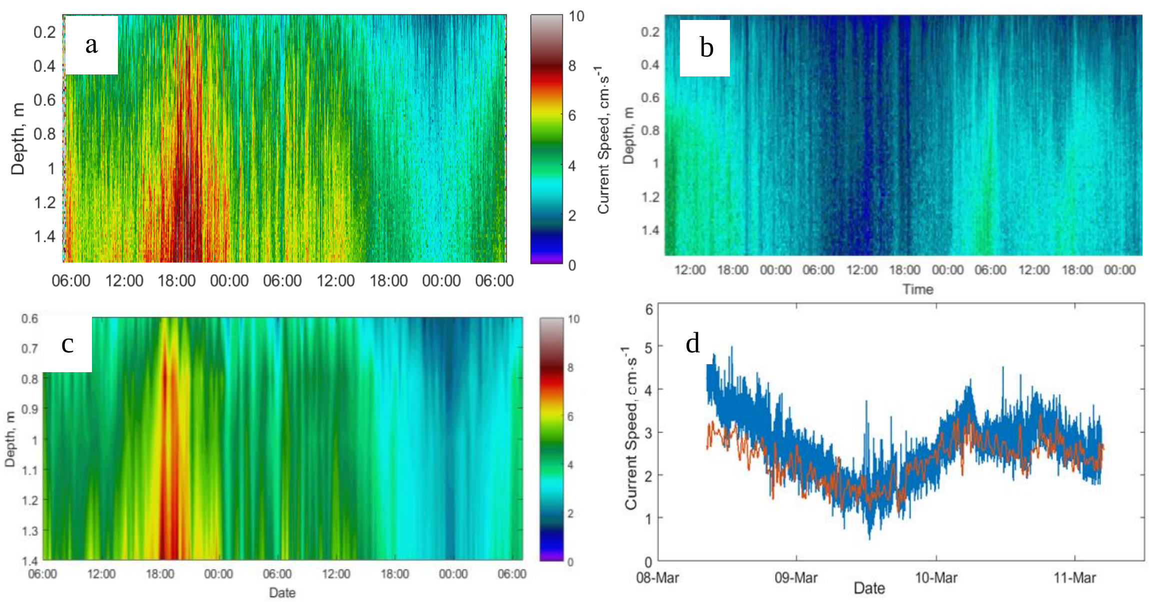

Fig. 2. Vertical velocity profiles at Station 1 (a, c) and Station 2 (b) measured by the acoustic Doppler profiler Aquadopp (a, b) and the electromagnetic loggers INFINITY (c). Panel (d): flow velocity at 1 m under ice from a single INFINITY logger (thin red line) and the Aquadopp velocity record from the same depth (a thick blue line).

3. Results.

The obtained data on spatial and temporal dynamics allowed the first direct quantitative assessment of the mixing intensity in the under-ice boundary layer of Lake Baikal. In an area with weak under-ice currents (Station 2), the TKE dissipation rates ε varied around a value of 10^{-9} W/kg, which is a threshold between turbulent and laminar conditions. In turn, the average ε in the vicinity of the jet-like subglacial current (station 1) was two orders of magnitude higher, characteristic of developed turbulence (Fig. 3). The values of ε increased towards the water-ice boundary that indicated shear generation of turbulence by the flow near a solid surface.

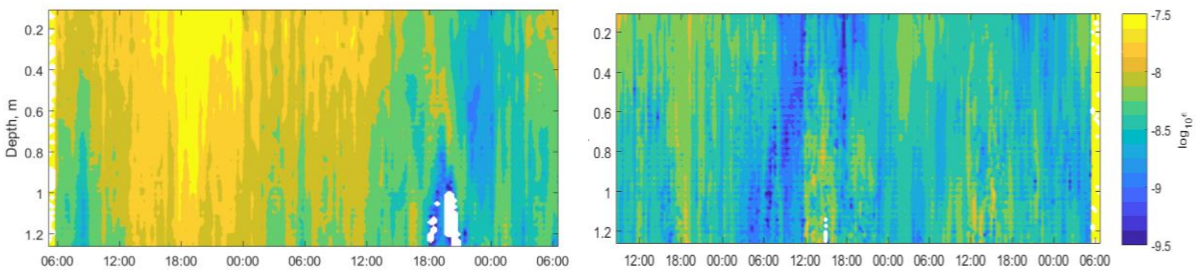

Fig. 3. The rates of dissipation of the TCE in the area of the jet stream (station 1, on the left) and in the region of weak currents (station 2, right).

This fact served as a qualitative proof of the presence of a layer of constant turbulent stress ("logarithmic" layer) under ice of Baikal and allowed estimation of the flow velocity range at which a logarithmic layer is formed, as well as quantitative characteristics of the boundary layer (roughness parameter the depth of the ice surface z_0 and the relationship between the mean current and the intensity of mixing). The presence of a layer of constant turbulent stress (shear velocity) u_* is an important property of the developed shear turbulence, so that the velocity shift is described by the logarithmic law,

$$\frac{\partial U_{mean}}{\partial z} = \frac{u_*}{\kappa z} \qquad \textbf{[1]}$$

or

$$U_{mean}(z) = \frac{u_*}{\kappa} ln(\frac{z}{z_0})$$

where U_{mean} is the average velocity of horizontal flow in the boundary layer, z is the turbulent pulsation length scale equal to the distance from the lower boundary of the ice, z_0 is the roughness parameter for the ice surface, and κ is the von Karman constant. The presence of such a layer suggests a local balance between production and dissipation of TKE, that is:

$$\varepsilon = u_*^2 \frac{\partial U_{mean}}{\partial z} = \frac{u_*^3}{\kappa z} \qquad \textbf{[2]}$$

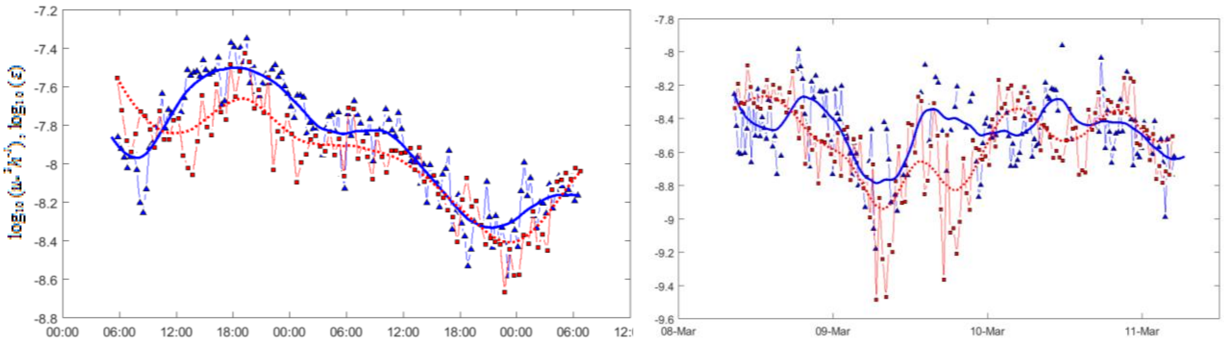

Fig. 4. Dissipation rates (red line and circles) and TKE production at 1 m depth (blue line and triangles), in the region of the jet stream (station 1, left) and in the region of weak currents (station 2, right). Bold lines - values filtered by a moving average with a window in 48 hours.

A direct comparison of the measured dissipation rates ε and the turbulent energy production u_*^3/z, calculated from the mean current profiles, unambiguously confirm the presence of a local balance between production and dissipation in the majority of the flow velocity range (Fig. 4). The balance is disturbed only at current speeds < 2 cm s^{-1}, with a corresponding drop of ε up to 10^{-9} W kg^{-1} (station 2, March 9, 2017, cf. Fig. 1b). In the same period, the vertical flow profiles show a significant deviation from the logarithmic form, indicating laminarization of the boundary layer under these conditions. The boundary value of the dynamic velocity for the transition to turbulent regime is $u_* \approx 1.0$ mm s^{-1}, (in the region of jet flows $u_* = 1.5$-3.0 mm s^{-1}).
On the basis of a local balance between production and dissipation of turbulent energy in the boundary layer, a direct relationship ("bulk" formula) was established between the mean velocity U_z of the current at a depth z and the intensity of turbulence under ice: $\log_{10}(u_*^3 k^{-1}), \log_{10}(\varepsilon)$

$$u_*^2 = C_D U_z^2 \quad \textbf{[3]}$$

where the coefficient of resistance C_D for $z = 1$ m was found equal to $2.6 \cdot 10^{-3}$ and was checked by independent velocity measurements (Fig. 5, left panel). This allowed us to test - and confirm - the hypothesis on the proportionality of the heat flux at the water-ice boundary Q_{iw} to the Kolmogorov velocity scale v_k:

$$K \propto V_K \propto (\nu\varepsilon)^{\frac{1}{4}} \propto \nu^{\frac{1}{4}} u_*^{3/4} \quad \textbf{[4]}$$

so that the water-ice heat flux is determined as

$$Q_{iw} = C_q K \Delta T \quad \textbf{[5]}$$

where $\nu \approx 10^{-7}$ m^2 s^{-1} is the kinematic viscosity of water, ΔT is the temperature drop in the viscous boundary layer, and C_q is the proportionality constant to be determined. Using Equation (2), the values of the dissipation rates were restored from the average flow velocities for the entire available observation period and verified by direct measurements of ε (Fig. 5, right panel).

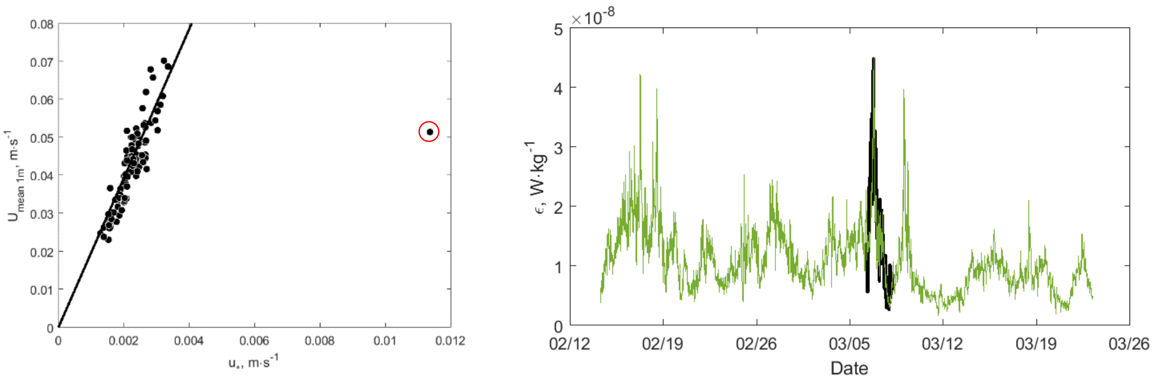

Fig. 5. (Left) The relationship between the mean flow velocity and the turbulent stress, red circle marks a single outlier; (right) the approximation of the dissipation rate of the TKE as a function of the mean flow based on the "bulk" formula (a thin green line), and the measured values of the dissipation rate of the TKE (black solid line).

Subsequently, the values of ε were used in Eqs. (4-5) for calculating the heat flux from water to ice and verified by alternative Q estimates from the heat balance and from the numerical model (Fig. 6). The thickness of the viscous sublayer, determined from the temperature data, was 1-2 mm, with a temperature drop ΔT of about 0.07 K, which corresponded to $C_q \approx 0.5$. The practical value for estimating flows from routine measurements and in modeling has a modified formula in which the temperature at the outermost boundary of the viscous sublayer is replaced by the temperature T_z at some depth z, outside the boundary "logarithmic" layer (which varies little with depth, since it corresponds to temperature mixed convective layer). For this case, the coefficient $C_q \approx 0.075$, so that the flow can be determined only from the flow velocities and temperatures:

$$Q = C_q C_D^{\frac{3}{8}} \nu^{\frac{1}{4}} U_z^{3/4} z^{-1/4} (T_z - T_f) \qquad \textbf{[6]}$$

where $C_q = 7.5 \cdot 10^{-2}$, $C_D = 2.6 \cdot 10^{-3}$ (for z = 1 m), T_f – the freezing temperature of freshwater.

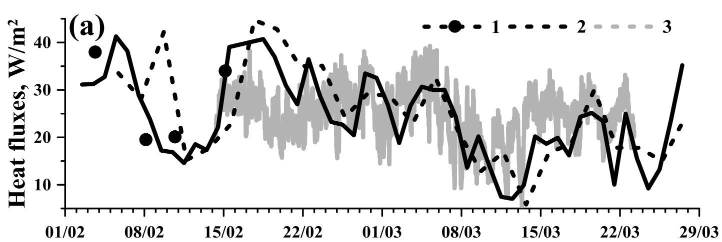

Fig. 6. Heat flux at the ice-water interface determined by Eq. [6] (gray line) vs. flux calculations from the heat budget within the ice cover (black solid line) and from the numerical model of the ice growth (black dashed line). See (Aslamov et al. 2014) for description of modeling and the heat budget methods.

Acknowledgments

This study is part of the joint Russian-German project ‘IceBound’ funded by the German Research Foundation (DFG KI-853/11-1) and by the Russian Foundation for Basic Research (15-55-12378 ННИО_а)

References

Aslamov, I. A., Kozlov, V. V., Kirillin, G. B., Mizandrontsev, I. B., Kucher, K. M., Makarov, M. M., Gornov A. Yu,. & Granin, N. G. (2014). Ice–water heat exchange during ice growth in Lake Baikal. Journal of Great Lakes Research, 40(3), 599-607.

Wiles, P. J., Rippeth, T. P., Simpson, J. H., & Hendricks, P. J. (2006). A novel technique for measuring the rate of turbulent dissipation in the marine environment. Geophysical Research Letters, 33(21). DOI: 10.1029/2006GL027050

Field Study of Anchor Ice Occurrence and Disappearance and Material Circulation in Cold Regions River

Hirotaka SUZUKI[1], Masahiro HASHIBA[1], Yasuhiro YOSHIKAWA[2], Hiroshi YOKOYAMA[3]
1 Fukuda Hydrologic Centre, Hokkaido, Japan
hashiba@f-suimon.co.jp
2 Kitami institute of technology, Hokkaido, Japan
yoshi@mail.kitami-it.ac.jp
3 Civil Engineering Research Institute for Cold Region, Hokkaido, Japan
yokoyama-h22ab@ceri.go.jp

Anchor ice is a phenomenon to accumulate of frazil ice on the river bed. This is formed due to the super cooling and a shallow, turbulent section of the river. In this study we observed a continuous observation of air temperature, water temperature, stone temperature, water level in Syuku-syu-betsu River and Yubetsu River, and we could successfully capture from the occurrence to the disappearance of anchor ice using the underwater video camera. The anchor ice began to occur from riverbed in early morning and spread to the ground area while increasing the thickness and finally covered with the riverbed stone. When the sunshine was getting strong, the anchor ice gradually became thin and disappeared. As a result, Firstly, we found the critical element of the anchor ice occurrence-disappearance was keeping supercooling condition. Secondary, it was found when the temperature of the stone was rising above the water temperature due to influence of sunshine, the anchor ice disappeared. On the other hand, we attempted to analyze two-dimensional flow calculation and spatial distribution of photo image analysis of an anchor ice. As a result, we found spatial distribution of anchor ice was proportional to the Froude number. Next to we conducted the impact of anchor ice on material transport in ice-covered river. We analyzed the contained algae of an anchor ice. As a result, a lot of algae (diatoms) existed in the anchor ice. When the one day cycle (occurrence and disappearance) of anchor ice repeated, the algae biomass tended to decrease. The reason for this phenomenon was considered that the growth rate of algae was shorter than the one-day cycle of the anchor ice.

1.Introduction

In cold regions rivers are frozen during winter due to decrease air and water temperature.
Fig. 1 shows a conceptual diagram of river ice formation.
According to Ashton's previous study (1986), when the state of zero air temperature continued, river water became super cooling (0 ° C. or less), and crystals of frazil ice were occurred in the river. As the frazil ice flows down to the downstream, it accumulated on the water surface and formed an ice sheet. In the upstream and small river with a steep gradient, the frazil ice transported to the riverbed material due to turbulence flow, and formed sherbet-like ice called anchor ice. Shen et al. Devised an equation to calculate the thickness of the anchor ice that simplified the complex process of forming anchor ice, and It was clarified the growth of anchor ice was caused to heat exchange between the frazil ice at the super cooling and the riverbed.
Malenchak et al. (2006) constructed a numerical calculation model (CRISS 2 D) using this equation and clarified that the growth rate of anchor ice had influence of crystal ice concentration, flow velocity, and water depth. From the spatial distribution model of anchor ice, Bisaillon et al. (2007) was clarified as the occurrence condition was that the average flow velocity was faster and the depth of water was shallower. In addition, Froude number was needed above 0.22 on average. If it was below 0.10, anchor ice was not occurred.
Furthermore, Tremblay et al. (2013) carried out field observations in time series on the Stoke River in Canada on the cycle of occurrence of anchor ice.
However, there were few observation cases in actual river, because it was difficult to specify where anchor ice occurred. Regarding material containing anchor ice, especially algae, there were few research cases and it was not sufficiently elucidated.
In this study, in order to elucidate the occurrence condition of anchor ice, we conducted a time series observation from the occurrence to disappearance. We also conducted on-site observations of the plane surface distribution of anchor ice. In addition, we investigated material(especially algae) contained in anchor ice according to time series observation, and examined relationship of the anchor ice occurrence condition and substances contained in anchor ice.

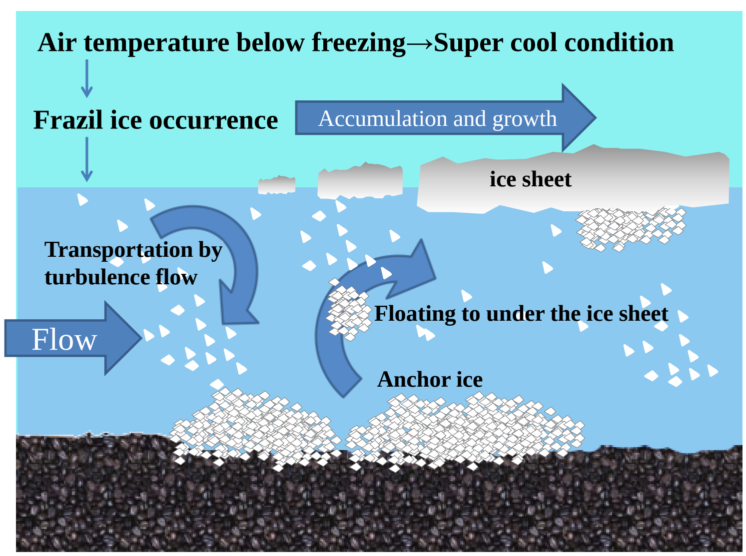

Fig. 1. Conceptual diagram of river ice formation

2. Time series field observation of anchor ice occurrence and disappearance (Syuku-syu-betsu River)

a) Field observation point and observation period

The site observation point is Syuku-syu-betsu River, a secondary river of the Saru River water system in the Hidaka district of Hokkaido. The observation period was from December 27, 2011 to May 2, 2012.

b) Observation method

In order to acquire continuous weather data, a thermometer (MC accuracy: ± 0.15 ° C or less), a water temperature gauge (JFE Advantec. MDS-Mk V / T, resolution: 0.015 ° C, accuracy: ± 0.05 ° C) and a hydraulic pressure gauge Electrical Industry Co., Ltd. MC-1100, accuracy ≤ ± 0.1% FS) was installed on river bank and riverbed.

Also, in order to grasp the formation and disappearance of anchor ice, an IP camera (Panasonic BB-HCM735) capable of continuously acquiring image data of 640 × 480 pixels was installed and photographing was performed at one minute intervals.

Since the commercial power source could not be secured locally, the power generation section used two solar panels of 195 W and made 8 storage batteries of 12 V - 105 A / hr. In addition, in order to enable day and night continuous shooting, we used an ultra-high intensity LED spotlight (18 LED for 12 V) and 10 W solar panel.

c) Observation result

Figure 2 shows the occurrence situation picture of the anchor ice extracted from the continuous shooting with the fixed point camera and continuous data of the temperature, the water temperature and the water level.

c-1) Full open surface (without anchor ice)

From December 25, 2011 to January 12, 2012, average temperature during this period was -6.9 ℃, snowfall amount was 38 cm, and the river surface was not still covered with ice. Diurnal fluctuation was observed in plus temperatures during the day, and average water temperature was also 0.5 ℃. Under this condition, no anchor ice occurred.

c-2) Full open surface (anchor ice occurrence)

From January 12, 2012, the occurrence of anchor ice was confirmed on the entire riverbed. The amount of snowfall was 30 cm, the average day temperature was -11.3 ° C, and the day the temperature was below 0 ° C even during the day continued. The river water temperature was constantly maintained at 0.1 ° C and was in the super cooling. Furthermore, on January 18 - 23, the water level temporarily rose due to the river construction work.

c-3) Overall ice covered (with anchor ice)

From January 29, 2012 gradually freezing from river banks, on February 1, 2012, all of the open channels were covered with ice. The days during which the average daily temperature was -9.3 ° C and the lowest temperature was below -20 ° C lasted around 5 days. The super cooling at the water temperature of 0.1 ℃ was maintained and anchor ice was present.

c-4) Partial ice covered (with anchored ice)

On February 7, due to the influence of warm air, the temperature temporarily exceeded 4 ° C and the water temperature rose to 1.4 ° C, partial breakup had occurred of the center of the river.

Anchor ice remained under the ice sheet, but the anchor ice had disappeared where there was no ice covered.

c-5) Partial ice covered (anchor ice disappearance)

After March 8th, the average temperature was -2.0 ° C, and it was often plus air temperature during the day and the water temperature changed to 1.4 ° C on the average, so the ice covered area decreased and the anchor ice disappeared.

c-6) After breakup

There was rain with a total rainfall of 58.5 mm from April 3 to April 4, 2012, and the water level rose sharply by about 1 m in about 8 hours, so it completely melted on April 4.

From this results, it was found that maintaining the super cooling of water temperature was an important factor for the presence of anchor ice.

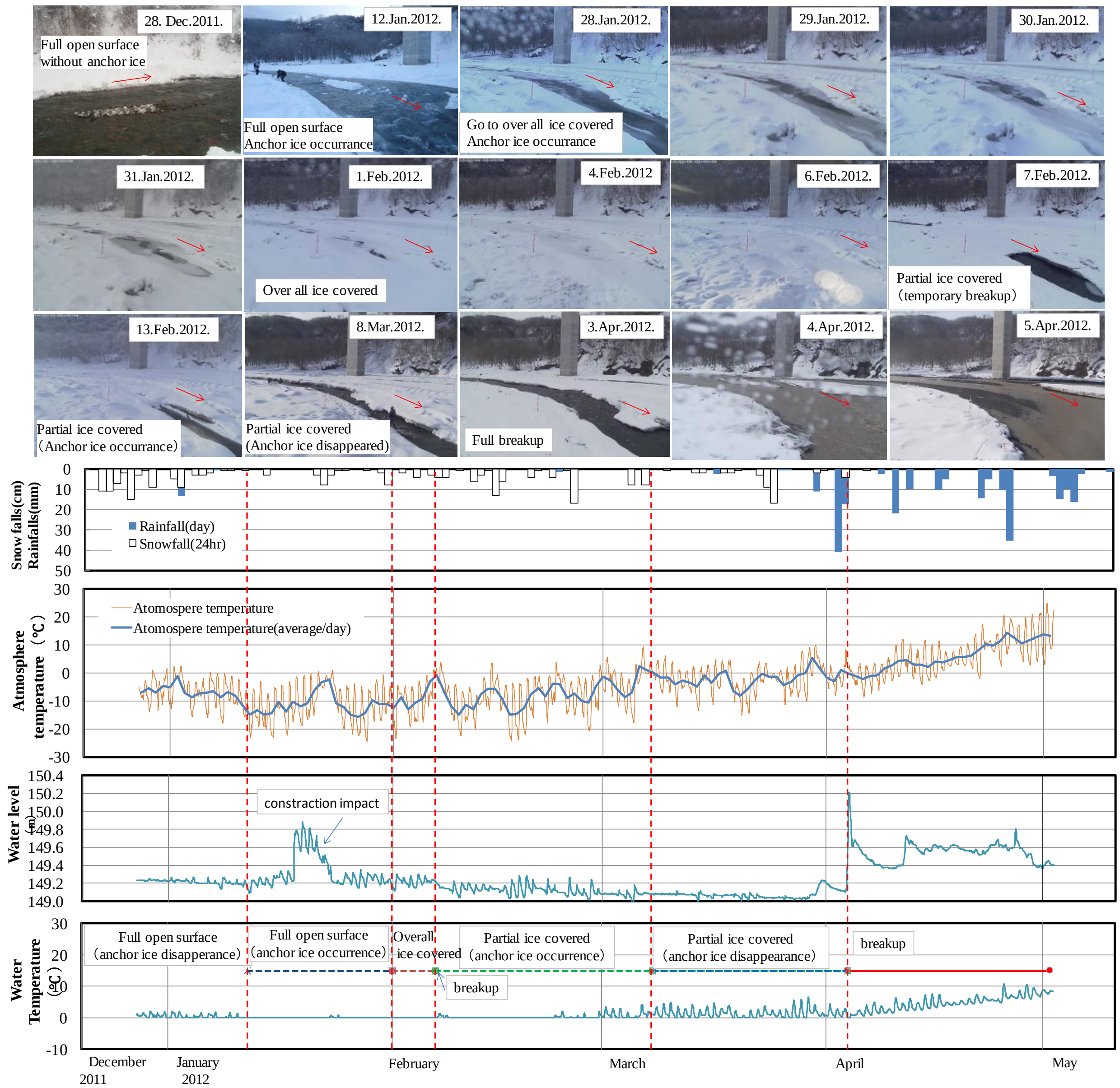

Fig. 2. Continuous field observation of anchor ice occurrence and disappear

3. One Day cycle of anchor ice occurrence and disappearance(Yubetsu River)

Next, in order to observe one day cycle behavior of anchor ice, we conducted a time series observation of water temperature, riverbed temperature, illuminance.

a) Field observation point and observation period

The site observation point is a secondary river of the Yubetsu River located in east of Hokkaido. The observation period was from January 26, 2017 to February 3, 2017.

b) Observation method

For the water temperature observation we used the JFE Advantec. MDS-Mk V / T(resolution: 0.015 ° C, accuracy: ± 0.05 ° C). For the riverbed temperature observation, we conducted to hole the riverbed stone and then we installed temperature gauge(Alec Electronics MDS-Mk V / T) into the stone as shown the center of photograph （①-④） in Figure 3.

For the underwater illuminance observation, we used the JFE Advantec. MDS-Mk-V/L. We installed the underwater camera(Brinno TLC200Pro) with LED light for observation of one day cycle of anchor ice behavior.

c) Observation result

In Figure 3, Anchor ice occurred when the observed water temperature dropped below 0 ° C. At this time the stone temperature also drops to the same extent.

The water temperature recovers quickly to around 0, but the stone has a high specific heat, so the temperature rise is slow. In the meantime, the occurrence of anchor ice has continued.

As daylight falls and the underwater illuminance increases, the temperature of the stone rises and becomes higher than the water temperature. At the same time anchor ice will disappear.

In addition, the picture of underwater camera showed that the anchor ice occurred on the ground at night(②), it became maximum in the early morning(③) and disappears in the morning(④).

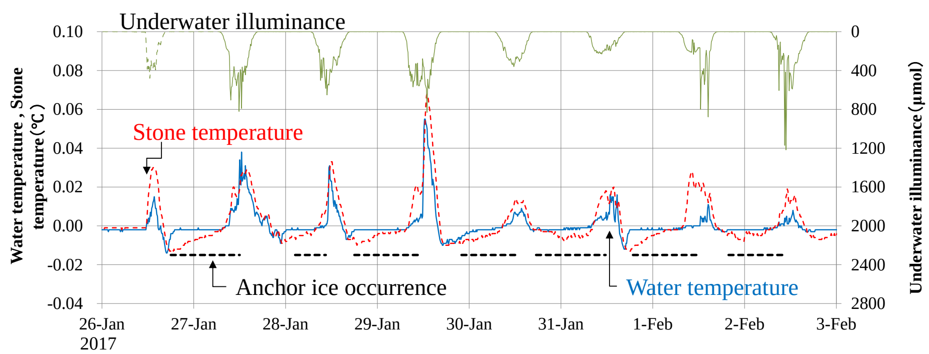

①18:00 28-Jan: none anchor ice ②1:00 29-Jan: anchor ice occurrence

③4:00 29-Jan: anchor ice maximum ④11:00 29-Jan: anchor ice disappearance

Fig. 3. One Day cycle of anchor ice occurrence and disappearance

4. Plane distribution of anchor ice(Syuku-syu-betsu River)

a) Froude number of anchor ice occurrence place

The Froude number affecting the anchor ice occurrence condition was calculated from the plane flow velocity distribution and the river bed shape distribution.

A section of 20 m in the crossing direction of the river and 20m in the direction of the downward flow axis was set within the fixed point photograph image range on December 27 to 28, 2011 in Syuku-syu-betsu River. Before the occurrence of the anchor ice, and the section in the cross direction 0.5 m, Survey of riverbed shape at 1.0 m intervals. Using the river bed mesh data, plane distribution of flow was calculated by plane two-dimensional flow calculation by Nays-2D of iRIC. The calculation lattice is divided by 40 × 40, the difference method of the advection term of the equation of motion is CIP method of high precision difference scheme, and the downstream water level which is boundary condition was obtained by equal current calculation. The initial water surface shape at the upstream end is set by setting the water level for on-site measurement from the relationship of water level(H) and discharge (Q):HQ equation of the separate host bridge in 2012 ($Q = 92.86\ (H-149.06)^2$), setting the average discharge in the winter period to $3m^3$/sec, it was given by uniform-flow calculation. The coefficient of roughness was given uniformly 0.04 based on the low discharge observation result (November 28, 2012: water level 149.20m, discharge $4.11m^3$/sec, average flow velocity 1.12m/sec). The Froude number was 0.2 or more over the whole area as shown in Figure 4., which coincided with the anchor ice generation condition (0.2 or more) in Bisaillon(2007).

b) Plane distribution of anchor ice and Froude number

On January 26, 2011, a photograph of a survey section (20 m × 20 m) taken from a different host

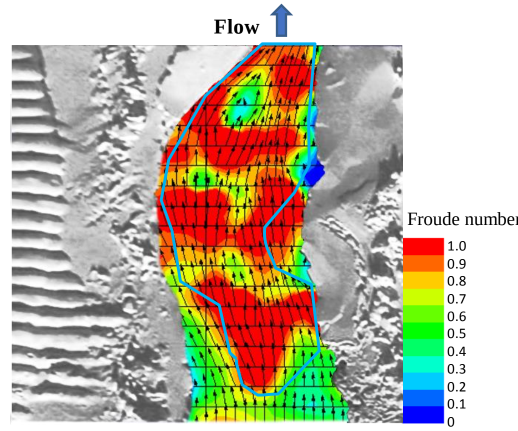

Fig. 4. Distribution of Froude number

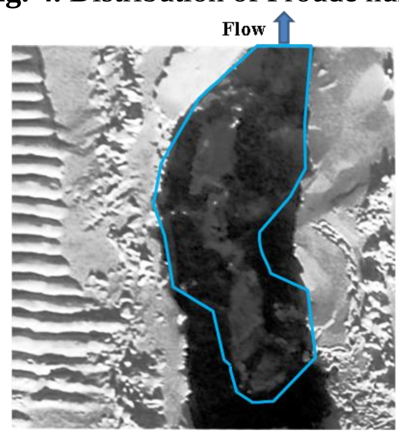

Fig. 5. Distribution of Anchor ice

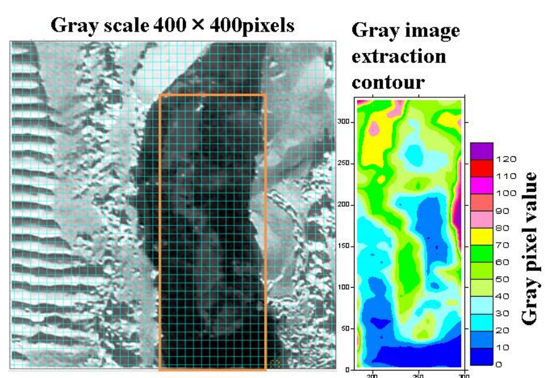

Fig. 6. Image analysis of Anchor ice

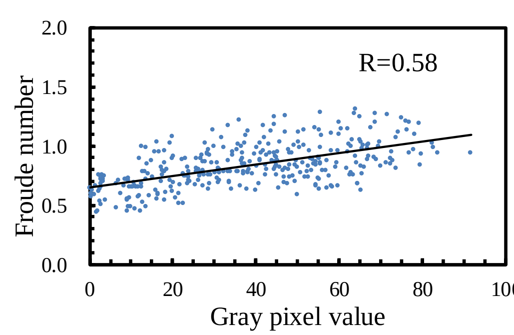

Fig. 7. Relationship of Froude number and Gray pixel value

bridge was geometrically corrected and shown on the plane in Figure 5. At this point, the water surface was open, but the anchor ice of the river bed was clearly visible throughout the whole area. Also, as the clear part of the anchor ice surrounded by the frame in Figure 6 and the part with large Froude number in Figure 5 generally coincided, it was suggested the relevance.

This picture was divided into 400 × 400 pixels, which is the same as the plane two-dimensional flow calculation, and gray scale pixel values were extracted from the shade of color in the lattice frame shown in Figure 6. Image processing software used open source “Image J” developed at National Institutes of Health (NIH)). The gradation of a pixel was represented by a numerical value of 0 to 255 bytes, and as the number increased, it became black to white. In the lattice frame, in the part close to the shoreline, since the Froude number became a high numerical value, it was removed as an abnormal value. As a result, the anchor ice clear part and the unclear part were quantified, and the relationship between the pixel value and the Froude number was shown in Figure 7. Although the variation was seen in the pixel value, the correlation coefficient was 0.58. Therefore the Froude number had a proportional relationship. From this, it was suggested that a clear distribution of anchor ice appears as the Froude number is larger.

4. Effect of anchor ice on algae circulation(Yubetsu River)

a)Algae contained in anchor ice

In the Yubetsu River, during the observation period, the algae contained in anchor ice was a total of 58 species, 46 diatoms, 5 green algae, 3 yellow dinoflagellates algae and 4 blue-green algae. The biomass of algae in anchor ice is shown in Figure 8.

As anchor ice disappeared on February 19 and March 18, 2014, we collected the frazil ice under the ice sheet instead of anchor ice.

The biomass of algae was the largest on December 25, 2013 immediately after the occurrence of anchor ice, and the dominant species was a feather-like diatom in the upper rank.

In diatoms, *Hydorurus foetidus* became the dominant species in yellow flagellous algae, while *Hannaea arcus*, *Cymbella minuta*, *Gomphoneis okunoi*, *Nitzchia* spp. Accounting for about 80% of the total.

Anchor ice contained algae such as diatoms, the algae biomass was the highest in the first anchor ice, and tended to decrease each time the diurnal variation repeated. The reason for this phenomenon was considered that the growth rate of algae was shorter than the one-day cycle of the anchor ice.

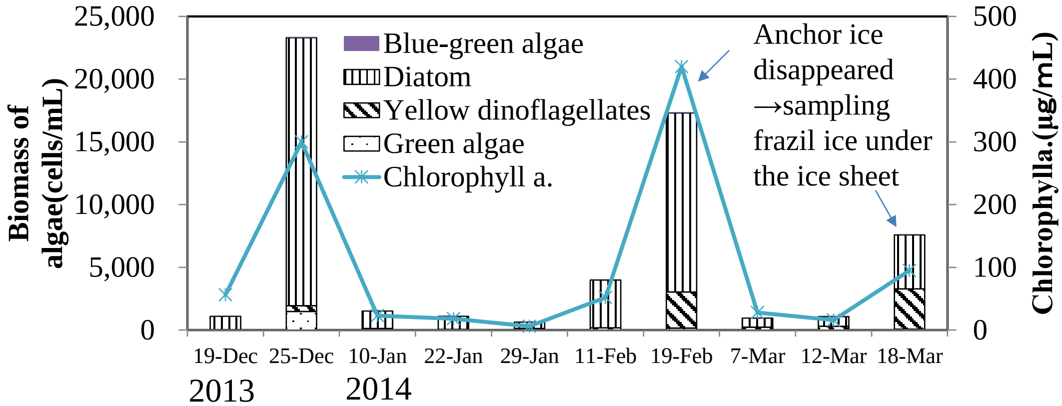

Fig. 8. Time series change of algae in the anchor ice

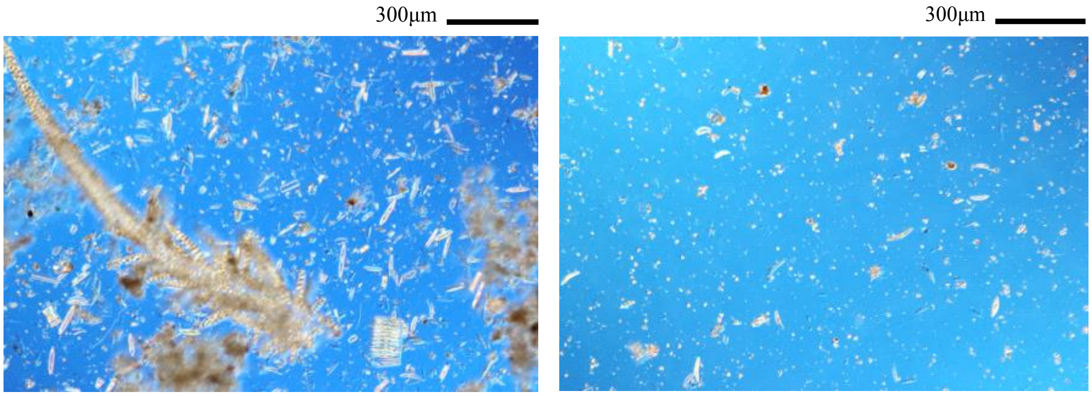

Before flash of anchor ice (Dec. 25, 2013)   After flash of anchor ice(Jan. 10, 2014)

Fig. 9. Microscope in the anchor ice

5. Summary

We succeeded in the field observation of the occurrence of anchor ice and the plane distribution and examined the occurrence condition using meteorological data and hydraulic data. Furthermore, the substance contained in the anchor ice was analyzed, and it became clear that algae peculiar to the ice-river contained. The research results obtained are as follows.

(1) Anchor ice occurred and it was found that super cooling of river water due to temperature decrease is an important factor as a condition to be present. Also, it was found that the temperature of the riverbed due to solar radiation is related to disappearance.

(2) The occurrence cycle and plane distribution of the anchor ice has a proportional relationship with the Froude number, and the distribution of the anchor ice is clear as the Froude number is larger.

(3) Anchor ice contains algae such as diatoms, the algae biomass tended to decrease each time the one day cycle (occurrence and disappearance) of anchor ice repeated. The reason for this phenomenon was considered that the growth rate of algae was shorter than the one-day cycle of the anchor ice.

Acknowledgments

This work was supported by JSPS KAKENHI Grant Number JP18K04361.

References

Ashton.G.D.:River and Lake Ice Engineering Colorado, USA,Water Resource Pubulication,1986.

Shen H.T., Wang D.S., WasanthaLal A.M. Numerical Simulation of River Ice Processes, Journal of Cold Regions Engineering , ASCE9(3),107-118.1995.

Malenchak J., Morris M., Shen H.T., Doering J. Modeling Anchor Ice Growth at Sundance Rapids, Proceedings of the 18thIAHR International Symposium on Ice, 2006.

BisaillonJ.F., Bergeron N.E. Modelling anchor ice presence-absence in gravel bed streams, Proceedings of the 14th CRIPE Workshop on Hydraulics of Ice Coverd Rivers,2007.

Tremnlay P., Leconte R., Lacey R.W.J., Bergeron N. Anchor ice cycles: observations from field study on the Stoke River, CGU HS Committee on River Ice Processes and the Environment 17th Workshop on River Ice, pp. 47-54, 2013.

International Association for Hydro-Environment Engineering and Research
Supported by Spain Water and IWHR, China

24th IAHR International Symposium on Ice
Vladivostok, Russia, June 4 to 9, 2018

Thermodynamics and Consolidation of Fresh Ice Ridges for Different Scale and Configuration

Evgenii Salganik[1], Knut Vilhelm Høyland[1]
[1]Sustainable Arctic Marine and Coastal Technology (SAMCoT), Centre for Research-based Innovations (CRI), Norwegian University of Science and Technology, Trondheim, Norway
Department of Civil and Environmental Engineering, NTNU, 7491, Trondheim, Norway
evgenii.salganik@ntnu.no, knut.hoyland@ntnu.no

Ice ridges are formed from deformed ice under atmospheric cooling. Interaction of first-year ice ridges with structures often gives highest loads. This process can be modelled in ice basins under controlled environment in contrast to field experiments, where most key parameters for consolidation analysis are unknown or uncertain. A series of experiments have been conducted to study model-scale fresh ice ridge development. The effect of initial rubble size, temperature, and configuration on consolidated level growth was observed in experiments and described analytically. Scale-dependent model was developed, taking into account main thermodynamic processes governing model-scale fresh ridge consolidation: conduction in the ice, sensible heat storage in the ice and convection in the air. Results of numerical and analytical models and experiments showed that consolidated layer growth was significantly faster than level ice for small-scale experiments. This difference is governed not only by the ridge initial macro-porosity (volumetric liquid fraction) and temperature but also by block length, width, freeboard, and orientation. Experimental setup and instrumentation are described providing measuring techniques for the convectional heat transfer coefficient, consolidated layer and level ice thickness, and heat fluxes at the newly formed ice and initial ice rubble.

This study provides the understanding of the main differences between the thermodynamics of fresh model-scale and full-scale ice ridges. It can be a basis for saline ridge consolidation analysis, where there is a presence of solution gradients in both ice and water underneath. Study results can provide additional information about data that should be collected in future field investigations and laboratory experiments, and about parameters that could be controlled to perform basin tests with necessary and realistic model-scale ridge configuration.

Introduction

In recent years, the part of deformed sea ice is increasing. Physical parameters of broken ice features can be studied in the field, but these investigations are time-consuming and usually cannot provide data about ridge formation process, initial conditions before consolidation, and about potential full-scale loads on offshore structures and vessels. It literally means that almost all the parameters governing consolidation process are unknown or quite uncertain: initial macro-porosity, initial size, orientation, salinity and temperature of broken ice blocks (rubble) forming the ridge, and thickness of the snow above the ridge.

Scale basin tests can be used for the design of new structures. However, scale models of ice ridges also have disadvantages: complications with scaling down of ice microstructure, mechanical properties and performing natural ridge formation. Significant scaling of ice mechanical properties is possible only using dopants, which makes solidification process more complicated because of temperature dependent liquid fraction of model ice. According to Griewank and Notz (2013), the dopant concentration in growing ice depends strongly on an experimental scale and dopant density at different temperatures and concentrations. The research goal is to study ice ridge solidification in different scales to be able to predict its growth rate in basin and laboratory tests and to provide a better understanding of ridge thermodynamics in general.

Theory

Consolidation is mainly governed by ridge thermodynamics, most of the information can be received from thermistor strings. However, thermistors usually provide data about temperature distribution in one dimension while ridge consolidation is a multidimensional process. The temperature profile in the air above the ice is non-linear in the range of boundary layer. Ice surface temperature depends on the ratio between conduction in the ice and convection in the air, so it can be estimated from temperature gradient in ice and convectional heat transfer coefficient $\mathrm{H_{ia}}$ mainly depending on air velocity. The temperature profile in the ice during freezing is usually non-linear because some part of higher heat flux at the top surface is covering the amount of sensible heat to cool down the ice with growing thickness to transport heat.

According to Griewank and Notz (2013), sensible heat changes the ice growth insignificantly so in most cases linear temperature profile can be assumed. It is a weak assumption for fresh ice ridges and even weaker assumption for sea ice ridge, because during ridge solidification not only newly formed ice but also surrounding rubble should be cooled down to the equilibrium temperature profile. Temperature profile from voids can provide information about consolidated layer ice growth, while profiles from ice rubble can tell about the heat that is stored, extracted and conducted through it. The difference between these two profiles can show how strong heat fluxes in the horizontal direction are. The consolidated layer thickness $\mathrm{h_c}$ is assumed as the minimum thickness of newly formed ice after ridging process. The ratio of the consolidated layer and surrounding level ice thickness is called the degree of consolidation $\mathrm{R = h_c/h_i}$.

In previous publications and engineering standards, ice ridges are usually assumed as a homogeneous media with small pores evenly distributed in its volume. This simplification provides a simple one-dimensional solution of consolidation problem based on the amount of freezing degree-days and initial macro-porosity η_0 where the ratio between the consolidated layer and surrounding level ice thicknesses is $h_c/h_i = 1/\sqrt{\eta_0}$ (Leppäranta, 1993). Coupling of conduction in the ice, convection in the air and additional sensible heat needed for rubble cooling can be implied to this solution (Adams et al., 1960) giving significant scale effect of level ice and consolidated layer growth rate ratio (Fig. **3**). This solution is correct for small and mostly horizontally oriented blocks. Level ice h_i and consolidated layer thickness h_c can be found as:

$$\Delta T dt = \frac{1}{2}\rho L dh_i\left(\frac{h_i}{k}+\frac{1}{H_{ia}}\right)\left(1+\sqrt{1+\frac{4}{3}\frac{c_p\Delta T}{L}\left(\left(\frac{H_{ia}h_i}{k}\right)^3-1\right)\Big/\left(\frac{H_{ia}h_i}{k}\right)^3}\right); \tag{1}$$

$$\Delta T dt = \frac{1}{2}\rho L_c dh_c\left(\frac{h_c}{k}+\frac{1}{H_{ia}}\right)\left(1+\sqrt{1+\frac{4}{3}\frac{c_p\Delta T}{L}\left(\left(\frac{H_{ia}h_c}{k}\right)^3-1\right)\Big/\left(\frac{H_{ia}h_c}{k}\right)^3}\right); \tag{2}$$

$$L_c = L\eta_0, \tag{3}$$

where t is the freezing time; ΔT is the difference between water freezing and air ambient temperatures; ρ is the ice density; L is the ice latent heat; L_c is the latent heat of consolidated layer; k is the ice thermal conductivity, and c_p is the ice specific heat capacity.

This analytical approach is valid if the ice ridge can be described as a homogeneous media. Full-scale ridge development consists of three main phases: initial, main and decay (Høyland and Liferov, 2005). The initial phase of ridge consolidation can be included into the described analytical model by varying the value of initial porosity η_0. According to Chen and Høyland (2016) only 80 % of specific heat energy of 20 cm thick ice block can be transferred to the new ice formation. This correction was used to evaluate the value of initial porosity change $\Delta\eta = \eta - \eta_0$ for the analytical mode:

$$\Delta\eta = 0.8(1-\eta)\frac{c_p(T_f - T_0)}{L} \tag{4}$$

Convectional heat transfer coefficient H_{ia} for steady laboratory conditions can be back-calculated from equation (1) using experimental level ice thickness for corresponding time and air temperatures.

Experimental setup

Twenty tests were conducted to study the influence of rubble blocks scale, orientation and initial temperature on consolidation rate. Fresh ice was cut into pieces with a prescribed size of $L \times w \times 10$ cm, cooled down to the chosen temperature T_0, placed into the water tank with side thermal insulation, and frozen under laboratory conditions with air temperature T_a of -15°C (Fig. **1**). Ice blocks were vertical or inclined by 30° from water level surface. The thickness of ice blocks w was 2, 4 and 6 cm; the length L was 15 cm and 25 cm. The initial thickness for both level ice and the consolidated layer was 0, the initial water temperature was 0°C, the initial ice blocks temperature was -1, -15 and -24°C. The size of side insulation box was 10x30x25 cm. Above water block height varied for different tests in the range of 0–3 cm. Two thermistor strings with the length of 100 cm and 15 cm were installed to measure water, ice and air temperatures. Initial macro-porosity values η_0 were close to 0.4 and were obtained from photo images. In the full-scale ridges, macroporosity values are in the range of 11–45 % (Høyland, 2007). Both level ice and consolidated layer thicknesses were measured directly after each experiment.

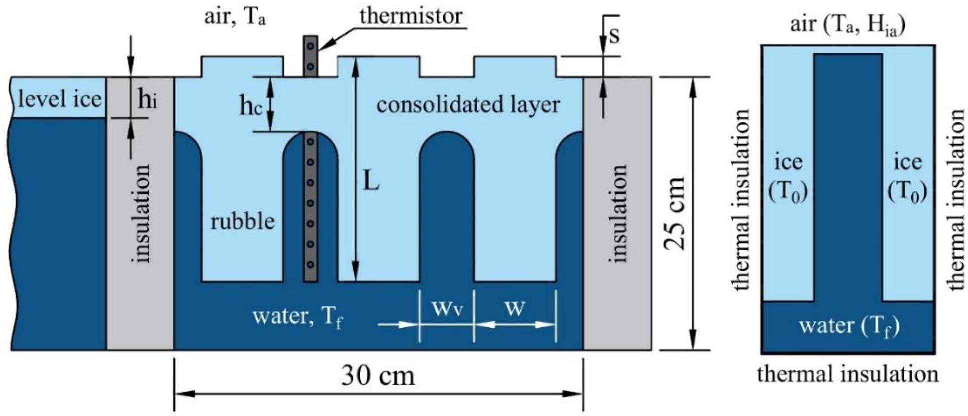

Fig. 1. Scheme of the experimental setup and numerical model setup at starting time.

a) b)

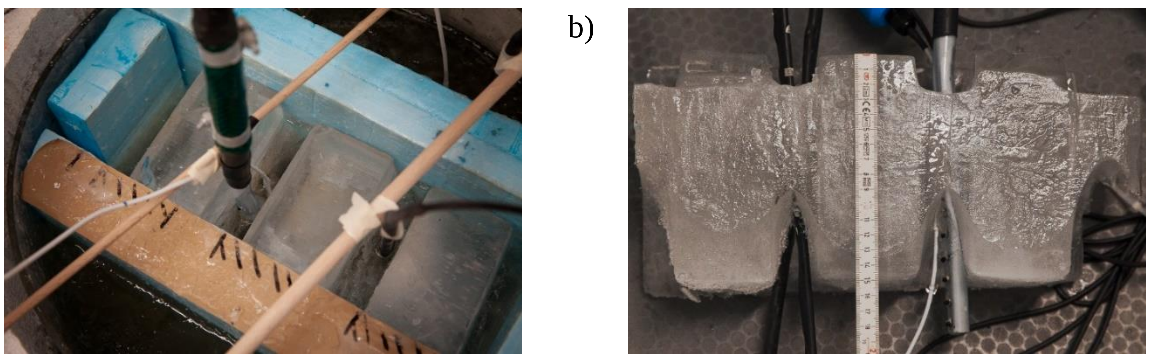

Fig. 2. a) Experimental setup and b) model ridge after consolidation.

Numerical model

The ridge consolidation process was modelled using finite element analysis simulation software COMSOL Multiphysics 5.2a. Two materials, fluid water, and solid ice, were used. Heat transfer in fluid and laminar flow packages were coupled for water simulation. The position of the ice-water boundary was defined by Stefan energy balance condition, where the difference of heat fluxes in two materials is equal to the amount of new solid formed or melted (Alexiades et al., 2003). This model requires following material parameters: thermal conductivity, heat capacity, density, the coefficient of thermal expansion, latent heat of fusion and kinematic viscosity. These values were obtained using the Gibbs SeaWater Oceanographic Toolbox of TEOS-10 (Feistel et al., 2010) and from Schwerdtfeger (1963). Thermal boundary conditions were defined as thermal insulation from sides of ice and bottom of the water, and as external convection with a constant heat transfer coefficient H_{ia} at the top. The value of $H_{ia} = 20\,W/m^2K$ was used based on level ice growth rate in the laboratory.

Results

Ice growth rate depends both on air ambient temperature T_a and heat transfer coefficient H_{ia}, so it is practical to present consolidation process as a function of level ice thickness h_i via degree of consolidation $R = h_c/h_i$. It is also practical to present experimental results normalized over different ridge porosities η_0 as $R\sqrt{\eta_0}$. This factor shows the difference between idealized consolidated layer thickness, which is $1/\sqrt{\eta_0}$ times larger than of surrounding level ice, and actual thickness of the consolidated layer from the experiments or from the model. Values of $1/\sqrt{\eta_0}$ for h_c/h_i can be only realized with following assumptions: infinite heat transfer coefficient H_{ia}, zero thermal inertia $c_p\Delta T$, and infinitely small block size. Consolidation factor $R\sqrt{\eta_0}$ with these assumptions is equal to 1 (Fig. **3**a).

Analytical solution, described in equation (2), is based on homogeneity assumption, and, according to the provided experiments, significantly overestimates consolidation when level ice thickness h_i is smaller than the distance between blocks $w_v = w\eta_0/(1-\eta_0)$ (Fig. **3**b).

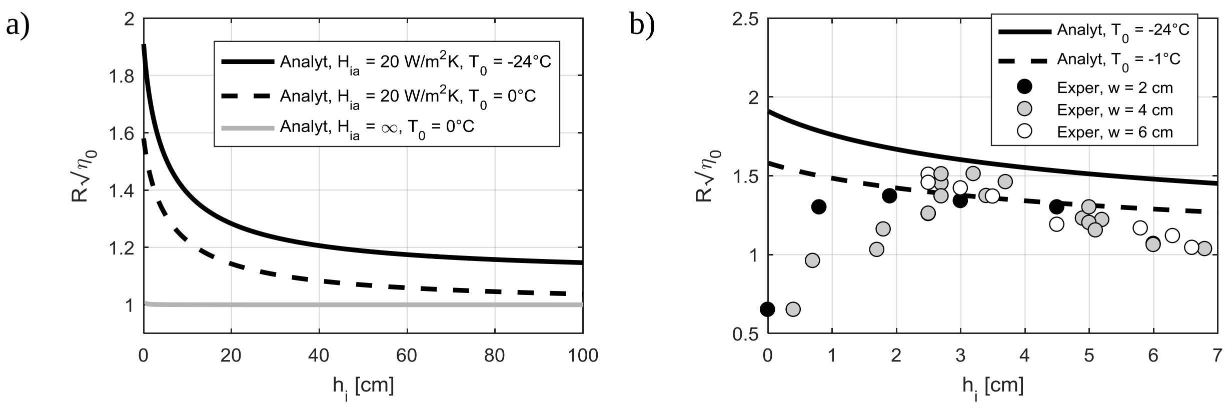

Fig. 3. Ratio of consolidated layer and level ice thickness $R = h_c/h_i$ multiplied by the square root of initial porosity $\sqrt{\eta_0}$ vs level ice thickness h_i a) for large scales and analytical solution and b) for small-scale experimental and analytical values.

For experiments with thinner ice blocks, consolidation layer thickness is faster approaching the analytical solution. Numerical modelling results can explain lower values of consolidation $R\sqrt{\eta_0}$ for later stages of experiments: solidification rate is slower when consolidation layer thickness is approaching to the values of block length L, solidification rate is higher for larger above water block height s or sail of the model ridge (Fig. **4**).

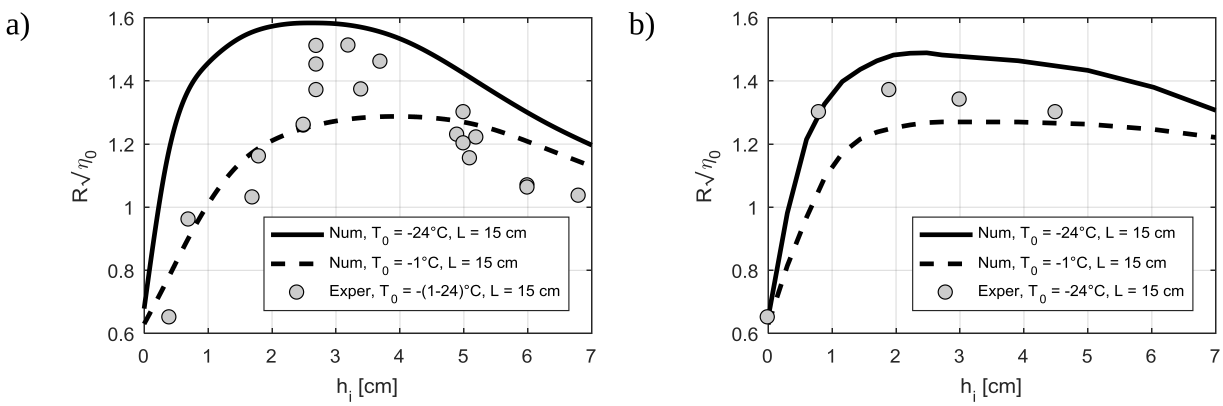

Fig. 4. Product of the degree of consolidation and square root of porosity $R\sqrt{\eta_0}$ vs level ice thickness h_i from numerical simulations and from experiments a) for 4 cm wide blocks and b) 2 cm wide blocks.

In the 1D analytical model, the block length L is infinitely large and there is no sail. There is no significant effect on experimental consolidation rate from block orientation and initial temperature. At the same time, both analytical and numerical models are predicting maximum experimental values of consolidation $R\sqrt{\eta_0}$ only with taking into account block initial temperature T_0. For all the provided experiments consolidated layer was up to 2.2–2.8 times thicker than surrounding level ice while the idealized solution for porosity value of 0.4 gives values of $R = 1.6$.

Discussion

According to numerical and experimental results not only initial ice thickness and temperature, but also block length and sail height, are affecting ridge consolidation rate. Consolidated layer thickness from simulations and experiments is approaching 1D analytical solution from equation (2) after surrounding level ice is reaching values close to ridge block thickness w. When the consolidated layer thickness is close to the ridge block length L, growth rate is becoming slower than according to the analytical solution. Presence of above water ice (ridge sail) is changing the initial ratio between convection and conduction and increasing consolidation rate.

The strong effect from initial ice temperature was not observed in experiments, but according to simulation results, extraction of sensible energy $c_p(T_f - T_0)$ during initial phase has a significant effect on consolidation process. The effect of initial rubble temperature on consolidation ratio $R\sqrt{\eta_0}$ is scale dependant. According to analytical solution for consolidated layer growth and initial porosity change from equation (4), simulation results are converging to 1D model if only some part of the initial sensible energy is going to be spent on new ice growth. These values are also scale dependant: 70 % and 60 % of sensible energy for 4 cm blocks and 15 cm.

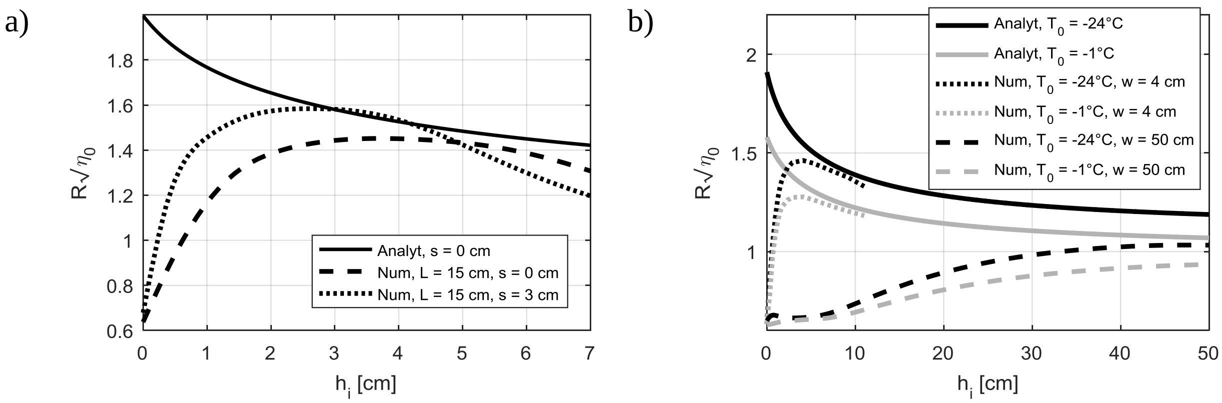

Fig. 5. Product of the degree of consolidation and square root of porosity $R\sqrt{\eta_0}$ vs level ice thickness h_i a) for $w = 4$ cm, $T_0 = -24℃$ and different sail height s and b) for 4 cm and 50 cm wide blocks from 1D analytical solution and from numerical simulations.

During the initial stage, consolidated layer with vertically oriented blocks is growing as fast as surrounding level ice (Petrich et al., 2007), while during the main phase its thickness is close to the scale-dependent 1D analytical solution from.

Conclusions

Analytical solution for one-dimensional fresh ice ridge consolidation is provided showing the significantly faster growth of consolidated layer in comparison to surrounding level ice for smaller scales. Experiments were conducted showing that this scale effect is significantly stronger for thinner ice blocks. Finite element model for ridge consolidation in different scale and configuration is described and confirmed by experimental data. For all the provided experiments consolidated layer was up to 2.2–2.8 times thicker than surrounding level ice. When the consolidated layer thickness is close to the ridge block length, the growth rate is becoming slower than according to the one-dimensional analytical solution. Presence of above water ice (ridge sail) is increasing consolidation rate. Study results can be used for basin-scale experiments and full-scale ridge investigations.

Acknowledgements

The authors wish to acknowledge the support of the Research Council of Norway through the Centre for Research-based Innovation, SAMCoT, and the support of the SAMCoT partners.

References

Adams, C. M., French D.N. and Kingery W. D., 1960. Solidification of sea ice. Journal of Glaciology, 3(28), 745-760.

Alexiades, V., Hannoun N., and Mai, T.Z., 2003. Tin Melting: Effect of Grid Size and Scheme on the Numerical Solution," Proc. 5th Mississippi State Conf. Differential Equations and Computational Simulations, pp. 55–69.

Ashton G.D., 1989. Thin Ice Growth. Journal of Water Resources Research. Vol. 25, No. 3, pp. 564–566.

Chen, X. and Høyland, K.V., 2016. Laboratory Work on Heat Transfer in Submerged Ice, Theory, Experimental Setup and Results. Proceedings the 23rd IAHR International Ice Symposium on Ice, Ann Arbor, USA.

Feistel, R., Wright D. G., Jackett D. R., Miyagawa K., Reissmann J. H., Wagner W., Overhoff U., Guder C., Feistel A. and Marion G. M., 2010. Numerical implementation and oceanographic application of the thermodynamic potentials of water, vapour, ice, seawater and air. Part 1: Background and equations. Ocean Science, 6, 633 – 677.

Griewank, P. J. and Notz, D., 2013. Insights into brine dynamics and sea ice desalination from a 1-D model study of gravity drainage. Journal of Geophysical Research: Oceans, 118(7):3370–3386.

Høyland, K.V., Liferov, P., 2005. On the initial phase of consolidation. Cold Regions Science and Technology. (41, 1), pp. 49-59.

Høyland, K.V., 2007. Morphology and small-scale strength of ridges in the North-western Barents Sea. Cold Reg. Sci. Technol. 48 (3), 169–187.

Leppäranta, M., 1993. A review of analytical models of sea- ice growth. Atmosphere-Ocean, 31, pp. 123-138.

Petrich, C., Langhorne P. J., and Sun Z. F., 2007. Formation and structure of refrozen cracks in land-fast first-year sea ice. Journal of Geophysical Research: Atmospheres, 112:C04006.

Salganik, E., Høyland, K. V. and Shestov A., 2017. Thermodynamics and Consolidation of Ice Ridges for Laboratory Scale. Proceedings – International Conference on Port and Ocean Engineering under Arctic Conditions.

Schwerdtfeger, P., 1963. The thermal properties of sea ice. J. Glaciol. 789–807.

24th IAHR International Symposium on Ice
Vladivostok, Russia, June 4 to 9, 2018

A Semi-Empirical Pod Model for USCGC Icebreaker Mackinaw Part II – the Model

Michael Lau
National Research Council of Canada
1 Arctic Ave, St. John's, NL
Wai-Hung.Lau@nrc-cnrc.gc.ca

A semi-empirical pod model is developed based on experimental data for the USCGC Mackinaw to predict propulsion forces for the icebreaker driven by twin podded propulsors. The experiments are conducted in straight-ahead motion with the azimuth angle of one of the twin pods steered in a range from 0 to 180°. In this pod model, assumption was made to extend the test data to the full range of 360° azimuth angles and advance coefficients.
Since all the tests are carried out in straight ahead motion only with a constant heading, analysis was performed to extend these functions to general cases of arbitrary planar motions. Three pod models were presented with varying degrees of complexity. Model I is the simplest model, applying the nondimensional longitudinal and transverse force coefficients obtained from the straight-ahead motion at known advance coefficient and azimuth angle directly to any motion. In Model II, the influence of geometrical drift angle local to the pods is added to Model I. In Model III, the influence of hull-pod interaction on the geometrical drift angle is added to further refine the model treatment. These models are implemented in the NRC/OCRE-RC's in-house maneuvering simulation software OSIS-IHI and their validity assessed. The comparison of Model III with comprehensive model test and limited sea trial data shows good agreement. Based on the validation results, it is concluded that the final model (Model III) can be used successfully for motion simulation of pod-driven ships.

1. Introduction

In recent decades, podded propulsors have become popular owing to, among other things, their excellent capability in maneuvering. The propulsion forces and moments due to pods can be simulated numerically based on empirical models developed from model test data. At the NRC's Ocean, Coastal and River Engineering Research Centre (OCRE-RC), a semi-empirical pod model has been developed and incorporated into its in-house ship maneuvering in ice simulation software OSIS-IHI (Ocean-Structure Interactions Simulator - Ice-Hull Interaction), based on experimental data of the USCGC Mackinaw (Akinturk and Lau, 2011). The experiment is conducted in straight-ahead motion with the azimuth angle steered in a range from 0 to 180^{o}. Regression equations were obtained to describe the pod performance for a full range of azimuth angle θ from 0 to 360^{o} and advance coefficient J. Lau (2018) summarizes the empirical data and their analysis.

The test data are measured only in straight forward ship motion with a constant heading ψ, and the pod forces could be quite different at the same θ and J when the ship turns; therefore, the influences of hull-pod interaction, wake fraction, flow rectification coefficient and thrust deduction were investigated to extend these test data to general cases of arbitrary planar motions. This paper presents result of these analyses which result in a semi-empirical model. This model is capable of modeling pod performance for arbitrary ship maneuvers. Section 2 describes details of the semi-empirical model. Model validation is given in Section 3. The conclusion and recommendation are given in Section 4.

2. Semi-Empirical Pod Model

Three versions of the semi-empirical model were developed. Model I is the simplest model, applying the nondimensional longitudinal and transverse force coefficients, $K_{Fx}(J,\delta)$ and $K_{Fy}(J,\delta)$, at known advance coefficient J and steering angle δ directly to any motion. In Model II, the influence of geometrical drift angle β_{podG} local to the pods is added to Model I. In Model III, the influence of hull-pod interaction on the geometrical drift angle is added to further refine the model treatment.

2.1 Pod Model I

When a ship is steered by deflecting a rudder angle δ to maneuver in any 2-D motion at advance speed u, transverse speed v and yaw rate r, the motion is governed by the following maneuvering equations defined about the centre of gravity:

$$
\begin{aligned}
&(m-X_{\dot{u}})\dot{u} = X_{uu}u^2 + mvr + F_x \\
&(m-Y_{\dot{v}})\dot{v} - Y_{\dot{r}}\dot{r} = Y_v v + (Y_r - mu)r + Y_{v|v|}v|v| + Y_{r|r|}r|r| + Y_{vrr}vr^2 + Y_{vvr}v^2 r + F_y \\
&(I_{zz} - N_{\dot{r}})\dot{r} - N_{\dot{v}}\dot{v} = N_v v + N_r r + N_{r|r|}r|r| + N_{v|v|}v|v| + N_{vrr}vr^2 + N_{vvr}v^2 r + M_z
\end{aligned}
\quad [1]
$$

where the motion control forces provided by Pods A and B are forces F_x in longitudinal and F_y in transverse directions and the moment M_z around the ship gravity centre, respectively:

$$F_x = F_{xA} + F_{xB}, \;\; F_y = F_{yA} + F_{yB}, \; M_z = (F_{yA} + F_{yB})x_{pod} + (F_{xA} - F_{xB}) | y_{pod} | \qquad [2]$$

where the pod position (x_{pod} , y_{pod}) refers to the hull-fixed system. The functions $K_{Fx}(J, \delta)$ and $K_{Fy}(J, \delta)$ are obtained for Pod A and B directly from model test data (Lau, 2018). Therefore, for a given advance coefficient J and rudder angles δ_A and δ_B , the known functions $K_{FxA(B)}(J, \delta)$ and $K_{FyA(B)}(J, \delta)$ could be directly applied to predict the control forces:

$$F_{xA(B)} = -K_{FxA(B)}(J, \delta)\rho n^2 D^4, \;\; F_{yA(B)} = -K_{FyA(B)}(J, \delta)\rho n^2 D^4 \qquad [3]$$

where ρ is the water density, n the propeller revolutions and D the propeller diameter. Since the non-dimensional forces $K_{FxA(B)}$ and $K_{FyA(B)}$ are measured on the mounting base of the pods in the longitudinal and transverse directions, $F_{xA(B)}$ and $F_{yA(B)}$ are the actual forces on the hull generated by the pods, respectively. These forces were modeled in the semi-empirical model to simulate ship maneuvering.

Model I is only applicable to straight-ahead motion because the rudder angle can only correctly represent the relative orientation between the incoming flow and pod in this simple case. For any other planar motion, the functions $K_{Fx}(J, \delta)$ and $K_{Fy}(J, \delta)$ cannot be applied directly. Model I is tested in OSIS software to simulate Mackinaw turning at $\delta_A = \delta_B =$ 45 deg and $n_A = n_B =$ 314 rpm at full power to illustrate the deficiency of this simple model treatment. The OSIS prediction was benchmarked with data taken from CMS (2010). The benchmark data are confidential and cannot be released at this time; however, for the same simulation condition, the diameter simulated in OSIS for Model I is around 16% lower.

2.2 Pod Model II

The incoming flow relative to pods or conventional rudders has major influence on pod or rudder performance. Pod Model II addresses the deficiencies of Model I by a treatment of geometrical drift angle and pod forces. The incoming flow relative to pods is dependent upon both geometrical rudder angle δ and local geometrical drift angle at the center of gravity β_{podG} (Figure 1). For a turning motion, the local geometrical drift angle β_{podG} and the magnitude of the local velocity $\vec{V}_{podG}$ (or incoming flow -$\vec{V}_{podG}$) at the pod are as follow:

$$\beta_{podG} = -\tan^{-1}\frac{v + x_{pod} r}{u - y_{pod} r}, \; V_{podG} = \sqrt{(u - y_{pod} r)^2 + (v + x_{pod} r)^2}\,. \qquad [4]$$

The effective rudder angle $\delta_{effect} = \delta + \beta_{podG}$ is introduced here to represent the relative orientation between the incoming flow and the pod. The pod propeller is now subject to incoming flow -$\vec{V}_{podG}$ at the relative angle δ_{effect} instead of the geometric rudder angle δ. It is obvious that for straight-ahead motion $\delta_{effect} = \delta$ and $\vec{V}_{podG} = u$ due to $v = r = \beta_{podG} = 0$. Since the pod works under the condition that the incoming flow $-\vec{V}_{podG}$ is orientated at the effective rudder angle δ_{effect}, the corresponding advance coefficient becomes $J = V_{podG}/nD$ and the pod forces components along and perpendicular to the incoming flow, $K_{Fx}(\frac{V_{podG}}{nD},\delta_{effect})$ and $K_{Fy}(\frac{V_{podG}}{nD},\delta_{effect})$, instead of $K_{Fx}(\frac{u}{nD},\delta)$ and $K_{Fy}(\frac{u}{nD},\delta)$ when the difference of wake influence between $\beta_{podG} = 0$ and $\beta_{podG} \neq 0$ is ignored (see Figure 2).

A virtual hull may be referenced to a two-dimensional hull-fixed system ($\xi\ \eta$), where the positive ξ direction is along the local total velocity $\vec{V}_R$. Therefore, $K_{Fx}(\frac{V_{podG}}{nD},\delta_{effect})$ and $K_{Fy}(\frac{V_{podG}}{nD},\delta_{effect})$ are the pod force components given in the $\xi\ \eta$ system, i.e. $K_{F\xi} = K_{Fx}(\frac{V_{podG}}{nD},\delta_{effect})$ and $K_{F\eta} = K_{Fy}(\frac{V_{podG}}{nD},\delta_{effect})$, which should be converted to K_{Fx} and K_{Fy} as control forces in the maneuvering Equation 1. In Figure 3, $F_{\xi} = K_{F\xi}\rho n^2 D^4$ is plotted to further illustrate this matching.

Finally, the measurements $K_{Fx}(\frac{u}{nD},\delta)$ and $K_{Fy}(\frac{u}{nD},\delta)$ can be mapped to $K_{F\xi}$, $K_{F\eta}$ as follows:

$$K_{F\xi} = K_{Fx}(\frac{V_{podG}}{nD},\delta_{effect}) = K_{Fx}(\frac{\sqrt{(u - y_{pod}r)^2 + (v + x_{pod}r)^2}}{nD},\delta + \beta_{podG}) \quad [5]$$
$$K_{F\eta} = K_{Fy}(\frac{V_{podG}}{nD},\delta_{effect}) = K_{Fy}(\frac{\sqrt{(u - y_{pod}r)^2 + (v + x_{pod}r)^2}}{nD},\delta + \beta_{podG})$$

and $K_{F\xi}$, $K_{F\eta}$ can be converted to K_{Fx}, K_{Fy} in the real hull-fixed system:

$$K_{Fx} = K_{F\xi}\cos\beta_{podG} + K_{F\eta}\sin\beta_{podG},\ K_{Fy} = -K_{F\xi}\sin\beta_{podG} + K_{F\eta}\cos\beta_{podG} \quad [6]$$

Model II is also tested in OSIS to simulate the Mackinaw turning performance in the same condition as that for Model I (45° rudder angles and 314 rpm for both pods). Now the turning diameter is 63% higher than that given in the CMS document. Although Model II is more reasonable than Model I, the result is poorer, which implies that some important factors are missing in Model II and further refinement was performed resulting in Model III.

2.3 Pod Model III

The influence of hull-pod interaction, i.e. thrust deduction and wake, was analyzed and its effect on the pod performance was incorporated in Model III. The pod propeller contributes to two components of resistance. One is the appendage resistance included in the measurement K_{Fx}.

Another component is an additional resistance induced due to the flow around the hull disturbed by a working propeller. This additional resistance is accounted for by an equivalent reduction in thrust. Therefore, the control forces in the maneuvering Equation 1 are $(1-t)\tilde{F}_{xA}$ and $(1-t)\tilde{F}_{xB}$, where t is the thrust deduction.

The wake, induced by the hull moving in water, reduces the flow speed in the longitudinal direction and diverts flow transversely. The influence on the longitudinal speed is represented by the wake fraction w, whereas the influence on the transverse speed by the rectification coefficient γ. The wake fraction w could reduce the local incoming flow at pod from ship speed u to $(1-w)u$ in straight ahead motion as a usual application. But in an arbitrary motion the wake fraction is a function of geometrical drift angle β_{podG} obviously. The function relationship may be expressed simply as $we^{-K\beta_{podG}^2}$, where w is wake fraction at $\beta_{podG}=0$ and $K=4.0$ based on model experiments, proposed by Hirano (1980). Then the x-component of local velocity at pod is written as $(1-we^{-K\beta_{podG}^2})(u-y_{pod}r)$. For the rectification coefficient γ, the y-component of local velocity at pod reasonably seems to be $\gamma(v+x_{pod}r)$. However, Kose (1982) and Inouse (1981) pointed out that the better expression is $\gamma(v+\chi x_{pod}r)$, where χ is suggested to be in the range 1.814 to 2.0. The rectification coefficient γ should be a function of geometrical drift angle β_{podG} similar to wake fraction, but no available information is found; so, it is kept constant in the preliminary model.

Therefore, the geometrical drift angle $\beta_{podG}=-\tan^{-1}\dfrac{v+x_{pod}r}{u-y_{pod}r}$ is replaced by the so-called "real" drift angle β_{pod} and incoming flow V_{pod} to predict pod forces as:

$$\beta_{pod}=-\tan^{-1}\frac{\gamma(v+\chi x_{pod}r)}{(1-we^{-K\beta_{podG}^2})(u-y_{pod}r)},V_{pod}=\sqrt{[(1-we^{-K\beta_{podG}^2})(u-y_{pod}r)]^2+[\gamma(v+\chi x_{pod}r)]^2} \qquad [7]$$

Finally, the measurement $K_{Fx}(\dfrac{u}{nD},\delta)$ and $K_{Fy}(\dfrac{u}{nD},\delta)$ can be mapped to the modified equations:

$$K_{F\xi}=K_{Fx}(\frac{1}{(1-w)}\frac{V_{pod}}{nD},\delta_{effect})=K_{Fx}(\frac{\sqrt{[(1-we^{-K\beta_{podG}^2})(u-y_{pod}r)]^2+[\gamma(v+\chi x_{pod}r)]^2}}{(1-w)nD},\delta+\beta_{pod}) \qquad [8]$$

$$K_{F\eta}=K_{Fy}(\frac{1}{(1-w)}\frac{V_{pod}}{nD},\delta_{effect})=K_{Fy}(\frac{\sqrt{[(1-we^{-K\beta_{podG}^2})(u-y_{pod}r)]^2+[\gamma(v+\chi x_{pod}r)]^2}}{(1-w)nD},\delta+\beta_{pod})$$

and K_{Fx}, K_{Fy} in the hull-fixed system become:

$$K_{Fx}=K_{F\xi}\cos\beta_{pod}+K_{F\eta}\sin\beta_{pod},\quad K_{Fy}=-K_{F\xi}\sin\beta_{pod}+K_{F\eta}\cos\beta_{pod}. \qquad [9]$$

It should be indicated that the advance coefficient in above Equation 8 is $\frac{1}{(1-w)}\frac{V_{pod}}{nD}$ but not $\frac{V_{pod}}{nD}$ because the wake fraction has been introduced into incoming flow V_{pod} in Model III.

2.3.1 Approximate hull-pod interaction parameters

The reliable way to obtain the hull-pod interaction parameters, i.e., thrust deduction t, wake fraction w and rectification coefficient γ, is via experiments with respect to different geometric drift angle β_{podG}. In the absence of direct measurement, empirical data available in open literature are used. In this model, t and γ are assumed independent of β_{podG}, though this may cause inaccuracy in the treatment. The thrust deduction and wake fraction are given by Holtrop (1984) as:

$$t = 0.325C_B - 0.1885D/\sqrt{BT}\ ,\ \ w = 0.3095C_B + 10.0C_B[(1+k)C_F + C_A] - 0.23D_p/\sqrt{BT} \quad [10]$$

where B is beam, T draught, C_B block coefficient, k form factor, C_F frictional coefficient and C_A is the model-ship correlation. For Mackinaw, t is equal to 0.1383; and since C_F is as function of advance speed, w is also a function of advance speed, estimated from Equation 10. The rectification coefficient $\gamma = 0.364$ is measured for a Series 60 model by Kose (1982), which is proved to be sensitive to turning performance.

As in Models I and II, the same simulation is repeated for the condition of $\delta_A = \delta_B = 45°$ and $n_A = n_B = 314$ rpm to compare with turning diameter provided in the CMS document. The simulation result from the OSIS is 10% higher in this case. The value of 0.364 for γ was measured for another ship, and if γ is adjusted slightly to 0.3, the simulated turning diameter matches that provided in the CMS document. This preliminary verification suggests that Model III is acceptable. The model can further be improved by a better estimation of this rectification coefficient.

3. Validation

The semi-empirical Model III was implemented in OCRE-RC's OSIS simulation software and a validation exercise was conducted by comparing the OSIS simulation results with those obtained from CMS's Polaris simulation under identical test conditions. The simulation at CMS is conducted using its existing pod model developed for the Mackinaw. Since the propellers used in the OCRE-RC's and Polaris models are different, and thus generate different thrust at the same propeller speed, the validation is conducted at the same propeller power outputs, which corresponds to 130.5 rpm and 180 rpm for the OCRE-RC and Polaris models, respectively.

A range of rudder angles from 0 to 60^{o} was imposed and the corresponding turning motion was simulated using OSIS and Polaris. The results are summarized in Figure 4(a) for turning diameter and Figure 4(b) for advance speed. The turning diameter obtained from sea trials of the

Mackinaw at $\delta_A = \delta_B = 35^\circ$ is also given in Figure 4(a). Figure 4 shows a good agreement among the OSIS simulation, Polaris simulation and limited sea trial data.

4. Conclusion and Recommendation

Experiments with scale model of the USCGC Mackinaw driven by pods were conducted in straight-ahead motion with the azimuth angle steered in a range from 0 to 180^o. A semi-empirical model was developed to predict propulsive forces of pods for the full range of 360^o azimuth. By incorporating hull-pod interaction into this model, it can be applied to any planar motion including turning. This semi-empirical model has been implemented in OCRE-RC's OSIS-IHI software and CMS's Polaris simulator. Based on the validation results, it is concluded that the final model (Model III) can be used successfully for motion simulation of pod-driven ships. However, refinement of the thrust deduction and rectification factor estimations is recommended for further improvement of the model.

5. References

Akinturk, A. and Lau, M., 2011. Manoeuvring performance of podded propulsors behind a ship. Ships and Offshore Structures 6(3):223-230.

CMS, 2010, Description of ship model MACK01S GLIB USCGC Mackinaw service version 10. Doc No MACK01S ver.10/04-Jan-2010, Centre for Marine Simulation, Marine Institute St. John's, Newfoundland and Labrador.

Hirano, M., 1980, On calculation method of ship manoeuvring motion at initial design phase. The Society of Naval Architects of Japan, vol. 147.

Holtrop, J., 1984, A statistical re-analysis of resistance and propulsion data. International Shipbuilding Progress, vol. 31.

Inouse, J., Hirano, M., Kijima, K., and Takashina, J., 1981, A practical calculation method of ship manoeuvring motion. International Shipbuilding Progress, vol. 28.

Kose, K., 1982, On a new mathematical model of maneuvering motions of a ship and its application. International Shipbuilding Progress, vol. 29.

Lau, M., 2018. A semi-empirical pod model for USCGC icebreaker Mackinaw: Part I – The empirical data. Proceedings of the 24th IAHR International Symposium on Ice, Vladivostok, Russia.

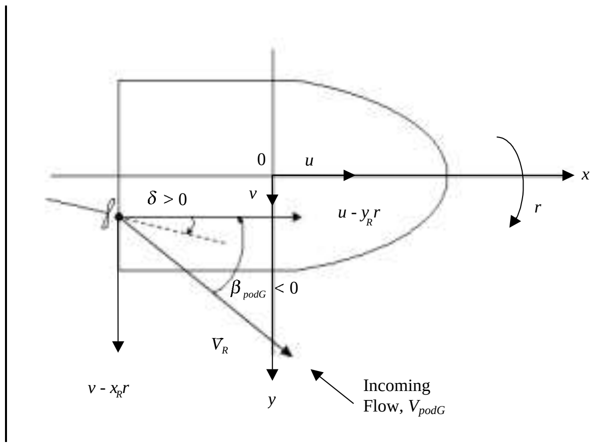

Fig. 1. Local geometric drift angle at pod β_{podG} in a turning motion

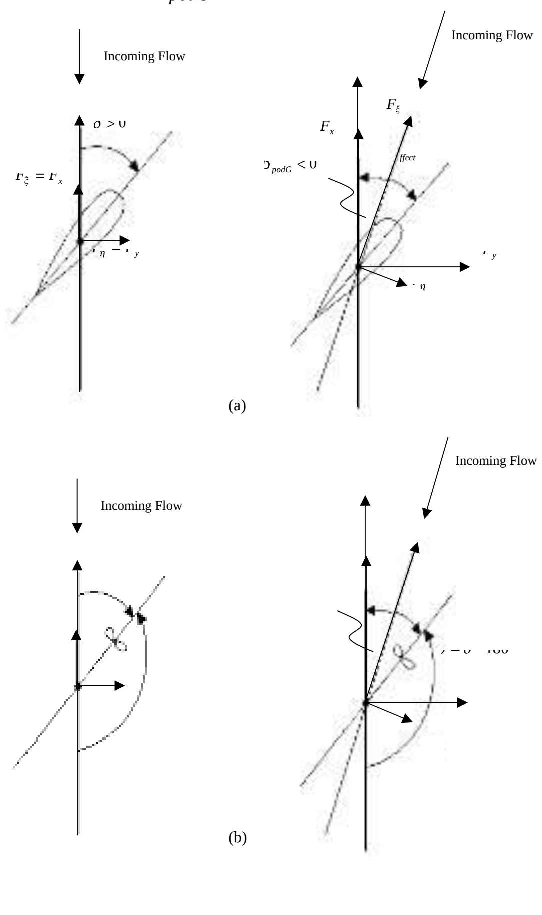

Fig. 2. (a) The forces F_ξ , F_η , F_x and F_y on the conventional rudder at β_{podG} ;
(b) Forces F_ξ , F_η , F_x and F_y on the Pod at β_{podG}

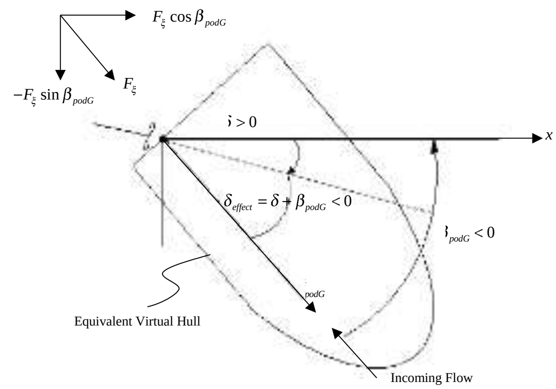

Fig. 3. $K_{F\xi} = K_{Fx}(\frac{V_{podG}}{nD}, \delta_{effect})$, mapped from existing function $K_{Fx}(\frac{u}{nD}, \delta)$

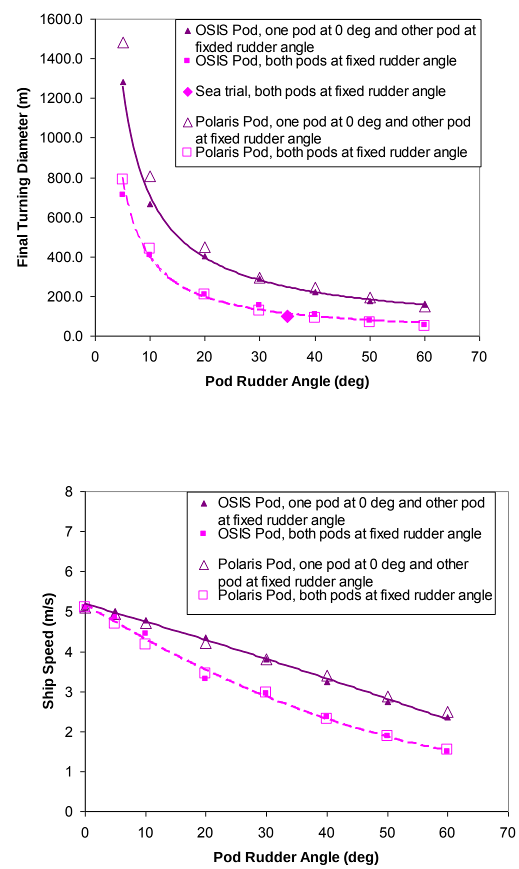

Fig. 4. Comparison of predictions from OSIS and Polaris simulations for turning in open water: (a) Turning diameter
(b) Steady speed

International Association for Hydro-Environment Engineering and Research
Supported by Spain Water and IWHR, China

24th IAHR International Symposium on Ice
Vladivostok, Russia, June 4 to 9, 2018

Influence of Cohesive Stiffness on Cohesive Element Method Based Simulation of Ice-Structure Interaction

Dianshi Feng (ceefd@nus.edu.sg)
Jin Zhang (zhangjin@nus.edu.sg)
Department of Civil and Environmental Engineering, National University of Singapore
Block E1A, #03-03, No.1 Engineering Drive 2, Singapore 117576
Kim Thow Yap (kimthow.yap@keppeltech.com)
Keppel Technology & Innovation, Singapore
#11-03/04 Keppel Bay Tower, Singapore 098632
Sze Dai Pang (ceepsd@nus.edu.sg)
Department of Civil and Environmental Engineering, National University of Singapore
Block E1A, #07-03, No.1 Engineering Drive 2, Singapore 117576

Cohesive element method (CEM) is currently being advanced to improve the simulation accuracy of ice-structure interactions. Cohesive stiffness is an important numerical parameter that affects both the computational cost and prediction accuracy. In this study, the effects of initial cohesive stiffness such as introducing an additional compliance or changing the wave propagation profile in numerical simulations were studied using CEM models constructed in LS-DYNA. The influence of cohesive stiffness on the prediction of ice loads was analyzed for both ice flexure and ice crushing failure cases. Recommendations are made accordingly on the initial stiffness of cohesive elements for different ice-structure interaction scenarios to balance between computational cost and accuracy of prediction.
Keywords: Cohesive element method; initial stiffness; additional compliance; wave propagation; ice-structure interaction.

1. Introduction

Cohesive element method (CEM), an approach first introduced by Hillerborg et al. (1976) for studies in damage of concrete, is widely used to simulate fracture for a variety of engineering materials like metals, ceramics, polymers and composites, and has recently been applied to study the ice interaction with offshore structures (Gürtner, 2009; Hilding et al., 2011; Kuutti et al., 2013). In this approach, cohesive elements are inserted at the interfaces between discretized bulk elements, and thus provide propagation paths that potential cracks can follow. The continuum mechanical response of material is captured by the bulk elements while damage and cracking are modeled by the cohesive elements. Compared with other numerical methods like Discrete Element Method (DEM), Particle-in-Cell (PIC) Method, Smooth Particle Hydrodynamics (SPH), Extended Finite Element Method (XFEM), the CEM has the advantage at physically simulating the ice fracture and fragmentation process while simultaneously satisfying conservation laws.

Unlike conventional elements in finite element analysis (FEA), the cohesive elements do not represent any physical material, but describe the tractive forces to be applied on adjacent bulk elements to resist them from being pulled apart. The constitutive behavior of cohesive elements is described by a traction-separation law (TSL) which may be defined in two approaches according to the initial loading phase, i.e. intrinsic (Xu and Needleman, 1994), and extrinsic (Kubair and Geubelle, 2003). In the intrinsic approach, the TSL has an initially elastic region; once the maximum traction value is reached, the failure process initiates and the traction reduces to zero as the separation increases up to a critical value which is generally determined based on energy dissipation. An extrinsic TSL has an initially infinite stiffness which means the initial response is rigid, thus only relies on the modelling of the failure portion of the cohesive law. Unlike the initially elastic interface elements, the extrinsic cohesive elements would require the introduction of a separate criterion to decide when to insert new surfaces through duplication of nodes at the onset of fracture (Camacho and Ortiz, 1996); to do so, the sophisticated tracking of complex structural information is needed since the elements deform continuously during analysis.

For the widely used intrinsic cohesive models, the initial slope k_0 of TSL should be determined carefully as it affects both the computational cost and the accuracy of simulation. In CEM simulation of ice-structure interaction which requires the modelling of extensive ice fracture and fragmentation, zero-thickness cohesive elements are preferred to minimize the effects of volume loss caused by the erosion of interface elements. For zero-thickness cohesive elements, k_0 should be infinitely high in theory. However, from the numerical point of view, an extremely stiff initial response should always be avoided in practical analyses as it will cause high computational cost and could result in numerical instabilities. On the other hand, a low cohesive stiffness can cause artificial reduction of overall structural stiffness or artificial additional compliance (Blal et al., 2012), and may alter the wave propagation (Espinosa and Zavattieri, 2003), leading to unrealistic predictions of structural response and damage evolution.

In this paper, the effects of initial cohesive slope on overall structural stiffness in static condition and wave propagation in dynamic condition were investigated using CEM models constructed in LS-DYNA. Its influence on ice-structure interaction simulations was analyzed for both ice flexure and crushing scenarios, and the results were compared and discussed with the intention to balance computational cost and required accuracy of prediction.

2. Effects of initial cohesive stiffness

On overall structural stiffness

In CEM simulation of ice-structure interaction, the additional compliance introduced by intrinsic cohesive elements reduces the overall stiffness of ice. The artificial reduction of stiffness f can be easily derived using a simple 1D "bulk-cohesive model", and the expression is as follows:

$$f = 1 - \frac{1}{1 + E_{bulk} / k_0 l_{ele}} \quad \textbf{[1]}$$

where E_{bulk} is the Young's modulus used for bulk elements, k_0 is the initial cohesive stiffness and l_{ele} is the mesh size. According to this equation, for a particular simulation case (where E_{bulk} is determined from the simulated material), the artificial reduction of overall stiffness f is a function of mesh density l_{ele} and cohesive stiffness k_0. If the mesh density is fixed, lower f is expected when higher k_0 is used; while if k_0 is kept constant, higher f will be seen for finer meshes, which is easy to understand since finer mesh means the insertion of more cohesive elements.

However, in practical ice-structure interaction simulations, f may be affected by other factors as well, e.g. contact modelling. Fig. 1 shows a numerical test using an ice beam model constructed in LS-DYNA. The ice beam is discretized in two ways: one using pure bulk elements; and the other using bulk elements interspersed with zero-thickness cohesive elements. The beam is fixed supported at one end and loaded at the other. E_{bulk} = 5 GPa, ρ = 910 kg/m^3 and ν = 0.3 are used for bulk elements, and various combinations of mesh sizes and cohesive stiffness were used for comparison.

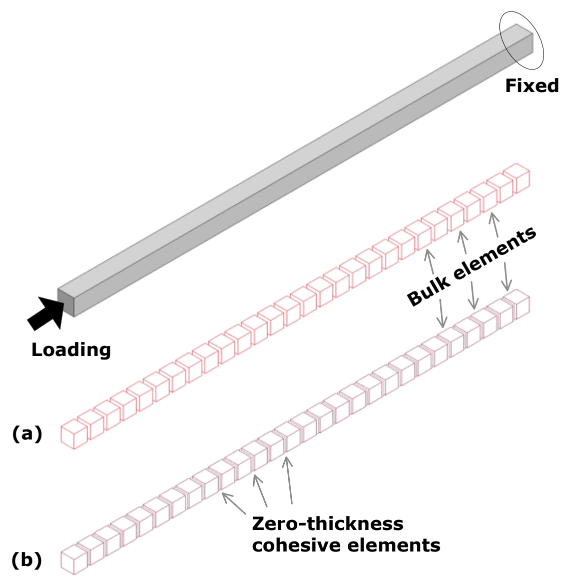

Fig. 1. Ice beam meshed in two ways: (a) pure bulk elements, and (b) bulk elements interspersed with zero-thickness cohesive elements.

Through comparing the slopes of force-displacement curves predicted by models with and without cohesive elements, the reduction of overall stiffness caused by cohesive elements could be obtained. Fig. 2 compares the predicted stiffness reductions, under tensile and compressive loadings, along with the analytical solution for different l_{ele} and k_0 values. It can seen that the predicted stiffness reduction under tensile loading corresponds well with the analytical solution, while it is different in the compressive loading case. Under compression, the predicted stiffness reduction is smaller than the analytical value, which can be attributed to the contact defined between bulk elements; furthermore, the deviation between prediction and analytical solution increases as cohesive stiffness or mesh size decreases.

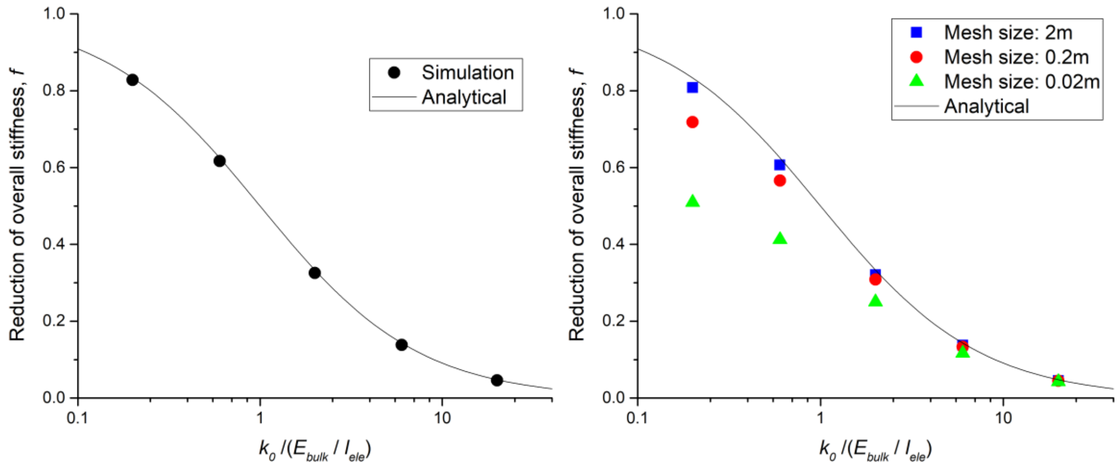

(a) (b)

Fig. 2. Comparison of predicted additional compliance with the analytical solution, under (a) tensile loading, and (b) compressive loading.

In practical analyses, if possible, one should choose appropriate l_{ele} and k_0 values to make sure that the combination results in minimal stiffness reduction (i.e. tail part, right side in Fig. 2); For example, if the selected initial cohesive stiffness k_0 for zero-thickness cohesive elements satisfies:

$$k_0 \geq 20E_{bulk} / l_{ele} \qquad \textbf{[2]}$$

by applying this criterion, the overall stiffness reduction would be less than 5%. However, it should also be noted that achieving a minimal stiffness reduction generally results in longer computational times.

<u>On wave propagation</u>

Another critical aspect of the cohesive stiffness effects concerns the wave propagation. If the wave propagation is substantially affected due to the insertion of cohesive elements, the damage progress and failure pattern predicted in simulations might be very different from the real case. Espinosa and Zavattieri (2003) performed numerical tests both in tension and in shear, and reported that the elastic wave propagation speeds remain nearly unchanged when $k_0 \geq 10E_{bulk}/l_{ele}$.

Fig. 3 presents an example of how the elastic wave propagation of ice model might be affected by applying different cohesive stiffness. The compressive wave traveling through a pure bulk model of an ice bar is plotted in Fig. 3a, and is taken as the benchmark. The results predicted by CEM model with low cohesive stiffness (k_0 = $0.2E_{bulk}/l_{ele}$) and high cohesive stiffness (k_0 = $20E_{bulk}/l_{ele}$) are shown in Fig. 3b and Fig. 3c, respectively. Clearly, the low stiffness model predicts a fictitious wave profile while the high stiffness model predicts one that is close to the expected wave profile.

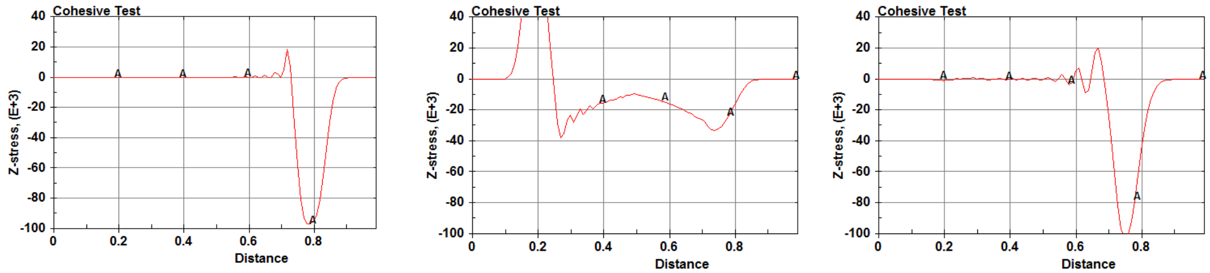

(a) (b) (c)

Fig. 3. (a) Expected wave profile for a compressive wave travelling through an ice bar, (b) erroneous wave profile for a cohesive model with low stiffness $k_0 = 0.2E_{bulk}/l_{ele}$, (c) matching wave profile for a cohesive model with sufficiently high stiffness $k_0 = 20E_{bulk}/l_{ele}$.

3. Influence on simulation of ice-structure interaction

Flexural failure of ice

Fig. 4 depicts the CEM model for simulating level ice interaction with a wide sloping structure (α = 50°), in which case the dominant failure is bending crack. The ice is modelled with elastic bulk elements with zero-thickness cohesive elements inserted along all the inter-element boundaries perpendicular to the length direction. The buoyancy force of water is simulated by attaching discrete spring elements to the nodes of bulk elements.

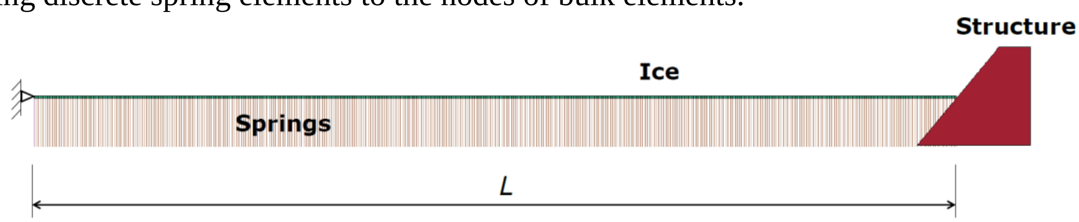

Fig. 4. Numerical model for simulating flexural failure of ice.

Elastic properties used for bulk elements are: E = 6 GPa, ρ = 910 kg/m^3 and ν = 0.3; stress-based TSL curves with T_{max} = 0.5 MPa but with different initial stiffness ranging between 1E10 Pa/m (or $0.83E_{bulk}/l_{ele}$) to 1E12 Pa/m (or $83.33E_{bulk}/l_{ele}$) are used. Three ice thicknesses, h = 0.5 m, h = 1.0 m and h = 2.0m, are considered for analysis. The length of the ice sheet model L = 200 m is used as the preliminary analysis shows that the simulation converges for all three ice thicknesses when L is larger than 200 m.

Fig. 5 plots the ice breaking load and breaking length as a function of initial cohesive stiffness, respectively; and the dotted lines show the analytical solutions according to Croasdale (1980):

$$F_B = 0.68\xi\sigma_f w/(\left(\frac{E}{\rho_w g h^5}\right)^{0.25} - 0.68\xi/h) \quad \textbf{[3]}$$

$$l_B = \frac{\pi}{4}\left(\frac{4EI}{k}\right)^{0.25}$$ **[4]**

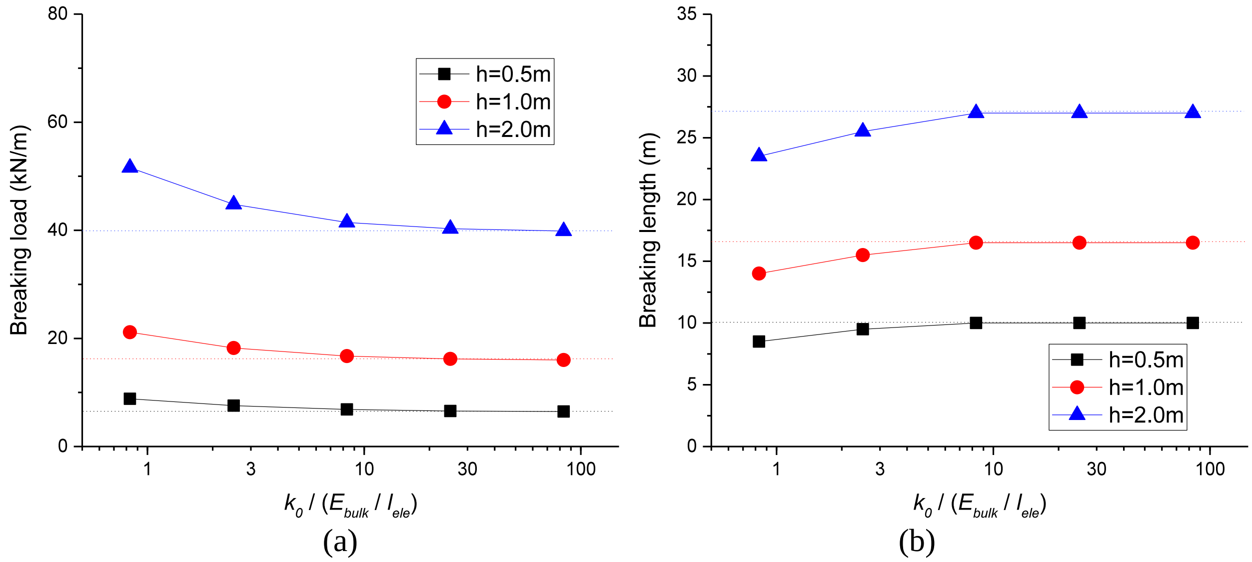

Fig. 5. Effect of initial stiffness on predicted (a) ice breaking load and (b) ice breaking length.

The simulation results show that as the initial slope k_0 of TSL decreases, the ice breaking load increases while the breaking length decreases. This trend can be understood through Equations (3) and (4). If E in equations reflects the apparent modulus of the bulk cohesive system, it becomes lower as cohesive stiffness is lowered, and this will lead to larger F_B and smaller l_B consequently. It is also found that higher k_0 will make the predicted ice breaking loads and breaking length values tend towards the analytical solution.

Crushing failure of ice

The influence of initial cohesive stiffness on ice crushing was studied using the CEM model as shown in Fig. 6a, which simulates the level ice interaction with a lighthouse structure. The ice is 8.4 m x 8.4 m x 2.1 m in size and moves at a constant velocity of 0.15 m/s towards a fixed cylinder structure which has a diameter of 4.2 m. The ice sheet was discretized into cubic brick elements, 0.3 m in size, which are interconnected by zero-thickness interface cohesive elements. A plate modelled with rigid brick elements was placed under the ice to approximately simulate the support provided by water base.

Bulk and cohesive parameters used in the analysis were referenced from Gurtner (2009) and Hilding et al. (2011). TSL curves with the same peak traction (T_{max} = 1.0 MPa) and fracture energy (G_f = 5200 J/m^2), but with different initial stiffness values, 5E8 Pa/m, 5E9 Pa/m, 5E10 Pa/m and 5E11 Pa/m (or 0.03, 0.3, 3.0 and 30 times of E_{bulk}/l_{ele}, respectively), are applied for comparison. Fig. 6b and Table 1 compare the simulation results of ice force and CPU time costed for simulation running. It is shown that the predicted ice force is not sensitive to the change of initial cohesive stiffness k_0 unless an extremely low value, like 5E8 Pa/m ($0.03E_{bulk}/l_{ele}$) is used, which will lead to very high additional compliance, in turn translating to the obvious under-prediction of ice force. Furthermore, as the last column of table 1 shows, the computational cost rises fast with increasing k_0, so an intermediate initial stiffness might be adopted accordingly to strike a balance between computational time and accuracy.

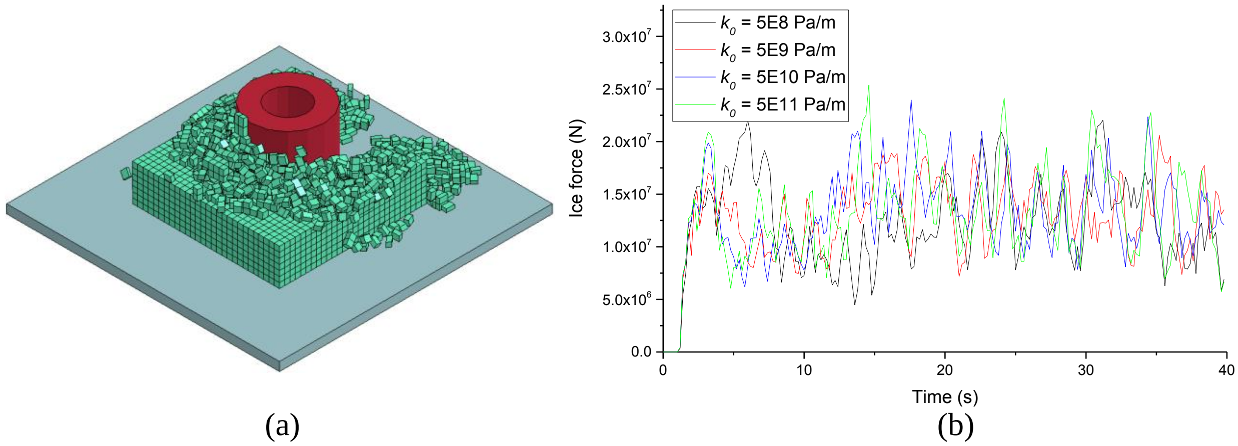

Fig. 6. (a) Modelling of ice crushing against a vertical structure, and (b) force-time histories predicted using different initial stiffness of traction-separation law.

Table 1. Comparison of predicted ice forces and computational costs using different k_0 of TSL.

$k_0/(E_{bulk}/l_{ele})$	Ice force (MN)		CPU time (hrs)
	mean	std	
0.03	12.8	3.6	29
0.30	14.0	3.2	29
3.00	14.0	3.4	79
30.0	14.0	3.9	124

4. Discussions

The influence of initial cohesive stiffness on predicted ice loads is quite different for flexural failure (ice interaction with sloping structures) and crushing failure (ice interaction with vertical structures) of ice. A very clear increasing trend of ice breaking load is observed in the former case when the cohesive stiffness becomes lower; while in the latter case, the ice load appears to be nearly unaffected among a wide range of cohesive stiffness investigated. The difference can be attributed to distinct failure modes in two scenarios. The failure mechanisms are less complex for the ice flexure case where bending crack is the dominant failure mode and the cohesive elements in mode I fracture play a more important role as compared to the bulk elements. Therefore the ice load is more sensitive to the change in cohesive parameters. In the case of ice crushing, it is a more complex situation where the bulk elements undergo extensive plastic deformation and govern the energy dissipation. Hence, the global ice load is relatively more sensitive to the overall fracture properties (peak traction T_{max} and fracture energy G_f) used for cohesive elements but less affected by the TSL shape or initial stiffness k_0 (except for the case when the elastic response of ice becomes unrealistic if extremely low k_0 is used).

As a result, the recommendations given on the initial cohesive stiffness used for simulation of ice flexure and ice crushing may differ in practical applications. Judgement is required to achieve a balance between computational cost and required accuracy of prediction.

5. Conclusions

In this paper, numerical studies on the additional compliance and wave propagation effects relating to the initial cohesive stiffness were carried out. The influence of cohesive stiffness on simulation of ice interactions with sloping structures as well as vertical structures was analyzed. It is found that the influence of cohesive stiffness may differ for the scenarios where ice flexural failure or ice crushing failure is the dominant failure mechanism. Judgement is required accordingly on the initial stiffness values of cohesive elements to balance between computational cost and required accuracy of prediction.

Acknowledgments

The authors would like to thank the National Research Foundation of Singapore, Keppel Corporation and National University of Singapore for supporting this work done in the Keppel-NUS Corporate Laboratory. The conclusions put forward reflect the views of the authors alone, and not necessarily those of the institutions within the Corporate Laboratory.

References

Blal, N, Daridon, L, Monerie, Y and Pagano, S., 2012. Artificial Compliance Inherent to the Intrinsic Cohesive Zone Models: Criteria and Application to Planar Meshes. International Journal of Fracture, 178, 71 83.

Camacho, G and Ortiz, M., 1996. Computational modeling of impact damage in brittle materials. Int. J. Solids Structures, 33, 2899-2938.

Croasdale, KR., 1980. Ice forces on fixed, rigid structures. IAHR Working Group on Ice Forces on Structures, U.S. Army Cold Regions Research and Engineering Laboratory, Special Report 80-26, 34-106.

Espinosa, H and Zavattieri, P., 2003. A grain level model for the study of failure initiation and evolution in polycrystalline brittle materials. Part I: Theory and numerical implementation. Mechanics of Materials, 35, 333-364.

Gürtner, A., 2009. Experimental and Numerical Investigations of Ice-Structure Interaction. Doctoral thesis, Norwegian University of Science and Technology.

Hilding, D, Forsberg, J and Gürtner, A., 2011. Simulation of Ice Action Loads on Offshore Structures. 8th European LS-DYNA Users Conference, Strasbourg.

Hillerborg, A., Modéer, M. and Petersson, E., 1976. Analysis of crack formation and crack growth in concrete by means of fracture mechanics and finite elements. Cement Concrete Res., Vol.6, pp. 773–782.

Kuutti, J, Kolari, K and Marjavaara, P., 2013. Simulation of Ice Crushing Experiments with Cohesive Surface Methodology. Cold Regions Science and Technology, 92, 17-28.

Kubair, DV and Geubelle, PH., 2003. Comparative analysis of extrinsic and intrinsic cohesive models of dynamic fracture. Int. J. Solids Structures, 40(15), 3853-3868.

Xu, XP and Needleman, A., 1994. Numerical simulations of fast crack growth in brittle solids. J. Mech. Phys. Solids, 42(9), 1397-1434.

International Association for Hydro-Environment Engineering and Research
Supported by Spain Water and IWHR, China

24th IAHR International Symposium on Ice
Vladivostok, Russia, June 4 to 9, 2018

A Semi-empirical Pod Model for USCG Icebreaker Mackinaw Part I – The Empirical Data

Michael Lau
National Research Council of Canada
1 Arctic Ave, St. John's, NL
Wai-Hung.Lau@nrc-cnrc.gc.ca

A semi-empirical pod model is developed based on experimental data for the USCGC Mackinaw to predict propulsion forces for the icebreaker driven by twin podded propulsors. The experiments are conducted in straight-ahead motion with the azimuth angle of one of the twin pods steered in a range from 0 to 180^{o}. In this pod model, assumption was made to extend the test data to the full range of 360^{o} azimuth angles and advance coefficients. Analysis was then performed to allow these test data for application of any planar motion including turning by considering hull-pod interaction.
This is Part I of a two-part paper. In this paper, the results from ice tank tests are presented. These include steering moment generated by the propulsors, thrust and torque of the propellers and the forces exerted on the hull at the location of the connection of the propulsors. The procedure to extend the empirical data to the full range is then presented. The agreement between static and dynamic data and the symmetry of the data is considered.

1. Introduction

In recent decades, podded propulsors have become popular owing to, among other things, their excellent capability in maneuvering. The propulsion forces and moments due to pods can be simulated numerically based on an empirical model developed from model test data. Ship simulators require such a model to simulate pod-driven ships. At the NRC's Ocean, Coastal and River Engineering Research Centre (OCRE-RC), a semi-empirical pod model has been developed and incorporated into its in-house ship maneuvering in ice simulation software OSIS-IHI (Ocean-Structure Interactions Simulator - Ice-Hull Interaction), based on experimental data of the USCGC Mackinaw (Akinturk and Lau, 2011). This model is also implemented in CMS's (Centre for Marine Simulation in Memorial University) marine simulators.

The experiment is conducted in straight-ahead motion with the Pod Azimuth angle steered in a range from 0 to 180^{o}. The semi-empirical model is then extended to cover the full range of 360 degrees as well as accounting for the different wake effects during turning (Lau, 2018).

This is Part I of a two-part paper. In this paper, the results from ice tank tests are presented. Section 2 summarizes the empirical data and their analysis. Regression equations were obtained to describe the pod performance for a full range of azimuth angle θ from 0 to 360^{o} and advance coefficient J. The conclusion is given in Section 3.

2. Experiments and Regression Model

The twin-podded propellers were tested in their typical operational configuration, i.e., the tractor mode, with a 1:15.62 scale model of USCGS icebreaker Mackinaw (Akinturk and Lau, 2011). The model was towed straight-ahead at various speeds while the azimuth angle of one of the twin pods steered in the range of 0 to 180^{o}. Two types of conditions were simulated for the pods during the experiments: static tests, in which the azimuth angle of the one of the pods was fixed at a certain azimuth angle for the duration of a run; and dynamic tests, in which the one of the pods was continuously steered from 0 to 360^{o} azimuth. Figure 1 shows a typical test set up. Figure 2 shows the two Mackinaw model pods. The pod located at the port side was designated Pod A, and the starboard side as Pod B. The basic geometry of the model propeller is summarized in Table 1. For details of the experiment, please refer to Akinturk and Lau (2011).

The drift angle β at the centre of gravity is defined as positive anti-clockwise from the x-axis in the direction of ship velocity $\vec{V}$, i.e. $\beta = -\tan^{-1}\dfrac{v}{u}$, where u and v are the components of $\vec{V}$ on the x- and y-axes respectively. This coordinate system is illustrated in Figure 3, where the Earth-fixed planar reference frame is denoted by ξ and η.

The thrust T and torque Q on the propeller shaft, and the longitudinal F_x and transverse F_y forces generated on the model ship hull by the pods were measured and non-dimensionalized. These are the thrust coefficient K_t, torque coefficient K_q, non-dimensional longitudinal K_{Fx} and transverse K_{Fy} force coefficients, respectively. The non-dimensional forces K_{Fx} and K_{Fy} are defined as:

$$K_{Fx}(J,\delta_R) = -F_x / 0.5\rho n^2 D^4 \quad \text{and} \quad K_{Fy}(J,\delta_R) = -F_y / 0.5\rho n^2 D^4 \qquad [1]$$

where ρ is the water density, n the propeller revolutions and D the propeller diameter. K_{Fx} and K_{Fy} are functions of advance coefficient $J = \frac{u}{nD}$ and steering angle δ_R. Since the non-dimensional forces K_{Fx} and K_{Fy} are measured on the mounting base of the pods in the longitudinal and transverse directions, F_x and F_y are the actual forces on the hull generated by the pods, respectively. These forces were modeled in the semi-empirical model to simulate ship maneuvering.

The torque coefficient K_q is defined as follows:

$$K_q(J,\delta_R) = Q / 0.5\rho n^2 D^5 \qquad [2]$$

It is used to estimate the shaft power according to the following equation:

$$P_S = 2\pi K_q \rho n^2 D^5 / \eta_R \, \eta_S \qquad [3]$$

where η_R and η_S are rotation and shaft coefficients, respectively. The thrust coefficient K_t is not used in the model at the current stage of software development.

Regressions are performed on these test data to obtain K_t, K_q, K_{Fx} and K_{Fy} as functions of J and δ_R, where $J = \frac{u}{nD}$ is advance coefficient, u is advance speed, n is propeller revolution and D is propeller diameter. For the static test, a second order polynomial is applied, whereas a sixth order polynomial is necessary for the dynamic test.

Table 2 gives a list of static and dynamic tests, the measurements from which the semi-empirical model was built. The relationship between azimuth angle θ and corresponding rudder angle δ is shown in Figure 4 and the following equation:

$$\theta = \delta + 180 \text{ or } \theta = \delta - 180 \ (\delta \in [-180,\ 180]) \qquad [4]$$

2.1 Static Test Data

In the static tests, Pod A remains in normal operating mode (at -180 degrees) and Pod B is varied between certain angles to starboard as previously listed in Table 2 (as shown in Figure 5). Since Runs 95, 96 and 97 are conducted under the same condition, i.e. $\theta_A = \theta_B = -180°$, regression is made for combined data in these runs (see Figure 6).

Measurement from the three runs agreed well except for K_{Fy}; however, the K_{Fy} are small, and in the case of $\theta_A = \theta_B = -180$ °, K_{Fy} should and is set to 0. These regression equations are implemented in the model to simulate the performance of the pods at azimuth angle $\theta = -180$ ° (i.e. $\delta = 0$). Note that K_t is greater than K_{Fx}, which means that the measurement K_{Fx} includes the thrust and appendage resistance of the pod.

However, the performance in static tests is measured only within the range $\theta_B = -180$ ° to 0. These data will be extended to $\theta_B = 0$ to +180° using the results of the dynamic tests.

2.2 Dynamic Test Data

The dynamic test is conducted only at $J = 0.2$ (advance speed V = 0.6 m/s, propeller revolution n = 15 RPS) to measure performance of the Pod A with azimuth angle $\theta_A = 0$ to 360° whereas θ_B of Pod B is fixed at -180°, as illustrated in Figure 7. The dynamic test includes Runs 82 and 83 with identical test conditions; hence, we combined these data for regression analysis. The regression curves of K_{Fx} , K_{Fy},, K_t and K_q from Runs 82 and 83 are presented in Figure 8.

Now the data obtained from the static tests from Pod B are combined with the data of Pod A from the dynamic tests to extend the data set to other J values. Given the symmetric positions of Pods A and B, it is assumed that K_{Fy} for Pod A in the static range of $\theta_A = 0$ to -180° corresponds to negative K_{Fy} for Pod B on the range $\theta_B = 0$ to +180°.

Figure 9 shows that the dynamic data match the static data well at $J = 0.2$ for K_{Fx} and K_{Fy}, which implies that it is reasonable to extend static data at other advance coefficents to the full range of $\theta_A = 0$ ° to 360° by following the trend of the dynamic curve. Since the dynamic data show an approximate symmetry about $\theta_A = 180$ °, it is expected that the error due to this extension would be small.

2.3 Procedure to Extend Empirical Data to the Full Range

Extension of the empirical data to the full range of azimuth angles and advance coefficients relies on the agreement between static and dynamic data and the symmetry of the data. To account for imperfect symmetry, let azimuth angles θ_{A1} and θ_{A2} be the symmetric angle about 180 degrees, i.e., θ_{A1} = -45 deg corresponds to θ_{A2}= 45 deg. Since in the dynamic test (at $J = 0.2$) we have measurement for $K_{Fx1}(\theta_{A1})_{J=0.2}$ at $\theta_{A1} < 180$ ° and $K_{Fx2}(\theta_{A2})_{J=0.2}$ at the symmetric angle $\theta_{A2} = 360 - \theta_{A1} > 180$ °, the following equation can be established:

$$(K_{Fx2})_{J=0.2} = (K_{Fx1})_{J=0.2}\,(1 + \alpha\,) \qquad [5]$$

where the modification ratio α is a small number that is a function of θ_{A1}, i.e. $\alpha(\theta_{A1}) = \left[K_{Fx2}(360 - \theta_{A1})_{J=0.2} - K_{Fx1}(\theta_{A1})_{J=0.2}\right] / K_{Fx1}(\theta_{A1})_{J=0.2}$. It is assumed that this modification ratio α could be applied to other J at θ_{A2}, i.e.:

$$\left(K_{Fx2}\right)_J = \left(K_{Fx1}\right)_J \left(1+\alpha\right) \qquad [6]$$

and $K_{Fx2}\left(J,\theta_{A2}\right)$ is simply scaled from known $K_{Fx1}\left(J,\theta_{A1}\right)$ and $\alpha\left(\theta_{A1}\right)$. This ratio $\alpha\left(\theta_{A1}\right)$ can be derived from the dynamic data at $\theta_{A1} = 0$ to 180° before applying it to data for $\theta_A = 180°$ to 360°. Figure 10 shows the performance at $\theta_A = 0°$ to 360°. Figure 11 shows the K_q $\theta_A = 180°$ to 360°. In this model K_q is used to predict power and the agreement between static and dynamic tests looks acceptable. Figure 12 predicts pod performance at $\theta_B = -120°$ and +120° to illustrate the different performance of Pod B at θ = 180° to 0° and θ = 0 to +180°. In this figure the curves for $\theta_B = -120°$ are the best fit of test data and the points for $\theta_B = +120°$ are data extended using Equation 6.

For this case, the maximum difference predicted for K_{Fx} between $\theta_B = -120°$ and +120° is 17%, which corresponds to approximately 8% for the maximum difference for K_{Fy}. The regression equations for the coefficients $K_{Fx}\left(J,\theta\right)$, $K_{Fy}\left(J,\theta\right)$, $K_q\left(J,\theta\right)$ for the full range of azimuth angle $\theta \in [0,\ 360]$ are ready for implementation in the semi-empirical model as empirical data.

5. Conclusion

Experiments with scale model of the USCGC Mackinaw driven by pods were conducted in straight-ahead motion with the pod azimuth angle steered in a range from 0 to 180 degrees. This paper summarizes the empirical data and their analysis. Regression equations were obtained to describe the pod performance for a full range of Pod Azimuth angle θ from 0 to 360^o and advance coefficient *J*, which are ready for implementation in any semi-empirical model as empirical data. Lau (2018) gives an example of such implementation.

6. References

Akinturk, A. and Lau, M., 2011. Manoeuvring performance of podded propulsors behind a ship. Ships and Offshore Structures 6(3):223-230.

Lau, M., 2018. A semi-empirical pod model for USCGC icebreaker Mackinaw: Part II – The model. Proceedings of the 24th IAHR International Symposium on Ice, Vladivostok Russia.

Fig. 1. Experimental set-up of the model in the ice tank

Table 1. Basic geometry of the model propeller

Diameter	200 mm
Number of blades	4
Section thickness form	NACA 66 (DTMB modified)
Pitch distribution	P/D =1.0, constant
Hub taper angle	15 degrees
Skew and rake distribution	zero

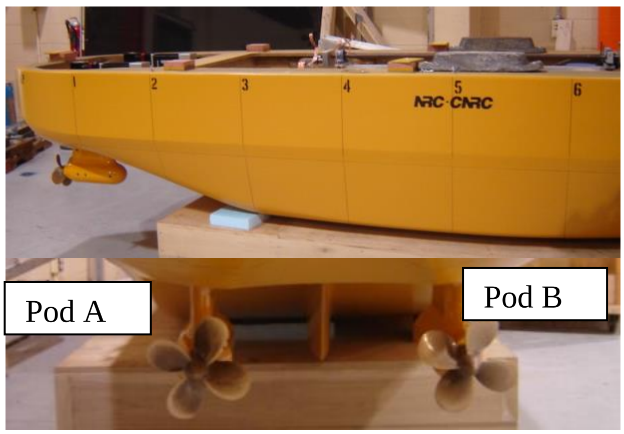

Fig. 2. Aft view of the model hull (top), and the pod designation used in the experiments (bottom)

Table 2. A list of static and dynamic tests

Run	Pod A θ_A	Pod B θ_B	Corresponding Rudder Angle δ_B
STATIC_084	-180	-355	-175
STATIC_085	-180	-175	5
STATIC_086	-180	-170	10
STATIC_087	-180	-165	15
STATIC_088	-180	-150	30
STATIC_089	-180	-120	60
STATIC_090	-180	-90	90
STATIC_091	-180	-60	120
STATIC_093	-180	0	180
STATIC_095	-180	-180	0
STATIC_096	-180	-180	0
STATIC_097	-180	-180	0
DYNAMIC_082	0 ~ 360	-180	0
DYNAMIC_083	0 ~ 360	-180	0

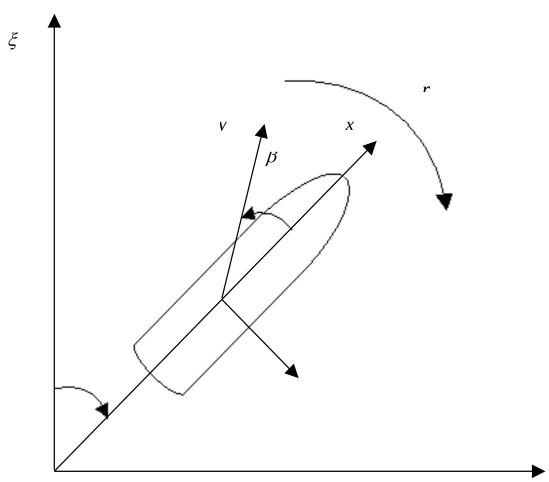

Fig. 3. Definition of the hull-fixed coordinate system

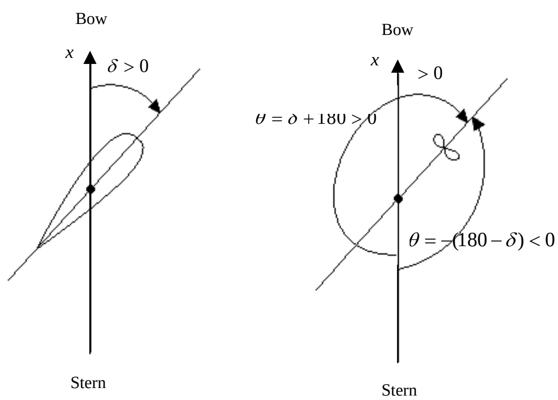

Fig. 4. Azimuth angle θ and corresponding rudder angle δ

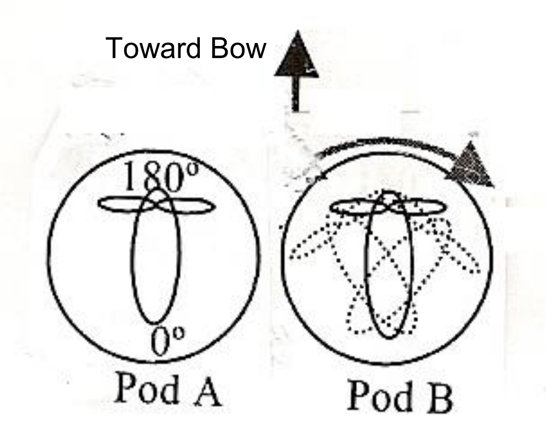

Fig. 5. Azimuth angle θ_A and θ_B in static tests

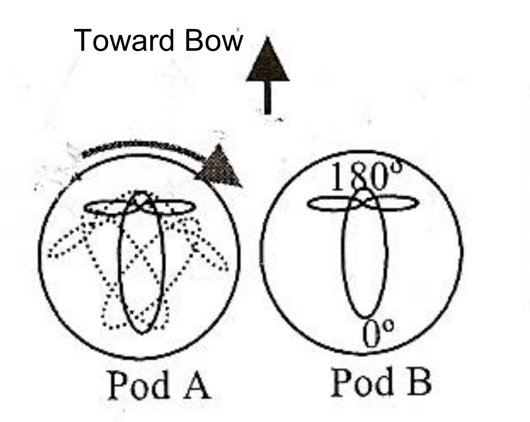

Fig. 6. Azimuth angle θ_A and θ_B in dynamic tests

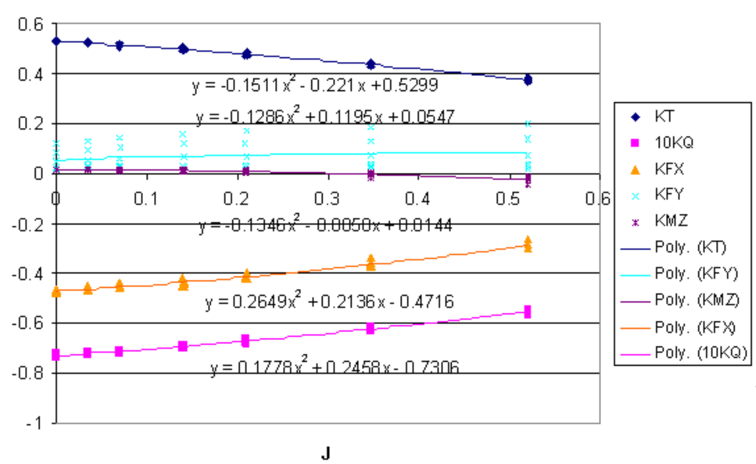

Fig. 7. Performance at azimuth angle $\theta_A = \theta_B$ =-180 deg (Average of Run 95, 96 and 97)

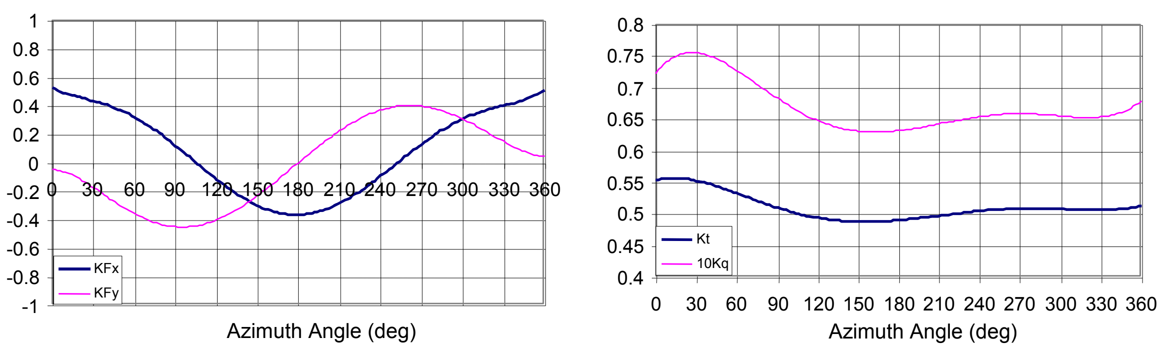

Fig. 8. Regression data of dynamic tests Runs 82 and 83: (Top) unit and transverse force coefficients and (Bottom) thrust and torque coefficients vs. azimuth angle

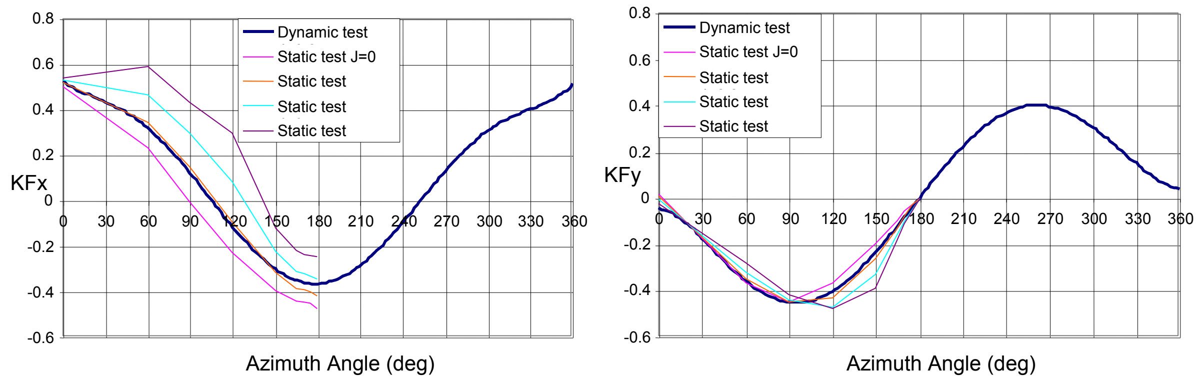

Fig. 9. Measurement of K_{Fx} and K_{Fy} in static and dynamic tests

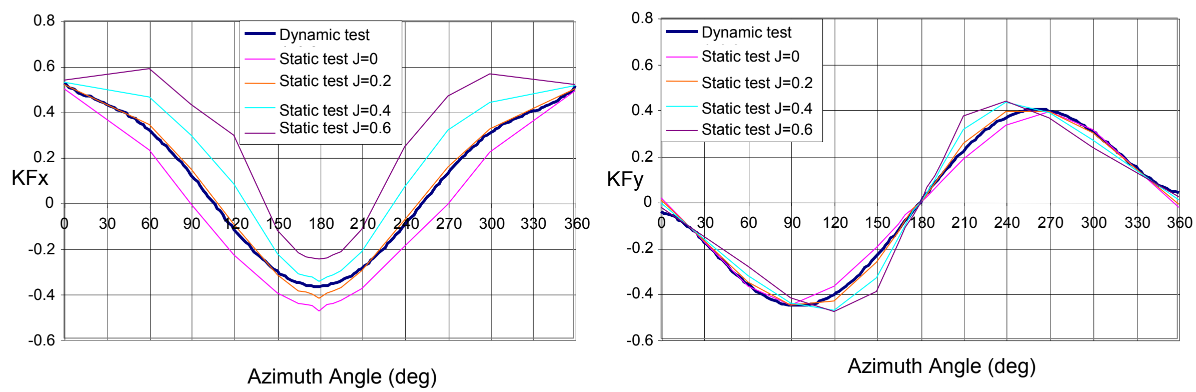

Fig. 10. K_{Fx} and K_{Fy} for $\theta_A = 0°$ to 360°

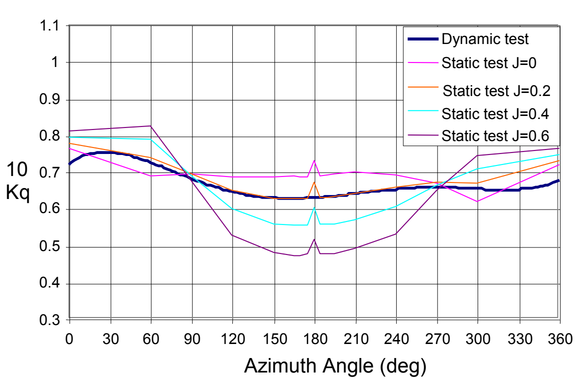

Fig. 11. K_q extended from 180° to 360° in static tests

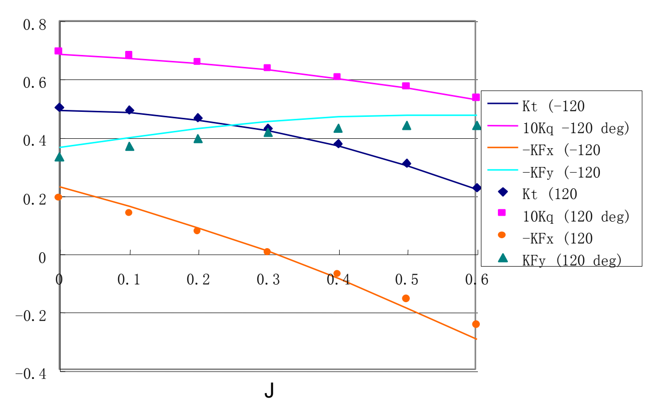

Fig. 12. Performance predicted at $\theta_B = +120°$ and extended to $\theta_B = -120°$

International Association for Hydro-Environment Engineering and Research
Supported by Spain Water and IWHR, China

24th IAHR International Symposium on Ice
Vladivostok, Russia, June 4 to 9, 2018

Melting of Lake Ice: Measurements and Modelling

Matti Leppäranta[1], Georgiy Kirillin[2], Elisa Lindgren[1]
[1]*Institute of Atmospheric and Earth Sciences, University of Helsinki, Helsinki, Finland*
2Leibniz-Institute of Freshwater Ecology and Inland Fisheries, Berlin, Germany
matti.lepparanta@helsinki.fi,
kirillin@igb-berlin.de

Melting of lake ice is driven primarily by solar radiation. Complications arise from large variability of optical properties of ice in the melting season. To gain more understanding of the melting process, field experiments have been performed in Finnish lakes from the boreal zone to Arctic tundra. In particular, an extensive research program was carried through in Lake Kilpisjärvi in the tundra zone in 2013–2014. The surface area of the lake is 37.1 km^2, and the maximum depth is 57 m. The heat budget in the melting season was dominated by the radiation balance, and turbulent heat fluxes were small except that occasionally sensible heat flux was large. The strong solar radiation leads to internal melting, and under the ice water warms up resulting in convective mixing. The fractions of surface melting, internal melting and bottom melting depend on weather and structure. Radiation transfer through the ice was measured using photo-synthetically active radiation (PAR) irradiance sensors. The data obtained was also used as the reference of mathematical model development. In this model ice and liquid water can co-exist in a grid cell when the temperature is at the melting point. The model is able to predict melting and deterioration of lake ice but the solar radiation sub-model needs further work. The output provides ice thickness and porosity, which tell of evolution of ice strength in the melting season.

1. Introduction

Fennoscandian Arctic tundra zone extends over high altitudes in the Scandinavian mountain chain. The northwest corner of Finnish Lapland is located in this zone. There lakes are frozen for 7–8 months annually. The ice cover consists of congelation ice and snow-ice with snow cover on top, and the annual maximum thickness of ice is close to one meter. The thickness of snow on land varies due to topography and it is also around one meter. Ice grows from November to April and melts during May–June. As in general in frozen lakes, the ice cover largely decouples the water body from the atmosphere and, consequently, weakens turbulence, mixing, sunlight, and level of oxygen in the water body. In the area the polar night lasts two months, and due to the snow cover the lakes are dark for 3–4 months each winter. The primary motivation of recent research of tundra lakes has been their climatology, ecology and fishery (Salonen et al. 2009; Kirillin et al. 2012), and interaction with the atmosphere (Yang et al. 2013). For the past decades, in most mid-latitude lakes freeze-up has come later and breakup earlier year-by-year (e.g., Magnuson et al. 2000) while for Arctic lakes there is less data. Lei et al. (2012) found no significantly change in breakup.

Here the heat budget of Lake Kilpisjärvi in the Finnish Arctic tundra is examined for the melting period. This lake is a medium-size clear-water lake. The research was performed jointly between the University of Helsinki and the Leibniz-Institute of Inland Waters and Fisheries, Berlin (Graves et al. 2014; Kirillin et al. 2014; Lindgren 2015). Due to safety issues, fieldwork on melting lake ice has been problematic, and the lack of data has been notified. For the present research field campaigns were performed in two years. Melting of lake ice is driven primarily by solar radiation. Ice melts at the boundaries and in the interior, with fractions depending on the solar radiation balance and surface and bottom heat balances. Complications arise from large variability of optical properties of ice in the melting season.

The results of the heat budget analysis in Lake Kilpisjärvi are presented below based on fieldwork in the melting periods in 2013–2014. The data include solar radiation, air–lake fluxes and evolution of ice and snow thickness. Monitoring data of the weather conditions and the lake hydrology were also utilized. The net surface heat flux was compared with the melting rates of ice and snow that provided an excellent condition to validate the total incoming heat flux. The surface heat balance was dominated by net solar radiation, net longwave radiation, and sensible heat flux. The specific ice cover deterioration results provide new insight into the physics of ice breakup.

2. Field data

Lake Kilpisjärvi is located at 69°03’N 20°50’E, 473 m above sea level. The distance to the shore of the northern North Atlantic Ocean is about 60 km. The lake is in the northwest end of a long valley, fells rising up to 1000 m elevation (500 m from the lake surface) on both sides, and the maximum fetch is 6.2 km. The surface area is 37.1 km^2, and the average and maximum depths are 19.5 m and 57 m, respectively. The inflow comes from small mountain brooks, and outflow is in the southeast to River Könkämäeno and further to the Baltic Sea. There are no industrial or agricultural activities in the drainage basin, apart from reindeer herding. In Kilpisjärvi village at the lake there are less than 100 inhabitants but annually close to 40,000 tourists visit the region.

In the northwest bay of the lake there is a routine ice and snow monitoring station of the Finnish Environment Institute (Korhonen 2005). Observations are made at every 5–15 days. The mean freezing and breakup dates were November 9 and June 18 in the period 1952–2015, and the earliest and latest breakup date were June 2 and July 1, respectively. The surface temperature increases to 10–15°C at about August 10th. The average maximum annual ice thickness was 89 cm (the range was 77–114 cm), reached in April. Local weather data were available from the Kilpisjärvi Biological Station (KBO) and weather station Enontekiö Kilpisjärvi Kyläkeskus (EKK) of the Finnish Meteorological Institute. The annual mean air temperature (1962–2015) was between –4ºC and –1ºC, with mean monthly air temperatures below 0ºC from October to April. Snow thickness on ground was on average 90 cm in March–April.

The field experiments were carried through in Lake Kilpisjärvi in May–June 2013–2014. Temperature and light conditions in snow, ice and water were collected at 10-minute time intervals (Lindgren 2015). Light measurements were made using PAR (Photosynthetically Active Radiation, 400–700 nm) irradiance sensors. Automated data collection was complemented by regular manual ice observations. Also, CTD sounding data were collected from the water body. First manual data were collected from the ice, but later a small boat was needed when the ice cover had become more open and fragile

3. Heat budget

The heat content of Lake Kilpisjärvi consists of sensible heat and latent heat. A convenient reference is the heat content (E_0) of the lake at isothermal liquid state at 0ºC. The actual heat content per unit area is then $E = E_0 + \Delta E$, where

$$\Delta E = \frac{1}{A}\left(\int_V \rho c T dV - \int_A \rho_i L h dA\right) \qquad [1]$$

Here A is the lake surface area, V is lake volume, ρ is density, c is specific heat, T is temperature in ºC, L is latent heat of freezing, h is ice thickness, and the subscript i stands for ice; in the volume integral ρ and c may represent liquid water ($T \geq 0$°C) or ice ($T \leq 0$°C). The water balance is taken zero, i.e. inflow, evaporation/sublimation, and precipitation are assumed to compensate for their net mass flux in the outflow to the River Könkämäeno. It is further assumed that the inflow and outflow do not significantly influence the heat budget. The heat content changes only by the solar source and fluxes at the top and bottom surfaces:

$$\frac{d}{dt}\Delta E = Q_n = (1-\alpha)\gamma Q_s + Q_0 + Q_b \qquad [2]$$

where Q_n is net flux, Q_s is incoming solar radiation, α is albedo, γ is the proportion of solar radiation penetrating into the lake (about the same as the proportion of optical band), Q_0 is surface heat balance, and Q_b is the heat flux from the bottom. The surface heat balance is

$$Q_0 = (1-\alpha)(1-\gamma)Q_s + Q_{La} - Q_{L0} + Q_c + Q_e + Q_P \qquad [3]$$

where Q_{La} and Q_{L0} are the terrestrial radiation fluxes from the atmosphere and from lake surface, respectively, Q_c and Q_e are sensible and latent heat fluxes, and Q_P is the heat flux from precipitation.

Results of ice melting

The ice cover consists of three principal layers: congelation ice, snow-ice and snow. Occasionally there may be slush sub-layers in the snow or snow-ice layer. In Lake Kilpisjärvi, average snow and snow-ice thickness correspond to snow accumulation by about 75 cm, which is less than snow accumulation on ground (on average 90 cm), largely due to drifting of snow. Maximum ice thickness is reached in March – April (Table 1), and melting of ice begins in May, as soon as snow has melted. Melting of ice then progresses by about 2 cm per day solid ice thickness equivalent.

Table 1. Seasonal and average ice characteristics in the study winters. Comparison to climatology is also provided (Lei et al. 2012): freeze-up and breakup from 1952–2010, ice thickness from 1981–1990, and snow from 1977–2010.

	2013	2014	Mean	Standard deviation
Maximum ice thickness (cm)	95	97	89	7.7
- congelation ice	75	45	70	17.3
- snow-ice	20	52	20	17.1
- day of occurrence	10 March	30 April	14 April	14.9 d
Maximum snow thickness[1]	23	20	37	9.1
- date of occurrence	10 April	25 April	4 March	34.4 d
Ice breakup date	3 June	19 June	18 June	6.8 d

[1]Snow on lake ice

Lake ice cover is a good sensor for the heat budget. The heat content in the ice cover is mainly latent heat and it can be determined from the thickness of ice layers:

$$\Delta E_l = -[\rho_i(h_{ci} + h_{si}) + \rho_s h_s - \rho_w h_{sw}]L \qquad [4]$$

i

where h_{ci}, h_{si} and h_s are the thicknesses of congelation ice, snow-ice and snow layers, h_{sw} is the equivalent thickness of liquid water in the ice, and ρ_i, ρ_s, and ρ_w are the ice, snow and water densities. Heat needed to melt the ice equals ΔE_l. Melting takes place at the boundaries and in the interior, so that ice becomes porous and fragile, breaks due to its own weight into brash ice, and thereafter disappears very quickly. After this breakage event, the heat balance changes since albedo becomes close to open water albedo and turbulence in the water brings more heat from below.

Weather conditions were unusual during the 2013 field campaign. Colder than average winter resulted in maximum ice thickness of 95 cm. At the end of May an extraordinarily warm, clear weather followed, with daytime maximum air temperatures reaching 25°C. Ice and snow thickness recordings by Finnish Environment Institute showed that the 20 cm thick snow covering the lake ice started to melt in the beginning of May, whereas the ice melting started in mid-May after most of the snow was gone. Narrow ice-free margins, moats, had formed along the shoreline by May 24 and became wider as the melting progressed. Ice break-up took place on June 3, preceded by warm but windless days which kept the fragile ice cover unbroken. On the break-up day, the average wind speed rose to 4–5 m s^{-1}, and the about 90 % ice-coverage disappeared in 10–15 hours.

In the beginning of the field campaign, ice thickness ranged lake-wide in 37–60 cm with a 0–4 cm layer of slush partly covering the ice. Ice thickness was measured only on two days (May 25 and 26) since thereafter the ice cover was too fragile to move on. Overall, the ice cover was very patchy. When the ice was dry and appeared white, the bearing capacity remained significant almost until the break-up day, whereas in some areas the ice was dark-coloured and wet, internal melting having turned the 30–40 cm thick ice to candled ice. At the PAR-station, between the installation and dismantling ice thickness decreased from 50 cm to 25 cm resulting in an extremely rapid melting, averaging to 4.5 cm per day corresponding to net heat flux of 160 W m^{-2} into the ice.

In the winter 2014, the maximum ice thickness reached 97 cm. The 20 cm thick snow began to melt in the end of April and the snow had disappeared by the end of May. Ice thickness stayed around 90 cm until the middle of May when the ice melting started to progress. The prevailing weather during the field campaign was cold compared to 2013: the daytime maximum temperature stayed mostly around +5°C and at night-time the temperature dropped close to 0°C, the coldest recorded value being –3.1°C. Ice break-up took place on June 19, which is close to the long-term average. Snow was absent in the beginning of the 2014 field campaign apart from slush patches. Melting of ice had just started, and average ice thickness across a line in the lake decreased from 97 cm on May 20 to 69 cm on May 26. At the same time the thickness of the slush layer increased from 3 cm to 13 cm as the solid uppermost layer of ice melted and exposed an unfrozen layer that had been trapped underneath. Until May 24, the freeboard of ice was positive i.e. the water level in a drill hole was below the top of the ice layer, but on May 26 after the increase in the amount of slush, the freeboard turned negative on average by –2.5 cm. The ice thickness observations at the fixed PAR-station showed, that over the six days the initial thickness of 90 cm decreased to 82 cm resulting in a melt rate of 1.3 cm per day.

The incoming solar radiation was measured directly at Kilpisjärvi biological station. The albedo used was based on the observed surface properties and earlier field results (Arst et al. 2008; Lei et al. 2011) and assumed to be a constant equal to 0.3 in 2013 and 0.5 in 2014. The emitted longwave radiation from the surface was obtained by assuming that the surface temperature was at the melting point. The turbulent fluxes were obtained with the bulk aerodynamic formulae. No precipitation events took place in either year and this flux does not account for.

The resulting heat fluxes are shown in Fig.1. In 2013 the radiation balance was clearly dominated by the incoming solar radiation. The daily cycle peaked at 420 W m^{-2} in most days due to the dominating clear sky conditions but in June 2 and 3 the weather was more cloudy. Net longwave radiation was smaller staying between –55 W m^{-2} and 50 W m^{-2}. Surprisingly, it was not only acting as a heat loss term, but instead contributed a small amount of heat for ice melt. This is due to the exceptionally warm weather. Turbulent heat exchange between the ice and relatively warm air was strong and had a clear daily cycle. Sensible heat flux stayed positive over the ten days of field campaign peaking up to 100 W m^{-2} at daytime and decreasing close to zero at the nights. The daily averages were between 18 W m^{-2} and 45 W m^{-2}. Latent heat flux, on the other hand, was negative as usual but the absolute value had a smaller magnitude. Except for the night-time hours, when the net surface heat flux decreased below zero, the lake ice was gaining a lot of heat. The daily maximum reached as high values as 450 W m^{-2}, and on average the daily surface heat budget was within 116–219 W m^{-2}. The observed melting rate and the heat budget were well in agreement.

In 2014 cloudy weather and higher albedo were the reasons for a relatively low net shortwave radiation (Fig. 1). The maximum daily solar heating was 300 W m^{-2}, and the daily average was on May 22 as low as 45 W m^{-2} while the highest value reached only 141 W m^{-2} on May 24. As normal, ice surface was cooled down by net longwave radiation that stayed negative over the whole field campaign, the daily averages varying between –13 W m^{-2} and –62 W m^{-2}. The turbulent heat exchange was rather low and did not contribute much to the heat balance. Sensible heat flux remained slightly positive, except in May 26, the maximum peaking at 50 W m^{-2}. The daily averages were between –3 W m^{-2} and 17 W m^{-2}. Likewise, latent heat flux was very low, between zero and –20 W m^{-2}, with daily averages from –3 W m^{-2} to –13 W m^{-2}. When these rather small surface fluxes were combined, the net became down to –40 W m^{-2} at night-time, while the daytime values peaked at 240 W m^{-2}. On average the surface was gaining heat daily from 32 W m^{-2} to 93 W m^{-2}. The observed low melting rate (1.3 cm day^{-1} at the PAR site) supports these results.

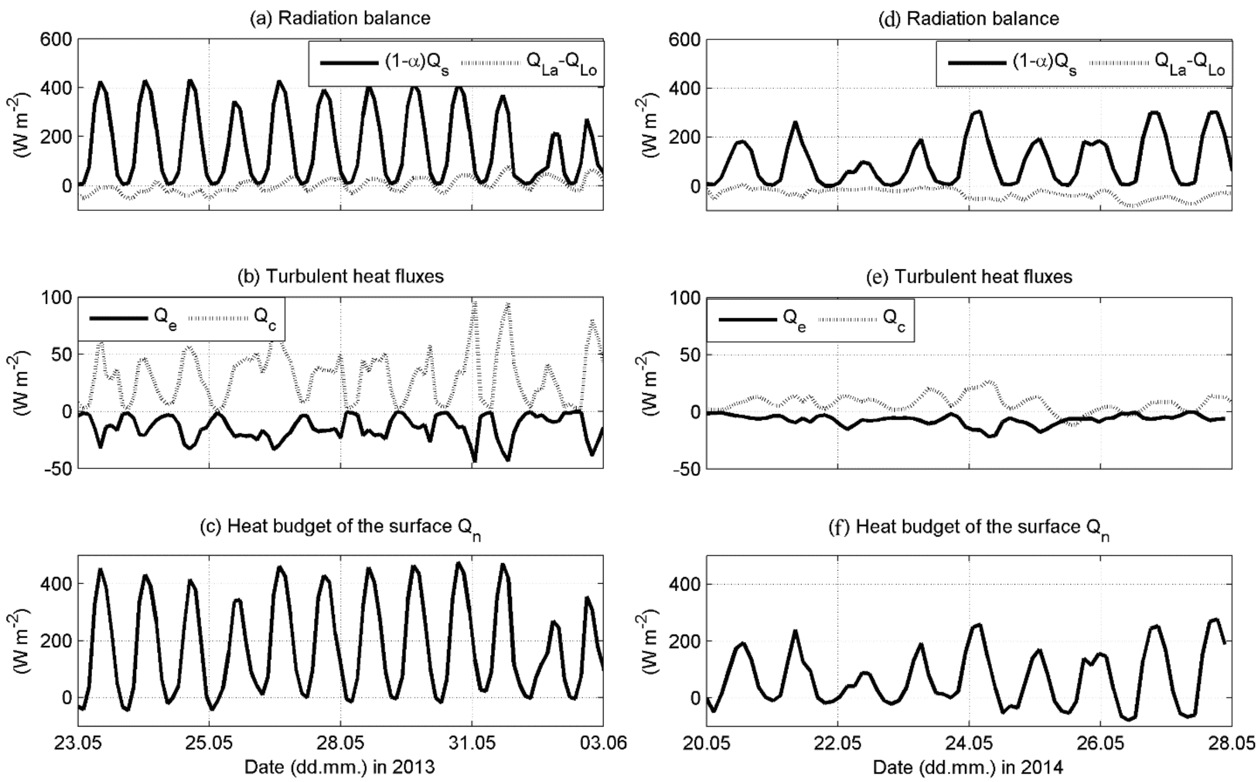

Fig. 1. Surface heat budget in 2013 (a-c) and 2014 (d-e) in Lake Kilpisjärvi. (a) and (d) are net solar radiation $(1-\alpha)Q_s$ and net longwave radiation $Q_{L0} - Q_{La}$, (b) and (e) are turbulent latent Q_e and sensible Q_c heat fluxes, and (c) and (f) are the net heat fluxes to the lake $\mathrm{Q_n}$.

PAR irradiance measurements showed the highly different conditions in 2013 and 2014. In 2013 the prevailing condition was clear sky, and the level of radiation was over 600 W m^{-2} at noon. The surrounding mountains shade the lake during the polar day when the solar altitude is low and thus the irradiance dropped to almost zero at night-time. Thinning congelation ice allowed a lot of light to penetrate the ice cover, and already on May 26 the under-ice irradiance was 350 W m^{-2} increasing gradually to 450 W m^{-2} on May 31. The ice was melting with a rate of 4–5 cm day^{-1}. Measurements from 2014 showed higher variation in incoming irradiance due to more cloudy conditions. The radiation level under the ice was low, 30 W m^{-2}, as expected with the 80–90 cm thick ice with layer of highly scattering snow-ice. The maximum PAR-irradiance over the six days did not change. In the congelation ice, 24.5 cm over the ice bottom and 12.5 cm below the snow ice–congelation ice interface, the irradiance responded more strongly to the variations at the surface; the maximum 200 W m^{-2} was measured on May 24 but mostly the daytime irradiances remained around 100 W m^{-2}.

In 2013 the light attenuation in the ice changed significantly over the six days. The attenuation coefficient decreased from 0.8 m^{-1} to as low as 0.2 m^{-1}. This was caused by ice melting, which firstly decreased the ice thickness by 4.5 cm per day and, secondly, resulted in the gas pockets filling with melt water. In 2014 the attenuation coefficient remained almost as constant of 1.7 m^{-1} over the five days of measurements. This was due ice conditions not changing drastically during the field campaign and due to the presence of the snow-ice layer.

The vertical distribution of heat content of ice is expressed as

$$\Delta E_i(z) = \rho_i L\nu(z) + \rho_i c_i[1 - \nu(z)]T(z) \qquad [5]$$

where ν is ice porosity. Since $\nu = 0$ for $T < 0°C$ and $\nu \geq 0$ for $T = 0°C$, Eq. (5) can be split into evolution equations for porosity and temperature to give a realistic picture of the progress of melting (see Leppäranta et al. 2013; Leppäranta 2015). Forcing takes place by solar radiation and, as long as there are temperature gradients, by heat conduction. In the full melting stage just porosity increases by solar radiation penetrating into the ice. Then there are feedbacks since the internal melting also influences the transparency of ice.

4. Final remarks

Ice melting in an Arctic tundra lake has been examined based on field data in years 2013 and 2014. The former year was exceptional with strong solar flux from clear sky and exceptionally warm air temperatures up to 25°C resulting in positive net longwave radiation and significant sensible heat flux. The average melt rate was 4.5 cm d^{-1}. In 2014 the sky was mostly cloudy and air temperature was below 5°C, ice melting rate was 1–2 cm d^{-1} which is lower than normal. The breakup date is strongly tied to solar radiation and takes place in June after the sunrise of the polar day, and therefore the sensitivity to climate variations is low.

Further work is ongoing on melting ice for the mechanical breakage, the water body beneath, and ice–water interaction (see Graves et al. 2014; Kirillin et al. 2014). Modelling work is also ongoing with a two-phase (water + ice) model (Leppäranta 2015). The model is able to predict melting and deterioration of lake ice and further the evolution of ice structure to predict the change of mechanical properties of ice in the melting season.

Acknowledgements

Our field research was based in Kilpisjärvi Biological Station of the University of Helsinki. The station director, Professor Antero Järvinen and technician Mr. Oula Kalttapää are greatly acknowledged for use of station facilities and help. Ms. Cecilia Äijälä and Mr. Tom Kokkonen are thanked for help in the fieldwork. This work is a contribution of the Nordic Center of Excellence Cryosphere–Atmosphere Interactions in a Changing Arctic Climate (CRAICC) and has also been supported by the Academy of Finland (project #140939).

References

Arst, H., Erm, A., Herlevi, A., Kutser, T., Leppäranta, M., Reinart, A., and Virta, J., 2008. Optical properties of boreal lake waters in Finland and Estonia. Boreal Environment Research 13(2), 133–158.

Graves, K., Laval, B.-E., Forrest, A., and Kirillin, G., 2014 Under-ice circulation, modified by Earth's rotation, in an arctic lake. Proc. 22nd IAHR Symposium on Ice, Singapore.

Kirillin, G., Engelhardt, C., Forrest, A., Graves, K., Laval, B.-E., Leppäranta, M. and Rizk, W., 2014 Standing waves during ice breakup in a polar lake. Proc. 22nd IAHR Symposium on Ice, Singapore.

Kirillin, G., Leppäranta, M., Terzhevik, A., Bernhardt, J., Engelhardt, C., Granin, N., Golosov, S., Efremova, T., Palshin, N., Sherstyankin P., Zdorovennova, G. and Zdorovennov, R., 2012 Physics of seasonally ice-covered lakes: major drivers and temporal/spatial scales. Aquatic Ecology 74, 659–682.

Lei R., Leppäranta, M., Erm, A., Jaatinen, E., and Pärn, O., 2011. Field investigations of apparent optical properties of ice cover in Finnish and Estonian lakes in winter 2009. Estonian Journal of Earth Sciences 60(1), 50–64.

Lei, R., Leppäranta, M., Cheng, B., Heil, P. and Li, Z., 2012. Changes in ice-season characteristics of a European Arctic lake from 1964 to 2008. Climatic Change 115, 725–739.

Leppäranta, M., 2015. Freezing of lakes and the evolution of their ice cover. 301 p. Springer-Praxis.

Leppäranta, M., Järvinen, O., and Mattila, O.-P., 2013. Structure and life cycle of supraglacial lakes in the Dronning Maud Land. Antarctic Science 25(3), 457–467.

Lindgren, E., 2015. Ice break-up in an Arctic lake – investigating Lake Kilpisjärvi [in Finnish]. MSc thesis, University of Helsinki, Department of Physics.

Magnuson, J.J., Robertson, D.M., Benson, B.J., Wynne, R.H., Livingstone, D.M., Arai, T., Assel, R.A., Barry, R.G., Card, V., Kuusisto, E., Granin, N.G., Prowse, T.D., Stewart, K.M., and Vuglinski, V.V., 2000. Historical trends in lake and river ice cover in the Northern Hemisphere. Science 289, 1743–1746.

Salonen, K., Leppäranta, M., Viljanen, M., and Gulati, R., 2009. Perspectives in winter limnology: closing the annual cycle of freezing lakes. Aquatic Ecology 43(3), 609–616.

Yang, Y., Cheng, B., Kourzeneva, E., Semmler, T., Rontu, L., Leppäranta, M., Shirasawa, Km. and Li, Z., 2013. Modelling experiments on air-snow interactions over Kilpisjärvi, a lake in northern Finland. Boreal Environment Research 18, 341

24th IAHR International Symposium on Ice
Vladivostok, Russia, June 4 to 9, 2018

Peak ice loads and buckling in ice-inclined structure interaction

Janne Ranta[1,2], Arttu Polojärvi[1,2], Jukka Tuhkuri[1,2]
[1]*Aalto University, School of Engineering, Department of Applied Mechanics*
P.O. Box 14300, FI-00076 Aalto, Finland
[2]*Sustainable Arctic Marine and Coastal Technology (SAMCoT), Centre for Research-based Innovation(CRI), Norwegian University of Science and Technology, Trondheim, Norway*

e-mail: janne.ranta@aalto.fi

Our earlier statistical studies on interaction of ice with an inclined structure suggest that ice loads only depend on a relatively small number of parameters. The complexity of the interaction process yields a largely scattered peak ice load values, which makes the data analysis of load data challenging. In this paper, which is a summary of the results observed by Ranta et al. (2018b), we present peak load observations from a large number of simulations and show that a simple buckling load model, having only two ice parameters, explains the peak loads well. The results highlight the importance of buckling phenomenon in ice-structure interaction processes.

Introduction

Development of safe Arctic operations requires reliable prediction of maximum sea ice loads. The study presented here uses 2D combined finite-discrete element method (2D FEM-DEM) simulations to study ice sheet buckling as a mechanism to limit ice loads. Figure 1 illustrates our simulations, which have a floating and continuous ice sheet pushed against an inclined rigid structure. The initially intact ice sheet fails into a rubble pile of ice blocks.

An important feature of discrete element simulations is that they can describe force chains (Peters et al., 2005). In the case of ice-structure interaction, the force chains are chainlike groups of ice blocks, or ice floes, that transmit the loads from the intact ice sheet to the structure. Existence of force chains at peak load events in similar ice-structure interaction processes as studied here was observed by (Paavilainen and Tuhkuri, 2013).

This paper gives a summary of the results observed by Ranta et al. (2018b), who analyzed the effect of the force chain buckling on maximum ice loads on an inclined structure. We first describe our simulations and a buckling model, which is based on the assumption that the ice sheet has broken into individual ice floes in the vicinity of the structure. After this, we demonstrate that the buckling model predicts the peak ice loads in our simulations well, and yields floe size predictions that corresponds to those observed in full-scale.

Simulations

We performed our 2D FEM-DEM simulations using an in-house code of the Aalto University ice mechanics group. The code is based on the models described in Hopkins (1992) and Paavilainen et al. (2009). The ice sheet was formed by discrete elements connected with Timoshenko beams. These beams were linearly elastic up to a failure criterion for sea ice (Schreyer et al., 2006), and then went through an energy dissipating cohesive softening leading to failure. Discrete elements were used to treat contact interactions between the ice blocks and the ice and the structure. Paavilainen et al. (2011) and Paavilainen and Tuhkuri (2012, 2013) validated the model against full- and model-scale data.

We ran six sets of simulations, S1...S6, summarized by Table 2. Each of the sets S1...S6 contained 50 simulations, which only differed by the initial vertical velocity perturbation v_0 (see Figure 1). The initial velocity v_0 was of the order of 10^{-12} m s^{-1} at the free edge of the ice sheet and

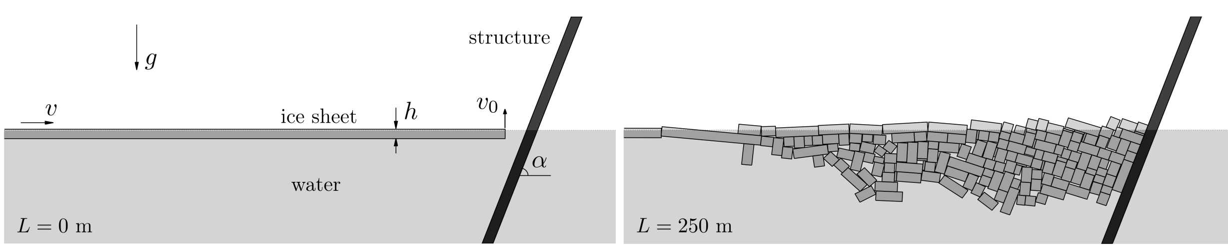

Fig. 1. Simulated ice-structure interaction process: snapshots from instances of $L = 0$ m and 250 m of ice (thickness h) pushed against an inclined structure (angle α) with velocity v. Small initial vertical velocity v_0 was applied to the right end of the ice sheet at $L = 0$ m.

had an unique value for each simulation in a set. As the data in Figure 2 demonstrates, this was enough to yield different ice-structure interaction processes for the simulations in each set. The sets S1. . .S6 differed from each other by the values of h and σ_p.

Figures 2a and b illustrate how the maximum peak load F^p events differed between simulations: the F^p events in them occurred at a different time and yielded a different F^p value. The close-ups of the Figure 2b illustrate, that the peak load events were not due to sudden impact loads. The ice behavior in these F^p events could be captured with a buckling model presented in Figures 3a and b, which, respectively, show the model in its initial and buckled state.

The buckling model of Figures 3a and b consists of a rigid rod, which simulates a rigid ice floe of length L_f, lying on an equilibrium on an elastic foundation modeling water. The modulus k of the elastic foundation, chosen after the specific weight of water, was $\rho_w g$, where ρ_w is the mass density of the water and g the gravitational acceleration. We used a model that included a floe rather than an intact ice sheet, since the ice sheet had virtually always broken into ice floes in the vicinity of the structure when F^p events occurred.

The buckling model can describe different buckling modes depending on the values of the spring constants K_1 and K_2 of the springs at the ends of the floe. Table 3 shows the different modes together with the corresponding K_1 and K_2 values. Out of the four modes of the table, modes 1 and 2 assume that the elastic bending of the intact ice sheet does not have a role in a peak load event. Modes 3 and 4, on the other hand, assume that the elastic ice sheet behind the buckling floe generates a lateral support for the left end of it. The buckling load P for the model is (Ranta et al.,

Table 1. Summary of the simulation parameter values.

	Parameter	Unit	Value		Parameter	Unit	Value
General	Gravitational acceleration	$\mathrm{m\,s^{-2}}$	9.81	Ice	Thickness (h)	m	0.5, 0.875, 1.25
	Ice sheet velocity	$\mathrm{m\,s^{-1}}$	0.05		Effective modulus	GPa	4
	Drag coefficient	-	2.0		Poisson's ratio	-	0.3
	Slope angle	deg	70		Density	$\mathrm{kg\,m^{-3}}$	900
Contact	Plastic limit (σ_p)	MPa	1, 2		Tensile strength	kPa	600
	Friction coefficient	-	0.1		Shear strength	kPa	600
Water	Density	$\mathrm{kg\,m^{-3}}$	1010				

Table 2. Sets S1. . .S6 of repeated simulations. Each set consisted of 50 simulations.

Set	h [m]	σ_p [MPa]	Set	h [m]	σ_p [MPa]
S1	0.5	1	S4	0.875	2
S2	0.5	2	S5	1.25	1
S3	0.875	1	S6	1.25	2

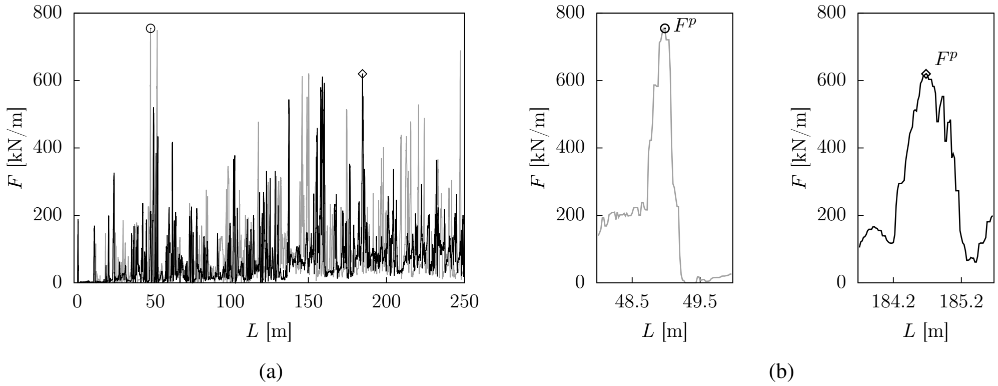

Fig. 2. Ice load F records from two simulations: (a) two F records plotted against length L of pushed ice and (b) close-ups showing the maximum peak ice load F^p events. These simulations differed by the initial velocity perturbation v_0 (Figure 1). The ice thickness $h = 1.25$ m and the plastic limit $\sigma_p = 1$ MPa.

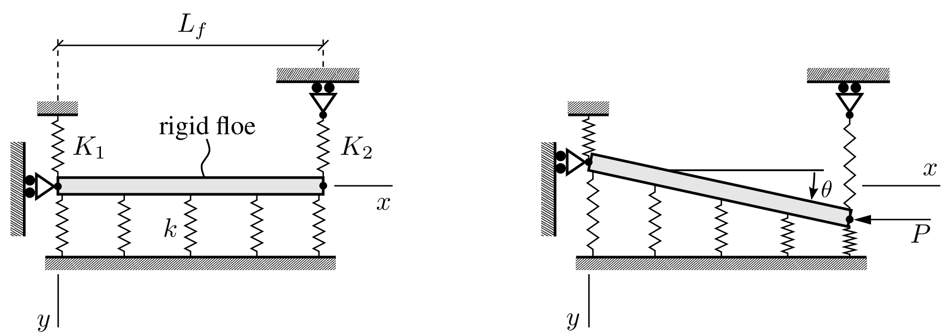

Fig. 3. The buckling model we used in its initial (left) and buckled (right) states. The model consisted of a rigid ice floe of length L_f resting on an elastic foundation with modulus k presenting water. Springs K_1 and K_2 modeled the boundary conditions for the buckling modes of Table 3. Compressive force P is due to the other floes or the structure. Figure is from Ranta et al. (2018b).

2018b)

$$P = \frac{k^2 L_f^3 + 4k(K_1 + K_2)L_f^2 + 12K_1K_2L_f}{12(kL_f + K_1 + K_2)}. \quad \textbf{[1]}$$

The characteristic length $L_c = \sqrt[4]{4EI/k}$ of a beam on elastic foundation (Hetényi, 1979) is introduced into Equation 1 by substitution of $L_f = \chi L_c$, where χ is a dimensionless buckling length factor defined below. As Ranta et al. (2018b) shows, L_c allowed us to express P for all buckling modes of Table 3 in form

$$P = a(\chi)\sqrt{kEI}, \quad \textbf{[2]}$$

where $a(\chi)$ is a buckling-mode-dependent dimensionless multiplier given in Table 3. This equation can be used to study the relation between buckling and peak loads as follows. As the input for the analysis, the F^p value from each simulation, together with the simulation parameters (k, E and I), are collected. These are substituted to the previous equation, which is then solved for $a(\chi) = F^p/\sqrt{kEI}$. If buckling had limited the F^p values, the $a(\chi)$ values for all simulations should be approximately equal; the F^p values should become normalized by factor $\sqrt{kEI}$.

Results

Figure 4a shows the maximum peak ice load F^p values from all of our simulations. Additionally, it shows the mean F^p values with their standard deviations for the simulations of each set S1…S6. While the F^p values from the simulations in a given set show scatter, the mean F^p values of the sets S1…S6 are seen to differ considerably, up to about 500 %, mainly due to the difference in ice thickness h between the sets (Ranta et al., 2016). The variation between the F^p values yielded by the simulations in each set is largely due to the stochasticity of the ice loading process (Ranta et al., 2016, 2018c,a).

The values of $a(\chi)$ (Equation 2), solved using the F^p data of Figure 4a, are shown in Figure 4b, and indicate that the peak load events are related to buckling. All of the mean $a(\chi)$ values are in the same range. There is no dependency between the $a(\chi)$ and h. There is some scatter in $a(\chi)$ data, but the mean $a(\chi)$ values differ by about 15 % at maximum. In other words, the F^p values are remarkably well normalized by factor $\sqrt{kEI}$ of Equation 2. This suggests that buckling limits the peak ice load values; Multiplying F^p by $1/\sqrt{h^3}$ yields normalized $a(\chi)$ data. The scatter in $a(\chi)$ data is mostly due to the boundary and loading conditions, which in individual F^p events differ from those in our idealized buckling model.

As $a(\chi)$ appears constant, we can solve χ to estimate the lengths $L_f = \chi L_c$ of buckling floes (see Figure 5). The data points of Figure 6 are the χ values from all simulations in sets S1…S6 for modes 2-4 of Table 3. (For each $a(\chi)$ value, we get four values for χ, one for each mode, as

Table 3. Four buckling modes considered in our study with the corresponding spring constants K_1 and K_2 (Figure 3). The buckling load $P = a(\chi)\sqrt{kEI}$, where $a(\chi)$ is a mode-dependent multiplier. Factor χ gives the buckling length as described in the text. Table is from Ranta et al. (2018b)

mode		K_1	K_2	$a(\chi)$
1		0	0	$\frac{\chi^2}{6}$
2		∞	0	$\frac{2\chi^2}{3}$
3	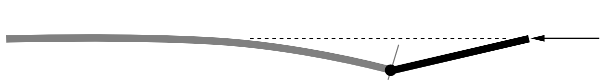	$\frac{1}{2}kL_c - \frac{3}{4}\frac{P}{L_c}$	∞	$\frac{12\chi + 8\chi^2}{9\chi + 12}$
4	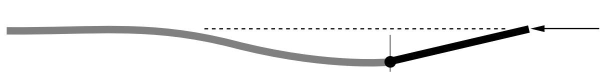	$kL_c - \frac{P}{2L_c}$	∞	$\frac{12\chi + 4\chi^2}{3\chi + 6}$

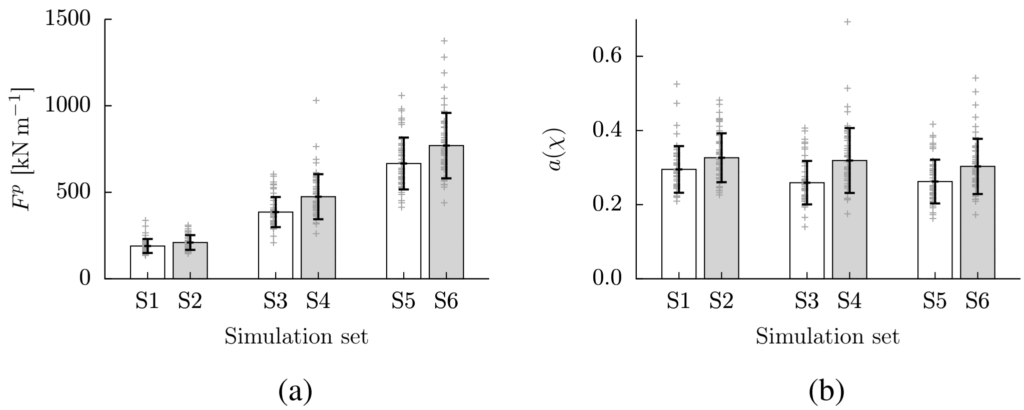

Fig. 4. The values of (a) maximum peak ice loads F^p from all simulations in sets S1 . . . S6 (see Table 2) and (b) dimensionless $a(\chi)$ values (see Equation 2) derived using all F^p data. The graphs show the mean values and standard deviations for the F^p and $a(\chi)$ data of each set.

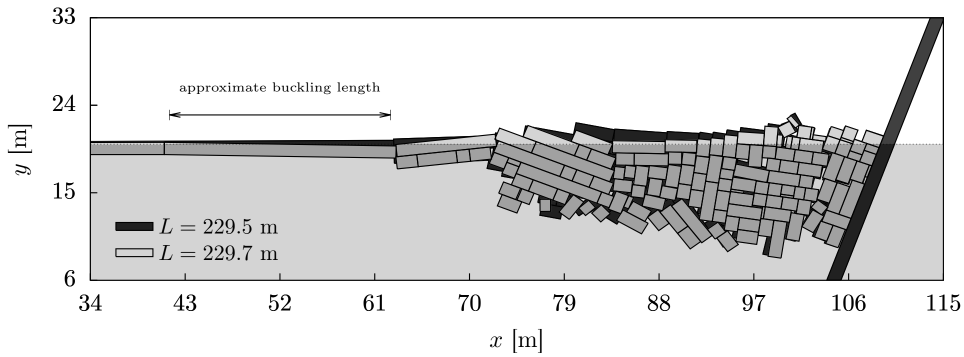

Fig. 5. This simulation reached F^p at $L = 229.5$ m. The figure also shows the model at $L = 229.7$ m (four seconds later). Buckling occurred at $x \approx 61$ m. The line in the figure illustrates the approximate buckling length. Here h and the plastic limit σ_p were 1.25 m and 2 MPa, respectively. Figure is from Ranta et al. (2018b).

described by Table 3.) The mean χ value for mode 1 was 1.32 ± 0.2, but χ factors for mode 1 are not shown in the figure, as this mode is physically unfeasible. It is justified to assume $L_f < L_c$, as the floes breaking off of the intact ice sheet in bending (occurring prior the peak load event) would have the length of about L_c at maximum. This means that χ should fulfill a condition $0 < \chi \leq 1$ (roots $\chi < 0$ are obviously not feasible).

The two horizontal lines of Figure 6a correspond to the χ values, which we calculated for the reported minimum (Lau et al., 1999) and maximum (Frederking, 1980) values for average breaking lengths of an ice sheet in a full-scale ice-structure interaction process (Li et al., 2003). Interestingly, almost all of the χ values resulting from the simulated ice-structure interaction processes fall between these limits, which gives confidence to both, our buckling and FEM-DEM, models.

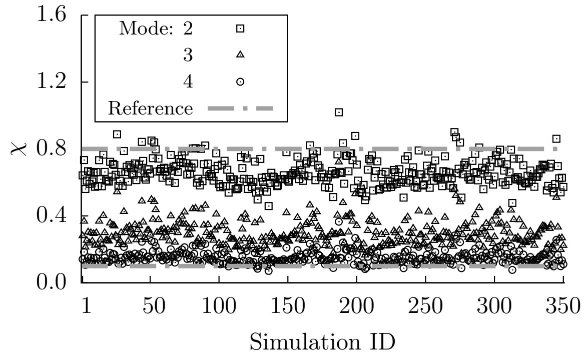

Fig. 6. The dimensionless χ factor values for buckling modes 2 and 4 of Table 3 using the $a(\chi)$ values of Figure 4b. The two horizontal dash-dot lines correspond to full-scale observations on maximum and minimum breaking lengths (Li et al., 2003). Figure is from Ranta et al. (2018b).

Conclusions

This paper has summarised the work by Ranta et al. (2018b) on the limits of the peak ice load values during a simulated sea ice failure process against an inclined rigid marine structure. The peak ice load data from ice-inclined structure processes was normalized with good accuracy by multiplying the load values with $1/\sqrt{h^3}$. This suggests that the peak ice loads in ice-inclined structure interaction process are governed by buckling. Our simplified buckling model quantifies the force chain buckling-related peak ice load values in an ice-inclined structure interaction process. The success of the model is due to it accounting for the individual ice floes in front of the structure. The buckling model predicts floe lengths, which match our observations. The floe lengths fall between the limits for observed ice floe lengths yielded by ice-structure interaction processes in nature.

Acknowledgements

The authors wish to acknowledge the support from the Research Council of Norway through the Centre for Research-based Innovation SAMCoT and the support from all SAMCoT partners.

References

Frederking, R. (1980). Dynamic ice force on an inclined structure. In *Physics and Mechanics of Ice. Tryde P. ed. IUTAM Symposium*, pages 104–116, Copenhagen.

Hetényi, M. (1979). *Beams on elastic foundation: Theory with applications in the fields of civil and mechanical engineering*. Ann Arbor: The University of Michigan Press.

Hopkins, M. (1992). Numerical simulation of systems of multitudinous polygonal blocks. Technical Report 92-22, Cold Regions Research and Engineering Laboratory, CRREL. 69 p.

Lau, M., Molgaard, J., Williams, F., and Swamidas, A. (1999). An analysis of ice breaking pattern and ice piece size around sloping structures. In *Proceedings of OMAE99, 18th International Conference on Offshore Mechanics and Arctic Engineering*, pages 199–207, St. John's, Canada.

Li, F., Yue, Q., Shkhinek, K., and Kärnä, T. (2003). A qualitative analysis of breaking length of sheet ice against conical structures. In *Proceedings of the 17th International Conference on Port and Ocean Engineering under Arctic Conditions, POAC'03*, pages 293–304, Trondheim, Norway.

Paavilainen, J. and Tuhkuri, J. (2012). Parameter effects on simulated ice rubbling forces on a wide sloping structure. *Cold Regions Science and Technology*, 81:1 – 10.

Paavilainen, J. and Tuhkuri, J. (2013). Pressure distributions and force chains during simulated ice rubbling against sloped structures. *Cold Regions Science and Technology*, 85:157 – 174.

Paavilainen, J., Tuhkuri, J., and Polojärvi, A. (2009). 2D combined finite–discrete element method to model multi-fracture of beam structures. *Engineering Computations*, 26(6):578–598.

Paavilainen, J., Tuhkuri, J., and Polojärvi, A. (2011). 2D numerical simulations of ice rubble formation process against an inclined structure. *Cold Regions Science and Technology*, 68(1-2):20–34.

Peters, J., Muthuswamy, M., Wibowo, J., and Tordesillas, A. (2005). Characterization of force chains in granular material. *Physical Review E - Statistical, Nonlinear, and Soft Matter Physics*, 72(4).

Ranta, J., Polojärvi, A., and Tuhkuri, J. (2016). The statistical analysis of peak ice loads in a simulated ice-structure interaction process. *Cold Regions Science and Technology*, 133:46–55.

Ranta, J., Polojärvi, A., and Tuhkuri, J. (2018a). Ice loads on inclined marine structures - virtual experiments on ice failure process evolution. *Marine Structures*, 57:72–86.

Ranta, J., Polojärvi, A., and Tuhkuri, J. (2018b). Limit mechanisms for ice loads on inclined structures: Buckling. *Cold Regions Science and Technology*, 147:34 – 44.

Ranta, J., Polojärvi, A., and Tuhkuri, J. (2018c). Scatter and error estimates in ice loads - results from virtual experiments. *Cold Regions Science and Technology*, 148:1–12.

Schreyer, H. L., Sulsky, D. L., Munday, L. B., Koon, M. D., and Kwok, R. (2006). Elastic-decohesive constitutive model for sea ice. *Journal of Geophysical Research*, 111(C11S26).

International Association for Hydro-Environment Engineering and Research
Supported by Spain Water and IWHR, China

24th IAHR International Symposium on Ice
Vladivostok, Russia, June 4 to 9, 2018

An Estimation of the Ice Resistance in the Oblique Condition

Hyun Soo Kim
Department of Naval Architecture and Ocean Engineering, Inha Technical College
Inharo100, Nam-gu, Incheon, Republic of Korea
hyunsookim@inhatc.ac.kr
Bumsu Go, Donghwa Han, and Jae-bin Lee
Department of Naval Architecture and Ocean Engineering, Inha University
Inharo100, Nam-gu, Incheon, Republic of Korea
rhqjatn8@naver.com, hdh7900@naver.com, beeny06@gmail.com

In general, studies on the ice resistance have been carried out for the breaking and clearing performance of the icebreaker. However, in the case of FPU (floating production unit) for resource development in the Arctic region, it is necessary to estimate the ice resistance in the oblique condition to ensure safety. Thus, although estimation of the ice resistance in the oblique condition is significant, there has not been enough research until recently. In this paper, we suggest algorithms for estimating the ice resistance in the oblique condition, and we used a pre-development program to estimate the ice resistance in the oblique conditions. The analysis results of the existing program for ice resistance were verified to be within 10% of the average error rate compared to the model test results. This paper shows results of the ice resistance which was calculated in the oblique condition, and the change of the ice resistance is shown according to various oblique angles in pack ice.

Introduction

Countries around the world are increasingly interested in resource development in the Arctic due to global warming. Recently, the Arctic coastal states (such as Russia, USA, and Canada) are pursuing infrastructure construction projects for resource development in the Arctic region. Because the offshore structures in the Arctic are exposed to the ice in the sea, to ensure the safety of the structures, the calculation of the ice resistance is of paramount importance for offshore structures. For this, it has been studying that estimation of the ice resistance which has the highest factor on the offshore structure among the external environmental conditions of the Arctic region.

According to the US Geological Survey (UGGS), the Arctic region is estimated to account for about 20% of the world's Undiscovered oil and gas exploration resources. For this reason, recently, interest in resource and exploration development in the Arctic region is increasing worldwide. In this environment, the floating offshore structure for deep water resource development needs location optimization, and it is necessary to apply dynamic position keeping control system and mooring system simultaneously.

To optimize the position keeping of floating offshore structures in ice environments, the ice loads in the sea are an essential factor and platform shapes with minimal load on the ice must be developed. To be estimated the ice resistance of a floating offshore structure for resource development in the Arctic region, the oblique conditions must be considered. However, estimation of the ice resistance using the empirical formula has been limited to the icebreaker. That is, estimation of the ice resistance using the empirical equation has been proposed under the condition that the propulsion direction and the axis of the icebreaker ship coincide with each other.

In this paper, a modified ice resistance empirical equation for calculating the ice resistance under the oblique condition is presented, and the ice resistance is estimated for the pack ice.

Approach for calculating the ice resistance

1. Total ice resistance

Estimation of the ice resistance algorithm within non-oblique condition for level ice is based on the Spencer (Spencer, 1992) estimation theory, and it is calculated as the linear sum of four independent ice resistance components as shown in the following equation [1].

$$R_{Total} = R_{Breaking} + R_{Clearing} + R_{Buoyancy} + R_{Openwater} \qquad [1]$$

where, the $R_{Buoyancy}$ is the buoyancy resistance caused by the buoyancy of the ice flowing below the hull, and the $R_{clearing}$ is the clearing resistance that occurs when pushing the pieces of ice present in the direction of the hull.

The $R_{breaking}$ is the ice breaking resistance which occurs when a flat ice plate is broken. The pack ice resistance is calculated without considering the $R_{breaking}$, and it can be expressed by the following Equation [2]. Since the Spencer empirical equation assumes the total ice resistance as a linear sum of the components of each ice resistance, therefore we define the resistance of the pack ice without considering the breaking resistance as in Equation [2]. In case of a hydrodynamic resistance ($R_{Openwater}$), it occupies a minimum impact in the total ice resistance and is not considered in this paper.

$$R_{Total} = R_{Clearing} + R_{Buoyancy} \quad [2]$$

2. Ice buoyancy resistance

To be calculated the ice buoyancy resistance, geometric information on the estimated object is extracted and applied to the empirical equation. Figure 1 is diagrams of the ship information for calculating the ice buoyancy resistance and are defined as Equation [3]. It is based on the empirical equation for estimating the ice buoyancy resistance of Enkvist (Enkvist, 1972).

$$R_{Buoyancy} = R_{sp} + R_{sf}$$

$$R_{sp} = \frac{\sum_0^{L/2} L_i \sum_0^B \rho_{\nabla} g h \bar{s} b_i}{L/2}, \quad R_{sf} = \sum_0^{L/2} L_i \sum_0^B f_g \rho_{\nabla} g h b_i \sin\beta \quad [3]$$

where, ρ_{Δ} represents the density difference between water and ice, L_i is the length between each section, b_i is the perimeter of each section, $\bar{s}$ represents the average depth of ice cubes immersed in water. h is the ice thickness, g is the gravitational acceleration, B is the breadth of the hull, and f_g is the coefficient of friction.

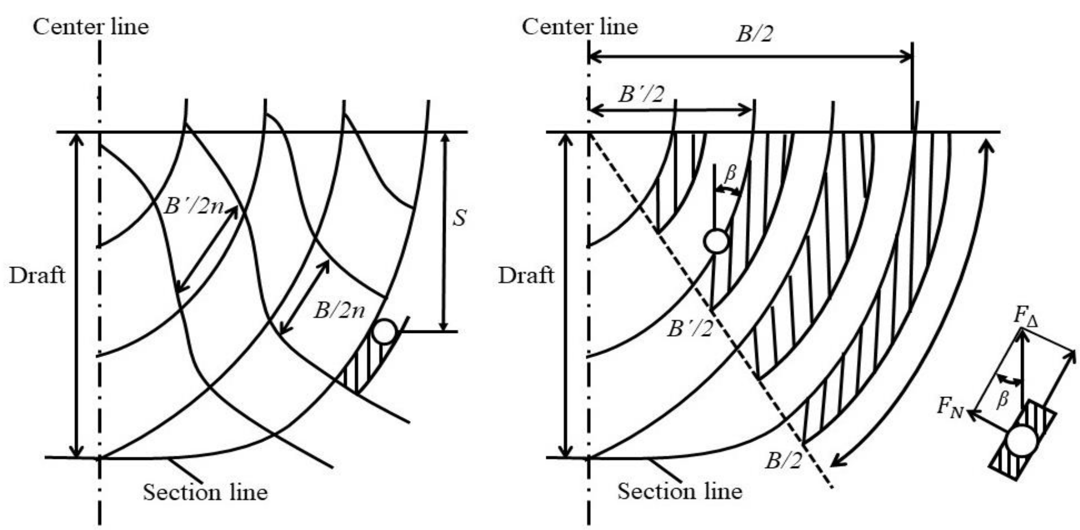

Fig. 1. Schematic of section line for buoyancy ice resistance

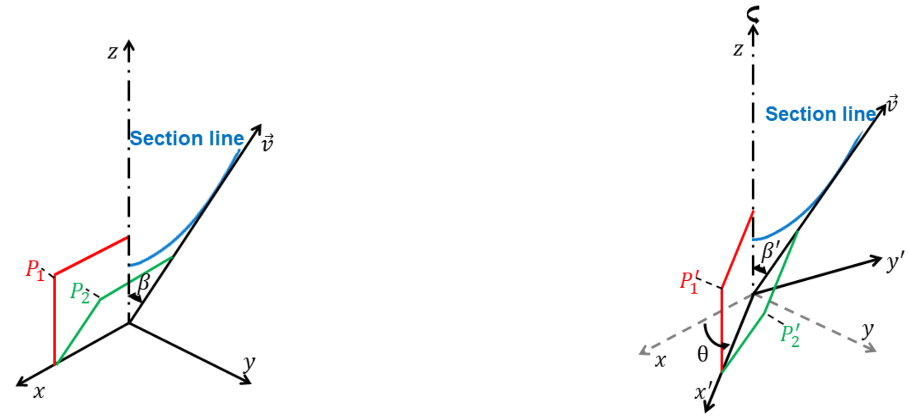

(a) Non-oblique condition (b) Oblique condition

Fig. 2. Schematic of β in oblique condition for buoyancy ice resistance

As shown in Figure 2, in case of applying the oblique condition, it is assumed that the β of the section line (perpendicular to the propulsion direction) applied to the buoyancy resistance is differently extracted and applied to the empirical formula. Figure 2 graphically shows that beta is differently extracted before and after application of angle. Figure 2(a) can be obtained by calculating the angle between the P_1 plane and the P_2 plane when the condition is non-conditional. On the other hand, Figure 2(b) shows the angle between the rotation-transformed P_1' plane and P_2' plane when the angle of rotation is the θ angle, and the calculated the β' can be derived.

3. Ice clearing resistance

The calculation for ice clearing resistance was applied as an empirical formula of Ionov (Poznyak and Ionov, 1981) as the following Equation [4], and it is schematized in Figure 3. The ice condition of Equation [4] is non-oblique that has been presented previously.

$$R_{Clearing} = 2\rho_i ghB \times Fr_B \left[K_3' \int_0^{L/2} \frac{\{y'(x)\}^2}{\cos\alpha} dx + K_3'' f_g \int_0^{L/2} \frac{y'(x)}{\cos\alpha} dx \right] \tag{4}$$

$$Fr_B = \sqrt{\frac{V_s}{g \cdot B}}$$

where, y is the length function representing the line breadth, ρ_i is the density of ice, h is ice thickness, f_g is the friction coefficient, and g is the gravitational acceleration. K_3' and K_3'' are 1.0 and 0.5, respectively.

Finally, Fr_B is the Froude number for the hull breadth, V_s is the ship speed, and B is the hull breadth. The ice clearing resistance cannot be calculated merely by applying an oblique angle like the ice buoyancy resistance. In the ice buoyancy resistance, there is no need to modify Equation [3] when considering the hull section information applied in Figure 2. That is, it is calculated by applying the changed β in consideration of the change of the reference axis (propulsion direction) with the oblique angle. To overcome this problem for ice clearing resistance, in this paper, we propose modified equation for ice clearing resistance based on the existing empirical equation as following Equation [5].

$$R_{Clearing} = 2\rho_i g h W_{max} \times Fr_B \left[K_3' \int_0^{L/2} \frac{\{y'(x)\}^2}{\cos\alpha} dx + K_3'' f_g \int_0^{L/2} \frac{y'(x)}{\cos\alpha} dx \right]$$

$$Fr_B = \sqrt{\frac{V_s \sin\theta}{g \cdot 2(W_{max} \sec\theta - L\tan\theta)}} \qquad [5]$$

$$W_{max} = L\sin\theta + 0.5B\cos\theta$$

Figure 3 shows the geometric hull information on the ice clearing resistance when rotating the waterline of the hull by θ at non-oblique conditions. In Figure 3, the W_{max} is the maximum length from the reference axis (propulsion direction) to the waterline of the hull at draft depth in oblique condition. The W_{max} in the oblique condition can be substituted for hull breadth B in non-oblique conditions as defined in Equation [5] ($W_{max}=L\sin\theta+0.5B\cos\theta$), and Froude number ($Fr_B$) is also defined as W_{max}. Meanwhile, at an arbitrary on the load waterline, the angle α with the reference axis (propulsion direction) is transformed to the angle α' by the oblique angle θ.

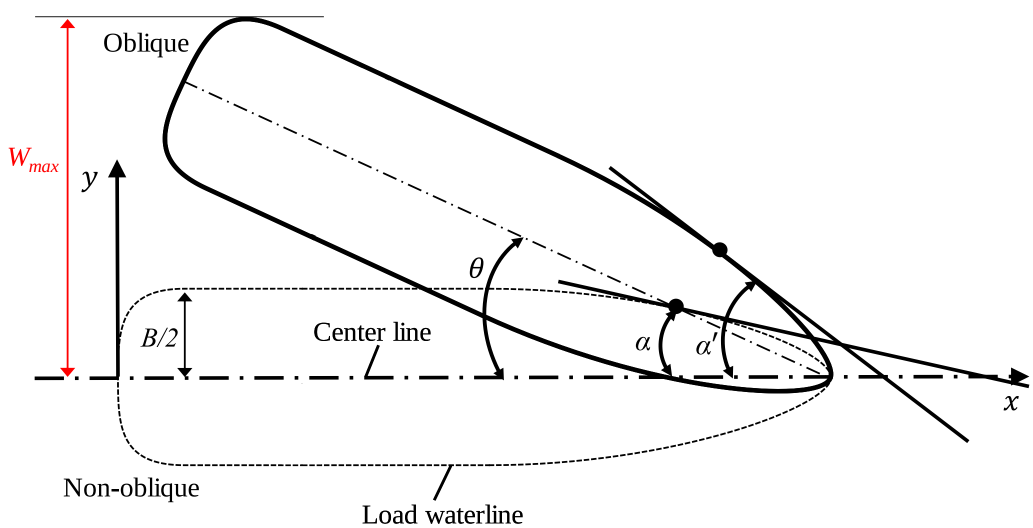

Fig. 3. Schematic of α' and W_{max} in oblique condition for the ice clearing and breaking resistance

Estimation of the Ice Resistance

The effect of each factor on ice clearing and buoyancy resistances were evaluated by calculating the ice resistance according to oblique angles in pack ice. Table 1 summarizes the analysis conditions of the oblique condition, and the FPU is used for the ice resistance estimation object, and the ice conditions are considered for pack ice (100% concentration). The oblique angles are estimated from 0° to 30° at 10° intervals, and ship speed is considered as 1.5 knots. As mentioned, in this paper, ice resistance is not considered to open water condition.

Table 1. Input variables for calculation of ice resistance in oblique condition

Items	values
Ship Speeds	1.5 knots
Flexural Strength	800 kPa
Ice Thickness	1.5 m
Elastic Modulus	2 GPa
Friction Coefficient	0.05 (Ice and Ship)
Density	880(ice), 1000(water) kg/m^3

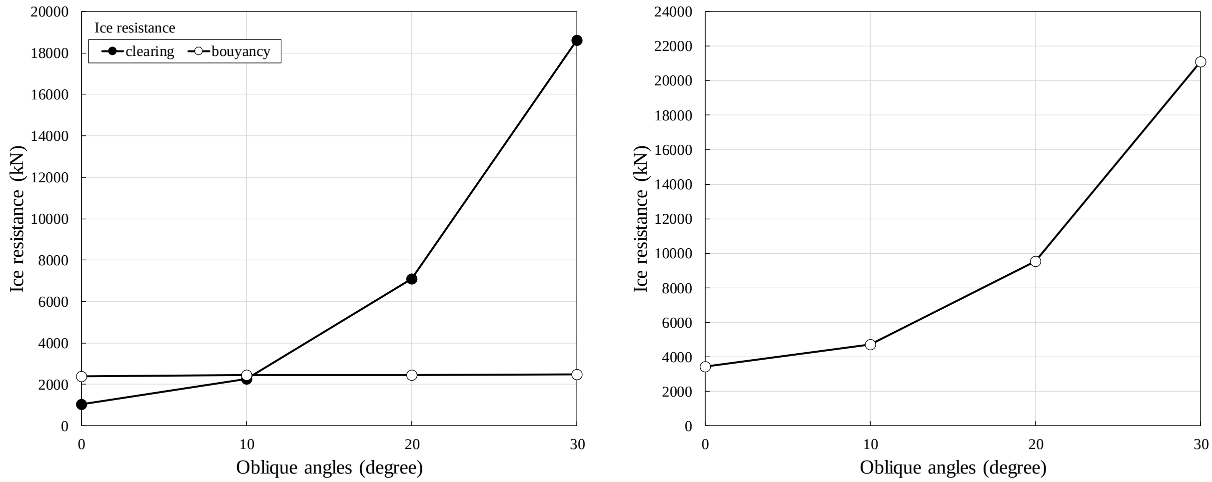

(a) Ice resistance components (b) Pack ice (100% concentration)

Fig. 4. The ice resistance with the oblique angles

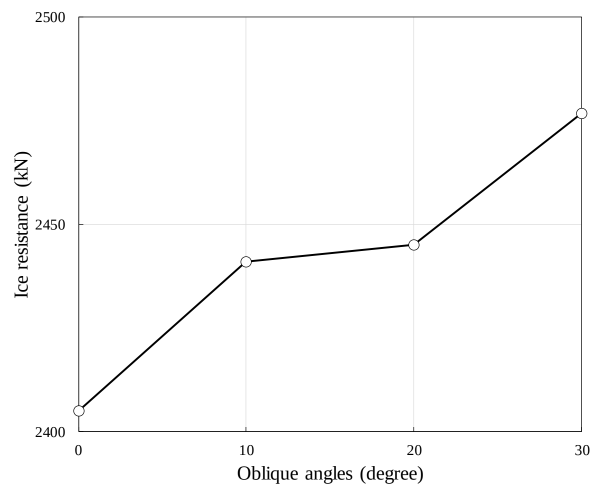

Fig. 5. The ice buoyancy resistance with the oblique angles

Figure 4 shows the ice resistance according to the oblique angle at 1.5 m of ice thickness and 1.5 knot speed. It is found that the total ice resistance increases nonlinearly with increasing oblique angle.

In Figure 4(a), the buoyancy resistance was evaluated to be higher than the clearing resistance and breaking resistance until the oblique angle of 10 degrees, but the tendency was reversed after 10 degrees. These tendencies are likely to be different if the ship speed and ice thickness are significant as a result of arbitrary ship speed and ice thickness. Also, the ice clearing resistance is largely increased nonlinearly with the oblique angle, and the rate of increase of the clearing resistance was calculated to be larger. Notably, when the oblique angle is 30 degrees, the ice clearing resistance is estimated to be about nine times higher than the ice buoyancy resistance. The variation of the buoyancy resistance according to the oblique angle was evaluated to be very small. It can be seen that the influence of the change of the section line according to the oblique angle on the resistance value is small. The buoyancy resistance of Figure 4(a) is shown in Figure 5, and the variation of the buoyancy resistance according to the oblique angle can be confirmed more clearly. In Figure 4 (b), the ice resistance for pack ice (100% concentration) was evaluated as the sum of the ice clearing and buoyancy resistance.

Conclusion

In this paper, to estimate the ice resistance of the oblique condition, a new equation is presented by modifying the existing empirical equation and applied to the FPU ship to estimate the ice resistance according to the oblique angle. We calculated the ice resistance according to an oblique angle to evaluate the effect of oblique condition on the ice resistance component. The clearing resistance was estimated to have the most significant effect on the oblique angle, and the buoyancy resistance was the smallest. The ice resistance for pack ice had nonlinearity depending on the oblique angle. It is concluded that the model test is needed to verify the ice resistance using the proposed modified equation for ice resistance. Lastly, this study can be useful to the position keeping of floating offshore structures in ice environments.

Acknowledgments

This research is supported by “Development of hull form of year-round floating-type offshore structure based on the Arctic Ocean in ARC7 condition with dynamic positioning and mooring system” through the Ministry of Trade, Industry, and Energy(MOTIE) (10063405, 2018).

References

Enkvist, E., 1972. On the Ice Resistance Encountered by Ships Operating in the Continuous Mode of Icebreaking. The Swedish Academy of Engineering Sciences in Finland 24.

Poznyak, I.I. and Ionov, B.P., 1981. The division of icebreaking resistance into components, proceeding of the 6th STAR Symposium. New York U.S., 249-252.

Spencer, D., 1992. A Standard Method for the Conduct and Analysis of Ice Resistance Model Tests. Proceeding of the 23rd American Towing Tank Conference, New Orleans U.S., 301-307.

Shimanskii and Yu.A., 1938. Conditional standards of ice qualities of a ship. Engineering Consulting and Translation Center (ECTC), New York.

IAHR AIRH International Association for Hydro-Environment Engineering and Research
Supported by Spain Water and IWHR, China

24th IAHR International Symposium on Ice
Vladivostok, Russia, June 4 to 9, 2018

Experimental and Theoretical Considerations on Water Depth and Force on Onshore Structures Driven by Run-Up Tsunami Wave in Ice-Infested Waters

Shinji KIOKA and Maiko ISHIDA
Civil Engineering Research Institute of Hokkaido
Hiragishi 1-3-1-34, Toyohira-ku, Sapporo, 062-8602, Japan
kioka@ceri.go.jp
Takahiro TAKEUCHI
Hachinohe Institute of Technology
No.88-1, Oobiraki, Myo, Hachinohe, Aomori, 031-8501, Japan
take@hi-tech.ac.jp

Sea ice carried to land by tsunamis has been reported to cause serious damage to private houses and bridges from the impact of the ice floes (e.g., in the 1952 Tokachi-Oki Earthquake). In this study, some new experimental results and theoretical considerations were added to reexamine the phenomena of run-up tsunamis containing ice in addition to our previous studies.

We suggested the following mechanisms/processes behind the action of force caused by a tsunami with ice. After the collision force imparted by the ice floes acts on structures, the tsunami flow is blocked by the formation of ice jams between the structures, and a large static force also acts on the structures because of the ice jam formation. Even after the water subsides, horizontal force caused by ice pile-up, such as active earth pressure, remains. It was confirmed that the active pressure and the residual force could be estimated by Rankine's earth pressure theory when ice fragments were regarded as Mohr-Coulomb materials. A simple theoretical model was developed to estimate the water depth and the tsunami force on structures caused by tsunami run-up flow using only a parameter as the open ratio instead of structure width and pitch, which was modeled by analogy to the occurrence of a negative bore caused by the sudden closing of a sluice gate. The validity of the simple theoretical model was also confirmed by the further experimental results in this study. It was also found that, when the ice jam formed, although there was dispersion in the water depth in front of the structures and there was no clear difference between the open ratios, the water depth was roughly the same value as that in the case with less than 0.3-0.4 of the open ratio under a no-ice.

1. Introduction

If a tsunami arrives at the coast in ice-infested waters, run-up waves carrying ice may cause greater damage than a tsunami without ice due to their static and/or dynamic action occurring in ice-floe-laden flows. A tsunami with sea ice floes has been reported to cause serious damage to private houses and bridges from the impact of the ice floes (e.g., in the 1952 Tokachi-Oki Earthquake). Run-up of sea ice to the shore and of river ice along rivers along with some minor damage to land structures caused by ice collisions were also confirmed during the 2011 Great Tohoku Tsunami on the coast of the Kuril Islands (Kaistrenko et al., 2012). Sea ice run-up, river ice collision with sluice gates, water surface elevation caused by ice-related blockages (ice jams) and other phenomena also have been observed in Japan (Yoshikawa et al., 2012, Abe et al., 2014). Accordingly, there is an urgent need for studies and measures concerning inundation flow caused by ice-carrying tsunamis (for evacuation facilities, etc.). We have so far conducted a model experiment involving onshore run-up of a tsunami containing sea ice floes with focus on ice jams and pile-up formations between structures, and examined tsunami loads acting on structures and water depths around structures in conditions with and without ice (Kioka et al., 2015, 2016). The collision force and fracture mechanism of sea ice were also studied through medium-scale experiments and numerical calculation (Kioka et al., 2010, 2012). In addition, a quasi-three-dimensional DEM of a run-up tsunami with ice floes was developed with consideration of vertical motion to simulate pile-up and ice jam formations, and an example of simulation results was presented [Kioka et al.,2016]. Although this simulation method is still in the development stage, it was expected to be useful in the formulation of disaster mitigation plans including hazard maps (e.g., structure arrangement, evacuation plans). While this paper reviews the results of a previous model experiment on run-up tsunamis containing ice, some new experimental results and theoretical considerations were added to reexamine the phenomena of run-up tsunamis.

2. Model Experiment on Run-up Tsunami

2.1 Experimental Method and Conditions

Although the experimental method is the same as the previous study [Kioka et al., 2015], it is described briefly here. As shown in Fig.1., a tsunami was generated by quickly opening the gate as in a dam-break, under the condition where sea ice floes drifted ashore, which then ran up to level land after propagating up a uniform slope of 1/20 (scale: 1:100). Several prism-shaped structures were lined up horizontally on land. The water storage depth (h_{0u}) on the upstream side of the gate (0.12-0.22m), and the width W (2-8cm) of and interval B (4-15cm) between structures were changed. The ice floe models were made from rectangular polypropylene plates (Kunimatsu et al., 1993) whose sides ranged from 1.5 cm to 10 cm in length with thickness of 5 mm. These were arranged such that the average side length was equivalent to 3 cm (3m in full scale). Although the

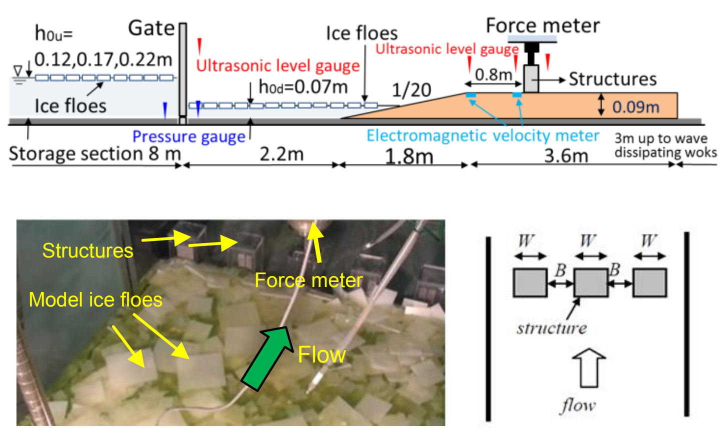

Fig. 1. Experimental setup

density and the dynamic friction coefficient of the model ice are roughly the same as those of natural sea ices, the fracture strength and the elastic modulus of the model ice do not match dynamically at full scale. Therefore, evaluation of the collision force imparted by the ice floes was excluded. The collision force and fracture mechanism of ice were examined separately through a medium-scale experiment and numerical calculation (Kioka et al., 2010, 2012).

2.2 Fundamental mechanisms of run-up tsunami with ice floes

We suggested the following mechanisms/processes behind the action of force caused by a tsunami with ice [Kioka et al, 2015, 2016]: After the collision force imparted by the ice floes acts on structures, the tsunami flow is blocked by the formation of ice jams between the structures, and a large static force also acts on the structures because of the water level rise and hydrostatic pressure on the gaps between the structures (inter-structural spaces) due to the ice jam [see Fig.2, 3].

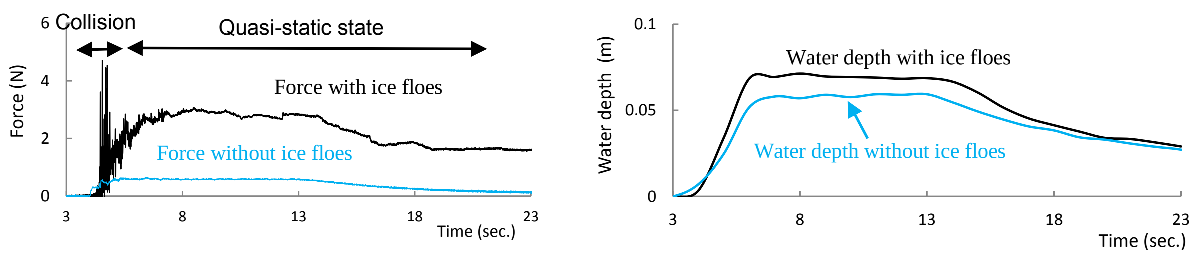

Fig. 2. An example of time-history of water depth in front of the structure and streamwise force on the structure under ice-jam formation, and a comparison with those without ice floes (W=4cm, B=9cm, h_{0u}=17cm)

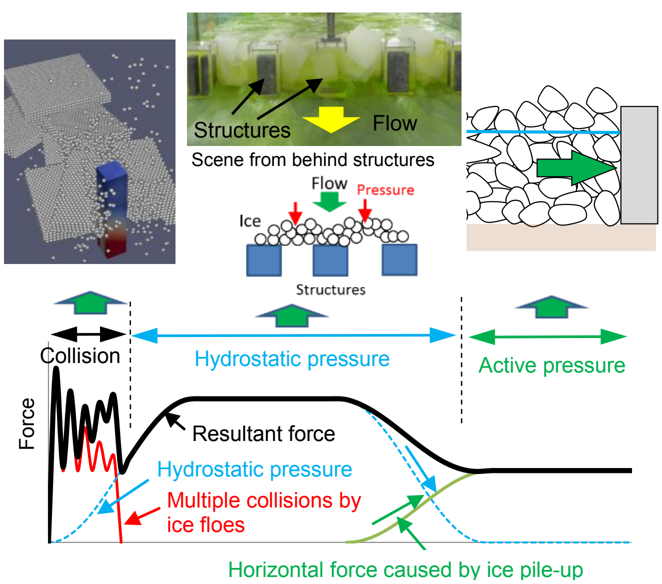

Fig. 3. Model for action process of tsunami force with ice floes

Thus, in addition to the collision force, the presence of a large static force over a long time could also become a threat against structures. In the past, the ice jams that formed between the legs of jacket type oil platforms caused the platforms to collapse due to the increase in drag force (Wang, 1983). However, the water level rises to a certain degree caused by a group of structures even in the case of flow without ice floes, as shown in Fig.2. Even after the water subsides, horizontal force caused by ice pile-up, such as active earth pressure, remains. Fig.3 outlines the concept behind the action of force with ice. In the end, the tsunami force with ice floes is the resultant force of i) collision, ii) hydrostatic force and iii) active forces as indicated by the thick line in Fig.3.

2.3 Active pressure caused by ice pile up

As in the previous section, active pressure generates by pile-ups and ice floes to replace hydrostatic force in accordance with the reduced water level (reduction of buoyancy acting on ice floes), eventually resulting in a continued steady residual force (at zero water level) as shown in Fig.3. Here, from the analogy of earth pressure, let us apply Rankine's earth pressure theory to the mechanical model when ice fragments are regarded as Mohr-Coulomb materials (see Fig.4). As shown in Fig.4, the pressure distribution by ice pile-up is assumed to be as follows. While the pressure increases linearly toward the water surface (triangular distribution) above water, it also increases linearly toward the water surface below water (trapezoid distribution) due to the buoyancy of ice floes. The resultant force on a structure caused by the active pressure in the gap between adjacent structures can be shown as Eq. (1).

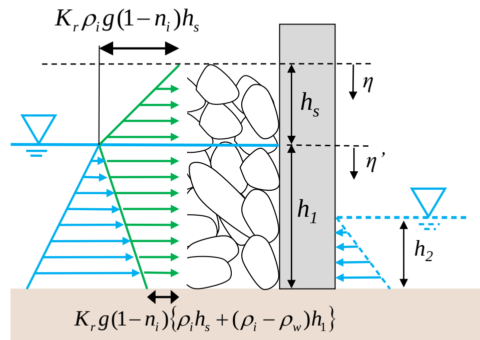

Fig. 4. Mechanical model for active pressure by ice pile-ups

$$F_{ip} = (W+B)\left[\int_0^{h_s} K_r \rho_i g(1-n_i)\eta d\eta + \int_0^{h_1} K_r g(1-n_i)\{\rho_i h_s + (\rho_i - \rho_w)\eta'\}d\eta'\right]$$
$$= (W+B)\frac{K_r g(1-n_i)}{2}\left\{\rho_i (h_1 + h_s)^2 - \rho_w {h_1}^2\right\} \qquad [1]$$

where, ρ_i and ρ_w represent the density of ice and water, respectively. h_1 and h_2 represent the water depth upstream and downstream from the structures and h_s is the pile-up height above the water surface, respectively. ϕ_i and n_i represent the internal friction angle and the void ratio, respectively, when the ice fragments are regarded as Mohr-Coulomb materials. K_r is the coefficient of the active earth pressure as shown in the following equation.

$$K_r = \tan^2(45 - \phi_i / 2) \qquad [2]$$

In the end, the hydrostatic pressure upstream and downstream from the structures is added to the total force acting on the structure.

Fig.5 shows examples of a time-history of force on the structure and their comparisons with calculated values using the above formula when ϕ_i and n_i are assumed to be 30 deg. and 0.3, respectively. From this figure, it can be assumed that the active pressure generated by ice pile-ups replaces the hydrostatic force in accordance with the reduced water level.

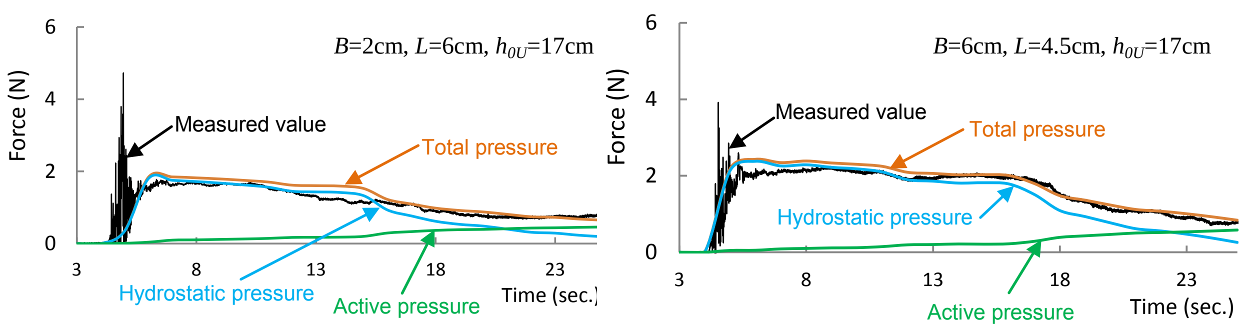

Fig. 5. Examples of stream wise force on the structure under ice-jam formation and their comparisons with the theoretical forces during static state

The theoretical total forces during the quasi-static state caused by the active and hydrostatic forces agree well with the measured forces. Accordingly, the above formula or the basic concept of active pressure - the forces caused by hydrostatic pressure, active pressure and their total pressure - by ice pile-up are considered appropriate. Even after the water subsides, a certain level of active pressure caused by ice pile-up remains. Accordingly, we also have to continue to be alert to the steady residual force even after the tsunami recedes.

3. A simple theoretical model for estimating the water depth and the tsunami force on structures caused by tsunami run-up flow in conditions with and without ice

We have introduced just one parameter, "*open ratio,*" instead of structure width (W) and pitch (B) for the case of some prism-shaped structures arranged in a row on land, and developed a simple theoretical model that uses the open ratio for estimating the water depth and the tsunami force in the steady state caused by dammed tsunami flow by a group of structures in addition to ice jam formation [Kioka et al.,2015]. In this study, we added further experimental results (the test case of B=6cm) to revalidate the theoretical model, and characteristics of the water level rise under the ice jam formation were also reexamined. This phenomenon can be modeled by analogy to the occurrence of a negative bore caused by the sudden closing of a sluice gate as shown in Fig.6. When the run-up flow is dammed by the structures, part of the flow exits through gaps between the structures, and the remaining part of the flow propagates upstream as a hydraulic bore. We now consider the domain between the centers of two adjacent structures (B_1) in the model, assuming that the flow velocity (v_2) and the water depth (h_2) between the structures are uniform. While v_1 and h_1 represent the mean velocity and the water depth in front of the structures, respectively, v_0 and h_0 respectively represent the mean velocity and the initial run-up water depth in the case without structures. Also, w is the wave velocity of the negative bore, and P_1, P_2 and P_e are the hydrostatic pressures in each section and in the sudden contraction of the channel, respectively. We assume that the fluid body between the upstream and downstream including the bore upstream from the structures (dotted line) moves to the domain indicated by the heavy line after a time of δt, and the laws of conservation of mass and momentum for the fluid body can be expressed as shown in Eqs. (3) and (4), respectively. The subscript I and II indicate the state of the fluid at a time of t and after a time of δt, respectively.

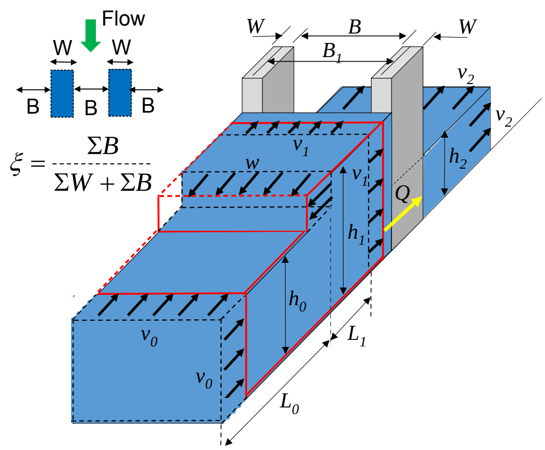

Fig. 6. Simplified hydraulic model

$$\int_{V_I} \rho_w dV = \rho_w (h_1 L_1 + L_0 h_0) = \int_{V_{II}} \rho dV = \rho_w \{ (L_1 + w\Delta t + v_1 \Delta t) h_1 + (L_0 - v_0 \Delta t - w\Delta t) h_0 \} \quad [3]$$

$$\begin{aligned} \delta M &= \int_{V_I} \rho_w v_I dV - \int_{V_{II}} \rho_w v_{II} dV \\ &= \rho_w \left[(L_1 + v_1 \delta t) h_1 v_1 + (L_0 - v_0 \delta t) h_0 v_0 + w \delta t (h_1 - h_0)(-w) - \left(L_1 v_1 h_1 + L_0 v_0 h_0 \right) \right] \\ &= \delta t \sum F = \frac{\rho_w g}{2} \left(h_0^2 - h_1^2 \right) \delta t \end{aligned} \quad [4]$$

The laws of conservation of mass and momentum of the fluid between the upstream and the downstream from the structures are simplified as shown in Eqs. (5) and (6), respectively.

$$Q = B_1 v_1 h_1 = B_2 v_2 h_2 \quad [5]$$

$$\rho_w Q (v_2 - v_1) = P_1 - P_2 - P_e = B_2 \frac{\rho_w g}{2} \left(h_1^2 - h_2^2 \right) \quad [6]$$

The volume flowing from the gaps between the structures (Q) is assumed to be equal to the product of the inflow ($v_0 h_0$) and the rate of f depending on the open ratio of ξ as shown in Eq. (7).

$$Q = f(\xi) B_1 v_0 h_0 \quad [7]$$

where, $\xi = \Sigma B / (\Sigma B + \Sigma W)$, $\quad f(0) = 0$, $\quad f(1) = 1$

If we introduce the relations as in Eq. (8), Eq. (9) for the water depth h_1 as λ can be obtained from the above equations.

$$f(\xi) = \xi^n, \qquad \lambda = h_1 / h_0, \qquad Fr = v_0 / \sqrt{g h_0} \quad [8]$$

$$\lambda^4 - \lambda^3 - (1 + 2Fr^2)\lambda^2 + (1 + 4Fr^2 \xi^n)\lambda - 2Fr^2 \xi^{2n} = 0 \quad [9]$$

Also, we have the following equation for h_2 as λ_d ($=h_2/h_0$) when B_2/B_1 can be regarded as ξ.

$$\lambda_d{}^3 - \left[\lambda_d{}^2 + \frac{2Fr^2 \xi^{2n-1}}{\lambda} \right] \lambda_d + 2Fr^2 \xi^{2n-2} = 0 \quad [10]$$

Fig. 7 shows the relationship between the open ratio ξ and the water depths upstream and downstream under the steady state and their comparisons with calculated values in the cases of n=1.3 and Fr=0.9, respectively. When ice floes do not exist, h_1 increases and h_2 conversely decreases with a decrease in ξ, and h_1 or h_2 takes the same value if ξ becomes the same value regardless of any combination of W and B (or regardless of each value of W or B) (see Fig.7 (a)).

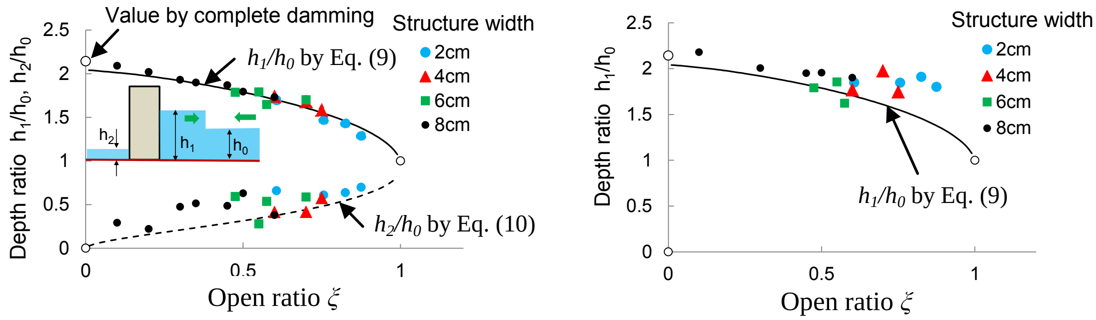

(a) the case without ice floes (b) the case with ice floes

Fig. 7. The relationship between the open ratio ξ and the water depths upstream and downstream under the steady state and their comparisons with calculated values

Therefore, we can assume that unified description by ξ can be possible. While the result calculated by Eq. (9) for h_1 agrees well with the trend of experimental values, that for h_2 gives a slight underestimation and there are still issues to be solved to improve the model for h_2. When the ice jam forms, although there is dispersion in h_1 and there is no clear difference between the open ratios, h_1 is roughly the same value as that in the case with less than 0.3-0.4 of ξ under a no-ice condition (see Fig.7 (b)). The same theoretical curve of h_1/h_0 as in case where ice floes do not exist is also indicated in Fig.7 (b). The gaps between the structures are not completely blocked even though the ice jam forms, and the patterns of the ice jams, which also vary even under the same experimental conditions, would also influence the water depth. This may correspond to the fact that there are no clear differences in h_1 between ξ as shown in Fig.7 (b) once an ice jam forms.

Next, let us estimate the force on the structure under the steady condition. As mentioned above, since this force is caused by the hydrostatic pressure, the force in the case without ice floe, which is normalized by W and h_0, can be expressed as follows.

$$F/\rho_w gWh_0^2 = \frac{1}{2}\left\{(h_1/h_0)^2-(h_2/h_0)^2\right\}=\frac{1}{2}\left(\lambda^2-\lambda_d^2\right) \qquad [11]$$

where, the water depth behind the structures was assumed to be h_2. When the ice jam forms, the force is the resultant force caused by the hydrostatic pressure and the active pressure due to the ice pile-up considering their pressures on the gap between the adjacent structures (inter-structural spaces). Although the estimation of the water depths upstream and downstream from the structures under the steady state will be left as a future issue, if we use the water depth in the case without ice as a lower limit, the normalized lower limit force by W and h_0 will be,

$$F/\rho_w gWh_0^2=\frac{1}{2}\frac{1}{1-\xi}\left[\left(\lambda^2-\lambda_d^2\right)-K_r(1-n)\left\{\frac{\rho_i}{\rho_w}\left(\lambda+\frac{h_s}{h_0}\right)^2-\lambda^2\right\}\right]\approx\frac{1}{2}\frac{1}{1-\xi}\left(\lambda^2-\lambda_d^2\right) \qquad [12]$$

In the steady state, the active pressure can be ignored as shown in Fig.5 because sufficient buoyancy acts on ice floes. Accordingly, we consider only the hydrostatic pressure in Eq. (12).

If we assume complete wall-like blockages in inter-structural spaces as the upper limit, the force can be obtained by substituting the solution in Eq. (9) that assumes ξ=0 for λ and by substituting zero for λ_d in Eq. (10). Fig.8 shows the relationship between ξ and the streamwise forces on the structure under the steady state and their comparisons with calculated values, and this figure corresponds to Fig.7. When ice floes are not present, the calculated value of the force by Eq. (11) agrees well with the trend of experimental values. Also, even when ice jams form, the experimental values fall between the upper limit and the lower limit. Therefore, the validity of the simple theoretical model that includes the water depths as mentioned above can be verified. The difference in the forces between the conditions with versus without ice floes becomes large for a greater ξ. Thus, when an ice jam forms, we also should take into consideration the static load acting on a structure caused by the hydrostatic pressure exerted on the gaps between the structures, which will increase for a greater ξ. However, although it is presumed difficult for ice jams to form with an increase in ξ, such conditions of ice jam formation remain issues to be addressed in the future.

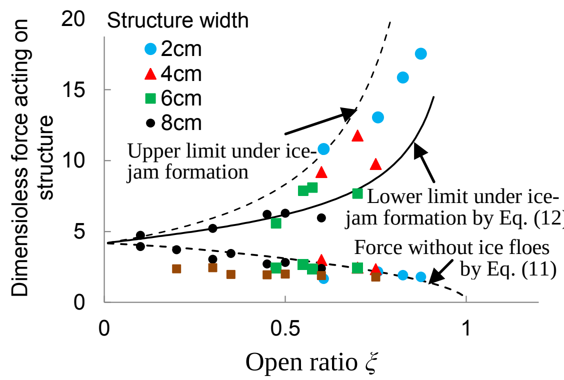

Fig. 8. The relationship between ξ and the streamwise forces on the structure under the steady state and their comparisons with calculated values

Thus, the validity of the simple theoretical model was also confirmed by the further experimental results in this study.

4. Conclusions

While this paper reviewed the results of a previous model experiment on run-up tsunamis containing ice, some new experimental results and theoretical considerations were added to reexamine the phenomena of run-up tsunamis.

We suggested the following mechanisms/processes behind the action of force caused by a tsunami with ice. After the collision force imparted by the ice floes acts on structures, the tsunami flow is blocked by the formation of ice jams between the structures, and a large static force also acts on the structures because of the water level rise and hydrostatic pressure on the gaps between the structures (inter-structural spaces) due to the ice jam. Even after the water subsides, horizontal force caused by ice pile-up, such as active earth pressure, remains. Accordingly, we also have to continue to be alert to the steady residual force even after the tsunami recedes. It was confirmed that the active pressure by ice pile-up could be estimated by Rankine's earth pressure theory when ice fragments were regarded as Mohr-Coulomb materials. A simple theoretical model was developed to estimate the water depth and the tsunami force on structures caused by tsunami run-up flow without ice using only a parameter as the open ratio instead of structure width and pitch, which was modeled by analogy to the occurrence of a negative bore caused by the sudden closing of a sluice gate. The validity of the simple theoretical model was also confirmed by the further experimental results in this study.

In the future, while we will take into consideration various shapes of structures and several arrays of the structure, we also plan to investigate the detailed conditions of ice-jam formation.

5. References

Abe, T., Yoshikawa, Y., Satoh, Y., Itoh, A. and Yamaguchi, S., 2014. Research on the effects of river tsunami with ice floes on structures, Proc the 22nd IAHR International Symposium on Ice, 671-678.

Kaistrenko, V., 2013. Manifestation of the 2011 Great Tohoku Tsunami on the Coast of the Kuril Islands: A Tsunami with Ice, Pure Appl. Geophys., 170 (6-8), 1103-1114.

Kioka, S., Yamamoto, Y., Sugawara K., Endo, T. and Takeuchi, T., 2010. Medium-scale Experiment and Numerical Simulation using 3-D DEM for the Impact Load by an Ice Floe against a Pile Structure, Proc. 20th IAHR International Symposium on Ice, 110.

Kioka, S., Takeuchi, T. and Kanie, S., 2012. Medium-scale Experiment and Numerical Simulation for the Impact Load by an Ice Floe against a Pile Structure, J. JSCE, Ser. A2 (Applied Mechanic), 68(2), 423-432.

Kioka,S., Takeuchi, T. and Watanabe, Y.,2015. Characteristics of Sea Ice floes Run-up caused by Tsunami Considering Ice Jams and Ice Pile-ups around Structures, Proc. 25th International Offshore and Polar Engineering Conference (ISOPE), 3, 778-782.

Kioka, S., Takeuchi, T. and Maruta, N. 2016. Fundamental Study for Physical Experiments and Numerical modelling of Ice-Jams and Ice Pile-ups Driven by Run-Up Tsunami Wave, Proc. 23th IAHR International Symposium on Ice.

Wang, Q.J., 1983. A Tentative View on Ice Load Applied on Jacket Platforms in Bo-hai Gulf, Proc. International Conference on Port and Ocean Engineering under Arctic Conditions (POAC), 2, 930-939.

Yoshikawa, Y., Abe, T. and Hirai, Y., 2012. Simulation of Ice Jam generated by Tsunami in the Mu River, J. JSCE, Ser. B2 (Coastal Engineering), 68 (2), 416-420.

International Association for Hydro-Environment Engineering and Research
Supported by Spain Water and IWHR, China

24th IAHR International Symposium on Ice
Vladivostok, Russia, June 4 to 9, 2018

Verification of Ice Measurement Data by SWIP and ADCP and Observation of River Ice Time Series Behavior in Teshio River

Masahiro HASHIBA[(1)],Yasuhiro YOSHIKAWA[(2)],Hiroshi YOKOYAMA[(3)]
1) Fukuda Hydrologic Centre, Hokkaido,Japan e-mail (hashiba@f-suimon.co.jp)
2) Kitami institute of technology,Hokkaido,Japan e-mail (yoshi@mail.kitami-it.ac.jp)
3) Civil Engineering Research Institute for Cold Region, Hokkaido, Japan
e-mail (yokoyama-h22ab@ceri.go.jp)

This study aimed to analyze field data on the behavior of river ice and hydraulic phenomena during river ice breakup collected using non-contact acoustic devices of SWIP (Shallow Water Ice Profiler), ADCP (Acoustic Doppler Current Profiler) and Echo-Sounder.
Firstly, we conducted an experiment with a large water tank (height 2.44m, capacity 10.65m^3) in order to check the accuracy of these acoustic devices. To simulate the large water tank into the ice-covered river, 1) we set the ice block which was 0.15m thickness on the surface and 2) we set the snow which was adjusted low density(0.375g/cm^3) and high density(0.482g/cm^3) under the ice block as a pseudo frazil ice. We measured between top of the device and bottom of the ice in the tank at an interval of 0.2 m from bottom to pseudo ice using an auto elevating the acoustic device set upward. We compared with direct measured length and each device measured length. In the experimental results, regardless of the type of acoustic device, direct measured length and device measured length were almost same and standard deviations were from 0.03 to 0.04 m. Also, regardless type of these devices, it was showed that measured border of ice was the bottom of ice sheet or frazil ice regardless density. Secondary, in the field study, we observed the behavior of river ice and hydraulic phenomena seen in the Teshio River using SWIP and ADCP. It was found that the rising of water levels during ice breakup tended to lag behind the maximum flow rate because of ice accumulation as well as ice jams formed in the upstream part of the river. A phenomenon was observed in which ice fragments and frazil that were formed upstream and flowed downstream moved under river ice. It was found that the Froude number under ice-covered conditions remains at about 0.1, and that the coefficient of roughness tended to decrease because of changes in river ice thickness. Based on analysis of the field data collected, we proposed the possibility that ice-transport capacity could be described using a dimensionless flow strength formula.

1.Introduction

The water level of river is important observation data for river administrator to manage flood management, water source, and river environment. The water level of river is influenced by river runoff, channel cross-sectional shape, and riverbed roughness. Also, the water level of the ice-covered river is affected by the change in the cross sectional area due to river ice and the change of roughness of the river ice. In particular, the water level of a river fluctuates greatly at the early stage of freezing and at the time of breakup. For this reason, it is important for river administrators to know the ice movement of rivers. Regarding past study, acoustic instruments (ADCP, SWIP and Echo sounder) which were installed riverbed were possible to measure continuously river ice thickness. These studies showed that noncontact acoustic instruments were effective for measurement of river ice, but quantitative accuracy verification of each acoustic instrument has not been done. In addition, the continuously field observation data at the time of ice-covered river was necessary because there were few cases of past research.

However, it was hard to observe enough at the time of breakup because of danger.

In this study, we carried out accuracy verification noncontact acoustic instruments in the experiment using big tank. In addition, we carried out field observation using these instruments installed on the riverbed during ice-covered period. The authors compared and verified the obtained observation data and the past research results and examined the hydraulic phenomenon at the time of deicing and the behavior of river ice.

2.Experiment of quality assurance of acoustic instruments

a) Acoustic instruments

SWIP (Shallow Water Ice Profiler, 546kHz, ASL Environmental Sciences) is an instrument that measures accumulation of ice bottom surface and frazil ice from ultrasonic back scattering intensity. ADCP (Acoustic Doppler Current Profiler, WorkHorse Sentinel 1200kHz, Teledyne RD Instruments) is an instrument that measures the flow velocity of each set layer from ultrasonic beam doppler shift. In addition, it has a bottom tracking function for measuring the distance from the target and the relative speed, and the change points of backscattering intensity to estimate the density difference. A single beam acoustic sounder (PS-20R type 200kHz, Kaijo Co., Ltd.) is a device that measures distance from the instrument to the target with vertical single beam.

b) Structure of experimental apparatus

Figure 1 shows the outline of the large tank. The height 2.44m× width 2.00m × depth 2.18m, capacity 10.65m^3. This size was considering the ultrasonic wave of the ADCP irradiation angle 20° not directly striking the wall surface. In order to observe inside the water tank by using a clear vinyl chloride plate of 20 mm thick on the front side and to prevent abnormal echoes of the ultrasonic wave, the material to be used was made of wooden 2.4 cm thick water resist veneer plywood. The instruments were installed on a stand which can be stopped at any depth by electric winch along the guide rails in the large tank.

In addition, a water level gauge (North-one KADEC 21-MIZU Accuracy ± 2 cm: 0.1% F.S / 20 m) was installed on the stand to be used for verifying depth of equipment. Before the start of the experiment, we added crushed ice into the large tank to keep under the 4℃ to be closer to the temperature in actual river.

c) Experimental materials

As shown in Table 1, the experimental materials were made under five conditions combining water, ice sheet and frazil ice (low density, high density). The ice sheet was placed with 50 × 50 × 30 × 15 cm thick plate-shaped ice on the surface of the water without gaps. Frazil ice (low density) was installed in a thickness of about 40 cm under the water surface without shaping or compressing the snow accumulated naturally. The ice sheet + frazil ice has two layers of plate-shaped ice with a thickness of 15 cm in the upper layer and frazil ice (low density) with a thickness of 40 cm in the lower layer. In the ice sheet + frazil ice (high density) + frazil ice (low density), plate ice of 15 cm thick in the upper layer, frazil ice (high density) 40 cm thick in the middle layer, frazil ice 40 cm thick in the lower layer Density) was set up to have a three-layer structure.

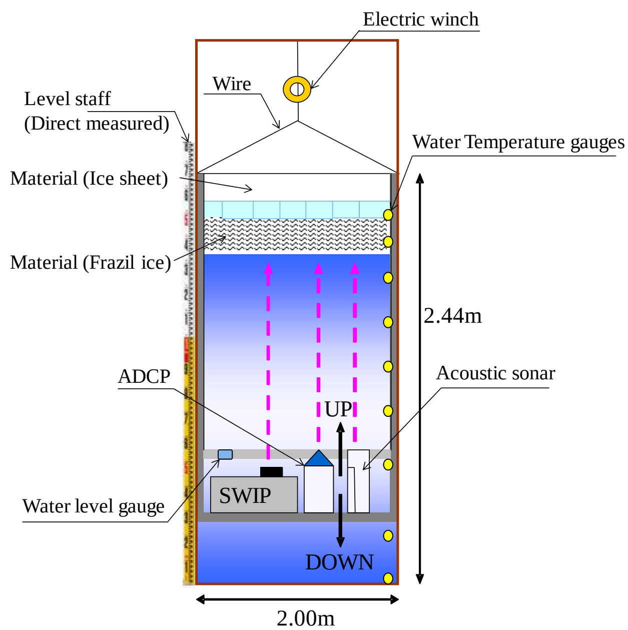

Fig.1. Outline of the large tank for experiment

d) Experiment method

Measurement of equipment was carried out at a water depth of 0 to 2.0 m at intervals of 0.2 m using a lift. Observation of SWIP was interval of 1 sec, and it was obtained with 60 pings, resolution (Gain1).

Table1. Experimental materials and preparation method

No	Simulated ice	Material
1	Water	Tap water
2	Ice sheet 0.15m thickness	Plate-shaped ice of 50×30×15cm was used as a filing (density: $0.966 g/cm^3$)
3	Frazil ice(low density) 0.4m thickness	Use snow accumulated naturally (low frazil density: $0.375 g/cm^3$)
4	Ice sheet+Frazil(low density) 0.55m(0.15m+0.4m) thickness	Plate-shaped ice+snow accumulated naturally
5	Ice sheet+Frazil(high density)+Frazil(low density) 0.95m(0.15m+0.4m+0.4m) thickness	Compressed snow by person (High-density frazil ice was squeezed in a container of 34 × 50 × 30 cm and compacted, and one having a weight of 35 kg or more was used. High frazil density: $0.492 g/cm^3$)

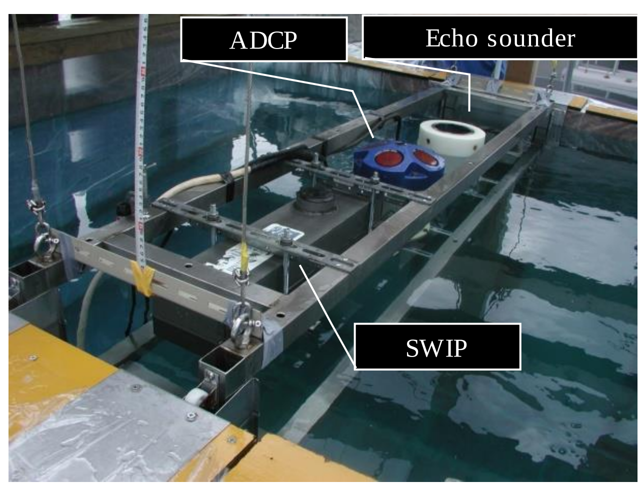

Fig. 2. Acoustic instruments for experiment

The measured value of ADCP was acquired with high resolution high resolution mode (WM 8), layer thickness of 5 cm, ping number setting of 30, bottom tracking (BM 5) was 30 pings, ADCP backscattering intensity was 5 cm in the depth direction with a difference of more than 30 dB in water depth as the boundary. The echo sounder reads the self-registered paper of the backscattering intensity, and corrected it using the water temperature in the tank. Directly measured the water surface, the bottom of the ice sheet and the bottom of the frazil ice with visual observation with a measuring staff directly.

e) Experimental results

In the experimental results, the direct measured values are on the horizontal axis and the measured values of each instrument on the vertical axis, shown in Figure 3.

In the case of only water, SWIP and acoustic sounding machine coincided with direct measurement values on the water surface, but ADCP bottom tracking and ADCP backscattering intensity could not capture the water surface.

In the case of the ice sheet, all instruments coincided with the direct measured values of the ice bottom. It was indicated that the measurement accuracy was high at flat ice.

In the case of upper ice sheet and lower frazil ice, all instruments measured the bottom of frazil ice. The ADCP bottom tracking and ADCP backscattering intensity were coincide with the direct measured values, whereas the error of about 0.11 m for SWIP and about 0.25 m for single beam acoustic sounder had occurred.

As ADCP spreads at a beam angle of 20 °, it is inferred that the point directly coincides with the measured value as it measured the point near the side wall to be measured directly.

However, the difference in the measured value with respect to the change in water depth is constant in any of the instruments.

In additon, it is confirmed that the measurement accuracy is high because the standard deviation is as small as 0.03 to 0.04 m in each instrument.

There was no clear difference in measured value due to difference in frazil ice density.

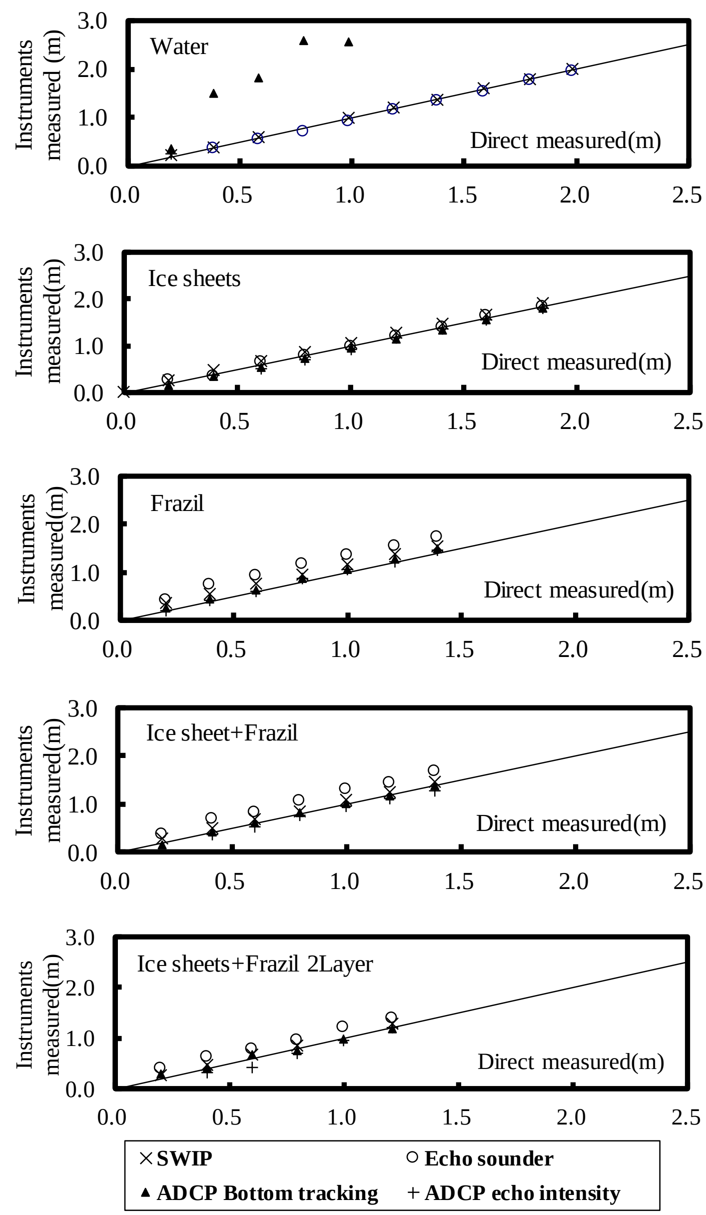

Fig. 3. Result of instruments assurance

3. Field observation results

a) Observation point and method

The target river is a Maruyama gauging station located 30 km from the estuary of Teshio River located in the northern part of Hokkaido, and the observation period was from December 2009 to March 2010. We installed the acoustic instruments (SWIP, ADCP and echo sounder) in the riverbed. In addition, a light wave phase difference detection type snow depth meter (Niigata Denki Co., Ltd.) was installed on the tower to obtain the snow surface height.

b) Observation result

Figure 4. shows precipitation, wind direction wind speed, temperature water temperature, river ice and frazil ice contour by SWIP, vertical flow velocity contour under river ice by ADCP, river ice moving speed. The upper surface of the maximum scattering intensity of SWIP is consistent with ADCP bottom tracking, the height of the river ice bottom surface obtained by the echo sounder and fluctuates in phase with the water level. The point frame in the figure shows the early stage of breakup and the temperature rapidly increased from -12.6 ° C. to + 10.7 ° C. in 32 hours from 7:00 to 25 at 15:00 on February 2010, From the time ~ 26th at 6 o'clock, rainfall of 30 mm has been cumulatively observed, there is a sudden rise of the water level, increase of the flow velocity, movement of the river ice occur. The details of the early stage of breakup (February 25 - March 5, 2010) are shown in Figure 5.

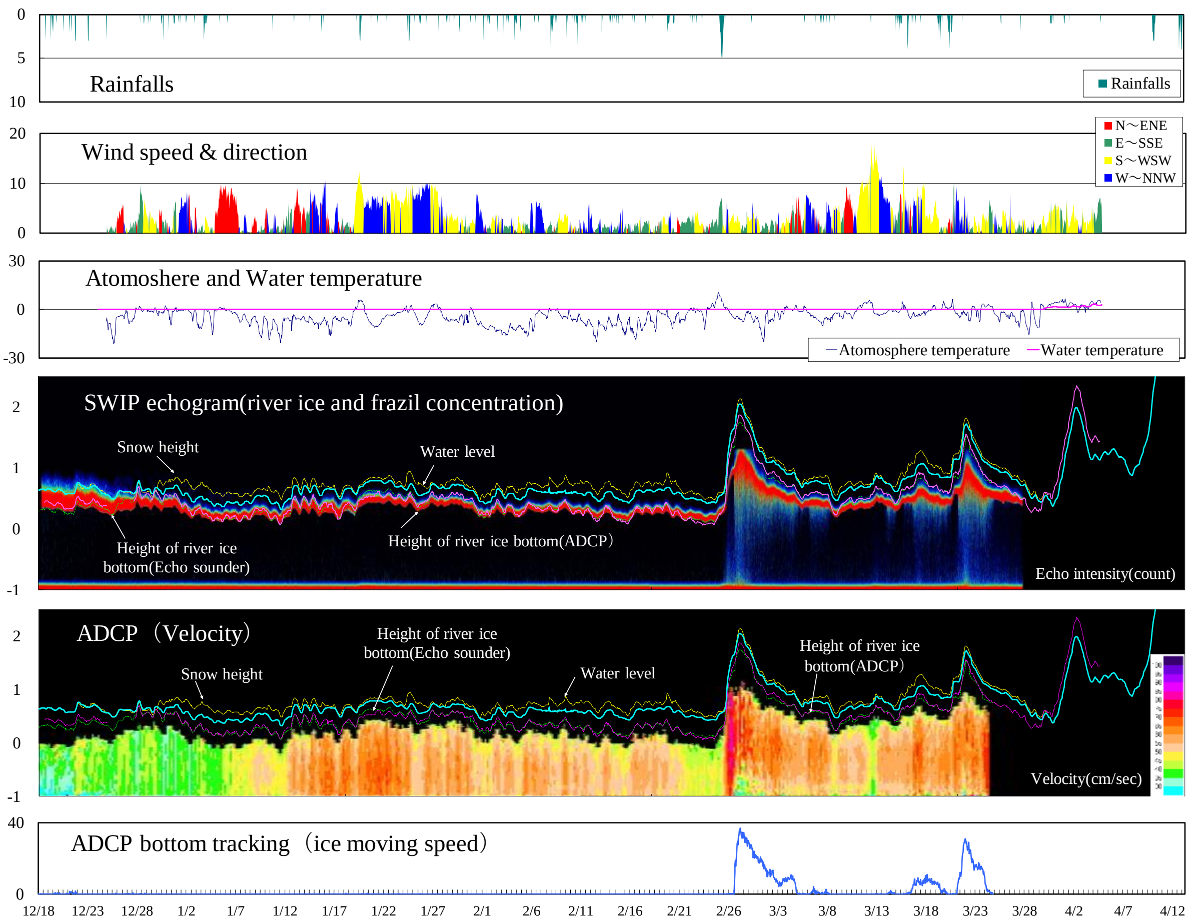

Fig. 4. Field observation using acoustic instruments result

Here, the thickness of river ice indicates the thickness from the height of the snow surface to the height of the bottom surface of the river.

In Figure 6-①, the river ice begins to move after the peak of the flow velocity, and accumulation of frazil ice was seen under the bottom of the river ice. This phenomena was presumed that crushed ice / frazil ice was flowing from the upstream and was diving below the bottom of the river ice.

After that, the flow velocity decreased, the water level rose by about 1.3 m and peaks. There was a time difference of about 24 hours between the flow velocity and the water level peak.

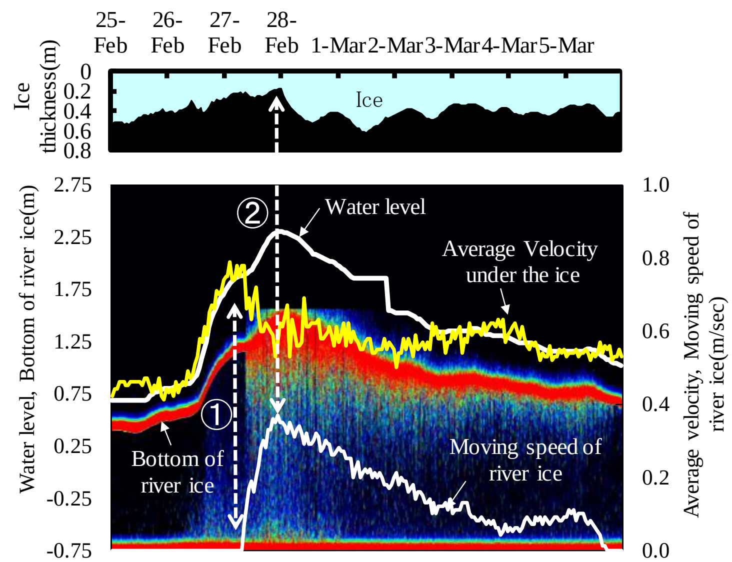

Fig. 5. Behavior of river ice and hydraulic condition at breakup

It was presumed that the water level was rising due to the accumulation of ice jam, and the flow velocity has decreased due to the influence of backwater.

In addition, in Figure 6-②, because the peak of the river moving speed (maximum 0.4 m/sec) and the peak of the water level were coincided and the river ice thickness became the thinnest, it was suggested that ice breakage may have occurred due to contact with flowing crushed ice and frazil ice.

4. Verification of observation data

a) Changes over time of composite roughness coefficient and Froude number

Time series change of river ice thickness and roughness is shown in Fig. The roughness was calculated from the Manning equation (1) , with the roughness n_0 of the river ice and bed combined, using the measured values of ADCP and measured water level gauge.

$$v = \frac{1}{n_0} \cdot R^{\frac{2}{3}} \cdot I_e^{\frac{1}{2}} \tag{1}$$

υ [m / sec]: average flow velocity (vertical mean), n_0: composite roughness (river ice and bed), R: hydraulic radius, I_e: energy gradient. Since it was completely ice-covered during the observation period, iced perimeter S_i [m], wetted perimeter S_b [m], river width B [m], cross sectional area A [m], effective water depth h_w [m], $B >> h_w$, it can be assumed that $i \approx S_b \approx h_w$, so the hydraulic radius R can be expressed by equation (2).

$$R = \frac{A}{S_i + S_b} \cong \frac{A}{2B} \cong \frac{h_w}{2} \tag{2}$$

The calculated roughness is the composite roughness of the ice sheet and the riverbed, but after January 19, when the water level gradient stabilizes, the roughness tends to decrease with time

regardless of the increase or decrease of the river ice thickness. This is estimated that the smoothing the bottom surface of river ice due to flow caused to decrease the roughness.
In the dotted frame in Figure 6., the roughness became higher due to accumulation of crushed ice or frazil ice at the time of breakup.

Froude number Fr of ice formation was calculated from equation (3).

$$Fr = \frac{U_w}{\sqrt{g(\frac{A}{B})}} \qquad (3)$$

U_w [m/sec]: ADCP average flow velocity, A [m^2]: cross sectional area, B[m]: water surface width
Kishi states that the condition of complete ice river ice formation is determined by temperature, precipitation and Froude number, there is a possibility of complete ice at $F_r \leq 0.2$, and it does not freeze if $F_r \fallingdotseq 0.4$ is exceeded. The examination result is shown in Fig. 8, but it has been changing at $F_r \fallingdotseq 0.1$ throughout the period, consistent with the condition of complete ice removal of Kishi.

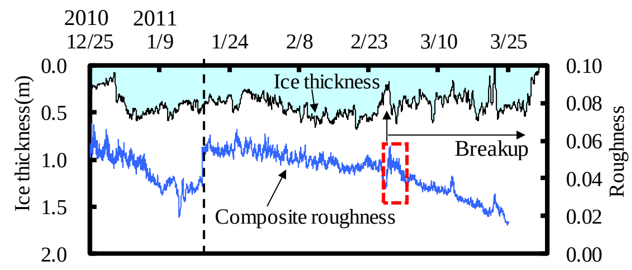

Fig. 6. Relationship of ice thickness and roughness

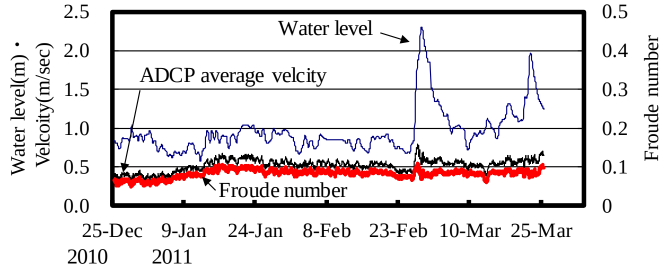

Fig. 7. Froude number at the ice-covered

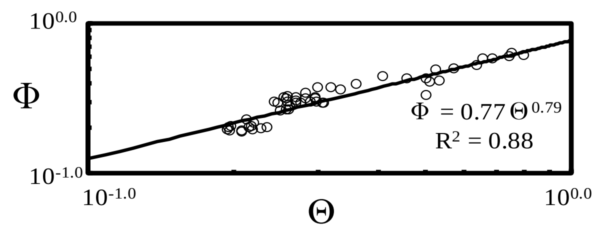

Fig. 8. relationship between the moving speed of river ice and the dimensionless tractive force

b) River ice movement speed and water level, flow velocity, dimensionless tractive force
In order to see the relationship between the moving speed of river ice and the dimensionless tractive force, with reference to the relationship between the movement amount of frazil ice and the dimensionless tractive force studied by Shen and others, the frazil ice particle diameter d was set to river ice thickness was substituted for the study. Shen and others are shown in equations (4) and (5).

$$\Theta = \frac{U_*^{\,2}}{gd(\frac{\rho - \rho_{ice}}{\rho})} \qquad (4)$$

$$\Phi = \frac{q_{ice}}{d\sqrt{(gd(\frac{\rho - \rho_{ice}}{\rho}))}} \qquad (5)$$

U_*[m/sec]:friction velocity($U_*^{\,2} = \sqrt{gRI}$) , g: gravitational acceleration , d[m]:river ice thickness, ρ [g/cm^3]: density of ice, ρ_{ice} [g/cm^3]: density of river ice, R: radial depth (≈ effective water depth / 2), I: energy gradient ≈ water level gradient.
In this study, ρ was 1g/cm^3 and ρ_{ice} was 0.8g/cm^3 from the measured value on February 25, 2010. Where q_{ice} = movement of river ice.

Substituting into the equation (5) as velocity (V_{ice}) × river ice thickness (d), it becomes equation (6).

$$\Phi = \frac{V_{ice}}{\sqrt{(gd(\frac{\rho - \rho_{ice}}{\rho}))}} \tag{6}$$

From Figure 8., the correlation between the non-dimensional river moving speed Φ and the dimensionless sweeping force Θ is obtained and is elated by the power approximate expression. From this, it is shown that the transport capacity of river at the time of deicing can be studied by a concept similar to riverbed material transport.

5. Summary

As a result of verifying the measurement accuracy of SWIP, ADCP and acoustic sounder, the measurement error is constant irrespective of water depth, the standard deviation of measured value and measured value of each device is as small as 0.03 ~ 0.04 m, the measurement accuracy is high. The following observations were obtained from the field observation results on the hydraulic phenomenon at the time of deicing and the behavior of river ice. Due to rapid temperature rise and rainfall, the flow velocity becomes faster and as the flow velocity peaks, the river ice moves to the downstream. Moving river ice stays on the bottom of the river ice and increases the synthetic roughness of the river, so the flow velocity slows and the water level rises. In addition, the peak of the moving speed of river ice coincided with the peak of the water level.
In addition, it has been confirmed that the Froude number changes at about 0.1 at the time of complete ice formation, that the composite roughness coefficient decreases with time, the new dimension knowledge such that the dimensionless river moving speed is associated with the dimensionless sweeping power was gotten. The new observation method of this research showed that it is possible to observe the hydrological phenomenon at the time of deicing and the behavior of river ice. This fact indicates that this observation method will be one of long-term monitoring techniques for ice covering ice.

Acknowledgments
This work was supported by JSPS KAKENHI Grant Number JP18K04361.

References

Yoshikawa.Y.,Watanabe. Y.,Hayakawa. H. and Hirai. Y. : Measurement of Manning roughness coefficient and Frazil Thickness using ADCP in Ice Covered River, 14th Biennial Conference ERB 2012, pp.192-195,2012.

J.R.Marko and M.Jasek,2009.Estimation of Frazil Particle Size and Concentration from SWIPS Measurements in the Peace River:an Assessment of Options and Prospects.15th CRIPE workshop on River Ice,St.Johb’s .Nfld.

George D. Ashton : Froude criterion for ice-block stability，Journal of Glaciology，vol.13，No.68，307-313，1974.

Kishi. T.,Nakao. K.: On ice formation and winter drought in Hokkaido, Annual academic lecture presentation summary, Japan Society of Civil Engineers,No.16,pp79-80, 1961.(Japanese)

H.T.Shen・D.S.Wang : Undercover Transport and Accumulation of Frazil Granules，Journal of Hydraulic Engineering，vol.121，No.2，pp184-194，1995.

International Association for Hydro-Environment Engineering and Research
Supported by Spain Water and IWHR, China

24th IAHR International Symposium on Ice
Vladivostok, Russia, June 4 to 9, 2018

Ice-Induced Vibrations of Model Structures with Various Dynamic Properties

Cody C. Owen, Hayo Hendrikse
Department of Hydraulic Engineering at Delft University of Technology
Building 23, Stevinweg 1, 2628CN Delft, the Netherlands
C.C.Owen@tudelft.nl, H.Hendrikse@tudelft.nl

For the design of offshore structures in regions with ice-infested waters, the prediction of interaction between floating level ice and the support structure is essential. If the structure is vertically sided at the ice-structure interface and certain ice and structural conditions exist, then the phenomenon known as ice-induced vibrations can develop. Recently, an ice-structure interaction model has been developed and validation has been attempted based on dedicated experiments. This study extends the validation by investigating the capabilities of the analytical model in predicting the indentation speed range for the frequency lock-in regime of ice-induced vibrations with various input parameters. Implementation of these various input parameters seeks to address the challenge of adapting the analytical model from the reference input parameters to scenarios with other structural properties. Using these various input parameters, the analytical model can demonstrate accurate prediction of frequency lock-in vibrations as observed in the experiments when the mean global ice load in crushing is properly estimated. For the cases when the mean global ice load was not properly estimated, either unsuitable scaling between input parameters, undesirable behavior of the model ice during the experiments, or a combination thereof may be the cause. Overall, this study serves to establish the range of applicability for the analytical model in terms of accurate prediction of frequency lock-in vibrations between model ice and various structures and discusses the sensitivity of the analytical model with respect to the input parameters. This study is an important step towards application of the analytical model for full-scale scenarios.

1. Introduction

For the design of offshore structures in regions with ice-infested waters, the prediction of interaction between floating level ice and the support structure is essential. If the structure is vertically sided at the ice-structure interface and certain ice and structural conditions exist, then the phenomenon known as ice-induced vibrations can develop. Some ice-structure interaction models have attempted to predict ice-induced vibrations, but issues have arisen regarding their range of applicability for various dynamic properties of the structures (Jeong et al., 2010; Kärnä et al., 2013; Muhonen, 1996). Recently, a phenomenological model has been developed and validation has been attempted based on dedicated experiments (Hendrikse et al., 2018). These experiments belong to an extensive model-scale testing campaign as part of the Ice-induced Vibrations of Offshore Structures (IVOS) project and were conducted by the Hamburg Ship Model Basin (HSVA). From the validation attempt of the analytical model, input parameters to define the model ice behavior were derived with a reference structure.

With the previously determined input parameters, experiments from the IVOS project with similar ice conditions but with structures that differ from the reference structure are simulated to investigate the capabilities of the analytical model. This validation focuses on assessing the predictive capabilities of the analytical model in determining the indentation speed range within which the frequency lock-in regime of ice-induced vibrations develops. The working principle is that if the mean global ice load magnitude is properly estimated in the analytical model, then the frequency lock-in regime should be predicted correctly regardless of the structural properties. Determining an accurate global ice load level is dependent on the scaling from the predetermined reference parameters and to other parameters. In this study, it is proven that proper estimation of the global ice load by the analytical model can produce results that correspond well with experimental observations in the frequency lock-in regime of ice-induced vibrations. Furthermore, scaling of the reference parameters to different ice conditions as input to the analytical model for prediction of the frequency lock-in regime is attempted and the results are expounded.

2. IVOS Experimental Campaign

The Phase 1 and Phase 2 experiments of the IVOS campaign with model ice were conducted between 2015 and 2016 by HSVA in their Large Ice Basin (Ziemer et al., 2017). Model structures with various configurations of size, cross-sectional geometry (shape) at the ice-structure interface, fundamental natural frequency, and stiffness were utilized for indentation tests in model ice over a range of indentation speeds (Hinse et al., 2017). Figure 1 illustrates the test apparatus and size and shape of the model structures of the IVOS experiments that are specifically chosen for this study. Detailed ice properties were recorded for each of the experiments and the pertinent measurements, and their use, are elaborated in Section 5.

3. Analytical Model

The analytical model used for this study is described in Hendrikse et al. (2018) and further explanation of the physical basis and derivation is given by Hendrikse (2017). The reference parameters to define the HSVA model ice behavior have been determined in Hendrikse et al. (2018) and are shown in Table 1.

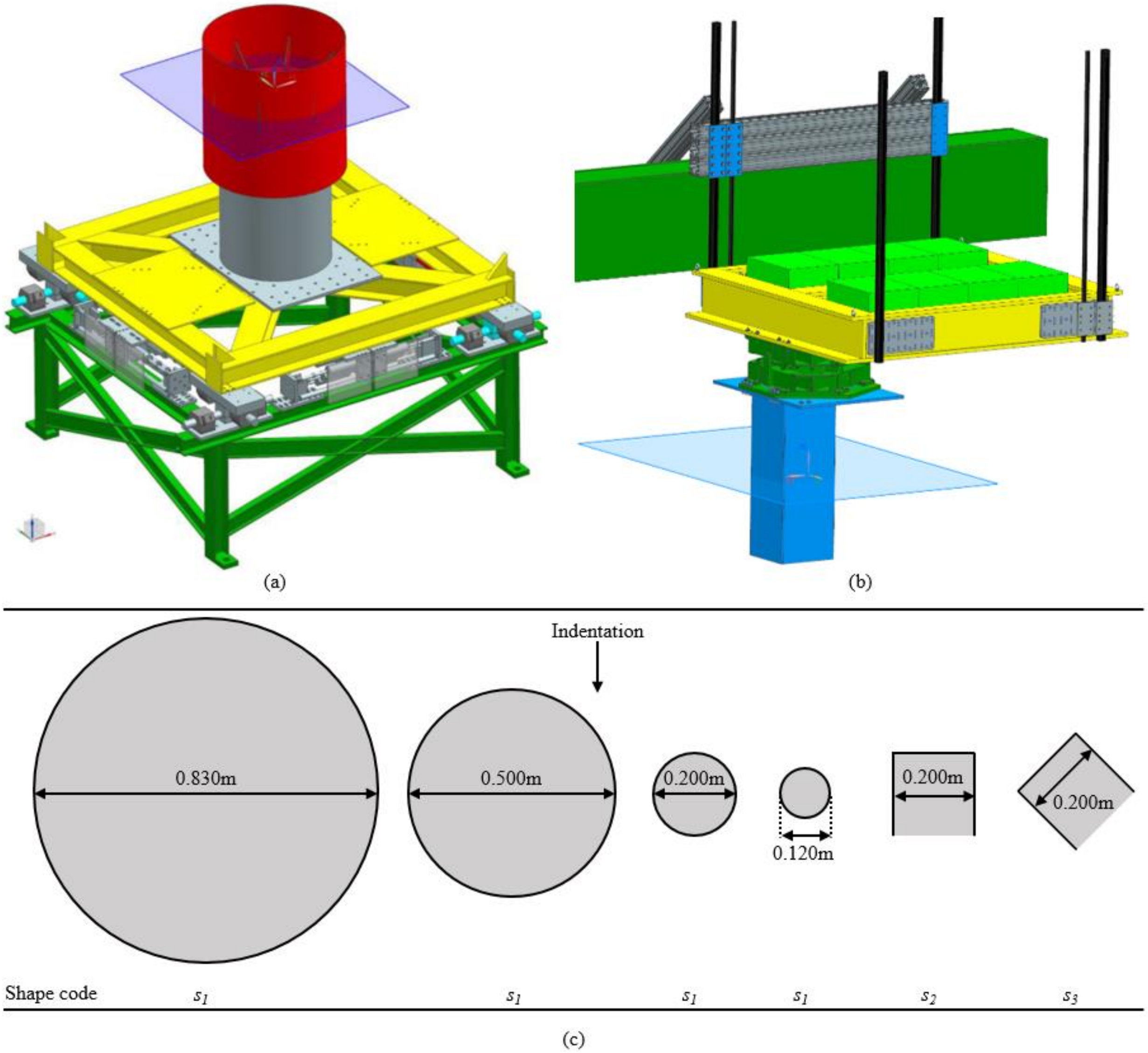

Fig. 1. Schematics of the test apparatus and size and shape of select model structures from the IVOS experiments, of which (a) is the Phase 1 test apparatus; (b) is the Phase 2 test apparatus; and (c) is the schematic of model structure cross-sections with shape and shape code, size, and orientation of indentation (Hinse et al., 2017; Ziemer et al., 2017).

Table 1. Reference input parameters from HSVA model ice for the analytical model derived from the indentation experiment with the rigid reference structure (Hendrikse et al., 2018).

$K_{2,ref}$ [N m^{-1}]	$C_{2,ref}$ [N^3 m^{-1} s]	$K_{1,ref}$ [N m^{-1}]	$C_{1,ref}$ [N m^{-1} s]	N_{ref} [-]	$r_{max,ref}$ [m]	$\delta_{f,ref}$ [m]
$5.091\cdot10^4$	$1.05\cdot10^9$	$5.372\cdot10^3$	$1.7021\cdot10^4$	39	$2.9\cdot10^{-3}$	$2\cdot10^{-3}$

4. Scaling Approach

The reference input parameters with subscript *ref* in Table 1 are the result of specific ice conditions, the HSVA model ice in this case, and a structure with distinct size and shape. For the different ice conditions observed during the experiments and for the shapes of the various model structures, the reference input parameters are scaled according to Hendrikse et al. (2018) as follows:

$$
\begin{aligned}
&N = N_{ref}\,(d / d_{ref})\\
&K_2 = K_{2,ref}\,(\sigma / \sigma_{ref})\,(h / h_{ref})\,s_s(s,s_{ref})\\
&C_2 = C_{2,ref}\,(\sigma / \sigma_{ref})\,(h / h_{ref})\,s_s(s,s_{ref})\\
&K_1 = K_{1,ref}\,(\sigma / \sigma_{ref})\,(h / h_{ref})\,s_s(s,s_{ref})\\
&C_1 = C_{1,ref}\,(\sigma / \sigma_{ref})\,(h / h_{ref})\,s_s(s,s_{ref})\\
&r_{max} = r_{max,ref}\\
&\delta_f = \delta_{f,ref}
\end{aligned}
\qquad \textbf{[1]}
$$

which assume a linear dependence of the mean global ice load in crushing on structural width d, compressive ice strength σ, ice thickness h, and shape factor $s_s(s,s_{ref})$. Note that the variable for the shape factor from Hendrikse et al. (2018) is changed from $f_s(s,s_{ref})$ to $s_s(s,s_{ref})$ for clarity in this article. It has been observed experimentally and analytically that indentation shape affects the global ice load level when comparing structures of similar size (Korzhavin, 1971; Owen, 2017). As a preliminary method to substantiate the effect of load level on specific indentation shapes, an elastic-plastic indentation model with different shapes of indenters is employed (Yu et al., 1996). The rigid model structure utilized to obtain the reference input parameters had a square cross-section with side-first indentation in the model ice sheet; therefore, the reference shape s_{ref} is defined as rectangular. The shape s of indentation of the structures considered in this study are circular s_1, rectangular s_2, and triangular s_3. For the shapes that differ from the reference shape, the shape factor $s_s(s,s_{ref})$ is determined by the elastic-plastic indentation model as the ratio between the loads from the shape s and from the reference shape s_{ref} for indenters of equivalent size and for equivalent ice conditions. Based on the model ice properties and the sizes and shapes of the model structures, the indentation model predicts shape factors $s_s(s,s_{ref})$ for the circular and triangular shapes of roughly 0.8 and 0.7, respectively, when compared to a rectangular shape with shape factor $s_s(s,s_{ref})$ of 1.0. These results generally agree with the findings by Korzhavin (1971) and Owen (2017). These shape factors are selected as inputs to the numerical model as shown in Equation 1 and implemented in Section 5.

5. Simulation Parameters

The input parameters to the analytical model for the simulations are shown in Table 2. Each structure is simulated as a single-degree-of-freedom oscillator, which follows the design objective of the test apparatus from the IVOS experiments. The fundamental natural frequency f_s and stiffness K_s of each model structure were provided by HSVA (Hinse et al., 2017). The damping as a ratio of critical damping ζ_s was determined by logarithmic decrement from a relaxation test for each of the structures (Owen, 2017). It was observed during the experiments that the properties of the model ice varied spatially throughout the basin and among the different ice sheets. To capture effects of the variation in ice properties on the ice-structure interaction, a range of ice thickness h and compressive strength σ are considered for the simulations. Each structure is subjected to three different ice condition cases in the simulations. In the first case, the mean ice thickness and mean compressive ice strength as determined from the corresponding experiments are simulated. The second case considers the minimum ice thickness observed during any of the corresponding experiments and 10% less than the minimum compressive ice strength computed from any of the corresponding experiments. Finally, the third case considers the maximum ice thickness observed during any of the corresponding experiments and 10% greater than the maximum compressive ice strength computed from any of the corresponding experiments. As suggested by HSVA, the 10% variation for the compressive ice strength is included because the compressive ice strength values were computed based on only one sample location for each of the ice sheets. The mean load adjustment factor is disregarded for the first set of simulations and is addressed in Section 6.

For each trial, simulations are performed from an indentation speed of 0.003 m s^{-1} to 0.150 m s^{-1} with increments of 0.001 m s^{-1} as performed in the experiments. The initial conditions of the structure for each simulation are defined as the final conditions of the structure from the simulation of the previous indentation speed. This is chosen to recreate the stepwise increase in consecutive indentation speeds as done in the experiments. Each simulation is executed for 20 seconds and the final 10 seconds are exclusively considered for statistical analysis of the steady-state response.

6. Comparison of Experiments and Simulations

To compare the experiments and simulations regarding the frequency lock-in regime of ice-induced vibrations, criteria are defined to identify this particular regime. As a basic criterion, the frequency lock-in regime of ice-induced vibrations can be defined by the ratio of the maximum structural velocity and the indentation speed, known as β, between 1.0 and 1.5 (Hendrikse, 2017). Following this definition, the experiments and simulations are examined for recurring instances when β is between 1.0 and 1.5, when the structural response is quasi-sinusoidal near the fundamental natural frequency, and when the global ice load periodically is amplified ensuing the time when the relative velocity between ice and structure is low. For this study, adequate development of frequency lock-in vibrations is achieved for the experiments when the aforementioned criteria are met for at least three consecutive cycles. The choice of at least three consecutive cycles is made in an attempt to inclusively identify frequency lock-in vibrations as a result of nearly constant ice conditions. But because the ice conditions were known to vary substantially for a given indentation speed, requiring more consecutive cycles could potentially exclude indentation speeds during which frequency lock-in vibrations develop. The simulated results are considered frequency lock-in vibrations when the aforementioned criteria are met for a majority of the time history.

Figure 2 shows the comparison between the experimental observations of frequency lock-in vibrations and the predicted lower and upper bounds within which the frequency lock-in regime of ice-induced vibrations develops. The predicted bounds for frequency lock-in vibrations are in close agreement with the experimental observations. Frequency lock-in vibrations are observed below the predicted lower bound for most of the experiments, which is explained in Section 7. Not all of the experiments contained an indentation speed resolution required to yield a complete range for the frequency lock-in regime. But for the experiments with sufficient indentation speed resolution, the predicted upper bounds for frequency lock-in vibrations that are higher than experimentally observed (see trials T6 and T9 in Figure 2) can be explained by an improper estimation of the mean global ice load in crushing. This is further discussed in Section 7.

To quantify the effect of proper estimation of mean global ice load in crushing on the range of indentation speeds during which frequency lock-in vibrations develop, a mean load adjustment is applied as a factor in the same manner as the shape factor (see Table 2). The mean load adjustment factor is determined a posteriori by computing the ratio of the simulated mean load and the experimental mean load in crushing for the highest experimental indentation speed. Applying this factor and repeating the simulations, the simulated bounds for frequency lock-in vibrations generally fit better with the experimental observations (see Figure 3). However, no frequency lock-in vibrations are predicted for trials T2 and T3 in Figure 3 with the mean load adjustment. The mean global ice loads obtained from the experiments corresponding to trials T2 and T3 were highly influenced by flexural behavior of the ice; this is explained in Section 7.

Figure 4 exemplifies the result of proper mean global ice load level estimation in terms of global ice load and structural displacement time traces in the frequency lock-in regime. A low-pass filter with cutoff frequency of 49 Hz was applied to the experimental global ice load signal to attenuate noise from the data acquisition power source, and was applied to the simulated ice load signal for comparative consistency.

7. Discussion

Based on general trends from the experiments, the analytical model can demonstrate accurate prediction of the range of indentation speeds within which frequency lock-in vibrations develop. However, this accurate prediction is predicated on proper estimation of the mean global ice load level by the analytical model. For the mean global ice load level to be properly estimated using the input parameters that differ from the reference parameters, a type of scaling must be applied. Reviewing Figure 2 and Figure 3, it can be deduced that the linear scaling in Equation 1 may not be suitable for the various dynamic properties that differ significantly from the reference parameters. But it is not clear whether the type of scaling or the flexural behavior of the model ice is the cause.

It was observed that the spatial variations in ice conditions were substantial during the IVOS experiments with model ice. These variations in ice conditions mean that, during an experiment, the mean global ice load changed not only with indentation speed but also with the ice properties. The ice conditions, such as ice thickness and uniaxial compressive ice strength, were not reported for the entirety of each ice sheet and thus could not be accurately simulated. Moreover, nearly steady-state ice-structure interaction for statistical analysis cannot be reliably observed during experiments with such large spatial variation in ice conditions. In addition, the flexural behavior of the model ice was such that ice failure in crushing was not always the dominant failure mechanism and, as a result, the mean global ice load differed from the predictions. Out-of-plane, downward bending and failure of the ice sheet was consistently observed in the experiments for the lower indentation speeds, which reduced the mean global ice loads and limited the development of ice-induced vibrations. For example, intermittent crushing vibrations did not properly develop for any of the IVOS experiments because of the flexural behavior of the model ice. In the case of low indentation speeds for the Phase 2 experiments, the ice bending resulted in conditions suitable for frequency lock-in vibrations. These conditions are not included in the analytical model and therefore would not be predicted.

Table 2. Input parameters to the analytical model for simulation of the IVOS experiments.

Trial name	Shape code	$s_s(s,s_{ref})$ [-]	d [m]	f_s [Hz]	K_s [kN m^{-1}]	ζ_s [%]	h [m]	σ [kPa]	Mean load adjustment factor [-]
T0_0	s_1	0.8	0.830	5.45	2230	1.5	0.048	81	0.28
T0_1							0.044	61	
T0_2							0.052	106	
T1_0	s_1	0.8	0.830	2.65	490	3.0	0.046	98	0.21
T1_1							0.042	58	
T1_2							0.049	131	
T2_0	s_1	0.8	0.500	5.47	2220	2.0	0.031	90	0.24
T2_1							0.026	81	
T2_2							0.034	99	
T3_0	s_1	0.8	0.500	7.60	3020	2.9	0.031	80	0.36
T3_1							0.028	72	
T3_2							0.033	88	
T4_0	s_1	0.8	0.200	5.78	1930	2.4	0.042	97	0.41
T4_1							0.040	87	
T4_2							0.045	107	
T5_0	s_1	0.8	0.500	5.47	2030	1.7	0.043	72	0.32
T5_1							0.040	65	
T5_2							0.047	79	
T6_0	s_1	0.8	0.120	5.40	1935	1.0	0.041	136	1.13
T6_1							0.038	122	
T6_2							0.044	150	
T7_0	s_2	1.0	0.200	4.18	1290	1.8	0.048	125	0.89
T7_1							0.045	104	
T7_2							0.051	160	
T8_0	s_3	0.7	0.283	5.59	1915	2.2	0.044	110	0.55
T8_1							0.040	99	
T8_2							0.047	121	
T9_0	s_2	1.0	0.200	5.4	1950	1.7	0.045	110	0.81
T9_1							0.042	99	
T9_2							0.048	121	

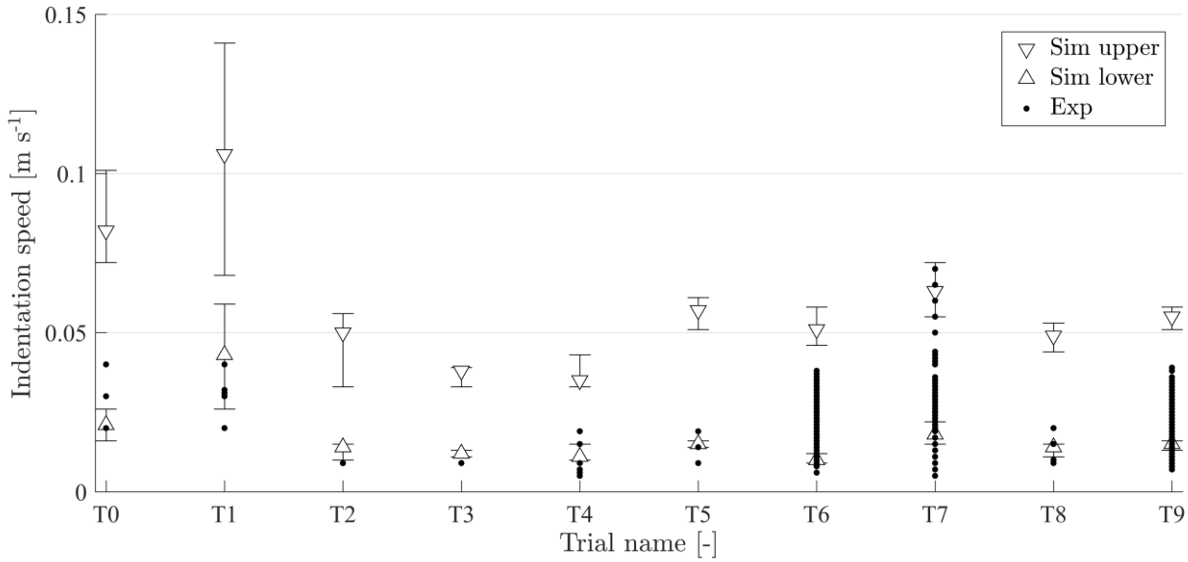

Fig. 2. Comparison of simulated (Sim) lower and upper bounds for frequency lock-in regime and observed (Exp) frequency lock-in vibrations from the experiments. Each simulated bound is represented by a triangle with a higher and lower error bar indicating simulation results from the mean, maximum, and minimum ice condition cases, respectively.

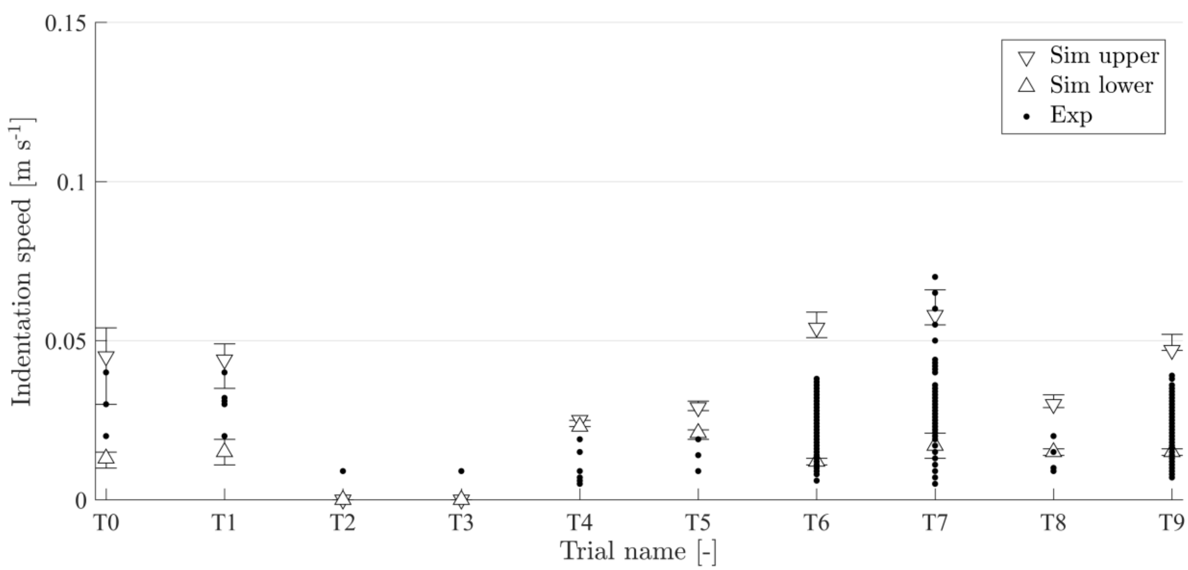

Fig. 3. Comparison of simulated (Sim) lower and upper bounds for frequency lock-in regime with mean load adjustment and observed (Exp) frequency lock-in vibrations from the experiments. Each simulated bound is represented by a triangle with a lower and higher error bar indicating simulation results from the mean, minimum, and maximum ice condition cases, respectively.

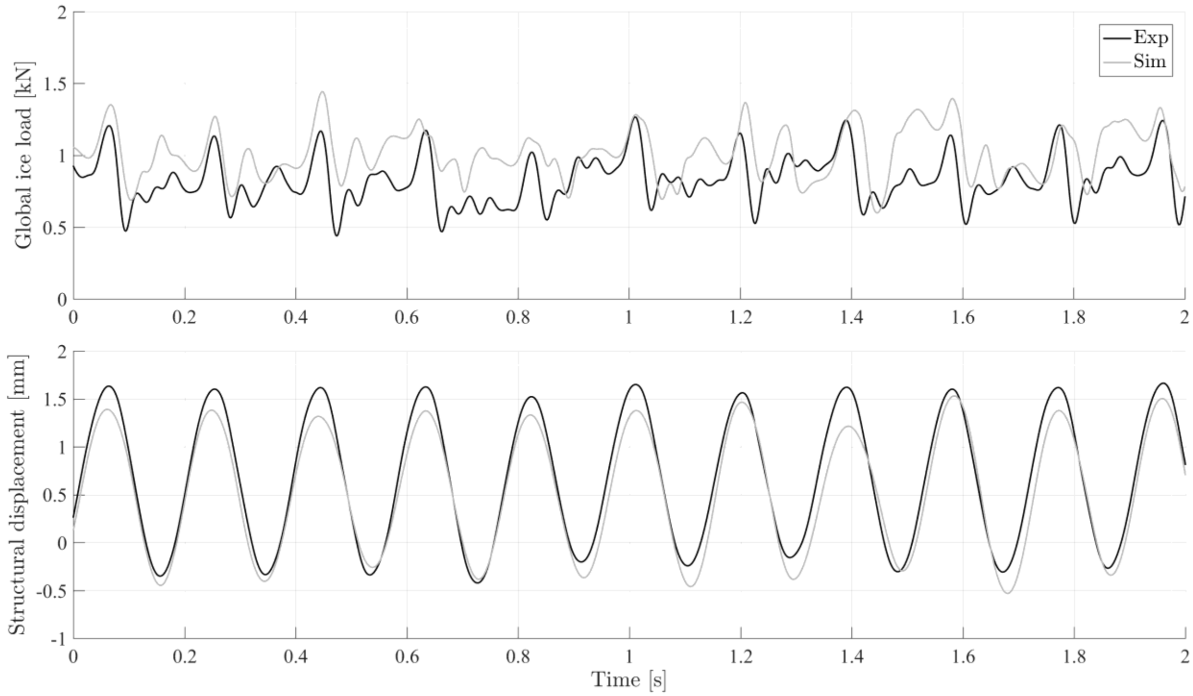

Fig. 4. Comparison of global ice load and structural displacement time traces in the frequency lock-in regime from experimental (Exp) results and simulated (Sim) results with mean ice conditions (trial T9_0) and mean load adjustment at an indentation speed of 0.029 m s^{-1}.

8. Conclusion

Experiments in model ice from Phase 1 and 2 of the IVOS project have been simulated using the analytical model with reference input parameters from a reference structure and accurate predictions of the frequency lock-in regime for each experiment have been shown. Proper estimation of the mean global ice load level in crushing is demonstrated to be very important for accurate prediction of the range of indentation speeds during which frequency lock-in vibrations develop. It is proposed that further research is focused on simulating more experiments with different ice conditions and structures while still utilizing the reference input parameters as determined in Hendrikse et al. (2018). Moreover, the experiments should comprise ice-structure interaction during which the ice fails only in crushing.

Acknowledgements

The authors gratefully acknowledge the support from the SAMCoT CRI through the Research Council of Norway and all of the SAMCoT partners. In particular, the authors wish to thank partners involved in the IVOS project: DNV GL, Engie SA, Kvaerner AS, Multiconsult AS, Shell Technology Norway AS, Total E&P Norge AS, and project coordinator HSVA.

References

Hendrikse, H. (2017). Ice-induced vibrations of vertically sided offshore structures. PhD Dissertation, Delft University of Technology, Faculty of Civil Engineering and Geosciences, Delft.

Hendrikse, H., Ziemer, G., and Owen, C. C. (2018). Experimental validation of a model for prediction of dynamic ice-structure interaction. Cold Regions Science and Technology, 1-63.

Hinse, P., Müller, F., and Ziemer, G. (2017). IVOS Progress Report: April 2017. Hamburg: HSVA.

Jeong, S. and Baddour, N. (2010). Comparison of characteristic failure frequency models for ice induced vibrations. JP Journal of Solids and Structures, 4(3):115–137.

Kärnä, T., Andersen, H., Gürtner, A., Metrikine, A., Sodhi, D. S., Loo, M., Kuiper, G., Gibson, R., Fenz, D., Muggeridge, K., Wallenburg, C., Wu, J.-F., and Jefferies, M. G. (2013). Ice-induced vibrations of offshore structures - looking beyond ISO 19906. In Proceedings of the 22nd International Conference on Port and Ocean Engineering under Arctic Conditions, page 12, Helsinki, Finland.

Korzhavin, K. (1971). Action of ice on engineering structures. (U. A. Technical Report Translation TL260, Trans.)

Muhonen, A. (1996). Evaluation of three ice-structure interaction models. PhD thesis, Helsinki University of Technology.

Owen, C. C. (2017). Ice-induced vibrations of vertically sided model structures: Comparison of structures with circular and rectangular cross-section subjected to the frequency lock-in regime. Delft University of Technology. Delft: Delft University of Technology.

Yu, W., and Blanchard, J. P. (1996). An elastic-plastic indentation model and its solutions. Journal of Materials Research, 11(9), 2358-2367.

Ziemer, G., and Hinse, P. (2017). Relation of maximum structural velocity and ice drift speed during frequency lock-in. Port and Ocean Engineering under Arctic Conditions, (pp. 1-12). Busan.

International Association for Hydro-Environment Engineering and Research
Supported by Spain Water and IWHR, China

24th IAHR International Symposium on Ice
Vladivostok, Russia, June 4 to 9, 2018

An Experimental Study of Saline Ice Growth

Xiaodong Chen[1, 2], Knut Hoyland[2], Shungying Ji[1]
1 Dalian University of Technology, Dalian, China
2 Sustainable Arctic Marine and Coastal Technology (SAMCoT),
Centre of Research-based Innovation (CRI).
Norwegian University of Science and Technology, Trondheim, Norway
chenxiaodong@mail.dlut.edu.cn

To study the growing process of saline ice, fresh water ice were submerged into saline water with different salinities (0, 9.11, 22.4, 32.6ppt) and temperatures (0.2, -1.6, -1.75℃). During the warming-up process, the temperature was measured by thermistor string while the ice-water interface was recorded by photographing. From the result, it shows that the ice temperature is independent on water salinity. However, the ice growth is strongly influences by water salinity and temperature. In the saline ice growth, the interface appears a needle period, in which duration is dependent on the difference between freezing point and water temperature. The result denotes that the ice needle exists throughout the experiments. Due to the needle size is dependent on the temperature difference, the ice texture behaves granular in the early stage and columnar in the late stage. For saline ice, the ice growth is driven by latent and convective energies. Therefore, the new ice growth increases with increasing water temperature and has complicated trend with water salinity.

1. Introduction

The sea ice growth is fundamental importance both on the thermal and mechanical properties of sea ice (Weeks and Ackley, 1986). During the ice ridging, the cold ice falls into warm water and builds the consolidated layer by refreeze ice (Høyland, 2002). The texture of bonding part is believed to dominate mechanical strength and driven by the thermal process (Leppäranta et al., 1995). During the ice growth, the majority of the salt is rejected to concentrate the underlying water while part of it is trapped into the sea ice (Thomas and Dieckmann, 2010). The rejection brings a thin layer with increased salinity. The salt concentration enhances the heat transfer between sea ice and sea water (Middleton et al., 2015). From fieldwork measurements, the brine drainage geometries are found to be various through locations (Cole and Shapiro, 1998). Gough et al measured the development of ice micro-structure in the Antarctic through a whole winter, and it shows that the ice salinity varies and is dependent on the ice growth history (Gough et al., 2012). In the mid-winter of the Antarctic (mid-May), the supercool water is studied and represented by platelet ice, which is observed near the ice-waster interface depending on the water temperature (Leonard et al., 2006). At high ice growth rate, the solute convection is limited due to most of the salt is trapped into ice crystal (Worster and Wettlaufer, 1997).

From an imaging method, the channel of brine repelling is visualized from growing process of saline ice. The images show that the each single salt-rejection channel only lasts over a short time(Middleton et al., 2015; Middleton et al., 2016). It means that the rejection period is related to ice grain size. Based on a work of brine fluxes from ice growing, it appears a critical time, where sale rejection is limited within this value (Wells et al., 2011). It is reasonable to assume that, the critical time represents ice growth speed. For the needle-ice growing in cold air, it is driven by air temperature and humidity (Grab, 2001). It means that the ice crystal forms as long as the condition reaches freezing criterion. The interface condition influences the convection efficient and heat transfer process. Chen et al performed series of submerging test to investigate heat transportation between ice and water. During the tests, it is shown that heat convection is strongly dependent on geometry of ice-water interface and brine drainage (Chen et al., 2017; Chen and Høyland, 2016).

In this work, submerging experiments are carried out to study the thermal behavior and water-ice interface condition during the process.

2. Experiment description

2.1 Experiment setup

In this paper, the setup is design to represent the natural ice grow scenario, where ice-water interface advances downward. The fresh ice is insulated with only bottom surface exposed to warm water. In this way, the ice grows in natur

al direction and the salt is expel

led downwards driven by gravity. The ice temperature and thickness are measured by thermistor string and photographing respectively. The specific details of the strings and thickness measurement are further explained by Chen et al (Chen and Høyland, 2016).

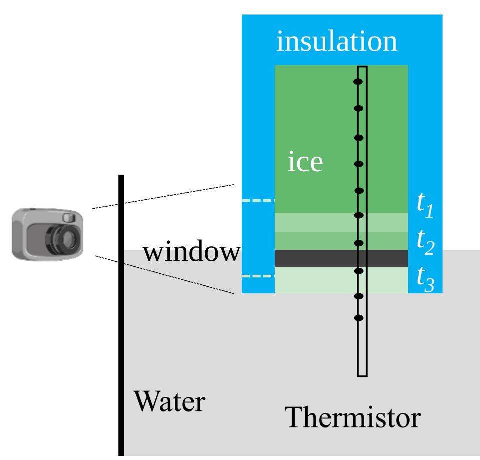

Fig. 1. Experiment setup sketch.

2.2 Sample description

For saline ice growth, the water salinity is essential since it is connected to freezing point and salt rejection. Besides, the temperature difference between freezing point and environment temperature limits the ice growth speed. The salt expelling together with ice growth speed dominate the saline ice texture. To study the influence of water salinity and temperature difference on ice growth, the experiments were performed on various conditions, as given in Tab.1. In this paper, the water salinity crosses a critical value 24.7ppt, where the maximum density of salt water appears at freezing point. It means the cold water becomes heavy and leads to strong convection.

Table 1. Sample parameter matrix.

No.	Ice temperature [℃]	Water temperature [℃]	Ice salinity [ppt]	Water salinity [ppt]
1	-32±1	0.2±0.1	0±0.05	0±0.1
2	-33±1	0.2±0.1	0±0.05	9.11±0.1
3	-33±1	0.2±0.1	0±0.05	22.4±0.1
4	-32±1	0.2±0.1	0±0.05	32.6±0.1
5	-32±1	-1.6±0.1	0±0.05	32.6±0.1
6	-32±1	-1.75±0.05	0±0.05	32.6±0.1

3. Result and discussion

Based on the experiment introduced, the experiments were carried out in NTNU cold laboratory. During each test, the ice surface and temperature were monitored by photographing and thermistor strings respectively. From the visual information of ice-water interface, we further calculated the ice growth and ice needle behavior.

3.1 Ice temperature

Fig.2 shows the time history of average temperature from the initial ice part of all samples. In Fig.2 (a), it gives the average temperature history of sample in the water with difference salinities. And the temperature variation of sample submerging in the water with various temperature is given in Fig.2 (b). In overall, all the temperature curves follow a closed trend, which has a climb-up beginning and gentle increase afterward. At the beginning of each test, the temperature gradient is large since the low initial temperature and therefore leads to a strong conduction. During this stage, the temperature behaves a fast-increasing. In the later stage, due to the temperature gradient goes down, the increase becomes gentle.

It is interesting to see a similar time history of average temperature. In Fig.2(a), for different water salinity, the heat transfer coefficient (h) has different values. When water temperature is 0.2 ℃, the h No.4 (32.6ppt) test should be the highest since the density difference becomes. For the same water salinity (Fig.2(b)), the samples share a same h and therefore No.6 test experiences the strongest convection due to a large temperature difference. However, neither h nor temperature difference make a major difference on temperature history. It is because in all the tests, the thermal resistance to conduction within ice is much higher than the resistance to convection across the ice-water boundary. The data shows that the conduction dominates the ice temperature.

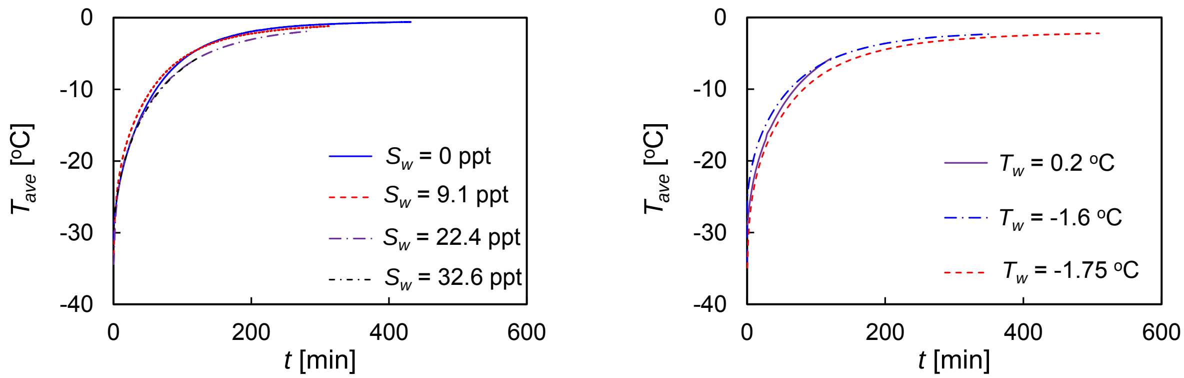

a. Ice temperature under various water salinity b. Ice temperature under various water temperature

Fig. 2. Average temperature history.

3.2 Ice growth

In Fig.3, it gives the ice growth from the tests with difference water salinities and water temperatures. The tests are finished once ice starts melting. In Fig.3(a), it shows that the water salinity influences both ice growth rate and final ice growth. Although the freezing point is lower, the ice growth in 9.1ppt water seems higher than that in fresh water. This is due to the new ice in No.2 test is saline and consumes less energy. In the test with high water salinity, the surface temperature is colder due to the freezing point is lower. This leads to a large surface-environment temperature difference and more heat is released by convection. Thus the ice growth is weakened as shown from the samples with 22.4ppt and 32.6ppt in Fig.3(a). For the tests with various water temperature, it appears significant difference on ice growth as shown in Fig.3(b). The one with T_w= -1.75℃ has a final ice growth of three centimeter, which is almost three times of that in warm water. In these tests, the main difference is convection condition due to the various environment temperature. It means that the ice growth is strongly influenced by heat convection. Overall, the true factors influencing ice growth are convection and ice salinity. The former one decides the total amount energy on ice growing while the latter one denotes the portion of solid ice.

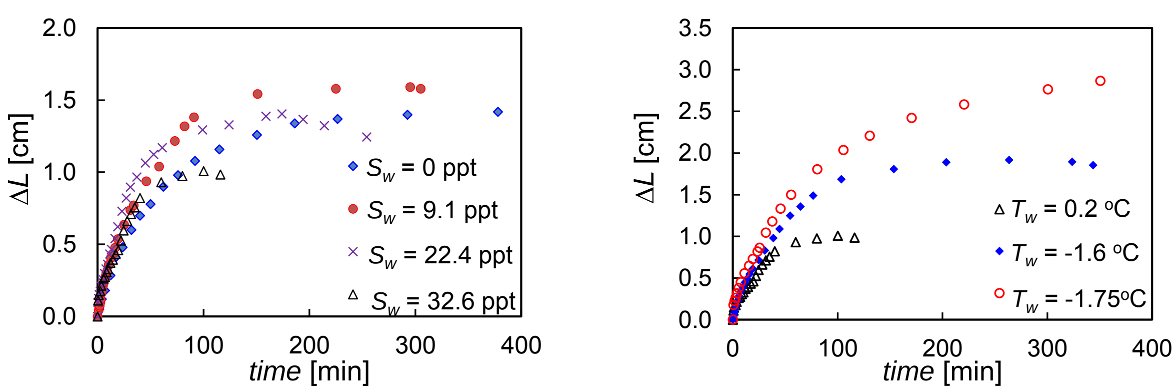

a. Ice growth under various water salinity b. Ice growth under various water temperature

Fig. 3. Ice growth history.

3.3 Morphology of ice water interface

The major distinguishment between fresh ice grow and saline ice grow is the salt rejection. When saline ice grows and ice-water interface downwards, salt irons are rejected from ice. The rejection leads to high salt concentration zone. Since the freezing point decreases with increasing salinity, the high concentration forms a supercool layer. This phenomenon is more convenience to be described by interface morphology. Without salt rejection, a planar interface is preferred throughout the fresh growth process while a lamellar interface forms in saline ice growth.

In Fig.4, it gives ice front condition from No.5 test at difference time. At the beginning of the test, the interface is planar, as shown in t_1. When the test proceeds to t_2, the needles at the interface grows to a visible size. At the time of t_3 (Fig4(c)), the size of needles is increased and can be clearly observed. The surface becomes smooth at the end of the test, as shown in Fig4(d). Accordingly, the sketches of each stage are shown in Fig.4(e)-(h). For the ice growing in saline water, the lamellar structure exists throughout the experiments. However, the environment condition influences the size of the needles. Conventionally, the surface is assumed to be flat for small size.

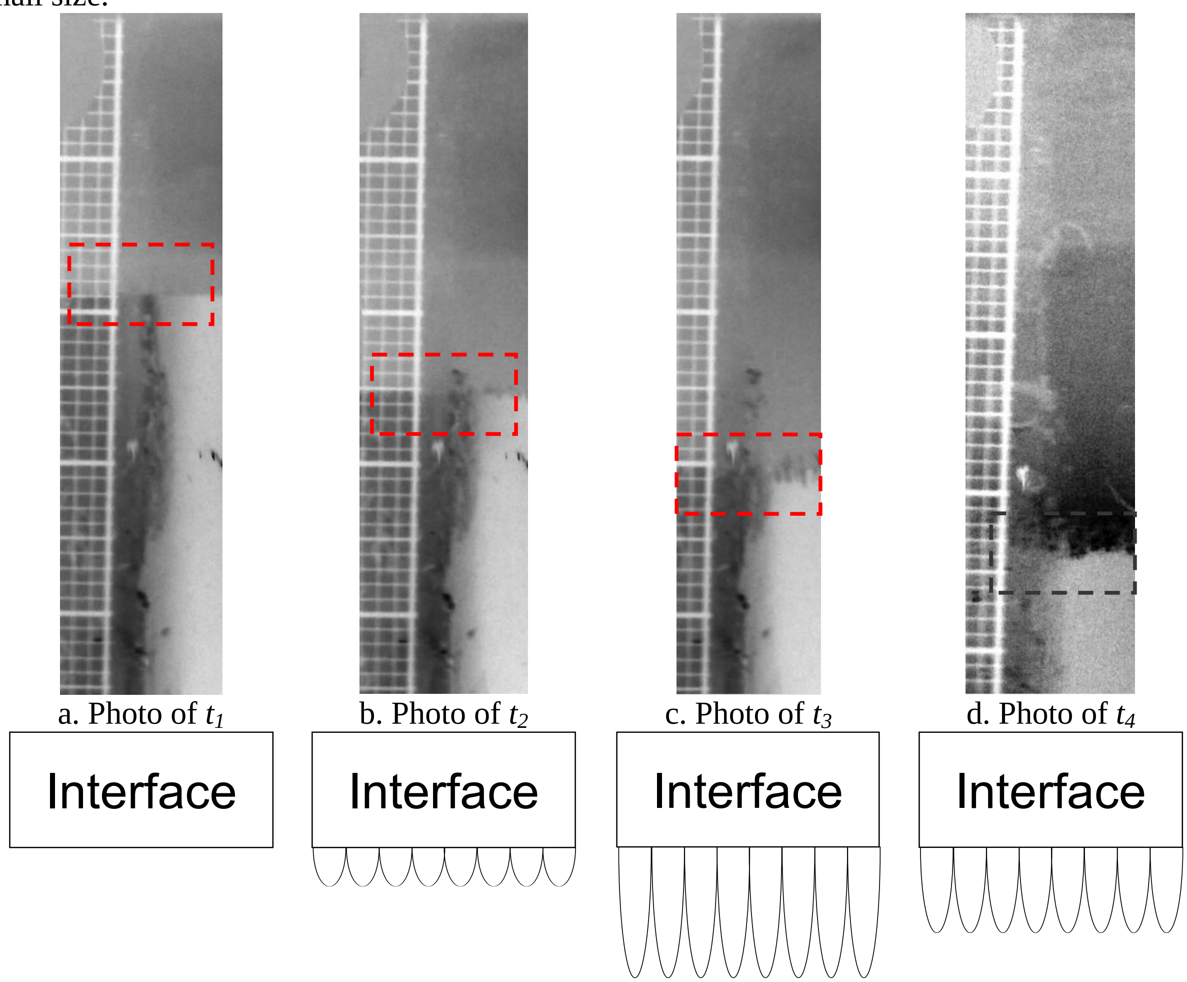

a. Photo of t_1 b. Photo of t_2 c. Photo of t_3 d. Photo of t_4

e. Sketch of t_1 f. Sketch of t_2 g. Sketch of t_3 h. Sketch of t_4

Fig. 4. The development of ice needle.

The growing mechanism is critical for the formation of ice texture and salt rejection. Based on the thin section from No.5 test, we suggest that the saline ice grows in the following procedure: 1. Driven by the temperature, first layer of ice columnar forms at cold front and leaves high concentration brine in the between. 2. The high salinity of brine leads to a closing of columnar and result in needles. 3. The concentration gradient induces mass convection and decreases the water salinity, where second layer columnar starts growing. The process is shown in the sketch of Fig.5, where thin section of No.5 test is given. The upper part of the new ice (red box) owns finer ice grains compared with lower part (yellow box). It seems that the constant water salinity results in difference grain size due to the temperature history. Based on the ice growth history, it shows that the grain shape is dependent on the ice-growing rate. When ice grows in a high rate, the water keeps a high concentration due to the salt rejection. The ice grain closes when the water reaches certain salinity. Therefore, the size of grain is dependent on both water salinity and ice growth rate.

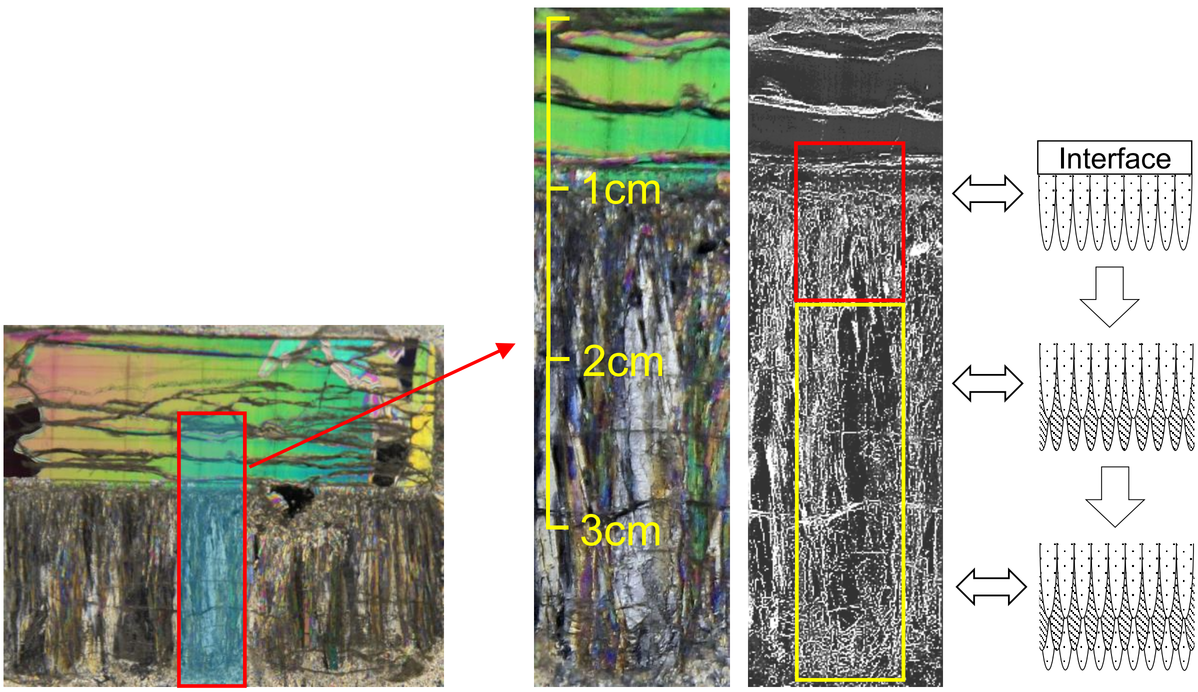

Fig. 5. The ice growth process. (The left is thin section from No.5 test)

Since temperature difference drives the ice growing, it is also related to the development of ice needles. During the ice growing, the needles can be observed when the length reaches certain values, as shown in Fig.4. In Fig.6 gives the beginning and end time of ice needle condition in each test. It is shown that the duration is dependent on the difference between environment temperature and freezing point. The longest duration is 325 minutes in No.6 test while the shortest is 65 minutes in No.2 test. Besides, for fresh water test, the ice needle does not reach a visible size.

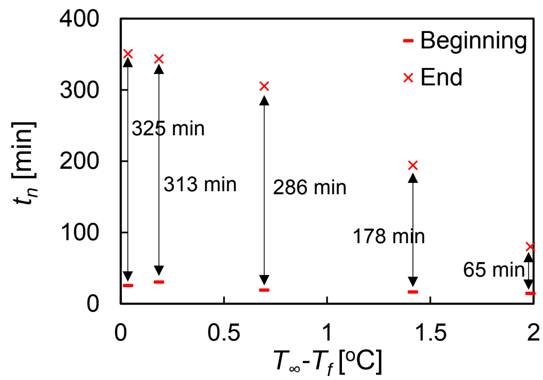

Fig. 6. The duration of needle.

4. Conclusion

In this paper, the thermal process of saline ice growing is studied by submerging tests. The experiments were performed on various water salinities and temperatures. The main conclusion are as following:

(1) The internal thermal resistance is much higher than external resistance, thus the ice temperature is independent on water salinity, which represents heat convection.

(2) The ice growth is related to water temperature and salinity. The new ice thickness decreases with increasing water temperature while has complicated relation with water salinity.

(3) For saline ice, the water-ice interface owns a lamellar structure throughout the growing process. The size of ice needles has negtive correlation with difference between freezing point and water temperature.

Acknowledgments

The work was supported by Chinese Scholarship Council (CSC). The authors furthermore wish to acknowledge the support of the Research Council of Norway through the Centre for Research-based Innovation SAMCoT, and the support of all SAMCoT partners, Johan Wåhlin and Håkon Dahle for the helping in laboratory, Per Østensen and Bent Lervik for the support in instrumentation.

References

Chen, X., Høyland, K. and Ji, S., 2017. The Determination of Heat Transfer Coefficient on Water-ice Surface in a Free Convection, Proceedings of the 24th International Conference on Port and Ocean Engineering Under Arctic Conditions, Busan.

Chen, X. and Høyland, K.V., 2016. Laboratory Work on Heat Transfer in Submerged Ice, Theory, Experimental Setup and Results, Proceedings of the 23rd International Symposium on Ice (IAHR), pp. 4868615.

Cole, D.M. and Shapiro, L.H., 1998. Observations of brine drainage networks and microstructure of first - year sea ice. Journal of Geophysical Research Oceans, 103(C10): 21739-21750.

Gough, A.J., Mahoney, A.R., Langhorne, P.J., Williams, M.J.M. and Haskell, T.G., 2012. Sea ice salinity and structure: A winter time series of salinity and its distribution. Journal of Geophysical Research Oceans, 117(C3): 1-12.

Grab, S., 2001. Needle ice observations from the high Drakensberg, Lesotho. Permafrost & Periglacial Processes, 12(2): 227-231.

Høyland, K.V., 2002. Consolidation of first-year sea ice ridges. Journal of Geophysical Research Oceans, 107(C6): 15-1–15-16.

Leonard, G.H., Purdie, C.R., Langhorne, P.J., Haskell, T.G., Williams, M.J.M. and Frew, R.D., 2006. Observations of platelet ice growth and oceanographic conditions during the winter of 2003 in McMurdo Sound, Antarctica. Journal of Geophysical Research Oceans, 111(C4): -.

Leppäranta, M., Lensu, M., Kosloff, P. and Veitch, B., 1995. The life story of a first-year sea ice ridge. Cold Regions Science & Technology, 23(3): 279-290.

Middleton, C., Thomas, C., Escala, D., Tison, J.-L. and De Wit, A., 2015. Imaging the evolution of brine transport in experimentally grown quasi-two-dimensional sea ice. Procedia IUTAM, 15: 95-100.

Middleton, C.A., Thomas, C., De Wit, A. and Tison, J.L., 2016. Visualizing brine channel development and convective processes during artificial sea-ice growth using Schlieren optical methods. Journal of Glaciology, 62(231): 1-17.

Thomas, D.N. and Dieckmann, G.S., 2010. Chapter 2. Growth, Structure and Properties of Sea Ice. Wiley - Blackwell, 23-77 pp.

Weeks, W.F. and Ackley, S.F., 1986. The growth, structure, and properties of sea ice, The geophysics of sea ice. Springer, pp. 9-164.

Wells, A.J., Wettlaufer, J.S. and Orszag, S.A., 2011. Brine fluxes from growing sea ice. Geophysical Research Letters, 38(4): 37-53.

Worster, M.G. and Wettlaufer, J.S., 1997. Natural Convection, Solute Trapping, and Channel Formation during Solidification of Saltwater. Journal of Physical Chemistry B, 101(32): 6132--6136.

International Association for Hydro-Environment Engineering and Research
Supported by Spain Water and IWHR, China

24th IAHR International Symposium on Ice
Vladivostok, Russia, June 4 to 9, 2018

Real time monitoring and Forecasts of Land fast Sea Ice in the Baltic Sea

Bin Cheng[1], Juha Karvonen[1], Marko Mäkynen[1], Zeliang Liao[2]
Jiechen Zhao[2] and Timo Vihma[1]
[1)] Finnish Meteorological Institute, Erik Palménin aukio 1,
Helsinki Finland
[2)] National Marine Environmental Forecasting Centre, Dahuisi, Haidian Division, 100081,
Beijing, China
bin.cheng@fmi.fi;
Juha.karvonen@fmi.fi;
Marko.makynen@fmi.fi;
zeliang.liao@hotmail.com;
zhaojiechen@outlook.com;
timo.vihma@fmi.fi

We have developed and tested a novel monitoring and forecasting system for the Baltic Sea land fast sea ice and snow thickness. The system is composed of real-time measurements of snow and ice temperature and thickness by the high-resolution Snow and Ice Mass Balance Array, known as SIMBA; A high-resolution thermodynamic snow/ice model (HIGHTSI) forecasts using ECMWF 10-days weather forecasts as external forcing; and SENTINEL-1 and RADARSAT-2 SAR imagery and a classification algorithm to identify land fast sea ice area. We provide daily land fast sea ice thickness and snow thickness products. The SAR imagery can also provide further ice information, such as total ice deformation along the land fast ice boundaries, and location of the major ship tracks across the land fast ice field. The purpose of this extended abstract is to document the compositions and setup of the snow and sea ice monitoring and forecasting system for the Baltic Sea Land Fast Ice (BALFI) service. We are aiming to establish a sustainable BALFI service for the Baltic Sea in the coming ice seasons.

1. Introduction

Baltic Sea is covered by ice in every winter. Smooth winter navigation in the Baltic Sea relies heavily on accurate sea ice information. Ice fishing and skiing are very popular outdoor activities in winter-spring season on the land-fast ice zone of the Baltic Sea. Over thick land-fast ice roads can be established between main land and populated islands to speed up transportation compared to the use of ferries. Land-fast ice also allows transport of material to or from islands without piers for large ships. However, one needs to know and be aware of snow and sea ice thickness in order to avoid dangerous situations. Therefore, better snow and ice information of the Baltic Sea for the authorities and public is vitally important.

Finnish Meteorological Institute (FMI) will demonstrate a new coastal downstream service for the Baltic Sea: Baltic Sea landfast ice extent and thickness (BALFI), starting from the winter 2018-2019. The BALFI service includes a derived product (landfast ice extent and thickness) based on two existing CMEMS Baltic Sea products, and additionally, on SENTINEL-1 and RADARSAT-2 SAR imagery, sea ice thermodynamic model HIGHTSI run at FMI, and available operational in-situ snow and sea ice data. The service will also give information on snow thickness on landfast ice, dynamic ice parameters (e.g. total deformation) along the landfast ice boundaries, and locate major ship tracks across the landfast ice field. The product will be operationally generated on a daily basis and distributed (via web-portal) at Sodankylä National Satellite Data Center (NSDC, see http://nsdc.fmi.fi/) of FMI. The BALFI development is funded by a Mercator Ocean tender (Development and promotion of demonstrations of CMEMS downstream services).

The in-situ snow and thickness data is provided by weekly manual measurements at fixed locations organized by Finnish Ice Service, and by a new type of ice mass balance buoy (IMB) entitled as “high-resolution Snow and Ice Mass Balance Array (SIMBA)” (Jackson, et al, 2013). The SIMBA buoys are composed of a very high spatial-resolution thermistor string. The temperature profiles have been used for the energy balance studies in seasonally ice-covered seas, lakes and polar ice cover (Cheng et al., 2014, Hoppmann et al., 2015, Lei, et al, 2018). Snow and ice thickness can be derived from the SIMBA temperature profiles manually (Cheng et al., 2014) or automatically (Liao et al., 2017, Zhao et al., 2017).

In winter 2017/2018, two SIMBA buoys have been deployed on land-fast ice south of Hailuoto island and in the Kalajoki Archipelago (Fig.1) to monitor snow and ice thickness. In this extended abstract we focus on the installation of SIMBA monitoring system and snow and ice thickness retrieval from SIMBA temperature profiles, and on simulation of snow and ice thickness using the HIGHTSI snow/ice thermodynamic model (Launiainen and Cheng, 1998). We provide an overview on the generation of the BALFI products.

Real time monitoring of land fast sea ice

Point measurement

Since winter seasons 2012/2013, the SIMBA buoys have been deployed in the Baltic Sea at two locations (Fig. 1) on land fast ice to monitor the snow and ice thickness evolution. For safety reasons, the deployment were often made in January when ice thickness was at least 20 -30 cm. The sensor positions at ice surface, freeboard level and ice bottom were measured. The thermistor chain borehole remained exposed (Fig. 2) to ensure a proper refreezing of it. A SIMBA buoy measures vertical temperature profiles four times daily. The temperature profiles are transmitted to a data server on a daily basis through the Iridium satellite network. A script is run daily to download the SIMBA measurements from the SIMBA data server to a FMI local computer and the vertical temperature readings are illustrated (Fig. 3). The vertical coordinate are converted from sensor numbers to the vertical depth (cm). We have developed an automated algorithm to process SIMBA temperature data to snow and ice thickness. The principle of the algorithm is based on heat flux continuation through the air-snow- ice-water system and measurements of the vertical temperature profile with a high accuracy and vertical resolution (Liao et al., 2018). The algorithm has worked reasonable well for the Polar conditions. A preliminary investigation, however, suggested that the algorithm does not work well for the Baltic Sea ice. The problem lies in the detection of the ice bottom as the ocean temperature at the ice bottom in the Baltic Sea is much higher than that in the Arctic Ocean due to low salinity of the Baltic Sea. A further improvement of the algorithm is under way. Hence, for the 2017/2018 ice season, the SIMBA data analyses were still largely manual.

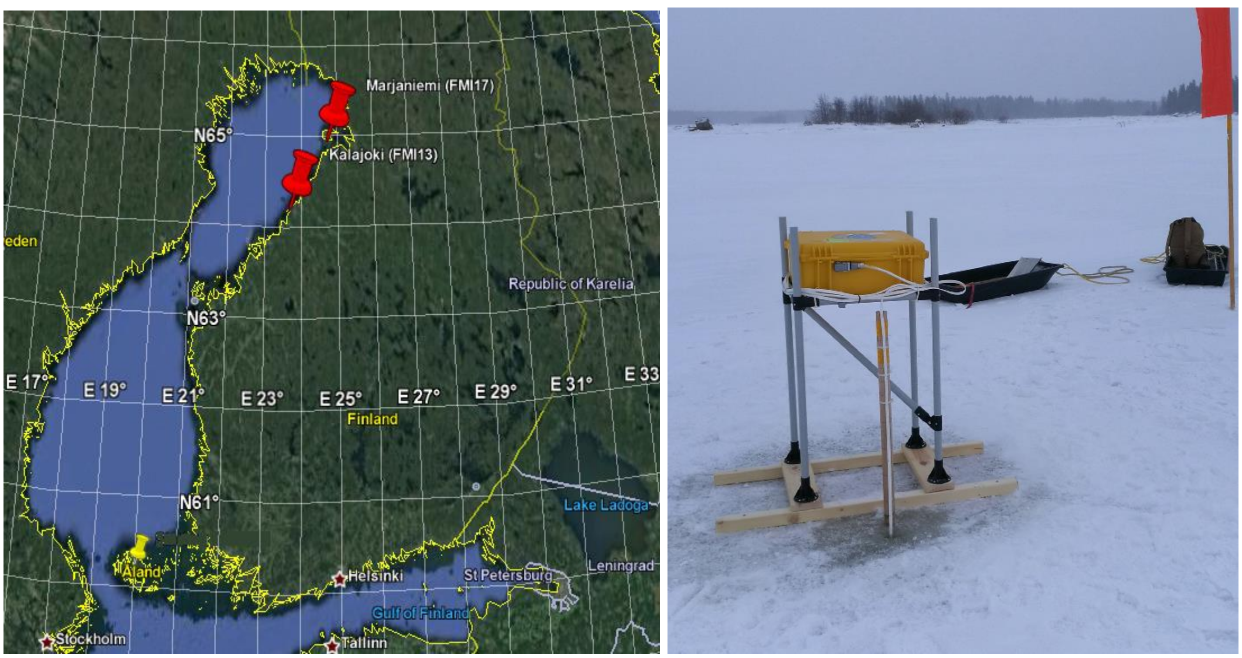

Fig. 1. a) Partial Baltic Sea domain. The red pins represent the spots where SIMBA ice mass balance buoys were deployed. b) Onsite photo of SIMBA deployed at Kalajoki on 18 January 2018.

Figure 3 showed the examples of latest visualization of SIMBA measured vertical temperatures. Here two profiles represented vertical temperature on 26 January and its evolution after some days on 7 February at Hailuoto site. The light blue and red lines mark the initial ice surface and bottom, respectively. The green dashed line is the ice bottom on 26 January and the blue line is the ice bottom on 7 February. The SIMBA buoys were recovered on 17 April. At Hailuoto site (Fig.2), the surface was at sensor S82 level. There was some 6 cm hard snow. The total ice thickness was 66 cm at the time when buoy was recovered. The ice bottom sensor was S117.

During the measurement period, the ice bottom growth was (117-103)*2 = 28 cm. Compared with the initial ice thickness of about 36 cm, the snow-ice was roughly 2 cm.

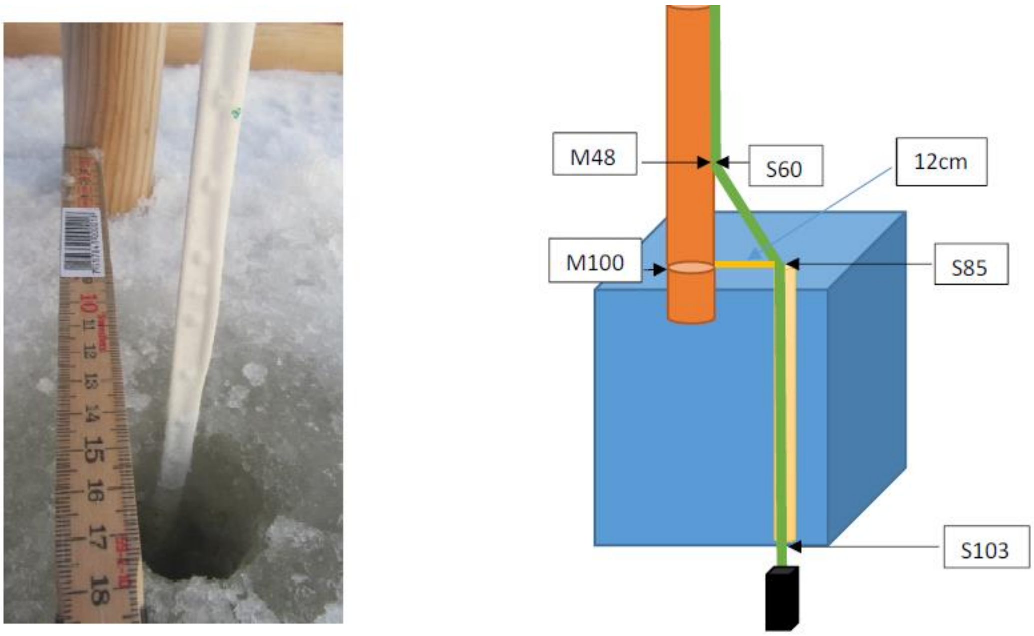

Fig. 2. a) A close look of thermistor string placed in the borehole. B) Schematic illustration of supporting wooden stick (Orange bar) and attached thermistor string (green segments) along the vertical direction through air-ice-ocean. M100 and M48 refer to the initial reference marks on the wooden-stick, S60, S85 and S103 are the initial sensor positions. The black block is a weight attached to the bottom of the thermistor string to ensure that the sensor chain to be vertically straight.

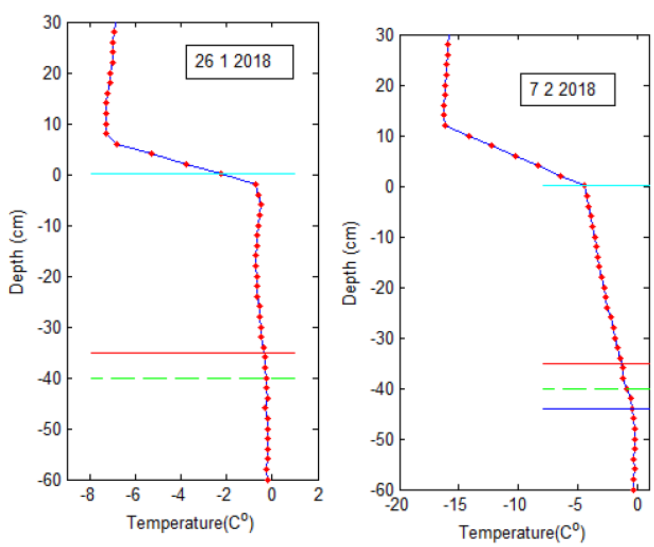

Fig. 3. Examples of vertical temperature profiles from air downward into snow-ice-ocean.

Downstream Baltic Sea Land Fast Ice (BALFI) Service

The BALFI products and the end-user service portal are currently under development. The BALFI demonstration will start in Nov/Dec 2019 and continue for at least until June 2021. Information about the BALFI service is available at: http://nsdc.fmi.fi/services/Copernicus_Marine_Service/BALFI.

SENTINEL-1 and RADARSAT-2 SAR imagery, two CMEMS Baltic Sea products, HIGHTSI model data as well as numerical weather prediction model forecasts data are used to create the BALFI products. The full technical diagram of the BALFI is prescribed in Figure 4. The SIMBA snow and ice thickness data will be used at first for validation activities, and later also as input data for the BALFI products. The BALFI products are generated daily during the Baltic Sea ice season (Nov/Dec to June), with areas of new SAR image acquisitions updated. The products will cover the whole Baltic Sea, with a spatial resolution of 1 km.

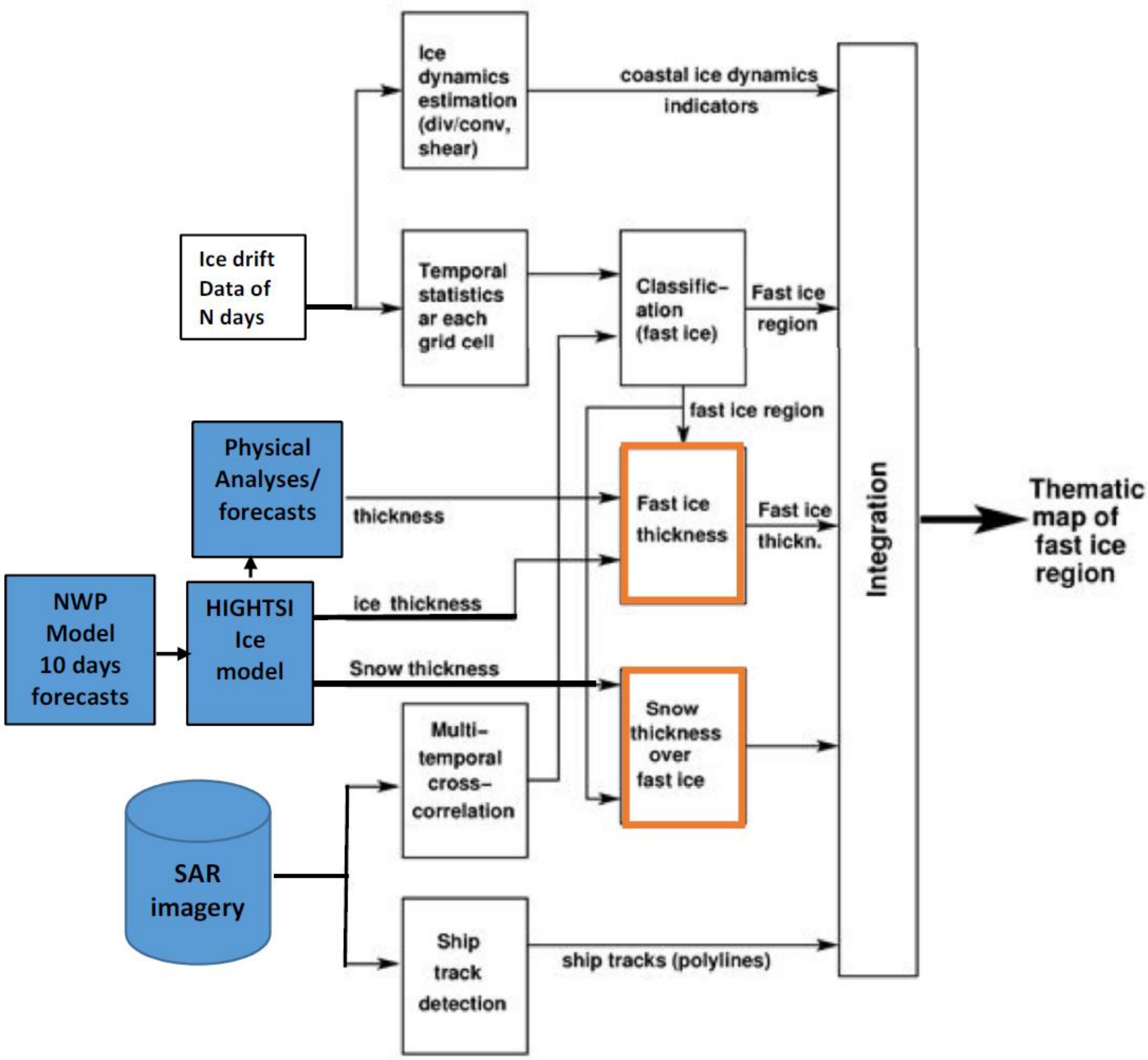

Fig. 4. Schematic production chain of the BALFI products. The colored frames are the major components of this study.

Snow and sea ice forecasts

The land fast sea ice is immobile, and thus the mass balance is controlled by the thermodynamic process. We applied a high resolution 1-D snow/ice thermodynamic model (HGHTSI) to predict snow depth and ice thickness. HIGHTSI is a process model used to accurately resolve the evolution of snow/ice thickness and temperature profile (Launiainen and Cheng, 1998). The external weather forcing variables for HIGHTSI were taken from the short-term forecasts of the European Centre for Medium- Range Weather Forecasts (ECMWF) numerical weather prediction (NWP) model. The ECWMF variables we applied so far are wind speed, air temperature, moisture, cloudiness and snow precipitation. The weather data for the entire Baltic Sea domain has a spatial resolution of about 7.5 km. The entire Balti Sea has 7635 sea grid points (Fig. 5). The impact of ice drift was taken into account by incorporating sea ice concentration (SIC) product into the HIGHTSI model. When a grid cell is at least partly covered by sea ice (SIC > 20%), the ice growth is calculated at that particular grid cell. If the ice concentration at a certain grid cell is reduced below 20 %, the ice thickness will remain at the value of the previous time step. The calculation of ice growth is resumed once the ice concentration is again larger than 20 %. The oceanic heat flux is parametrized as a function of the SIC value. This assumption is based on the assumption that where increasing amounts of open water are usually associated with increasing solar energy absorbed by the ocean, consequently increasing the oceanic heat flux.

The sea ice forecast was initialized in early December 2017. The initially we set up a thin ice thickness of about 0.02 m and in-ice temperature of -0.25°C for the entire domain. We applied an initialization procedure of Yang et al. (2013) to identify when sea ice start to form in the Baltic Sea. Once the weather conditions favor ice formation, HIGHTSI run was carried out each day. For each day the initial snow and ice thickness at each grid is from 24 h forecasts of the previous day (Fig 6).

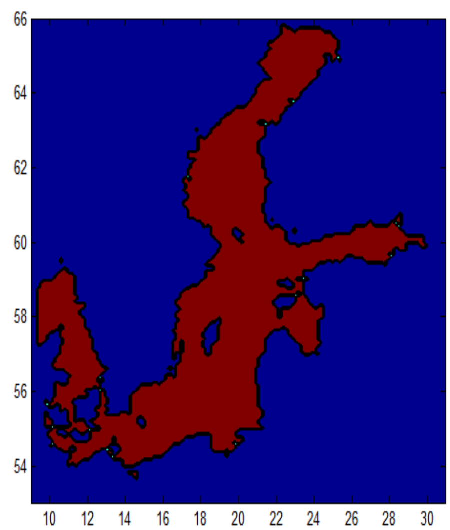

Fig. 5. The Baltic Sea domain. The land (blue) and sea (red) mask. The spatial resolution of sea grid is 0.133 degree in longitude and 0.0665 degree in latitude.

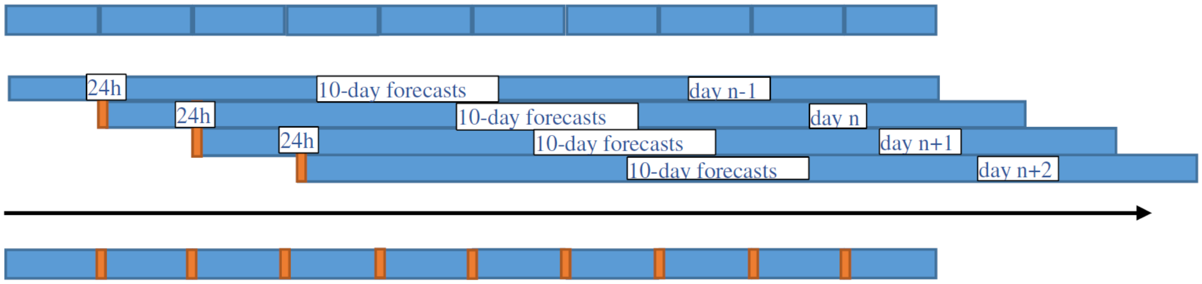

Fig. 6. Time line of HIGHTSI model forecasts and daily BALFI product production. The small blue segment represent one day. The orange represent the 24 h sea ice forecasts.

The production of the BALFI product in terms of timeline was arranged in the following way: on day N, HIGHTSI is operated using ECWMF 10 day forecasts as external input. The initial snow and ice conditions are read from day (N-1)'s 24 h forecasts. The day N's 24 h snow and ice thickness forecasts results are picked up and combined with the SAR data to provide land fast ice thickness and snow thickness (Fig. 7). In the following day N+1, the HIGHTSI model is operated using N day's 24 h snow and ice forecasts as initial conditions and (N+1) day's ECWMF weather forcing data as weather forcing. So eventually we generate a time series of snow and ice thickness products.

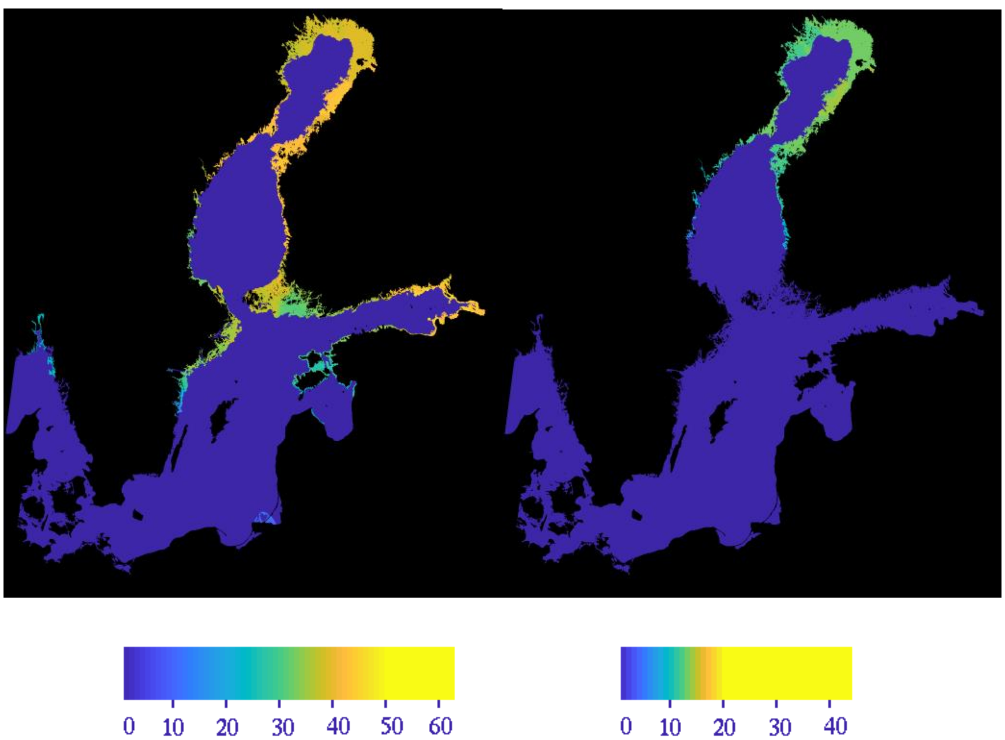

Fig. 7. Ice and snow thickness over land fast ice calculated by HIGHTSI model on April 4, 2018. The land fast ice extent was extracted from SAR imagery.

Final remarks

We described a novel monitoring and forecasting system for the Baltic Sea land fast sea ice and snow thickness. The major components are 1) The SENTINEL-1 and RADARSAT-2 SAR imagery and a classification algorithm to identify land fast sea ice area; 2) A high-resolution thermodynamic snow/ice model (HIGHTSI); 3) Daily product of ECMWF 10-days weather forecasts, and 4) the high-resolution Snow and Ice Mass Balance Array (SIMBA). The system has been tested on a quasi-operational trail during the winter 2017/2018. This is a very preliminary summary of the BALFI system. A validation of the BALFI products are underway, for example, the *in situ* snow and ice thicknesses measured by local ice observers on weekly basis are under investigation and will be used to compare with the SIMBA derived snow and ice thickness. A user-friendly web-demonstration portal is also under construction and is expected to be ready for the next winter season.

Acknowledgments

This study is funded by a Mercator Ocean tender (Development and promotion of demonstrations of CMEMS downstream services) and the Academy of Finland under contract No. 283101

References

Cheng, B., Vihma T., Rontu, L., Kontu, A. Kheyrollah Pour H., Duguay C. and Pulliainen, J. 2014. Evolution of snow and ice temperature, thickness and energy balance in Lake Orajärvi, northern Finland, Tellus A 2014, 66, 21564.

Hoppmann, M., M. Nicolaus, P. A. Hunkeler, P. Heil, L.-K. Behrens, G. König-Langlo, and R. Gerdes. 2015. Seasonal evolution of an ice-shelf influenced fast-ice regime, derived from an autonomous thermistor chain, J. Geophys. Res. Oceans, 120, 1703–1724, doi:10.1002/2014JC010327.

Jackson, K., Wilkinson, J., Maksym, T., Meldrum, D., Beckers, J. and co-authors. 2013. A novel and low cost sea ice mass balance buoy. J. Atmos. Ocean. Tech. 30(11), 26762688. DOI: 10.1175/JTECH-D-13-00058.1

Launiainen, J., and Cheng, B. 1998. Modelling of ice thermodynamics in natural water bodies, Cold Reg. Sci. Technol., 27(3), 153-178.

Lei, R., Cheng, B., Heil, P., Vihma, T., Wang, J., Ji, Q. and Zhang, Z. 2018. Seasonal and interannual variations of sea ice mass balance from the Central Arctic to the Greenland Sea. Journal of Geophysical Research: Oceans, 123. https://doi.org/10.1002/2017JC013548

Liao Z., Cheng B., Zhao J., Vihma T., Yang Q., Zhang L. 2017 An automated algorithm for detection of snow and ice thickness on the basis of data from SIMBA sea ice mass balance buoy. The 32th International Symposium on Okhotsk Sea and Sea Ice, 19 - 22 February, 2017 Mombetsu, Hokkaido, Japan.

International Association for Hydro-Environment Engineering and Research
Supported by Spain Water and IWHR, China

24th IAHR International Symposium on Ice
Vladivostok, Russia, June 4 to 9, 2018

Optics of Melt Ponds on Arctic Sea Ice

Peng Lu[1], Zhijun Li[1], Bin Cheng[2], Matti Leppäranta[3]
1.State Key Laboratory of Coastal and Offshore Engineering,
Dalian University of Technology, Dalian, China
lupeng@dlut.edu.cn
2.Finnish Meteorological Institute, Helsinki, Finland
3.Institute of Atmospheric and Earth Sciences, University of Helsinki, Helsinki, Finland)

Melt ponds are important and inevitable issue as dealing with the dramatic decay of current Arctic sea ice. The melt pond properties and its effect on Arctic sea ice mass balance has been studied extensively in recent years. However, there are still some shortcomings in the studies. For example, the pond albedo is still associated with pond depth according to field observations many years ago. Pond color is never examined and only treated as an additional feature of meltwater on ice surface. And partitioning of solar energy in melting sea ice is still difficult to measure in summer Arctic. In this study, a radiative transfer model was adopted to investigate the optics of melt ponds on Arctic sea ice, including issues mentioned above. The results show that the present model has the capability to model the optics of melt ponds on Arctic sea ice, which produced comparable results with previous data on the melt-pond albedo and color. It can be also implemented into sea-ice thermodynamic models to improve our understanding of the effect of melt ponds on surface heat budget and mass balance. More validation data are still necessary to compare with the modelling results.

1. **Introduction**

Melt ponds on Arctic sea ice surface in summer have attracted much attention from scientists because of their important role as illustrating the rapid decay of Arctic sea ice in summer in recent decades. They can cover up to 50% of the ice surface and lower the surface albedo from as high as 0.8 (snow) to as low as 0.15 (Perovich and Polashenski, 2012). The albedo evolution generates a positive ice-albedo feedback mechanism, which enhances the melting of ice, alters the physical and optical properties of sea ice, and even affects the salt and heat budget of the ocean surface layer (Landy et al., 2014).

Efforts have been made in different aspects through field observations, remote sensing, and numerical modelling. For examples, the spatial and temporal distribution of melt ponds on sea ice surface has been investigated, to find the possible relationship between melt pond evolution and sea ice decay within a relative long period (Webster et al., 2015). Melt-pond albedo and its evolution during its life cycle has been observed, to reveal the role of melt ponds in the albedo-feedback mechanism (Perovich and Polashenski, 2012). The mechanism of melt pond formation and evolution has been explored, to explain the influence of melt-pond development on sea ice melt (Polashenski et al., 2017).

However, there are still some uncertainties in these previous studies. For example, the pond albedo is still associated only with pond depth according to field observations many years ago. Pond color is never examined and only treated as an additional feature of meltwater on ice surface. And partitioning of solar energy in melting sea ice is still difficult to measure in summer Arctic. Therefore, a radiative transfer model (RTM), initially developed to parameterize melt-pond albedo (Lu et al., 2016), was employed in this study to address these issues. The framework of the RTM is summarized in Section 2. Section 3 discusses the variations in melt-pond albedo, color, and energy partitioning in melting sea ice. And conclusions are drawn in Section 4.

2. Model Setup

In the spectral RTM for melt ponds in Lu et al. (2016), sea ice with melt ponds was simplified to comprise of three plane-parallel layers: meltwater, underlying ice, and ocean beneath ice (Fig. 1), without considering the horizontal inhomogeneity of sea ice. In each layer of the model, radiation transfer was simplified as two streams, upwelling irradiance $F^{\uparrow}(z, \lambda)$ and downwelling irradiance $F^{\downarrow}(z, \lambda)$. These are governed by two coupled first-order differential equations, which describe how irradiance is lost due to absorption, and lost and gained due to scattering, under the assumptions of diffuse incident solar radiation and isotropic scattering (Flocco et al., 2015). Given continuity of radiation fluxes at each interface, the irradiance in both directions in each layer can be calculated as well as the surface albedo α_{λ} and transmittance T_{λ}.

A two-stream model is employed instead of a more advanced RTM such as the Monte Carlo approach (Light et al., 2003). This is because the two-stream model is mathematically straightforward, and an analytical solution is available for model validation. Moreover, different studies have revealed that the results of the two-stream RTM agree well with field measurements on sea ice (Flocco et al., 2015; Lu et al., 2016). The limitations of such model lie to assumptions of diffuse incident solar radiation in the air and isotropic scattering in the ice. The former assumption is not a major problem in Arctic summer because sky is often covered with low stratus cloud (Perovich, 1990). The latter one is also not badly biased for melting sea ice, because the geometric structure of porous sea ice becomes more irregular that can favor isotropic scattering in the ice (Leppäranta et al., 2003).

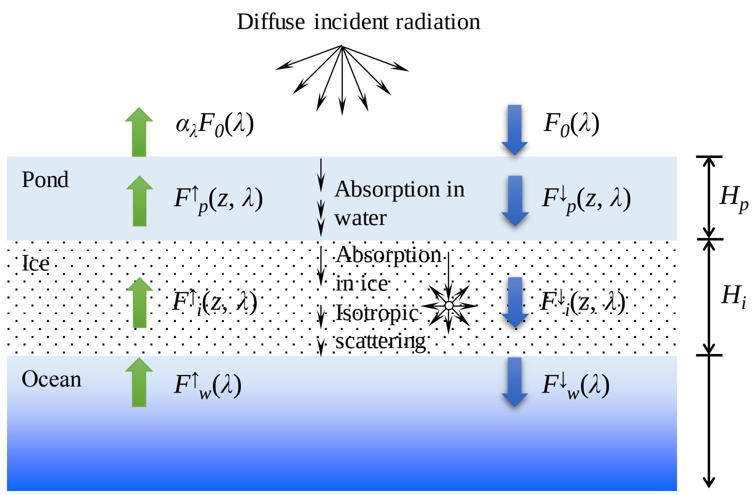

Fig. 1. Schematic graph of the radiative transfer model for melt ponds on Arctic sea ice. $F_0(\lambda)$ is the incident solar irradiance. $F^{\uparrow}(z, \lambda)$ and $F^{\downarrow}(z, \lambda)$ are the upwelling and downwelling irradiances, and z is the depth, with subscripts p, i, w for the layer of meltwater, underlying ice, and ocean respectively. H_i is the thickness of underlying ice, H_p is the pond depth, α_λ is the spectral melt-pond albedo, and λ is the wavelength, covering the solar spectrum from 300 nm to 2500nm.

The IOPs of each layer are defined by the wavelength-dependent scattering coefficient σ_λ and absorption coefficient k_λ. They have been fully discussed in Lu et al. (2016), and therefore their results are used here. The incident solar irradiance $F_0(\lambda)$ measured by Grenfell and Perovich (2008) under an overcast sky at noon in August with the solar disk not visible, is employed as a representation of Arctic summer.

3. Results

3.1 Melt-pond Albedo

Variations of the boardband melt-pond albedo with both pond depth H_p and ice thickness H_i are investigated. H_p was assumed to vary between 0 and 0.5m, and H_i varied between 0.5 and 5.0 m. The results are shown in Fig. 2.

The broadband albedo α (Fig. 2a) varied within the range (0.2–0.4) comparable with the observations by Perovich and Polashenski (2012). For thin ice (H_i < 1 m), α depended mainly on H_i, but with increasing H_i, α was first sensitive to both H_i and H_p and finally only on H_p for H_i > 3 m. For incident solar radiation, pond water is an absorbing medium, while ice is an absorbing or scattering medium, depending on the wavelength. As H_i < 1 m, an increase in ice thickness will significantly enhance the upwelling irradiance through backscattering in ice, namely increasing the surface abledo. While for H_i > 3 m, any further increase in H_i will not change the backscattered irradiance very much, but inceases in H_p will reduce the downwelling irrdiance that penetrates through the melt ponds, reducing the surface albedo as a result. According to the variations in Fig. 2a, the broadband melt-pond albedo α can be expressed by:

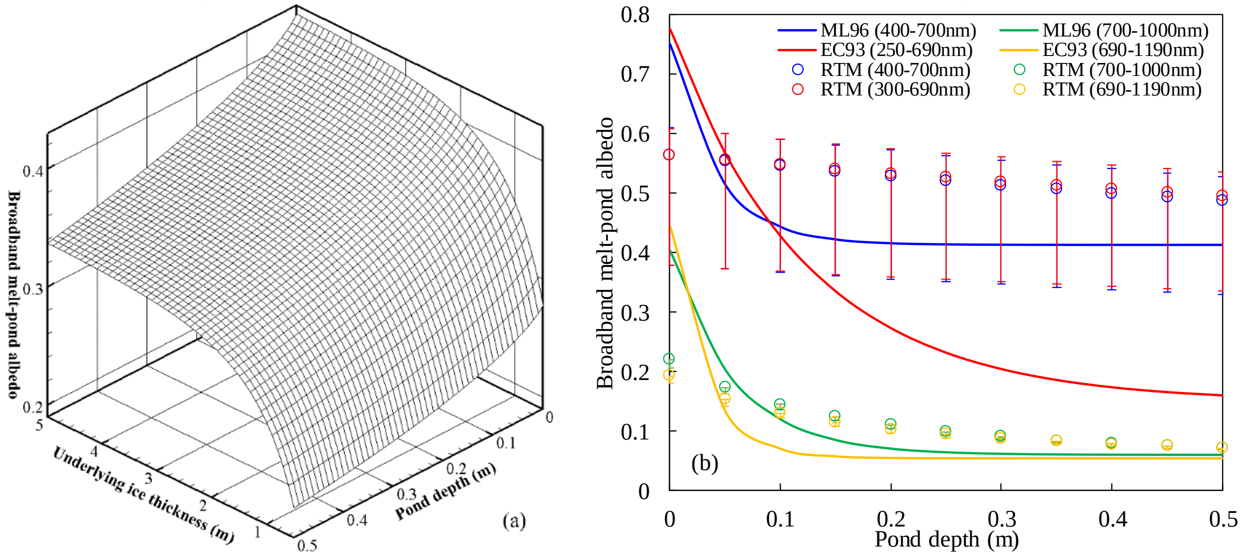

Fig. 2. (a) Variations in the boardband melt-pond albedo α with underlying ice thickness H_i and pond depth H_p. (b) Comparisions of the simulated melt-pond albedo using the RTM with previous paramaterizations, including Morassutti and Ledrew(1996) (ML96) and Ebert and Curry (1993) (EC93).

$$\alpha = \begin{cases} 1.2H_i & H_i \le 1\text{ m} \\ 0.5H_i + 0.8H_p & 1\text{ m} < H_i \le 3\text{ m} \\ 2.5H_p & 3\text{ m} < H_i \end{cases} \qquad \textbf{[1]}$$

This is in contrast to the parameterization in Morrassutti and Ledrew (1996) and Ebert and Curry (1993). The formmer studied 2-m-thick FYI and 2.5–6.0-m-thick MYI, and the albedo changed only with the H_p in both studies. The Arctic sea ice thickness in the current summer is seldom beyond 2 m, and is different from the situations twenty years ago, thus our model is maybe more realistic.

For any given pond depth, the parameterized pond albedo values are widely spread (Fig. 2b). The different spectral windows employed in the various studies may partly explain the differences. Of these results, EC93 (690–1190 nm) gave the smallest pond albedo, similar with that of ML96 (700-1000 nm), partly attributing to the enhanced absorption in water of longer-wavelength radiation. EC93 (250–690 nm) gave much more realistic pond albedo for deep ponds, and the albedo decreased significantly with the pond depth. Variations in the pond albedos predicted by ML96 (400–700 nm) are different to that by EC93 (250–690 nm), but similar to EC93 (690–1190 nm). The results of present RTM considered an underlying ice thickness of 1.5 m, and errors due to H_i are presented by the vertical bars in Fig. 2b. The positive bars denote the values for H_i = 2.5 m and negative bars for H_i = 0.5 m. The RTM results agree well with the paramaterization in EC93 (690–1190 nm) and ML96 (700-1000 nm). In this band, the influence of ice thickness is negligible because of the strong absorption of water. But the difference between the RTM results and EC93 (250–690 nm) and ML96 (400–700 nm) is considerably large for deep ponds. For ponds shallower than 0.1 m, the parameterized pond albedo showed an exponential variation with pond depth because exponential functions were applied, while the present result varied more moderately with pond depth, similar to the modeling in Makshtas and Podgorny (1996).

3.2 Melt-pond Color

Albedo sensed by spectral radiometers represents the spectrum upwelling irradiance from the pond surface, but the color of a melt pond is actually the response of human eyes to this irradiance, which consists of the reflected solar radiation from the pond surface and the backscattering radiation from ice and water below. A colorimetric method to describe the color of a melt pond has been developed by Lu et al. (2018b) using the upwelling irradiance from the pond surface, therefore it can be employed here to investigate the variation of pond color with the properties of the surface lid. The pond depth and underlying ice thickness are altered here, and variations in the color of melt ponds are shown on Fig. 3. The color is a vector comprising of red, green and blue intensities in the RGB color space.

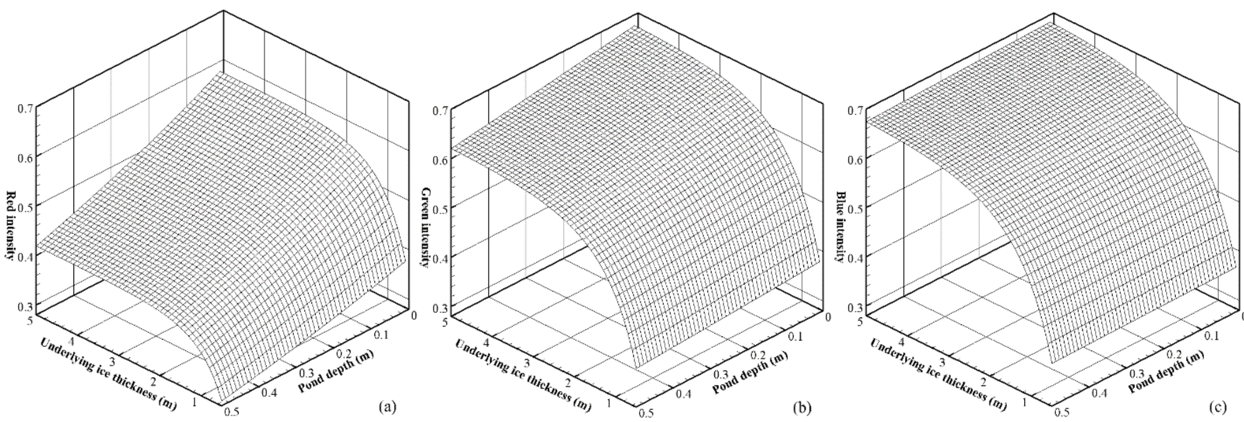

Fig. 3. Variations of melt-pond color in the RGB color space with underlying ice thickness H_i and pond depth H_p: (a) red intensity, (b) green intensity, and (c) blue intensity.

In Fig. 2a, the melt-pond albedo is sensitive to H_i for thin ice, but to H_p for thick ice. The behavior of the three primary colors is somewhat different. The red component in Fig. 3a increases mostly with increasing H_i for thin ice ($H_i < 1.5$ m), but with increasing H_p for thick ice ($H_i > 1.5$ m), similarly with Fig. 2a. However, the green and blue components in Figs. 3d and 3c change only with H_i and almost not at all with H_p, except for very thick ice with $H_i > 4$ m. In other words, deeper pond water makes the color bluish rather than gray because red light is more easily absorbed by pond water. Basically, melt ponds on FYI in Arctic are shallow and flat, resulting in various gray color tones, while melt ponds on MYI may have relative larger depth ranges and more complex geometrical patterns, displaying green and blue (Webster et al., 2015). These agree with the variations in Fig. 3.

The only quantitative measurements for pond color were conducted by Istomina et al. (2016) on the Arctic sea-ice surface during the R/V Polarstern cruise ARK27/3 IceArc 2012. A digital camera was used to take photographs of melt ponds, and the color information was extracted to associate with measured pond depth and underlying ice thickness. Using the measured H_i and H_p, the pond color can be reproduced and compare with the in-situ observations, as shown on Fig. 4. The simulated pond color agrees well with the in-situ measurements by Istomina et al. (2016). The measured H_p was in the range of 8–40 cm and H_i in the range of 33–256 cm, producing varying pond color with a red intensity in the 0.3–0.6 range, a green intensity within 0.4–0.8, and a blue intensity within 0.4–0.8. The simulated red, green, and blue intensities of pond color were within 0.3–0.5, 0.4–0.6, and 0.4–0.6 respectively. The agreement is acceptable because H_i and H_p are the only variables in the present model, but in-situ environmental conditions such as sky conditions and ice optics were different from pond to pond and of course not completely consistent with the definitions in the model. In other words, this experiment underlines the importance of H_i and H_p in determining the surface appearance of melt ponds (Lu et al., 2016).

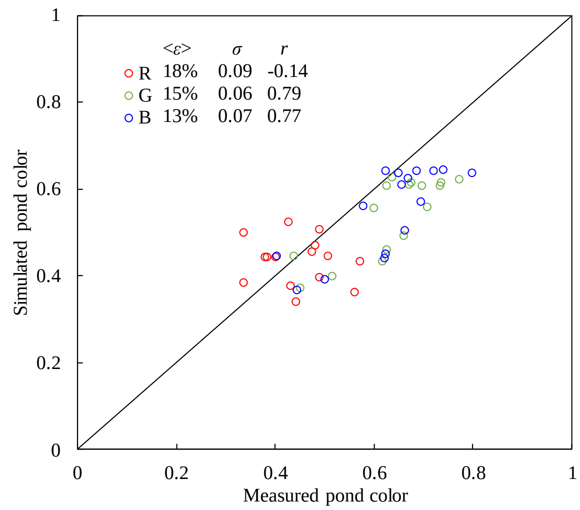

Fig. 4. Comparisons of simulated melt-pond color with field measurements in Istomina et al. (2016). r is the correlation coefficient between simulated and measured color. σ is the root-mean-square error, and $<\varepsilon>$ is the mean of relative error in simulated color.

3.3 Energy Partitioning in Sea Ice

After the upwelling and downwelling irradiances in each layer were calculated, the solar radiation absorbed by the layer can be determined straightforwardly using the changes in the net irradiance, $F_{net}(z, \lambda) = F^{\uparrow}(z, \lambda) - F^{\downarrow}(z, \lambda)$ (Lu et al., 2018a). The fraction of incident solar radiation reflected back by the pond surface has been shown in Fig. 2a, and the fractions absorbed by melt pond, by underlying ice, and by ocean beneath ice are shown in Fig. 5.

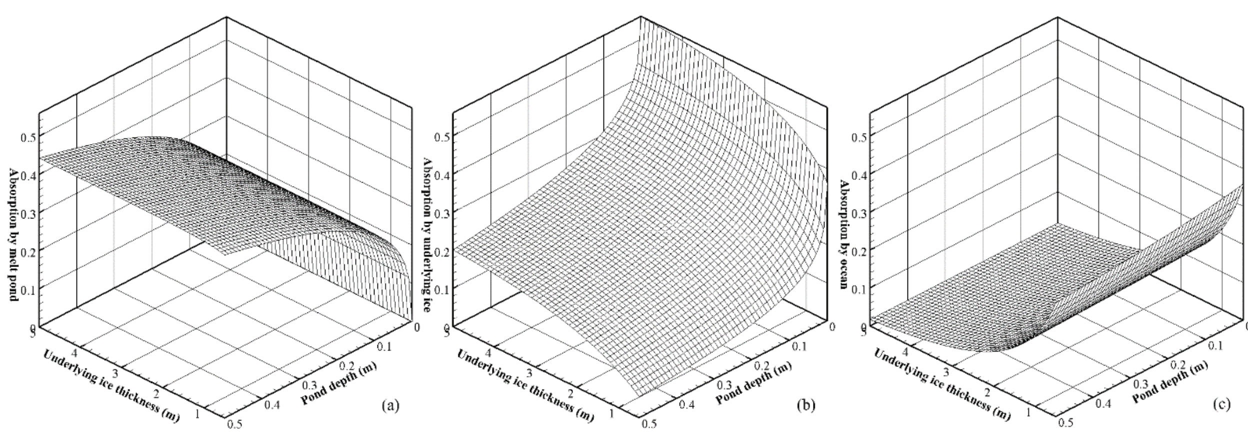

Fig. 5. Variations in the fractions of incident solar radiation absbdorbed by (a) melt pond, (b) underlying ice, and (c) ocean beneath ice with underlying ice thickness H_i and pond depth H_p.

The portion of solar energy absorbed by the melt pond increases only with increasing pond depth (Fig. 5a). The positive effect of backscattering in thicker underlying ice on absorption in melt ponds seems negligible. While the portion absorbed by underlying ice varies in a more complicated way (Fig. 5b). This can be explained by the counteracting effect of pond and ice to the energy absorption in ice. For a deep pond on thin ice, an increase in ice thickness will significantly enhance the absorbed energy of the underlying ice. For a shallow pond with thick ice, a decrease in pond depth also greatly benefits the absorption by ice. However, for medium values of H_p and H_i, the positive effect of an increase in H_i can be completely counteracted by the negative effect of an increase in H_p. The fraction of incident solar radiation absorbed by ocean beneath ice equals to the transmittance, which depends mostly on H_i, and slightly on H_p (Fig. 5c). This result agrees with Lu et al. (2016). That is, the portion of solar energy that penetrates to the ocean beneath the ice increases only when the ice becomes thinner, because the extinction effect of ice to the penetrating radiation (absorption + scattering) is stronger than that of water (absorption).

4. Conclusions

A two-stream radiative transfer model was employed to investigate the extent to which the melt-pond albedo α is dependent on the pond depth H_p and thickness of the underlying ice H_i. The results revealed that α depends on the H_i for thin ice (H_i < 1 m) and on the H_p for thick ice (H_i > 3 m). This is in contrast to the parametrizations in Ebert and Curry (1993) and Morassutti and Ledrew (1996). In dealing with the current thin ice in the Arctic, a new parameterization in Eq. (1) as a function of both H_p and H_i is more suitable than the depth-dependent melt-pond albedo. The upwelling irradiance from the pond surface is employed to determine the color of the melt pond using a colorimetric method. An increase in H_i enhances both the green and blue intensities of pond color, whereas the red intensity is sensitive to H_i for thin ice and to H_p for thick ice, similar to the behavior of melt-pond albedo. The pond color reproduced by the model agrees well with field observations for Arctic sea ice in summer, supporting the validity of this study. Both H_p and H_i pose an important impact on the partitioning of solar radiation in melting sea ice. The transmitted solar energy into the ocean is sensitive only to H_i. The portion absorbed by melt pond increased only with H_p, and the variations in the portion by the underlying ice were seen to be complex because of the counteracting effects of pond and ice to the energy absorption in ice.

The present model has the capability to model the optics of melt ponds on Arctic sea ice, which produced comparable results with previous data on the melt-pond albedo and color. It can be also implemented into sea-ice thermodynamic models to improve our understanding of the effect of melt ponds on surface heat budget and mass balance. More validation data are still necessary to compare with the modelling results.

Acknowledgments

This research was supported by the National Natural Science Foundation of China (41676187 and 41376186), and the Global Change Research Programme of China (2015CB953901).

References

Ebert, E.E., and Curry, J.A., 1993. An intermediate one-dimensional thermodynamic sea ice model for investigating ice-atmosphere interactions. J. Geophys. Res., 98(C6), 10085–10109.

Flocco, D., Feltham, D.L., Bailey, E., et al., 2015. The refreezing of melt ponds on Arctic sea ice. J. Geophys. Res. Oceans, 120(2), 647–659.

Grenfell, T.C., and Perovich, D.K., 2008. Incident spectral irradiance in the Arctic Basin during the summer and fall. J. Geophys. Res., 113(D12), doi:10.1029/ 2007JD009418.

Istomina, L., Melsheimer, C., Huntemann, M., et al., 2016. Retrieval of sea ice thickness during melt season from in situ, airborne and satellite imagery, Proc. IGARSS-2016, Beijing, China, 7678–7681.

Landy, J., Ehn, J., Shields, M., et al., 2014. Surface and melt pond evolution on landfast first-year sea ice in the Canadian Arctic archipelago. J. Geophys. Res. Oceans, 119(5), 3054–3075.

Leppäranta, M., Reinart, A., Arst, H., et al., 2003. Investigation of ice and water properties and under-ice light fields in fresh and brackish water bodies. Nordic Hydrol., 34(3), 245–266.

Light, B., Maykut, G.A., and Grenfell, T.C., 2003. A two-dimensional Monte Carlo model of radiative transfer in sea ice. J. Geophys. Res., 108(C7), 3219, doi:10.1029/2002JC001513.

Lu, P., Cheng, B., Leppäranta, M., et al., 2018a. Partitioning of solar radiation in Arctic sea ice during melt season. Oceanologia, In press.

Lu, P., Leppäranta, M., Cheng, B., et al., 2016. Influence of melt-pond depth and ice thickness on Arctic sea-ice albedo and light transmittance. Cold Reg. Sci. Technol., 124, 1–10.

Lu, P., Leppäranta, M., Cheng, B., et al., 2018b. The color of melt ponds on Arctic sea ice. The Cryosphere, 12, 1–15.

Makshtas, A.P., and Podgorny, I.A., 1996. Calculation of melt pond albedos on arctic sea ice. Polar Res., 15, 43–52.

Morassutti, M.P., and Ledrew, E.F., 1996. Albedo and depth of melt ponds on sea-ice. Int. J. Climatol., 16, 817–838.

Perovich, D.K., 1990. Theoretical estimates of light reflection and transmission by spatially complex and temporally varying sea ice covers. J. Geophys. Res. 95 (C6), 9557–9567.

Perovich, D.K., and Polashenski, C., 2012. Albedo evolution of seasonal Arctic sea ice. Geophys. Res. Lett., 39, L08501, doi:10.1029/2012GL051432.

Polashenski, C., Golden, K.M., Perovich, D.K., et al., 2017. Percolation blockage: A process that enables melt pond formation on first year Arctic sea ice. J. Geophys. Res. Oceans, 122(1), 413–440.

Webster, M.A., Rigor, I.G., Perovich, D.K., et al., 2015. Seasonal evolution of melt ponds on Arctic sea ice. J. Geophys. Res. Oceans, 120(9), 5968–5982.

International Association for Hydro-Environment Engineering and Research
Supported by Spain Water and IWHR, China

24th IAHR International Symposium on Ice
Vladivostok, Russia, June 4 to 9, 2018

Modeling Thermodynamic Behavior of Seasonal Ice-Covered Reservoir

Nan Li[1], Youcai Tuo[2], Yun Deng[2], Hung Tao Shen[3]
[1]Yalong River Hydropower Development Company, Ltd., Chengdu, 610051, China.
linanscu@163.com
[2]State Key Laboratory of Hydraulics and Mountain River Engineering, Sichuan Univ., Chengdu, 610065, China.
tyxl200496@163.com and dengyun@scu.edu.cn
[3]Dept. of Civil and Environmental Engineering, Clarkson Univ., Potsdam, NY 13699-5710, U.S.A.
htshen@clarkson.edu

A laterally-averaged tow-dimensional thermal-ice model for seasonal ice-covered reservoir is developed. In this model, two-dimensional flow and water temperature distributions are solved by the finite volume method with the k-ε turbulent model. Supercooling and frazil ice, and the formation of initial ice cover are considered. Thermal growth and decay of the ice cover is modeled by vertical heat transfer and heat exchanges at air-ice and ice-water interfaces. The model was applied to the 153 km-long Fengman Reservoir on Songhua River. Simulation result showed a good agreement with field data in both vertical water temperature distribution and ice thickness. Effects of inflow water temperature on thermodynamic behavior of ice and water in reservoir are discussed.

1. Introduction

In cold regions, hydrodynamic and thermal conditions of reservoirs are affected by ice conditions. A few reservoir models considered the thermal-ice regime or the growth and decay of ice in reservoirs have been developed (e.g. Findikakis and Law, 1999; Xiao et al. 2004; Gebre et al., 2014; Oveisy and Boegman, 2014). However, some important ice phenomena, such as the supercooling of water and the formation and transportation of frazil ice, were not considered in these models.

In this paper, the WWL model (Deng et al. 2001, Tuo et al. 2011) is extended to the WWL-ICE model, to allow the model to simulate more complete thermal-ice processes of reservoir. The model is applied to the 153 km-long Fengman Reservoir located in the middle reach of the second Songhua River, Jilin, China. Effects of inflow water temperature on thermodynamic behavior of ice and water in the Fengman Reservoir are discussed.

2. Model Description

The WWL model is a laterally-averaged two-dimensional water temperature model. It has been used to simulate water temperature variations in deep reservoirs, and successfully applied to several large reservoirs (e.g. Deng et al., 2011; Tuo et al., 2011). In the WWL-ICE model, thermal-ice processes including supercooling, frazil ice transport, and the thermal growth and decay of ice cover are considered. In addition, the wind stress on the water surface is considered in the momentum equations.

2.1 Water temperature and frazil concentration

When the water temperature Tw ≥ 0 ℃, the governing equation of water temperature is

$$\frac{\partial BT_w}{\partial t}+u\frac{\partial BT_w}{\partial x}+w\frac{\partial BT_w}{\partial z}=\frac{\partial}{\partial x}\left[B\left(\alpha+\frac{\nu_t}{\sigma_T}\right)\frac{\partial T_w}{\partial x}\right]+\frac{\partial}{\partial z}\left[B\left(\alpha+\frac{\nu_t}{\sigma_T}\right)\frac{\partial T_w}{\partial z}\right]+\frac{1}{\rho_w C_p}S_h \qquad \textbf{[1]}$$

where, B is the river width, m; T_w is the water temperature,℃; u and w are the components of water velocity, m s^{-2}; α is the thermal diffusion coefficient of water, m^2 s^{-1}; ν_t is the kinematic eddy viscosity, m^2 s^{-1}; σ_T is the turbulent Prandtl number; ρ_w is the density of water, kg m^{-3}; C_p is the specific heat of water, J kg^{-1} $℃^{-1}$; S_h is the heat input that come from the air, the ice cover, and the solar radiation:

$$S_h=\begin{cases}\varphi_{aw} & \text{The heat fluxes at air-water interface without the ice.}\\ \varphi_{wi} & \\ \dfrac{\partial B\varphi_z}{\partial z} & \text{The heat exchanges at ice-water interface with the ice.}\end{cases} \qquad \textbf{[2]}$$

$$\varphi_z$$

When the water temperature Tw < 0 ℃, the water is suppercooled and frazil ice forms. The frazil production can be calculated from the heat exchange between the supercooled water and frazil crystals. The frazil production will release latent heat contribute to water temperature change (Shen et al. 1995). The frazil ice transport can be calculated by:

$$\frac{\partial(BC_v)}{\partial t}+u\frac{\partial(BC_v)}{\partial x}+(w+v_b)\frac{\partial BC_v}{\partial z}=\frac{\partial}{\partial x}\left(B\varepsilon_x\frac{\partial C_v}{\partial x}\right)+\frac{\partial}{\partial z}\left(B\varepsilon_z\frac{\partial C_v}{\partial z}\right)+BS_i \qquad \textbf{[3]}$$

where, v_b is the buoyant velocity of frazil; ε_x and ε_y are the longitudinal and vertical turbulent diffusion coefficient, respectively, $m^2\ s^{-1}$; and S_i is the source term due to the thermal growth of the frazil ice.

2.2. Ice cover formation and thickness change

The formulation on cover formation in the reservoir is based on the method of Huang et al. (2012). In addition, the model assumes ice cover will form when the frazil concentration C_v >0.8 in the surface layer. Thermal growth and decay of the cover is calculated based on heat condition across the snow and ice cover thicknesses taking into consideration of the possible melting from the top and bottom surfaces of the ice cover (Shen and Chiang 1984).

2.3. Wind stress

The wind shear on the water surface is determined by the wind speed along the river, which can be expressed by the formulation:

$$\tau_{aw}=C_{wind}\rho_a|V_w|V_w \qquad \textbf{[4]}$$

where, τ_{aw} is the wind shear stress (along the river); C_{wind} is the wind drag coefficient; V_w is wind velocity at 10 m above the water surface along the river, m/s; ρ_a is the density of the air, kg m^{-3}. This term is added to hydrodynamic equation as a source term on the surface layer.

3. Model calibration and validation

The WWL-ICE model is calibrated and validated with field data of Fengman Reservoir during the 2010-11 winter. These data include the vertical water temperature profiles, outflow temperatures and ice cover thicknesses. In the numerical simulation, a structured mesh with grids of 20 ~ 800 m in the longitudinal direction and 0.3 ~ 3.0 m in the vertical direction was used. The observed water temperature data on June 25, 2010 were taken as the initial conditions of the temperature field. The simulation was carried out for 321 days with 30s time steps.

Figure 1 shows the comparison of the vertical water temperature distributions between the simulated results and the observed data. Figure 2 shows the comparison of the daily-averaged outflow temperatures between the simulated results and the observed data. Figure 3 shows the comparison of simulated and observed ice thicknesses near the Fengman Dam. Compared with the observed ice cover length, the simulated errors of ice cover length were 8.7% (December 20, 2010), 1.3% (February. 22, 2011), and 3.8% (April 3, 2011), respectively. Figure 4 shows the inflow water temperature at the upstream boundary.

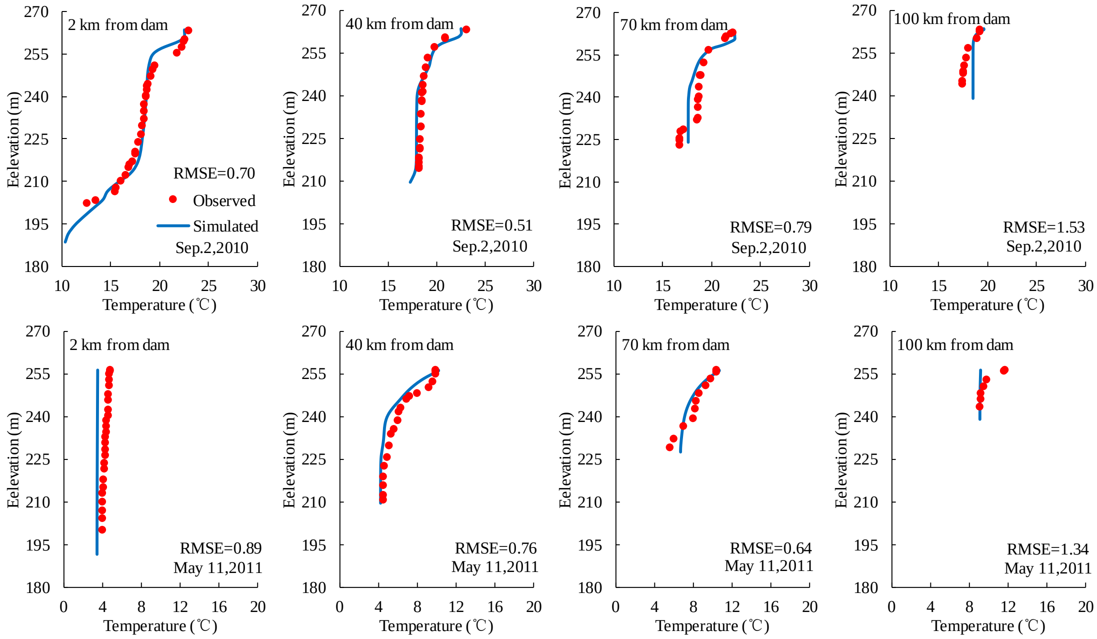

Fig. 1. Comparison of simulated and observed vertical temperature distributions

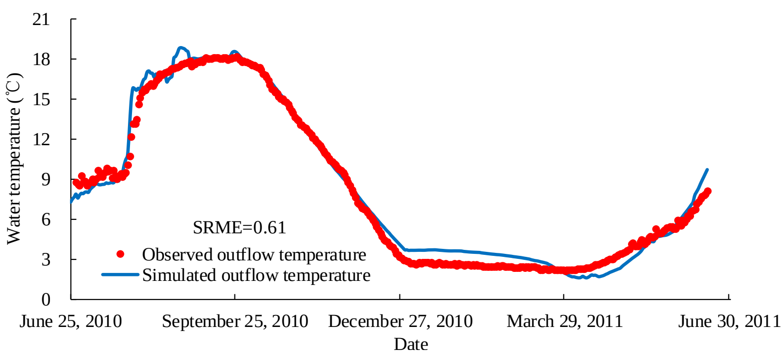

Fig. 2. Comparison of the simulated and observed daily-averaged outflow temperatures

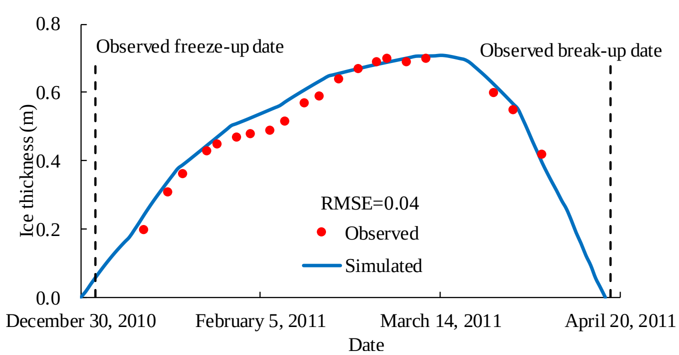

Fig. 3. Comparison of the simulated and observed ice thicknesses near the dam

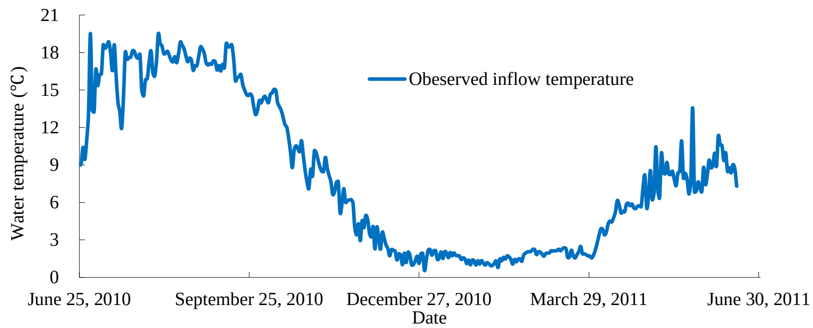

Fig. 4. The observed daily-averaged inflow temperature

4. Effect of inflow temperature on ice conditions

Simulations for two cases with different inflow temperatures were made to show the potential effects on ice conditions in the reservoir. In Case A, the inflow water temperature at the upstream boundary is the observed field condition (see Figure 4), while in Case B, the inflow water temperature is set at 0.1℃. Both cases use the same reservoir operation and meteorological conditions during the 2010-11 winter and the water temperature field on Oct. 31, 2010, as the initial condition.

Figure 5 shows the comparison of the 2D water temperature distributions on Nov. 10, 2010, before the ice period between Case A and Case B. The obvious difference between these two cases is the water temperature distribution in the upstream end of the reservoir. In Case A, a uniform vertical water temperature distribution with an average temperature of 6.0~7.0 ℃ occurs in the upstream end of the reservoir, due to the high inflow temperature. In Case B, a uniform vertical water temperature distribution with an average temperature of 0.05℃ occurs in the upstream end of the reservoir, and a vertical-inverse water temperature distribution with 2.0~3.5℃ temperature difference between the surface and bottom of reservoir occurs in 40 ~ 47 km from the upstream end of the reservoir.

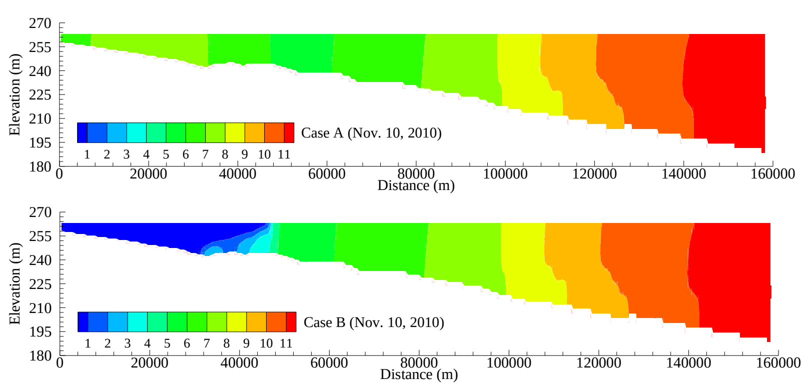

Fig. 5. Comparison of the 2D water temperature distributions between Case A and Case B

Figure 6 shows the frazil ice and ice cover distributions in the upstream portion of the reservoir in Case B. With the averaged air temperature drops to -9.2℃ in early December, the frazil ice forms in the area 32~33 km from the upstream end of the reservoir on December 8, 2010. The concentration of frazil ice reaches its peak value and the frazil ice transports to the area 45 km from the upstream end of the reservoir on December 20, 2010. The initial ice cover forms in the area 30 km from the upstream end of the reservoir and progresses towards the dam on December 11, 2010. Due to the development of ice cover, the heat loss from the surface water is cut off and the production of the frazil ice is decreased. In early January, the whole reservoir is ice-covered and no frazil ice exists.

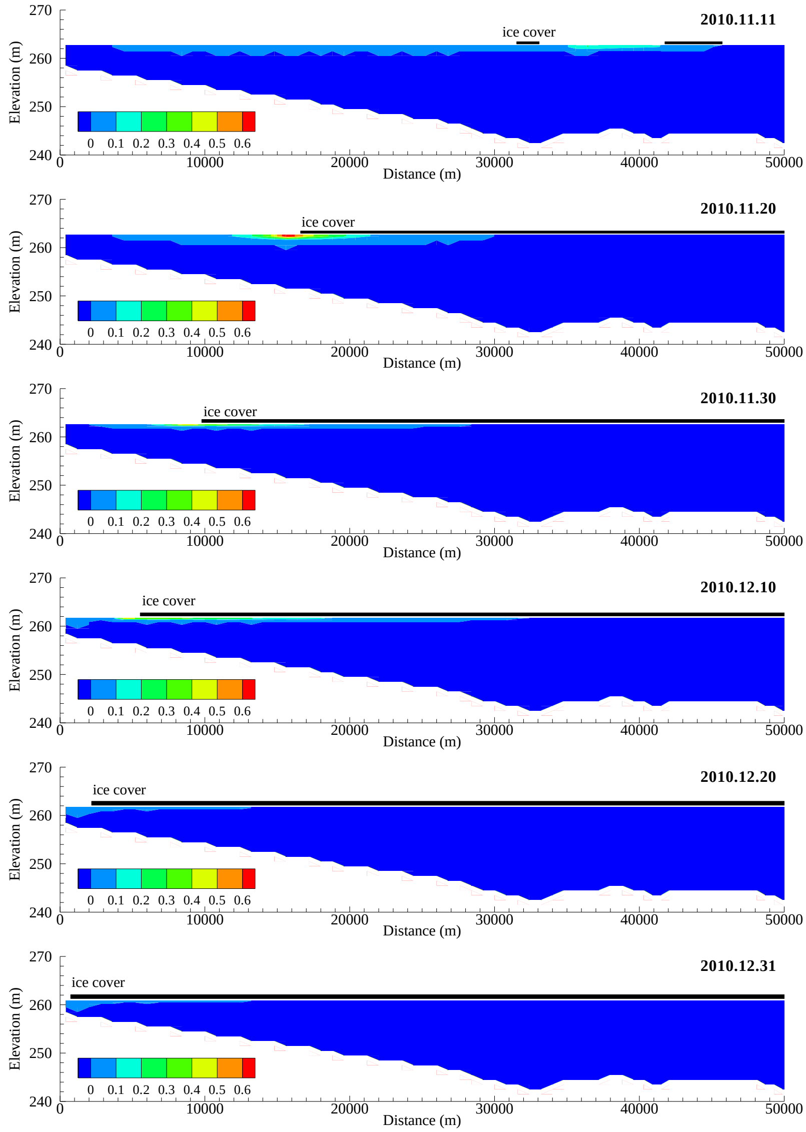

Fig. 6. Frazil ice concentration and ice cover distributions in the upstream portion of the reservoir of Case B

Figure 7 is the comparison of the ice cover during the freeze-up period between Case A and Case B. In Case A, the initial ice cover forms in middle reservoir, the ice cover develops towards to the dam and upstream end, and the cover reaches the dam on January 2, 2011. The upstream end of the reservoir remains open during the winter in Case A, due to the high temperature inflow. In Case B, the initial ice cover forms in the area that close to the upstream end of the reservoir on December 11, 2010, and the whole reservoir is ice-covered on January 1, 2011.

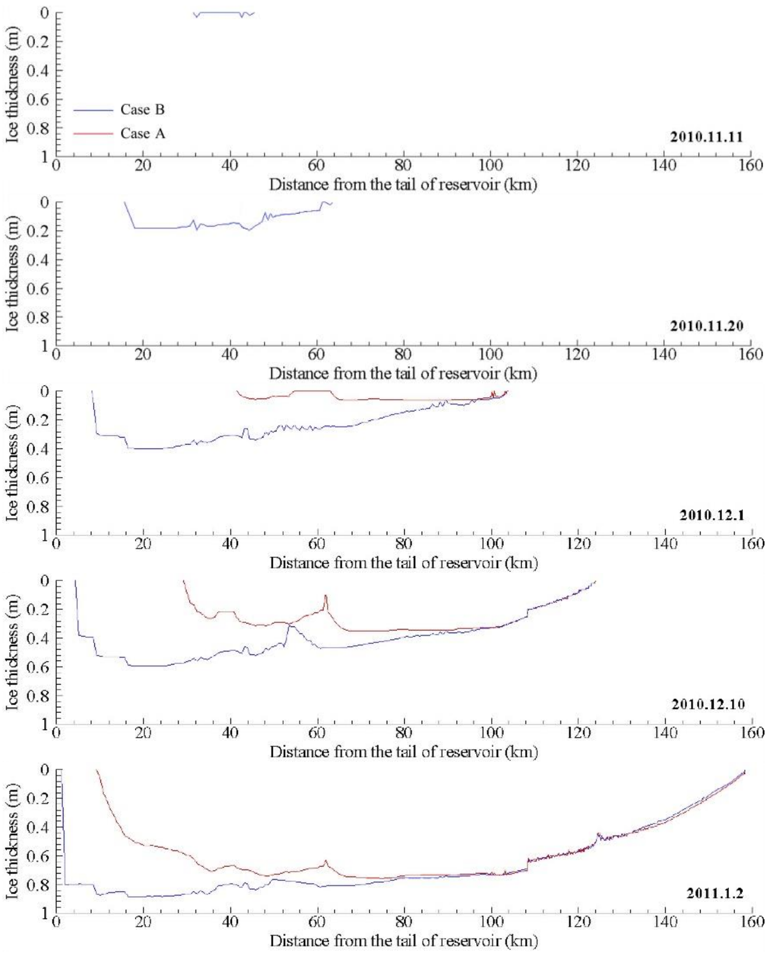

Fig. 7. Comparison of the ice cover between Case A and Case B

5. Conclusions

The WWL model is extended to consider ice processes including supercooling of water, ice cover formation, frazil ice transport, and the surface wind stress. This new model, WWL-ICE, is calibrated and validated with field data of Fengman Reservoir for the winter of 2010-11. The validation results indicate that the model is suitable for simulating the variation of water temperature, outflow temperature and ice conditions.

Using the WWL-ICE model, effects of inflow water temperature on the thermal-ice of the reservoir are discussed. The inflow temperature changes the thermal distribution in the tail end of the reservoir. With a low temperature inflow, supercooling of water occurs and frazil ice forms, and production of frazil ice leads to the rapid development of ice cover in the upstream end of the reservoir. With a warmer temperature inflow, the water temperature gradually drops to 0 ℃when flows to the middle reach of the reservoir.

Acknowledgments

This research was supported by National Key R & D Program of China (Grant No. 2016YFC0502207) and the National Natural Science Foundation of China (Grant No. 91547211).

References

Deng, Y., Zhao, W.Q., Li, J., and Luo, L., 2001. Simulation on thermal stratification of the huge-cubage and deep reservoirs. In: Proceedings of the 29th IAHR Congress, Beijing, pp. 584-593.

Deng, Y., Tuo, Y.C., Li, J., Li, K. F., and Li, R., 2011. Spatial-temporal effects of temperature control device of stoplog intake for Jinping I power station. Sci. China 54 (S1), 83-88.

Findikakis, A.N., and Law, A.W.K., 1999. Wind mixing in temperature simulations for lakes and reservoirs. J. Environ. Eng. 125 (5), 420-428.

Gebre, S., Boissy, T., and Alfredsen, K., 2014. Sensitivity to climate change of the thermal structure and ice cover regime of three hydropower reservoirs. J. Hydrol. 510 (6), 208-227.

Huang, F.B., Shen, H.T., and Knack, I.M., 2012. Modeling Border Ice and Cover Progression in Rivers, Ice Research for a Sustainable Environment, Proceedings, 21th IAHR Ice Symposium, June, Dalian. pp. 139-149.

Oveisy, A., and Boegman, L., 2014. One-dimensional simulation of lake and ice dynamics during winter. J. Limnol. 73 (3), 441-453.

Shen, H.T., and Chiang, L., 1984. Simulation of growth and decay of river ice cover. J. Hydraul. Eng. 110 (7), 958-971.

Shen, H.T., Wang, D., and Lal, A.M.W., 1995. Numerical Simulation of River Ice Processes, Journal of Cold Regions Engineering, ASCE, 9 (3), 107-118.

Tuo, Y.C., Li, J., Deng, Y., and Liang, R.F., 2011. Effects of water temperature on spawning ground of Chinese Sturgeon in Three Gorges Reservoir. In: International Conference on Electric Technology and Civil Engineering, Lushan, 5916-5919.

Xiao, J.M., Jin, L.H., Xie, Y.G., and Huo, Y.D., 2004. Study on mechanism of formation and melting of reservoir ice cover in cold area. J. Hydraul. Eng. 6, 80-85 (in Chinese).

International Association for Hydro-Environment Engineering and Research
Supported by Spain Water and IWHR, China

24th IAHR International Symposium on Ice
Vladivostok, Russia, June 4 to 9, 2018

Experimental studies of ice influence as a factor of the frozen soils deformation activity

Aleksey Marchenko
Department of Arctic Technology, UNIS, P.O. Box 156, Longyearbyen, Norway, N-9171
aleksey.marchenko@unis.no
Nicolai Vasiliev
The Laboratory of Static Research of Soils ,JSC "Vedeneev VNIIG"
21, Gzhatskaya , St. Petersburg 195220, Russia
nicolaivasiliev@hotmail.com
Artem Nesterov
Peter the Great St. Petersburg Polytechnic University (SPbPU)
29, Politechnicheskaya, St. Petersburg 195251, Russia
artyom_nesterov-@mail.ru
Yuri Kondrashov
KPIF AO Atomenergoproekt, 9, Molodezhnaya , Kurchatov 307251, Russia
jurok_rm@mail.ru
Aleksandr Alhimenko
Peter the Great St. Petersburg Polytechnic University (SPbPU)
29, Politechnicheskaya, 195251 St. Petersburg, Russia
a.alhimenko@mail.ru

Phase transformations of ice in seasonally frozen soils are an inalienable part of the Earth's cryosphere and affect the balance of the external heat of our planet. These processes depend on natural and technogenic changes in the environment. That is why for the design of engineering structures, built in the Arctic world regions, it is necessary to have a complete conception for the formation mechanism of the stress-strain state of such soils in a wide range of thermal loads. The study of the nonstationarity of ice, as an important component of considered medium, is an actual problem. New method for measuring the temperature deformations of frozen soils using fiber-optic Bragg grating sensors can serve as a solution. In the course of the experiments, cylindrical samples of previously frozen soils saturated with water of different salinity were tested.
Keywords: thermal expansion; frozen soil; ice; sand; clay; fiber-optic sensors;

1. Introduction

Building and operation of engineering constructions in cold regions meet difficulties due to the formation and propagation of thermal contraction cracks. Because of the extreme cold weather, the depth of the cracks reaches a few meters, with opening widths of 15~20 cm. Over the next few months, the snow melts; the remaining water fills the cracks and then freezes under the influence of cold flux from the permafrost. These tiny cracks penetrate into the permafrost (Figure 1) (Petersen *et al.*, 2015). In the summer months, water fills the cracks, freezes and expands. It influences the crack growth and the formation of ice wedges. As this process continues over many years, ice wedges can reach the size of a swimming pool. The ice wedge usually appears in a polygonal pattern, known as an ice wedge polygon. As a result, destruction of engineering constructions and underground utility systems may happen. The cracks constitute an especially great danger for earth-filled dams, piles encased with soil, roads, underground storage areas, airfield pavements, power transmission lines, pipelines, communication cables, and other linear structures.

The formation of thermal contraction cracks is directly connected with the thermal expansion/contraction of frozen soils. This paper is dedicated to the experimental study of thermal expansion of frozen soils saturated with fresh or saline water. We investigate the dependence of the coefficient of thermal expansion from the soil content and temperature. This knowledge is necessary for the design of engineering structures in the coastal zone of the northern seas.

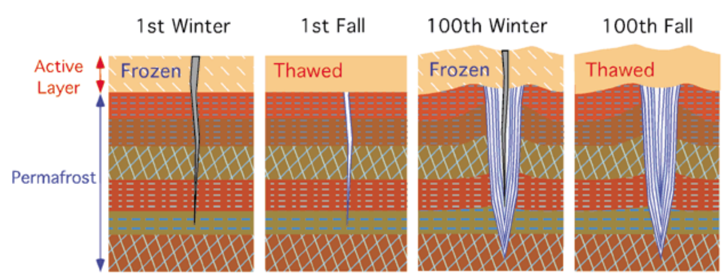

Fig. 1. Seasonal evolution of ice wedges

Experimental investigations of thermal deformations of frozen soils started in the 1930s (Fedosov, 1935). A complex nonlinear character of the deformations due to the cooling was ascertained later by (Votyakov, 1975; Ershov, 1990; Cheverev, 2004). Thermal deformations of frozen soils have abnormal properties (expansion due to cooling and contraction due to heating) in a certain range of temperatures due to the presence of unfrozen, or bound, water in frozen soils. Properties of the bound water in cryogenic soils are discussed in the analytical review (Cheverev, 2003). Negative values of the coefficient of thermal expansion are explained by the gradual freezing of the bound water during the soil cooling.

Several methods of determining the amount of unfrozen water in frozen soil are known: the method based on measurement of the thawing temperature (Grechishchev *et al.*, 1983), the method of measuring the amount of heat for heating the soil and melting the ice in a sample (Patent RU2034110, 1995), and the calorimetric method (*Guidance on Physical, Thermal and Mechanical Properties of Frozen Soils*, 1973). All of these methods involve determining multiple deliverables, are time-consuming, and are not accurate enough. The method for determining of soil deformations with dial indicators does not have sufficient measurement accuracy (Votyakov, 1975).

In the present paper we describe the method and the results of direct measuring of thermal expansion/contraction of frozen soil samples with Fiber Bragg Gratings (FBG) strain and temperature sensors. The experiments are performed with soil samples with different grain-size distribution, water saturation, and salinity. Earlier this method was used to investigate thermal expansion of saline ice (Marchenko *et al.*, 2016).

2. Instrumentation

FBG sensor is a periodic grid with 40,000 cells burned by two laser beams inside the fiber with diameter of 9 μm. The grid length is 1 cm. Each FBG sensor reflect the light signal of a certain wavelength, depending on the grid characteristics, tension and temperature of the fiber. The incoming light signal is generated in the optical fiber by the source LED in the spectral range 1,500~1,600 nm. The wavelengths reflected by the FBG sensors are registered and analyzed by a spectrometer. To register changes inside a calibration device, a constant temperature is maintained in one of the sensors. The spectrometer, calibrator, and analyzer of the incoming optical signals are combined in one unit with four channels designed and manufactured in the company Advance Optic Solutions GmbH (Dresden). Every channel of the unit can transfer information from 16 FBG sensors embedded in the same fiber.

FBG thermistor string and strain sensor are shown in Figure 2. Fiber cable with FBG temperature sensor is protected from mechanical deformations by thin metal tube of 1 mm diameter. The FBG thermistor string includes 12 FBG sensors embedded in the same fiber with 1 cm distance between neighbor sensors. The FBG thermistor string is protected from mechanical deformations by thin metal tube of 1 mm diameter and 25 cm length. The thermistor string is welded with optical fiber protected by blue plastic. The accuracy of temperature measuring and nominal resolution is correspondingly equal to 0.4 °C and 0.08 °C. Strain sensor is embedded in the middle part of the fiber protected by transparent plastic with working length about 20 cm. The fiber inside transparent plastic is going through the screw and welded to fiber cable protected by yellow plastic. The strain sensor is mounted on a sample and pretended using two screws and bolts. The resolution of the strain sensors is 10^{-6} (1 μstrain), and the accuracy is 5×10^{-6} (1 μstrains).

The change of the wavelength ($\Delta\lambda$) of the light reflected by the Bragg grating is proportional to the fiber extension ($\Delta L/L$) and the change of the fiber temperature (ΔT):

$$\frac{\Delta\lambda}{\lambda} = \mathrm{GF}\cdot\frac{\Delta \mathrm{L}}{\mathrm{L}} + \mathrm{TK}\cdot\Delta\mathrm{T} \qquad \textbf{[1]}$$

where GF = 0.719, "calibration factor"; TK = 5.5×10^{-6}, “thermal elongation factor”; L is the reference length of the fiber; λ is the reference length of the light reflected by the Bragg grating. The value of $\Delta\lambda$ is measured by the spectrometer. From Equation 1 it follows that temperature changes of the fiber ΔT should be known for the calculation of the fiber strain $\Delta L/L$. In the experiment, the temperature of the strain sensor was measured by the FBG temperature sensor. The FBG thermistor string was installed to measure temperature inside the soil sample.

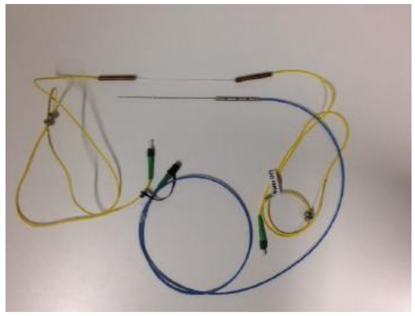

Fig. 2. FBG thermistor string with blue plastic housing of the fiber and strain sensor with yellow plastic housing of the fiber.

3. Experiments

The soil samples were installed within the metal frame used for the mounting of the fiber with FBG sensors (Figure 3). The fiber with FBG strain sensor was fixed between the metal frame and the steel slab, lying on the surface of the sample. The vertical screws exclude possible horizontal displacements of the slab along the sample. It allows avoid the complicated procedure of fixing the sensors on the sample itself (Grechishchev *et al.*, 1983) and simplify the mounting of FBG sensors. The distance between the slab and the frame decreases when the sample elongates. In this case the strain sensor indicates contraction. In case when the sample becomes shorter the strain sensor indicates expansion. The sample strain is calculated according to the strain sensor reading as follows:

$$\varepsilon = \frac{\Delta L_s}{L_s} = -\frac{\Delta L}{L}\frac{L}{L_s}, \qquad \textbf{[2]}$$

where L is the initial distance from the frame to the sample surface, and L_s is the initial length of the sample.

a) b)

Fig. 3. (a) View of the tested sample; (b) the rig for the tests

Samples of different porosity, density, and water content were prepared in the cold laboratory of the University Centre in Svalbard (UNIS). The samples had the form of thick-walled cylinders 20 cm high, with the outer diameter 13 cm and the inner diameter 2 cm (Figure 3a). The physical characteristics of the soils are presented in Table 1. The water content of the sand samples was preset as equal to 15% and for clay samples, 35.5%. The water saturation ratio S_r for sand samples was equal to 0.72~0.86 and for clay samples, 0.90~0.96. Saturation was performed using fresh water or seawater with salinity of 34.3ppt. For clay samples the densities of them were approximately equal. The fine and silt sands had the characteristics presented in Table 2. The fine sand was considered to have no less than 75% content of particles > 0.1 mm by weight; and the silt sand had less than 75% content. For sand sifting, the sieves of international standard ASTM and the vibrating table Retsch AS 200 were used.

The soil samples were preliminarily cooled before testing: the sand samples to 0 °C and the clay samples to −5 °C. Then each sample was placed in the cold room and the FBG strain sensor and thermistor string were mounted on the sample. All electronic devices, the LED source, the spectrometer, and the PC were installed outside the cold room. The temperature of the cold room was changed every 6 hours. The processes of moisture movement or squeezing was not taken into account.

Table 1. Characteristics of the tested soils

Type of soil	Water content, W (%)	Type of water used for saturation	Density (g/cm^3)	Void ratio, e	Saturation factor, S_r
Fine sand	15.0	Fresh	2.04	0.544	0.76
Silt sand	15.0	Saline	2.13	0.479	0.86
Fine sand	15.0	Saline	2.01	0.568	0.72
Clay (Cambrian)	35.5	Fresh	1.83	0.991	0.96
Clay (Kaolin)	35.5	Fresh	1.80	1.085	0.91
Clay (Cambrian)	35.5	Saline	1.83	0.991	0.96
Clay (Cambrian)	35.5	Saline	1.79	1.097	0.90

Table 2. Grain-size distribution of fine and silt sands

Particle size, mm	≥0,6	≥0.3	≥0.15	≥0.075	<0.075
Silt sand, mass, g	1,250	1,250	1,000	1,500	
Fine, mass, g	1,000	1,500	1,500	700	300

4. Results

The experiments on thermal deforming of frozen soil samples were performed respectively in the temperature ranges: from 0 to −12 °C (sand samples) and from −5 to −12 °C (clay samples). The results of the experiments are presented in Figures 4–9.

The strain–temperature curves of fine-sand samples saturated with fresh or saline water are presented in Figure 4. In the first cycle of temperature change, the sample saturated with fresh water expanded when its temperature decreases from −1 °C to −7.5 °C and contracted when the temperature further decreases to −11 °C. In the second cycle, the expansion of the sample was not so large at the same condition because the ice inside the sample didn't melt completely during the 6-hour period of heating. The strain patterns of the sample saturated with saline water are different: the sample expanded as the temperature decreases to −12 °C and contracted as the temperature increases to 0 °C in the both cycles of the temperature change.

The soil expansion under the cooling is explained by the gradual formation of ice from unfrozen water inside the soil. Figures 5 and 6 show the sample strain and the air temperature measured near the sample versus the time. The range of thermal strains in the samples saturated with fresh water is much less than that in the samples saturated with saline water.

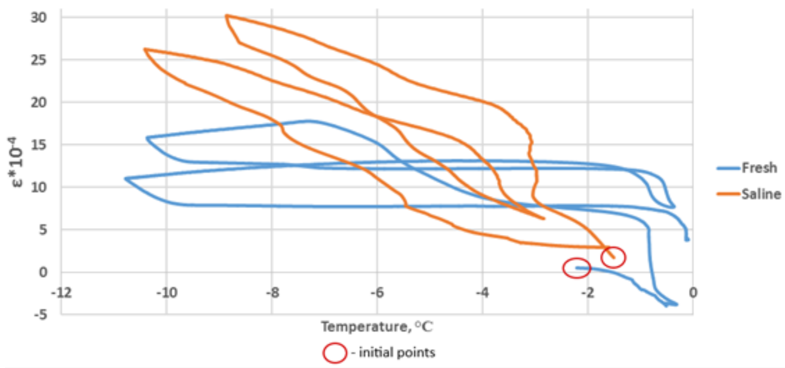

Fig. 4. The strain–temperature relationships of the fine-sand samples saturated with fresh or saline water

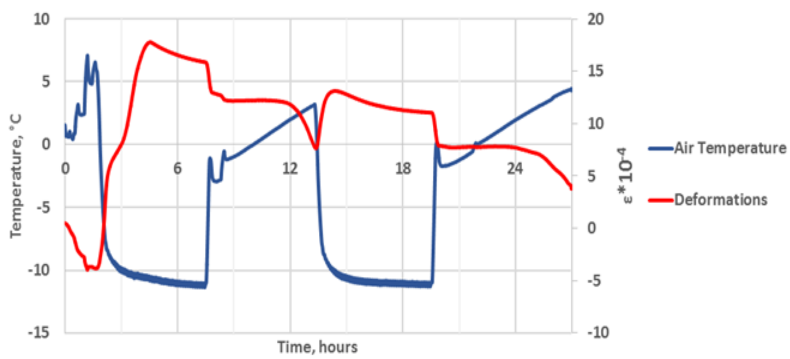

Fig. 5. The change of the strain compared with the air-temperature change in the cold room for the sand sample saturated with fresh water

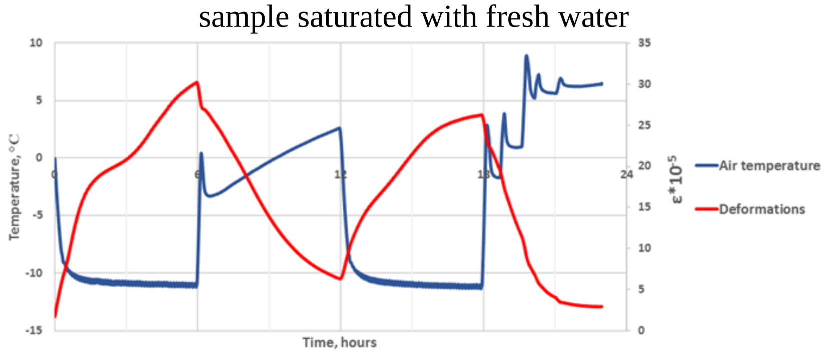

Fig. 6. The change of the strain compared with the air-temperature change in the cold room for the sand sample saturated with saline water

The strain–temperature curves for the Cambrian and Kaolin clay samples saturated with fresh water are shown in Figures 7–9. From Figure 8 it is seen that the Cambrian clay sample shrunk continuously during 6 hours when the air temperature near the sample was -11^{o}C. The strain rate of the sample changed the sign when the air temperature increased to -4^{o}C. Similar deformations of Kaolin clay samples occurred with lower strain rates (Figure 9).

The hysteresis is described in terms of strain-temperature dependencies during the "cooling–heating" cycles of soil samples. In clays the hysteresis loops are wider (Figure 7) than in sands (Figure 4) because of the higher content of unfrozen water in finely dispersed soils (Cheverev, 2003).

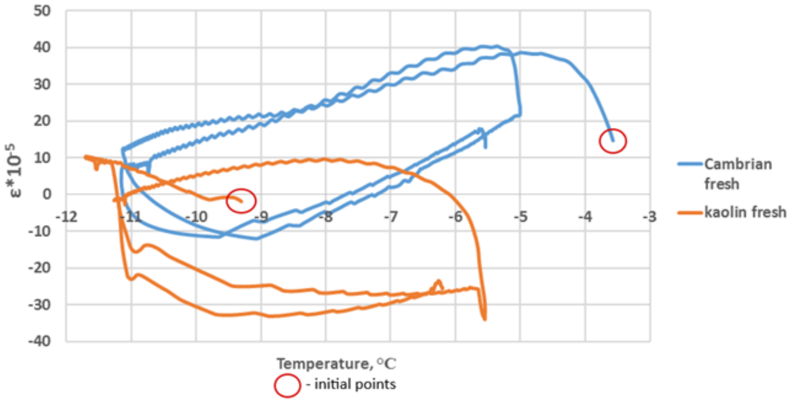

Fig. 7. The strain–temperature relationships of the Cambrian and Kaolin clay samples saturated with fresh water

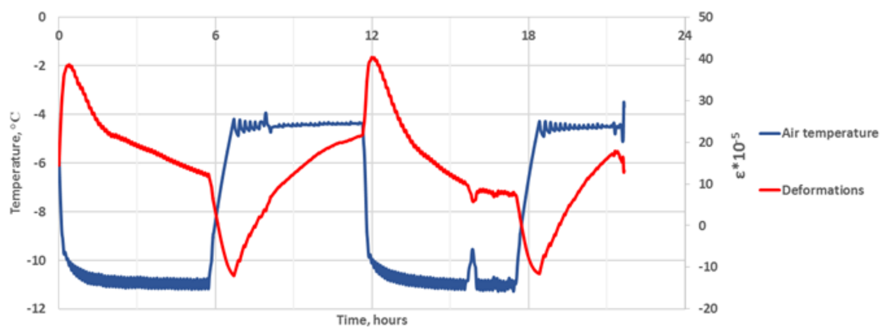

Fig. 8. The change of the strain compared with the air-temperature change in the cold room for the Cambrian clay sample saturated with fresh water

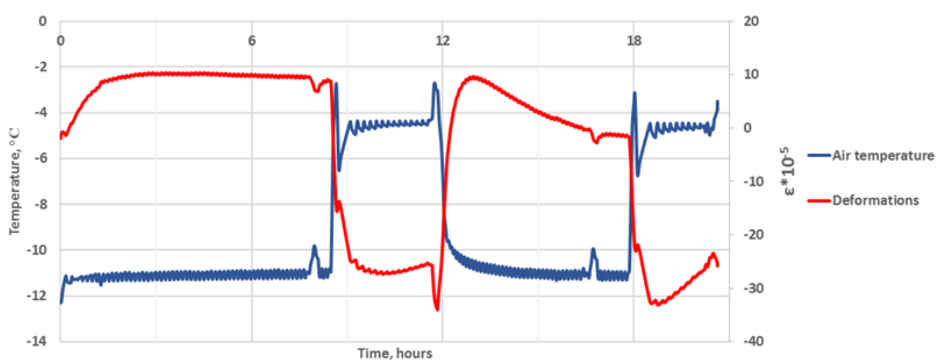

Fig. 9. The change of the strain compared with the air-temperature change in the cold room for the Kaolin clay sample saturated with fresh water

5. Conclusions

- New method of measurement of thermal deformations of frozen soil samples was developed based on the use of optical fiber sensors with Bragg grating.

- A number of tests on determining the thermal response of soils on cycling temperature changes specific for natural conditions were performed. Soil samples containing Cambrian or Kaolin clay, silt or fine sand were saturated with fresh or saline water and tested.
- The results obtained are regarded as preliminary. On the basis of the method developed, a number of further experiments are planned in future for gathering statistical data and performing more detailed analysis of physical processes in frozen soils at cyclic changes of the temperature.

The results of the tests can be used for the study of geo-cryological processes (thermokarst, thermal erosion, frost cracking and heaving, suffusion) in earth dams of the frozen type and in other structures in the permafrost and arctic shelf zones. These processes are even more intensive under the severe climatic conditions of the permafrost zone due to the large thermal and moisture gradients and the resulting complex thermal stress–strain state in the structures (Chzhan and Velikin, 2014).

6. Acknowledgments:

The investigations were performed with the support of the Innovation Centre SAMCoT (Sustainable Arctic Marine and Coastal Technology), a project of the Norwegian scientific fund.

7. References

(Cheverev VG, 2003). Properties of bound water in cryogenic grounds. Earth Cryosphere, 7(2): 30–41. (in Russian)

(Cheverev VG, 2004). Nature of cryogenic soils. Moscow: Nauchnui Mir., pp. 234. (in Russian)

(Chzhan RV, Velikin SA, 2014). Safety of small and medium dams in permafrost regions. Sciences in Cold and Arid Regions, 6(4): 331–339. DOI: 10.3724/SP.J.1226.2014.00331.

(Ershov ED, 1990). Geocryology. Moscow: Nedra, pp. 559. (in Russian)

(Fedosov AE, 1935). Physical and Mechanical Processes in the Soil at Freezing and Thawing. Moscow: Transgelitizdat, pp. 48. (in Russian)

(Grechishchev SE, *et al.*, 1983). New methods of studying the composition, structure and properties of frozen soils. "Nedra", Moscow. (in Russian)

(Guidance on physical, thermal and mechanical properties of frozen soils). [Rukovodstvo po opredeleniiu fizicheskih, teplofizicheskih i mekhanicheskih kharakteristik merzlykh gruntov]. 1973. Moscow.194p. (in Russian)

(Marchenko AV, Lishman B, Wrangborg D, *et al.*, 2016). Thermal Expansion Measurements in Fresh and Saline Ice Using Fiber Optic Strain Gauges and Multipoint Temperature Sensors Based on Bragg Gratings, Hindawi Publishing Corporation. Journal of Sensors, 2016: 5678193. DOI: 10.1155/2016/5678193.

(Patent RU2034110, E01D 1/00, 1995).

(Petersen J, Sack D, Gabler RE, 2015). Fundamentals of Physical Geography. 2nd Edition. Cencage Learning, http://www.physicalgeography.net/fundamentals/contents.html

(Votyakov IN, 1975). Physical and mechanical properties of frozen and thawed soils of Yakutia. Novosibirsk: Nauka. pp. 176. (in Russian)

International Association for Hydro-Environment Engineering and Research

Supported by Spain Water and IWHR, China

24th IAHR International Symposium on Ice
Vladivostok, Russia, June 4 to 9, 2018

Experimental study on the seepage flow through the ice jam

Kolerski Tomasz*, Bratnikow Małgorzata**
Gdansk University of Technology, Department of Civil and Environmental Engineering
Narutowicza 11/12, 80-233 Gdańsk, Poland
**tomasz.kolerski@pg.edu.pl **malbratn@student.pg.edu.pl*

In light of the observed climate change, there is a need for better understanding of river ice processes for managing water resources in the cold regions. Ice jams produce significant resistance which may cause rise of water level and flooding. The jam resistance is only referred to the roughness of its underside, and this approach lead to exceptional roughness coefficients which has no physical explanation. Number of evidences and facts showed the analogy between the seepage flow in the ice jam and flow in open channel over rough, permeable bed. Base on the experiments where flow over rough, gravel bed was investigated it was concluded that the velocity over the bed is not zero, thus the seepage flow in the gravel exists. Taking all this into consideration, experiments conducted on ice jam model can help to develop theories on gravel bed, as well as during the study some theories from permeable bed can be adopted.

This paper describes the first approach to gain preliminary understanding on the flow resistance of river ice jams. The study was carried out using the facilities at Gdansk University of Technology (GUT) where all hydraulic experiments were conducted. Experiments were proceed in hydraulic laboratory as a scale model of the real ice jam, because measurements in rivers are extremely dangerous and nearly impossible due to the risk of ice jam release during the surveying of the water velocity. Therefore scale model was set up to reproduce the typical condition observed in rivers. Since the facility on Gdansk University of Technology has no possibility to lower the room temperature to below freezing, the material similar to the ice was used instead (polypropylene, PP). Results shown that significant amount of water discharge formed the seepage flow through the jam voids.

1. **Introduction**

In cold and temperate regions of the world, wintertime operation of river systems is a key element in managing surface water resources. Climate change, either natural or anthropogenic, could have serious implications in the management of water resources. In addition to changes in mean conditions, global warming produces more extreme events caused by climate variability. Aside from more frequent extreme floods and droughts, it was also observed that more ice jam events have occurred in warmer winters (Jones et al. 2004), and cold spells have become more frequent (Shabbar and Bonsal 2003). River ice is known to affect many of the world's rivers. In the Northern Hemisphere about 60% of rivers experience significant seasonal effects of river ice (Prowse 2005). In the United States alone, there have been over 14,000 ice jam events observed between 1950 and 1999 (White and Eames 1999). The formation of river ice jam has serious effects on extreme floods, low winter flows, inland navigations, hydropower productions, sediment regime, and riparian structures. While the economic cost of ice-induced extreme events is significant, river ice can also have serious implications on environmental and ecological effects. These concerns bring the added urgency to the quantitative understanding of river ice processes.

River ice jams can produce extensive blockage of river flow and severe flooding due to the reduction of flow area by the jam mass as well as its excessive flow resistance, i.e. the head loss (Ashton 1986). Based on field data, Nezhikhovskiy related Manning's roughness coefficient n_i to its thickness for ice covers formed by accumulations of ice floes, dense slush, and loose slush to thickness (Nezhikhovskiy 1964). Existing empirical formulations attributed the entire jam resistance to the undersurface resistance of the jam, but relate the jam resistance to jam thickness with no theoretical basis (Shen 2010):

For breakup jams:

$$n_i = 0.0690H^{-0,23}t^{0.54} \text{ for t > 0.5 m} \quad \textbf{[1]}$$

$$n_i = 0.0593H^{-0,23}t^{0.77} \text{ for t < 0.5 m} \quad \textbf{[2]}$$

For freeze up jams:

$$n_i = 0.0262H^{-0,23}t^{0.54} \quad \textbf{[3]}$$

in which, H = depth of flow under the jam; and t = jam thickness. Base on the Thames River ice jam data Beltaos (1988, 1993) developed theory on seepage flow through the voids of the jam having effect on hydraulic resistance. He relates the resistance to the water discharge flow through the jam by incorporating water surface slope. The seepage flow Qp, through the voids of the jam was expressed as (Beltaos 1988):

$$Q_p = \lambda A\sqrt{S} \quad \textbf{[4]}$$

Calibrated mathematical model DynaRICE was implemented to the Thames river reproducing the historical ice jam case from February 1986. Simulation results shown that the significant percentage of the total discharge forming the seepage flow (Kolerski 2016, Kolerski, Huang, Shen, 2016). In this study the percentage of the seepage flow was calculated based on the calibration of the water level and ice thickness measured during the 1986 ice jam event. The amount of seepage flow varied along the jam structure and reached 6% of the total discharge (Figure 1.).

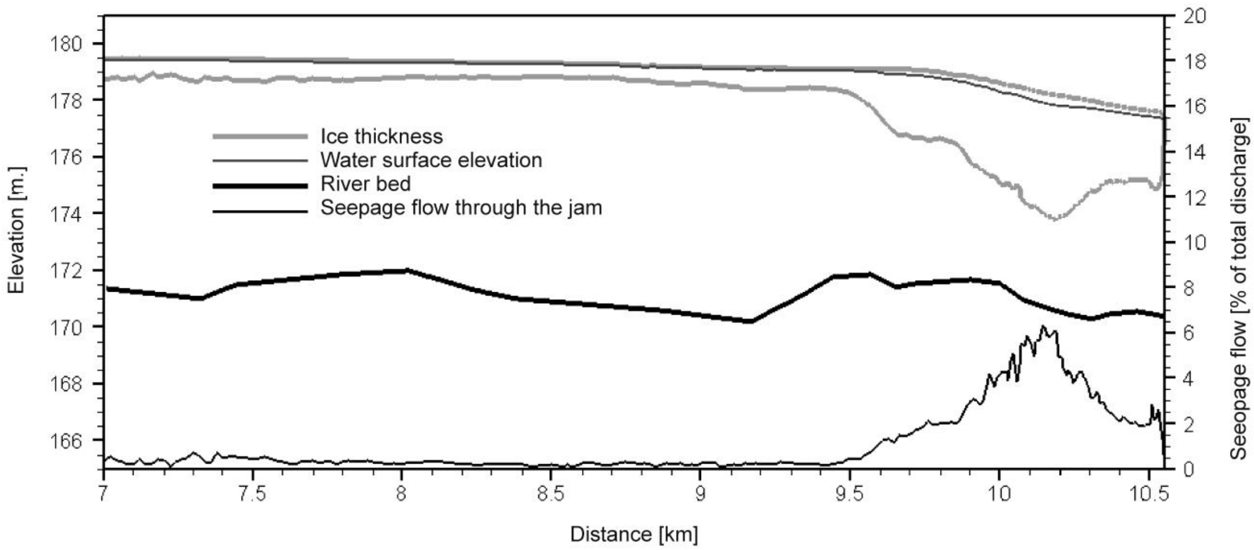

Fig. 1. Longitudinal profile of the simulated ice jam thickness and seepage flow through the jam voids, Thames River case

A preliminary analysis of the seepage flow resistance and the flow resistance of the undersurface of the jam, showed that the resistance due to the seepage flow is the dominating part of the jam resistance (Fan et al. 2016). Authors proved that in ice jammed channels, the total energy loss comprises of those due to the bed shear stress, the shear stress on the undersurface of the jam, and the energy loss due to the seepage flow through the jam. The total friction slope, S_f, between two cross sections can be expressed as:

$$S_f = S_{fb} + S_{fi1} + S_{fi2} = \frac{(P_b\tau_b + P_{i1}\tau_{i1} + D_t)}{\rho g A} \quad \textbf{[5]}$$

in which, S_{fb},S_{fi1} and S_{fi2} are friction slopes correspond to the bed resistance, resistance due to the undersurface roughness of the jam, and the resistance due to the seepage flow through the jam, respectively; ρ = water density; A = average flow area under the jam between two cross sections; $P_b$and τ_b = bed wetted perimeter and shear stress, respectively; P_{i1} and τ_{i1} = ice cover wetted perimeter and shear stress, respectively; and D_t = seepage drag on ice particles in the jam. Through a detailed analysis of the seepage flow resistance and the resistance due to the undersurface roughness of jams, the study by Fan et al. 2017, showed that the seepage flow resistance increases with the jam thickness and the flow resistance due to the undersurface roughness of the jam remains relatively constant. Moreover, the contribution of the resistance due to the undersurface roughness is relatively small compared to the seepage flow resistance.

The seepage flow resistance is a dominating part of the jam resistance excepted for a portion of the jam near its head, where the jam thickness is small with negligible seepage flow. In this study, experiments were conducted to study the flow resistance of ice jams with particular attention to the seepage flow effects for developing theories on these processes.

Number of evidences and facts showed the analogy between the seepage flow in the ice jam and flow in open channel over rough, permeable bed. Base on papers by Nikora et al, 2001, 2007, Manes et al 2009. As well as Gupta and Pudyal (1985), where flow over rough, gravel bed was investigated, it was concluded that the velocity over the bed is not zero, thus the seepage flow in the gravel exists. Taking all this into consideration, the analogy with flow in open channel over permeable surfaces could be found, where the channel bed is made of rough stones and boulders, as well as for regulated rivers where bed is stabilized by gabion baskets or mattress. Therefore experiments conducted on ice jam model can help to develop theories on gravel bed, as well as during the study some theories from permeable bed can be adopted.

2. Research methodology

In order to verify the research hypothesis, series of physical experiments were conducted where water velocity profiles were measured under and inside the ice rubble. Experiments were proceed in hydraulic laboratory as a scale model of the real ice jam, because measurements in rivers are extremely dangerous and nearly impossible due to the risk of ice jam release during the surveying of the water velocity. Therefore scale model was set up to reproduce the typical condition observed in rivers. Since the facility on Gdansk University of Technology has no possibility to lower the room temperature to below freezing, the material similar to the ice was used instead. Number of possible materials was tested such as lightweight concrete (with expanded clay aggregate), polyethylene and wood but polypropylene (PP) was finally accepted to be good imitation for the river ice. The density of polypropylene (920 kg/m^3) is very close to the density of ice (917 kg/m^3). Also the unity price of polypropylene is acceptable and the material properties will not change during the experiment due to soaking in the water. PP board was cut into required size parcels with dimension of 40 x 40 mm. The small size of single parcel helped to produce uniform distribution of ice in the jam and to get smooth velocity profiles inside the jam. Material was placed directly to the water in the upstream section of the flume, and the jam was formed due to existence the permeable barrier in the downstream section of the flume. The barrier was made of wire mesh with clearance of 10 mm, which allowed the water to flow without significant resistance but the PP material was stopped. The jam length, produced by the supplied material was sufficient to achieve equilibrium condition within short section of the rubble.

After the scale model of the ice jam was produced, the measurements of the water velocity profiles were made. The goal of the experiments was to get full profile of the water velocity under and within the ice rubble. To measure the seepage flow velocity, a micro velocity meter with sensor diameter not larger than 40 mm was needed. This type of instrument will allow direct measurements within the rubble without interaction with the material, which could cause collapsing of the jam or changing its features. Knowing the proportion between under - jam discharge and seepage flow calculations were made which can lead to establishing the better theory on hydraulic resistance in the case of ice jam.

3. Hydraulic experiment

The experimental study has been preceded in summer 2016, in small flume in the hydraulic laboratory of Department of Civil and Environmental Engineering, Gdansk University of Technology (Figure 2). 10 mm polypropylene boards were used to imitate ice. The material was cut to the parcels of the dimension 40 x 40 mm. Due to the lack of founding, only 1,5 m^2 was purchased which could produce the jam with length of 0,7 m and average thickness of 0,1 m, and thickness at the toe reached 0,16 m. The width of the jam was limited by the flume width which was 0,38 m. Water velocity was first measured by use of self-made Pitot tube. In order to measure the small water velocity, the scale of the tube was installed on slat sloped to the horizontal plane on 10^o angle. Unfortunately, Pitot tube was not reliable, and results produced by the instrument may not be trusted. Therefore the decision was made to not use this device in further measurements.

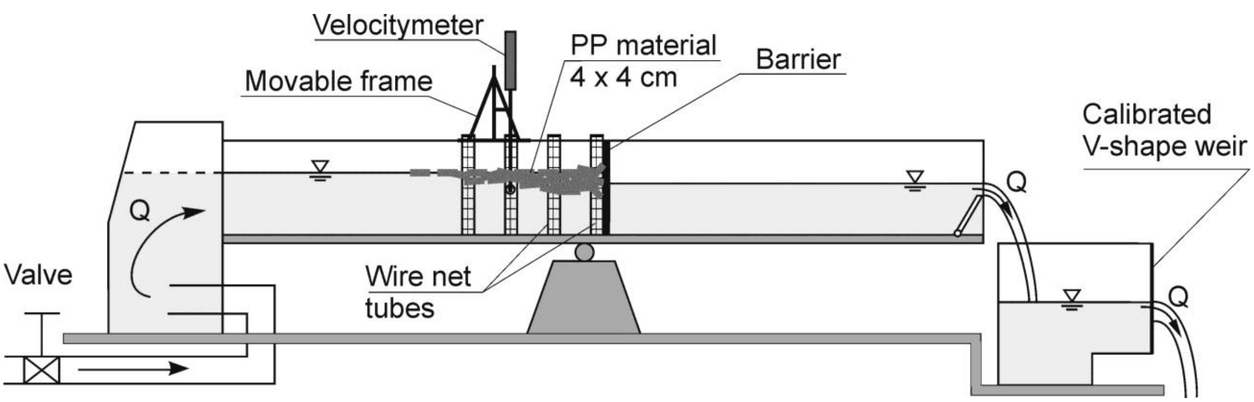

Fig. 2. Layout of the laboratory flume and the locations of the instrumentation in small flume of the Gdansk University of Technology (GUT)

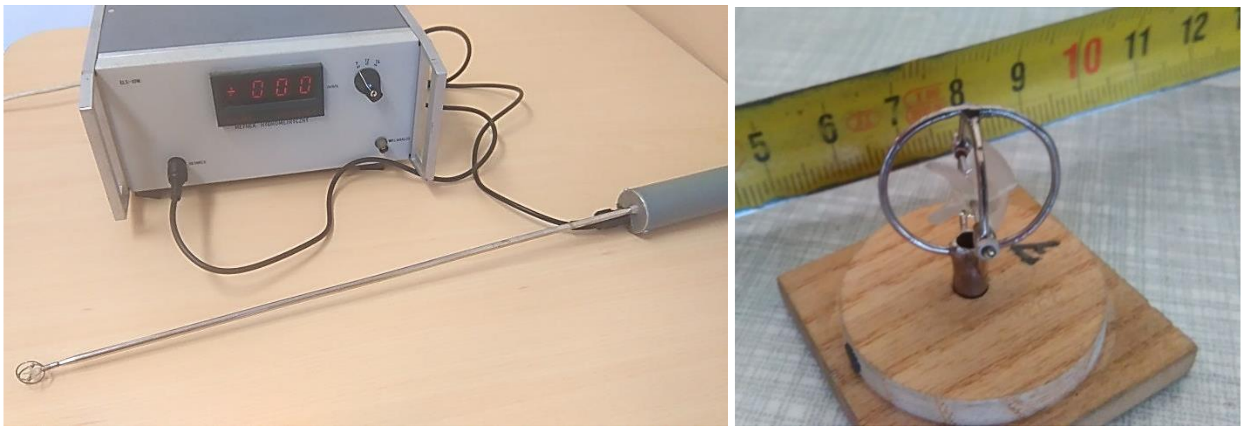

Fig. 3. Propeller type micro-velocity meter with the counting device (a); propeller in a casing basket – measuring tape's scale in centimeters (b)

Further water velocity measurements were made with use of the micro velocity meter, which was self-made instrument constructed by faculty of Institute of Hydro-engineering Polish Academy of Science in eighties last century. The device is propeller type, electromagnetic meter which include micro propeller with diameter of 10 mm, installed inside the 25 mm protective basket (Figure 3). The propeller rotate on the horizontal ax causing interference noise on the sensor installed at the end of the rode. The calibrated signal was next transfer to the counting device where velocity of flowing water was displayed with accuracy of 1 mm/s and the range of the measurements was 0,02 – 2 m/s. The velocity meter was validated prior to the experiments, by comparison the measured velocity recorded by ADV meter and HEGA propeller type velocity meter, showing sufficient accuracy. The micro velocity meter is very fragile instrument, and it required special shields in a form of steel wire net tubes of dimeter of 30 mm (Figure 5.). The tubes were installed in four, previously selected locations along the jam and the velocity was measured inside them. The first profile was at the jam toe (3,5 cm upstream of the barrier), and the next tubes were installed with 0,2 m spacing in upstream direction (see Figure 2 and photograph on Figure 5).

Fig. 4. Ice jam model in GUT hydraulic laboratory, flow direction from left to right

4. Results

All results collected during the laboratory experiments are presented below in a form of velocity plots for each profile (Figure 5) and a table summarizing the seepage flow percentage calculated based on the measured velocities.

The results shown significant amount of flow goes through the jam reaching nearly 40% of total discharge in the profile near the barrier. The average porosity of the entire jam was estimated to reach 54%, which was calculated based on jam thickness and amount of material used in the model. By analogy with the ground flow, the porosity of the material may play important role in the seepage, however this parameter was not tested and requires further studies. The profile I, where the larges seepage occurred, was set inside the jam toe. In this location almost half of the cross section was filled with the material causing significant blockage of the water flow. The water velocity distribution shown two zones from which in the area near the water surface the low velocity occurred (below 0,1 m/s). In the zone below the mid line of the jam thickness, water velocity increases significantly, reaching the maximum at the underside of the jam formation.

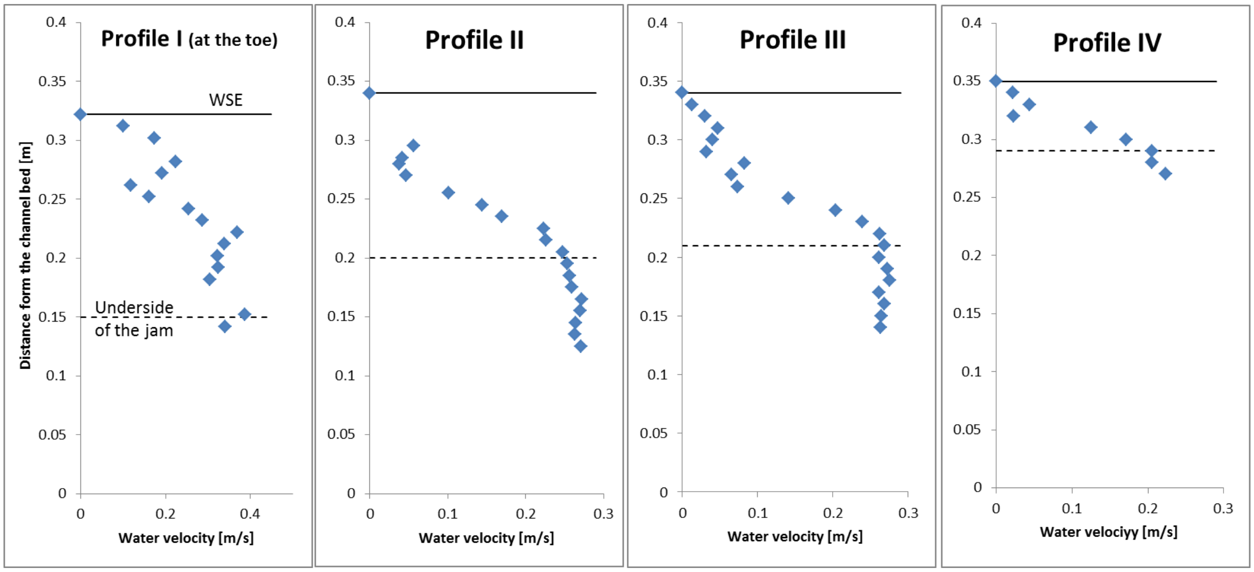

Fig. 5. Water velocity profiles measured inside and under the jam (Profiles spaced by 0,2 m distance and Profile I was measured at the toe)

Table 1. Measured seepage flow through the jam voids

Profile	Seepage flow [% of the total discharge]
I	**36**
II	**19**
III	**16**
IV	**5**

5. Conclusions

Experimental results shown significant percentage of the flow is seeping through the jam. The seepage water velocity reaching its maximum value at the underside of the jam and its only slightly lower than water velocity under the jam. The effect of the porosity and parcel size is considered to play important role in the seepage mechanism, however both were not tested at the current study.

Below all errors and malfunctions of the preliminary tests are pointed out. The results are now considered as the conclusions to improve the future tests to avoid further problems:

a) Insufficient amount of PP material caused that the modeled jam was short and barely reached equilibrium state.
b) Small flume width in comparison to the size of single parcel caused scattered velocity profiles with significant effect of the boundary condition.

c) The used instrumentations were in low quality and caused many problems, including overwarming the device (propeller-type velocity meter) or producing not reliable results (Pitot tube).
d) Micro velocity meter was very fragile, and could not be placed in the jam without shields. The protection tubes produced local velocity fields different form the velocity inside the jam.

References

Ashton, G. D. (Ed.), 1986. River and lake ice engineering. Water Resources Publication.

Beltaos, S., 1988. Configuration and properties of a breakup jam. Canadian Journal of Civil Engineering, 15(4), 685-697.

Beltaos, S. (1993). Numerical computation of river ice jams. Canadian Journal of Civil Engineering, 20(1), 88-99..

Fan L., Mao Z., Shen H.T., 2016. Hydraulic Resistance of River Ice Jams, Journal of Hydrodynamics, Ser. B, Accepted for publication.

Gupta, A. D., & Paudyal, G. N., 1985. Characteristics of free surface flow over gravel bed. Journal of irrigation and drainage engineering, 111(4), 299-318.

Jones, K.F., Friddell, J.E., Daly, S.F., and Carrie, M.V., 2004. Severe winter weather in the continental U.S. and global climate cycles, ERDC/CRREL TR-04-19, 87p.

Kolerski, T., 2016. Modelowanie matematyczne zjawisk lodowych na wodach śródlądowych, Wydawnictwo Politechniki Gdańskiej,

Manes, C., D. Pokrajac, I. McEwan and Nikora V., 2009. Turbulence structure of open channel flows over permeable and impermeable beds: A comparative study. Physics of Fluids, 21: 125109.

Нежиховский, Р. А., 1964. Коэффициенты шероховатости нижней поверхности шуголедяного покрова. Труды ГГИ (Государственный гидрологический ин-т), Ленинград, 1964, вып. 110, с. 54—82.

Nikora, V., Goring, D., McEwan, I., & Griffiths, G., 2001. Spatially averaged open-channel flow over rough bed. Journal of Hydraulic Engineering, 127(2), 123-133.

Nikora, V., McEwan, I., McLean, S., Coleman, S., Pokrajac, D., & Walters, R., 2007. Double-averaging concept for rough-bed open-channel and overland flows: Theoretical background. Journal of Hydraulic Engineering, 133(8), 873-883.

Shen, H. T., 2010. Mathematical modeling of river ice processes. Cold Regions Science and Technology, 62(1), 3-13.

Shen, H. T., 2016. River ice processes. In Advances in Water Resources Management (pp. 483-530). Springer International Publishing.

White, K.D. and Eames, H.J. 1999. CRREL ice jam database. USA Cold Regions Research and Engineering Laboratory, Ice Engineering Information Exchange Bulletin No. 9.

International Association for Hydro-Environment Engineering and Research
Supported by Spain Water and IWHR, China

24th IAHR International Symposium on Ice
Vladivostok, Russia, June 4 to 9, 2018

Hardmetry Method for Assessing the Concrete Resistance to Aggressive Ice Impacts

Alexey A. Sklyarov[1], Tatiana E. Uvarova[1], Galina S. Slavcheva[2], Egor E. Pomnikov[1]
[1] Offshore and Structure Mechanics Department, School of Engineering
Far Eastern Federal University, 8 Sukhanova St., Vladivostok, Russia, 690090
[2] Voronezh State Architecture-Construction University,
84 20th Anniversary of October St., Voronezh, 394008
aleksey_saa@mail.ru;
uvarova.te@dvfy.ru
gslavcheva@yandex.ru;
pomnikov.ee@dvfu.ru

The main factor affecting the reliability of marine ice-resistant platforms (MIRP) is the ice regime in the construction site and, as a result, ice loads and impacts on the structure. One of such impacts in the water areas with a dynamic regime of ice cover drift is ice abrasion. The concrete in the variable-level zone from the drifting ice cover effect contributes to the loss of the structure concrete elements thickness in the variable level zone, causes the danger of reinforcement exposure and its accelerated corrosion in the marine environment and, therefore, may lead to a reduction in the strength characteristics of these structural elements. The task of increasing the concrete resistance to the ice cover abrading impacts is directly related to the studies of their deterioration resistance and the requirements determination for the composition and concretes exploited structure in the Arctic seas.

The article substantiates the prerequisites of the hardmetry use for the concrete resistance evaluation to ice abrasion as a method of obtaining an independent direct quantitative resistance index that is correlated with the concrete destruction processes during ice abrasion and independent of the ice impacts parameters.

The applying possibilities and adapting existing hardmetry methods testing for concrete as a brittle heterogeneous material have been estimated. The rationale for the optimal method, procedure and algorithm for estimating the concrete hardness is discussed, and the tests results of specimens that prove the determining possibility the integral concrete hardness based on a statistically reliable hardness evaluation of each of its structural elements are presented.

To predict and regulate the concrete resistance to ice abrasion, it is proposed to identify the relationship between the integral hardness index of the concrete surface and the found depth values of ice abrasion, considering the variation in speed, temperature and ice pressure, performed in the period from 2007 to 2014 on a special unit for studying ice abrasion effects on various types of building materials.

Key words: hardmetry, abrasion, concrete, hydrotechnical constructions, estimation method.

Introduction

The problem of reliability and durability of technical means of offshore development oil and gas fields in recent decades is one of the most relevant in the world. The main operational factor affecting the reliability of such facilities in the Arctic regions is the marine area ice regime and, as a consequence, the ice loads and impacts on the structures. Practical experience of their exploitation shows that there is a probability of loss of the structure bearing capacity (structural element) from relatively moderate effects of high frequency. As a result of dynamic influences, the surface contacting with ice is constantly exposed to ice abrasion, which can lead to exposure of the reinforcement, to changing the cross-section and to loss of the bearing capacity of the structure as a whole [5].

The results of long-term studies of the ice cover and its impact on hydraulic structures suggest that the problem of ice abrasion can be divided into two parts:

- ice impacts causing abrasion, the main ones being contact pressure, the length of the abrasion path and the interaction speed, ice strength and temperature;
- the resistance of the material to the abrading action of ice.

At present, a significant amount of scientific research has been done on the first part of the problem of ice abrasion [8, 9, 10]. As a result, considerable experience has been accumulated in modeling ice impacts and predicting the structures behavior in various design situations. Experimental studies of the ice abrasion process made it possible to obtain empirical models of ice abrasion concrete resistance [6, 7], reflecting the concrete wear process intensity depending on the parameters of ice impacts.

However, the second part of the abrasion problem associated with the study and the behavior forecasting of the materials themselves is currently not being given due attention. Accumulated quantitative data only reflect the concrete strength relationship with the ability to withstand ice abrasion. In particular, for concrete it is assumed that in order to provide sufficient resistance to ice abrasion, it is necessary to regulate its strength (at least 70 MPa) [2]. The standard concrete mechanical characteristics, including strength, are not direct quantitative characteristics of abrasion resistance, since in the testing process, compression failure and bending are reproduced. In the process of abrasion by ice, concrete is destroyed as a result of fundamentally different phenomena. To regulate the ice abrasion resistance, to predict its behavior, an adequate quantitative resistance index is necessary, on the one hand, correlated with the processes of concrete destruction under ice abrasion, on the other - independent of test conditions and parameters of ice impacts, but determined by the composition characteristics and the material structure.

An analysis of the existing methods complex for evaluating mechanical testing of materials has made it possible to pay attention to hardness as a promising method for solving this problem. However, existing hardness methods have been developed and widely used to evaluate the hardness of metals, i.e. homogeneous materials with their characteristic elastoplastic properties [1, 4]. Concrete is a brittle heterogeneous material, so there is a problem of adaptation for concrete of solid-metal methods used for metals.
Concerning, in this paper, it is proposed to consider the hardmetry possibilities as a method of obtaining a direct quantitative indicator of the concrete resistance to ice abrasion. There are following reasons for this.

First, the similarity of the abrasion process mechanism [8] and the testing process for hardness [1]. This is of fundamental importance, since the measurement principle itself, when obtaining information about the material properties, must simulate the operational impact and be adequate to the operational processes. From this point of view, it is the hardness test process that completely simulates the concrete surface destruction mechanism under the ice abrasive action (Table 1).

Table 1 Ice abrasion processes and processes in the hardness test implementation

Processes from the action of frictional forces in the abrasion contact interaction "ice-concrete"	Processes with indentation of the tip into the surface of the test body during the hardness test
The displacement of concrete and the formation of a scratch	Replacement of the material and formation of a roller around the print
Deformation and microcracking of a certain volume of concrete around the scratch	Deformation and microcracking of a certain amount of material around the fingerprint
A new surface formation	A new surface formation
Friction of ice on contact with the material surface	Friction of the tip when penetrating the material
Heat release	Heat release

Secondly, there is an analogy between the quantitative characteristics of ice impacts and the local impact on the material when assessing its hardness. On the one hand, the amount of ice abrasion depends mainly on the ice contact pressure on the structure surface. The calculation method [3] allows estimating the contact stress at any point in the structure abrasion zone, taking into account the different interaction scenarios. On the other hand, the hardness value can be considered as a parameter of the material local resistance to the stress on the interaction contact area, since it corresponds to the average contact pressure per unit surface when the tip is pressed in.

Thus, it is the hardness characteristic that corresponds most adequately to the mechanism of material destruction and the loads parameters during ice abrasion. This article presents the results of the author's studies evaluating the applying and selecting possibility the optimal hardmetry method for concrete testing, the procedures and algorithm for evaluating the concrete hardness are substantiated.

Materials, equipment, measurement process

To verification the test procedure, the authors of this article tested 8 samples of concrete grade B60 at the age of more than 1 year. To prepare for the tests, the samples of the cube 10 × 10 × 10 cm were sawn into two halves, followed by grinding the test surface.

To study the static hardness of the concrete samples surface, the Qness Q150A+ equipment was used (Table 2). The hardness measurement in this equipment is carried out automatically in the prescribed trajectory. In the testing process, the sample is fixed on the magnetic table of the hardness meter, the measurement points grid position on the sample surface is assigned, and the sample surface is photographed. As a result, a common plot of the measured surface hardness values, tables and graphs with hardness values for each specific point is plotted, and the tested samples surface images are obtained.

Table 2 Technical characteristics of the Qness Q150A+ hardness meter

Range of test loads	9,81-2450 N
Test height / depth	187/180 mm
Subject table	Motorized 170 × 250 mm with travel stroke X260/Y166 mm
Maximum mass of samples	50 kg
Accessories, additional equipment, software	Holders of samples, indentors, lenses, ***Qplx control*** software modules and software, built-in optical system, camera

After the measurements are complete, the data is exported to Microsoft Excel spreadsheets. Further, the data on the concrete structural elements are filtered through a visual comparison of the concrete surface photo with the measurement points coordinates.

The optimal method substantiation, procedures and algorithm for evaluating the concrete hardness

At the first stage of the experiment, a hardmetry method was chosen which can be adapted for concrete testing. To determine the hardness of the concrete samples surface, four methods were considered: according to Rockwell, Brinell, Vickers and Knoop, which are currently most widely used in industrial tests. In these methods, the hardness test is realized by static pressing a hardened steel ball, a diamond pyramid with a square base and with an angle between the opposite faces of 136º and a diamond cone with an angle at the top of 172º.

In the Brinell, Vickers and Knoop tests, hardness is calculated as the ratio of the vertical load to the print surface area of the corresponding tip. When testing hardness using the Rockwell method, the indentation is indented in two steps: first, the tip is pressed with preload, and then the main load is applied. The measured parameters are the difference in penetration depths of the tip under the action of the main load and preload, measured without removing the preload.

During the tests, it was found that methods for determining hardness by measuring the indentation on the material surface (Brinell, Vickers, Knoop) cannot be used to study the concrete samples hardness. On the concrete surface, the prints had fuzzy boundaries, which is due to the heterogeneous concrete structure and the fracture fragile nature, and therefore an estimate of the print area resulted in significant errors (Figure. 1). Thus, only the Rockwell method can be used from the evaluated methods for testing the concrete hardness.

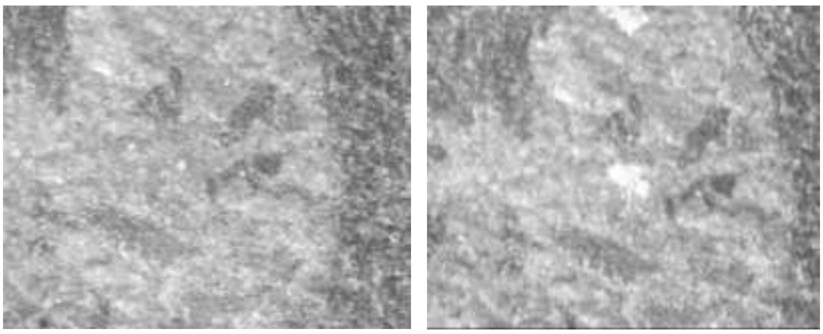

Fig. 1. A photograph of the concrete surface before and after measurement.

At the second stage of the experiment, the procedure and algorithm for estimating the concrete hardness by the Rockwell method was substantiated

Selection of indenter. For Rockwell tests, the following indentors are used: No. 1 - diamond cone (Figure 2, a), No. 2 - ball ∅1.5875 mm (Figure 2, b), No. 3 - ball ∅3,175 mm (Figure 2, c). During the tests, the following was established:

- when using indenter No. 1, a systematic error was observed because of the indenter small size, which in more than 50% of the measurement points fell into the pores, which led to negative values of the hardness index;

- indentor No. 3 does not provide an opportunity to identify the hardness of concrete individual structural elements because of its large size,

- indentor No. 2 allows to conduct an accurate measurement of the structural concrete hardness (coarse aggregate, binder and their contact zone).

Indenter No. 2 is considered optimal for evaluating the concrete hardness as an inhomogeneous material, since this indenter makes it possible to record different characteristics of the hardness of concrete structural constituents.

Load selection. For indentor № 2 (∅1.5875 mm), the Qness Q150A+ equipment allows to apply the normative loads of 15,30,45 kgf. It is established that when loads of 30 and 45 kgf are applied, the surface layer of the concrete sample is significantly destroyed, which leads to a high measurement error. The load of 15 kgf is a necessary and sufficient value of the standard load, which was used for further tests.

Determine the number of measurement points. For a 10×10 cm sample of concrete, the hardness measurement area measures 5×5 cm. According to regulatory requirements, the interval of breaking must not be less than two diameters of the indenter tip. Therefore, within the measurement area, measurement fields were created with an interval between the application points of the load 2.5; 5; 7.5 mm. It is established that the most accurate results are obtained from 19×19 points with an interval of 2.5 mm between them (Figure 3). The increase in the measurement interval leads to considerable errors in the hardness measurement, since a small number of measurement points makes it impossible to obtain statistically reliable hardness characteristics of concrete structural constituents.

a b c

Fig. 2. Indenters used in Rockwell hardness measurement: a - diamond cone, б - ball ∅1.5875 mm, c - ball ∅3,175 mm.

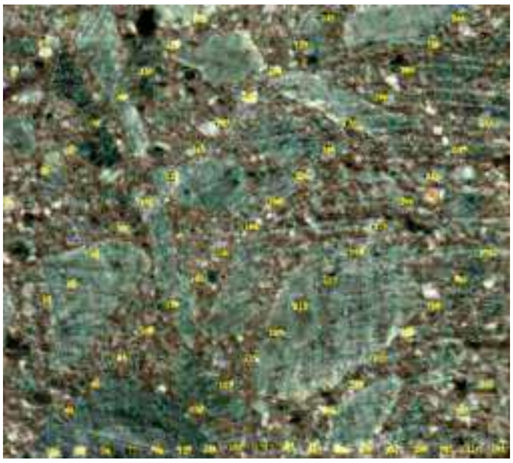

Fig. 3. Location of load points on the sample.

Results of measurements of test samples of concrete.

In Figure. 4, (a) shows the total distribution of surface hardness values of 8 test concrete samples obtained after rejecting hardness negative values that correspond to the indenter ingress into the pores. The distribution total histogram (Figure. 4, a) has a pronounced positive asymmetry, and the hardness values vary in the interval h∈{5,22;98,22}. This type of distribution is a natural consequence of the concrete structure heterogeneity, a significant difference in the hardness of its structural elements. In accordance with the data on the load application points location, the measurement data were stratified according to the concrete structural elements (Figures 4, b, c, d) with the rough errors rejection by the Romanovskii criterion. The data statistical processing made it possible to calculate the hardness following values of concrete grade B60 and its structural elements (Table 3).

Table 3 Concrete class B60 hardness characteristics

Statistical characteristics of hardness	Surface			
	total	coarse aggregate	cement stone	contact zone
Average hardness value	73,86	86,85	63,91	65,01
Standard deviation of hardness values	19,4	11,4	16,4	18,9
Standard deviation of mean values from samples	2,1	1,9	2,7	6,9

The obtained data indicate sufficient convergence and reproducibility of the measurement results. The method makes it possible to obtain reliable data on the concrete surface integral hardness and the hardness of its individual structural elements, which determines the hardmetry using possibility as a concrete testing method.

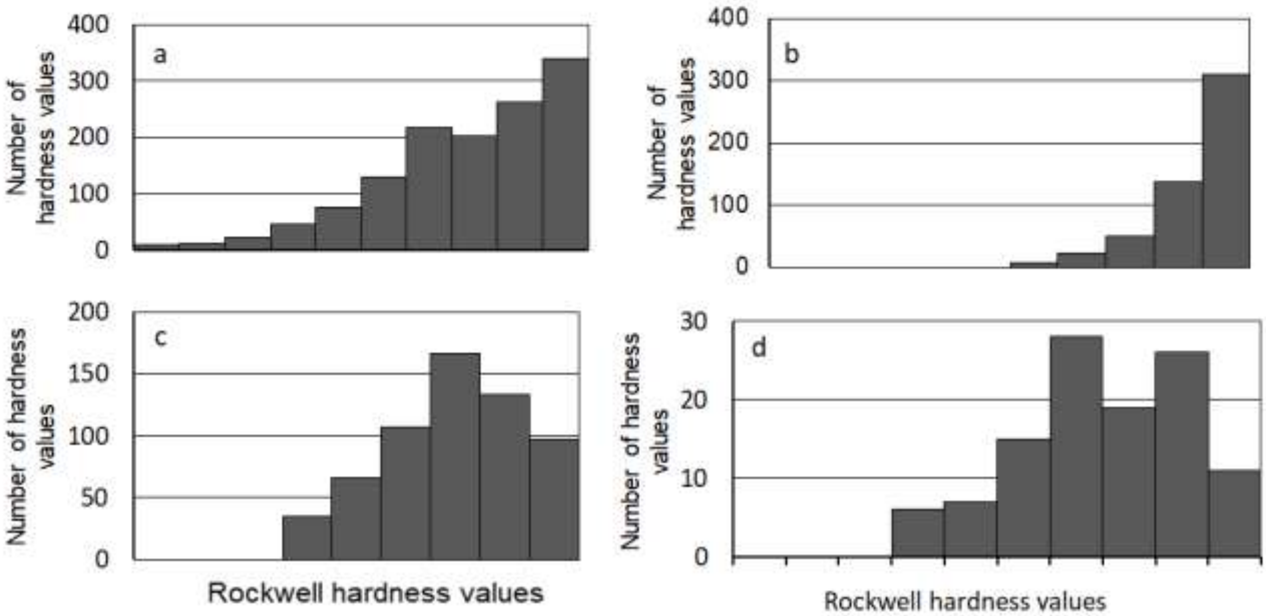

Fig. 4. Hardness values distribution of the concrete samples surface:
a - total, b - large aggregate, c - cement stone, d - contact zone

Conclusion

Analysis of the ice abrasion process mechanism and the hardness testing process mechanics allowed us to conclude that the hardness characteristics are most adequately correlated with the material destruction mechanism and the ice abrasion loads parameters. Based on this, hardmetry is considered as a method for assessing the concrete resistance to ice abrasion, and hardness is taken as a direct quantitative measure of this resistance.

To assess the concrete hardness, the Rockwell method is the best one. The rational parameters of the measurement process are: a normative load of 15 kgf, use of an indenter with a ball tip ∅1.5875 mm, an interval between measuring points of 2.5 mm.

Statistical analysis of the verification tests data has shown the hardmetry method reliability and the possibility of its use for assessing the concrete surface integral hardness and its individual structural elements.

The research development is expected in the following areas:

- obtaining quantitative estimates for the ratio of structural elements hardness of various classes concrete;

- substantiation of the requirements to the method for determining the integral hardness index of concrete taking into account the heterogeneity of its structure;

- analysis of correlation relationships between the integral hardness index of concrete various types and the values of their ice abrasion, depending on the ice impacts parameters;

- analysis of correlation relationships between the integral hardness index of concrete various types and its standard mechanical properties;

- the structure modeling and justification of the requirements for the concrete composition with the ice abrasion resistance optimum value.

The the results obtained perspective, in our opinion, consists in introducing the hardness index as an independent indicator in the overall complex of the concrete properties assessments, which must be regulated to ensure its durability when operating hydraulic structures in arctic conditions.

References

1. Grigorovich V.K. Hardness and microhardness of metals. Moscow: Izd-vo Nauka, 1976, 230 p.

2. ISO 19906-1: 2011. Oil and gas industry. Constructions of the Arctic shelf. Moscow: Standartinform, 2011.

3. Uvarova T.E. Method for determining the ice abrasion depth, Systems. Methods. Technology. 2011, № 4 (12). pp. 46-52.

4. ASTM E140-07 Standard Hardness Conversion Tables for Metals Relationship Among Brinell Hardness, Vickers Hardness, Rockwell Hardness, Superficial Hardness, Knoop Hardness, and Scleroscope Hardness. Olin College, US, 2007, 21 p.

5. Bekker A.T., Uvarova T., Jacobsen S., Pomnikov E., Kim L., Fossa K.T. Concrete Ice Abrasion due to Ice-indentation Pore Pressure. Proc. of the 1th International Congress on Durability of Concrete (ICDC–2012), Trondheim, Norway, 2012.

6. Bekker A.T. Problems of the Ice Cover Abrading Action on Legs of Concrete Offshore Structures, Workshop on Ice abrasion concrete structures. 2007, N 10, pp. 26-25.

7. Bekker A.T., Uvarova T.E., Pomnikov E.E. Calculation of Ice Abrasion for the Lighthouses Installed in the Gulf of Bothnia. Proc. of the 21th Conf. on Port and Ocean Engineering under Arctic Condition (POAC 11), Montreal, Canada, 2011.

8. Huovien S. Abrasion of Concrete Structures by Ice, Cement and Concrete Research. 1993, vol. 23, N 1. pp. 69-82.

9. Itoh Y., Tanaka Y., Saeki H. Estimation Method for Abrasion of Concrete Structures Due to Sea Ice Movement. Proceedings of the Forth International Offshore and Polar Engineering Conference, Osaka, Japan, 1994, vol. 2, P. 545–552.

10. Takeuchi T., Nakazawa N., Mikami T. et al. Abrasion of Offshore Structure due to Sea Ice Movement. Proc. of 15th International Offshore and Polar Engineering Conference, Seoul, Korea, 2005, p. 729–732.

International Association for Hydro-Environment Engineering and Research
Supported by Spain Water and IWHR, China

24th IAHR International Symposium on Ice
Vladivostok, Russia, June 4 to 9, 2018

Space-time evolution of ice conditions in long distance water conveyance channels

Jinbo Yang
Department of Hydraulics Research, Changjiang River Scientific Research Institute, Wuhan, Wuhan, Hubei, 430010, China
E-mail:yangjb1225@163.com
Yanhua Nie
Department of Hydraulics Research, Changjiang River Scientific Research Institute, Wuhan, Wuhan, Hubei, 430010, China
E-mail: 54277262@qq.com
Wengang Duan
Department of Hydraulics Research, Changjiang River Scientific Research Institute, Wuhan, Wuhan, Hubei, 430010, China
E-mail:ckydwg@163.com

Long distance water diversion project is an important engineering measure to solve the allocation of water resources. In the cold area, the winter freezing of water conveyance project affects the normal operation of the channel. This paper studies the space-time evolution of ice in winter long distance water conveyance project based on the prototype observation data of the winter ice. In the field of time, the different ice conditions of border ice, moving ice, ice cover, ice thickness and ice melting are studied. The effect of temperature, water temperature and water flow on the time of ice age is considered. In the field of space, according to the different channels of winter ice conditions, the ice range of channel of the long distance water diversion project is analyzed. The main frozen channel and buildings are determined. It provides technical support for winter operation of long distance water conveyance project.
Keywords: long distance water conveyance project; ice conditions; space-time distribution;

1. Introduction

The spatial distribution of water, soil and human resources in China is not harmonious. There are more water in the south and less water in the north. The middle route of south - to - north water diversion project was established, in order to alleviate the serious shortage of water resources in north China, optimize the allocation of water resources and improve the ecological environment. In 2008, the Beijing - Shijiazhuang section of the project began emergency water diversion to Beijing. In December 2014, the whole line was completed and put into operation.

Since the operation of the project, ice has been frozen every winter, that affects the efficiency and safe operation of water transportation in winter. Through several winter ice prototype observation[1-3], channel icing is mainly related to meteorology, channel flow and channel layout. In space, The section of the project in Henan province is located in the southern, and the climate is relatively warm in winter, and generally it doesn't freeze. The section of the project in Hebei province is the downstream part of the project, which is easy to freeze with the cold winter. In Hebei Province, the ice age in the cold winter season is wide, and the ice age is long and the ice condition is serious. In the warm winter year, the ice extent of the channel is small, and sometimes it does not freeze. The ice situation in the middle line of the south to north water transfer is very complex.

2 Conditions for development of ice

2.1 Water conveyance project

The main line of the middle route of the south to North Water Diversion Project is 1277km. The average water volume of the canal head is 9 billion 500 million m3 for many years. The flow of the canal head is designed to be 350m3/s. The flow of the end of the canal is 50m3/s. The way of water transportation is the open channel, the local pipe culvert is supplemented. The building along the line includes the control gate, the water diversion port, the retreating sluice, the inverted siphon, the tunnel, the aqueduct, the dark culvert and so on. The project uses the normal operation mode before the gate, without on-line reservoir regulation, and has limited storage capacity. The middle route of the south to North Water Diversion Project spans 33~40 north latitude. Under the influence of cold climate in winter, the Hebei section of the main canal has ice problems. The main canal will run in complex operating conditions, such as ice transport, flow of ice and water, ice cover and so on. Ice calamities such as ice plug may appear in the aqueduct, the inlet of the inverted siphon, the inlet of the tunnel, the bend and so on[4-7].

According to the operation experience of winter in recent years, the main icing range of the main canal is located in the Shijiazhuang to Beijing section (referred to as the Jingshi Section). The section of the Shijiazhuang ancient canal in the south of this section is controlled by the sluice, the north to the north of the Juma River, the total length of 228km. The 14 sluice along the line divides the Jingshi Section into 13 "canal pools" in series, the single pool is long 9~27km. The flow rate Q=170~50m3/s is gradually reduced from south to north, the design bottom width is b=26.5~7.5m, the design depth is h=6.0~3.8m, the design surface width is B=51~27m, the average velocity of the design section is V=1.00~0.75m/s, and the design of the Froude number of water is Fr=0.161~0.117. The longitudinal slope of the canal is i=1/25000~1/20000 slow, and the roughness of the open channel is n=0.015. The water conveyance lines are located in mountainous and hilly areas, with inverted siphons, tunnels, nd aqueducts. The buildings, bends and narrow cross sections change the layout and hydraulic conditions of the channel, which is easy to induce ice jam danger.

2.2 Weather conditions

The frozen section of the project is located in Hebei province. It has many sunny days in winter, and the climate is dry and cold, with little rainfall. The average temperature of the area in the region begins to turn negative in the next ten days of November and turn positive in February In the next year. Taking the data of Tangxian County meteorological station as an example, the measured temperature characteristic values in the last 5 years are shown in Table 1. The average temperature of day is -1.7~-6.0℃ in January. The negative accumulated temperature is -100~300 ℃.The minimum temperature is -9.0~-18.6℃. And the temperature characteristic values of different years differ greatly. In the cold winter, the winter climate was most typical in 2015~2016 in figure 1. In January 17, 2016, there was a cold wave of more than 20 years. The temperature lasted for a long time below the -10 ℃. The measured lowest gas temperature dropped to -18.6℃. The cold climate provided the thermal conditions for the ice production.

Table 1. The characteristics of winter water transport temperature in the last 5 years

Winter	Minimum temperature （℃）	Average temperature in January （℃）	Negative accumulated temperature （℃）
2011~2012	-12.9	-3.6	-194.8
2012~2013	-14.8	-5.0	-299.7
2013~2014	-11.6	-2.4	-173.0
2014~2015	-9.0	-1.7	-109.3
2015~2016	-15.6	-4.0	-161.0
2015~2016	-18.6	-6.0	-241.1

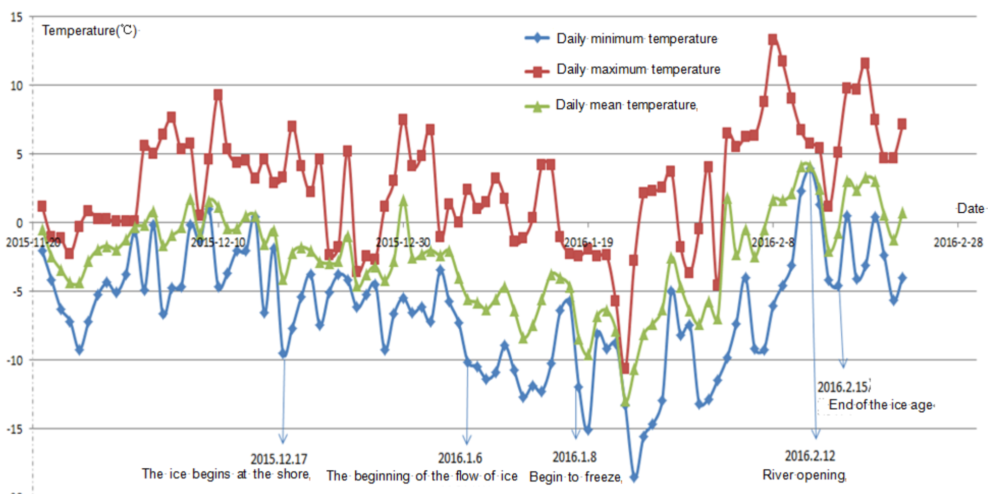

Fig. 1. Temperature change process in winter of 2015~2016

2.3 Hydraulic condition

Since 2008, the operation of the project can be divided into 2 stages in winter. Before 2014, it is temporary water in Jingshi Section before 2014. The water source area is the Huangbizhuang reservoir, Wangkuai reservoir and Angezhuang reservoir in Hebei province. It is only water supply in Beijing. It has the characteristics of short transportation channel line, small diversion flow and relatively simple dispatch.

After 2014, the whole line of middle line begins to run with supplied by the Danjiangkou reservoir, mainly supplies water to cities along Beijing, Tianjin, Henan and Hebei. Taking the Beijing section as an example, the water transport flow rate of the glacial period in the last 5 years is Q=11~30m3/s, as shown in Table 2, in which the flow of water in the annual glacial period is the largest in 2015~2016, and the average flow rate of the North anti horse river sluice is 30.7m3/s (the channel design flow is Q=50m3/s), accounting for 61.4% of the design flow of the canal section. During the winter operation, the channel depth is h=2.8~4.5m, the average velocity of v=0.25~0.67m/s, Fr=0.033~0.142, especially the flow velocity of the aqueduct reaches 0.67~0.81m/s, which provides the dynamic condition for the ice movement.

Table 2. Water transport in 5 Winter

Winter	The flow of Beijuma control sluice	
	Actual flow（m3/s）	Actual flow accounts for the percentage of design（%）
2011~2012	17.0	34.0
2012~2013	11.0	22.0
2013~2014	11.5	23.0
2014~2015	13.0	26.0
2015~2016	30.7	61.4

3 Characteristics of ice growth and elimination

3.1 Main ice phenomenon

According to the prototype observation, the glacial period of the main canal can be divided into three stages: ice age, freezing period and river opening period.

In the beginning of Ice period, Shore ice and flow ice are the main ice formation. At the beginning of winter, when the temperature dropped to -6 ℃, shore ice began to appear on both sides of the main canal in figure 2. When the air temperature falls below -8℃, there is ice drift in the main cana，in figure 3. The surface ice is the main form of drift ice, and the ice provides material conditions for the downstream of the canal.

Fig. 2. Shore ice

Fug. 3. Surface flow ice

During the freezing period， Ice cover is frozen and ice cover is thickened. During the formation of the ice sheet， the ice movement in the upper reaches of the canal and the inlet of the downstream buildings form a blockage to form the initial ice sheet. Then the upstream ice continues to accumulate at the front edge of the initial ice sheet to track the frozen channels. Generally, all single canal pools can be frozen within 2~3 days. With the increase of negative accumulated temperature, the thickness of ice sheet gradually increases. Then a certain balance is reached, the maximum thickness can reach 30cm.

During the opening of the river, the ice cover melted, only the remaining shore ice. As temperatures rise, the middle part of the ice sheet begins to thaw and melt away. First of all, the middle part of the ice cover is open. The remaining ice on both sides of the bank will fall off and move downstream, then gradually melt away in figure 4.

Fig. 4. Ice during the opening of the channel

3.2 Time and space distribution of ice

There are many factors that affect the development of ice conditions. The spatial and temporal distribution of ice is very complex. See Table 3. In fields of time, ice age generally begins in December, and end in February or March. The glacial period was 63~98d. The time nodes of the characteristics of the ice age were different in each year. In the winter of 2012~2013, the beginning time of the ice age is the earliest and the ending is the latest. The beginning time of the winter ice age in 2015~2016 is the latest.

Table 3. Characteristic glacial time node

Winter	Initial ice date	End ice date	Freezing date	River opening	Glacial period（day）	Freezing day（day）
2011~2012	2011-12-16	2012-02-23	2012-01-20	2012-02-18	70	30
2012~2013	2012-12-01	2013-03-08	2012-12-24	2012-02-24	98	62
2013~2014	2013-12-14	2014-02-24	2013-12-23	2014-02-20	73	60
2014~2015	2014-12-03	2015-02-07	2014-12-26	2015-02-04	67	41
2015~2016	2015-12-16	2016-02-17	2016-01-14	2016-02-15	63	32

In space, Freezing range of ice cover of the main canal is 80~400km. The freezing length of ice cover varies greatly under different winter climate conditions. 2014~2015 the winter temperature is warmer and the channel ice cover is 86km long. The winter of 2015~2016 is the most typical cold winter,. The glacial period lasted 63 days, and the ice cover was frozen for 32 days. The channel length of the frozen section is 363km. Among them, the 113km section of Puyang River - North Juma River is a stable freezing section.

The measured maximum ice cover thickness is 14~32cm in 5 winter. In 2012~2013, the ice cover is the thickest 32cm in winter. In the winter of 2015~2016, the thickness of the ice was measured by 28cm. In space, the thickness of ice cover gradually thickens from south to north. For a single section, the ice in the core is thin with thick in the shore, and the maximum ice thickness near the shore is 46cm.

Table 4. Ice cover thickness

Winter	Frozen canal length（km）	Maximum ice thickness in the middle of cross section（cm）
2011~2012	218	24
2012~2013	226	32
2013~2014	218	14
2014~2015	86	14
2015~2016	363	28

3.3 Analysis of ice age scheduling scheme

According to operation experience in recent years, winter is between December and March next year. The middle route of the south to North Water Diversion Project generally adopts ice age water conveyance mode. Reduce the water conveyance flow, reduce the flow condition, and make the ice sheet form as soon as possible. The time and space scope of scheduling are discussed. Under the condition of safe engineering in winter, the efficiency of main canal water conveyance in winter is improved.

In the scheduling time, there are different climatic conditions in winter, the beginning of the ice period and the end time of the main canal are different. The time of the ice period scheduling scheme should be adjusted according to the different climatic conditions. In the cold winter, the ice time of the project is long and the time of the ice period should be extended.

In the warm winter year, the ice age is short and the ice age scheduling time should be extended. In the space aspect, in the cold winter, the ice area is wide, the water diversion gate which is affected by the glacial period is more, the ice period scheduling range increases, and the ice cream is avoided. In the warm winter year, the ice area of the channel is small, the whole line is not frozen, and the ice period scheduling scope should be reduced.

4 Conclusion

In this paper， we understand the evolution of ice and ice in the main canal. The influence of climate, hydrodynamic force, geographical location and engineering layout on ice process is analyzed. The optimization idea of winter operation scheme for main canal was preliminarily explored. The climatic conditions of warm winter and cold winter, the time and space adjustment strategy of the main canal in winter are analyzed, which provide the technical support for the safe operation of the long distance water conveyance project in winter.

5 Acknowledgments

In end, thanks for the support of National Key R&D Program of China, NO: 2017YFC0405003.

References

1 (Duan, W. G., Yao, X., et al.,2016). Analysis and safety scheduling of water transport in long distance water diversion open channel[J], South-to-North Water Transfers and Water Science & Technology,14 (6), 96-104.

2 (LIU M K, et al.,2011).Analysis of hydraulic response of long distance control canal system during freezing period[J], Journal of Agricultural Engineering, 27 (2),20-27.

3 (WEN, S. Y.， YANG, J. B., et al.,2015). A prototype observation of the winter ice situation in the middle line of the south to North Water Transfer Project in the year 2014～2015[J], Journal of Yangtze River, (22),99-102.

4 (WU, J. J.,2002) Analysis of the formation and evolution mechanism of ice in the river and numerical simulation of ice plug and water internal ice[D]. Tsinghua University.

5 (YANG, K. L., et al., 2002) Simulation of river ice jam[J]. Water Resources and Hydropower Engineering, 10, 40-47.

6 (WANG, J.,2007) Formation mechanism of ice plug and simulation analysis of velocity field under ice cover and two phase flow of ice particles[D]. He Fei: Hefei Polytechnic University.

7 (LI, Z. J.，HAN. M., et al.,2005) Current situation and research progress of ice thickness variation in field monitoring[J], Progress in Water Science, 16(5), 753-757.

International Association for Hydro-Environment Engineering and Research
Supported by Spain Water and IWHR, China

24th IAHR International Symposium on Ice
Vladivostok, Russia, June 4 to 9, 2018

Analytical Review of the Regulatory Framework of Requirements to the Performance Characteristics of Material in Relation to the Conditions of Their Operation in the Offshore Structures in Arctic Conditions

Shavkat Shukhratovich Rafibaev, Alexandra Denisovna Grabareva, Antonina Iosifovna Midyukova
Offshore and Structure Mechanics Department, School of Engineering Far Eastern Federal University, 8 Sukhanova St., Vladivostok, Russia, 690090

Article is analytical review of the regulatory framework of requirements to the performance characteristics of material in relation to the conditions of their operation in the offshore structures in arctic conditions.For review, international standards were used. Based on review of different types of standards the analysis of information on material requirements was performed and divided into two parts: requirements for concrete and requirements for steel.

There are different approaches to the assignment of material requirements in standards. Features of the operation of different structural parts and environments that affect structure are not fully taken into account when selecting material characteristics in each document. Constant references to the other regulations do not give a general idea of how to choose characteristics based on given operating conditions. It was also noticed that some of the standards give information about the use of material with some characteristics in certain conditions or in certain parts of structure.

The use of various materials in the construction of offshore structures in different countries is complicated by the availability of different approaches to the assignment of material requirements. In this paper, the main regulatory documents that can be applied to the design of engineering structures on the shelf of the Arctic seas were considered.

1. International Standards ISO 19906 Petroleum and natural gas industries – Arctic offshore structures

This standard names the minimum specified 28 days strength for concrete exposed to abrasion and scouring actions, which shall be equal to, or exceed, 45 MPa. It also refers to ISO 19903 that specifies a minimum strength of 40 MPa for offshore concrete structures exposed to sea water, and concrete compressive strength on cylinders at 28 days of at least 60 MPa in parts of the structure where severe abrasion due to ice, pebbles, sand, or silts is anticipated [3].

For structural reinforced concrete exposed to chlorides under freezing and thawing conditions (in tidal zone) it also names the water/cement ratio (shall not exceed 0.40) and the air content for aggregates of different size.

2. National adoption of International Standards GOST R 54483-2011 (ISO 19900:2002) Oil and gas industry. Offshore platforms for oil and gas production. General requirements

This document refers to other documents: Normative values of the properties of materials should be determined in accordance with the instructions of the current domestic regulatory documents, as well as international standards that are applicable in the Russian Federation [7].

GOST R ISO 19906 Petroleum and natural gas industries – Arctic offshore structures

This document has exactly the same information as ISO 19906 except that for concrete exposed to abrasion and scouring actions, the minimum specified 28 days strength shall be 60 MPa. It also has reference to ISO 19903 considering minimum compressive strength of concrete for structures exposed to seawater and in parts of the structure where severe abrasion.

BS EN ISO 19903:2006 Petroleum and natural gas industries. Fixed concrete offshore structure

According to standard for concrete exposed to seawater and stored oil, the characteristic cylinder strength at 28 days should not be less than 40 MPa.

The effective water/cement ratio shall not be greater than 0.45. In the splash zone and areas that can be exposed to severe frost action - not higher than 0.40. [2]

Concrete subjected to freezing and thawing shall have adequate frost resistance. This requirement may be considered satisfied if the air content is at least 4 % for a maximum particle size of 40 mm, or at least 5 % for a maximum particle size of 20 mm (for Portland and Portland composite cements with fly ash or silica and with more than 80 % clinker). With clinker contents less than 80 %, the frost resistance shall be demonstrated by appropriate testing methods to evaluate scaling and freezing/thawing resistance.

The document also gives information about cement content for the splash zone (not less than 400 kg/m3) and for reinforced or pre-stressed concrete outside the splash zone, where it depends on the maximum size of aggregate, as follows:

- 360 kg/m3 for aggregates up to 20 mm;
- 320 kg/m3 for aggregates from 20 mm to 40 mm.

BS EN ISO 19902:2007 Petroleum and natural gas industries. Fixed steel offshore structures

This standard regulates the strength group and toughness class for steel. Document explains two approaches on material selection: material category (MC) and design category (DC). Both methods can be used. DC approach has been very successfully used within the offshore industry for many years.

As material selection criteria, standard propose: yield strength requirements, structure exposure level, lowest anticipated service temperature. [1]

Once the criteria have been established, the steel selection process follows the logical sequence of one of approaches.

In the MC approach the steel selection is based on the interrelation of the structure's exposure level, the material yield strength and toughness, and the component consequence ranking. Thickness is considered in connection with component type.

The DC approach allows wider discretion in selecting the appropriate material strength group and toughness class on the basis of a component's criticality rating: DC 1 to DC 5, with DC 1 being the most critical.

3. Interstate Standards (GOST) GOST 26633-2015 Heavyweight and sand concretes. Specifications

This GOST gives classification of concrete based on different features: compressive strength, frost resistance, water tightness, abradability. [5]

There is an appendix A of this document "Additional requirements for concrete intended for different areas of construction, and materials for their preparation". However, the requirements to the properties of concrete are not regulated clearly. There are only requirements to the properties of raw materials for these concrete and it has reference to SP 35.13330.2011 Bridges and culverts.

GOST 31384-2008 Structural concrete and reinforced concrete protection against corrosion. General technical requirements

This GOST has requirements for concrete depending on exposure classes just like SP 28.13330.2012 Protection against corrosion of construction: minimum concrete strength class

(B), minimum cement consumption (kg/m3), minimum air content (%), and other requirements regarding components or agents. [6]

In addition, it has requirements for concrete of structures operating under alternating temperature conditions that name minimum concrete grade for frost resistance and concrete grade for water tightness depending on consequence category and working conditions: operating mode characteristic and outdoor winter design temperature.

4. Sets of Rules (design guides)

SP 58.13330.2012. Hydraulic Structures. Basic statements
This standard extends to newly designed, under construction, operated, reconstructed and subjected to liquidation river and marine hydraulic structures of all types and classes. [13]

Document does not have any information regarding material requirements but has reference to SP 35.13330.2011 Bridges and culverts.

SP 41.13330.2012 Concrete and reinforced concrete hydraulic structures

This document regulates concrete classes for compressive strength and axial tension, which should be taken in accordance with tables 3 and 4 of this document, depending on the values of design concrete resistances determined in accordance with the instructions in Sections 8, 9, 10 of this code.

The rules recommend the following classes of concrete for compressive strength: B5; B7,5; B10; B12,5; B15; B17,5; B20; B22,5; B25; B27,5; B30; B35; B40. [12]

Frost resistance requirements apply only to concrete, which is located in the zone of variable level of water, and external above water concrete. The concrete frost resistance grade should be assigned depending on climatic conditions of the construction area and the number of calculation cycles (shifts) of alternate freezing and thawing during the year (according to long-term observations), taking into account operating conditions.

The rules recommend the following grades of concrete for frost resistance: F50; F75; F100; F150; F200; F300; F400; F500; F600; F700; F800; F1000.

For structures and parts of structures in the zone of variable level of water (including a two-meter zone above it), the concrete grade for frost resistance is taken from Table 1 of this document. For the above-water zone of structures, concrete grades for frost resistance are assigned taking into account atmospheric influences, but not below F100 - for mild, F150 - for severe and F200 - for especially severe climatic conditions.

The water tightness concrete grade is assigned depending on the pressure gradient, defined as the ratio of the maximum head (m) to the thickness of the structure (m), and the temperature of the water in contact with the structure (°C), taking into account the aggressiveness of the environment given in SP 28.13330.

The rules recommend the following grades of concrete for water tightness: W2; W4; W6; W8; W10; W12; W14; W16; W18; W20.

If there is a need for concrete to meet the requirements to resistance to abrasion by a flow of water with sediment loads or to resistance to cavitation, the class of concrete for compressive strength should be not lower than B25, the concrete grade for frost resistance must not be lower than F300, and the waterproof grade of concrete shall not be lower than W8.

SP 28.13330.2012 Protection against corrosion of construction

This document has requirements for concrete depending on exposure classes that represent:
- action of sea water (constant exposure to water, cyclical exposure to water or air, aerosols, but without direct contact with sea water);
- alternate freezing and thawing, in the presence or absence of anti-icing salts;
- chemical and biological aggressive environment.

The requirements are: minimum concrete strength class (B), minimum cement consumption (kg/m3), minimum air content (%), and other requirements regarding components or agents. These are used taking into account the tables regulating concrete grades for water tightness, diffusion permeability, frost resistance. [10] The approximate matching of the permeability parameters of concrete is given.

Appendix “Ж” has requirements for concrete of structures operating under alternating temperature conditions that name minimum concrete grade for frost resistance depending on working conditions: operating mode characteristic and outdoor winter design temperature.

It is mentioned that higher requirements for frost resistance should be imposed on concrete of reinforced concrete structures subjected to simultaneous action of variable freezing and thawing and aggressive fluid (chlorides, sulfates, nitrates and other salts), but the requirements are not regulated.

Recommendations on use of specific grades of steel for medium aggressive and highly aggressive fluids or soils are proposed. Steel grades 12ГН2МФАЮ, 12Г2СМФ и 14ГСМФР with a yield strength of at least 588 MPa are allowed and steel with higher strength is allowed only after research.

SP 35.13330.2011 Bridges and culverts

This standard regulates the requirements to the properties and design characteristics of concrete classes for compressive strengths B20, B22.5, B25, B27.5, B30, B35, B40, B45, B50, B55 and B60. The design resistances, the modulus of elasticity of concrete under compression and tension, the ultimate specific creep strains of concrete, the limiting relative deformation shrinkage are established only for these classes of concrete.

Grades of concrete and mortar for frost resistance, depending on the climatic conditions of the zone of construction, location and type of structures are regulated (Table 7.5) to F500, grades for water tightness - to W8. [11]

Concerning the requirements for concrete for resistance to chemically and biologically aggressive environment - there are no clear regulations, there is a reference to the requirements of SP 28.13330.

SP 16.13330.2011 Steel structures

This document regulates the use of steel for structures, taking into account the group of structures, the design temperature, the requirements for toughness and chemical composition. It also gives some recommendations on providing fire resistance limit (45 min) for all groups of open structures regardless of the design temperature. Information on the characteristics of steel for hydraulic structures and arctic conditions is absent. [9]

ND 2-020201-013 Rules for the Classification, Construction and Equipment of Mobile Offshore Drilling Units and Fixed Offshore Platforms

The category of steel with thickness equal to 50 mm or less for a particular platform's component can be chosen depending on the design temperature of the structural material and the responsibility of this element.

The use of steel with thicknesses exceeding the regulated ones is possible only after a special agreement with the Register, when meeting the requirements for the characteristics of viscosity and cold resistance. [18]

Compressive strength of concrete classes meeting the value of guaranteed strength are B30, B35, B40, B45, B50, B55 and B60 (if properly justified and agreed with the Register, it is allowed to use the concrete compressive strength classes B70 and B80). Classes can be chosen depending on the values of strength of concrete in compression and in axial tension (if needed).

Freezing resistance grades: F100, F150, F200, F300, F400, F500 and F600 specified depending on operational conditions and the number of repeated cycles of freezing and thawing per year.

5. Normative documents approved by the relevant departments, used as recommendations

VSN 41.88 Design of ice resistant stationary platform

These recommendations advice to take steel grades and their design resistance for ice resistant platforms according to the table of mandatory annex 4 of this document. Table contains steel, type of product, mechanical properties, design yield strength and function of steel. There is also a reference to SP 16.13330.2011 and SP 28.13330.2012.

As for concrete, which are in operation within the limits of exposure to seawater, its spray and in contact with ice fields and the bottom of the seabed, it must satisfy the requirements of SP

41.13330.2012. However, it still mentions that prismatic strength of concrete in the zone of variable water level should not be less than 40 MPa. For other cases, the minimum class of concrete for strength is established in accordance with the requirements of SP 63.13330.2012 and SP 41.13330.2012. [4]

Minimum concrete grades for water tightness and frost resistance are established based on Table 18 of this document. The table is based on temperature and humidity exposure zones.

There is also the note that this table is composed for the winter temperatures of the outside air minus 40 °C and below. At estimated winter temperatures of outside air below minus 20 ° C to minus 40 °C, below minus 5 °C to minus 20 °C and minus 5 °C and higher, the concrete grade for frost resistance should be reduced against the requirements of the table for one, two and three grades respectively.

6. Conclusion

Based on review of different types of standards the analysis of information on material requirements was performed and divided into two parts: requirements for concrete and requirements for steel.

Concrete requirements consist of a few parameters, which are compressive strength, or concrete grade for compressive strength, frost resistance grade, water tightness grade, cement consumption, air content and water/cement ratio (Table 1).

Table 1. Concrete requirements in reviewed standards

STANDARDS / PARAMETERS	GOST R 54483	SP 58.13330.	SP 41.13330.	GOST 31384	SP 28.13330.	GOST 26633	SP 35.13330.	GOST R ISO 19906	ISO 19906	BS EN ISO 19903	VSN 41.88	ND 2-020201-013
Compressive strength (concrete grade)	↲	-	✓	↲	✓	↲	✓	✓	✓	✓	✓	✓
Frost resistance grade	↲	-	✓	✓	✓	↲	✓	-	-	-	✓	✓
		-	✓	✓	-		✓	-	-	-	✓	✓
Water tightness grade	↲	-	-		✓	↲	-	-	-	✓	-	-
Cement consumption	↲	-	-	↲	✓	↲	-		✓	✓	-	-
		-	-		-		-		✓	✓	-	-
Air content	↲			↲		↲		↲				
Water/cement ratio	↲			-		↲		↲				

Note: "✓" – presents in standard
"-" – doesn't present in standard

"↲" – has reference to another standard

Steel requirements are specified as the use of exact grades of steel with required thickness. The methods of steel selection changes from standard to standard (Table 2).

Table 2. Steel selection in in reviewed standards

	Requirements
VSN 41.88	Steel grade (GOST and TU) SP 16.13330.2011 and SP 28.13330.2012
SP 58.13330.	-
SP 28.13330.	For medium and high aggressive fluids or soils - steel grades
SP 35.13330.2011	-
SP 16.13330.	Steel grade (GOST), Toughness, Chemical composition
GOST R 54483 (ISO 19900)	-
ISO 19906	ISO 19902
GOST R ISO 19906	ISO 19902
BS EN ISO 19902	Steel grade (US and European specifications)
ND 2-020201-013	Steel category (A, B, D, E, F) and thickness limitations

There are different approaches to the assignment of material requirements in standards. Some of the documents require the use of other standards in addition with their own requirements. Due to special conditions, in which offshore ice-resistant platforms are placed, selection of material become a very hard work that requires operation of many documents.

References

1. BS EN ISO 19902, Petroleum and natural gas industries – Fixed steel offshore structures
2. BS EN ISO 19903, Petroleum and natural gas industries – Fixed concrete offshore structures
3. ISO 19906:2010 Petroleum and natural gas industries – Arctic offshore structures
4. ВСН 41.88. Проектирование ледостойких стационарных платформ. Ведомственные строительные нормы (экспериментальные). – М. : Миннефтепром, 1988. – 136 с.
5. ГОСТ 26633-2015 Бетоны тяжелые и мелкозернистые. Технические условия. – М. : Стандартинформ, 2016. – 11с.
6. ГОСТ 31384-2008 Защита бетонных и железобетонных конструкций от коррозии. Общие технические требования. – М. : Стандартинформ, 2010.
7. ГОСТ Р 54483-2011 (ИСО 19900:2002) Нефтяная и газовая промышленность. Платформы морские для нефтегазодобычи. Общие требования. – М. : Стандартинформ, 2012.
8. НД №2 – 020201 – 013 Правила классификации, постройки и оборудования плавучих буровых установок и морских стационарных платформ. – Санкт – Петербург: Российский морской регистр судоходства, 2014. – 483 с.
9. СП 16.13330.2011 Стальные конструкции. Актуализированная редакция СНиП II-23-81* (с Изменением N 1) – Минрегион России. – М.: ОАО "ЦПП", 2011.

10. СП 28.13330.2012 Защита строительных конструкций от коррозии. Актуализированная редакция СНиП 2.03.11-85 (с Изменениями N 1, 2) – М. : Минрегион России 2012.
11. СП 35.13330.2011 Мосты и трубы. Актуализированная редакция СНиП 2.05.03-84* – М. : Минрегион России 2010.
12. СП 41.13330.2012 Бетонные и железобетонные конструкции гидротехнических сооружений. Актуализированная редакция СНиП 2.06.08-87 – М. : Минрегион России 2012.
13. СП 58.13330.2012 Гидротехнические сооружения. Основные положения. Актуализированная редакция СНиП 33-01-2003 – М. : Минрегион России 2012. – 41 с.

International Association for Hydro-Environment Engineering and Research
Supported by Spain Water and IWHR, China

24th IAHR International Symposium on Ice
Vladivostok, Russia, June 4 to 9, 2018

Inhomogeneity of sea ice

Aleksandr T. Bekker, Aleksandr E. Farafonov, Tatiana E. Uvarova, Anton A. Zverev
Offshore and Structure Mechanics Department, School of Engineering Far Eastern Federal University, 8 Sukhanova St., Vladivostok, Russia, 690090
bekker.at@dvfu.ru
farafonov.aye@dvfu.ru
uvarova.tye@dvfu.ru
zverev.aa@students.dvfu.ru

In this paper, we outline the brief bases for the need to take into account the spatial inhomogeneity of the properties of the ice cover. Long-term results of the study of the heterogeneity of the ice cover are presented. The analysis of the results and comparison of data from long-term field studies performed in the Amur Bay and Novik basin has been performed.

Keywords: strength properties of the ice cover, inhomogeneity of ice fields, ice strength.

Introduction

The development of explored reserves of oil and gas on the shelf of the Sea of Okhotsk will significantly improve the situation in the fuel and energy complex of the Far Eastern region, provide raw materials for the chemical industry, and create new jobs.

Analysis of technical means and methods of development of deposits shows that the most promising method is the above-water method, which requires the construction of unique marine ice-resistant platforms (IRP). However, the development of the shelf deposits of the northern and Far Eastern seas is constrained by the fact that a number of technical problems have not been adequately solved. In particular, the operation of such platforms in the freezing seas is complicated by the impact of ice cover on them.

Ice cover heterogeneity

Uncertainty, which is caused by inadequate exhaustion of sampling methods to determine the strength of ice, leads to the fact that the calculated values of ice loads are overestimated.

Ice loads on the structures of the continental shelf of the northern seas, in many cases, are predominant and, as a rule, affect the basic parameters of the structure.

The ice load from the drifting ice cover depends on many factors and in the general case it can be represented by the following expression:

$$F = f(k, d, h, V, R) \tag{1}$$

where k – is a coefficient that depends on the chosen interaction model and takes into account the various factors characteristic of this model (for example, the shape of the structure support, the speed of the ice during interaction, etc.);

d – is the characteristic dimension of the structure support;
h – is the thickness of the ice cover;
V – is the velocity of the ice cover;
R – is the design characteristic of ice strength.

The greatest uncertainty in expression 1 is the design strength of the ice. Based on numerous studies, the general dependence of the strength of sea ice on various factors can be represented as follows:

$$R = f_1(\Theta, S, \rho, \text{structure}) \tag{2}$$

where Θ - is the temperature of the ice;
S – is the salinity of ice;
ρ – is the density of ice;
structure – the structure of the ice field.

The structure of ice can be understood in a narrow (common sense) sense and in a broader sense. In the common sense, the structure of ice (the structure of the ice crystals, their orientation) was always assumed to be a structure, according to this there was a division into ice structures-polycrystalline, monocrystalline, etc. This structure undoubtedly affects the strength of the ice in the sample. But, given the high variability of the ice cover - in a broad sense it is possible to consider the structure on different scales. In these scales, four conventional structures of the ice field can be distinguished. Microstructure - orientation and size of crystals, interaction between crystals, characteristic size 30×30 cm (sample); ministructure - heterogeneity of ice properties in thickness and in plan, characteristic size 100×100 m (ice field); macrostructure - the structure of the ice cover as a whole for the ice season, taking into account its cohesion, the characteristic size - kilometers (ice field or several fields); megastructure - the structure of the ice cover as a whole for the period of operation, taking into account its cohesion, the characteristic size is tens or hundreds of kilometers (ice cover).

Phenomenological models are based, as a rule, on one common parameter, such as the calculated strength value Rc. This parameter characterizes the properties of ice throughout the destruction zone. Thus, in order to take into account, the spatial variability of the ice cover strength, a method of sampling ice is necessary, which makes it possible to take into account the inhomogeneity by means of a single criterion. At the initial stage, this criterion may be the ratio of the average ice strength in the fracture zone, defined as the arithmetic average of the strengths of the samples taken over the entire area of the proposed fracture site of the ice plate obtained as a result of testing small samples, to maximum strength. And although the use of values closes to the minimum strength instead of the average, looks more justified from the point of view of the process of destruction (the destruction occurs at points with minimum strength), the use of the proposed ratio lays a certain margin for strength.

Then the function describing the phenomenon of inhomogeneity takes the form (рис. 1):

$$F(S) = R_{aver}/R_{max} \tag{3}$$

where R_{aver} – average, by area, value of ice strength;
R_{max} – maximum strength value, for the same area;
S – square of the investigated area.

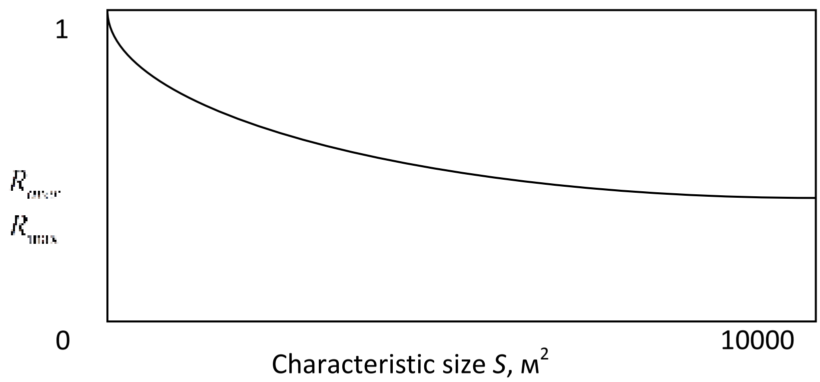

Fig. 1. The form of the function *F(S)*.

The form of the function is explained by the fact that the maximum maximum value of the ratio (3) can not be greater than 1. For large areas, of the order of $2\times10^3 \div 10\times10^3$ m^2, there will be an alternation of areas with high and low strength and, consequently, the ratio R_{aver}/R_{max} will be less than one.

To determine the design load, it is more convenient to use a coefficient that takes into account the spatial planed inhomogeneity of the ice properties, which in general will be described by the dependence:

$$k_н(S) = R_{aver}/R_{max} \tag{4}$$

This coefficient will depend on the characteristic size of the structure. The characteristic size of the fracture zone is adopted depending on the type of stress-strain state in the contact zone, the type of destruction of ice, and the geometric dimensions of the structure.

Full-scale studies of planned heterogeneity.

In accordance with the methodology developed by the Department of Hydrotechnics, the theory of buildings and structures of the FEFU, experimental studies were carried out in February 1996, 1999 - 2001 on the ice cover (fast ice) of the Amursky Bay in the city of Vladivostok. Further studies were carried out within the framework of the FEFU Winter School in 2015-2017 in the Novik Island, Russky Bay (Figure 2).

Fig. 2. Landfill for sampling (Novik Bay)

Based on the results of the processing of field data, ice strength distribution maps were constructed (Figure 3), which show that the zone of high ice cover strength alternates randomly with low strength zones. The dimensions of these zones also vary randomly.

For each polygon, distribution functions and basic statistical characteristics of strength were obtained (Table 1). As can be seen from the results, the average strength of the ice field varies from year to year, and the average strength for polygons within one year varies insignificantly, which is explained by the conditions of formation (genesis) of ice. Analysis of the distributions shows that the strength of ice obeys the normal distribution law (Figure. 4).

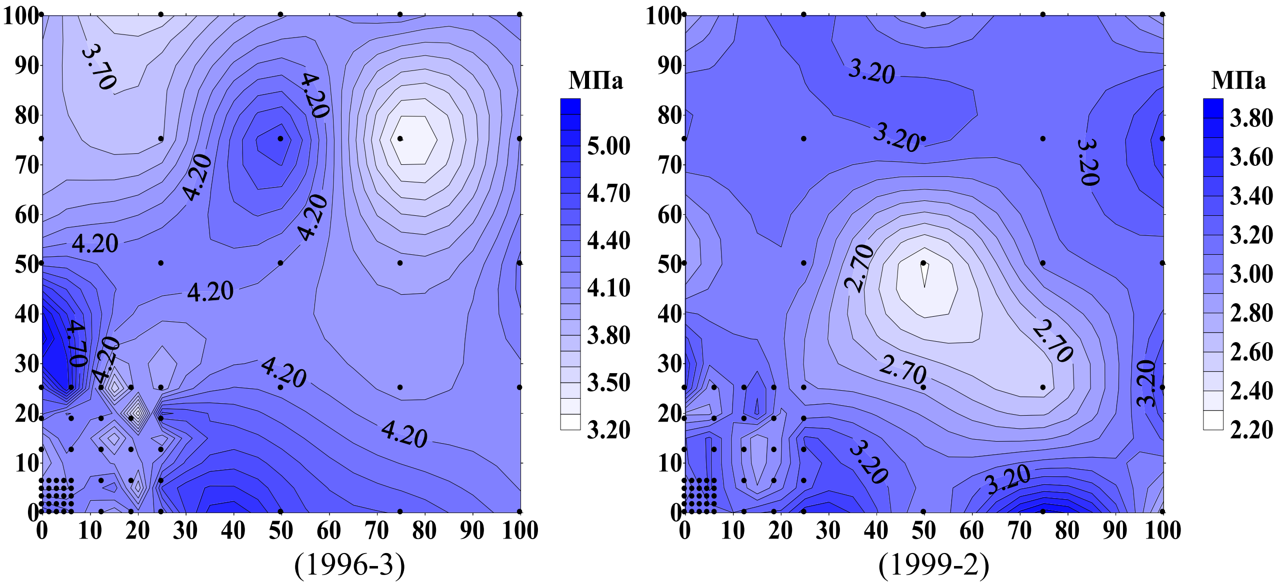

Fig. 3. Distribution of strength by polygons

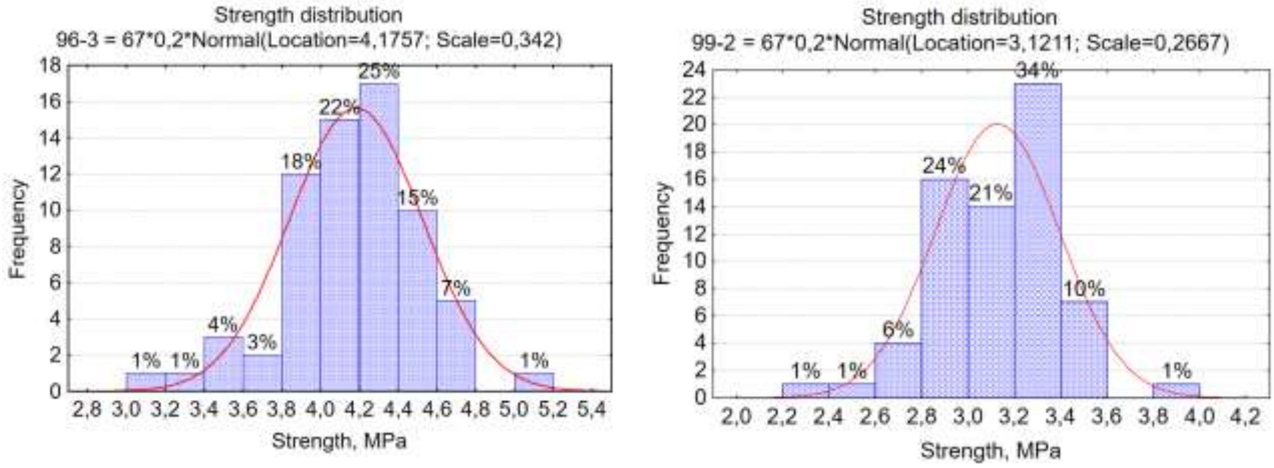

Fig. 4. Histograms of distribution of strength to polygons

To estimate the effect of spatial inhomogeneity and, consequently, its further consideration in determining the design strength of ice, the inhomogeneity coefficient is determined for each characteristic area as the ratio of the maximum strength to the average strength and the result is plotted on the plot of the spatial inhomogeneity coefficient versus the polygon area $k_н = f(S)$.

The study by the methods of correlation-regression analysis showed that the dependence $k_н = f(S)$ is most accurately described by a power function of the form $y = ax^b$ (Figure. 5) (Table 2). The high correlation coefficient (0.61-0.97) shows that the matched function adequately describes the relationship between the spatial inhomogeneity coefficient and the ice field area dimensions. Generalization and analysis of the results of full-scale studies have shown the presence of a spatial (in terms of) inhomogeneity of ice fields and its effect on the design strength of the ice field.

Analysis of the obtained graphs shows that for areas less than 1000 m^2 the value of the spatial inhomogeneity coefficient approaches unity, and, therefore, for structures with sizes up to 16 m it is necessary to take it equal to one. For areas of greater than 1000 m^2, the spatial inhomogeneity coefficient is recommended to be assigned to the upper envelope obtained as a result of plotting the curves obtained at different polygons and at different times. In addition, it is necessary to note the presence on the graph of the zone in which the change in the inhomogeneity coefficient occurs so insignificantly that these changes can be neglected. In this case, such a zone is observed for ice fields with an area of more than 5000 m^2.

Table 1. Approximating functions $k_н = f(S)$.

Years and No. of the test site	Ice temperature, ºC	$k_н=f(S)$
1996 - 1	-8,5	$y=0,896x^{-0,0208}$
1996 - 2	-8	$y=0,891x^{-0,022}$
1996 - 3	-4,5	$y=0,956x^{-0,0147}$
1999 - 1	-4,5	$y=0,923x^{-0,0119}$
1999 - 2	-4	$y=0,987x^{-0,0185}$
2000 - 1	-3	$y= 0,800x^{-0,0304}$
2000 - 2	-4	$y=0,809x^{-0,0318}$
2001 - 1	-5	$y=0,641x^{-0,0326}$
2015- East	-6,8	$y=1,0994x^{-0,042}$
2015- West	-4,7	$y=1,0985x^{-0,039}$
2016- East	-10,3	$y=1,1345x^{-0,045}$
2016- West	-11	$y=1,2363x^{-0,063}$
2017- East	-3,4	$y=1,4645x^{-0,097}$
2017- West	-3,38	$y=1,4988x^{-0,097}$

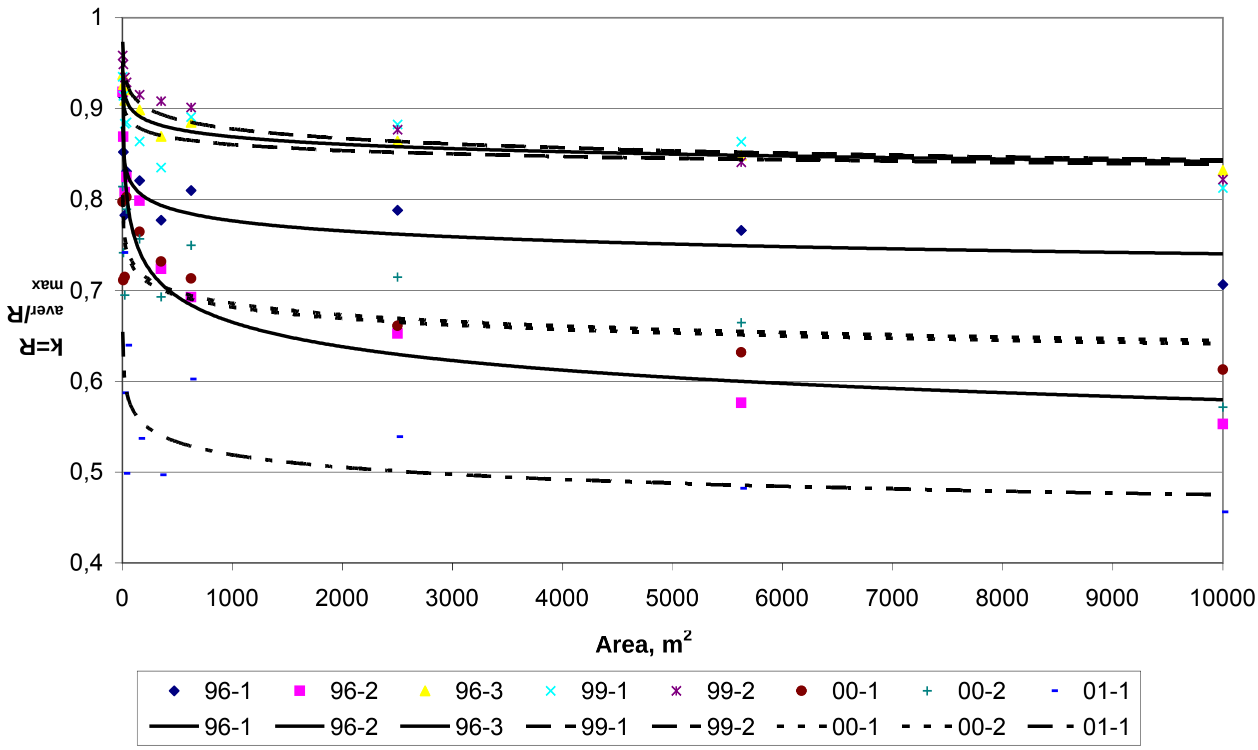

Fig. 5. Graph of the dependence of the inhomogeneity coefficient on the area of the ice field (Amursky Bay).

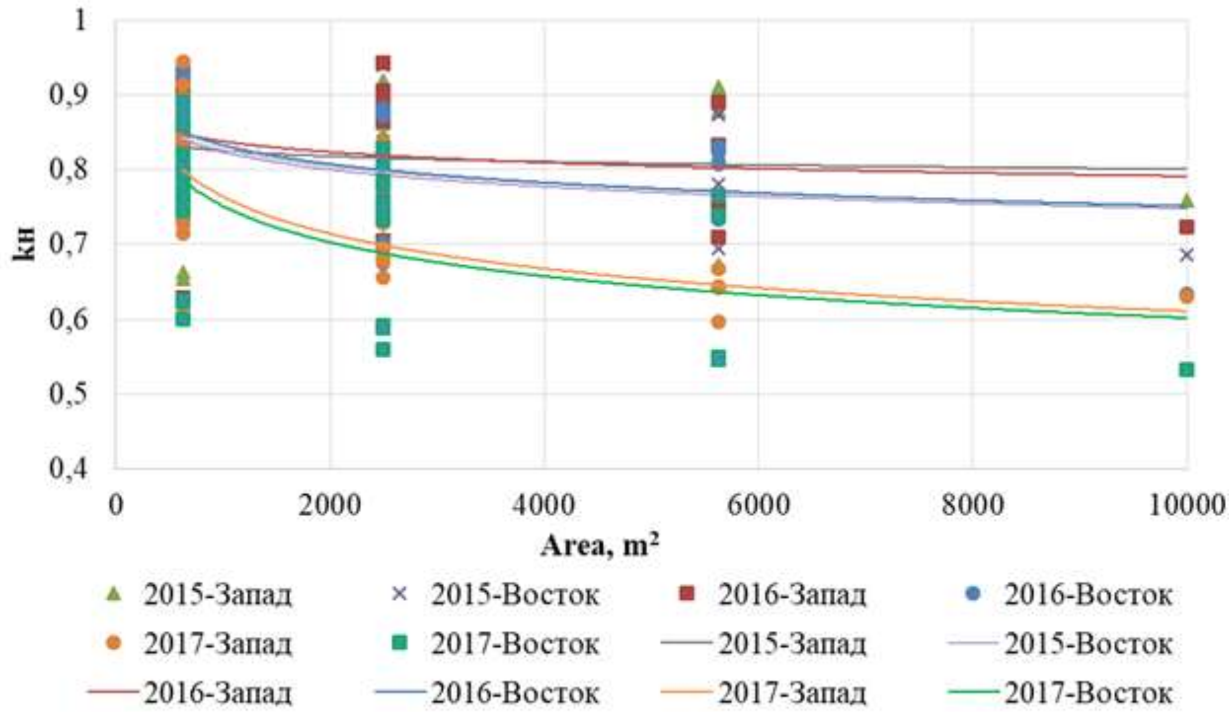

Figure. 6. Graph of the dependence of the inhomogeneity coefficient on the area of the ice field (Novik b.)

The discussion of the results

The processing of the results, carried out by the methods of mathematical statistics, showed that the distribution of the ice cover strength in the plan is random. It should be noted that the ice strength values vary widely, which confirms the high degree of variability in ice properties in the plan. Using the methods of mathematical statistics, the basic statistical characteristics of the strength distribution for each polygon were obtained. The average strength of the ice cover changes annually, which is caused by various external conditions.

Analysis shows that large areas of the ice cover are of order, alternating ice fields with high and low strength, and, consequently, the spatial inhomogeneity will be smaller. The graph of the dependence of the spatial inhomogeneity coefficient on the area of the polygon $k_и = f(S)$ has a constant form. The selection of the approximating function has shown that the dependence is most accurately described by a power function of the form $y = aX^b$.

Thus, the possibility of specifying the design strength of the ice cover by means of the inhomogeneity coefficient, determined by the results of full-scale tests, has been experimentally substantiated.

Analysis of the obtained graphs shows that, in the main for areas less than 1000 m^2, the inhomogeneity coefficient approaches unity, and therefore, for structures with a characteristic size in the contact zone of up to 15 m, the inhomogeneity factor must be taken equal to one.

For areas of large 1000 m^2, the inhomogeneity factor is recommended to be assigned to the upper envelope obtained as a result of plotting curves obtained at different polygons and at different times. In addition, it is necessary to note the presence in the graph of the region in which the change in the inhomogeneity coefficient is so insignificant that these changes can be neglected. In this case, such a zone is observed, starting with an area of 5000 m^2. The average value of the inhomogeneity coefficient for areas over 5000 m^2 during the observation period was 0.75. The maximum value of the spatial inhomogeneity coefficient for the same area was 0.91.

References

Bekker A.T., Definition of loading regime for offshore structure from drifting ice cover // Proc. Int. Symp. on the Okhotsk Sea and Sea Ice, Mombetsu, 1992, p. 302-306.

Farafonov A.E., Inhomogeneity of ice fields and its consideration in determining ice loads on marine hydraulic structures, FESTU, Vladivostok, 2006.

International Association for Hydro-Environment Engineering and Research
Supported by Spain Water and IWHR, China

24th IAHR International Symposium on Ice
Vladivostok, Russia, June 4 to 9, 2018

Preliminary study on icebreaking operation on the Middle and Lower Odra River

Tomasz Kolerski
Gdańsk University of Technology, Department of Civil and Environmental Engineering
Narutowicza 11/12, 80-233, Gdańsk Poland
tomasz.kolerski@pg.edu.pl

The Odra-Vistula Flood Management Project (OVFMP) is implemented with the assistance of international financial institutions, including the International Bank for Reconstruction and Development and the Council of Europe Development Bank, as well as with the support of funding from the Cohesion Fund and the state budget. Aside from others, the objective of the OVFMP is to increase flood protection for people living in selected areas of the Odra and Upper Vistula basins. The Odra-Vistula Flood Management Project consists of 5 components. In this paper the Component 1, Flood protection of the Middle and Lower Odra River will be discussed.
This component aims to enhance protection against summer floods and winter floods to the cities and smaller towns located along the Odra River. The activities will include, among others, the (re)construction of dikes and other bank protective works, dredging of the Odra riverbed and its channels, river training works, and the reconstruction of spur dikes. All mentioned works will be carried out to ensure the safety of icebreaking operation which requires sufficient depth over the entire river course. Five bridges also need to be raised to facilitate safe passage of icebreakers.
Within Lower and Middle Odra River the most significant flood risk is posed, in winter conditions, by ice jams created when flowing ice is stopped by existing obstacles such as shallow areas in the riverbed, narrowing of the riverbed and other obstacles caused by a result of sudden changes of the river current, backwater from sea waters and northern winds, which contribute to creation of ice jams (Lower Odra River runs a typically meridional course). This in turn causes damming of water and flooding of adjacent areas. The main aim of proposed tasks is to reduce possibility of creation of ice jams and to enable icebreaking which is the most efficient tool for minimizing risks of winter floods. These tasks will ensure safe passage of ice down the river and at the same time reduction of flood risk to adjacent areas.

1. Introduction

Ensuring and improving flood protection is one of the most important factors determining sustainable and stable social and economic development of regions and countries. Odra-Vistula Flood Management Project (OVFMP) assumes the implementation of the most urgent tasks in the field of flood protection within selected parts of river basins of the two largest Polish rivers, the Vistula River and the Odra River (Sweco 2017)

The project includes various activities carried out within the vast section of the Odra River with total length of approx. 440 km (within: Lower and Middle Odra River). All the work necessary for implementation are: (1) flood protection of areas in Zachodniopomorskie Voivodeship, (2) Flood protection on the Middle and Lower Odra, and (3) Flood protection of Słubice city (PCU 2015). The first and last tasks are mainly focusing on construction and modernization of existing embankments of the river, in order to increase security of adjacent areas, as well as works aimed at improving flow conditions for flood waters in the area between the embankments. Works planned for implementation in second task will result in improvement river conveyance for water and ice runoff during the spring or mid-winter breakup to reduce the ice jam flood risk. It is mainly focused on enabling operation of icebreakers on a long section of the river, which required ensuring of the river depth to the class III of the regional waterway which will allow navigation of the vessels with maximum draught 1,6-2,0 m (UNCE 2012). In addition, five bridges need to be raised to facilitate safe passage of the icebreakers underneath including but not limited to bridges shown on Figure 1(a) (Kreft, 2011).

2. Ice condition on the Odra River

The channel of the Oder River was regulated in early 19th century with corrections made in 1924-1941. River engineering works mainly concerned the use of a system of spurs located on both river banks for the so called low water level, however the efforts have never been completed. Currently the crowns, heads and main bodies of the structures are damaged to a varying extent, and a number of erosion potholes are found between the spurs (Kreft, Parzonka 2007). Despite significant alterations made to the riverbed, resulting from adjusting Odra River to the function of a waterway in the last centuries, the Valley maintained typical features of a large lowland river. The river source is in the Sudety Mountains and the mouth of the Odra is at the Baltic Sea, via Dąbie Lake and Szczecin Bay (Figure 1).

Ice phenomena on the Odra River are observed every season with some exceptions. Typically the first ice occur on Lake Dąbie, where static cover is formed during the due to low water velocity. If condition are suitable, frazil ice will be formed in the Odra River, which travels downstream and accumulate on the existing cover on Dąbie Lake. Thermal simulation of the ice cover formation on lake Dąbie have been proceeded to show the possible extend of the static ice cover. Air temperature recorded in February and March 2018 was used for the simulation. Water discharge is not observed on the East Odra or Regalica River (main inflow to the Lake Dabie – see Figure 1a) therefore typical flow conditions were used (low flow Q = 300 m^3/s and average flow Q = 575 m^3/s – data from Kundzewicz at al. 1999). Simulation results shown, that the static ice covers nearly entire lake. It leads to conclusion that for regular winter season ice cover will initiate at the Lake Dąbie and it will progress upstream through the accumulation of incoming surface ice. The progress of the dynamic ice cover is imitated by the stability conditions at the leading edge of the cover. In last decades, the maximum extend of equilibrium cover rarely reached Kostrzyń (Warta River outlet – Figure 1) or Słubice.

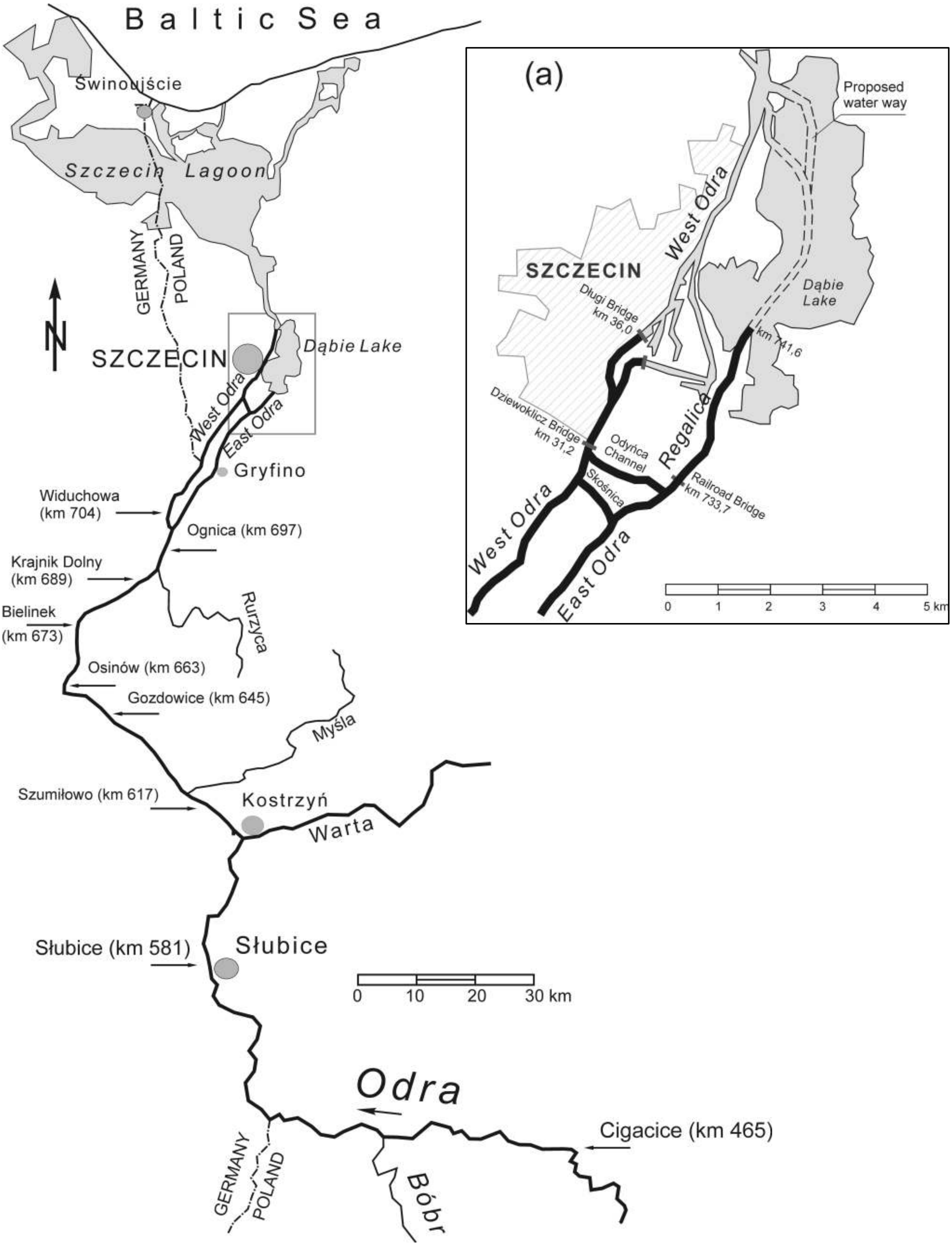

Fig. 1. Odra River in its lower and Middle section, (arrows indicate ice jam prone locations with river millage) together with a detail of the Szczecin Water Junction and lake Dąbie (a).

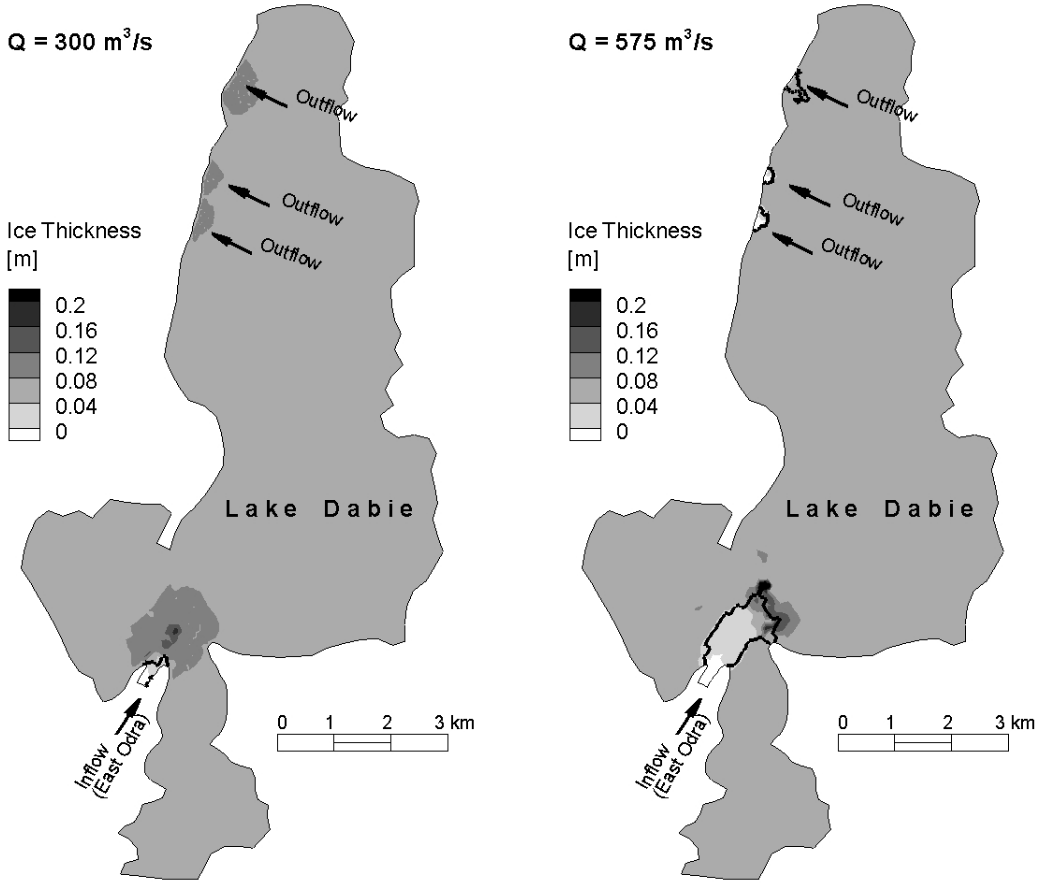

Fig. 2. Ice cover extend (black line) and thickness for air temperature data from February- Mach 2018, and variable water discharge

Ice formation and breakup on the Odra River may lead to severe jamming situations, which results for instance from the bad technical condition of river engineering structures and from years of neglect in water management. The situation is further amplified by hydraulic characteristic of the flow in the Lower Odra River which is strongly affected by hi water level on the Baltic Sea. Sea water set up together with northern wind is causing extensive backwater with effect observed up to Warta outlet (about 200 km). Locations of ice jam prone sections of the river were indicated on the map presented on Figure 1. In the paper two ice jam prone locations are analyzed: the border river section (km 571-586) in the vicinity of the Słubice and the sharp band on the Middle Odra near Cigacice (km 466-468).

2. Icebreaking operation

Numbers of possible ice breaking operations are available, however from technical and economical point of view the most reliable on the Odra River is to use specially designed vessels called icebreakers. To allow safe icebreaking operation the ship's power must be sufficient and the hull must have specific shape and be strengthened to withstand the ice load. Currently, there is a joint effort from German and Polish sides to relief winter flood risk by using 20 icebreakers.

Majority of the vessels are old and even though the fleet was recently updated by 4 new ships the average age of Polish icebreakers is 27 years and German is 44 years. Icebreaking operation is completed nearly every season, starting from lake Dąbie and continue upstream to release all ice jams on the Lower and Middle river sections. For the estuarine section of the East Odra, the ice could be additionally melted by using warm water, a coolant in the thermal power plant Grifice. The main obstacles for icebreakers in the Lower Odra are the bridges which in many cases have not enough clearance. In case of increased water level due to the ice jam the vertical clearance is too little for icebreakers to pass it safety. On the Middle Odra the biggest issue hampering the safe operation are the river depths, which may not exceed 1,0 m. To operate efficiently in Odra the icebreaker must have draught of about 1,8 m which is related to its horsepower required to break ice cover of thickness up to 30 cm (single floes) and exceeding 2 in case of ice jam.
Part of the project was proceeded to evaluate a "zero action" approach for the Odra, and to analyze the flood safety as a consequence of rejection of any further river engineering works. Those who support the continuation of the Odra River modernization maintain that building a river walls, longitudinal dykes with crosspieces on concave curves and in the passages between the curves, and spurs on convex banks is the best solution to the problem however not permanent. Opponents of the idea point to the fact that Western countries have ceased building dams and river engineering structures on lowland rivers. They claim that construction of other engineering structures would destroy naturally valuable areas, reserves, and Natura 2000 sites of conservation. Therefore it was desirable to recognize the ice condition in Lower and Middle Odra River in current state of the river bathymetry, and pointed out the possible problems related to winter water management and icebreaking operation.

3. Ice transport in the Słubice region (Lower Odra, km 571-586, Poland-Germany border)
Among others, the Lower River section in the vicinity of Słubice – Frankfurt is under constant surveillance due to its high risk of possible ice jam and flooding both cites in consequence. The main reason for hampering the ice flow is a bridge and longitudinal dyke narrowing the river to about 50% of its regular width. This leads to ice contraction and possible stoppage which may occur in case of high concentration of incoming ice. To check the ice condition in the vicinity of Słubice-Frankfurt bridge, mathematical model of 5 km of Odra River was build up to simulate ice run in the typical winter conditions. DynaRICE model was used as the most reliable and allowing simulation of dynamic balance between ice dynamics and river hydrodynamics (Shen 2010). The model was widely tested and successfully applied to number of domains including St. Clair River (Kolerski and Shen 2015) or Vistula River (Kolerski 2014). Boundary conditions for river hydrodynamics were set to represent flow conditions observed during core winter months. The data from Słubice gauging station were analyzed where daily water surface elevation is recorded. The station has also some ice thickness observations; however is mostly quantitative information of ice type. Detailed river bathymetry and the shoreline data were also used for the study. Simulation results for low flow condition and ice inflow of concentration 0,4 and initial thickness of 0,2 m were presented on Figure 3 in form of counter plot of ice thickness. Simulated results showed very fast process of ice accumulation and jamming which initiate at the bridge cross section and developed quickly upstream reaching the domain boundary after 24 hours.

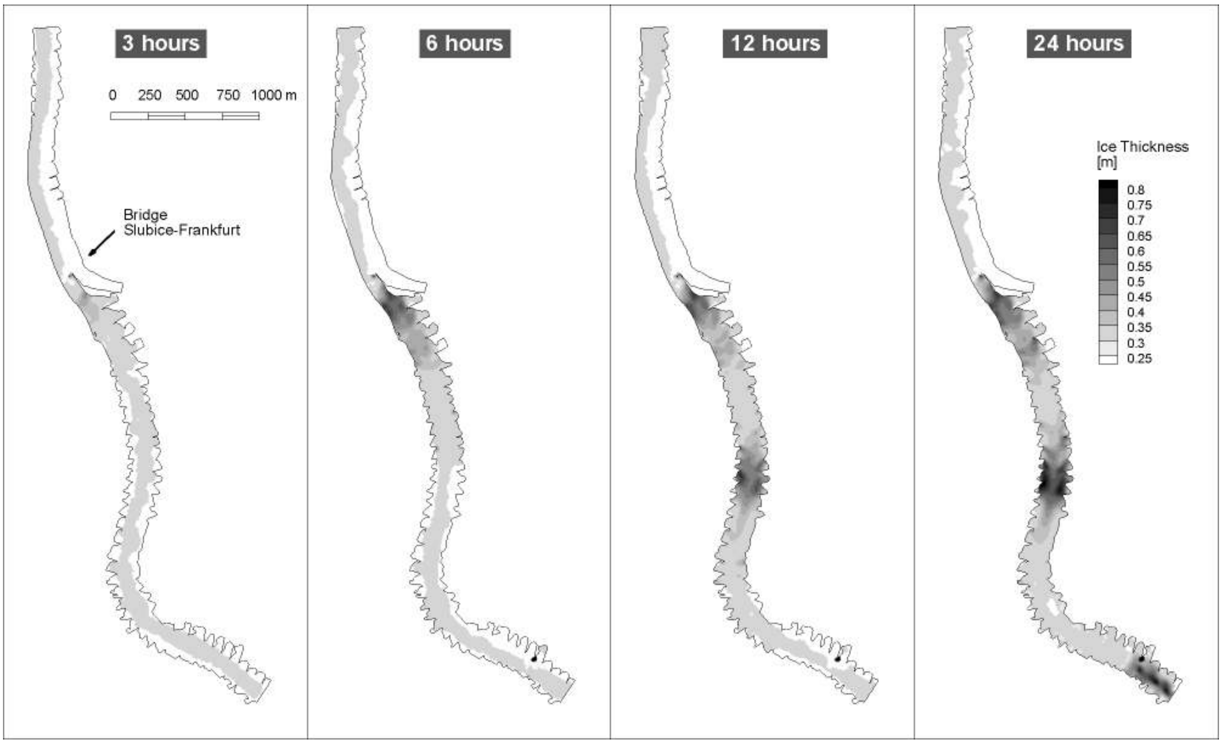

Fig. 3. Simulated ice thickness distribution in the Lower Odra River in the vicinity of the Słubice-Frankfurt bridge (km 551-586)

The simulated results were representative to the situation observed during the freeze-up as well as breakup operation. Mechanical breakup is proceeded in such way that icebreakers forming the ice free channel to release ice and water stored in the jams. Next the channel should be cleaned and widen to allow any additional ice to pass downstream without stoppage. Since the cross section near Słubice is significant river narrowing the ice could naturally accumulated there, which was confirmed by the numerical simulation. The model results shown that the process of ice accumulation will be very fast and if not released will lead to nearly 1,0 m jam. This ice formation if created downstream form operating icebreaker may be severe obstacle causing dangerous situation. To release ice jam with thickness up to 1 m and the range of about 3 km will require using icebreakers with significant horsepower. Since the horsepower of the icebreaker is related to its hull shape and draught, the river must have parameters allowing the large ship to operate safe. It leads to conclusion that to satisfy safety requirement on the Lower Odra, it modernization is needed. It could also be concluded to make use of those existing structures which are in a good condition to the extent possible.

4. Ice transport on the Middle Odra (Cigacice case, km 466-468)

The next simulation was proceed in the sharp river band on the Middle Odra where spur dikes on both river banks exists. The spurs as river training structures were built to enhance navigation and protect erodible banks but they origin form first river regulation (mid of the XIX century) and are in bad shape mostly. Existence of these structures affects intense vortex action which is set up at the streamward end of a spur dike. Intermittent vortices of lesser strength occur along both upstream and downstream face of the dike. This turbulence causes the bed material to be suspended causing scour hole that develops around the spur dike with extend determined by the

bed material's angle of response. Analyzing bed bathymetry extensive souring is visible on the concave bank of the bank and the river depth varies significantly along the thalweg.
Mathematical model was set up on the 2 km section of the river upstream of the gauging station Cigacice. For hydrodynamic boundary condition water discharge representing low flow condition was set up (Q = 84 m^3/s). In addition western wind with velocity of 10 m/s was simulated to study the effect of ice drifting towards the left, shallow bank of the river. Ice was supply at the model upstream with concentration of 0,3 and initial thickness of 0,2 m.
Simulation results showed that ice has tend to move close to nose of the spur dikes on the concave bank, where depths varies significantly (0,5 – 4,0 m) due to erosion and accumulation caused by the river training structures. In some locations ice settle on the river bottom causing anchored jam. Due to the western wind action, ice is pushed towards left bank, where is stopped on extensive shoals.
Icebreaking operation on The Middle Odra River must proceed continuously along both river banks. In case of ice stopped at the shallow part of the river its release may be impossible due to insufficient depth for the ships. In order to satisfy flood prevention during winter season Middle Odra must be regulated to satisfy required depth of about 2 m.

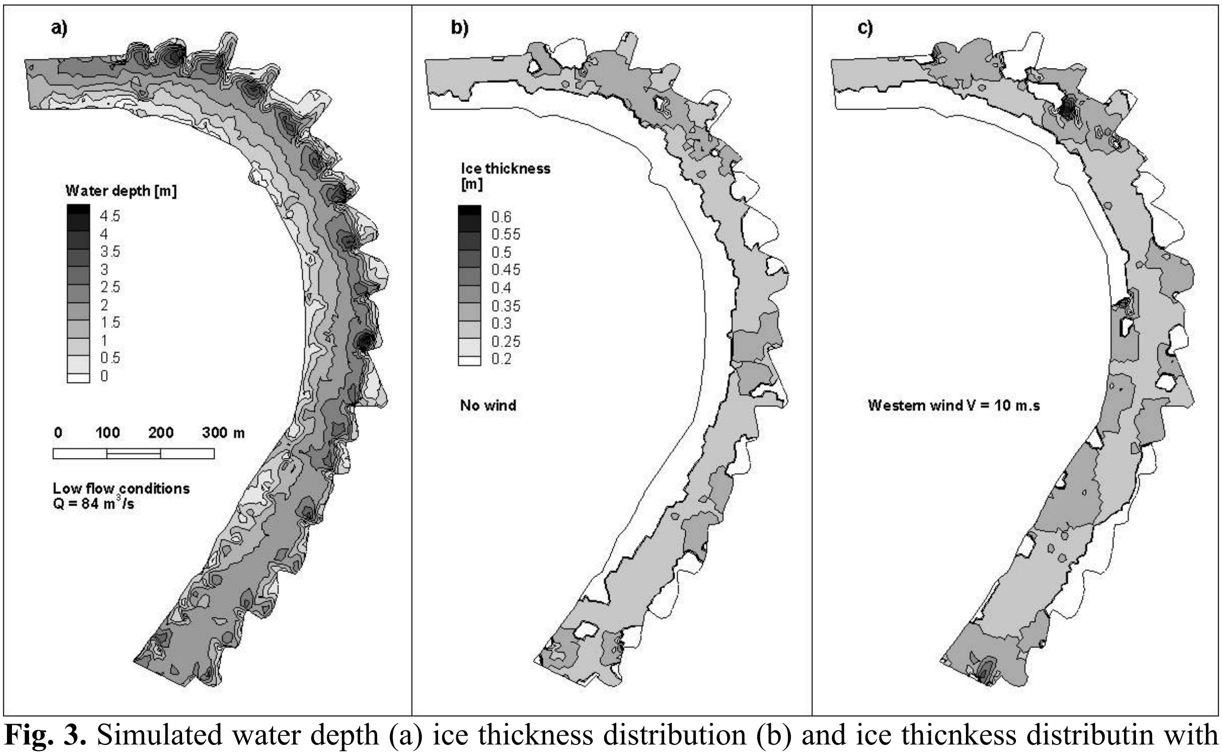

Fig. 3. Simulated water depth (a) ice thickness distribution (b) and ice thicnkess distributin with western wind (c) in the Middle Odra River near the Cigacice gauging station (km 466-468), for low flow conditions

Sumary

Concluding the practical experience of employees Water Resources Board in Szczecin (Kreft, 2011), and quantitative results of mathematical modeling presented above it must be said that icebreakers in the Odra River facing harsh ice conditions. It means that their power must be adequate and the design draught may not be less than 1,8 m. Opponents of river regulation claimed that similar to Danube or Elbe river vessels may be used in Odra, however on mentioned rivers ice jams occur occasionally and the thickness and range of historical jams were relatively small. It must be emphasized that ice conditions and parameters are side specific and cannot be directly transferred from other climatic zones to Polish rivers. It is important to study and describe qualitatively and quantitatively local ice condition on the Odra River. It could be done by implementation both, empirical and analytical approaches which must be well referred to historical observations. Based on results received from the ice research on the Odra River adequate technical solutions may be proposed. Results of above study confirmed the technical parameters of icebreakers to be used in the Odra River.

Acknowledgments
The study was supported by Sweco Consulting and was a part of the Odra-Vistula Flood Management Project – 8524 Pl, Sub-component 1A: Flood protection of areas in Zachodniopomorskie Voivodeship.

References

Sweco 2017. Odra-Vistula Flood Management Project; Environmental management plan for sub-component 1A : flood protection of areas in Zachodniopomorskie Voivodeship,

Project Coordination Unit, 2015, Project operations manual, Wrocław October, 2015

UNECE 2012, Map of European Inland Waterways, 5th ed.

Kreft, A., 2011, Icebreaking operation on Lower Odra River in winter season 2010/2011 Logistyka 6/2011 pp. 4837-4850 (in polish)

Kreft, A., Parzonka, W., 2007, Issues related to the modernization of river regulation structures on the border section of the Lower Odra river, Infrastructure and Ecology of Rural Areas 4/2, 2007, pp. 123–134 (in polish)

Kundzewicz, Z.W., Szamalek, K. and Kowalczak, P., 1999. The great flood of 1997 in Poland. Hydrological Sciences Journal, 44(6), pp.855-870.

Shen, H.T., 2010. Mathematical modeling of river ice processes. Cold Regions Science and Technology, 62(1), pp.3-13.

Kolerski, T. and Shen, H.T., 2015. Possible effects of the 1984 St. Clair River ice jam on bed changes. Canadian Journal of Civil Engineering, 42(9), pp.696-703.

Kolerski, T., 2014. Modeling of ice phenomena in the mouth of the Vistula River. Acta Geophysica, 62(4), pp.893-914.

International Association for Hydro-Environment Engineering and Research
Supported by Spain Water and IWHR, China

24th IAHR International Symposium on Ice
Vladivostok, Russia, June 4 to 9, 2018

Heavy Impact Test Site (HITS) Simulations

R. Gagnon[1], B. Quinton[2] and J. Mackay[3]
[1]OCRE/NRC; [2]MUN; [3]DRDC
[1, 2] St. John's, NL, Canada; [3]Halifax, NS, Canada
[1] Robert.Gagnon@nrc-cnrc.gc.ca; [2] f12bwq@mun.ca; [3] John.MacKay@drdc-rddc.gc.ca

OCRE/NRC is planning on establishing a new capability in its Large Ice Tank. The new facility, known as the Heavy Impact Test Site (HITS), will enable studies of a large massive object colliding with a massive hybrid ice-structure target, similar to ocean-going vessel collisions with ice masses. Numerical simulations utilizing coupled explicit ALE/FEA were used to estimate loads that could be achieved in the new facility. The simulations were also intended to assist with the design of the apparatus. When fabricated, the actual equipment will consist of a heavy-mass flooded structure that serves as a mock ship hull, to which actual grillage structures can be attached, and a large flooded hybrid ice-structure that serves as a substantial impacted 'ice mass'. Initially, three sets of striker-struck objects of differing sizes with approximate mass ratios of 1.00 (Large), 0.74 (Medium) and 0.55 (Small) were investigated for impact load generation capability. The simulations showed that the 'Small' impacting structure and impacted target objects could be used to generate sufficient impact loads to study collisions that involve grillage damage. This size is also the most feasible for practical handling purposes in the Ice Tank. Subsequently, two simulations were run using a naval vessel grillage, for an impact between stiffeners and an impact at a stiffener. The maximum plastic deflections of the plating were ~ 24 mm in the case where the impact occurred between stiffeners and ~ 11 mm when the ice impacted the plate in an area that had a stiffener behind it.

1. Introduction

Marine transportation in Arctic regions is seriously affected by the presence of glacial and sea ice masses. Of concern for ships (including naval vessels) are bergy bits and growlers (house-sized and car-sized glacial ice masses) and sea ice masses (either individual floes or smaller portions broken from floes). Detection of ice masses is sometimes difficult using marine radar in rough sea states. Should ice make contact with a ship's hull, the impact forces will depend on the masses of the vessel and ice, the hydrodynamics of the interaction, the ship structure, the shape of the ice mass and its local crushing properties. OCRE/NRC has been studying various aspects of the problem for several years, with the overall objective of creating a validated numerical model of ship/ice collisions using LS-Dyna™ software. The work has involved extensive physical model testing of a tanker transiting in proximity to bergy bits in NRC's Tow Tank (Gagnon, 2004a), impact experiments in NRC's Ice Tank using real growlers (Gagnon, 2004b) and strength and crushing experiments on iceberg ice and lab-grown ice (e.g. Gagnon, 2004c; Jones et al., 2003). A field study involving bergy bit impacts with an instrumented ship (Gagnon et al., 2008) was also conducted.

To facilitate a critical aspect of the simulations, i.e. validation, NRC is collaborating with DRDC to conduct ice impact testing of naval vessel hull structures in the NRC Ice Tank in St. John's, NL. This will involve using heavy-mass flooded structures for the ship hulls and large hybrid ice-structure masses to generate significant impact loads. OCRE/NRC successfully used this concept for the Growler Impact Tests conducted several years ago (Gagnon, 2004b). In the present case much larger masses would be involved (Figures 1 and 2). Apart from tests related to naval vessels there is a significant demand internationally for this type of facility because of so many planned activities for the Arctic (e.g. resource development, transportation, tourism, sovereignty issues, environmental monitoring). This new national NRC test facility will be known as HITS (Heavy Impact Test Site). The testing method will enable NRC to conduct heavy-mass high-load impact tests that do not require unrealistic high speeds and where hydrodynamic effects may be taken into account. Additionally, the apparatus will utilize NRC's pressure-sensing panel (Gagnon et al., 2009) so that representative pressure distribution patterns can be determined for the ice impacts that would be valid at least up until the point where the grillage starts to deform plastically.

The first planned use of HITS would be for DRDC. The purpose of that work will be to study the degree of damage that results when naval vessel grillage sections are subjected to ice impacts in conditions similar to the actual Arctic marine environment, including hydrodynamic effects. Parameters such as impact speed, impact angle and possibly hybrid ice object size will be varied. Here we report numerical simulations that were used to estimate loads, and grillage damage, that could be achieved in the new facility and that assist with the design of the HITS apparatus.

2. Assumptions and Design Constraints

All HITS experiments will be conducted in the OCRE/NRC Ice Tank, which is 12 m wide, 76 m long, and 3 m deep. The Ice Tank carriage has a maximum speed of 4.0 m/s, and can support attached experimental apparatus up to 12 m in length, 4 m in width, and up to 12 tonnes. The proposed HITS apparatus (Figures 1 and 2) will consist of two separate structures: a 'struck' object consisting of a large suitably-shaped and confined ice feature attached to a substructure of substantial mass; and a 'striking' object that is suspended from – and actuated by – the Ice Tank carriage, consisting of a ship's grillage structure and, potentially, the OCRE/NRC pressure sensing panel, supported by a substructure of substantial mass having an elongated shape. The impacted ice feature will be a 1 m diameter ice hemisphere.

3. Simulation Components and Setup

In order to ascertain the effect of the size and shape of the striking and struck objects on the overall possible impact force, three sets of striking and struck objects were created (Figure 3). The dimensions and masses of each of the objects are given, by 'set', in Table 1.

Table 1. Dimensions and masses for the three sets of structures shown in Figure 3.

Striking/Struck Combination	Striking Object Length [m] **	Striking Object Mass [tonne]*	Struck Object Width [m] *	Struck Object Mass [tonne]
Large	12	144	4	61.3
Medium	8.92	103.8	3	33.9
Small	6.64	73.8	2.2	18.8

* Note: This mass assumes that the entire volume of the structure is filled with water of density 1 tonne/m^3. Thus, only the structural steel-weight is exerting force on the Ice Tank bottom (struck object) or the Ice Tank Carriage (striking object), not the water-weight.

** Note: The striking object's shape is changing with the changing length, because its width and height must remain constant to accommodate the attached grillage.

'Dry' impact scenarios (as described below) involving a deformable ice hemisphere attached to the struck object, and a rigid impact plate attached to the striking object were performed, for an impact velocity of 1.5 m/s. The impact force time histories for each set are shown in Figure 4. Based on these results, and due to its more practically manageable size, it was decided that the 'Small' impact set provided an optimized solution for the HITS striking and struck objects, as the maximum 'dry' impact event was sufficient to deform a typical naval class grillage.

3.1. Estimated Grillage Dimensions

For the actual HITS apparatus the struck object must support a ship's grillage, so it is necessary that the structure supporting the grillage be considered. DRDC has indicated that the deformable grillage structure to be mounted on the HITS apparatus will likely have overall dimensions of approximately 1.8 m by 1.25 m. Based on previous experience with similar grillage impact problems, it was determined that the mass of the grillage, plus the structure providing the grillage's boundary conditions and securing the grillage to the HITS 'striking' apparatus, will be approximately 3 tonnes and require an area of approximately 2.8 m in width and 2.0 m in height.

Two configurations for the grillage structures were used in the simulations (Figure 5): 1. a 'plating impact' grillage, and 2. a 'stiffener impact' grillage. The 'plating impact' grillage sustains the impact primarily on the unsupported plate between two longitudinal stiffeners. The 'stiffener impact' grillage sustains the impact primarily at the location of the central longitudinal stiffener. Figure 6 shows a grillage mounted on the striking object.

3.2. Struck Object Ice Knob

The 'struck' object is shown in Figure 7. The hemispherical ice mass (a.k.a. the 'ice knob') is attached at the center of one of the structure's faces. A validated 'crushable foam' material model (Gagnon and Derradji-Aouat, 2006) was used to characterize the ice knob. To do this, LS-

Dyna's material model MAT_63 was used with the following inputs: Density = 870 kg/m^3, Young's Modulus = 9 GPa, Poisson's Ratio = 0.003, Tensile Stress Cutoff = 800 MPa, and the Yield Strength versus Volumetric Strain curve the same as that used by Gagnon and Derradji-Aouat (2006).

4. Meshing Considerations and 'Wet' Simulation Strategy

Following the methods of Gagnon and Wang (2012), the main large objects that do not interact with anything other than water and air, i.e. the striking object and the struck object, are given a large but adequately refined, mesh size that matches the mesh size of the water and air domains since they have to interact. Note that a mesh convergence study was conducted to in order to identify the adequate mesh size. On the other hand, the ice knob, deformable grillage and rigid impact plate must be finely meshed, since their interaction volume is much smaller, in order to capture the appropriate behaviors during the impacts. These relatively small and finely meshed objects do not have to interact with the water and air because the main hydrodynamic effects are captured by the interactions of the large striking and struck objects with the water and air. Furthermore, the deformable properties of the ice knob and grillage do not have to be active until they come into contact with one another, that is, they can be treated as rigid objects until the impacts occur. This is computationally very efficient, and LS-Dyna provides the user with the convenient option to run a simulation and control the properties of objects by setting precise times when their deformable properties become active during a simulation. The full air and water domains encompassing the striking and struck objects for a typical HITS simulation are shown in Figure 8.

With these aspects in mind the wet simulations involving the grillage were conducted by letting the striking object accelerate to the target speed of 1.5 m/s and then move through an adequate length of the water/air domain to create a realistic bow wave before actually making contact with the ice knob on the struck object. During this time the ice knob and the grillage were assigned rigid properties. Then, just before contact, the deformable properties of the ice knob and the grillage were switched on. This strategy ensured that the hydrodynamics of the interaction were adequately accounted for and that run times were only as long as necessary (roughly 25-35 hours using 28 CPU's on a HP Z820 Workstation).

5. Some 'Wet Case' Simulation Results

Figure 9 shows the force time series for three 'wet case' impact scenarios: Case 1. A 'rigid impact plate' (red), where a secondary impact is evident; Case 2. A 'plate impact' deformable grillage (green); Case 3. A 'stiffener impact' deformable grillage (blue). Figure 10 shows the Case 3 grillage impact where contours of stress are presented along with evident indentation of the plate, and bending/buckling of the stiffener and flange. Figures 11 shows the maximum deformable plate deflection for the Case 2 and Case 3 impact scenarios where the latter exhibits the lesser amount of deflection, as anticipated.

Figure 12 shows an image sequence from a 'wet case' simulation illustrating the complex and realistic waves generated as the striking object traverses a distance along the length of the water volume (i.e. the Ice Tank) on its way to impacting the ice knob (not visible) that is attached to the struck object. As expected, some bow wave induced surge and sway of the struck object occurred prior to the impact (data not shown here).

6. Conclusions

(a) Numerical simulations have shown that at a moderate striking object speed of 1.5 m/s the proposed small and manageable HITS apparatus is capable of generating the peak ice-impact loads shown in the Table 2 below for hits on rigid and deformable structures. Energy dissipation, due to permanent deformation of the grillage and ice, is included for two cases. **(b)** Mesh density was investigated for numerical convergence. Using three differing mesh sizes it was determined that the second and highest mesh densities produced very similar results. This confirmed that the second, and less computationally expensive, mesh density was appropriate to use. **(c)** The maximum plastic deflections of the naval grillage plating was ~ 24 mm in the case where the impact occurred between stiffeners and ~ 11 mm when the ice impacted the plate in an area that had a stiffener behind it.

Table 2. Maximum impact force, impact duration and energy dissipation for three simulations.

Striking Object Type	Maximum Impact Force (MN)	Impact Duration (s)	Energy Dissipation (kJ) Grillage ; Ice
Rigid Structure *Flat Surface* (no damage)	0.92	0.07	-------
Deformable Naval Grillage (plating impact with damage)	0.26	0.26	2.4 ; 1.6
Deformable Naval Grillage (stiffener impact with damage)	0.28	0.21	2.5 ; 1.6

7. Acknowledgements

The authors are grateful to NRC and DRDC for their support of this work.

8. References

Gagnon, R., 2004a. Physical Model Experiments to Assess the Hydrodynamic Interaction Between Floating Glacial Ice Masses and a Transiting Tanker. Journal of OMAE, Volume 126, Issue 4, pp. 297-309.

Gagnon, R., 2004b. Analysis of Laboratory Growler Impact Tests. Cold Regions Science and Technology, 39, 1-17.

Gagnon, R., 2004c. Side-Viewing High-Speed Video Observations of Ice Crushing. Proceedings of IAHR, St. Petersburg, Russia, Vol. 2, p. 289-298.

Gagnon, R.E. and Derradji-Aouat, A., 2006. First Results of Numerical Simulations of Bergy Bit Collisions with the CCGS Terry Fox Icebreaker. Proceedings of IAHR, Sapporo, Japan, Vol. 2, 9-16.

Gagnon, R., Cumming, D., Ritch, A., Browne, R., Johnston, M. Frederking, R., McKenna, R. and Ralph, F., 2008. Overview accompaniment for papers on bergy bit impact trials. Cold Regions Science and Technology, 52, 1–6.

Gagnon, R.E., Bugden, A., and Ritch, R., 2009. Preliminary Testing of a New Ice Impact Panel. Proceedings of POAC, Lulea, Sweden. Paper No. 33.

Gagnon, R.E. and Wang, J., 2012. Numerical Simulations of a Tanker Collision with a Bergy Bit Incorporating Hydrodynamics, a Validated Ice Model and Damage to the Vessel. Cold Regions Science and Technology 81, 26-35.

Jones, S.J., Gagnon, R.E., Derradji, A., and Bugden, A., 2003. Compressive Strength of Iceberg Ice. Canadian Journal of Physics, Vol. 81, No. 1 / 2, 191-200.

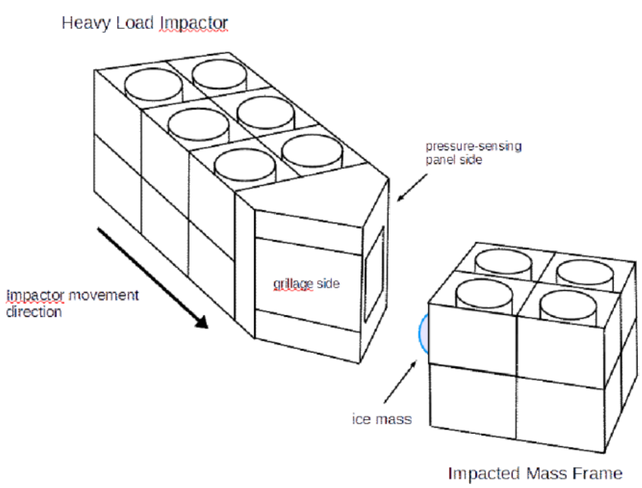

Fig. 1. Perspective-view configuration for heavy impact tests in the Ice Tank (pressure-sensing panel hits).

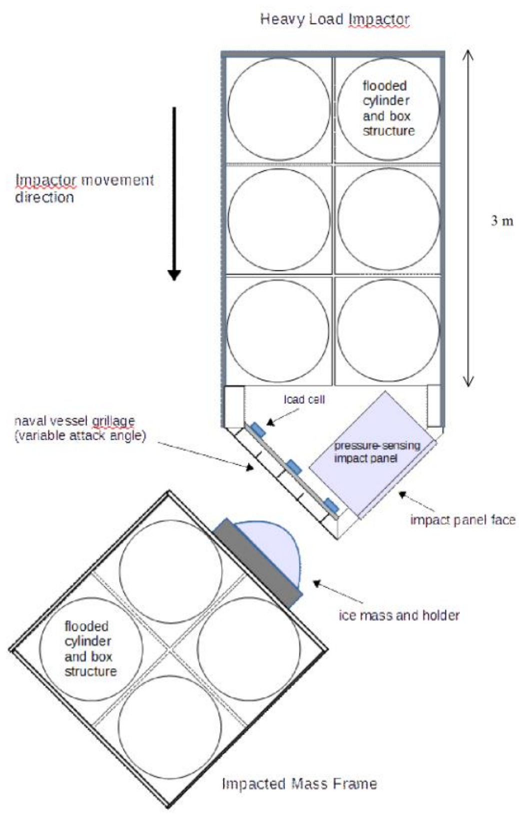

Fig. 2. Top-view configuration for heavy impact tests in the Ice Tank (grillage hits).

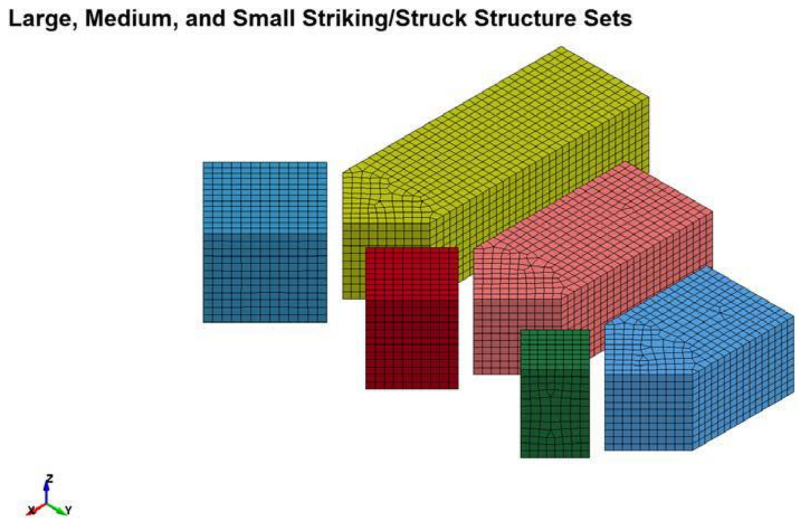

Fig. 3. ‘Large’ (top), ‘Medium’ (middle), and ‘Small’ (bottom) striking/struck object sets.

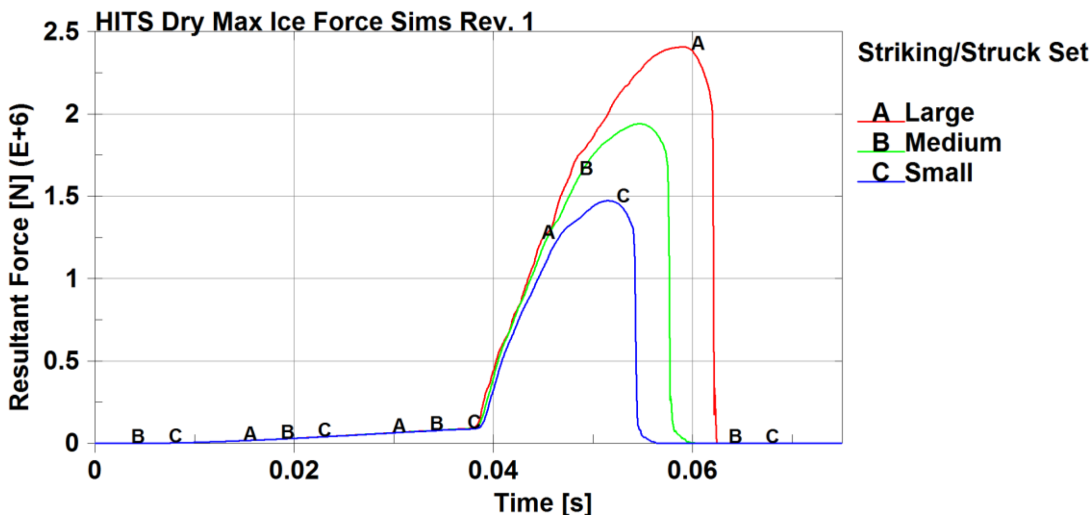

Fig. 4. Resultant ‘dry’ impact force for striking/struck sets.

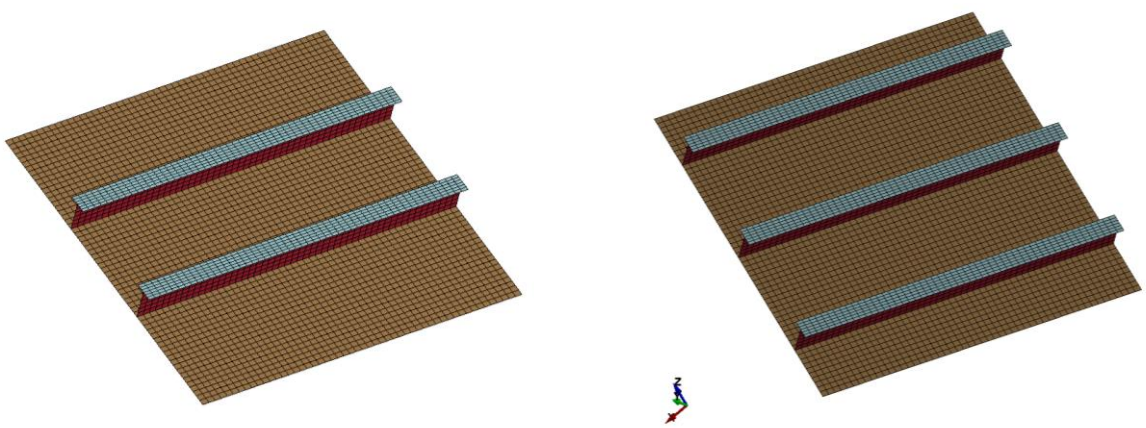

Fig. 5. Deformable ‘plate impact’ grillage mesh (left) and ‘stiffener impact’ grillage mesh (right), showing hull plating (brown), longitudinal stiffener webs (red), and longitudinal stiffener flanges (light blue).

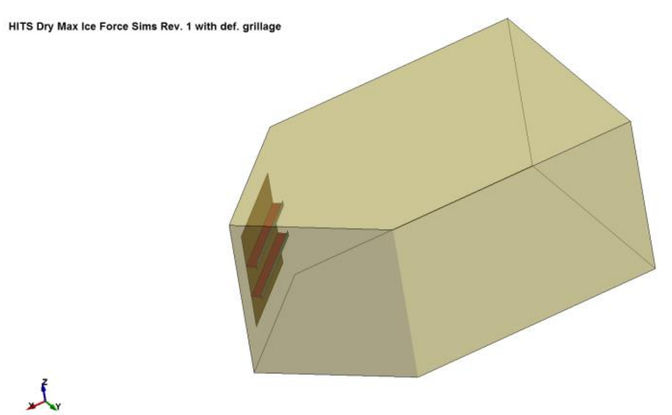

Fig. 6. ‘Plate impact’ deformable grillage shown attached to the rigid HITS striking object (transparent). The plating of the deformable grillage is coincident with the vertical portion of the striking object’s starboard ‘bow’.

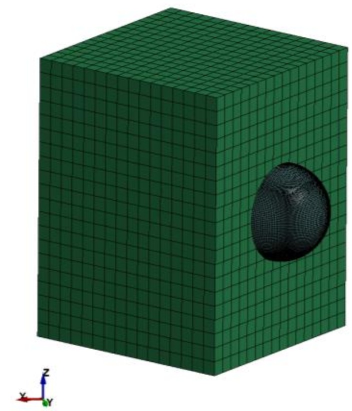

Fig. 7. The ‘struck’ object with the hemispherical ice knob attached at the center of one face.

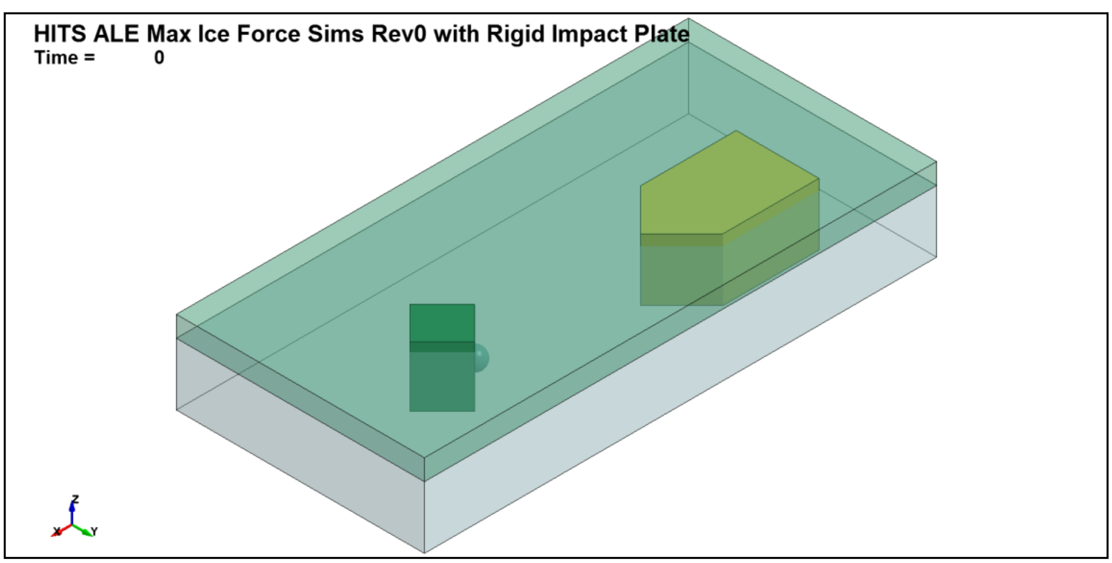

Fig. 8. ‘Wet’ HITS simulation components; air (transparent green), water (transparent blue), HITS struck object (solid green), ice hemisphere (solid blue), HITS striking object (solid yellow), rigid impact plate/deformable grillage (not visible).

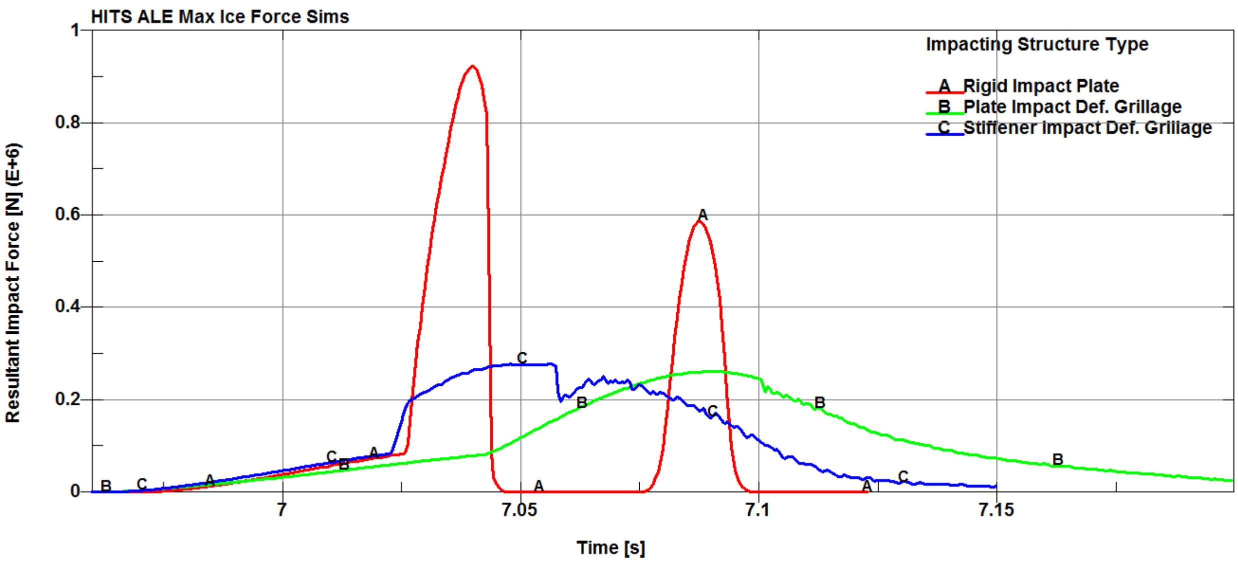

Fig. 9. Resultant force-time histories for the 'rigid impact plate' (red), the 'plate impact' deformable grillage (green), and the 'stiffener impact' deformable grillage (blue). The dip in the blue load record, at approximate time 7.06 s, is associated with buckling of the stiffener.

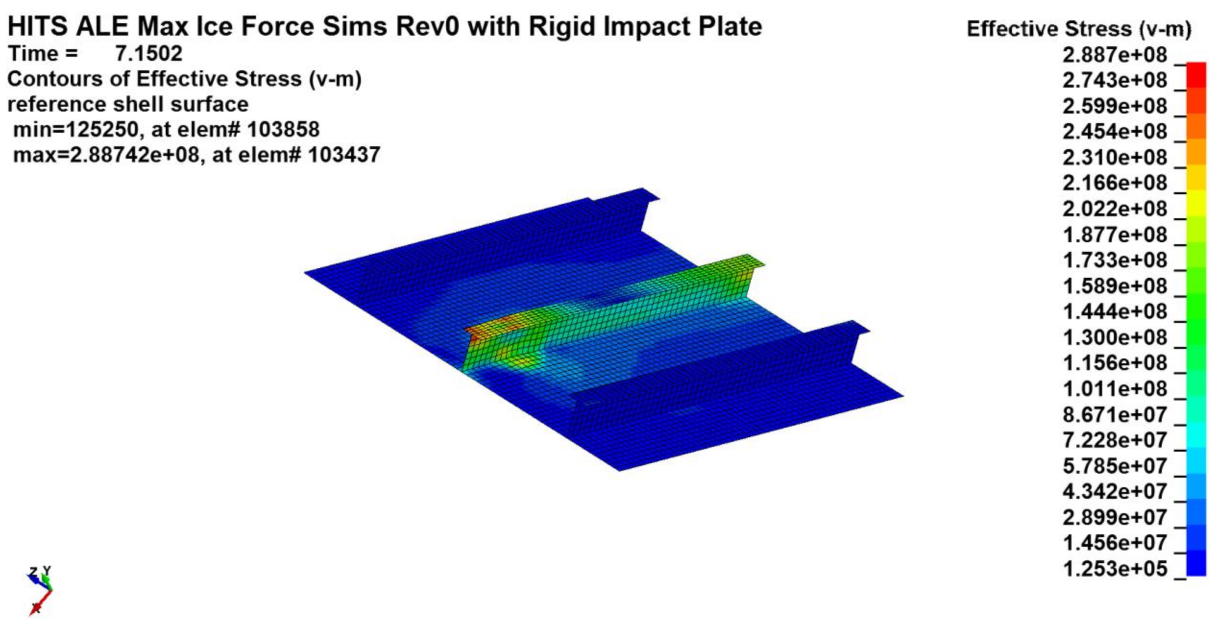

Fig. 10. Residual von Mises stress for the 'Wet' ALE 'stiffener impact' grillage case. Indentation of the plate, and bending/buckling of the stiffener and flange are evident.

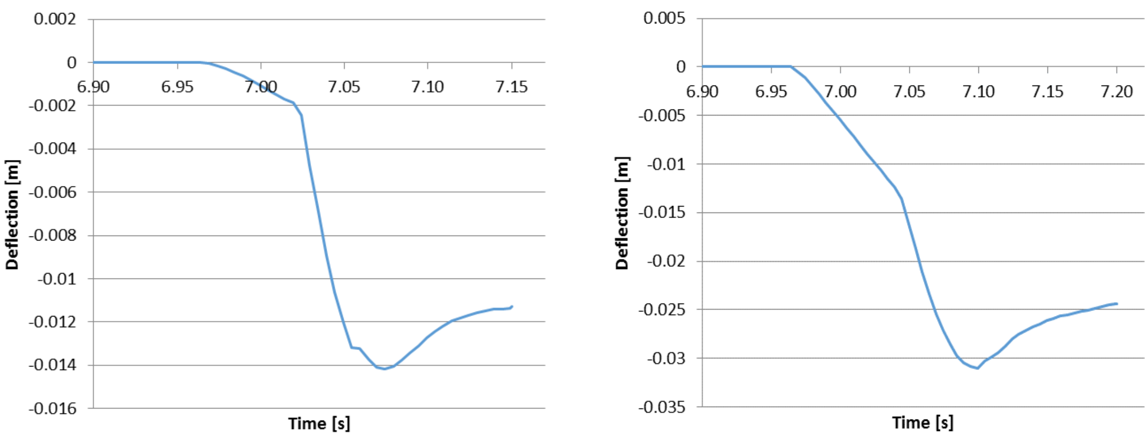

Fig. 11. Maximum deflection time histories for ‘wet case’ ice impacts on a deformable grillage plate at the location of a stiffener (left) and between stiffeners (right).

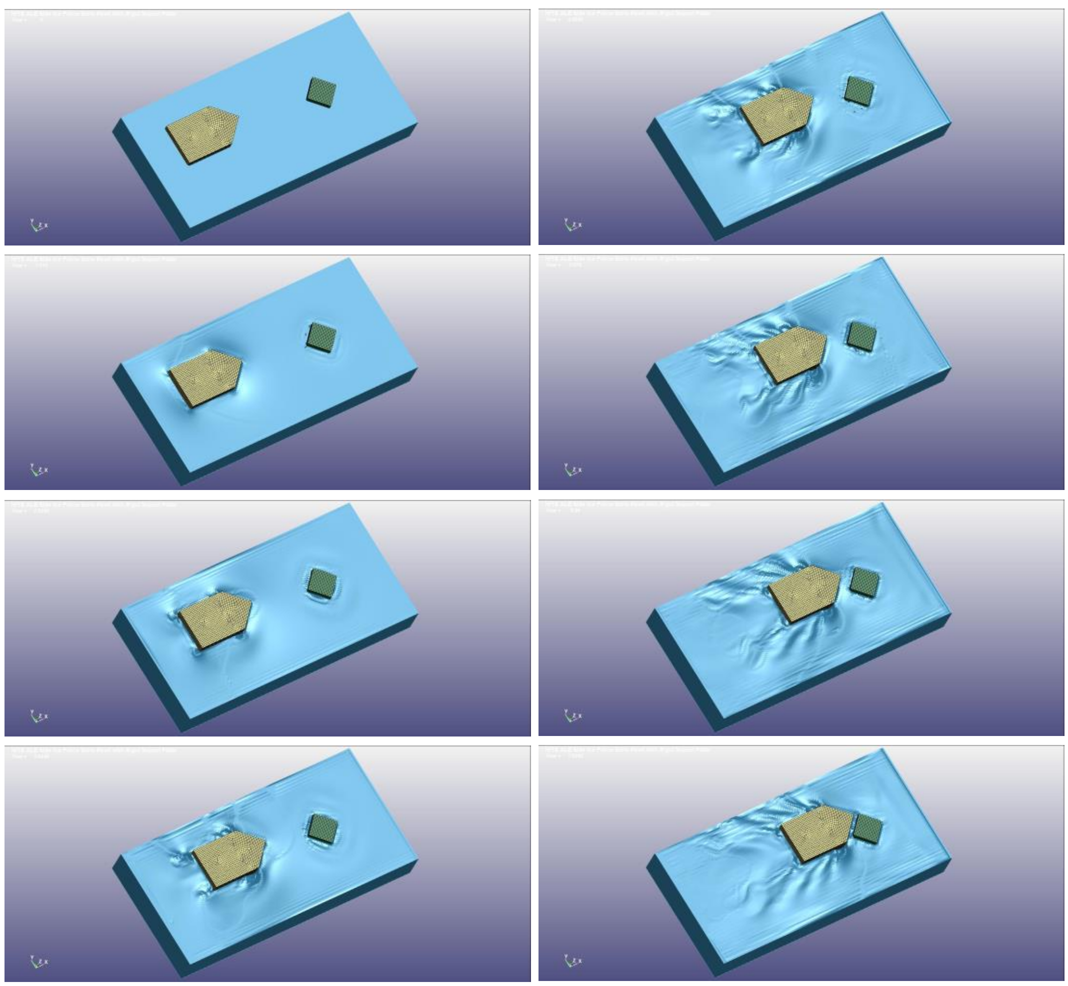

Fig. 12. Image sequence from top left to bottom right corresponding to the simulations in Figures 11 illustrating the realistic waves generated as the striking object (yellow) traverses a distance along the length of the ‘Ice Tank’, eventually impacting the ice knob (not visible) that is attached to the struck object (green). The bow wave of the striking object causes some surge and sway of the struck object prior to the impact.

24th IAHR International Symposium on Ice
Vladivostok, Russia, June 4 to 9, 2018

Constituents of Ice Navigation Systems from Ship Based Observations during Ice Transit of Kara Sea

Robert Bridges [1], Kaj Riska [1,2*], Philipp Griewank [4,3*], Philippe Lattes [1], Pierre Rampal [4], and Sylvain Bouillon [4,5*]

[1] *Total S.A., DSO/TEC/GEO, Courbevoie, France*
robert.bridges@total.com, philippe.lattes@total.com
[2] *Delft University of Technology, Netherlands*
k.a.riska@tudelft.nl
[3] *University of Cologne, Germany*
philipp.griewank@uni-koeln.de
[4] *Nansen Environmental and Remote Sensing Center, Bergen, Norway*
pierre.rampal@nersc.no
[5] *NUMECA International, Brussels, Belgium*
sylvain.bouillon@numeca.be
** Affiliation author is now working*

Operational feedback and in-situ data are required to develop reliable, safe and economic designs of ships and offshore structures. The data is also a prerequisite to determine marine operation feasibility, and to study uncertainty and variability in ice modelling and engineering. This paper outlines a ship transit of the Kara Sea and details the data and observations attained during the voyage. We gain insight into the ship's ice capabilities with and without icebreaker escort by comparing observed ice conditions and ship performance against ship speed and position. The paper also presents a shipboard ice observation method which is intended to reduce biases that arise from ships avoiding thick ice in favour of leads. Our observations highlight the need for a detailed and accurate ice navigation system to enable safe and efficient navigation. It is important that this ice navigation system takes the ship performance into account when determining possible strategic and tactical routes.

1. Introduction

An understanding of the sea ice environment is required for any voyage to be undertaken safely and efficiently, and especially for Arctic navigation in ice. Thus, prior to departing, and also during the voyages, navigational personnel must be aware of the present and forecasted ice conditions. Of equal importance is knowledge of the performance and capability of the vessel in ice. This is to be able to navigate a safe yet economical course, when the straightest and most economical course may lead to long voyage times due to transit difficulties in severe ice conditions for the ship's capability or even jeopardise the safety, whilst conversely navigation avoiding ice can increases the route length and journey time. Thus an understanding of both the ice conditions and the ship capability to transit the ice is required to determine the optimal deviations to be made in any given route under different range of ice conditions. In this paper, we use a transit voyage to obtain observational ice conditions data which can be used for the verification and validation of sea ice forecast models and associated experience of the ship performance that can be used to aid the ship navigation planning.

The International Code for Ships Operating in Polar Waters (Polar Code), adopted by the International Maritime Organisation (IMO 2015) and in force January 2017, requires a voyage planning tool to be approved by the Maritime Administration, which includes information of ice conditions along the intended route and historical ice data, as well as temperature data, places of refuge, information on marine mammals, and Search and Rescue (SAR). A methodology to assess operational capabilities and limitations in ice has been developed for the Polar Code, POLARIS, which relates the vessel ice class and ice conditions. Observational data from voyages form a feedback into development of such activities, as well as the various ice forecast models available and also under development. Forecasts are often made just prior to the voyage and complimentary to these charts are the satellite images, although noting the difference in time intervals and scales/accuracy. In actuality, different sources of information are used to improve accuracy and reliability of sea ice information, so it is important to obtain operational data to improve the reliability and accuracy.

While the climate community has increasingly studied the predictability of sea ice extent on a seasonal to annual time scale, e.g. Tietsche (2013) and Chevallier (2013), there is a strong tradition of operational ocean prediction systems that also include the Arctic, e.g. Tonani (2015). Recently there has been a push to develop higher resolved sea ice forecasts intended to help users operate inside the ice pack, while previously forecasts focused solely on predicting the location of the ice edge. Moving to higher resolution poses a host of challenges for the modelling community as the established sea ice models were designed for climate models and are poorly suited for the resolutions now desired for operational forecasting. As a result, various approaches are being tested to develop new models as well as the assimilation and evaluation methods required such as Wang (2016) and Shlyaeva (2016).

One of the ongoing efforts to produce a next generation sea-ice model capable of operating at all scales is the neXtSIM model under development at the Nansen Center in Bergen. neXtSIM is truly unique in that it uses a Lagrangian grid and employs a Elasto-Brittle rheology, Bouillon (2015) and Rampal (2016). The forecasting platform named neXtSIM-F has been constructed around the neXtSIM model. neXtSIM-F has been producing daily forecasts for the Barents and Kara Seas since October 2015. At the time of the voyage described in this paper neXtSIM-F was not yet operational, but the voyage was used to test a developmental version lacking thermodynamics and data assimilation. Example is shown in Figure 1.

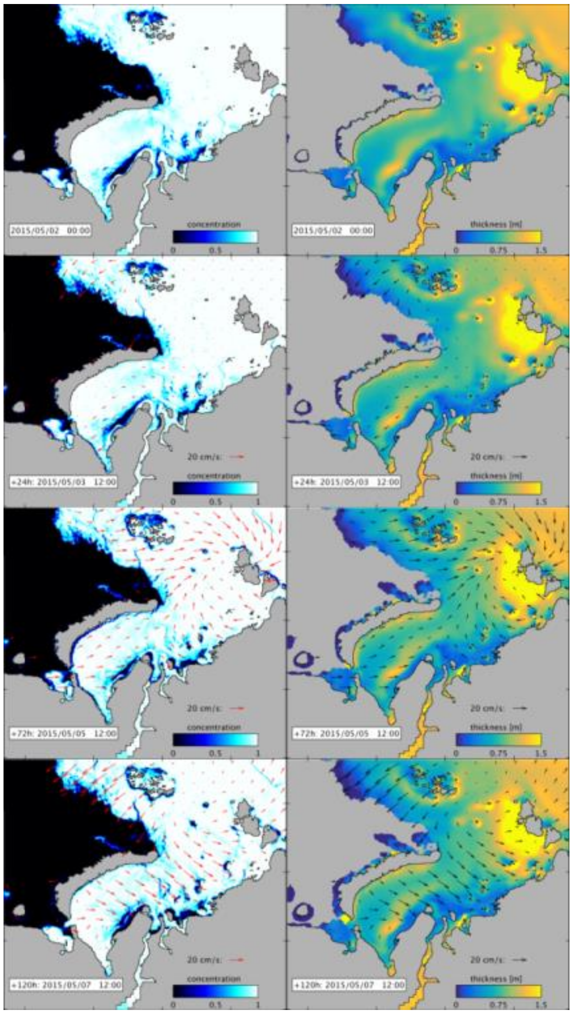

Figure 1. Example forecast with concentration (left) and ice thickness (right), NERSC.

Voyages in sea ice are frequently supported with various levels of ice information, generally six categories of information may be provided, with each varying with time scale and geographic scope, as noted by AIRSS (Transport Canada 1998). In an operational context of a specific voyage, and specifically for a Kara Sea voyage, the ice information is quite varied, as illustrated in Table 1. Here we neglect the long range forecast and climatological models, noting these would also require quite different specific information, such as atmospheric data, snow cover, or those related to melt stage, etc. This also does not differentiate between ship types or arrangements, for example those with longer parallel midbody may be more susceptible to besetment and conditions that create this would therefore be of greater significance, such as ice drift and wind.

To support ice information forecasts, monitoring, research, and development of ice charts, ship based observation data is often used. A range of observation techniques exist and have been utilised onboard ships, such as digital video and camera images, electromagnetic sounding (EM), satellite images as well as visual observations. In this paper we focus on the latter; visual observations.

A feature of visual observations, which can be challenging for the other techniques, is that visual observations can provide information about sea ice morphology that is not readily obtainable, such as ice deformation and brash ice conditions. It is however recognised that visual observations are often associated with a lower degree of accuracy, compared to more exact scientific methods, inherent from the observer dependent bias. However Suominen et al. (2016) noted similar results (of ice thickness) could be obtained with those from an EM device, although indicated a higher ice thickness than those from stereo camera measurements. This was expected from the floes breaking into pieces before arriving to the vicinity of the cameras. Thus, we can consider that visual ice observations provide a useful technique for ice characterisation.

Different methods of ice observations exist, such as MANICE (Environment Canada 2005). An early approach to categorise and standardise visual sea ice observations was Antarctic Sea ice Processes and Climate (ASPeCt), as developed by Worby and Alison (1999), which as the names suggests, was designed for Antarctic sea ice. An alternative approach is Arctic Ship-borne Sea Ice Standardisation Tool (ASSIST) which also includes guidance on estimating the properties of the sea ice. A programme for the collection and archive of visual observations of sea ice in the northern hemisphere conducted from ships using this method has been developed, IceWatch, and is outlined by Hutchings (2016).

Table 1. Example of ice condition information for strategic and tactical navigation.

Operational context		Information and data description	Level of resolution	Level of periodicity
Strategic	Short Term / Medium Range Planning for voyages	Forecasts for a period, issued weekly/monthly, and coverage on a regional chart of larger scale. The charts contain general descriptions of ice, e.g. types and concentrations	Low	Low
	Route selection; Kara Gate or North of Novaya Zemlya	Local detail ice conditions of Kara Sea region, especially ice ridging in Kara Gate		
	'Large' route deviations	Areas and regions to avoid based on ice (thickness) and identification of regions of open water		
Tactical	'Medium' deviations	Navigation route selection, e.g. based on satellite images for floe avoidance and regions of ice drift / compression		
	'Small' deviations	Local navigation using high resolution satellite and ice radar images. Also data at Port in near real time	High	High

2. Kara Sea Voyage

During May 2015 a voyage was made to supply a variety of material to the Sabetta Port construction. Authors, Robert Bridges (Ice Engineer with Total) and Philipp Griewank (working on the neXtSIM-F forecast platform), were given the opportunity to attend the ship to conduct ice observations. On the vessel they had no influence on the travel planning nor execution. The Kara Sea voyage provided an opportunity to validate ice navigation systems and the also gain understanding of the experience on the ship performance in ice as vessel navigation in the Kara Sea during the winter which requires efficient and safe navigation due to the presence of ice covered waters. The following summaries some of the activities that were observed following participation in the voyage:

- Acquisition of ice and metocean data to validate and verify ice forecast model. Validation includes correlation with ice conditions data, and verification with the ship crew on the reliability and usefulness of the forecasts. Also some recordings of metrological conditions were made, such as the general weather conditions, etc.
- Acquire logistics and navigation transit information for sea ice navigation models, and experience of ice navigation procedures, such as the ship operations that are employed by merchant ships whilst in ice, as well as the icebreaker escort operations.
- Capability and performance of ice strengthened ship. The ice performance of the vessel was recorded for various speeds in ice conditions and specific manoeuvres in relation to the ice-interactions.
- Observations of ice conditions in port and during port operations, such as berthing and with icebreakers, in brash ice channel and at berths.
- Cargo and crew operations particular to operations/equipment whilst in low temperatures. Review of the systems installed on the ship and operations in low temperatures, e.g. level of winterisation.

This paper summarises some observations, activities and results of data gained during a transit voyage of the Kara Sea to illustrate some of the salient points involved in ice navigation systems and the performance of ships in ice. This paper is composed of a general overview of the voyage purposes and goals, followed by a description of which observations were made with which methods. We then examine the ship voyage and the vessel ice capability, including POLARIS applied with our observations. Lastly, we compare the ship deviations to the observed ice conditions before summarising our results in our conclusions.

3. Voyage Route

The voyage took place May 2015 onboard a merchant cargo bulk carrier. The vessel particulars are:

Length	180 m
Breadth	23 m
Draught	9.91 m
Ice class	Arc4
Power	8238 kw

A summary of the voyage activity and route is shown in Figure 2. The weather was variable during the voyage, from sunny, raining, snowing, cloudy, and with fog. The journey was made with ‘constant’ light, i.e. at 00:00 it was still light, which allowed continuous visual observations. The temperature ranged from five to ten degrees in Arkhangelsk, seven to one in the White Sea, three to minus one in Barents, and one to minus three to in the Kara Sea.

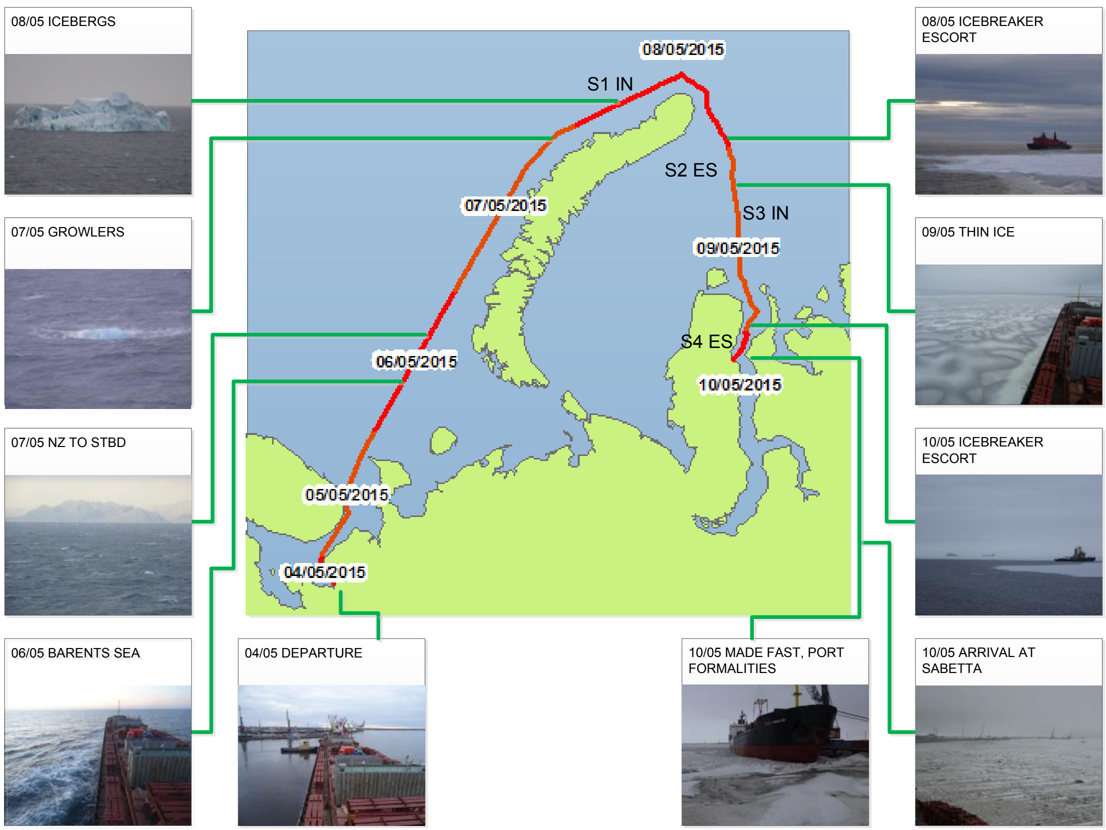

Figure 2. The ship route as measured by GPS from Arkhangelsk to Sabetta with photos illustrating ice and operating conditions. The orange and red colors represent one day’s journey and approximate regions of different operations indicated by four route segments.

In general, voyages in the Kara Sea have the potential to encounter sea ice from October to July. Late season voyages (October/December) will generally encounter recently formed ice, and large areas may become ice covered very quickly. Floes of ice will start coagulating and growing thicker, and by winter (January/April) first-year ice that may be very strong can be encountered. Early season voyages (May/July), and as is the case for the voyage, encounter sea ice that is beginning to deteriorate, but some can be near its maximum winter strength.

4. Observation Methods during the Voyage

During the voyage a series of observations were made visually, by camera, and GPS tracker, as well as those of the systems installed on the ship, such as thermometer and echo sounder. The observations are composed of the following aspects:

- Ice observations
- Metocean observations
- Ship observations

Ice observations were made to categorise the ice conditions into the following, and illustrative photos are shown in Appendix A to show some of the various ice conditions for navigation.

- Ice type and topography
- Concentration
- Floe size distribution divided into four; small, medium, large and vast, and with the proportion (%) of each size and ice thickness (*h*) recorded

Ice observations were made visually and by camera from the bridge, with estimation assisted by fixed measurement markings on the ship, for example, to correlate ice thickness of upturned ice or size of floes passing alongside. An extract of the ice observation recording is shown in Table 2. In this case we make three main approaches which are different compared to the methods of ice observations methods noted above i.e. ASPeCt, ASSIST, AIRSS, and MANICE. The first is in the distribution of ice. Typically three distinctions are made, Primary Secondary Tertiary, but here the four floes sizes distributions were categorised and then these allocated a percentage. The categories are broadly based on the World Meteorological Organisation nomenclature (WMO, 2014) for describing sea ice characteristics, however ice thickness is specific, rather than in large bands, as is now commonly adopted in sea ice models. The second difference was recording on a continuous basis, with observations noted when entering or exiting a different 'ice regime', rather than the periodic (over an hourly, half hour or ten minutes basis) used in other approaches. The last difference is the observations were based on all the ice visible. The intention being to capture the overall ice distribution, rather than that solely in contact with the ship being similar to that of ASSIST whereby the ice is viewed within 1 nautical mile, and as being an indicator of the ice conditions, and as an indicator if a so called 'ice regime' exists. This method of ice observations intends to reduce bias in the ship navigation whereby the ship will typically navigate around the worst ice and make use of leads or opening in the ice. This is often the case for previous ice observations being used for the purpose of investigating the local ice actions to the ship and thus the contact ice properties recorded. However, this information is necessary for characterisation often used in sea ice forecast models.

During escort operations, the channel width and performance of the icebreaker with additional breaking ice depending on the ice thickness, whilst the ice piece size variation was investigated by further analysis made from the photographs. Limited observations were made of ice ridges, predominantly of very small deformation ice rather than could be attributed to being fully formed ice ridges, and thus the ridge height and density were not included to high degree of observation. Likewise, limited observations of compression in the ice were observed. However, both these aspects play an important role in the ship performance in ice.

It is noted that during the voyage the vessel encountered other oncoming ships which had passed along the route to be navigated. The feedback from these vessels, giving warning of icebergs and descriptions of the ice conditions ahead was useful, and means of incorporating this into the ice navigation system should be made.

The general observations were made on the metocean conditions included the weather, wind, wave, temperature and snow/precipitation. Ship observations included the position, speed/distance, power, water depth and distance to icebreaker.

Table 2. Extract of ice observation recording showing total concentration, and composition of ice by concentration (%) and thickness (m) for different floe sizes.

				COMPOSITION							
			TOTAL	FLOE SIZE 1000m+		FLOE SIZE 500-50m		FLOE SIZE 50-5m		FLOE SIZE 5m-	
DATE	TIME	DESCRIPTION, ICE TYPE, COMMENTS	CONCET RATION	%	h	%	h	%	h	%	h
09/05/2015	11:00	LEVEL ICE	100	100	20						
09/05/2015	11:15	LEVEL ICE	95	80	20	20	20				
09/05/2015	11:08	LEVEL ICE	90	70	20	20	20			10	20
09/05/2015	11:14	LEVEL ICE	95	70	20			20	20	10	20
09/05/2015	11:50	LEVEL ICE	95							100	20
09/05/2015	11:59	LEVEL ICE	100	100	15						
09/05/2015	12:08	LEVEL ICE	40	100	15						
09/05/2015	12:14	LEVEL ICE	95	40	15	40	15	10	15	10	15
09/05/2015	12:25	LEVEL ICE	95	90	15			5	15	5	15
09/05/2015	12:30		95			50	20	25	20	25	20
09/05/2015	12:40		90			50	30	50	30		
09/05/2015	12:46		60							100	20
09/05/2015	12:58		90							100	20

5. Analysis of Ice Observation Data

The ice observations made during the voyage may be broadly categorised into four segments, a segment with icebergs and glacial ice, thick ice (with icebreaker escort), thin level ice, and finally the land-fast ice into port (under close tow by icebreaker).

The distribution of ice concentration, thickness and floe size is shown in Figures 3 to 5 for the different navigation modes and divided into four segments:

S1 IN — Segment is independent navigation from the first ice observation to the point of the icebreaker escort

S2 ES — Segment is the southward section with icebreaker escort

S3 IN — Segment is the continuation of the southward section as independent navigation from the point that the icebreaker left to the edge of the landfast ice

S4 ES — This is the final segment in landfast ice escorted by icebreaker

It can clearly be seen that the segment S1 is composed of icebergs and of low concentration, with the majority of small floe size, and high thickness ice. The segment S4 is completely in landfast ice and is simply the opposite of this, with high concentration (and floe size), but also with high thickness. The S2 and S3 segments with escort and independent navigation is composed of a variation of concentrations, with the escort segment tending towards greater concentrations and independent navigation lower concentrations. The floe distribution of escort navigation is clearly seen to be of larger size and an opposing trend for the independent segment of lower floe size. The ice thickness distribution is mostly composed of 1m for both navigation modes, then 0.3 to 0.4m for escort navigation and thinner 0.2m ice in the independent navigation segment.

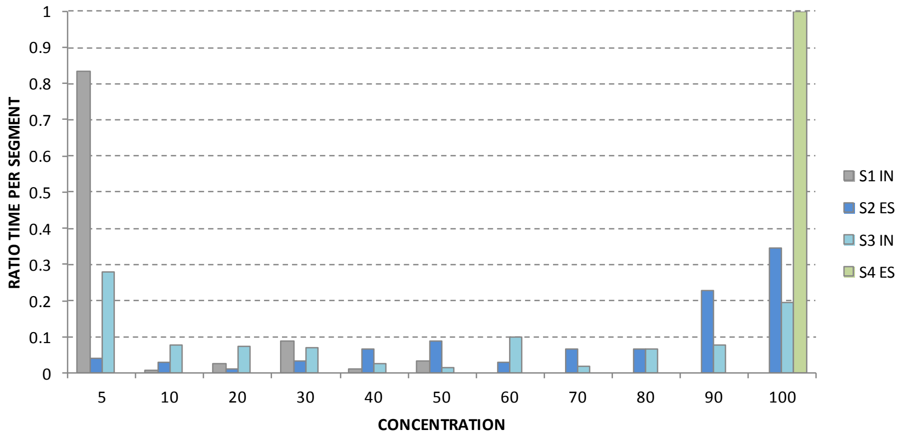

Figure 3. Time ratio of observed ice concentration distribution for each of the four route segments.

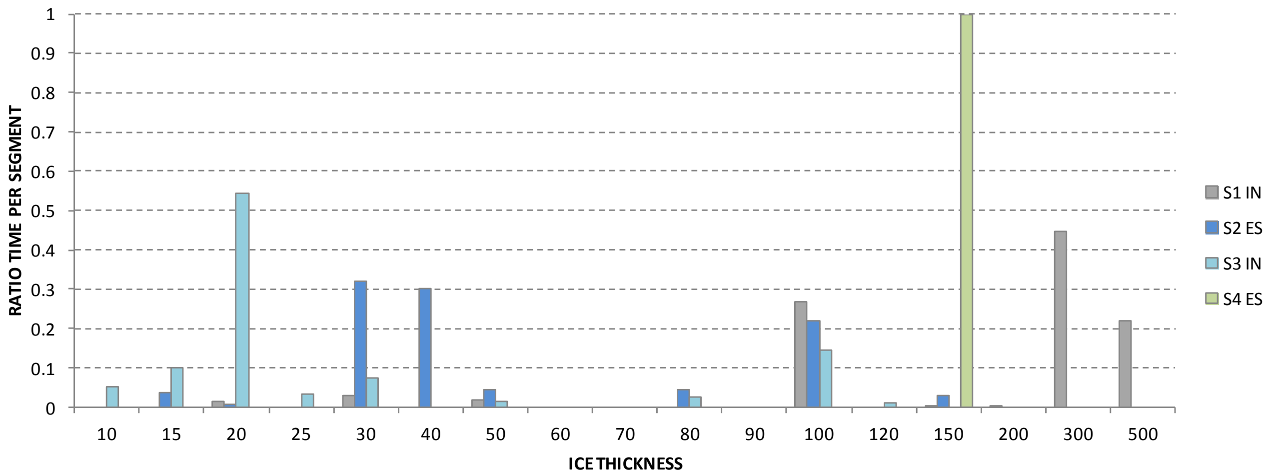

Figure 4. Time ratio of observed ice thickness distribution for each of the four route segments. 300 and 500 cm thicknesses observations are icebergs.

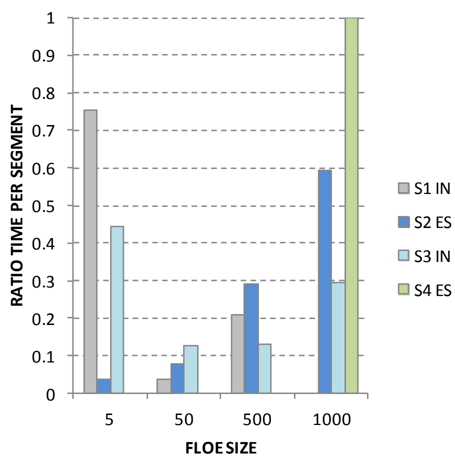

Figure 5. Time ratio of observed ice floe size distribution for each of the four route segments.

6. Ship Navigation

The following presents the different ship performance and navigation aspects observed during the voyage and presents some of the data acquired.

During the open water section, the ship speed was a smooth continuous level, with gradual changes only, due to changes in ship heading and the sea states. On reaching the region with icebergs, the speed was often changed, due to manoeuvring and navigating through the ice. This continues during the icebreaker escort in thick ice, with a decrease when entering a particularly thick section of ice. The thin ice navigation segment, during which the ship sailed independently, fluctuated, but as there were no route deviations, these should be closely correlated to the ice conditions. The final section was under towed escort in the brash ice channel and was a constant if rapidly fluctuating speed. Further, it was noted when entering the level landfast ice significant hull girder flexure was observed. Further statistical analysis of the ship data may be performed and related to theoretical and comparative results, although is not subject of this paper.

6.1. Vessel Ice Capability

The ship has an Ice class Arc4. According to the Russian Maritime Register of Shipping (RMRS 2016), this is intended for ship navigating in Arctic Seas. Based on the averaged quantitative data on permitted service area and ice service conditions presented in these rules, the ship is capable of navigating in the following ice conditions:

Operating independently with permissible speeds (of 6-8 knots):

- Winter/spring navigation — Open floating first year ice of 0.6m
- Summer/autumn navigation — Open floating first year ice of 0.8m

Operating in a channel following an icebreaker at a low speed (of 3 to 5 knots):

- Winter navigation — Thin first-year ice less than 0.7m
- Summer/autumn navigation — Medium first-year ice up to 0.9m

This is noted as being in reasonable agreement with the general capability noted of being 20 to 30cm independently. This also correlates with the observed ice conditions of independent navigation in 10 to 30cm at 10 to 13 knots. Taking due cognisance of this being a higher speed, but a lower ice thickness. The escorted operation is slightly different, with ice observations, being approximately 10 knots in 1m ice (Kara Sea) and 8 knots in 1.5m (Ob Estuary). Thus the Arc4 vessel proceeded at a higher thickness and higher speed than noted in the RMRS rules, however, extensive use of leads was made which could explain this.

6.2. Operational Ice Route with POLARIS

A methodology to assess operational capabilities and limitations in ice has been developed and proposed for the IMO Polar Code in MSC.1/Circ.1519 (IMO 2016). The system, currently referred to as POLARIS, is based on the Canadian system, the Arctic Ice Regime Shipping System (AIRSS). The system has quite a number of limitations and assumptions, as seen below in the following analysis.

The system uses the Finnish-Swedish Ice Classes (Transport Safety Agency, 2010) and International Association of Classification Societies (IACS 2016) Polar Class rules and links them to the ice conditions using the EGG code definitions, see Table 3 below. Using the below calculation for each ice regime, a positive RIO permits navigation, whilst negative restricts (safe speed).

$$RIO = (C1xRV1)+(C2xRV2)+(C3xRV3)+\ldots(CnxRVn)$$

Where *C1…Cn* are the concentrations (in tenths) of ice types within the ice regime, and *RV1…RVn* are the corresponding Risk Index values

Here it is noted that equivalency needs to be established for the RMRS Arc Ice Classes for use of this system. However, it is recognised that Arc4 is equivalent to Finnish-Swedish Ice Class IA, such as under HELCOM (Baltic Marine Environment Protection Commission, 2016), and the equivalency places this as equivalent to IACS PC7. However, these are attributed differently in POLARIS, see rows highlighted in Table 3 below. In this case, the ice class IA values have been used as being more conservative basis. It can be seen that this categorisation effectively permits operation for an Ice Class IA ship in conditions up to thin first-year ice, which has been attributed with an upper limit of a nominal ice thickness of 70cm. This is above those set out in the RMRS, as discussed previously.

In addition, POLARIS includes additional table of risk index values for conditions with ice decays. It is unclear at what point in time this is applicable, and so here again as conservative basis we neglect these values. A further aspect to note is the use of the terminology ‘ice regime’, which is used to describe an ‘area with a relatively consistent distribution of any mix of ice types, including open water to which POLARIS may be applied’. Here observations were made in near continuous time, often with ice conditions changing in minutes, and thus it is difficult to attribute how this ‘regime’ may be employed as the occurrences of what could be considered a consistent distribution of mix ice types was not often.

Table 3. Risk Index Values according to POLARIS (IMO 2016).

Category	Ice Class	Ice Free	New Ice	Grey Ice	Grey White Ice	Thin First Year Ice, 1st Stage	Thin First Year ice, 2nd Stage	Medium First Year Ice, 1m thick	Medium First Year Ice	Thick First Year Ice	Second Year Ice	Light Multi Year Ice	Heavy Multi-Year Ice
Upper limit cm			10	15	30	50	70	95	120	200	250	300	
A	PC1	3	3	**3**	3	2	2	2	2	2	2	1	1
	PC2	3	3	**3**	3	2	2	2	2	2	1	1	0
	PC3	3	3	3	3	2	2	2	2	2	1	0	-1
	PC4	3	3	**3**	3	2	2	2	2	1	0	-1	-2
	PC5	3	3	**3**	3	2	2	1	1	0	-1	-2	-2
B	PC6	3	2	2	2	2	1	1	0	-1	-2	-3	-3
	PC7	***3***	***2***	***2***	***2***	***1***	***1***	***0***	***-1***	***-2***	***-3***	***-3***	***-3***
C	IA Super	3	2	2	2	2	1	0	-1	-2	-3	-4	-4
	IA	***3***	***2***	***2***	***2***	***1***	***0***	***-1***	***-2***	***-3***	***-4***	***-5***	***-5***
	IB	3	2	2	1	0	-1	-2	-3	-4	-5	-6	-6
	IC	3	2	1	0	-1	-2	-3	-4	-5	-6	-7	-8
	none	3	1	0	-1	-2	-3	-4	-5	-6	-7	-8	-8

The results of applying POLARIS with the ice observations are shown in Figure 6. It can clearly be seen, that the values are above zero for the majority of the voyage. Indeed the results in the segment in thick ice, with escort (Kara Sea) have only three short sections of negative results, although recognising the route taken by the icebreaker avoided the most severe ice. Only the landfast ice segment is it clearly seen to require escort. Thus POLARIS appears to be somewhat biased for giving overly positive results, however it should be recognised that just because we had icebreaker support doesn't mean we truly needed it. Thus some caution should be made in using this system. In addition, for results between zero and minus ten, POLARIS suggests icebreaker escort may be used, although for vessels with ice class less than PC5 a speed limitation of 3 knots is stipulated, which was clearly not the case during this voyage.

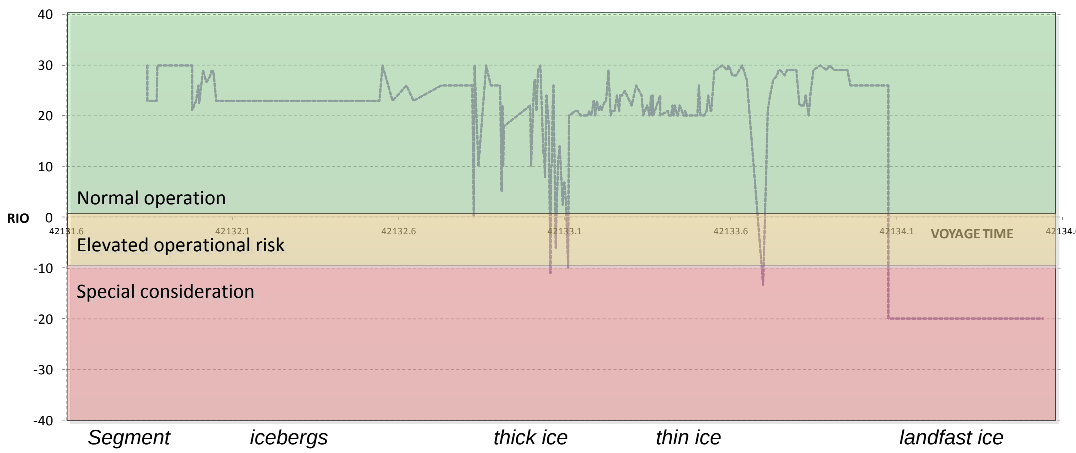

Figure 6. Ice observation data applying POLARIS (red and orange indicate negative results and green positive).

Thus it appears that specific ship characteristics and ice performance are not so well represented using the POLARIS system, and indeed does not mirror or incorporate some of the fundamental principles incorporated in the ice class rules such as hull form, engine power, etc. Further, whilst acknowledging the high risk value, whether lower ice classes, e.g. IC and IB, should even include assessment for multi-year ice is not a straightforward assessment.

6.3. Route Deviations due to Ice Conditions

During the voyage there were occasions and segments of navigation when the ice floes were noticeably thick, and thus it was considered to navigate around these. During this time, the vessel made use of leads in the ice and actively navigated around the worst ice features. This active navigation is discussed in this section.

The first time the ship made deviations from the planned route was whilst sailing the northern tip of Novaya Zemlya. Figure 7 shows an occasion whereby the vessel navigated around a large ice field.

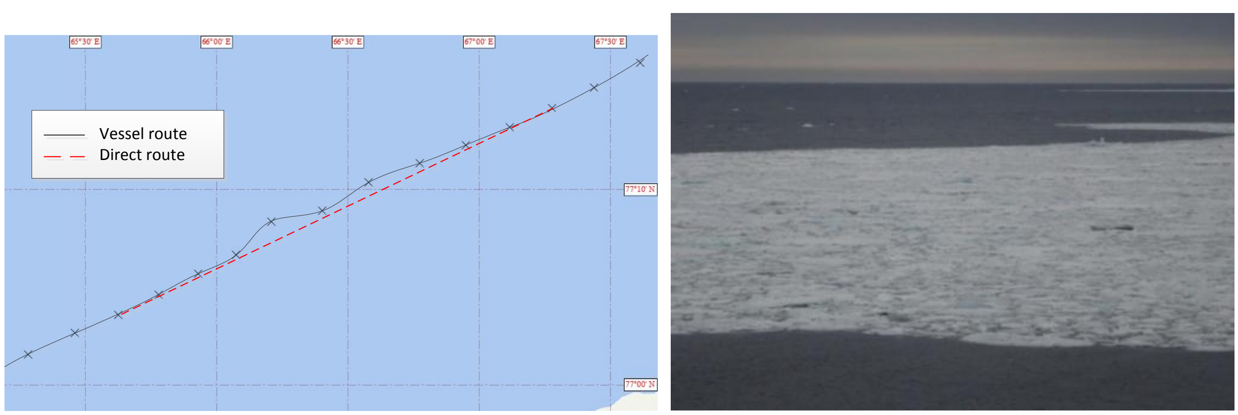

Figure 7. Route at Northern Novaya Zemlya with of deviation and image of ice region avoided. Small 'x' shows the measured GPS position every 15 minutes during S1 IN.

On reaching the tip of Novaya Zemlya and on the voyage southwards in the Kara Sea, the ship was escorted by icebreaker. During this segment the icebreaker employed active navigation around the worst ice conditions and made extensive use of leads. See Figure 8. During these escort operations, a variety of ice conditions were encountered. Often the navigation was in open water leads or in thin ice. On occasions, navigation was made through large floes, during which the channel width was noted as being that of the icebreaker, whilst the ice piece size varied and often large floes washed behind the icebreaker. On occasion, the radius of turn of the icebreaker was tighter than that of the ship's, and thus the sides of the vessel contacted the edges of the unbroken ice, highlighting the influence of ship manoeuvrability. It may be noted that the deviation under icebreaker escort has three distinct parts; that of a large arc, that of deviations along the route itself, and finally small route corrections and ice avoidance locally around the ship. Figure 9 shows the normalised ice observations and the route deviation as the distance taken from the direct route. It is clearly seen that in the thicker and higher concentration of ice there is greater route deviation.

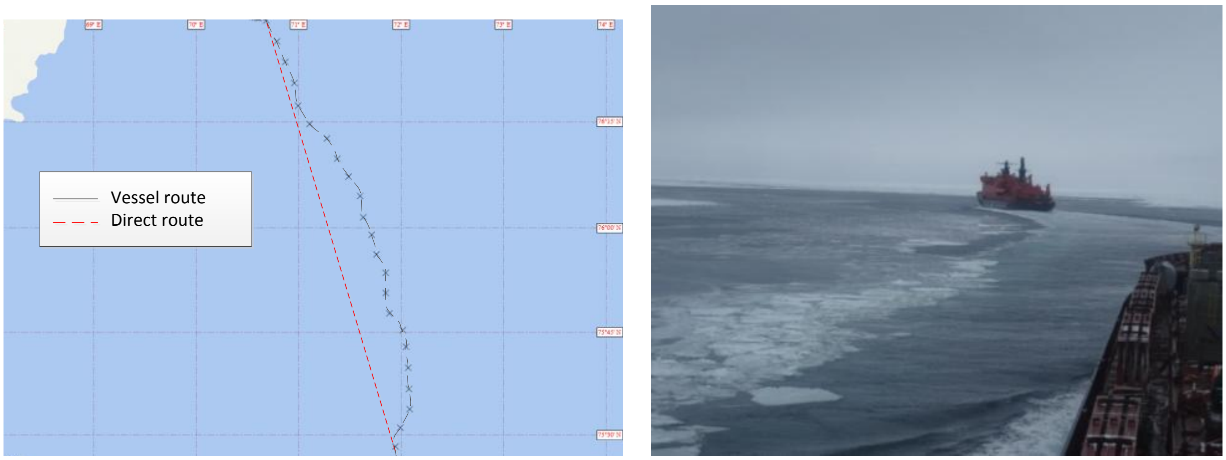

Figure 8. Escort track with *50 Let Pobedy*. Small 'x' shows the measured GPS position every 15 minutes during S2 ES.

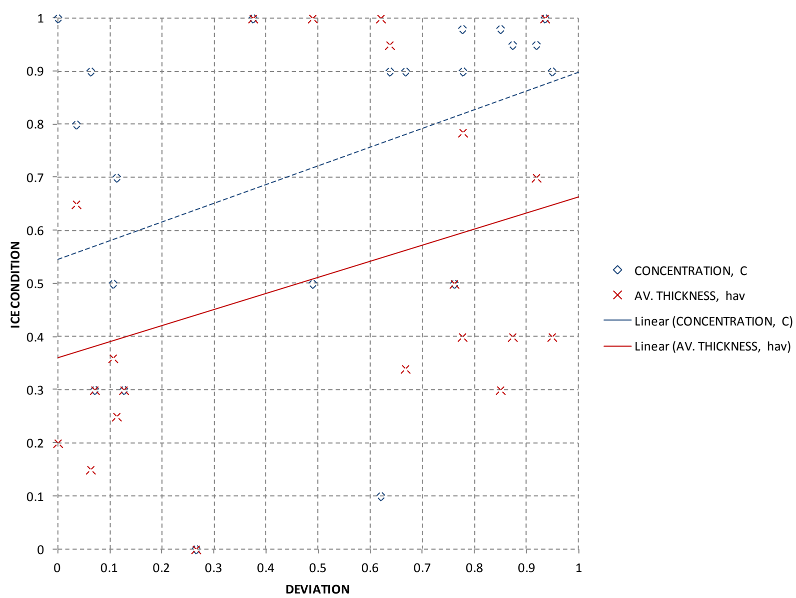

Figure 9. Normalised values of route deviations in different ice conditions during escort operation for S2 ES.

A final series of active navigation was observed in the Ob Estuary. Here, as with the earlier independent navigation in ice, avoidance of large thick ice floes was made. It should be noted that operation in a sea channel, i.e. a fixed route, would limit manoeuvrability and thus be unable to avoid these ice floes (e.g. due to restriction in channel width). The ice navigation system will need to therefore give a display of the situation so this can be assessed prior to entering the channel.

In all of these manoeuvres, the routeing was of tactical navigation. During the independent navigation, this tactical navigation was made based on visibility and experience. The track data may be further analysed for route deviations compared to ice conditions and ship speed. These deviations highlight that it is important to establish the limits of the ships in ice, and obtain the points in which the deviations in ship route are expected to be made based on the ice forecasts and charts, and feed these into the voyage planning and route selection criteria.

7. Summary

An ice information and forecast system is a perquisite for Kara Sea voyages to be undertaken safely and efficiently. The system must be useful and provide the required accuracy of data and presentation of the important ice conditions. To identify the content that should be addressed in providing useful ice charts and forecasts the navigation during the voyage highlighted the experience with Arctic shipping operations and the current operational procedures for safe and efficient navigation in ice.

Ice information is required to support tactical decision on the bridge of the ships, to determine the correct course and avoidance of critical ice features that pose risk to the ship operations. The information is required to detect floes and leads, however also regions of icebergs should be identified. Of particular importance is the ice thickness, especially when not employing any active navigation (ice avoidance and use of leads). Generally, the ice data of most importance is naturally noted as being the ice thickness, and concentration. This aligns with Timco (2007). Further, the location of vast floes (of significant thickness) is deemed useful. Here, the concern was, and also for glacial ice, avoidance of potential damage this may cause. Ridges are also noted as important, as are regions of compressions, although the latter generally assumed to be in relation to wind forecasts. Both charts and satellite images are useful, ideally on a daily basis, similar to the weather forecasts received. Thus, information in 'near' real time is important. Resolution needed for both tactical and strategic basis was observed.

The ice observations during the Kara Sea voyage provide a useful basis and valuable means of validation and verification of ice navigation systems for transit in the Kara Sea. Here we use visual observations made to characterise the ice conditions of the ship route. Further voyages would provide further necessary data correlation.

The input data, i.e. ice performance of the ship, in the ice navigation system is of importance. The RMRS values and POLARIS give differing performance characteristics. Here the latter is also noted due to the overly positive results gained from using this system. It is however important to establish the limits of the ships in ice, and also obtain the points in which the deviations in ship route will be made on the ice forecasts and charts, and feed these into the voyage planning and route selection criteria. Further work on these aspects is necessary and especially the route deviations and ship speed in ice may be further analysed and compared to theoretical models and predictions, to improve efficiency of ship navigation in the range of ice covered seas and safety of operations.

Acknowledgements

The support and assistance from Yamal LNG logistics is greatly appreciated as is also the Murmansk Shipping Company and ship crew.

References

Baltic Marine Environment Protection Commission, 2016. Safety of Winter Navigation in the Baltic Sea Area. Revised HELCOM recommendation 25/7.

Bouillon S., Rampal P. 2015: Presentation of the dynamical core of neXtSIM, a new sea ice model. Ocean Modelling 04/2015; 91. DOI:10.1016/j.ocemod.2015.04.005

Chevallier, M., D. Salas y Mélia, A. Voldoire, M. Déqué, and G. Garric, 2013: Seasonal Forecasts of the Pan-Arctic Sea Ice Extent Using a GCM-Based Seasonal Prediction System. J. Climate, 26, 6092–6104, doi: 10.1175/JCLI-D-12-00612.1.

Environment Canada 2005. MANICE Manual of Standard Procedures for Observing and Reporting Ice Conditions. Canadian Ice Servic. Revised 9th Edition, Meteorological Service of Canada.

Hutchings, J. K.; Hughes, N.; Orlich, A.; McFarlane, S.; Cowen, A.; Farmer, L.; Faber, M. K. Ice Watch: Standardizing and expanding Arctic ship based sea ice observations, Arctic Observing Summit 2016, 23pp.

International Association of Classification Societies, 2016. URI Requirements concerning Polar Class.

International Maritime Organisation, 2015. International Code of Safety for Ships Operating in Polar Waters, Resolution MSC.385(94) / Resolution MEPC.264(68).

International Maritime Organisation, 2016.Guidance on methodologies for assessing operational capabilities and limitations in ice, MSC.1/Circ.1519.

Ministry of Transport of Russia, 2013. Rules of Navigation in the Water Area of the Northern Sea Route.

Rampal P., Bouillon S., Ólason E., Morlighem M. 2016. neXtSIM: a new Lagrangian sea ice model. The Cryosphere 05/2016; 10(3). DOI:10.5194/tc-10-1055-2016

Russian Maritime Register of Shipping, 2016. Rules for the Classification and Construction of Sea-Going Ships, Part II, 2-020101-087-E_2.

Shlyaeva A., Buehner M., Caya A., Lemieux J.F., Smith G.C., Roy F., Dupont F., Carrieres T.: Towards ensemble data assimilation for the Environment Canada Regional Ice Prediction System Q.J.R.Meteorol.Soc.142: 1090 – 1099, January 2016 B DOI:10.1002/qj.2712.

Suominen M, Aalto H, Kulovesi J, Lensu M, Kujala P, Soal K, and Lehtiranta J. 2016. Ship-based visual Antarctic sea ice thickness measurements. 23rd IAHR International Symposium on Ice, Ann Arbor, Michigan USA, 8pp.

Tietsche, S., Notz, D., Jungclaus, J.H. et al. 2013. Predictability of large interannual Arctic sea-ice anomalies 2511. Clim Dyn. 2013 41. doi:10.1007/s00382-013-1698-8

Timco G.W. and Gorman R. 2007. Survey of Canadian Arctic Captains: Current Status and Research Needs, International Conference on Port and Ocean Engineering under Arctic Conditions, POAC-07, pp. 695-704.

Tonani M., Balmaseda M., Bertino L., Blockley E., Brassington G., Davidson F., Drillet Y., Hogan P., Kuragano T., Lee T., Mehra A., Paranathara F., Tanajura C.A.S., and Wang H. 2015. Status and future of global and regional ocean prediction systems, Journal of Operational Oceanography Vol. 8 , Iss. sup2.

Transport Canada, 1998.User Assistance Package for the Implementation of Canada's Arctic Ice Regime Shipping System (AIRSS), TP 12819, 50pp.

Transport Safety Agency, 2010. Finnish Swedish Ice Class Rules. Maritime safety regulation, TRAFI/31298/03.04.01.00/2010

Wang Q., Danilov S., Jung T., Kaleschke L., Wernecke A. (2016): Sea ice leads in the Arctic Ocean: Model assessment, interannual variability and trends, DOI: 0.1002/2016GL068696

Worby, A.P. and Allison I.1999. A technique for making ship-based observations of Antarctic sea ice thickness and characteristics. Part I: Observational technique and results. Antarctic Cooperative Research Centre Research Report 14, 63 pp., University of Tasmania, Hobart, Australia.

World Meteorological Organization (WMO) 2014. WMO sea-ice nomenclature. WMO/OMM/BMO No 259.TP.145.

Appendix A - Ice Conditions

Ice navigation systems require the incorporation of various ice conditions. Here some different ice conditions are shown with images taken during the voyage.

Low ice concentration
07/05

High ice concentration with glacial floe
07/05

Icebergs
08/05

Proceeding with icebreaker in thin ice
08/05

Icebreaker escort traversing section of thick ice
08/05

Navigation in small ice floes
09/05

Thin ice
09/05

Level ice navigation
09/05

Rotten and melting ice
09/05

High ice concentration in Ob Estuary
09/05

Ice floes in Ob Estuary
09/05

Turning in landfast channel during close tow
10/05

International Association for Hydro-Environment Engineering and Research

Supported by Spain Water and IWHR, China

24th IAHR International Symposium on Ice
Vladivostok, Russia, June 4 to 9, 2018

Corrosion Wears Additives for Ships Operation in Ice

V.A. Kulesh., N.G. Pets
Far Eastern Federal University.
vkulesh@mail.ru
Department of Shipbuilding and Ocean Engineering.
Russia, Vladivostok.
pecng85@gmail.com

The problem of reliability ensuring of marine facilities in the conditions of interaction with the ice is actual. Existing standards of reliability indirectly reflect the rules of Russian Maritime Register. The corrosion wear additives of shell plating and ice strake is important. Increase additives leads to an increase in the weight and cost of the ice reinforcement designs. In this paper, there are shortcomings in standardization of additives for corrosive wear for icebreakers and ice navigation vessels. The icebreaker service life may exceed 50 years. Corresponding additives for corrosion wear may exceed 25 millimeters. It is shown that project surcharges for corrosive wear should be related to wear rates in operation. It is also advisable to take into account the relationship between the rate of corrosion and ice pressures.

The issue of development of norms for surcharges for corrosive wear is considered in the work. First of all, this is accounting for protective coatings. A scheme for harmonizing the norms for surcharges of corrosive wear depending on the ice category for icebreakers, tugboats and other vessels is proposed. A way of differentiating surcharges for corrosive wear in different areas of the hull is proposed. Questions of planning and monitoring the life cycle of vessels are considered. The prospect of changing the ice category of the vessel during the life cycle is noted. Proposals can be used to develop the Russian classification system.

1. General information

The standardization of parameters that determine the reliability of ship hulls is based both on operational experience and on the level of scientific and technological progress achieved. If theoretical models are imperfect, preference should be given to experience.

The standardization of corrosion wear additives for the outer skin is carried out by classification societies. In the ice chapter of the current Rules for the Classification and Construction of Maritime Vessels of the Russian Maritime Register of Shipping (Rules for the classification and construction of sea-going ships, 2017)

$$\Delta s_{i\,0} = 0{,}75 T u, \qquad [1]$$

where T - is the planned lifetime of the ship, years; u - average annual reduction in thickness, given in tabular form, mm / year .

In carrying out measures to protect the outer skin from corrosion and abrasion (special coatings, clad steels, etc.), the determination of the value u is the subject of special consideration by the Register. In Fig. 1, for the fore part of the reinforcement, the values of average annual decreases are given, depending on the index of the ice category. In the middle and aft parts of the reinforcement value are less.

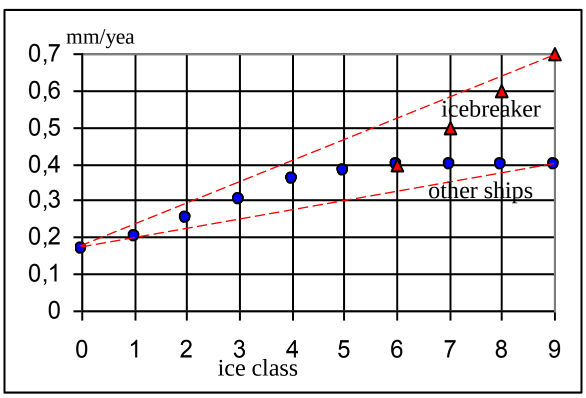

Fig. 1. Average annual reduction in thickness depending on the ice class of ships

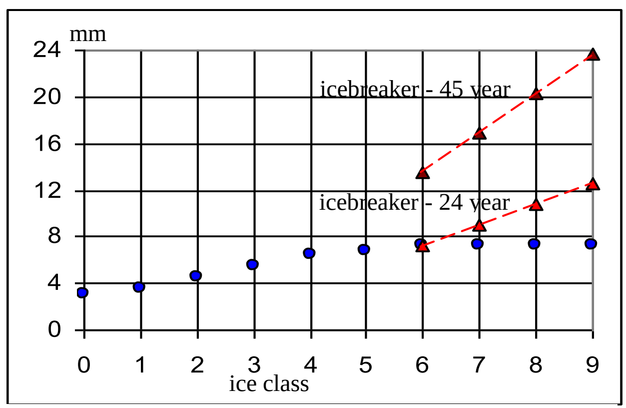

Fig. 2. Corrosion wear extensions depending on the ice class of ships

The growth trend in Figure 1 with the increase in the ice category is obvious. However, in the region of low categories (1-4), the growth rates seem overestimated. Indirectly, this is confirmed by the total lack of growth for high category (6-9) ships. The coincidence of values for vessels and icebreakers in category 6 is not entirely justified, since the proportion of navigation time in ice is lower for ships than for icebreakers. The growth rates for icebreakers are the highest.

A more complete representation provides a direct comparison of corrosion wear extensions, Fig. 2. Here, icebreakers and other vessels can be compared according with the planned service life. For the 24-year period, the corrosion wear additives for ships vary in the range from 3 to 7 mm, and for icebreakers - up to 13 mm.

2. Status of the issue

The service life of 24 years for icebreakers is clearly not sufficient. Therefore, in Fig. 2 the values for a service life of 45 years are additionally given. The values of the additives for icebreakers range from 14 to 24 mm .

The wear allowances, regulated during the design (Rules for the classification and construction of sea-going ships, 2017), can and should be linked to the permissible wear during operation (Rules for the Classification Surveys of Ships in Service, 2017). Currently, the Register in the area of ice reinforcement is most widely used for 20% wear allowance. Given this tolerance and the above allowances, it can be estimated that the thickness of the ice belt in the nose area of a small port icebreaker of the 6th category will be 70 mm, and the line icebreaker of the 9th category will reach 120 mm. Such thicknesses are overestimated and are not confirmed by experience. They force the use of special protective measures or take into account other factors.

The drawback of the current regulation of extensions (Rules for the classification and construction of sea-going ships, 2017) is that their extreme values, obtained in the waterline belt, spread in cross sections to the underwater part. Thus, a significant and unjustified weighting of the hull is produced.

Corrosion wear additives (Rules for the classification and construction of sea-going ships, 2017) do not have a direct connection with the intensity of ice loads. It is difficult to call optimal its indirect function, through the table for average annual decreases in thickness depending on the ice category and only 3 areas along the length of the vessel. The number of areas for icebreakers reaches 16.

The relationship between the wear of the outer skin and the intensity of the ice loads is beyond doubt. A significant factor affecting the intensity of ice loads is the displacement of vessels. However, under existing regulations within the same ice category, ships with a displacement of 1,000 tons and 100,000 tons will have the same surcharges.

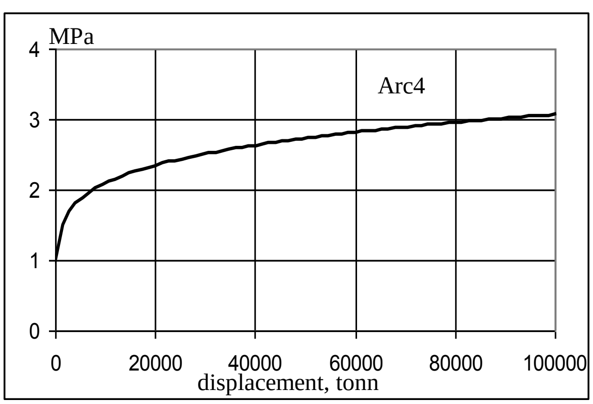

Fig. 3. The intensity of ice loads as a function of displacement (Arc4)

Figure 3 for the Arc4 category is an example of the change in the intensity of ice loads from vessel displacement. As can be seen, differences for small and large vessels reach up to 3-fold.

If we proceed from the fact that the regulation of ice requirements and additives in the part of experience was based on a relatively small group of ships of ice navigation with a displacement of 10-20 thousand tons, it is obvious that their extrapolation to numerous smaller vessels (e.g. tugboats and fishing vessels) significantly overstates the weight of the reinforcement.

In conclusion of this section it is important to return to the thesis on the necessity of interrelation of norms for classification and limits in the operation of ships. Currently, as noted above, the Registry (Rules for the Classification Surveys of Ships in Service, 2017) limits the permissible wear to 20% for outer skin in areas of ice reinforcement of ships built after 1990. In the practice of the Register of the USSR, a norm of 30% was adopted; in 1.5 more. It is with this in mind, a 1.5-fold decrease in the corrosion wear additives (Rules for the classification and construction of sea-going ships, 2017) is possible.

Further the possible ways of development the normalization of corrosion wear additives for work in ice have been considered.

3. Accounting for protective coatings

The quality and frequency of restoration of protective coatings can vary significantly. Figure 4 shows a scheme for reducing the thickness in time for a protective coating of low durability (up to 2.5 years) with a recovery period of 7.5 years.

The wear rates are not stable and can vary from zero values over a wide range. Therefore, the Rules (Rules for the classification and construction of sea-going ships, 2017) are based on the average annual (over long periods) thickness reduction, corresponding to the extreme values (tangent 1 in Fig. 4). In the special literature, for example (Maximadzhi A.I., et al. 1982), there is a possibility of a drop in average annual decreases with an increase in the period of observations (broken line 2 in Fig. 4).

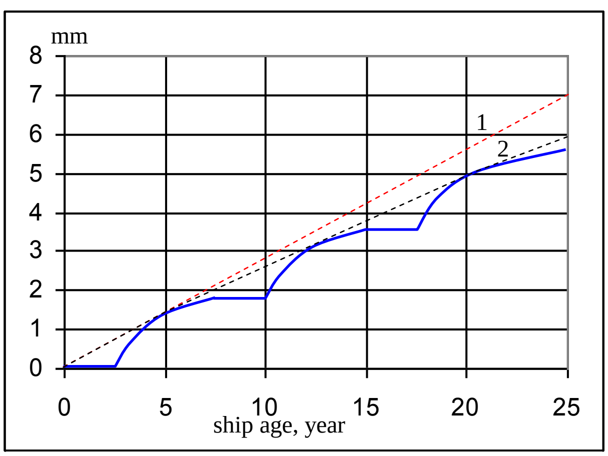

Fig. 4. Scheme for reducing the thickness of the outer skin, depending on the ship age provided of the periodic restoration of protective coatings

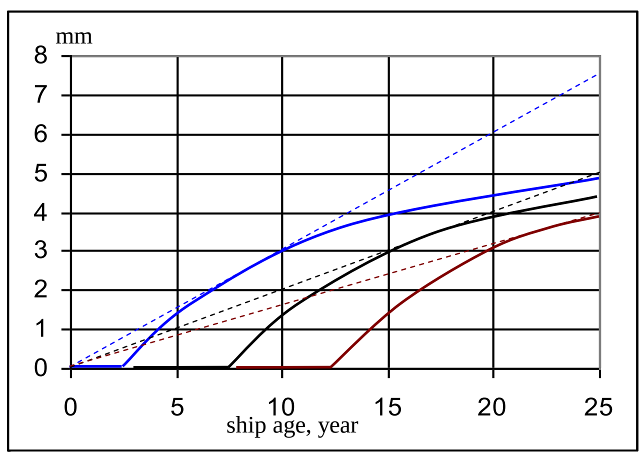

Fig. 5. Schematic diagram of accounting for different durability of protective coatings by the average annual reduction in thickness

In the mid-nineties of the twentieth century, the Norwegian Veritas in the developed system of monitoring the technical condition of vessels NAUTICUS applied mathematical models of deterioration with a gradation of periods of durability of coatings at 5, 10 and 15 years. Similar mathematical models of deterioration later became the basis of the European system CAS (Condition Assessment System).

The mathematical model of deterioration and tear with coatings as a function of the service life in the general case can be so

$$\Delta s(T) = \begin{cases} 0 & npu\, T \le T_n \\ a(T - T_n) + b(T - T_n)^c & npu\, T > T_n \end{cases}, \qquad \textbf{[2]}$$

where T is the service life of the ship, years; $T_п$ - durability of the protective coating, years.

The coefficients a, b and c in formula [2] can be determined on the basis of statistical data from the operating experience, for example the register ship database DEFHULL, subject to the boundary conditions.

Assuming that the nature of the wear curve after failure of the coating is not related to its longevity, different coatings will be reflected by shifting the wear curves along the horizontal axis, Fig. 5.

The tangents from zero to the deterioration trajectories in Fig. 5 provide analogs to the average annual thickness decreases in the Rules. As a result, the formula [1] can be represented in the form

$$\Delta s_{\acute{\imath}\,0} = 0{,}75 T u \cdot k_{\ddot{\imath}}\ , \qquad \textbf{[3]}$$

where k_Π - the proposed coefficient of accounting for protective coatings, depending on their durability and not more than 1.

As the longevity of the coatings, warranty periods of suppliers can act. Uncertainty or lack of warranty terms corresponds to the value of the coefficient 1.

4. Harmonization of the deterioration standardization

The existing gradation in the Rules (Rules for the classification and construction of sea-going ships, 2017) of the average annual decreases in thickness from ice categories is shown in Fig. 1 and for vessels is "convex". In the field of high categories and icebreakers, the character changes to "linear". Special studies on this issue show that wear associated with the intensity of ice loads and more correct is the "concave" nature of gradation. However, one cannot exclude the fact that with the increase in the ice category, the frequency and quality of protective coatings can increase. With this in mind, proposals for harmonizing the growth of average annual thickness decreases depending on the ice category on the basis of a simple "linear" principle may have the form shown in Fig. 6.

Here, "tugboats" and "icebreakers" are singled out as a separate group, since they have a higher share of the operational period in the ice. Below is a gradation for "other ships". As a result, the formula [1] for the nasal region of the reinforcements in the waterline belt in addition to [3] can be represented in the form

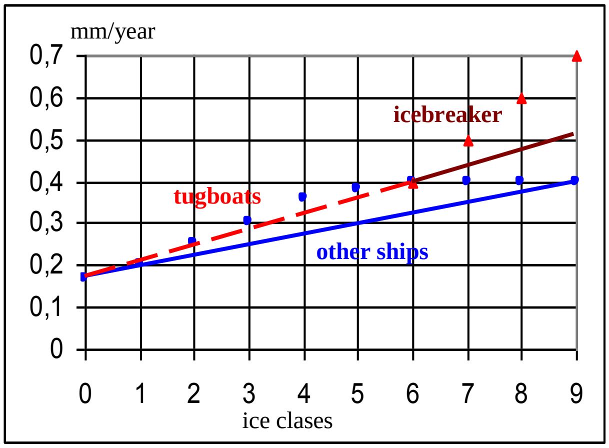

Fig. 6. The proposed scheme for the harmonization of average annual decreases in thickness (for the fore part of the reinforcements in the waterline belt)

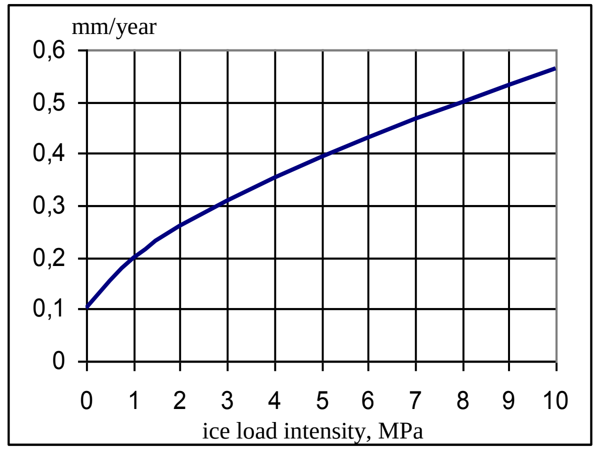

Fig. 7. Relationship between the average annual decrease in thickness and intensity of the ice load according to the Rules of the RS 1990

$$\Delta s_{í\,0} = 0{,}75T \cdot u_{Ic} \cdot k_{ĭ} \ , \qquad \textbf{[4]}$$

where u_{Ic} is the average annual decrease in thickness, determined by the formula

$$u_{Ic} = u_0 + k \cdot Ic \ , \qquad \textbf{[5]}$$

where u_0 is the base annual mean thickness reduction for the waterline variable belt in the existing Rules equal to 0.17 mm / year; k is a coefficient of 0.038 for tugs and icebreakers or 0.025 for other vessels; I_C is a numerical index of the ice category of the Register.

5. Relationship of wear and pressure rates

The drawbacks of the existing enlarged gradation of average annual decreases in thickness along the areas of the hull and the spread of high deterioration extensions of the waterline belt on the underwater part of the hull can be eliminated by directly linking them with the values of the intensity of the calculated ice loads. In Fig. 7 shows the relationship between mean annual thickness decreases and ice load intensity obtained in (Kulesh V. et al. 1995) based on data analysis in a wide range of vessels and categories - from small seiners to line icebreakers. In this case, the formula [1] for any region of the hull in addition to [3] can be represented in a more universal form

$$\Delta s_{í\,0} = 0{,}75T \cdot u(p) \cdot k_{ĭ} \ , \qquad \textbf{[6]}$$

where u(p) is the average annual decrease in thickness, determined by the formula

$$u(p) = u_m(1 + k_p \cdot p^{2/3}) \ , \qquad \textbf{[7]}$$

where u_m is the minimum value of the average annual decrease in thickness for the outer skin according to the Rules (in (Kulesh V., et al. 1995) the value 0.1 mm / year was used); p - the intensity of the calculated ice loads according to the current Rules, MPa; k_P - the coefficient of accounting for differences in the standardization of the intensity of ice loads under the 1990s Rules and the current.

The need to determine this coefficient is due to the fact that the existing ice classification is based on the criterion of ultimate strength (Appolonov E.M., 2014), in contrast to the fibrous and limited fluidity preceded by the criterion. This transition led to a change in calculated ice loads.

6. Planning and taking into account of the Life Cycle

Long-term experience of the Russian fleet shows that the preservation of the initial ice category during the entire planned service life of the vessel, which icebreakers can exceed 50 years, is not economically justified. The practice of lowering the ice categories of vessels with increasing age is wide spread. Decisions to lower the ice categories are usually taken in operation based on account the actual technical condition and with the aim of reducing repair costs in subsequent operation. Figure 8 shows an example from (Kulesh V., et al. 2014) monitoring the technical condition of the ice belt with a decrease in the ice category.

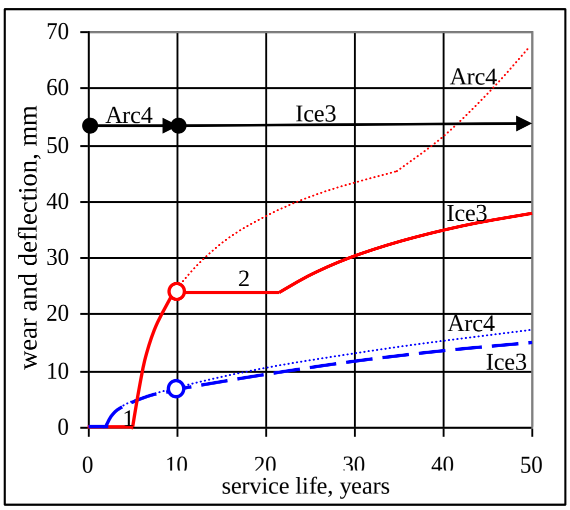

Fig. 8. An example of life-cycle management of s ship with a decrease in the ice category at the age of 10 years

As can be seen, the reduction of the category and the transfer of the vessel to the lighter conditions of operation make it possible to stop the progression of the deflections for a long period (designation 2) even in conditions of continued wear progression, but with lower rates. Planning a long life cycle of a ship at the design stage is very difficult. In the simplest case (with the category unchanged and under the assumption of a systematic restoration of the protective coatings), in determining the deterioration extensions, the planned life of the vessel - T can be reduced by the total longevity of all protection measures. Theoretically, this allows you to reduce the extensions for deterioration to zero values.

However, the above examples with icebreakers show the probability of a practical need for planning the life cycles of ships with changes in ice categories. In solving such problems, adjusting the allowance for deterioration alone will not be sufficient. Reduction of the ice category reduces the parameters of ice loads. As a result, the requirements for the component thickness reduce in terms of strength conditions. On the other hand, there are opportunities to increase the allowance for the deterioration of the skin. Theoretically, this may be equivalent to negative values of extensions for deterioration.

Of interest to ship owners may also be the tasks of overstating the ice category in the initial stages of operation, when high safety reserves still remain due to deterioration allowances. In addition, one can not ignore the possibility of the emergence of breakthrough technologies in the field of future super-resistant protective coatings over the decades could not be ignored.

7. Conclusion

The presented analysis of the existing practice standartization of additives of the external cladding of icebreakers and vessels operating in ice reflects shortcomings. These are the problems of accounting for protective coatings, the shortcomings of the graduation of allowances by category, the lack of direct connection with the intensity of ice loads, with deterioration standards and a number of others. Without their elimination, extensions can be significantly overestimated and increase the cost of ice reinforcements.

A scheme is proposed for taking into account the effect of the durability of protective coatings on the values of corrosion additives. The possibility of harmonization of the extra charges depending on the ice category is shown with the allocation of icebreakers, tugboats and other vessels. It is proposed to use a direct relationship between the annual average thickness decreases and the intensity of ice loads, which will allow determining the additives for deterioration, taking into account the size of the vessels and not spreading their high values in the ice belt to the underwater part of the hull.

Wide opportunities for optimizing the extensions for corrosion deterioration are revealed in a combination of planning and monitoring the life cycle of vessels. A special place here is the possibility of changing (lowering) the ice category with increasing deterioration and age of the vessel.

References

Российский Морской Регистр Судоходства, 2017. Правила классификации и постройки морских судов, СПб.

Российский Морской Регистр Судоходства, 2017. Правила классификационных освидетельствований судов в эксплуатации, СПб.

Максимаджи А.И., Беленький Л.М., Брикер А.С., Неугодов А.Ю., 1982. Оценка технического состояния корпусов морских судов. Ленинград, Судостроение – с.156

Апполонов Е.М., 2014. Предельная прочность арктических судов. ФГУП «Крыловский государственный научный центр», Санкт-Петербург – с.244

Kulesh V., Vinogradova N., 1995. Standardization of Corrosion Wear of Shell Plating for Ice Ships Operation. Proceedings of the International Northern Sea Route Symposium, Tokyo, 425-430.

Kulesh V., Ogay S., Voyloshnikov M., 2014. Monitoring of the processes of accumulation of defects of steel structures over time of ships operations. Proceedings of the 24 International Offshore and Polar Engineering. Vol. 4. Busan. Korea, 529-536.

International Association for Hydro-Environment Engineering and Research
Supported by Spain Water and IWHR, China

24th IAHR International Symposium on Ice
Vladivostok, Russia, June 4 to 9, 2018

Assessment of the Characteristics of Icebreakers and Ice Navigation Ships

T.I. Bessonova, V.A. Kulesh
Far Eastern Federal University.
Department of Shipbuilding and Ocean Engineering.
Russia, Vladivostok.
bess95@list.ru, vkulesh@mail.ru

Ice conditions of the seas and rivers of Russia are one of the most important factors that restrain the pace of development of transport processes, industrial potential and development of natural resources. Most of Russia's ports freeze and are forced to introduce ice navigation regimes that limit or prohibit the operation of ships with insufficient level of ice qualities.
Exploration and development of the Arctic and offshore, and plans to ensure year-round navigation along the Northern Sea Route (NSR), set the task of creating new specialized ships and polar icebreakers. Experience in the design, construction and operation of ice navigation ships (INS) has been accumulated in Russia. An important role was traditionally assigned to icebreakers and their escorts - the posting of caravans of ships. The movement of ships in the channel of the icebreaker obviously reduces the resistance and fuel expenditure.
In recent years, there have been trends in the significant growth of deadweight and the size of transport ships for navigation in ice, which outpaces the growth in the characteristics of icebreakers. Attempts to minimize the dependence of polar navigation on the icebreaking fleet lead to the search for new solutions, for example, to double acting ship (DAS). However, without combining innovations with experience, it is difficult to provide the necessary level of safety ice navigation processes.
The analysis and generalization of statistical data on the characteristics of icebreakers and transport tankers was carried out to determine their interrelationships in a wide range of changes in size, characteristics and ice categories. Data of the Russian Maritime Register of Shipping (the Register Book) were taken as a basis. Statistics reveal significant features and differences between conventional and linear icebreakers, including nuclear ones. The entire range of categories of icebreakers is practically covered. The main characteristics, including ice passability, are estimated at a given power.
Deadweight and ice category are proposed as an input parameter for transport tankers. Unfortunately, there are no statistical data on the highest ice categories. It is proposed to take into account new research by Russian colleagues. The paper proposes a method of estimating the main characteristics of ships in the whole range of Russian ice categories. The formulas are approved by comparisons with the new generation ships.
The results of the work can be used to plan the replenishment of the fleet and to assess the characteristics of ships and icebreakers in the early stages of design.

Assessment of the characteristics of icebreakers and ice navigation ships

Ice conditions of the seas and rivers of Russia are one of the most important factors that restrain the pace of development of transport processes, industrial potential and development of natural resources. Most of the Russian ports freeze and are forced to introduce ice navigation regimes that limit or prohibit the operation of ships with insufficient level of ice qualities.

Exploration and development of the Arctic and offshore, and plans to ensure year-round navigation along the Northern Sea Route (NSR), set the task of creating new specialized ships and polar icebreakers. Experience in the design, construction and operation of ice navigation ships (INS) has been gained in Russia. Herewith the important role was traditionally assigned to icebreakers and their escorts – ice-breaker support. The movement of ships in the ice channeling obviously reduces the resistance and fuel expenditure.

Fig. 1. Example of icebreaker support.

In recent years, there have been trends in the significant growth of deadweight and the size of transport ships for navigation in ice, which outpaces the growth in the characteristics of icebreakers. Attempts to minimize the dependence of polar navigation on the icebreaking fleet lead to the search for new solutions, for example, to double acting ship (DAS). However, without combining innovations with experience, it is difficult to provide the necessary level of safety ice navigation processes.

Fig. 2. Example of severe ice damage of ship's hull during independent navigation.

Ice damage of ship's hull with low ice categories is the most characteristic for independent navigation in broken ice. Sometimes such damages are severe and require the ship to be decommissioned. There are also cases of ice captivity and the death of ships in the continuous ice of the Arctic.

Icebreakers and ice navigation ships occupy a special place in the world shipbuilding industry. Ice reinforcements of ships with an equal deadweight can significantly increase the weight of ships and the power of propulsion system. The efficiency of the operation of such ships on water without ice is correspondingly reduced.

The development of Russia and shipping in ice, as well as the development of natural resources, pose the challenges of planning the replenishment of the fleet by new icebreakers and ice navigation ships with minimum costs and with maximum efficiency. Methods of assessing the main characteristics of ships prior to their design and construction offer solution. At the same time, the experience and trends in the development of the fleet should be taken into account to the maximum extent possible.

In this work, the main attention is paid to icebreakers of all types and tankers, the sizes of which reach the highest values. The entire range of ice categories of the Russian Maritime Register of Shipping (RMRS) is covered. Focus is only on the Register book data about before introduction of ice classification. The data of other ships and the results of the research work were additionally used to verify the formulas.

The basis of the statistical analysis is the data of the Register book on 24 icebreakers - from small port to linear nuclear. The data covered all 4 ice categories of the RMRS for icebreakers. Preliminary analysis showed that the features of linear icebreakers (power of more than 20 MWt) and differences from port icebreakers do not allow obtaining a general dependence with a high degree of reliability of approximation (R^2). As a result, at a given power (kWt), the displacement (t) of icebreakers can be estimated by formula

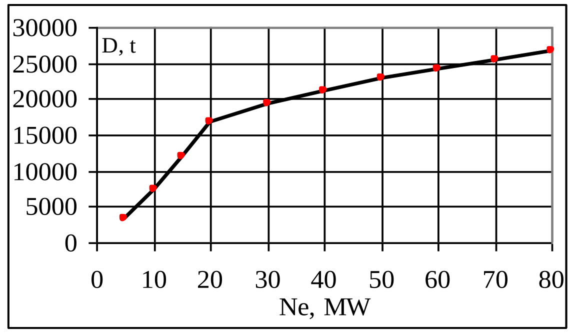

Figure 3. Relation between displacement and icebreakers power.

$$D = \min\begin{pmatrix} 0{,}1511 \cdot Ne^{1{,}1739} \\ 621{,}12 \cdot Ne^{0{,}3331} \end{pmatrix} \quad , \qquad R^2 \geq 0{,}93. \qquad \textbf{[1]}$$

The resulting relationship of these characteristics is reflected in Figure 3 and in Table 1.

Table 1. Calculations for icebreakers.

Power	MWt	5	10	15	20	30	40	50	60	70	80
Displace-ment	t	3323	7497	12066	16821	19253	21190	22825	24254	25532	26693
Length b. perp.	m	62,6	86,5	104,4	119,1	125,7	130,6	134,5	137,7	140,6	143,1
Breadth	m	18,1	22,1	24,8	26,9	27,8	28,5	29,0	29,4	29,8	30,1
Draught	m	5,7	7,3	8,5	9,4	9,9	10,2	10,4	10,6	10,8	10,9
Share of DW	%	28,7	25,3	23,6	22,4	20,9	19,8	19,0	18,4	17,9	17,5
Ice passability	m	0,71	1,00	1,22	1,41	1,73	2,00	2,24	2,45	2,65	2,83
by Register Rules	Ice passability	to 1 m		to 1,5 m		to 2 m		more than 2 meters			
	Shaft power	less than 11 MWt		more than 11 MWt		more than 22 MWt		more than 48 MWt			
	Classification	Icebreaker 6		Icebreaker 7		Icebreaker 8		Icebreaker 9			

The obtained correlations of the basic geometric characteristics of the icebreaker hulls can be estimated by the formulas presented below. Estimated length (m) may be set depending upon the displacement (t) of icebreakers.

$$L = 2{,}5123 \cdot D^{0{,}3966} \quad , \qquad R^2 = 0{,}99 . \qquad \textbf{[2]}$$

Breadth (m), depending on the design length (m) of icebreakers.

$$B = 1{,}4205 \cdot L^{0{,}6154} \quad , \qquad R^2 = 0{,}94 . \qquad \textbf{[3]}$$

Draft (m), depending on the design length (m)

$$d = 0{,}2125 \cdot L^{0{,}7938} \quad , \qquad R^2 = 0{,}87 . \qquad \textbf{[4]}$$

The most important characteristic for icebreakers is ice passability (h, м). «The maximum thickness of flat ice in which the ship can go steady speed is taken as ice passability, the strength of ice is 500 kPa, and the layer of natural snow cover is 20-25 cm» [Klimashevsky S., 2012]. The minimum speed of steady smooth motion in solid ice is 2 knots according to the Russian standards.

L. Tsoi proposed to determine ice passability (m) of ships and icebreakers by the formula, depending on the set of several parameters.

$$h = \frac{0{,}07 \cdot \cos^{3/2} \varphi \cdot \sin^{1/2}\left(\dfrac{\alpha_0 + \beta_0 + \beta_2}{3}\right)}{\sin^{3/2}\left(90^o - \beta_{10}\right)^2 \cdot \sqrt[6]{f_d} \cdot \sqrt[5]{L/B}} \cdot \sqrt[6]{D \cdot \sqrt{P_e / B}} \qquad \textbf{[5]}$$

where φ - stem angle to horizon, degree;

α_0 - load waterline slope in zero theoretical frame, degree;

$\beta_0, \beta_2, \beta_{10}$ - angles of side slope in 0, 2 and 10 theoretical frames, degree;

f_d - coefficient of dynamic friction of the hull with ice;

L, B - length and breadth of ship on constructive waterline, m;

D - displacement, t;

P_e - propeller thrust , t .

The formula [5] is rather cumbersome, requires a number of initial data, which are absent even in the early stages of design. It was modified by other authors for the sake of simplicity, but the angles of contours of hulls remained in the structure of formulas. On the other hand, the Rules of the RMRS, based on tradition, limit the angles of contours depending on the ice category. Statistical studies of the correlations between the design ice passability of icebreakers with the indicated characteristics and dimensions, as well as their combinations according to the type of formula [5], did not reveal any clear advantages. A high value of R^2 is provided by formula

$$h = 0{,}01 \cdot \sqrt{Ne} \qquad R^2 = 0{,}97 \qquad \textbf{[6]}$$

where Ne - power of the propulsion system, kWt.
The results of calculations of ice passability (m) according to formula [6] and comparison with design values for the example of 7 icebreakers are presented in Table 2 and in Figure 4.

Table 2. Comparisons of characteristics and ice passability of icebreakers.

	Names of icebreakers						
Characteristic	Lenin	Arctic	Moscow	Ermak	K. Sorok.	Mudyug	Taimyr
Length on const. waterline, m	124	136	112,4	130	121,3	73,5	140,8
Displacement, t	19240	23460	13290	20241	14914	5558	19600
Power, kWt	32300	55100	19120	30400	18180	10000	37500
Shaft power, kWt	28820	49600	16180	26470	16180	7000	32500
Thrust, t	330	480	226	320	181	87	295
Speed on water without ice, knots	19,7	20,8	18,3	19,5	19,4	17,4	20,2
Ice passability, m:							
Project	1,65	2,25	1,45	1,80	1,35	0,95	2,00
Calculated [6]	1,80	2,35	1,38	1,74	1,35	1,00	1,94
Contrast,%	8,9	4,3	-4,6	-3,1	-0,1	5,3	-3,2

a)

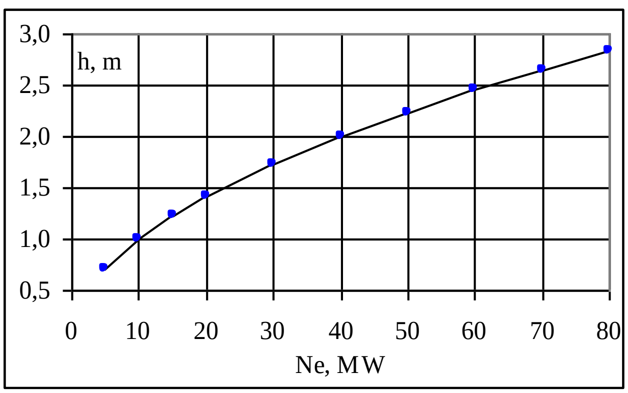

b)

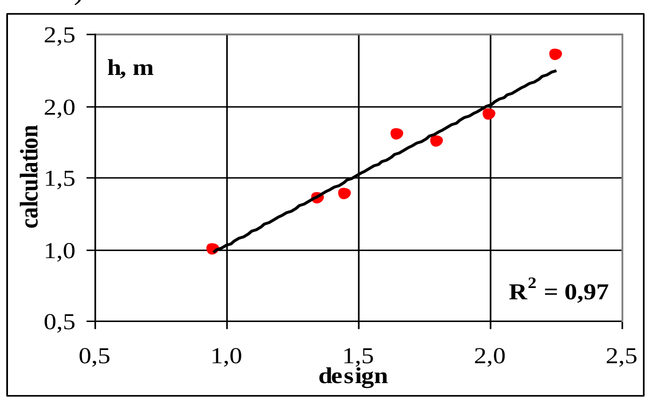

Figure 4. Estimated icebreakability of ice passability depending on the power of the propulsion system (a) and its relation to the project ice passability according to the data of 7 Icebreakers

Obtained formulas and given results provide the opportunity for the assessment of the major icebreaker characteristics and ship's lines according to power of the propulsion system in the full range of sizes, designation and ice categories.
The statistical analysis of the characteristics of tankers is based on the data of the Register book on 167 ships with the designation "oil tanker". The data covered tankers with ice categories not higher than Arc5 and with a displacement of not more than 30,000 tons. This determined the need to extrapolate the characteristics of ships to the area of higher ice categories - up to Arc9 and displacement - up to 120,000 tons. In this area, the experience of designing and building ships is little, and on its borders is absent. However, research in this area has started. For

instance, in work [Tarovik O., 2015], perspectives of construction of gas carriers for the Arctic with displacements in the range 80 000 - 90 000 tons were considered.

The most important characteristic for transport ships is the deadweight (DW). The cost of building ships is primarily related to their weight - light-ship weight (D_0). Figure 5 shows the relationship of these characteristics to ships without ice category (Ice 0) for ships with ice categories Arc5. With the same deadweight of 50,000 tons by weight, the tanker with Arc5 category can exceed the tanker without the ice category by 1.5 times.

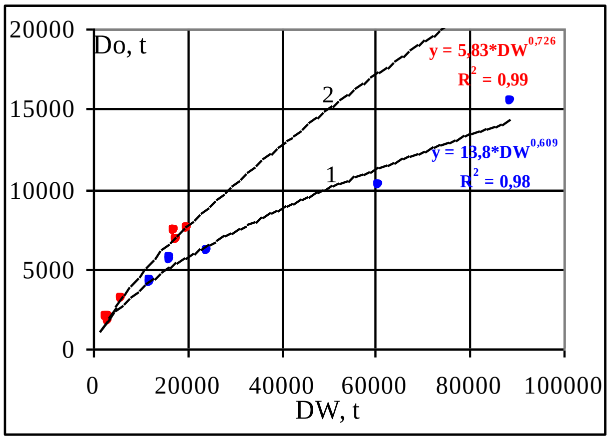

Fig. 5. The relationship between the light-ship weight and deadweight in the absence of the ice category (1) and for the Arc5 (2) category.

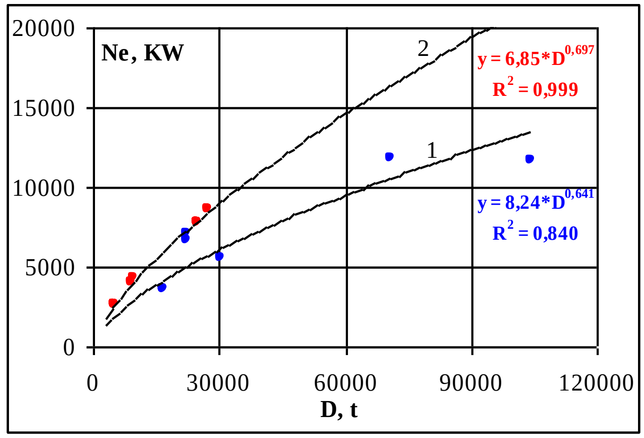

Fig. 6. Relationship between the power of ships and displacement in the absence of an ice category (1) and for the Arc5 (2) category.

A similar picture applies to the connection between the power of the propulsion system and the displacement of tankers (Figure 6). With the increase the ice category, the reliability index of the approximation increases – R^2 from 0,84 to 0,999. The reason may be that ships with Arc5 category were designed according to Russian standards, and ships without ice category in different countries.

Calculations showed that in the range of ice categories from 0 to 5, register ships with a deadweight of up to 20,000 tons increase their weight by an average of about 5% for each level of the category. With the increase in deadweight and ice category more than Arc5, the data from work [Tarovik O., 2015], were additionally taken into account. As a result, the light-ship weight (D_0, t) of tankers depending on the planned deadweight (DW, t) and the level of the ice category (ki) can be estimated by the formula

$$D_0 = \left(13{,}81 \cdot DW^{0{,}609}\right) \cdot \max\left[\frac{1}{1+\left(0{,}4222 \cdot DW^{0{,}117}-1\right) \cdot k_i/5}\right] \cdot \left[\underbrace{1+0{,}054 \cdot \left(k_i-5\right)^{1{,}6394}}_{\text{for } k_i>5}\right] \qquad [7]$$

The results of calculations using the formula [7] and comparison are shown in Figure 7. It also demonstrates the upper estimate for gas carriers in work [Tarovik O., 2015] and the position of a large polar tanker, name – “M. Ulyanov”. The weight of this tanker with category Arc6 is much higher than the calculated one according to the formula [7]. The reason may lie in impossibility to achieve the balance between ship weight and power of the propulsion system.

The power of propulsion system (Ne, kWt) as a function of the displacement (D, t) and the level of the ice category can be estimated by the formula

$$Ne = \left(8{,}24 \cdot D^{0{,}641}\right) \cdot \left(1 + 0{,}0723 \cdot D^{0{,}182} \cdot k_i / 5\right) \cdot \left[\underbrace{1 + 0{,}095 \cdot (k_i - 5)^{1{,}502}}_{\text{for } k_i > 5}\right] , \qquad \textbf{[8]}$$

where $D = DW + D_0$, t.

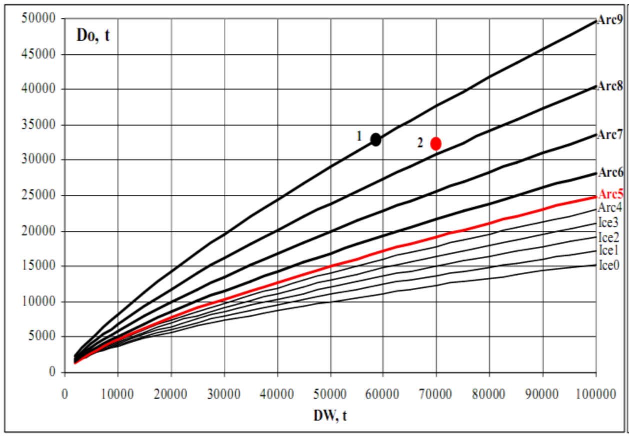

Fig. 7. Summary graph of relationships between light-ship weight and deadweight of tankers in all range of ice categories RMRS: 1 – estimate [Tarovik O., 2015] for gas-carrier Arc9; 2 – tanker "M. Ulyanov" Arc6

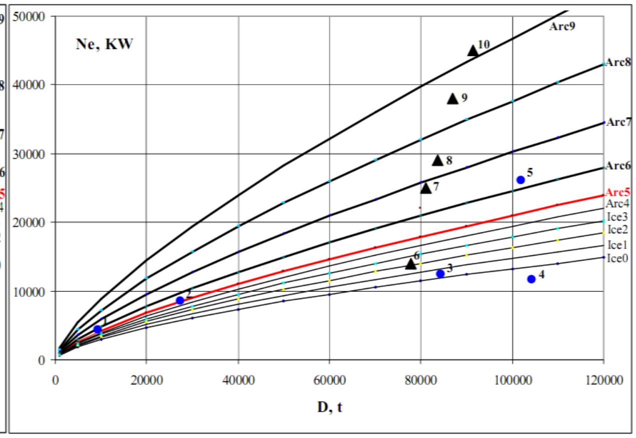

Fig. 8. Summary graph of relationships between power of the propulsion system and displacement of tankers in all range of ice categories: 1-5 – real tankers into class of RMRS; 6-10 – estimates [Tarovik O., 2015] for gas-careers (Ice0, Arc6 - Arc9)

The results of calculations using the formula [8] and comparison are shown in Figure 8. There are also positions of 5 tankers and estimates from work [Tarovik O., 2015] for 5 gas carriers. The designation - 5 in figure 8 refers to the mentioned tanker "M. Ulyanov" and shows that its power is close to that calculated for the category Arc6. Thus, the hulls of the tankers of this project are excessively heavier (Figure 7) or the power is understated. Comparison the resulting figures for other tankers with estimates [Tarovik O., 2015] for gas carriers shows good matching.

The correlations of the basic geometric characteristics of tanker hulls have been obtained and can be estimated using the formulas presented below. Length (m) depending on displacement (t) of tankers

$$L = 5{,}8905 \cdot D^{0{,}3215} \quad , R^2 = 0{,}89 \qquad \textbf{[9]}$$

The breadth of the ship (m), depending on the displacement (t) (Figure 9)

$$B = 1{,}1676 \cdot D^{0{,}2938} \quad , R^2 = 0{,}97 \qquad \textbf{[10]}$$

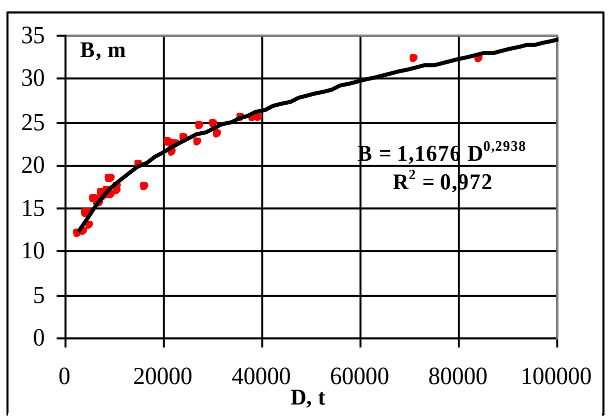

Fig. 9. Relation between displacement and breadth of tankers.

Draft (m), depending on the displacement (t) of tankers

$$d = 0{,}2344 \cdot D^{0{,}3587} \quad , \qquad R^2 = 0{,}77 . \qquad \textbf{[11]}$$

Depth (m), depending on the displacement (t) of the tankers

$$H = 0{,}2001 \cdot D^{0{,}4056} \quad , \qquad R^2 = 0{,}93 . \qquad \textbf{[12]}$$

Ice passability of tankers (m), depending on the propeller thrust (t) and the breadth (m), can be estimated using the formula in work [Kulesh V., 2018]

$$h = 0{,}45 \cdot \sqrt{P_e / B} \quad . \qquad . \qquad \textbf{[13]}$$

The obtained dependences make it possible to quickly evaluate the parameters of icebreakers and ice navigation tankers. It can be useful for comparing ships and feasibility studies of replenishing the fleet. In the latter case, the issues of safety and operational efficiency come to the fore, which were discussed earlier in work [Kulesh V., 2013], but are beyond the scope of this work.

References

Russian Maritime Register of Shipping. St. Petersburg., 2018. Rules for the classification and construction of sea-going ships.

Klimashevsky S.N., 2012. Calculation of ice passability of icebreakers and ice navigation ships, analysis of the shape parameters of the hull of these ships. Shipbuilding, №3, 11-15.

Tarovik O.V., 2015. Method for determining the masses of structures of ice reinforcement of transport ships at the early stages of design. Thesis of Cand. tech. sciences. FSUE Krylov State Research Center. St. Petersburg, 186.

Kulesh V.A., Lentarev A.A., Sharlay G.N., Motrich V.N., Moninets S.Yu.; Ed. A.A. Lentarev. - M, Morkniga, 2018. Exploitation of ships in polar waters: Textbook, 277.

Kulesh V., Ogay S., Voyloshnikov., 2013. M. Safety of Ships Navigation in ice and Operational Effectiveness. Proceedings of the Twenty-third International Offshore and Polar Engineering. Vol. 1. Anchorage, Alaska, USA, 1227-1234.

International Association for Hydro-Environment Engineering and Research
Supported by Spain Water and IWHR, China

24th IAHR International Symposium on Ice
Vladivostok, Russia, June 4 to 9, 2018

Double frequency radar system for field observation of ice condition

Hui Fu, Xinlei Guo, Kailin Yang, Tao Wang
State Key Laboratory of Simulation and Regulation of Water Cycle in River Basin, China
Institute of Water Resources and Hydropower Research, Beijing, China

The field measurement of the ice thickness and water depth distributions in a river, canal, or lake is one of the most important means of ascertaining and responding to an ice flood. A double-frequency radar system using frequencies of 100 and 1500 MHz radars was developed in the present study. The system was used to measure the ice thickness and water depths with 87 and 89 points, respectively, in the high-latitude Mohe section of the Heilongjiang River. Comparison of the measurements with those obtained by traditional drill-hole methods verified the accuracy of the proposed double-frequency radar system. The system was further used to measure the distribution of the ice thickness and water depth over a distance of 0.5 km in the Longdao Wharf section of the Heilongjiang River. The results were used to develop appropriate ice flood prevention methods. The high accuracy of the proposed double-frequency radar system promises to significantly improve the efficiency of prototype observations of ice thickness and water depth.
Keywords: Radar; Double frequency; Prototype measurement; Ice thickness; Water depth.

1. Introduction

Prototype field observation of the ice conditions of rivers, lakes, canals, and reservoirs is important to understanding the dynamic processes of ice and water and their coupling mechanism. It is also the basis for developing measures for preventing and mitigating ice disasters. Ice thickness and water depth are important parameters of such observations and their measurement methods can be generally divided into two types, namely, contact and non-contact measurements. Contact measurements include traditional drilling and the use of resistance heating lines and pressure sensors. These methods are considered to be the most reliable and have been in use for decades. However, in high-latitude areas, the temperatures during winter are generally about -30°C or lower, and the ice thickness is often more than 1 m, such as in the Heilongjiang River and Yellow River. In such areas the traditional ice thickness and water depth measurement methods have the disadvantages of low efficiency, low date volume, and high work intensity (Heil et al., 2006; Fu et al., 2010; Li et al., 2005; Huang et al., 2016). In recent years, Cui et al. (2015) have used the differences between the electrical resistance and temperature characteristics of air, ice, and water to partly overcome the disadvantages of traditional contact measurement methods. For example, they realized continuous contact measurement of the ice thickness and temperature gradient inside an ice layer through detection of the electrical resistance and temperature.

The non-contact measurement methods include sonar, satellite remote sensing, and ground-penetrating radar measurements. The equipment used for sonar ice condition measurement is the SWIP system produced by ASL Environmental Sciences. The system functions by transmitting and receiving ultrasonic pulse signals. It has the advantages of the ability to measure the ice thickness, water depth, and ice concentration(Marko and Jasek, 2008, 2010a, 2010b; Morse and Richard, 2009; Ghobrial et al., 2012, 2013). Satellite remote sensing survey is suitable for large-scale ice condition surveys, but is of limited accuracy (Helfrich et al., 2007; Hall et al., 2002). There has been continuous improvement in the accuracy of the ground-penetrating radar measurement method in recent years, with the technology offering the advantages of compactness, low cost, high efficiency, and applicability to large-scale ice condition measurements, among others. The method is currently in common use. Arcone (1987, 1991) conducted ice thickness measurements using an airborne ground-penetrating radar system, while Galley et al. (2009) applied the method to the thickness measurement of snow and ice in the estuary of the Churchill River using frequencies of 250 MHz and 1 GHz. Finlay et al. (2008) and Proskin et al. (2011) used a 500 MHz ground-penetrating radar to measure ice thickness, and a 120 MHz version to measure water depth. Holt et al. (2009) used a 50–250 MHz variable-frequency ground-penetrating radar to measure sea ice of thickness 1–7 m, and a 300–1300 MHz version to measure water of depth 0.3–1.0 m. Zhang et al. (2017) used a 200 MHz ground-penetrating radar to measure the ice thickness at the location of the Toudaoguai hydrological station along the Yellow River.

Although ground-penetrating radar systems are widely used for the measurement of ice thickness and water depth, the current single-frequency systems are incapable of accurate simultaneous measurement of ice thickness and water depth. This has prompted the development of a two-radar system that performs two measurements. However, such a system is not only subjected to greater workload, but there is also no guarantee of the measurement points of the ice thickness and water depth being exactly the same. The latter issue is a source of error in the ice condition measurements obtained by a two-radar system. To overcome the above problems, a double-frequency ground-penetrating radar system for the simultaneous measurement of ice thickness and water depth was developed in the present study. The system has a double-frequency ultra-wideband radar as its core component, and this is coupled with a high-precision Real-Time Kinematic (RTK) differential GPS positioning system for the real-time acquisition of the latitude and longitude coordinates of the measurement point.

2. Design principle

The basic principle of a ground-penetrating radar system is illustrated in Fig. 1. High-frequency short-pulse electromagnetic waves are transmitted into the ground from the transmitting antenna of the radar system placed on the ground. The waves encounter underground formations or targets of differing electrical properties and are reflected back to the ground surface where they are received by the receiving antenna of the radar system. Two-way travel time (t) in the measured medium can be calculated as follows (Galley et al, 2009):

$$t = \frac{\sqrt{d^2 + 4H^2}}{v} \qquad \textbf{[1]}$$

where H is the ice thickness or water depth, v is the propagation velocity of the electromagnetic waves in the measured medium, and d is the distance between the transmitting and receiving antennae of the radar system.

$$v = \frac{c}{\sqrt{\varepsilon}} \qquad \textbf{[2]}$$

where c=30 cm/ns, is the propagation velocity of the electromagnetic waves in a vacuum, and ε is the dielectric constant.

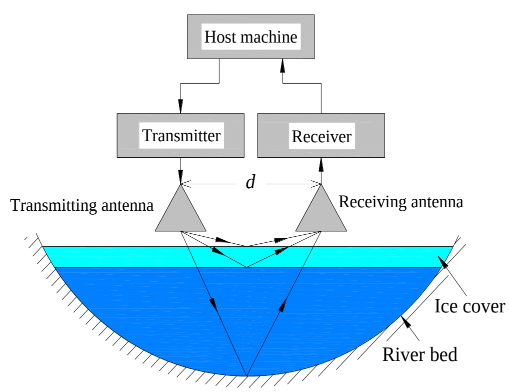

Fig. 1. Basic principle of the use of a ground-penetrating radar to measure ice thickness or water depth

The difference between the dielectric properties of different substances is the basis of the use of a ground-penetrating radar to detect a target medium. Commonly, the dielectric constant of air is 1, that of water is about 80, that of ice is 3-4, and that of sandstone (silt) is 5-30 (Davis and Annan, 1989). The differences among the dielectric properties of materials are thus obvious, and this enables the achievement of accurate measurements using a ground-penetrating radar. However, when using a ground-penetrating radar for depth measurement, there is a conflict between the measurement resolution and depth. A lower-frequency radar enables deeper measurement but affords a relatively low measurement resolution, resulting in decreased accuracy. The reverse is the case for a high-frequency radar, which has a limited measurement range in water. Hence, based on the characteristics of the thickness of river ice and water depth, a double-frequency radar system was developed, thus enabling the simultaneous measurement of ice thickness and water depth.

3. System composition and accuracy verification

3.1. System composition

The double-frequency radar system for ice thickness and water depth measurement is shown in Fig. 2. The system is 1.2 m long, 0.9 m wide, 0.4 m tall, weighs 15 kg, and can be used for field measurements by drawing by hand, a snowmobile, or hovercraft, among others (see Figs. 3 and 4). It main components are 1) a data acquisition and storage mainframe, 2) a double-frequency radar for measuring ice thickness and water depth, and 3) an RTK system for precise GPS coordinates measurement. With regard to performance, its ice thickness and water depth measurement ranges are respectively 0–6 m and 0–16 m, while its operating temperature range is -40–60°C.

Fig. 2. Radar system

Fig. 3. Manual measurement

Fig. 4. Drawing measurement

3.2. Verification of measurement accuracy of radar system

In December 2015 and April 2017, the stability, low-temperature performance, and measurement accuracy of the double-frequency radar system were verified by using it for ice thickness and water depth measurements in the Mohe section of the Heilongjiang River in the northernmost part of China (longitude 121°07–124°20′ E, latitude 52°10–53°33′ N) and the Togtoh section of the Yellow River (longitude 111°2′30″–111°32′ 21″ E, latitude 40°5′55″–40°35′15″), where ice dam disasters often occur.

The upper reaches of the Heilongjiang River are some of the coldest areas in China, characterized by an annual average temperature of below -2°C and a glacial period that lasts up to 6 months. Ice dams often occur along the 500 km riverway of the Heilongjiang River between the upper entrance of the Eerguna River and the entrance of the Huma River. Ice dams also occur very frequently in the vicinity of the Luogu River on Gucheng Island, Mohe County. The average temperature of the Luogu River is about -5°C, with the minimum winter temperature being as low as -59.5°C. The maximum ice thickness is above 2 m. Over the last 60 years covered by hydrographic records, the probability of an ice dam occurring along the river in a given year has been 40%. Ice dams that occurred in the Mohe County section of the Heilongjiang River generally measured 10–20 km, with backwater heights generally 6–8 m, and up to 13 m. Ice jams and ice dams also easily occurred in the Togtoh section of the Yellow River, where the annual glacial period lasts more than 3 months. These two areas were thus ideal for verifying the accuracy of the double-frequency radar system for ice thickness and water depth measurement (Yin et al., 2007) .

The ice thicknesses and water depths measured by the developed double-frequency radar system were compared with those measured by an L-type ice ruler (accuracy: 1 mm) and a pressure sensor (Type TDR-2050, RBR Ltd., Canada; accuracy: 0.05%), respectively.

3.2.1. Accuracy verification of radar system in Mohe County section of Heilongjiang River in 2015–2016

Form December 2015 to January 2016, an accuracy verification of the double-frequency radar system for ice thickness and water depth measurement was conducted in the Mohe County section of the Heilongjiang River for the first time. Twenty-one water depth contrast points and 19 ice thickness contrast points were set up for the measurements. The measurements obtained by the radar system, the L-type ice ruler, and the pressure sensor are shown and compared in Fig. 5. Under snow cover conditions, the average ice thickness measurement error of the radar system was 4.32%, with the errors at 12 of the 19 measurements points (i.e., 63.2%) being within 5%. The errors at four of the 19 measurement points (21.1%) were 5%–10%, while the errors at three points were over 10%, the maximum error being 12.44%. The average water depth measurement error was 3.97%, with the errors at 15 of the 21 measurement points (71.4%) being within 5%, while those at five points (23.8%) were 5%–10%. The significant errors at three of the ice thickness measurement points were due to accumulated ice jam, which is a multilayered discontinuous ice-air-ice structure. An ice jam has a complex structure, which alters the dielectric constant, resulting in the inapplicability of the dielectric constant of pure ice.

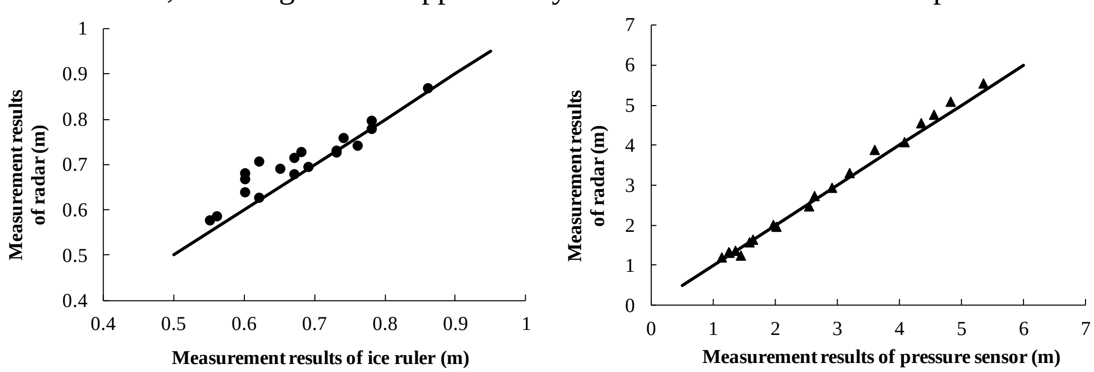

(a) Ice thickness **(b) Water depth**

Fig. 5. Comparison of the ice thicknesses and water depths in the Mohe County section of the Heilongjiang River measured by different methods in 2015–2016

3.2.2. Accuracy verification of radar system in Mohe County section of Heilongjiang River in 2017

In April 2017, a second round of tests were conducted in the Mohe County section of the Heilongjiang River using 58 ice thickness and water depth contrast points. The measurements results are shown in Fig. 6. As can be observed from the figure, the ice thickness and water depth measurements of the radar system are basically the same as those obtained by the traditional drill-hole methods using an L-type ice ruler and a pressure sensor, respectively. The average ice thickness measurement error of the radar system was 5.28%, with the errors at 46 of the 58 measurement points (79.3%) being less than 5%, while those at the 12 other measurement points (20.7%) were 5%–10%. The average water depth measurement error was 3.52%, with the errors at 24 of the 58 measurement points (41.4%) being within 5%, while those at 25 measurement points were 5%–10%, accounting for 58.6% of the total points.

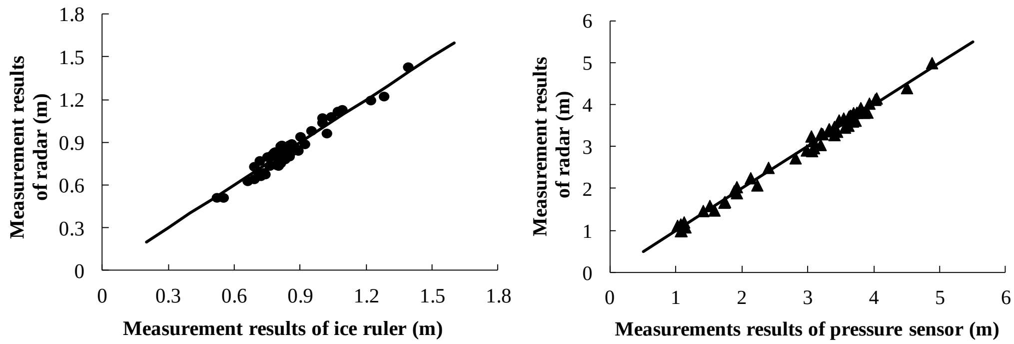

(a) Ice thickness **(b) Water depth**

Fig. 6. Comparison of the ice thicknesses and water depths in the Mohe County section of the Heilongjiang River measured by different methods in 2017

4. Application of developed radar system to prevention of ice flood

4.1. Prototype observation of Longdao Wharf section of Heilongjiang River

In April 2016, the developed double-frequency radar system was used to conduct a prototype observation of the ice thickness and water depth in the Longdao Wharf section of the Heilongjiang River in Mohe County, where ice flood disasters often occur. The observation covered a stretch of about 535 m. Because the RTK system was used to acquire the GPS coordinates in real time, the measurement results could be seamlessly integrated with a geographic information system (GIS). The specific measurement route is shown in Fig. 7. It can be observed from the measurement results shown in Fig. 8 that the ice thicknesses upstream and downstream of the Longdao Wharf section of the Heilongjiang River are respectively 0.9–1.0 and 0.8–0.9 m, while the corresponding water depths are about 3.0 and 6.0 m.

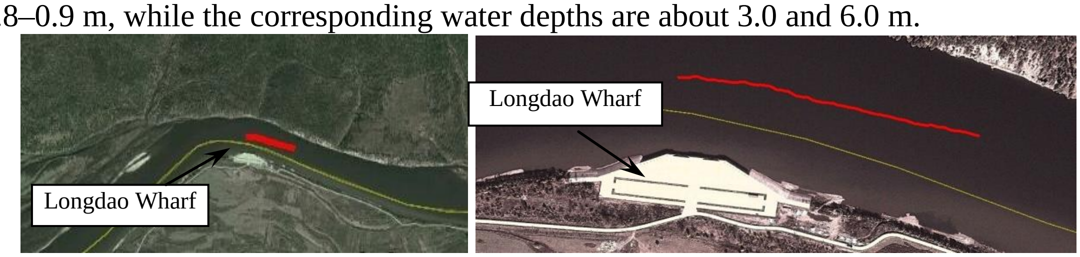

(a) Overall view **(b) Enlarged view**

Fig. 7. Satellite images of the measurement route along the Longdao Wharf section of the Heilongjiang River

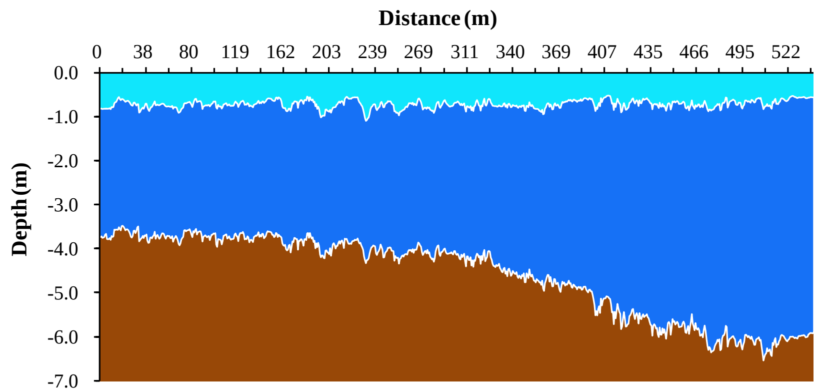

Fig. 8. Measured ice thickness and water depth along the Longdao Wharf section of the Heilongjiang River

Based on the measurement results, the frequent occurrence of ice dams in the Longdao Wharf section of the Heilongjiang River can be explained as follows: 1) The river curves in this section, resulting in increased resistance to ice flow. 2) Between upstream and downstream of the section, there is a significant decrease in the elevation of the river bed, resulting in a rapid increase in the water depth from 3.0 m to 6.0 m. This is accompanied by a 50% decrease in the water velocity, which causes accumulation of ice and the formation of an ice dam. The ice conditions upstream and downstream of the section substantiate the foregoing (see Figs. 9a and b). The upstream ice is very uneven and can be considered to form a narrow jam, whereas the downstream ice is very smooth and can be considered to form a juxtaposition jam.

(a) Surface of upstream narrow-jam ice (b) Surface of downstream juxtaposition-jam ice
Fig. 9. Ice jams in the Longdao Wharf section of the Heilongjiang River

Based on the ice thickness and water depth measurements, ice blasting was performed to prevent ice disasters in the Longdao Wharf section of the Heilongjiang River in 2016 and 2017 (see Fig. 10 and Fig. 11) (Liu et al., 2017). After the blasting, ice smoothly flowed through the section without accumulation. The developed double-frequency radar system thus enables the continuous acquisition of ice thickness and water depth data that can be used to obtain a better understanding of the reasons and nature of ice jams, and develop measures for preventing and dealing with ice disasters.

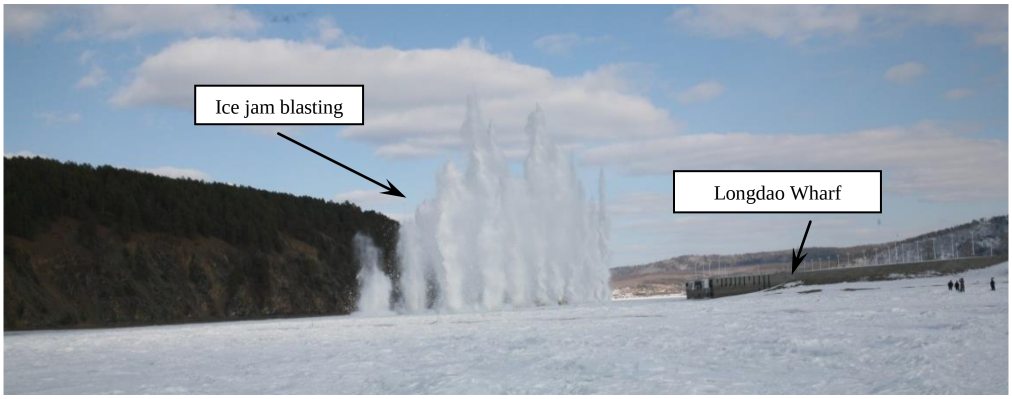

Fig. 10. Ice blasting to prevent ice disasters in the Longdao Wharf section of the Heilongjiang River

Before ice breakup **Ice breakup** **After ice breakup**

Fig. 11. Ice transportation situation in the Longdao Wharf section of the Heilongjiang River before and after ice blasting

5. Conclusion

A double-frequency radar system incorporating an RTK system for the prototype observation of ice thickness and water depth based on the differing dielectric constants of ice, water, and sediment was developed in this study. The system uses frequencies of 100 and 1500 MHz to measure water depth and ice thickness, respectively. In the demonstration of the developed system, a total of 87 ice thickness and 89 water depth measurement points were set up within the Mohe County section of the Heilongjiang River in the high-latitude part of China. Comparison of the measured ice thicknesses and water depths with those measured by an L-type ice ruler and pressure sensor showed that the average ice thickness and water depth measurement errors of the developed double-frequency radar system were about 4.93% and 3.84% respectively. Further, the ice conditions and the main reasons for the formation of ice dams in the Longdao Wharf section of the Heilongjiang River (about 0.5 km long) was examined using measurements obtained by the developed radar system. Based on the findings, ice blasting and the building of ice booms were suggested as measures for the prevention of ice floods.

Acknowledgments

This study was supported by the National Key Research and Development Program of China (grant numbers 2017YFC0405704, 2016YFC0400605 and 2016YFC0400603), the National Natural Science Foundation of China (grant number 51679263), and the IWHR Research & Development Support Program (grant numbers HY0145B912017, HY0145B642017 and SKL2017CGS04).

References

(Arcone, S.A., Delaney, A.J., 1987). Airborne river-ice thickness profiling with helicopter-borne UHF short-pulse radar. J. Glaciol. 33(115), 330-340.

(Arcone, S.A., 1991). Dielectric constant and layer-thickness interpretation of helicopterborne short-pulse radar waveforms reflected from wet and dry river-ice sheets. IEEE Trans. Geosci. Remote Sens. 29(5), 768-777.

(Cui, L.Q., Qin, J.M., Deng, X., 2015). Freshwater ice thickness apparatus based on differences in electrical resistance and temperature. Cold Reg. Sci. Technol., 119, 37-46.

(Davis, J.L., Annan, A.P., 1989). Ground-penetrating radar for high-resolution mapping of soil and rock stratigraphy. Geophys. Prospect. 37(5), 531-551.

(Fu, H.,Yang, K.L., Wang, T., 2010). Progress in the study of river ice hydraulics. South-to-North Water Trans. Water Sci. Technol. 2010, 8(1), 14-18.

(Finlay, P.I., Parry, N.S., Proskin, S.A., 2008). An overview of ice and bathymetric profiling using ground penetrating radar (GPR). Proceedings of the 19th IAHR International Symposium on Ice. International Association for Hydro-Environment Engineering and Research, pp.417-427 6-11 July 2008.

(Ghobrial, T.R., Loewen, M.R., Hicks, F.E., 2012). Characterizing suspended frazil ice in rivers using upward looking sonars. Cold Reg. Sci. Technol. 86(2), 113-126.

(Ghobrial, T.R., Loewen, M.R,. Hicks, F.E., 2013). Continuous monitoring of river surface ice during freeze-up using upward looking sonar. Cold Reg. Sci. Technol. 86(2), 69-85.

(Galley, R.J., Trachtenberg, M., Langlois, A., Barberm D.G., Shafai, L., 2009). Observations of geophysical and dielectric properties and ground penetrating radar signatures for discrimination of snow, sea ice and freshwater ice thickness. Cold Reg. Sci. Technol. 57(1), 29-38.

(Heil, P., 2006). Atmospheric conditions and fast ice at Davis, East Antarctica: a case study. J. Geophys. Res-Ocea. 111(C5), 101-112.

(Huang, W.F., Li, X.J., Jia, Q., Wang, N., 2016). Field observations and analysis of surface displacement of ice cover on reservoir . J. Hydraul. Eng. 47(12), 1585-1592.

(Helfrich, S.R., McNamara, D., Ramsay, B.H., et al., 2007). Enhancements to, and forthcoming developments in the Interactive Multisensor Snow and Ice Mapping System (IMS). Hydro. Process. 21(12), 1576-1586.

(Hall, D.K., Riggs, G.A., Salomonson, V.V., Digirolamo, N.E., Bayr, K.J, 2002). MODIS snow-cover products. Remote Sens. Environ. 83(1-2), 181-194.

(Holt, B, Kanagaratnam, P., Gogineni, S.P., Ramasami, V.C., Mahoney, A., 2009). Sea ice thickness measurements by ultrawideband penetrating radar: first results. Cold Reg. Sci. Technol. 55(1), 33-46.

(Li, Z.J., Han, M., Qin, J.M, Xi, Y.Z., Lu, P., 2005). States and advances in monitor of ice thickness change. Adv. Water Sci. 16(5), 753-757.

(Liu, Z.P., Wang, T., Guo, X.L., Fu, H., Yang, K.L, Peng, X.M., 2017). Breaking ice with explosive in Heilongjiang River. J. Hydraul. Eng. 48(2), 1-8.

(Marko, J.R., Jasek, M., 2008). Acoustic Detection and Study of Frazil Ice in a Freezing River during the 2004-2005 and 2005-2006 Winters. Proceeding of the 19th IAHR International Symposium on Ice. International Association for Hydro-Environment Engineering and Research, pp. 429-441 6-11 July 2008.

(Marko, J.R., Jasek, M., 2010a). Sonar detection and measurements of ice in a freezing river I: Methods and data characteristics. Cold Reg. Sci. Technol. 63(3), 121-134.

(Marko, J.R., Jasek,M., 2010b). Sonar detection and measurement of ice in a freezing river II: Observations and results on frazil ice. Cold Reg. Sci. Technol. 63(3), 135-153.
(Morse, B., Richard, M.A., 2009). Field Study of Suspended Frazil Ice Particles. Cold Reg. Sci. Technol. 55(1), 86-102.
(Proskin, S.A., Parry, N.S., Finlay, P., 2011). Applying GPR in Assessing the Ice Bridges, Ice Roads and Ice Platforms. Proceedings of the 16th Workshop on River Ice. CGU HS Committee on River Ice Processes and the Environment, pp.341-354 18–22 September 2011.
(Yin, F.Z., Li, G.F., Wang C.L., Xiao, D.F., 2007). Ice dam in Heilongjiang river. J. Heilongjiang Hydraul. Eng. Coll. 34(2), 23-26.
(Zhang, B.S., Zhang, F.X, Liu, Z.Y., Han, H.W., Li, Z.J., 2017). Field experimental study of the characteristics of GPR images of Yellow River ice. South-to-North Water Trans. Water Sci. Technol. 15(1), 121-125.

24th IAHR International Symposium on Ice
Vladivostok, Russia, June 4 to 9, 2018

Simulations on Ice-Structure Interaction in Shallow Water

Ida Lemström, Arttu Polojärvi, Jukka Tuhkuri
Aalto University, School of Engineering, Department of Applied Mechanics
P.O. Box 14300, FI-0076 Aalto, Finland
e-mail: ida.lemstrom@aalto.fi

The rubble pile forming during a shallow water ice-structure interaction process may ground. Grounding significantly affects the ice loading process and the magnitude of the ice loads induced on the structure. In this paper, we study this phenomenon and its effect on the ice loads based on numerical experiments on ice-inclined structure interaction. The simulations were performed using a two-dimensional combined finite-discrete method. The main interest of our study was to investigate the impact of the rubble pile grounding on the peak ice loads and on the ice loading process.

Introduction

Defining ice loads is essential when designing offshore structures for ice-covered seas. Many of these structures, such as bridges, lighthouses, wind turbines, offshore facilities, and ice barriers, are built in relatively shallow water, where the sea floor affects the ice loading process. This paper focuses on two-dimensional combined finite-discrete element method (2D FEM-DEM) simulations on ice loading processes on wide inclined shallow water structures. Earlier numerical studies on this topic has been carried out by Goldstein et al. (2013), while Karulin et al. (2007) conducted model model tests related to it. Furthermore, the process has been studied in full-scale by Marshall et al. (2011), Sudom and Timco (2009) and Timco and Wright (1999).

The paper describes how water depth, seabed angle, ice-structure friction and ice-bottom friction coefficients affect the horizontal global peak ice loads on an inclined structure. It also briefly studies how the ice loading process and the ice load distribution on the structure changes due to rubble grounding, which is likely to occur in shallow water. We start by describing our simulations and then present and discuss the results before concluding the paper.

Simulations

The 2D FEM-DEM code used to simulate the ice-structure-seabed interaction has been developed at Aalto University and it is described in detail in Paavilainen et al. (2009). The intact ice sheet is modelled using visco-elastic non-linear Timoshenko beam elements, which may fail in combined bending and shearing according to the cohesive crack model (Paavilainen et al., 2009). The interactions between the broken ice pieces are modelled using the discrete element method. The contact forces between the discrete elements are calculated based on an elastic-viscous-plastic normal force model and an incremental Mohr-Colomb tangential force model (Hopkins, 1992). The model has been validated against full- and model-scale data (Paavilainen et al., 2011; Paavilainen and Tuhkuri, 2012).

In the simulations here, an intact ice sheet was pushed with a constant velocity against an inclined rigid structure (see Figure 1). During the simulations, the initially intact ice sheet failed into separate ice blocks, which could interact with each other, the structure and the seabed. The main simulation parameters are presented in Table 1. The ice properties in the simulations were mostly based on Timco and Weeks (2010). In the simulations, the water depth D, the ice thickness h, the seabed angle β (in relation to horizontal, positive angle would be counterclockwise in Figure 1), the ice-structure friction μ_s and the ice-bottom friction μ_b were varied as shown in Table 1. For each of the set of variables, five simulations were run with varying initial vertical velocity of the free end of the ice sheet (maximum initial velocity was a fraction of mm s^{-1}). This variation in the initial velocity was enough to yield different ice-structure interaction processes for the five simulations with each parametrization. In total, 180 simulations were conducted for this study.

Figure 2 shows the global horizontal ice load F-records from two simulations with varying water depths. In the figure, F is plotted against the length L of the ice pushed against the structure. In order to remove peaks due to short impact loads, the data was filtered with a median filter using three neighboring values. The global peak horizontal load F of the two simulations are marked with a circle in the F-record. The snapshots in Figure 1 are from the peak load instants of the same simulations as in Figure 2.

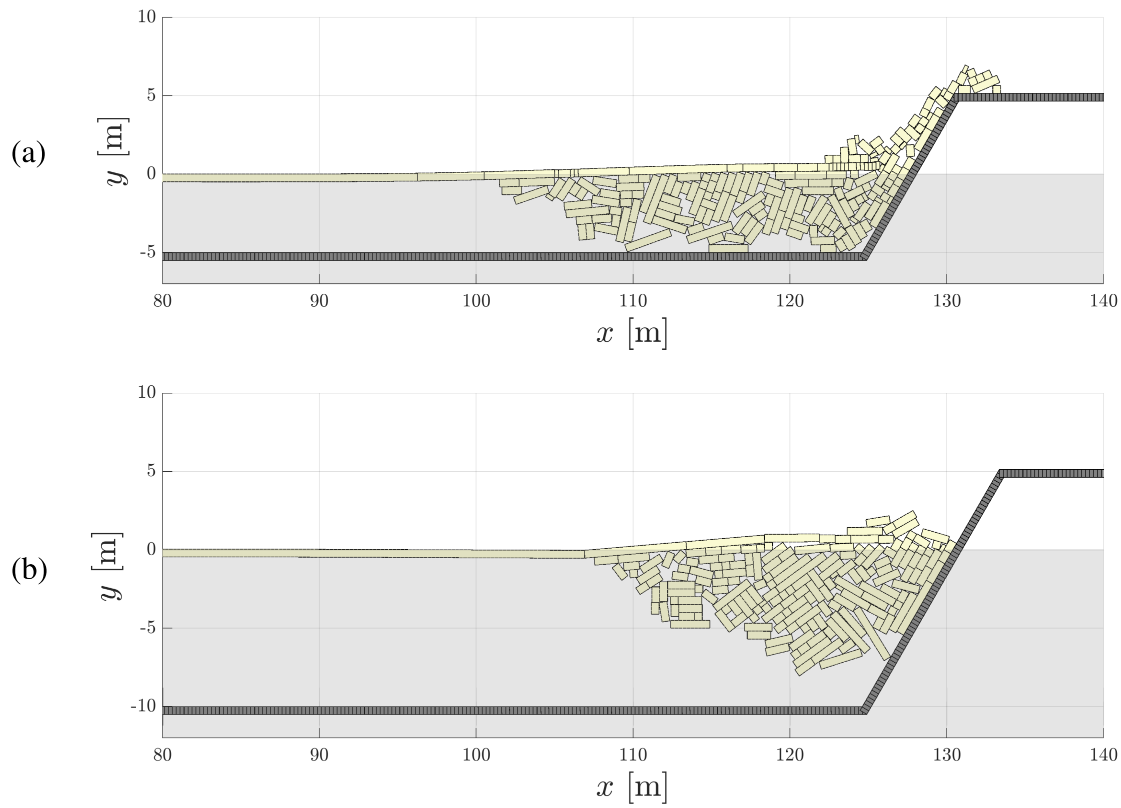

Fig. 1. Snapshots from two 2D FEM-DEM simulations on ice-structure interaction with water depths (a) 5 m and (b) 10 m. In these simulations, ice thickness h = 0.5 m, seabed angle β = 0°, ice-structure friction coefficient μ_s = 0.3 and ice-bottom friction coefficient μ_b = 0.3

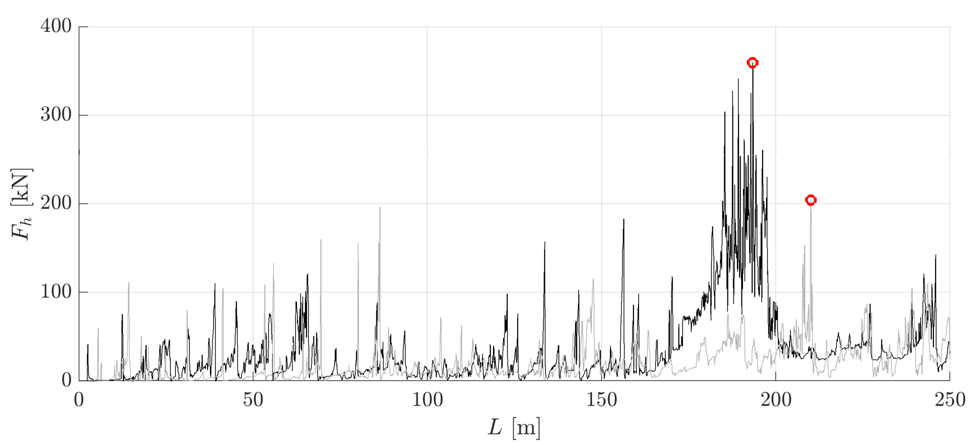

Fig. 2. Horizontal force F plotted against the length of the pushed ice L for two different simulations. The load records in black and gray are from simulations with water depths D = 5 m and D = 10 m, respectively. These cases are, respectively, presented in Figures 1a and b at the instants of the peak load F^{p} (marked with circles here). F^{p} in the case of $D = 5$ m was related to the overtopping event seen in Figure 1a.

Results

As mentioned above, this paper focuses on the effect of four parameters on peak ice load F^{p} values. The parameters of interest here were water depth D, seabed angle β, ice-structure and ice-bottom friction coefficients μ_s and μ_b, respectively. Table 2 illustrates the so-called factor effects of these parameters on F^{p} values. The factor effects estimate the mean change in F^{p} values as the parameter value is changed from the lower to the higher one, for example, the water depth D from 5 m to 10 m. Furthermore, Table 2 shows the 95% confidence intervals of the factor effects. A 95% confidence interval is the range of values, which with a 95% certainty contains the true mean value of the population.

Table 2 shows that from the studied parameters, μ_s had the greatest effect on F^{p} values. As μ_s increased from 0.1 to 0.3, F^{p} increased with approximately 130 kN. This is an about 30 % increase from the mean F^{p} value with $\mu_s = 0.1$. The 95% confidence interval for the factor effect of μ_s is clearly smaller than the factor effect itself (about 35 %). This implies that the range of the confidence interval for μ_s is acceptable, and the observation on its effect can be assumed to hold. Furthermore, the table shows that there is no noticeable factor effect for μ_b.

Also the water depth had a noticeable effect on the peak horizontal force as is further shown by Table 2. When the water depth increased from 5 m to 10 m, F^{p} values decreased with about 100

Table 1. Main simulation parameters of the 180 simulations of this paper.

	Parameter	Symbol	Unit	Value
General	Time step	Δt	s	$2.0 \cdot 10^{-5}$
	Element length	L_0	m	0.25
	Gravitational acceleration	g	m/s^2	9.81
	Ice sheet velocity	v_p	m/s	0.05
	Drag coefficient	d_c	-	2.0
Ice	Thickness	h	m	0.5, 1.25
	Effective modulus	E	GPa	4
	Poisson's ratio	v	-	0.3
	Density	ρ_i	kg/m^3	900
	Tensile strength	σ_f	kPa	600
	Shear strength	τ_f	kPa	600
Contact	Plastic limit	σ_p	MPa	2.0
	Ice-ice friction	μ_i	-	0.3
	Ice-structure friction	μ_s	-	0.1, 0.3
	Ice-bottom friction	μ_b	-	0.1, 0.3
Water	Density	ρ_w	kg/m^3	1010
	Depth	D	m	5, 10
Structure	Structure angle	α	$^\circ$	60
	Seabed angle	β	$^\circ$	0, 10, 20

kN. This observation is in line Polojärvi et al. (2016). The seabed angle also has an effect on F^{p} values, but this effect can only be observed when the sea bed angle changes from $\beta = 0°$ to $\beta = 10°$. A further increase in the angle does not affect the maximum load, as seen from the table.

Discussion

The results above indicate that the peak ice load F^{p} values increase as the water depth D decreases. Simultaneously, with decreasing D, the likelihood of rubble grounding increases (see Figure 1a). Hence, there is likely a grounding-induced change in the rubble pile-up process related to the increase in the F^{p} value. To study this change, we conducted a simple study on the load distributions on the structure by using equivalent force systems at the instant of F^{p}. (Force systems are equivalent, if they have the equal resultant force and torque about a given reference point.)

First, we replaced all horizontal contact forces F_i (both due to the intact ice and the ice blocks in the rubble) with their resultant F^{p}. Then we solved the y-coordinate y^{p} of the point of application of F^{p} by requiring that the torques induced by all contact forces F_i and resultant F^{p} were equal (only y^{p} is needed when just the horizontal load components are accounted for). In short, y^{p} for a peak load event of a simulation is solved from

$$\sum_{i=1}^{n} F_i y_i = F^{\mathrm{p}} y^{\mathrm{p}} \qquad \Rightarrow \qquad y^{\mathrm{p}} = \frac{\sum_{i=1}^{n} F_i y_i}{F^{\mathrm{p}}}, \tag{1}$$

where n is the number of contact forces acting on the structure and y_i is the point of application of the contact force F_i. A change in the y^{p} values, and in their scatter, with the change in D would be expected, if there was a noticeable change in the loading and rubble-pile up processes and in the load distributions on the structure.

Figure 3 presents the results of this analysis with both of the used h and D values. For the comparison of the data from the simulations with different h and D, we defined a normalized vertical distance $\hat{y}^{\mathrm{p}} = y^{\mathrm{p}}/D$ and normalized peak load $\hat{F}^{\mathrm{p}} = F^{\mathrm{p}}/\sqrt{h^3}$. In the latter, the normalizing factor $\sqrt{h^3}$ stems from a buckling model in Ranta et al. (2018). The buckling model is based on the observation, that the ice loads are limited by buckling of force chains (chain-like features of highly

Table 2. Factor effects and their 95% confidence intervals of water depth D, ice-structure friction μ_s, ice-bottom friction μ_b and seabed angle β on the peak horizontal force of the simulation. Base value refers to the mean peak load value with lower factor level.

Factor	Unit	Factor levels	Base value [kN]	Effect [kN]
D	m	$5 \rightarrow 10$	546	-105.4 ± 37
μ_s	-	$0.1 \rightarrow 0.3$	434	129.0 ± 35
μ_b	-	$0.1 \rightarrow 0.3$	457	21.2 ± 27
β	°	$0 \rightarrow 10$	540	-63.3 ± 47
β	°	$10 \rightarrow 20$	476	-13.0 ± 23

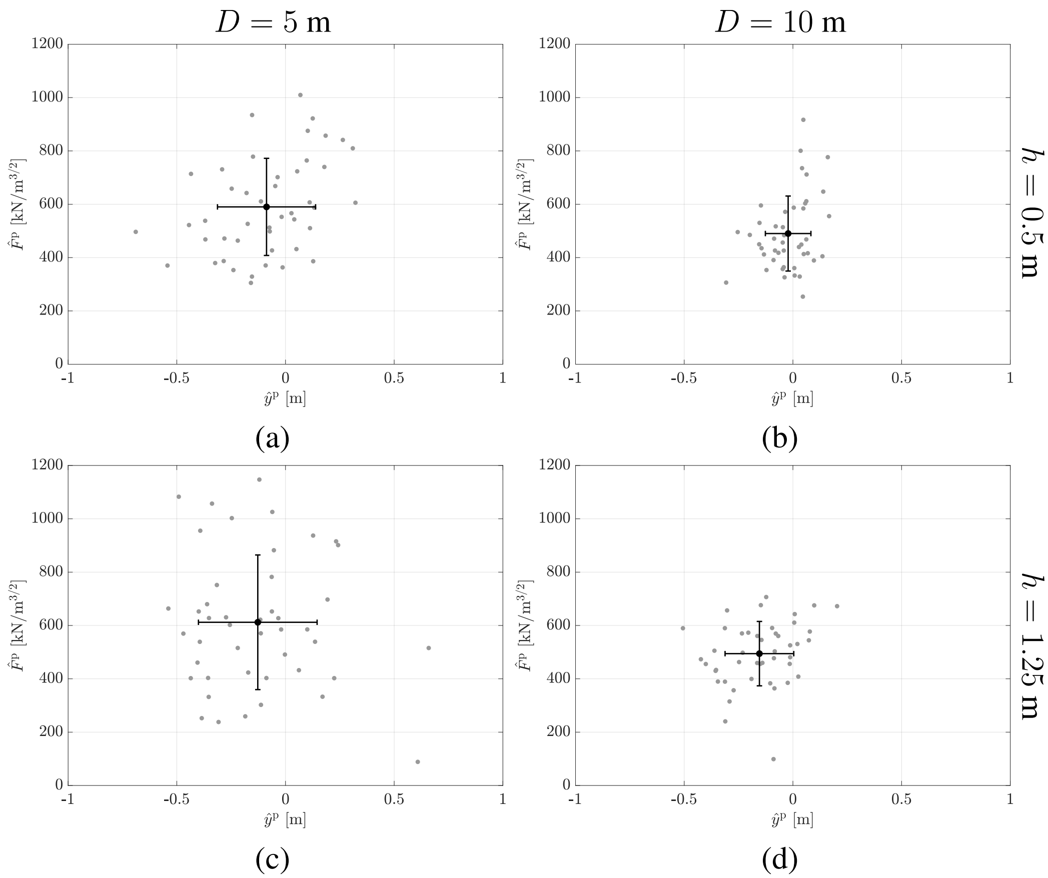

Fig. 3. The mean normalized peak horizontal forces $\hat{F}^{\mathrm{p}}$, plotted against the normalized distances from the waterline. The water depth and ice thickness in (a) was D = 5 and h = 0.5 m, in (b) was D = 10 m and h = 0.5 m, in (c) was D = 5 m and h = 1.25 m and in (d) was D = 10 m and h = 1.25 m.

compressed ice blocks transmitting the ice loads from the intact ice sheet to the structure). The mean values and the 95% confidence intervals for $\hat{F}^{\mathrm{p}}$ and $\hat{y}^{\mathrm{p}}$ data are also given in Table 3.

According to Figure 3 and Table 3, a decrease in water depth D affects y^{p} and, thus, the load distribution: the location of F^{p} appears to move downwards with decreasing D. Also, the stan-

Table 3. The mean normalized peak horizontal forces $\hat{F}^{\mathrm{p}}$, normalized distance from the waterline on the structure $\hat{y}^{\mathrm{p}}$ established according to the equivalent forces and systems and the 95% confidence intervals for different sets of water depths D and ice thicknesses h.

D [m]	h [m]	$\hat{F}^{\mathrm{p}}$ [kN/m$^{3/2}$]	$\hat{y}^{\mathrm{p}}$ [-]
5	0.5	590 ± 53	−0.087 ± 0.066
10	0.5	490 ± 41	−0.022 ± 0.031
5	1.25	612 ± 73	−0.128 ± 0.080
10	1.25	494 ± 35	−0.154 ± 0.046

dard deviation of $\hat{y}^{\mathrm{p}}$ increases significantly as D decreases, which is seen from Figures 3a-d. As D decreases, the probability of rubble grounding and large rubble piles in front of the structure increases. This tendency can be seen by a comparison of Figures 1a and b. An increased scatter in $\hat{y}^{\mathrm{p}}$ indicates that the grounded rubble piles in front of the structure transmit high loads to points on the structure, which are less well-defined than in the case of no grounding.

The normalization of the F^{p} data by the factor $\sqrt{h^3}$ works rather well, as the average $\hat{F}^{\mathrm{p}}$ values in Figures 3a-d are on the average in the same range. However, the scatter in the $\hat{F}^{\mathrm{p}}$ data increases with decreasing D. As mentioned above, the normalization factor $\sqrt{h^3}$ is based on the observation that buckling of the force chains is one of the main load limiting mechanisms for ice loads (Paavilainen and Tuhkuri, 2013; Ranta et al., 2018). Increasing scatter in normalized $\hat{F}^{\mathrm{p}}$ data with decreasing D suggests, that in shallow water the load limiting mechanism may differ from buckling. The increased scatter may, on the other hand, be due to grounded rubble supporting the buckling ice floes in a manner not accounted for by the buckling model.

Conclusions

This paper focused on two-dimensional combined finite-discrete element method simulations on ice loading processes on wide inclined shallow water structures. We showed how the water depth, seabed angle, ice-structure friction and ice-bottom friction coefficients affect the horizontal global peak ice loads. We also discussed the effect of rubble grounding on the ice loading process.

Acknowledgements

The authors acknowledge Business Finland, Aker Arctic Technology Inc., ABB Marine, Arctia Shipping, Technip Offshore Finland Oy, Suomen Hyötytuuli Oy, Finnish Transport Agency and Ponvia Oy for financial support through the ARAJÄÄ research-project.

References

Goldstein, R., Onishchenko, D., Osipenko, N., Shushpannikov, P., and Naumov, M. (2013). Grounded ice pile-up. 2D DEM simulation. In *Proceedings of the 22nd International Conference on Port and Ocean Engineering under Arctic Conditions*, Espoo, Finland.

Hopkins, M. (1992). Numerical simulation of systems of multitudinous polygonal blocks. Technical Report 92-22, Cold Regions Research and Engineering Laboratory, CRREL. 69 p.

Karulin, E., Karulina, M., and Blagovidov, L. (2007). Ice model tests of caisson platform in shallow water. *International Journal of Offshore and Polar Engineers*, 17(4):270–275.

Marshall, A., Jordaan, I., and McKenna, R. (2011). A two dimensional model of grounded ice rubble. In *Proceedings of the 11th International Conference on Port and Ocean Engineering under Arctic Conditions*, St. John's, Canada.

Paavilainen, J. and Tuhkuri, J. (2012). Parameter effects on simulated ice rubbling forces on a wide sloping structure. *Cold Regions Science and Technology*, 81:1 – 10.

Paavilainen, J. and Tuhkuri, J. (2013). Pressure distributions and force chains during simulated ice rubbling against sloped structures. *Cold Regions Science and Technology*, 85:157 – 174.

Paavilainen, J., Tuhkuri, J., and Polojärvi, A. (2009). 2D combined finite–discrete element method to model multi-fracture of beam structures. *Engineering Computations*, 26(6):578–598.

Paavilainen, J., Tuhkuri, J., and Polojärvi, A. (2011). Phenomena behind peak loads on inclined structure during a simulated ice pile-up process. In *The proceedings of the 21st International Conference on Port and Ocean Engineering under Arctic Conditions*, Montreal, Canada (electronic publication).

Polojärvi, A., Tuhkuri, J., Schneider, S., and Häsä, R. (2016). 2D FEM-DEM study on ice loads on shallow water structure. In *Proceedings of 23th IAHR International Symposium on Ice*, Ann Arbor, USA (electronic publication).

Ranta, J., Polojärvi, A., and Tuhkuri, J. (2018). Limit mechanisms for ice loads on inclined structures: Buckling. *Cold Regions Science and Technology*, 147:34 – 44.

Sudom, D. and Timco, G. (2009). Load reduction due to grounded ice rubble on the Molikpaq. In *Proceedings of the 20th International Conference on Port and Ocean Engineering under Arctic Conditions*, Espoo, Finland.

Timco, G. and Weeks, W. (2010). A review of the engineering properties of sea ice. *Cold Regions Science and Technology*, 60(2):107–129.

Timco, G. and Wright, B. (1999). Load attenuation through grounded ice rubble at Tarsuit Island. In *Proceedings of the 15th International Conference on Port and Ocean Engineering under Arctic Conditions*, Helsinki, Finland.

International Association for Hydro-Environment Engineering and Research

Supported by Spain Water and IWHR, China

24th IAHR International Symposium on Ice
Vladivostok, Russia, June 4 to 9, 2018

Review of wave-ice interaction studies

Hongtao Li, Raed Lubbad, Dennis Monteban
1) Sustainable Arctic Marine and Coastal Technology (SAMCoT),
Centre for Research-based Innnovation (CRI),
Norwegian University of Science and Technology, Trondheim, Norway
Høgskoleringen 7A, 7491 Trondheim, Norway
hongtao.li@ntnu.no

In the past several decades, sea-ice cover in the Arctic Ocean advances later than usual in the autumns and retreats earlier in the springs due to climate change. Concomitantly, total area of ice cover reduces and average ice thickness decreases. Consequently, open water areas increase and wave climate exacerbates. The interaction between waves and ice is strongly coupled and highly nonlinear. Ice refracts, attenuates, and scatters the waves. Reciprocally, waves bend, break and transport the ice around. From 1950s onwards, considerable scientific efforts have been made to study wave propagation in ice-covered waters. This paper summarizes the theoretical models, available in the open literature, for wave-ice interactions. Here, we discuss the assumptions, application ranges and limitations of these models. Moreover, we discuss the use of these theoretical models in operational wave models like WAVEWATCH III and present concerns about the parameterizations of the ice effects. Additionally, some applications of Synthetic Aperture Radar (SAR) remote sensing for studying ice effects on waves are presented. Finally, we identify the knowledge gaps in studying wave-ice interactions.

Introduction

Global climate change has complex implications for the Arctic Oceans. One example is the fiercer wave climates in the Arctic (Thomson et al., 2016). These severe waves are mainly attributed to the increasing fetch (Thomson and Rogers, 2014), which is a result of the reduction in the ice cover extent over the last decades (Vizcarra, 2018). Waves are one of the determinants for the spatial and temporal evolutions of sea ice. Waves break the ice (Kohout et al., 2016), transport it, accelerate its melting and induce collisions between the ice floes (McKenna and Crocker, 1990). On the other hand, ice refracts the waves (Squire et al., 1995), changes their dispersion relation, scatters and attenuates them (Wadhams et al., 1988).

In this study, we focus only on the effects of sea ice on the waves. Firstly, we list the different mechanisms that contribute to the wave attenuation. Then we provide a summary of the theoretical models, available in the open literature, for wave-ice interactions. Thereafter, we investigate the assumptions, application ranges and limitations of these models. Some of these models are recently implemented in the operational wave model WAVEWATCH III (henceforth WW3). In this paper, we also present a comparison of the implemented models along with other models. Additionally, Synthetic Aperture Radar (SAR) applications in studying change of waves due to ice are included. Finally, we discuss some of the knowledge gaps in the studies of wave-ice interaction.

Mechanisms to attenuate waves

Waves are attenuated due to scattering (Shen and Squire, 1998), turbulence (Shen and Squire, 1998, Squire and Shen, 1997), over-washing (Bennetts et al., 2015, Nelli et al., 2017), inelastic collisions between ice floes (McKenna and Crocker, 1992), inelastic bending of ice (thus fatigue) (Erber et al., 1993, Langhorne et al., 1998) and fracture of ice (Zhang et al., 2015). Among them, only wave scattering is a conservative process, which implies that the total wave energy is a constant, while forward-going wave energy reduces. The other processes, on the other hand, are all dissipative.

Theoretical models for wave-ice interaction

There have been intermittent efforts to develop theoretical models for wave-ice interaction since 1950s. These models are summarized in Table 1. The principal assumptions of each model are presented in the third and fourth columns (from left to right) of the same table. Abbreviations of these models, which are used in the remainder of this paper, are provided in the second column.

It is worthwhile to identify other assumptions of each model. WK neglects draughts of discrete mass points. GW model uses linear wave theory and thin elastic plate theory. Implicitly, plain strain state (see e.g. Logan (2012)) is assumed for the thin plate. Furthermore, small plate thickness relative to wavelength assumption leads to small normal stress in water depth direction that can be neglected. Lastly, it is assumed that the bottom of the plate is in contact with water all the time. Detailed derivation of resultant constitutive relation of the GW model can be found in Marchenko (2016). Regarding the viscous models (VSK, VSDD and VSLM), they are two-layer type models, in which the former two assume that the two layers are immiscible fluids. Same as for the GW model, all viscous and viscoelastic models assume upper layer always stays in contact with water. Note that Marchenko (2016) neglects inertia effect of ice when deriving the

VCM model. One common assumption of these models is small amplitude waves with small steepness.

Table 1. Wave-ice interaction models

Wave – ice interaction model		Ice	Water	Damping of wave energy from	Included in WW3	Selected wave number (Criteria)
Mass loading model	WK[1]	Discrete mass point	Inviscid	Scattering	No	2 real[12] (Geophysics relevant)
Thin plate model	GW[2]	Thin elastic plate	Inviscid	Scattering	No	2 real[13] (Geophysics relevant)
Viscous layer model	VSK[3]	Viscous fluid layer	Inviscid	Viscous damping in ice	No	1 complex (least damped wave mode)[3]
	VSLM[4]	Thin elastic plate	Viscous	Viscous damping in water	Yes[10]	1 complex
	VSDD[5]	Viscous fluid layer	Viscous	Viscous damping in ice and water	No	1 complex (closest to open-gravity wave with least attenuation)[14]
Viscoelastic model	VCWS[6]	Viscoelastic fluid layer (Voigt model)	Inviscid	Viscous damping in ice (linear dashpot)	Yes[10]	1 complex (closest to open-gravity wave with least attenuation)[6]
	VCFS[7]	Viscoelastic solid beam (Voigt model)	Inviscid	Viscous damping in ice (linear dashpot)	Yes[11]	2 complex (in first quadrant of complex plane)[15]
	VCRP[8]	Thin elastic beam	Inviscid	Damping forces due to vertical velocity of beam	No	2 complex (in first quadrant of complex plane)[15]
	VCM[9]	Viscoelastic solid (Maxwell model)	Inviscid	Viscous damping in ice (nonlinear dashpot)	No	1 complex (close to wave number of gravity wave)[16]

1. Weitz and Keller (1950), 2. Greenhill (1886) and Wadhams (1986), 3. Keller (1998), 4. Liu and Mollo-Christensen (1988), 5. De Carolis and Desiderio (2002), 6. Wang and Shen (2010), 7. Mosig et al. (2015), Li et al. (2015) and Fox and Squire (1994), 8. Mosig et al. (2015) and Robinson and Palmer (1990), 9. Marchenko (2016), 10. The WAVEWATCH III® Development Group (WW3DG) (2016), 11. Rogers (2017), 12. Squire et al. (1995), 13. Squire (1993) and Wadhams (1981), 14. De Carolis (2018), 15. Mosig et al. (2015), 16. Marchenko (2018).

Limitations of the theoretical models

WK fails to reproduce the progressive decay of waves, due to the lack of damping mechanisms in the ice-covered regions (see e.g. Squire et al. (1995)). In the GW model, viscous dissipation is absent. Thus the WK and GW models are applicable for sparse pancakes field and intact ice sheet, respectively (Zhao et al., 2015). The VSK and VSDD models are suitable for grease ice (Newyear and Martin, 1999, De Carolis and Desiderio, 2002). The VCWS model should, in principle, work for all the aforementioned ice types (Wang and Shen, 2010). The VSLM model appears to be more suitable for ice fields with high concentration (Liu et al., 1991). The VCFS model seems more applicable for low concentration ice fields (Squire, 2018), which is probably also true for the VCRP model.

The VSLM model adopts eddy viscosity to parameterize turbulence in the viscous boundary layer. Eddy viscosity is not measurable and it is usually used as tuning parameter to best-fit model results to field measurements (Liu et al., 1991). Undesirably, this parameter obtained from best-fit varies greatly for different field measurements. Similarly, the VCWS and VCFS models contain immeasurable quantities, i.e. equivalent viscosity and elasticity. Up to now, these two input model parameters are determined by inverse methods. Specifically, based on available measurements, they are estimated by minimizing the discrepancy between model results and corresponding measured quantities, such as total wave energy (Rogers et al., 2016), significant wave height (Li et al., 2017), wave attenuation coefficients (Li et al., 2015, Mosig et al., 2015) and complex wave number (Cheng et al., 2017). However, there are many limitations in using inverse method, such as possible interdependency among parameters, multiple solutions, measurement errors and low sensitivity of measurable output to input model parameters (Li et al., 2015). Another major limitation is that the roots selection criteria are not well defined, see Mosig et al. (2015) and Rogers et al. (2016) for VCWS and Collins et al. (2017) for VCWS and VCFS.

One common limitation of all available models is that they are based on linear theory, which implies that over-washing, rafting, ridging and collisions between ice floes are not accounted for explicitly. Owing to the utilization of linear wave theory, the above mentioned models only predict exponential attenuation (Squire, 2018). However, Squire (2018) and Kohout et al. (2014) found a distinct attenuation behaviour for large waves in western Arctic and Southern Ocean, respectively.

WW3 operational wave model

WW3 is a third generation spectral wave model that has been developed continuously to include wave-ice interaction effects (see The WAVEWATCH III® Development Group (WW3DG) (2016) and the sixth column of Table 1). The governing equation of this model is (presented here using the same concise form as in Cheng et al. (2017))

$$\frac{\partial E(f,\vec{x},\theta)}{\partial t}+\nabla_x \cdot c_g E(f,\vec{x},\theta)=(1-C)(S_{in}+S_{ds})+S_{nl}+CS_{ice} \qquad \textbf{[1]}$$

where $E(f,\vec{x},\theta)$ is the wave spectral density, f is the wave frequency, $\vec{x}$ is the spatial coordinate, θ is the wave propagation direction, t is time, c_g is wave group velocity, C is ice concentration, S_{in}, S_{ds}, S_{nl} and S_{ice} represent wind-wave interaction, wave energy dissipation due to white-capping, nonlinear interactions between different wave components and wave damping due to ice, respectively.

S_{ice} includes a dissipative term ($S_{ice,dis}$) resulting from friction and viscosity, and a conservative damping ($S_{ice,sc}$) induced by scattering (Zhao et al., 2015).

Comparisons of different theoretical models

Viscous and viscoelastic models for wave–ice interaction in principle address directly $S_{ice,dis}$ and c_g. $S_{ice,dis} = -2c_g k_i E$ (Rogers and Orzech, 2013), where k_i is the imaginary wave number. Both k_i and c_g can be obtained from the dispersion relations of these models. In contrast, WK and GW models conceptually deal with $S_{ice,sc}$ and c_g.

The viscoelastic models (VCWS, VCFS and VCRP) were compared by Mosig et al. (2015). They found that the dispersion relations of the VCFS and the VCRP models are analytically invertible for elasticity and viscosity. Hence, there is only one result of the inverse analysis for these models. Similarly, it is possible to show that the dispersion relation of VCM can be analytically inverted for the tuning parameter - creep constant. In contrast, the rheological parameter in the VCWS model can only be numerically found and non-unique solutions exist using the inverse analysis (Mosig et al., 2015).

Among all the previously mentioned models, only the VSLM model reproduces rollover. This phenomenon is a special wave attenuation behaviour, in which spatial wave attenuation coefficient increases first with frequency prior to decreasing steadily afterwards.

The theoretical models can be divided, based on their usage in real life, into two groups, i.e. 1) physics based models and 2) effective media continuum models (see Squire (2018) and references therein). The GW model belongs to first group, whereby physics are simulated to most extent for each solitary ice floe in ice field. Normally, the GW model is applied along with scattering theory to study wave attenuation and wave induced ice break-up (Kohout and Meylan, 2008, Dumont et al., 2011). Other models fall into the second category, where detailed physics are omitted and heterogeneous ice field is studied as a single entity. Effective media approach lumps together all attenuation mechanisms, scattering and dissipation, into effective viscosity. Nonlinear dissipation mechanisms such as collisions and ridging are accounted for in a linear manner in the second type model (Squire, 2018).

The comparisons of other features of the different models are summarized in Table 1. It is seen that only VCM includes a nonlinear term.

Mode-swap phenomenon inherited in VCWS model may explain the abrupt change of wave number profile with frequency, as shown in Figure 3 of Mosig et al. (2015), Figure 9 of Rogers et al. (2016) and Figure 7 of Collins et al. (2017). This behaviour was investigated extensively in Zhao et al. (2017). They found that outside the mode-swap region, gravity waves contribute most to the vertical motion. Following this, Cheng et al. (2017) selected the least damped propagating gravity wave. However, the efficiency of this root selection criterion should be further investigated. As demonstrated in Collins et al. (2017), the VCFS model displays similar discontinuity in the wave number profile.

Although the root finding criteria are not well-established yet, the VCFS and VCWS models have been implemented in WW3. The VCWS and the VCFS models together with the VSLM model that are embedded in WW3, awaits to be validated. To date, these models are not calibrated sufficiently against full-scale data for various ice types. This suggests that more field experiments including comprehensive ice property survey (such as ice thickness, elastic modulus and viscosity of ice, etc.) are needed (see e.g. Collins et al., 2017, Squire, 2018). In addition, concurrent and collocated measurements of wave height, wave period, wavelength and wave direction are necessary, in order to improve the calibration of these models. Recent progress in sensor technology makes it feasible, e.g. by applying stereo-imaging, SAR (see section 7 for details) and wave buoys in conjunction with marine radar (see Collins et al. (2017) and references therein).

As for WW3, many researchers questioned the current parameterization of S_{ice}, S_{ds}, S_{nl} and S_{in}. Li et al. (2017) questioned the validity of scaling down S_{in} and S_{ds} using fraction of open water. In addition to be suspicious of the current scaling of S_{in}, Rogers et al. (2016) claimed that present parameterization of S_{nl} in ice-covered waters requires in depth examination. Using physical arguments, Squire (2018) maintained that it is inappropriate to simply use ice concentration to scale S_{ice}. It can be seen that parameterizations of these parameters in WW3 are not resolved yet.

Apart from these issues, the debate on whether the rollover phenomenon does physically exist or not is still ongoing. Not all field studies report rollover and no laboratory experiment has yet captured this phenomenon (see Rogers et al. (2016), Li et al. (2017) and references therein). Although this question is not appropriately answered yet, researchers started to investigate the mechanisms, which contribute to this phenomenon. Wadhams et al. (1988) hypothesized that S_{in} and S_{nl} result in rollover. This is corroborated by study of Li et al. (2017) and references therein. However, little consensus is reached at this stage. Therefore, solid theoretical proof for the existence of rollover and lab test designed for this purpose are desired to understand the physical processes, which induce this behaviour.

SAR remote sensing used in ice-covered waters

Synthetic aperture radar (SAR) shows great potential for studying waves interacting with sea ice as it can be used day and night, independent of the weather and it covers large spatial areas. Wadhams et al. (1986) already mentioned the great potential SAR has and since then, SAR imagery was used to study wave parameter modulation in the marginal ice zone.

Some of the first spatial observations of ocean swell in sea ice by SAR were performed in the late 1980s during the Labrador Ice Margin Experiment (LIMEX). From the collected data, Liu et al. (1991, 1992) studied wave evolution in the marginal ice zone in terms of wave attenuation, refraction and dispersion. They found the characteristic rollover at high wave numbers from the

SAR-derived attenuation. Schulz- Stellenfleth and Lehner (2002) used ERS-2 SAR data to study wave damping of ocean waves by sea ice. A detailed theoretical analysis is provided, showing that the dominant wavelength and wave direction can be obtained. Wadhams et al. (2002) also used ERS-2 SAR data to study the wave-dispersion relation in frazil and pancake ice.

The quantitative analysis of SAR imagery in ice-covered regions could only provide an estimation of dominant wave direction and wavelength, until a study by Ardhuin et al. (2015) which estimated wave heights in sea ice in the presence of two ocean swell systems.

New operational satellites in service (e.g. Sentinel 1, TerraSAR-X) provide new opportunities to study the interactions of waves with sea ice due to their high spatial resolutions (e.g. Sentinel-1A wave mode products have a resolution of 4 m on the earth surface). Ardhuin et al. (2017) proposed an algorithm to determine elevation spectra and hence wave parameters. Their algorithm is supposed to work best when short waves are absent, i.e. beyond some tens of kilometers into the sea ice.

Gebhardt et al. (2016) utilized TerraSAR-X satellite scenes to analyze variations in peak wavelength of waves passing through marginal ice zone at the East coast of Greenland. They found an increase in peak wavelength, and the dispersion of waves is the same as in deep waters. Shen et al. (2018) used RADARSAT-2 SAR imagery for the same storm event and found that when waves travel into the marginal ice zone, the dominant wavelength increases, wave energy is attenuated and a shift in mean wave direction. Therefore, SAR imagery is consistent with in situ field observations and attenuation theory.

SAR imagery can provide wave information on a large scale, while in situ measurements provide limited spatial and finer temporal scale observations. A combination of these two provides a more detailed picture and shows great potential for studying wave-ice interactions. From SAR imagery, the dominant wavelength and wave direction can be determined in ice-covered oceans, while the retrieval of wave height is possible, though limited.

Conclusions

From this study, following conclusions are drawn:

1. The VSLM, VCWS and VCFS models appears to be the most desired models to simulate ice effects on ocean surface waves.
2. Large waves are attenuated differently from small and intermediate amplitude waves, which follow exponential attenuation law.
3. Wave mode selection criteria for the VCWS and the VCFS models urgently need improvement.
4. Ice property (such as viscosity, density and elastic modulus) and other oceanographic measurements (such as temperature and salinity profiles along water depth) are necessary to be measured in field campaign for studying wave propagation in ice cover.
5. Field and laboratory experiments are indispensable to conclude whether rollover physically exists and the mechanisms promote it.
6. Calibration and validation work is instrumental in ascertaining the fidelity of using the VSLM, VCWS and VCFS models in wave climate forecast in ice-infested waters.

7. Improved determination methodology for the tuning parameters, eddy viscosity used in viscous model, equivalent elasticity and viscosity, creep constant used in viscoelastic model, is required to reduce uncertainty in inverse analysis problem.

8. Exact effect of ice on S_{in}, S_{ds} and S_{nl} should be thoroughly examined.

9. Validation of scaling S_{ice} with ice concentration is required.

10. SAR remote sensing is an indispensable supplement to in situ measurements to provide a complete picture of the wave-ice interactions process.

11. SAR imagery from satellites can provide the dominant wavelength, wave direction and up to some extent wave heights in ice covered oceans.

Acknowledgement

The authors feel grateful towards the discussions with Knut Høyland, Aleksey Marchenko and Jens Olaf Pepke Pedersen. The authors wish to acknowledge the support from the Research Council of Norway through the Centre for Research-Based Innovation SAMCoT and the support from all SAMCoT partners.

References

Ardhuin, F., Collard, F., Chapron, B., Girard- Ardhuin, F., Guitton, G., Mouche, A. & Stopa, J. E. (2015). Estimates of ocean wave heights and attenuation in sea ice using the SAR wave mode on Sentinel- 1A. Geophysical Research Letters, 42, 2317-2325.

Ardhuin, F., Stopa, J., Chapron, B., Collard, F., Smith, M., Thomson, J., Doble, M., Blomquist, B., Persson, O., Collins, C. O. & Wadhams, P. (2017). Measuring ocean waves in sea ice using SAR imagery: A quasi-deterministic approach evaluated with Sentinel-1 and in situ data. Remote Sensing of Environment, 189, 211-222.

Bennetts, L. G., Alberello, A., Meylan, M. H., Cavaliere, C., Babanin, A. V. & Toffoli, A. (2015). An idealised experimental model of ocean surface wave transmission by an ice floe. Ocean Modelling, 96, 85-92.

Cheng, S., Rogers, W. E., Thomson, J., Smith, M., Doble, M., Wadhams, P., Kohout, A. L., Lund, B., Persson, O., Collins, C. O., Ackley, S. F., Montiel, F. & Shen, H. H. (2017). Calibrating a Viscoelastic Sea Ice Model for Wave Propagation in the Arctic Fall Marginal Ice Zone. Journal of Geophysical Research: Oceans [Online]. Available: http://dx.doi.org/10.1002/2017JC013275 [Accessed October 21, 2017].

Collins, C. O., Rogers, W. E. & Lund, B. (2017). An investigation into the dispersion of ocean surface waves in sea ice. Ocean Dynamics, 67, 263-280.

De Carolis, G. April 02, 2018 2018. RE: Questions regarding your paper - Dispersion and attenuation of gravity waves in ice: a two-layer viscous fluid model with experimental data validation. Type to LI, H.

De Carolis, G. & Desiderio, D. (2002). Dispersion and attenuation of gravity waves in ice: a two-layer viscous fluid model with experimental data validation. Physics Letters A, 305, 399-412.

Dumont, D., Kohout, A. & Bertino, L. (2011). A wave- based model for the marginal ice zone including a floe breaking parameterization. Journal of Geophysical Research: Oceans, 116.

Erber, T., Guralnick, S. & Michels, S. (1993). Hysteresis and fatigue. Annals of Physics, 224, 157-192.

Fox, C. & Squire, V. A. (1994). On the oblique reflexion and transmission of ocean waves at shore fast sea ice. Philosophical Transactions of the Royal Society of London A: Mathematical, Physical and Engineering Sciences, 347, 185-218.

Gebhardt, C., Bidlot, J.-R., Gemmrich, J., Lehner, S., Pleskachevsky, A. & Rosenthal, W. (2016). Wave observation in the marginal ice zone with the TerraSAR-X satellite. Ocean Dynamics, 66, 839-852.

Greenhill, A.-G. (1886). Wave motion in hydrodynamics. American Journal of Mathematics, 62-96.

Keller, J. B. (1998). Gravity waves on ice- covered water. Journal of Geophysical Research: Oceans, 103, 7663-7669.

Kohout, A., Williams, M., Dean, S. & Meylan, M. (2014). Storm-induced sea-ice breakup and the implications for ice extent. Nature, 509, 604.

Kohout, A., Williams, M., Toyota, T., Lieser, J. & Hutchings, J. (2016). In situ observations of wave-induced sea ice breakup. Deep Sea Research Part II: Topical Studies in Oceanography, 131, 22-27.

Kohout, A. L. & Meylan, M. H. (2008). An elastic plate model for wave attenuation and ice floe breaking in the marginal ice zone. Journal of Geophysical Research: Oceans, 113.

Langhorne, P. J., Squire, V. A., Fox, C. & Haskell, T. G. (1998). Break-up of sea ice by ocean waves. Annals of Glaciology, 27, 438-442.

Li, J., Kohout, A. L., Doble, M. J., Wadhams, P., Guan, C. & Shen, H. H. (2017). Rollover of Apparent Wave Attenuation in Ice Covered Seas. Journal of Geophysical Research: Oceans, 122, 8557-8566.

Li, J., Mondal, S. & Shen, H. H. (2015). Sensitivity analysis of a viscoelastic parameterization for gravity wave dispersion in ice covered seas. Cold Regions Science and Technology, 120, 63-75.

Liu, A. K., Holt, B. & Vachon, P. W. (1991). Wave propagation in the marginal ice zone: Model predictions and comparisons with buoy and synthetic aperture radar data. Journal of Geophysical Research: Oceans, 96, 4605-4621.

Liu, A. K. & Mollo-Christensen, E. (1988). Wave propagation in a solid ice pack. Journal of physical oceanography, 18, 1702-1712.

Liu, A. K., Vachon, P. W., Peng, C. Y. & Bhogal, A. (1992). Wave attenuation in the marginal ice zone during LIMEX. Atmosphere-Ocean, 30, 192-206.

Logan, D. L. (2012). A first course in the finite element method, Stamford, Conn, Cengage Learning.

Marchenko, A. Damping of surface waves propagating below solid ice. The 26th International Ocean and Polar Engineering Conference, 2016. International Society of Offshore and Polar Engineers.

Marchenko, A. 2018. RE: Question regarding your paper - Damping of surface waves propagating below solid ice. Type to LI, H.

Mckenna, R. F. & Crocker, G. B. (1990). Wave Energy and Floe Collisions in Marginal Ice Zones. In: MURTHY, T., PAREN, J., SACKINGER, W. & WADHAMS, P. (eds.) International Conference on Ice Technology. Downing College, Cambridge University, UK: Computational Mechanics Publications.

Mckenna, R. F. & Crocker, G. B. (1992). Ice- floe collisions interpreted from acceleration data during LIMEX ‘89. Atmosphere-Ocean, 30, 246-269.

Mosig, J. E., Montiel, F. & Squire, V. A. (2015). Comparison of viscoelastic- type models for ocean wave attenuation in ice- covered seas. Journal of Geophysical Research: Oceans, 120, 6072-6090.

Nelli, F., Bennetts, L., Skene, D., Monty, J., Lee, J., Meylan, M. & Toffoli, A. (2017). Reflection and transmission of regular water waves by a thin, floating plate. Wave Motion, 70, 209-221.

Newyear, K. & Martin, S. (1999). Comparison of laboratory data with a viscous two-layer model of wave propagation in grease ice. Journal of Geophysical Research: Oceans, 104, 7837-7840.

Robinson, N. J. & Palmer, S. C. (1990). A modal analysis of a rectangular plate floating on an incompressible liquid. Journal of Sound and Vibration, 142, 453-460.

Rogers, W. & Orzech, M. (2013). Implementation and testing of ice and mud source functions in WAVEWATCH III, NRL Memorandum Report. NRL/MR/7320-13-9462.

Rogers, W. E. (2017). Wave forecasting for the Marginal Ice Zone [Online]. Available: http://www.waveworkshop.org/15thWaves/index.htm [Accessed November 29 2017].

Rogers, W. E., Thomson, J., Shen, H. H., Doble, M. J., Wadhams, P. & Cheng, S. (2016). Dissipation of wind waves by pancake and frazil ice in the autumn Beaufort Sea. Journal of Geophysical Research: Oceans, 121, 7991-8007.

Schulz-Stellenfleth, J. & Lehner, S. (2002). Spaceborne synthetic aperture radar observations of ocean waves traveling into sea ice. Journal of Geophysical Research: Oceans, 107.

Shen, H., Perrie, W., Hu, Y. & He, Y. (2018). Remote Sensing of Waves Propagating in the Marginal Ice Zone by SAR. Journal of Geophysical Research: Oceans, 123, 189-200.

Shen, H. H. & Squire, V. A. (1998). Wave damping in compact pancake ice fields due to interactions between pancakes, Wiley Online Library.

Squire, V. A. (1993). A comparison of the mass-loading and elastic plate models of an ice field. Cold Regions Science and Technology, 21, 219-229.

Squire, V. A. (2018). A fresh look at how ocean waves and sea ice interact.

Squire, V. A., Dugan, J. P., Wadhams, P., Rottier, P. J. & Liu, A. K. (1995). Of ocean waves and sea ice. Annual Review of Fluid Mechanics, 27, 115-168.

Squire, V. A. & Shen, H. H. Ice floe collisions: a neglected attribute of wave dissipation in ice fields. The Seventh International Offshore and Polar Engineering Conference, 1997. International Society of Offshore and Polar Engineers.

The WAVEWATCH III® Development Group (WW3DG) (2016). User manual and system documentation of WAVEWATCH III® version 5.16, Tech. Note 329, NOAA/NWS/NCEP/MMAB, 329+ Appendices, Tech. Rep.

Thomson, J., Fan, Y., Stammerjohn, S., Stopa, J., Rogers, W. E., Girard-Ardhuin, F., Ardhuin, F., Shen, H., Perrie, W., Shen, H., Ackley, S., Babanin, A., Liu, Q., Guest, P., Maksym, T., Wadhams, P., Fairall, C., Persson, O., Doble, M., Graber, H., Lund, B., Squire, V., Gemmrich, J., Lehner, S., Holt, B., Meylan, M., Brozena, J. & Bidlot, J.-R. (2016). Emerging trends in the sea state of the Beaufort and Chukchi seas. Ocean Modelling, 105, 1-12.

Thomson, J. & Rogers, W. E. (2014). Swell and sea in the emerging Arctic Ocean. Geophysical Research Letters, 41, 3136-3140.

Vizcarra, N. (2018). Arctic sea ice maximum at second lowest in the satellite record [Online]. National Snow and Ice Data Center. Available: http://nsidc.org/arcticseaicenews/2018/03/arctic-sea-ice-maximum-second-lowest/ [Accessed March 29, 2018].

Wadhams, P. (1981). The ice cover in the Greenland and Norwegian Seas. Reviews of geophysics, 19, 345-393.

Wadhams, P. (1986). The seasonal ice zone. The geophysics of sea ice. Springer.

Wadhams, P., Parmiggiani, F. & De Carolis, G. (2002). The use of SAR to measure ocean wave dispersion in frazil–pancake icefields. Journal of physical oceanography, 32, 1721-1746.

Wadhams, P., Squire, V. A., Ewing, J. & Pascal, R. (1986). The effect of the marginal ice zone on the directional wave spectrum of the ocean. Journal of physical oceanography, 16, 358-376.

Wadhams, P., Squire, V. A., Goodman, D. J., Cowan, A. M. & Moore, S. C. (1988). The attenuation rates of ocean waves in the marginal ice zone. Journal of Geophysical Research: Oceans, 93, 6799-6818.

Wang, R. & Shen, H. H. (2010). Gravity waves propagating into an ice- covered ocean: A viscoelastic model. Journal of Geophysical Research: Oceans [Online], 115. Available: http://dx.doi.org/10.1029/2009JC005591 [Accessed September 04, 2017].

Weitz, M. & Keller, J. B. (1950). Reflection of water waves from floating ice in water of finite depth. Communications on Pure and Applied Mathematics, 3, 305-318.

Zhang, J., Schweiger, A., Steele, M. & Stern, H. (2015). Sea ice floe size distribution in the marginal ice zone: Theory and numerical experiments. Journal of Geophysical Research: Oceans, 120, 3484-3498.

Zhao, X., Cheng, S. & Shen, H. H. (2017). Nature of Wave Modes in a Coupled Viscoelastic Layer over Water. Journal of Engineering Mechanics, 143, 04017114.

Zhao, X., Shen, H. H. & Cheng, S. (2015). Modeling ocean wave propagation under sea ice covers. Acta Mechanica Sinica, 31, 1-15.

International Association for Hydro-Environment Engineering and Research

Supported by Spain Water and IWHR, China

24th IAHR International Symposium on Ice

Vladivostok, Russia, June 4 to 9, 2018

Simplified Model for Semi-Submersible Offshore Wind Turbine

Victor Flores Terrazas

Far Eastern Federal University

floresterrasas.v@students.dvfu.ru

In recent years there has been a growing interest in investigating offshore wind turbine structures and several different concept designs have been proposed. This work analyzes one such floating wind turbine concept design and its stability under loading from ice fields. Based from this analysis, a maximum allowable size of an ice field can be determined by using Russian standards. These calculations can be useful in deciding whether the design concept is suitable for operation under a determined arctic offshore area, given the specific conditions in the region.

1. Introduction

Due to the increasing interest in finding new ways of producing energy in a sustainable way, there has been a growing interest in developing technologies to harness offshore wind energy. Among the concept designs, there are some floating structures that offer certain advantages over fixed-bottom turbines, such as easier construction and installation and decommissioning. The design of a floating structure may be more complicated than a fixed-bottom turbine due to the hydrodynamics. Highly accurate simulations for these structures can be performed on a computer using specialized software. However, such software may not always be accessible to some users. This work presents a simplified method that uses a combination of readily available open source tools as well as licensed software that nowadays is widely used in many research centers, laboratories and academic institutions. In this work, a simplified model is introduced, based on dimensions and material properties of a concept of an offshore semi-submersible floating wind turbine (OFWT), proposed by the National Renewable Energy Laboratory. The turbine is assumed to be installed in ice-infested waters, where ice sheets and ice floes represent an operational hazard to the substructure of such OFWT. The analysis presented focuses on establishing a dimensional limit on the ice floe that the substructure can withstand, based on calculations of the Russian code SNiP to obtain a chart of varying floe area and thickness of the ice. This work considers the wind turbine model as a rigid body semi submerged in water. It is reported that offshore floating wind turbines have a larger allowable tilt than fixed-bottom offshore wind turbines (Bhattacharya, 2014). It has been suggested that a maximum allowable tilt of 10° (Huijs et al, 2014), which shall be considered as the main criteria for the stability analysis hereby presented.

2. Overview of offshore floating wind turbines

Most wind turbines nowadays are fixed to the seabed by a foundation, which can vary in design and function. The main engineering parameters used for designing a turbine foundation are the soil conditions and the loading on the turbine, such as the aforementioned wind loads, wave impact loads and, where applicable, ice sheet loads acting on the tower. The most common foundation-type substructures for offshore wind turbines can be categorized as: monopile, tripod, jacket, suction caisson and gravity based. Building and installing an offshore wind turbine can be a costly endeavor and it has been identified that its cost increases with respect to the water depth where it is installed. Thus, a floating substructure would be more cost effective for deep water projects.

Floating wind turbines are supported by a floating substructure and are typically very large structures, varying from 5,000 to 10,000 tons for 2 to 5-MW wind turbines. These types of structures offer feasibility for deep water projects, but they also have other advantages. They can be built onshore partially or in their entirety, and then transported to the installation site to be set in place. They also offer a degree of mobility when required. In the case where the structure needed to be moved, it can be done by transporting the structure without the need to completely dismantle the substructure. Likewise, these types of substructures can be more easily decommissioned, which affects the life cycle cost of the overall project.

The most common types of floating structures are ballast-stabilized spar-buoy, mooring line stabilized tension leg platform and buoyancy stabilized barge with catenary mooring lines. Floating wind turbines have six degrees of freedom (heave, surge, sway, yaw, pitch and saw) and they can be excited by wave, wind, ocean currents and ice loads (where applicable). They offer the key advantage that it can be assembled and commissioned near shore and transported afloat to the installation site.

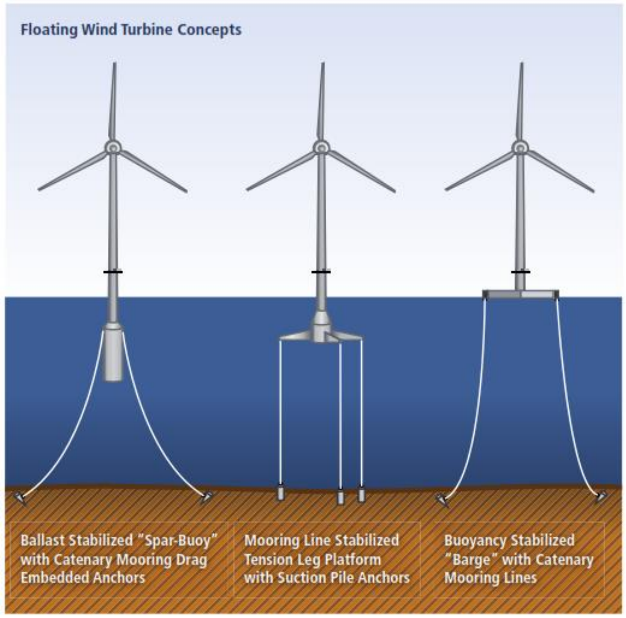

Fig. 1. Typical floating wind turbine designs (Edenhofer et al., 2011).

A semisubmersible substructure offers stability in heave following Archimedes Law, by balancing the total weight of the structure with the buoyancy force. Pitch and roll motions are stabilized by the action of restoring moments, which depend on the surface area of each column and the distance between them. The yaw, surge and sway are stabilized by the use of mooring lines, which maintain the stability of the system while allowing slowly varying motions (Karimirad, 2014).

3. Description of the model

The OC4 Semisubmersible Wind Turbine Model

The model selected for this analysis is largely based on the Offshore Code Comparison Collaboration Continuation (OC4) Phase II model. The OC4 was a code-to-code comparison collaboration led by the National Renewable Energy Laboratory in the U.S.A., whose active participants were laboratories and research centers from different countries. The goal was to run code simulations using different approaches to analyze the same structure to have a good point of comparison. This project involved the modeling of a semisubmersible floating offshore wind system developed for the DeepCwind project, which is a U.S.-based project aimed at generating field-test data for use in validating floating offshore wind turbine modeling tools (Jonkman et al, 2009). Thus, selecting this model for the present work is appropriate in order to compare the results with further research performed on this particular floating structure concept. The main characteristics of the wind turbine and substructure defined by the NREL are summarized in (Jonkman et al, 2009) and (Robertson et al, 2014). Based on the physical dimensions and the mechanical and material properties provided by the NREL, a model can be constructed using Computer Aided Design tools.

Description of the simplified model

The turbine can be modeled using finite element method (FEM) analysis software such as ANSYS or ABAQUS. The simplified model consists of a piece-wise approach. Thus, each of the loads needs to be separately calculated using different tools. The proposed model is represented in Figure 2.

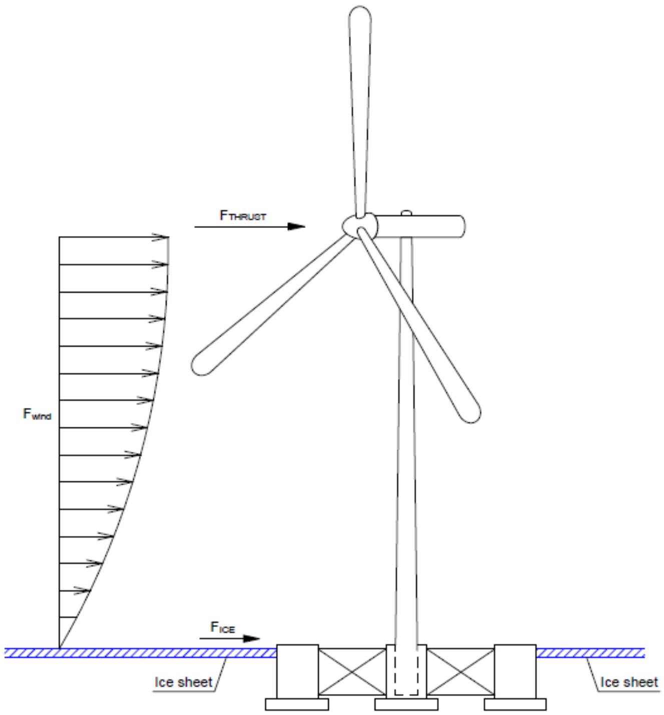

Fig. 2. Simplified wind turbine model.

The simplified turbine can be modeled using finite element method (FEM) analysis software such as ANSYS or ABAQUS. The model does not include the blades on the rotor but includes all other specifications as defined in (Jonkman et al, 2009) and (Robertson et al, 2014). The loads will then be calculated separately and included in the FEM analysis software. The main steps for the simplified model are shown in the flow chart in Figure 3.

4. Loads

For an elastic multi-body system, the structure may be divided into several bodies (Karimirad, 2012). Since the goal of the analysis is the stability of the structure, the structure is modeled as a single rigid body. The main loads are then modeled and applied to the structure. It is also assumed that during ice interaction, the structure follows the dynamics of a floating structure, but does not experience wave loads, due to the ice sheet preventing surface waves to exert any load on the splash zone of the structure. The simulation ran for 160 seconds. During the first 101 seconds, no loads were applied in order to allow for the structure to find its natural flotation point. At $t = 101\ s$, the wind loads and a horizontal load were applied as described below.

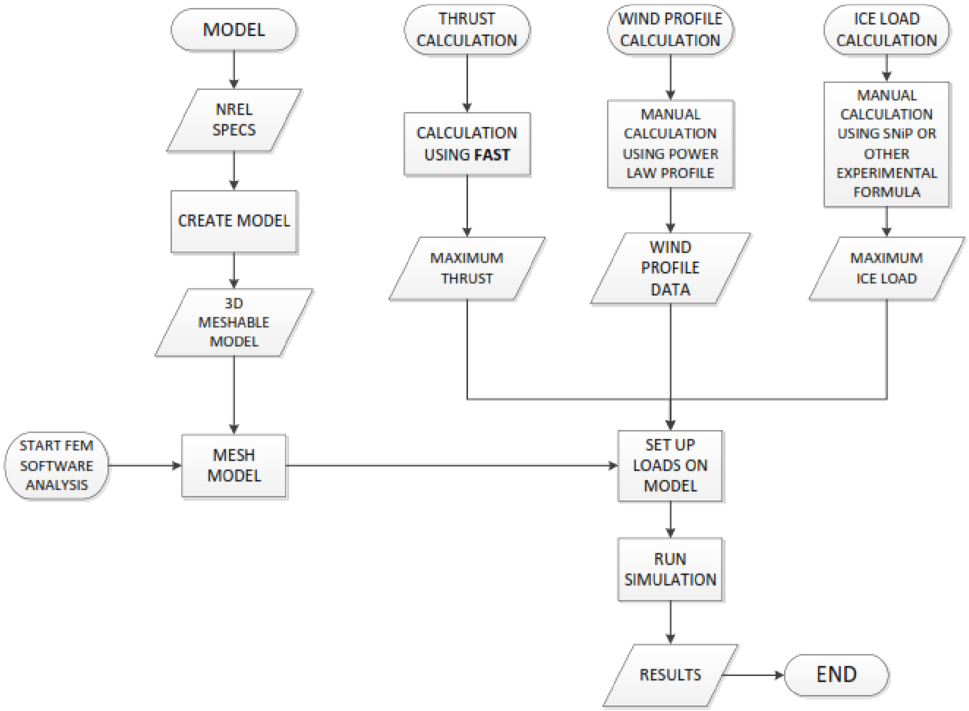

Fig. 3. Flow diagram for model construction.

Wind Loads

The wind loads applied to the model correspond to a uniform pressure corresponding to a 8 m/s wind velocity, which is within the working wind speed condition of the NREL turbine (Jonkman et al, 2009); a thrust force applied at the axis of the rotor, equivalent to the total wind force on the rotating blades, as per the blade element method theory. The thrust force was obtained by using NREL's code FAST (NWTC Information Portal), for a loading case of the aforementioned floating structure, under uniform wind speeds of $8\ m/s$, without ice loading, as a baseline load. The results of the rotor thrust are reported in Figure 4. The maximum thrust load acting on the rotor axis was found to be $582\ kN$, and this load was modeled as a concentrated load in ABAQUS.

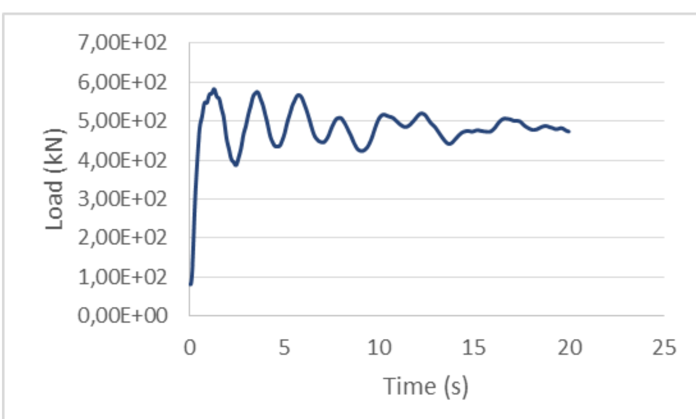

Fig. 4. Rotor thrust obtained from FAST.

An arbitrarily selected horizontal pressure applied at one of the floating columns on the substructure. The wind pressure p_w was obtained by using the load caused by a uniform wind pressure in (Chandrasekaran, 2016), by the formula:

$$p_w = \frac{1}{2}\rho_{air}C_w v^2$$

Where the air density ρ_{air} is $1.25\ kg/m^3$; the wind pressure coefficient is taken to be 0.95 and the wind velocity v is $8\ m/s$. The resulting uniform load was $38\ Pa$.

Horizontal Loads

A horizontal load was applied normal to one of the flotation columns. The magnitude of the load was arbitrarily chosen for each simulation run and it was applied gradually as a uniformly increasing load during a period of 10 s, after which it underwent an instantaneous unloading a subsequent uniform loading cycle for the next 10 s. This behavior corresponds to a frequency lock-in of a dynamic ice loading as described in (ISO, 2010).

5. Results

Determination of maximum ice load

Several simulations were run using a FEM software. In each simulation, a different ice load pressure was applied to the floating column, and the final maximum deflection of the tip of the hub was obtained. The wind loads on the tower and the rotor hub axis were identical at every run. Figure 5 shows the rotational displacement for each different load applied. The load was applied as a uniformly increasing loading cycle for each time step of 10 seconds, where unloading occurred and the load was applied again up until the load of each run. It was found that the maximum allowable load applied is $1.68x10^6\ MN$. At a load of $1.8\ MN$ the rotation was more than the allowable rotational displacement of 10° (Huijs et al, 2014).

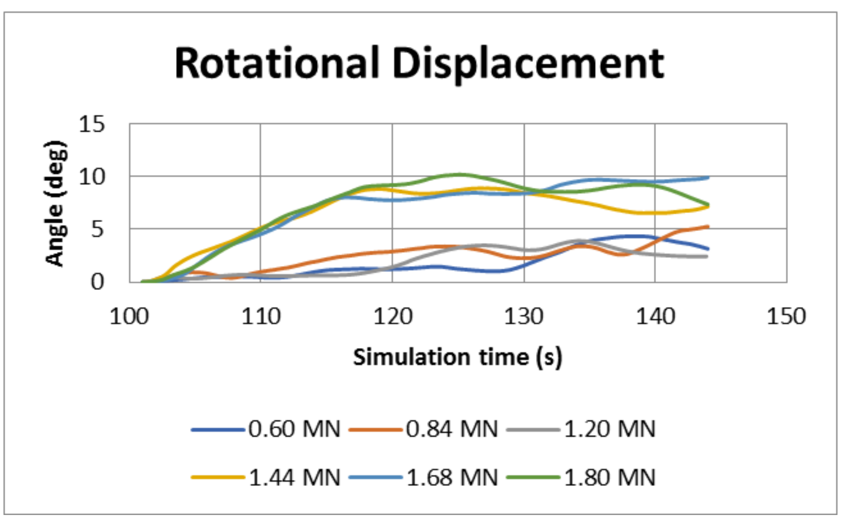

Fig. 5. Angle of rotational displacement for each loading case.

6. Conclusions

The present work presents an alternative for the analysis of the semisubmersible offshore wind turbine model proposed by the NREL. It is assumed that the model can be analyzed by breaking it down to fundamental models, which are easier to analyze separately. This method is proposed as a preliminary estimate of the behavior of the floating structure. Based on these analyses, early adjustments can be made to the concept. It is suggested that this method is used mainly as an indication of the order of magnitude of the parameters investigated. The results show the maximum horizontal load that it can withstand given the described conditions.

References

Bhattacharya, Subhamoy (2014). "Challenges in design of foundations for offshore wind turbines." Engineering & Technology Reference 1.1.

Chandrasekaran, Srinivasan (2016). Dynamic analysis and design of offshore structures. Springer.

Edenhofer, Ottmar, et al., eds (2011). *Renewable energy sources and climate change mitigation: Special report of the intergovernmental panel on climate change*. Cambridge University Press.

Huijs, Fons, Rogier de Bruijn, and Feike Savenije (2014). "Concept design verification of a semi-submersible floating wind turbine using coupled simulations." Energy Procedia 53 (2014): 2-12.

Ice Engineering - Engineering and Design (EM 1110-2-1612). Place of publication not identified: U.S. Army Corps of Engineers, n.d.. Internet resource.

ISO-19906 (2010). "19906: Petroleum and Natural Gas Industries–Arctic offshore structures." International Organization for Standardization, Geneva.

Jonkman, Jason, et al (2009). Definition of a 5-MW reference wind turbine for offshore system development. No. NREL/TP-500-38060. National Renewable Energy Lab.(NREL), Golden, CO, United States.

Karimirad, Madjid, and Torgeir Moan (2012). "A simplified method for coupled analysis of floating offshore wind turbines." Marine Structures 27.1: 45-63.

Karimirad, Madjid (2014). Offshore energy structures: for wind power, wave energy and hybrid marine platforms. Springer.

NWTC Information Portal (FAST). https://nwtc.nrel.gov/FAST. Last modified 04-January-2018; Accessed 26-March-2018

Robertson, Amy, et al (2014). Definition of the semisubmersible floating system for phase II of OC4. No. NREL/TP-5000-60601. National Renewable Energy Laboratory (NREL), Golden, CO.

SNiP 2.04.06-82 (1996). “Loadings and Influences On Hydraulic Engineering Structures (wave, ice and from courts)”, Moscow: Stroiizdat.

International Association for Hydro-Environment Engineering and Research
Supported by Spain Water and IWHR, China

24th IAHR International Symposium on Ice
Vladivostok, Russia, June 4 to 9, 2018

Method of Calculating the Ice Cover Parameters, Creating a Limit Ice Load on Marine Engineering Structures

Egor E. Pomnikov, Tatiana E. Uvarova, Anton A. Zverev
Offshore and Structure Mechanics Department, School of Engineering Far Eastern Federal University, 8 Sukhanova St., Vladivostok, Russia, 690090
pomnikov.ee@dvfu.ru
uvarova.te@dvfu.ru
zverev.aa@students.dvfu.ru

The main factor affecting the operating conditions and reliability of marine engineering structures is the ice regime of the sea area and as a result, ice loads and impacts on structures. Recently, the problem of assessing ice impacts on the offshore structures is one of the most important in the world. The article deals with a new approach to the assessment of the parameters of the ice cover, which allows ensuring the normal (safe) operation of the structure in ice conditions.
The aim of the work is to develop a methodology for calculating the parameters of the ice cover, namely the thickness and area of the ice formations that create the limit ice load on marine engineering structures, using the example of calculating for floating wind turbine.

Introduction
The relevance of the research topic is necessitated by the need to assess the parameters of the ice cover, allowing ensuring the normal operation of marine engineering facilitiesю The results of the research make it possible to solve the following problems:
- Definition of ice cover parameters for the limit ice load calculated for the structure;
- Determination of limit ice conditions for the safe operation of structures in the Arctic and subarctic seas;
- Choice site of installation for the structure, where the parameters of the ice cover does not exceed the limit ice load (which is very important for floating drilling platforms and vessels operated by the Arctic and subarctic seas);
- Characterization ice conditions to justify the application of the ice management method.

The solution of this problem is especially important for floating drilling rigs (platforms) and drilling vessels that are not designed for operation in severe ice conditions. Determination of the limit ice cover parameters, corresponding to normal operation for this type of facilities, allows determining the periods of safe operation of these facilities in ice conditions, to assess the possibility of extending these lifetimes by applying the ice management method.

Method of calculating the ice cover parameters for limit ice load
Method for estimating the ice cover parameters, creating a limit ice load on the structure, consists of the following stages.

1. Creation of the model of the structure
At this stage, the type and construction of the structure is determined and its design model is created.

2. Estimation of design loads on the structure.
The purpose of this calculation is to collect the loads acting on the structure. These loads are deterministic

3. Assessment of the maximum possible horizontal load acting on the structure
The purpose of this calculation is to determine the maximum horizontal load on a structure operating in the limiting state. The criterion of the limiting state for the structure is determined by the calculation purposes. For example, for fixed structures, this may be a criterion for the limiting state of the foundation soil, for floating drilling platforms and vessels - the limit riser deflection angle from the vertical position etc.

4. Assessment of the ice covers parameters for the limit the ice load.
The purpose of the calculation is to determine the ice floe parameters (ice thickness, area, drift velocity) for limit ice load calculated at stage 3.

The application of this method is shown on the example of determination of limit ice floe size for the stability of an offshore semi-submersible wind turbine.

Stage 1. Creating a model of the structure

1.1 Description of the construction of the structure
The reference design was that of a tri-floater semi-submersible substructure proposed by the National Renewable Energy Laboratory - NREL (Figure 1). The main characteristics of the wind turbine and substructure defined by the NREL are summarized in (Jonkman et al, 2009)

and (Robertson et al, 2014). Based on the physical dimensions and the mechanical and material properties provided by the NREL, a model can be constructed using Computer Aided Design tools.

1.2 Description of the design scheme of the structure

The turbine can be modeled using finite element method (FEM) analysis software such as ANSYS or ABAQUS. The simplified model consists of a piece-wise approach. Thus, each of the loads needs to be separately calculated using different tools. The proposed model is represented in Figure 2.

1.3 Direction of the maximum horizontal load

In the example, the maximum horizontal force is assumed to be the ice load. Therefore, direction and the point of application of the maximum horizontal force corresponds to the point of application of the ice load, and must be taken below the calculated water level by 0.25 hc, where hc – thickness of ice

Stage 2. Estimate of design loads for the structure.

The main loads are modeled and applied to the structure. There are wind loads, that are considered two loads: wind pressure and rotor thrus, and was calculated by Victor Flores Terrazas (2018). In this case, the horizontal load corresponds to the ice load applied at the level of the action of the ice cover and is a variable (Figure 2)

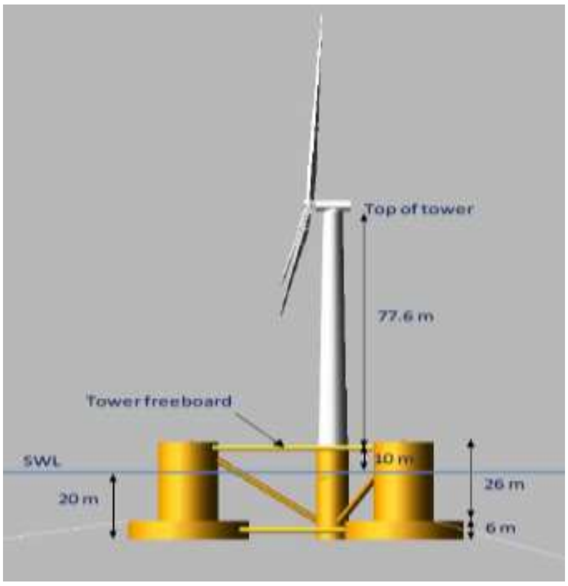

Fig. 1. The semisubmersible offshore wind turbine model.

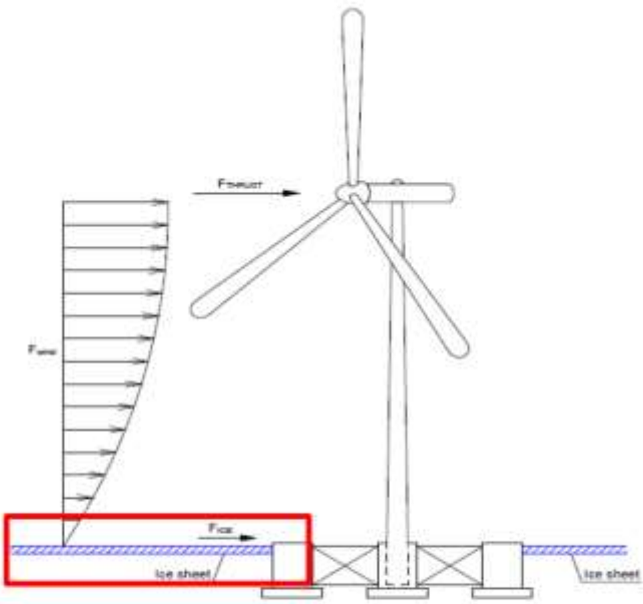

Fig. 2. The theoretical framework

Stage 3. Assessment of the maximum possible horizontal load acting on the structure

Purpose of the calculation is to determine the maximum horizontal load for the structure and determined according to the criterion of the maximum deflection of the tip of the hub from the vertical position at which normal operation conditions are satisfied. The allowable rotational the tip of the hub from the vertical position taken 10° (Huijs et al, 2014).

Several simulations were run using a FEM software. In each simulation, a different ice load pressure was applied to the floating column, and the final maximum deflection of the tip of the hub was obtained. The wind loads on the tower and the rotor hub axis were identical at every run. The load was applied as a uniformly increasing loading cycle for each time step of 10 seconds, where unloading occurred and the load was applied again up until the load of each run. It was found that the maximum allowable load applied is 1,68 MN (Victor Flores Terrazas, 2018).

Stage 4. Assessment of the parameters of the ice cover for the maximum value of the ice load.

Calculation of ice load

Level ice acting upon vertical structures may present flexural failure such as bending, buckling, splitting or crushing. The failure mode is mainly dependent on the loading rate, which is based on the velocity of the ice sheet pushing against the structure. Crushing is the failure mode that dominates ice actions for vertical structure scenarios.

The ice load exerted on a structure is calculated using the Russian Standards Code SNiP [8] and is defined by the formula:

$$F_{c,p} = 0.04 v h_d \sqrt{m A k_b k_v R_c \tan\gamma} \quad \textbf{[1]}$$

where v is the ice field velocity (m/s); h_d is the thickness of the ice field (m); m is the coefficient of support's outline in plan view; A is the maximum square area of the ice field (m^2); k_b is a coefficient based on geometry; k_v is a coefficient based on geometry and dynamic deformation; R_c is the ice compressive strength; γ is a half of the wedge angle of the support's front edge in plan at the level of applied ice effect, in degrees ($70°$ for semi-circular outline).

The load $F_{c,p}$ may not exceed the load $F_{b,p}$, defined as

$$F_{b,p} = m k_b k_v R_c b h_d \quad \textbf{[2]}$$

where b is the front width or support of the structure's section at ice load application level (m).

The ice load was arbitrarily chosen at each simulation run in order to analyze the stability of the structure under a different ice load. Thus, the wind force and pressure remained constant for every simulation run.

Determination of maximum ice floe size

Based on the SNiP guidelines for calculating ice loads on vertical structures, a Matlab code for ice load calculation was used to produce a chart of the loads depending on varying ice floe dimensions $A, h,$ ice field area in $m^2$and thickness in m, respectively. The compressive strength of the ice used for the calculations correspond to $R_c = 2\ MPa,\ m = 0.83$ and the constant values k_b and k_v were determined for each calculation based on the SNiP guideline.

The following initial data are used to estimate ice cover parameters for a given ice load value:
- the thickness of the ice fields varies from 0.1 m to 1.0 m in 0.1 m steps;
- the area of the ice fields varies from 5000 m to 150000 m^2 in steps of 5000 m^2;
- speed of ice fields 0.1, 0.3 and 0.5 m/s

Table 1 shows the results of the calculations with speed of ice floes 0.3 m/s. The numbers in hatch correspond to ice failure by crushing; the numbers in solid shade correspond to limit ice load, that equals to maximum horizontal load calculated on the stage 3.

Figure 3 shows the graphs of the maximum values of the thickness and area of the ice fields for the three selected velocities.

According to Fig. 3, at the example - the semisubmersible offshore wind turbine can resist to ice floes a thickness less than 0.3 m at any speed and area.

Table 1. Loads and ice field sizes traveling at 0.3 m/s

Velocity = 0.3 m/s										
A \ h	0.1	0.2	0.3	0.4	0.5	0.6	0.7	0.8	0.9	1
5000	0.071	0.142	0.252	0.381	0.504	0.682	0.863	1.031	1.195	1.357
10000	0.100	0.201	0.356	0.538	0.713	0.965	1.221	1.458	**1.689**	**1.920**
15000	0.123	0.246	0.436	0.660	0.873	1.181	1.495	**1.786**	**2.069**	**2.351**
20000	0.142	0.284	0.504	0.762	1.008	1.364	**1.726**	**2.062**	**2.389**	**2.715**
25000	0.159	0.317	0.563	0.851	1.127	1.525	**1.930**	**2.306**	**2.671**	**3.035**
30000	0.174	0.348	0.617	0.933	1.235	1.671	**2.114**	**2.526**	**2.926**	**3.325**
35000	0.188	0.375	0.666	1.007	1.334	**1.804**	**2.284**	**2.728**	**3.161**	**3.591**
40000	0.201	0.401	0.712	1.077	1.426	**1.929**	**2.441**	**2.916**	**3.379**	**3.839**
45000	0.213	0.426	0.756	1.142	1.513	**2.046**	**2.589**	**3.093**	**3.584**	**4.072**
50000	0.224	0.449	0.796	1.204	1.594	**2.157**	**2.729**	**3.261**	**3.778**	**4.292**
55000	0.235	0.471	0.835	1.263	1.672	**2.262**	**2.863**	**3.420**	**3.962**	**4.502**
60000	0.246	0.492	0.872	1.319	**1.747**	**2.363**	**2.990**	**3.572**	**4.138**	**4.702**
65000	0.256	0.512	0.908	1.373	**1.818**	**2.459**	**3.112**	**3.718**	**4.307**	**4.894**
70000	0.265	0.531	0.942	1.425	**1.887**	**2.552**	**3.229**	**3.858**	**4.470**	**5.079**
75000	0.275	0.550	0.975	1.475	**1.953**	**2.641**	**3.343**	**3.994**	**4.627**	**5.257**
80000	0.284	0.568	1.007	1.523	**2.017**	**2.728**	**3.452**	**4.124**	**4.779**	**5.430**
85000	0.293	0.585	1.038	1.570	**2.079**	**2.812**	**3.559**	**4.251**	**4.926**	**5.597**
90000	0.299	0.598	1.069	1.615	**2.139**	**2.894**	**3.662**	**4.375**	**5.068**	**5.759**
95000	0.299	0.598	1.098	1.660	**2.198**	**2.973**	**3.762**	**4.495**	**5.207**	**5.917**
100000	0.299	0.598	1.126	**1.703**	**2.255**	**3.050**	**3.860**	**4.611**	**5.343**	**6.070**
125000	0.299	0.598	1.255	**1.904**	**2.521**	**3.410**	**4.316**	**5.156**	**5.973**	**6.787**
150000	0.299	0.598	1.255	**2.086**	**2.762**	**3.736**	**4.727**	**5.648**	**6.543**	**7.435**

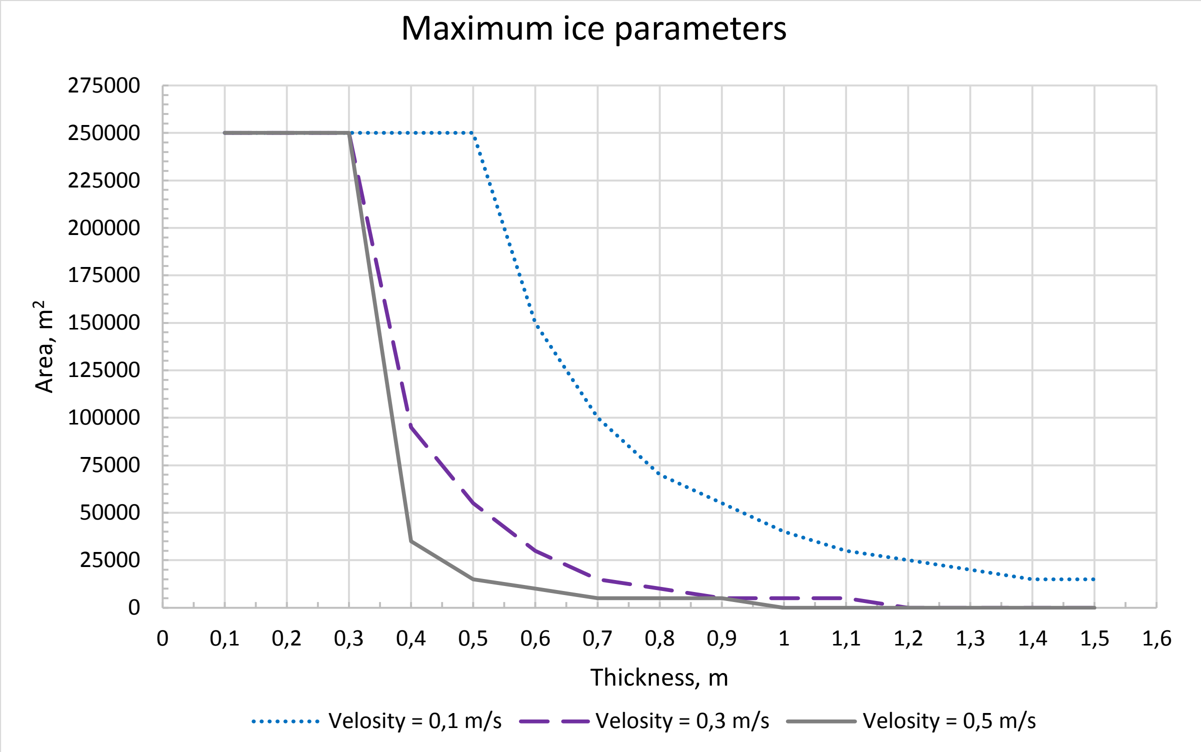

Fig. 3. Maximum ice floes parameters

Conclusions

This method is proposed as a preliminary estimate of the behavior of the engineering structure in ice condition. Based on these analyses, early adjustments can be made to the concept to adopt it to ice condition. It is suggested that this method is used mainly as an indication of the order of magnitude of the ice cover parameters for limit ice load of calculated structures.

This method is especially important for floating drilling rigs (platforms) and drilling vessels that are not designed for operation in severe ice conditions. Determination of the limit ice cover parameters, corresponding to normal operation of structure, allows determining the periods of safe operation of these facilities in ice conditions, to assess the possibility of extending drilling operations lifetimes by applying the ice management method.

References

Huijs, Fons, Rogier de Bruijn, and Feike Savenije (2014). "Concept design verification of a semi-submersible floating wind turbine using coupled simulations." Energy Procedia 53 (2014): 2-12.

Jonkman, Jason, et al, 2009. Definition of a 5-MW reference wind turbine for offshore system development. No. NREL/TP-500-38060. National Renewable Energy Lab.(NREL), Golden, CO (United States).

Robertson, Amy, et al, 2014. Definition of the semisubmersible floating system for phase II of OC4. No. NREL/TP-5000-60601. National Renewable Energy Laboratory (NREL), Golden, CO.

SNiP 2.04.06-82* (1996). “Loadings and Influences On Hydraulic Engineering Structures (wave, ice and from courts)”, Moscow: Stroiizdat.

Victor Flores Terrazas, 2018 Simplified model for semi-submersible offshore wind turbine / 24th IAHR International Symposium on Ice, Vladivostok, Russia, June 4 to 9, 2018.